Identifying and Overcoming Degradation Mechanisms in Layered Oxide Sodium-Ion Batteries

Laurence A. Middlemiss

Primary Supervisor: Professor Anthony R. West
Secondary Supervisor: Dr Denis Cumming
Industry Supervisor: Dr Ruth Sayers

Submitted for the Degree of Doctor of Philosophy

Faulty of Engineering
The University of Sheffield

December 2020

Declaration

This thesis is submitted in consideration for the award of Doctor of Philosophy.
It is believed to completely original, except where references are made.

Laurence A. Middlemiss

December 2020

Acknowledgements

First and foremost, I would like to thank my supervisor, Professor Anthony R. West, for his supervision and input throughout the project. With my PhD, I have been very fortunate to study under someone who has such a vast knowledge of solid state chemistry, and who is also highly experienced in the electrical properties of oxide materials. I would also like to express my gratitude to my industry supervisor, Dr Ruth Sayers, for her highly valued contribution to the project, and to my secondary supervisor, Dr Denis Cumming. I would also like to give a special mention to Dr Anthony Rennie for all the useful scientific discussion and help he gave me throughout my PhD.

I would like to take this opportunity to acknowledge the Centre for Doctoral Training in Energy Storage and its Applications for funding the research, with particular mention to the Centre managers, Sharon Brown and Tracey McNeilly, as well as the directors, Professor Andy Cruden and Professor Dave Stone. This project would not have been possible without collaboration from Faradion, to whom I express my gratitude. I would like to extend my thanks to all the staff at Faradion, in particular, Dr Jerry Barker, Dr Yang Liu, Rebecca Shutt, and Hamish Reid.

I would like to acknowledge Professor Derek Sinclair for all he did to keep the Department and lab running during my PhD, and thanks also to Dr Nik Reeves-McLaren for his help with all things X-ray related. Additional thanks go to the technical staff, Josie Whitnear and Kerry McLaughlin. I would like to thank all my fellow researchers who have made the experience both memorable and enjoyable during the past four years. All the CDT students, particularly Dr Jake Entwistle and Dr Laura Wheatcroft. Thanks are extended to my colleagues in the Functional Materials and Devices Group - my fellow group members: Dr Bo Dong, Dr Yun Dang, Dr Wan Fareen, as well as the Friday pub crew: Dr James Heath, Dr Emilio Pradal Velaquez and Wadir Kargar.

Lastly, but by no means least, I would like to thank my parents, David and Thérèse Middlemiss, without their continued support and encouragement this academic journey would not have been at all possible.

Abstract

A layered sodium quaternary transition metal oxide, $Na[Ni,Mg,Mn,Ti]O_2$, was studied as a potential Na-ion battery cathode candidate. The material was found to possess a mixed phase layered rock salt type structure, consisting of two individual polymorphs, with nominal formulae P2-"$Na_{0.64}[Mn_{0.8}Mg_{0.2}]O_2$" and O3-"$Na[Ni_{0.5}Mn_{0.5}]O_2$". From impedance measurements, the activation energy associated with the total conductivity of the material is 0.33(1) eV, and the layered oxide was found to be a mixed (ionic and electronic) conductor. Electrochemical testing revealed the material to possess a discharge capacity of 125 mAh g^{-1}, in a full-cell, as well as good rate capability and cycling stability: 95% charge retention after 200 cycles (at a discharge rate of 28 mA g^{-1}). From *in operando* X-ray diffraction measurements, the O3 polymorph is only present in the bottom ~ 20% state of charge (SoC), and above 4 V there is a significant alteration of the P2 structure, with evidence of an intergrowth "Z" phase. From galvanostatic intermittent titration technique (GITT) measurements, the P2-type phase was found to be the most conductive form of the cathode.

The individual P2-$Na_{0.64}[Mn_{0.8}Mg_{0.2}]O_2$ and O3-$Na[Ni_{0.5}Mn_{0.5}]O_2$ polymorphs were also studied separately. A solid solution was found to exist for $Na_x[Mn_{0.8}Mg_{0.2}]O_2$ ($0.5 \leq x \leq 1$), which can be indexed according to the hexagonal space group $P6_3/mmc$. The O3-$Na[Ni_{0.5}Mn_{0.5}]O_2$ polymorph formed over a narrow temperature range when synthesized in air. From impedance measurements, the P2-type material was more conductive that the O3. Electrochemical testing (*vs.* Na/Na^+) revealed the P2-$Na_{0.64}[Mn_{0.8}Mg_{0.2}]O_2$ material to have a discharge capacity of around 45 mAh g^{-1} and good initial cycling stability. The O3-$Na[Ni_{0.5}Mn_{0.5}]O_2$ layered oxide showed a higher specific capacity (~ 125 mAh g^{-1}) but poorer charge retention.

Electrochemical impedance spectroscopy (EIS) was performed on full-cell sodium-ion batteries consisting of a layered oxide cathode and a hard carbon anode. This was executed using both two- and three-electrode measurements (with an Na metal reference electrode) on a novel commercially-relevant pouch cell design. It was demonstrated across a range of formalisms that the sum of the positive and negative electrode impedances is similar to that of the full-cell

(within 6% difference). This indicates that this three-electrode configuration affords a superior measurement to many former cell designs. Furthermore, using a range of different complex formalisms to view impedance data, e.g. spectroscopic plots of *Z''* and *C'*, was found to afford a more in-depth analysis of the results; this allows for a more facile separation of electrode components across a range of frequencies.

Examining EIS data for a three-electrode cell measurement showed that an increasing cathode resistance dominates the impedance of these layered oxide Na-ion batteries during cycling. Modelling the response using ideal equivalent circuits found that the cathode impedance spectrum consists of three different resistive components. Comparison between the impedance results for different cell designs made it possible to assign these three components to separate physical elements of the sodium-ion battery. The cathode-electrolyte interface was found to be primarily responsible for an increase in the total cell resistance during cycling. Importantly, from performing impedance measurements during charge/discharge, the resistance of the cathode-electrolyte interface was found to increase dramatically above approximately 80% depth of discharge. These findings suggest that to optimise performance and extend battery life, these layered Na-ion cells should not be discharged below ~ 20% SoC.

The long-term performance of layered oxide Na-ion batteries was recorded with EIS measurements performed at regular intervals. A ‘knee point’ is observed to occur, after which capacity fading intensifies, eventually resulting in an end to the operational life of the battery. A reduced discharge rate recovers most of this capacity loss, indicating that the degradation is primarily due to a deterioration in ionic transfer rather than an irreversible loss of sodium or of active material. At the ‘knee point’, the resistance associated with the anode significantly increases, which is credited to a decrease in the conductivity of the carbon matrix due to structural degradation caused by successive Na insertion/extraction. In summary, it is hypothesised that while a charge-transfer resistance at the cathode is responsible for a limited capacity over the cycle life of the Na-ion battery, the major degradation mechanism at fault for eventual end of life is structural degradation of the hard carbon anode.

Contents

Acknowledgements……ii

Summary……..……..iii

Chapter 1 - Introduction…….…….....1

1.1 Batteries…….....1

1.1.1 Overview…….…...…….....1

1.1.2 Principle of Operation…….……..…..…...3

1.1.3 Basic Concepts…….……..…..…6

1.1.4 Definitions…….……...….....15

1.2 Sodium-Ion Batteries…….…….....21

1.2.1 Overview…….……..…...21

1.2.2 Anodes…….…….…..23

1.2.3 Electrolytes…….……..…25

1.2.4 Cathodes…….….26

1.3 Layered Sodium Oxides as Na-Ion Cathode Materials.....29

1.3.1 Classification and Structure…….…....29

1.3.2 Single Transition Metal Oxides…….....31

1.3.3 Multiple Metal Oxides…….…33

1.3.4 Mixed Phase Systems…….…....35

1.4 Performance Limiting Factors in Batteries…….....38

1.5 Impedance Spectroscopy of Batteries……..43

1.5.1 Studying Performance Limiting Factors in Batteries……..….43

1.5.2 Two-Electrode Impedance Studies……..…46

1.5.3 Three-Electrode Impedance Studies…….…...…48

1.5.4 Beyond Lithium-Ion Impedance Studies…….....….56

1.6 Aims……...…...60

1.7 References…….……...61

Chapter 2 - Experimental……..…….....77

2.1 Solid State Synthesis…….77

2.2 X-Ray Diffraction ……..……..…....78

2.3 Rietveld Refinement……...…..80

2.4 Scanning Electron Microscopy…….....83

2.5 Thermogravimetric Analysis……..... 84

2.6 Differential Scanning Calorimetry……..... 86

2.7 Battery Assembly……...…...87

2.8 Four Point Probe Conductivity Measurements……...…..88

2.9 Constant Current/Constant Voltage Cell Testing……..… 90

2.10 Cyclic Voltammetry……...… 92

2.11 Galvanostatic Intermittent Titration Technique……..… 93

2.12 *In Operando* X-Ray Diffraction……..…..... 96

2.13 Electrochemical Impedance Spectroscopy……...…..….. 97

2.13.1 Theory……...…97

2.13.2 Impedance Spectroscopy for Electroceramics…..…..108

2.13.3 Characterisation of Batteries by Electrochemical Impedance Spectroscopy…….....……..…115

2.14 References……...……...124

Chapter 3 – Structural Characterisation and Properties of Mixed Phase $Na[Ni,Mg,Mn,Ti]O_2$….....130

3.1 Introduction…….…….....130

3.2 Experimental……...…...…132

3.2.1 Materials……...…..132

3.2.2 X-Ray Diffraction……...…...132

3.2.3 Materials Characterisaton……..……132

3.2.4 Electrochemical Testing……..…..133

3.3 Results and Discussion…….....135

3.3.1 Structural Characterisation and Thermal Stability.....135
3.3.2 Electrical Properties…….....146
3.3.3 Electrochemical Testing…….....151
3.3.4 *In Operando* Studies……...…….160
3.4 Conclusions…….……...….171
3.5 References…….....173

Chapter 4 – Synthesis and Characterisation of P2-$Na_{0.64}$-$[Mn_{0.8}Mg_{0.2}]O_2$ and O3-$Na[Ni_{0.5}Mn_{0.5}]O_2$...178

4.1 Introduction……..178
4.2 Experimental……....180
4.2.1 Synthesis…….180
4.2.2 X-Ray Diffraction……...…180
4.2.3 Materials Characterisation……..181
4.2.4 Electrochemical Testing…….……182
4.3 Results and Discussion……..……..183
4.3.1 Synthesis and Structural Characterisation of P2-$Na_{0.64}[Mn_{0.8}Mg_{0.2}]O_2$…….183
4.3.2 Synthesis and Structural Characterisation of O3-$Na[Ni_{0.5}Mn_{0.5}]O_2$……..189
4.3.3 Electrical Properties of P2-$Na_{0.64}[Mn_{0.8}Mg_{0.2}]O_2$ and $Na[Ni_{0.5}Mn_{0.5}]O_2$…….....194
4.3.4 Electrochemical Testing of P2-$Na_{0.64}[Mn_{0.8}Mg_{0.2}]O_2$ and O3-$Na[Ni_{0.5}Mn_{0.5}]O_2$……...…200
4.4 Conclusions…….……204
4.5 References…….…..…...….206

Chapter 5 - Two- and Three-Electrode Impedance Spectroscopy of Layered Oxide Sodium-Ion Batteries…….209

5.1 Introduction…….209
5.2 Experimental……..…….……211
5.2.1 Cell Components……211
5.2.2 Cell Designs……...211
5.2.3 Testing Configuration……213
5.2.4 Testing Procedures…….214
5.2.5 Geometry Correction…….……215
5.3 Results and Discussion…….……...216
5.3.1 Performance Comparison of Two- and Three-Electrode Cells……216
5.3.2 Two-Electrode Impedance Studies……222
5.3.3 Three-Electrode Impedance Studies……..233
5.4 Conclusions…….244
5.5 References……...246

Chapter 6 – Investigating the Dominating Cathode Impedance in Layered Oxide Sodium-Ion Batteries……...…248

6.1 Introduction…….248
6.2 Experimental……...250
6.2.1 Cell Designs……...250
6.2.2 Cell Testing Procedures…….252
6.2.3 Analysis of Cell Data…….253
6.3 Results and Discussion……... 256
6.3.1 EIS After Charge/Discharge (Three-Electrode Cell)……....256
6.3.2 Assigning Cathode Resistive Components……....260
6.3.3 EIS During Charge/Discharge (Three-Electrode Cell)…….…...269
6.4 Conclusions…… 279
6.5 References…….…….. 281

Chapter 7 – Long-Term Cycling and Identifying Failure Mechanisms in Layered Oxide Sodium Ion Batteries…….……...284

7.1 Introduction……..……..... 284

7.2 Experimental…….....286

7.2.1 Cell Designs……...……286

7.2.2 Cell Testing Procedures…….286

7.3 Results and Discussion…….....288

7.3.1 Long-Term Performance of Sodium-Ion Cells….....288

7.3.2 Long-Term Impedance Studies of Sodium-Ion Cells……...291

7.4 Conclusions……..... 319

7.5 References……..... 321

Chapter 8 - Conclusions and Future Work…….....324

8.1 Conclusions…….....324

8.1.1 Structure-Composition-Properties-Performance Relationship in Layered Oxide Sodium-Ion Cathodes…….....324

8.1.2 Use of Impedance Spectroscopy to Determine Performance Limiting Factors in Prototype Commercial Na-Ion Batteries……..…..326

8.2 Future Work…….330

Appendices……..... 332

Appendix A Rietveld Refinement Parameters……..…..332

Appendix B Capacitor and Inductance Impedances……...335

Appendix C Mass Balancing of Sodium-Ion Cells……....338

Appendix D Differential Capacity Plots…….....339

Appendix E Capacity Plots (1-4.3 V)……..…...340
Appendix F Bragg's Law Calculations…….....…341
Appendix G *In Operando* XRD Patterns……...…342
Appendix H Starting Rietveld Model of
P2-$Na_{0.64}[Mn_{0.8}Mg_{0.2}]O_2$……..……..343
Appendix I XRD Pattern of $Na_{0.64}[Mn_{0.8}Mg_{0.2}]O_2$……...….344
Appendix J Warburg Impedance……...….345
Appendix K Circuit Fitting Example…….……....347
Appendix L MacMullin Numbers …….....…349
Appendix M Calendering Studies……...…...350
Appendix N DC Bias Three-Electrode Measurements….…….351
Appendix O Lithium-Ion Impedance Spectra……352

Chapter I

Introduction

1.1 Batteries

1.1.1 Overview

A growing global energy demand, coupled with a desire to reduce carbon emissions and mitigate climate change, has led to a move towards renewables, and away from fossil fuels. However, in order to facilitate the deployment of intermittent renewable energy sources, such as wind and solar, efficient and reliable energy storage is needed as a crucial accompaniment.[1] To date, of the various energy storage technologies, rechargeable batteries have proven one of the most promising. These have the advantage of being able to be made to a variety of different sizes and specifications, and are able to deliver electrical power instantaneously. Hence, they are not limited by location or energy source, and are used for a wide range of diverse applications. Figure 1.1 illustrates this dramatic growth in the global battery market over the past 30 years, with a breakdown of contributions from the different battery technologies.[2]

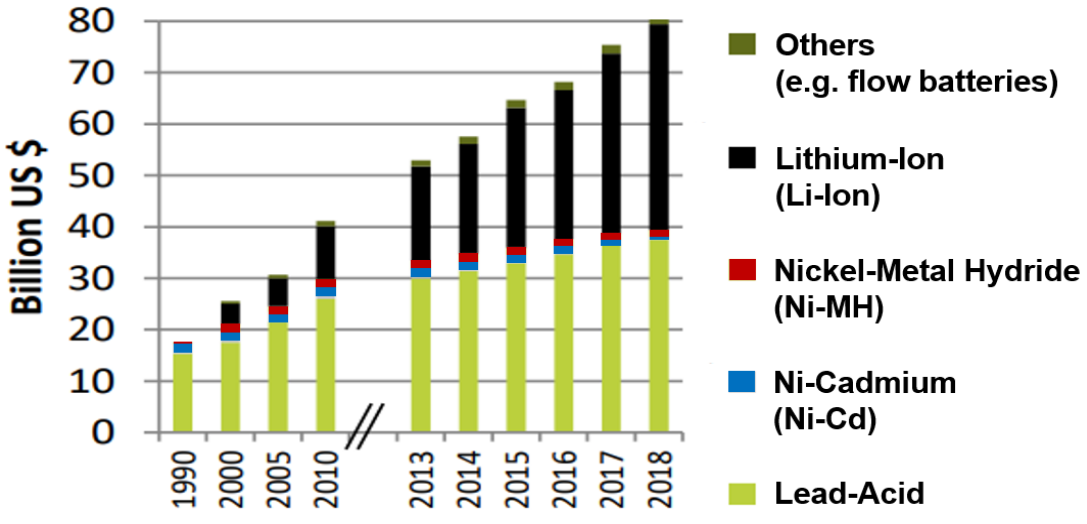

Figure 1.1 The world battery market 1990-2018. Adapted from reference 2.

Over the past decade, the world battery market has more than doubled, with the majority of this growth due to the increase in popularity of lithium-ion (Li-ion) batteries (LIBs). These have now overtaken lead-acid as accounting for the largest percentage of the global battery market. Li-ion technology first came to widespread attention in the 1980s with the discovery of layered transition metal oxide materials,[3] which were subsequently used in batteries that had two to three times the energy density of any that preceded it. Figure 1.2 compares the specific power and energy density of the most popular commercially-available rechargeable battery chemistries.[4] Today, LIBs have a specific energy greater than 100 Why/kg (at the cell level), and are capable of thousands of cycles during their lifetime.[5] Lithium-ion batteries were responsible for the portable consumer electronic boom in the 1990s, and their presence in everyday life is now ubiquitous. They are found in the mobile phones, laptops and tablets that people use on a regular basis, and are also becoming increasingly used in stationary applications, such as electricity grid storage, and in uninterruptible power supplies. Furthermore, lithium-ion batteries are currently at the forefront of the rapidly expanding electric vehicle (EV) sector.

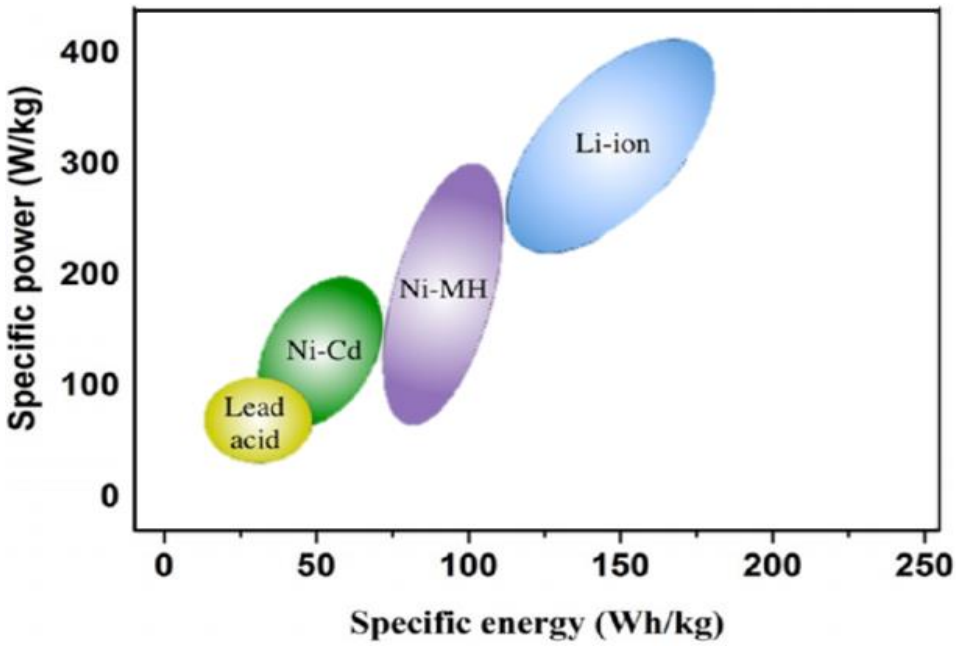

Figure 1.2 A Ragone plot comparing the power and energy densities of the most common rechargeable battery technologies. Adapted from reference 4.

However, concerns surrounding the long-term sustainability, cost and safety of lithium-ion batteries, have led researchers to seek alternative battery chemistries.[6] Of

the 'beyond lithium' technologies looked at to date, sodium-ion (Na-ion) batteries (SIBs) have received the most interest and development.[7] Sodium-ion batteries, in contrast to Li-ion, can be made from abundant and cheap materials, and are less susceptible to dangerous overheating.[8] Furthermore, several electrode materials have appeared in academic literature over the past few years, with energy densities comparable with those of their LIB counterparts.[9] Furthermore, in the commercial sector, Faradion, a British battery research company, has managed to develop a layered sodium transition metal oxide with a specific capacity similar to that of the commonly used Li-ion cathode material, lithium iron phosphate (LFP, $LiFePO_4$);[10] this has also been demonstrated to have an energy density on par with LFP at the cell level.

The ability to maintain a high capacity over time, i.e. battery cycle life, is an important performance criterion with respect to the widespread commercialisation of sodium-ion technology. Hence, an investigation into performance degradation and capacity fading in Na-ion batteries is imperative to fully characterise them and appreciate their worth. An identification of the problem interfaces and rate-limiting steps inside the cells is also of the utmost importance to completely understand their full potential. Furthermore, as cathode materials offer a lower Na-ion storage capacity than anodes, the ability to better understand the structure-composition-property relationship of sodium-ion cathode materials is also crucial. It is hoped that findings in these areas will, in the future, lead to an ideal Na-ion battery being developed with optimised energy density and power output.

1.1.2 Principle of Operation

An electrochemical cell either converts stored chemical energy into electrical energy or vice versa. A battery is a device consisting of one or more electrochemical cells connected to one another.* During the operation of a battery, a positively charged ion is removed from one electrode, transported through the electrolyte, and inserted into the other electrode. This is accompanied by an electron moving around the external circuit in order to balance the charges of the two electrodes; the electrolyte is an

* In this thesis, the word 'battery' refers to a single electrochemical cell, unless stated otherwise.

ionic conductor, but electronic insulator. An oxidation reaction occurs at the first electrode and a reduction reaction at the second one. The electrode, which electrons leave when the battery is supplying power (during discharge), is the negative terminal and is referred to as the anode. The electrode, which electrons enter during discharge, is the positive terminal and is referred to as the cathode. Electrons move in the opposite direction to current by convention, and so current flows from the positive terminal to the negative one (Fig. 1.3).

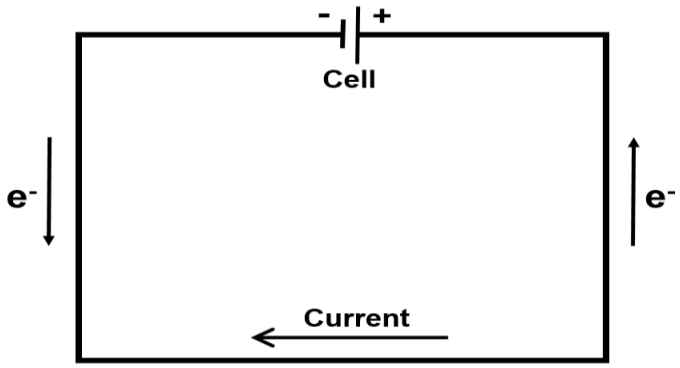

Figure 1.3 Electrons moving in the opposite direction to current flow in a circuit.

Certain batteries may only be discharged once; these are known as single-use or primary batteries. Secondary or rechargeable batteries may be charged and discharged several times during their lifetime.[†] The electrochemical reactions that occur in a battery at the separate electrodes may be described by what are known as half-reactions. Combining these together gives the overall redox reaction for the battery. The half-reactions that occur during the discharge of a sodium-ion battery are given below for the most common SIB electrode materials: a layered sodium transition metal oxide (NaT_MO_2) cathode and a hard carbon (C_6) anode. When the cell is discharged, Na^+ ions are removed from the hard carbon anode and migrate across the electrolyte to be intercalated into the sodium oxide cathode matrix. During charging, the same reactions occur, but in reverse.

Anode: $$xNaC_6 \rightleftharpoons xNa^+ + xe^- + xC_6$$

Cathode: $$Na_{1-x}T_MO_2 + xNa^+ + xe^- \rightleftharpoons NaT_MO_2$$

Overall: $$Na_{1-x}T_MO_2 + xNaC_6 \rightleftharpoons NaT_MO_2 + xC_6$$

[†] In this thesis, the word 'battery' refers to a rechargeable one, unless stated otherwise.

Chemical potential μ is energy that can be released/absorbed due to change in the number of particles of a particular species at a point in space. Electrochemical potential $\bar{\mu}$ also takes into account contributions from any electric forces at play, such as external electric fields and electrostatics.[11] Each chemical species has an electrochemical potential, which represents how easy it is to add more of that species to a particular location. Charged species always move from higher to lower electrochemical potential. In a lithium-/sodium-ion battery, the electrochemical potential of an electrode is determined by energies involved in both the electron transfer and Li^+ or Na^+ ion transfer.[12] Lithium is the smallest metal and very electropositive, meaning it has one of the greatest (most negative) electrochemical potentials. Hence, it is readily oxidised, making it a good candidate as an anode material. The higher the electrochemical potential (the less negative), the more readily a material is reduced, and the more suitable it is as a cathode material. Hence, the $\bar{\mu}$ of electrode materials in Li-/Na-ion batteries tend to be measured relative to that of lithium/sodium metal, respectively.

The electrochemical potential of a sodium-ion electrode is determined by how much energy is released/absorbed on removal/insertion of an electron and Na^+ ion from/into its structure. How easily a sodium ion is removed/inserted depends upon the specific site energy of the Na^+ ion, which is ultimately affected by its local environment.[13] Therefore, the elements the electrode possesses, and in particular the valence states, ionic radii, and electronegativity of these, is extremely important in determining its electrochemical potential. The crystal structure and electrode microstructure, e.g. particle size, are also contributing factors. For a cathode, the more energy released when electrons/Na^+ ions are inserted or removed, the higher its electrochemical potential, and the harder it is to insert/remove sodium into the structure. The electromotive force (emf) of an electrochemical cell, also known as open circuit voltage (OCV)[14], is defined as the difference in electrochemical potential of the cathode and anode divided by the elementary positive charge *e* (Eq. 1.1).[15] The elementary positive charge is the charge of an electron (1.60×10^{-19} coulombs).

$$V_{OCV} = \frac{\bar{\mu}_{cathode} - \bar{\mu}_{anode}}{e} \qquad (1.1)$$

Ideally, for a battery, the cathode should have a high electrochemical potential and the anode a low one, this will create a large potential difference (voltage) in the cell, which results in a greater energy density. However, the voltage needs to be within the electrochemical window of the electrolyte in order to avoid decomposition.[16] The electrochemical window is the energy gap (E_g) between the highest occupied molecular orbital (HOMO) and the lowest unoccupied molecular orbital (LUMO) of the electrolyte.[17] An anode which has an electrochemical potential below the LUMO of the electrolyte must be selected, and a cathode chosen with $\bar{\mu}$ above the HOMO (Fig. 1.4). If this is not the case, the electrolyte may either be reduced on the surface of the anode or oxidised at the cathode interface, and subsequently decompose.

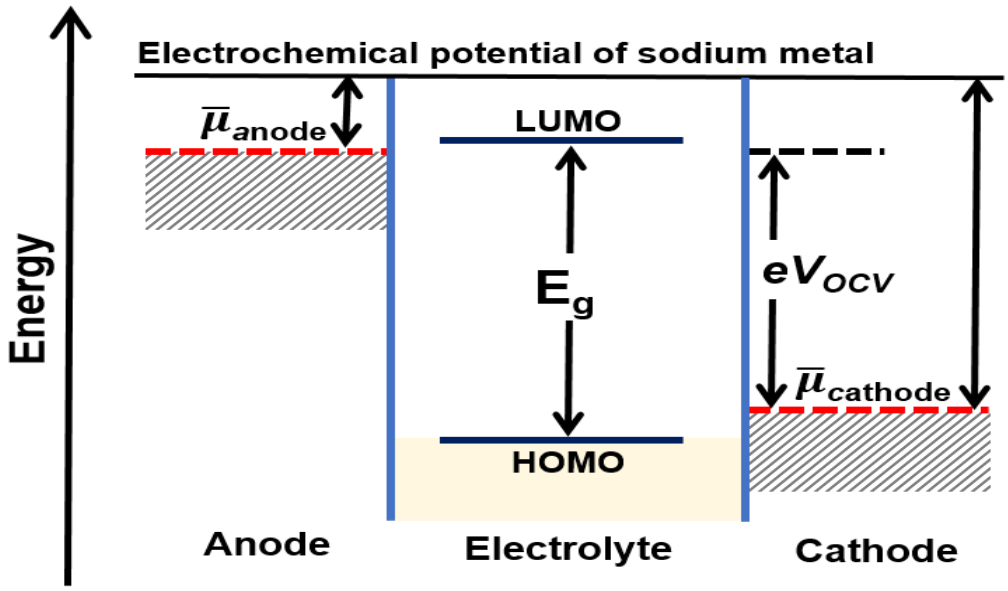

Figure 1.4 Schematic energy diagram of a sodium-ion battery at open circuit. The relative energies of the electrolyte window, E_g, and the relationship between the electrochemical potentials of electrodes and the HOMO and LUMO of the electrolyte are all shown.

1.1.3 Basic Concepts

1.1.3 (a) Current, voltage, and resistance

Electric current *I* (in ampere, A) is the rate of flow of charge *Q* (in coulomb, C) and is given by Equation 1.2.

$$I = \frac{dQ}{dt} \tag{1.2}$$

The charged species may be electrons or ions. Direct current (DC) means that current flows in one direction all of the time, and alternating current (AC) means that it changes direction and strength periodically (sinusoidally). Current may also be a combination of DC and AC. In order for the flow of charge to occur, a potential difference (voltage) is required. In a battery, voltage is a measurement of the difference in charge between the two electrodes. The more electrons there are at an electrode, the lower (more negative) its potential. Electrons will spontaneously flow from a negative potential to a positive one. The more electrons at the anode, the greater the charge separation between the two electrodes in a battery and the higher the overall voltage of the cell. During charging of a battery, an external power supply has a voltage greater than that of the cell, which forces electrons from the cathode to the anode, thus creating an overall positive cell voltage. During discharge, the load connected to the battery has a voltage which is lower than the voltage of the cell, meaning that electrons flow in the opposite direction, thus lowering the overall cell voltage. It is not possible to force a current through a circuit element without applying a voltage across the element. Similarly, it is not possible to produce a voltage without supplying current to force some place to have that voltage. It is sometimes said that a voltage causes current to flow, and sometimes that a current causes a voltage to be produced, but at the deepest level, the two are inseparable, and caused by charge separation.

Batteries can be cycled using either a constant current (galvanostatic) or a constant voltage (potentiostatic), see Section 2.9 for more on this. It is possible to either control the current and measure the voltage, or control the voltage and measure the current, but it is not possible to control both simultaneously. Manufacturers and scientists will often use advanced battery cyclers, which are capable of high precision currents, in order to test cells under different conditions. They are able to simulate battery loading, and can be automated with a custom program written by the user. Certain batteries, such as lithium-ion ones, operate over ‘tight’ voltage windows, as overcharging these cells causes damage. Overcharging an LIB causes metallic lithium plating to occur at the anode as Li^+ ions are reduced to Li metal, and simultaneously, electrolyte solvents are oxidised at the cathode, leading to flammable gases being produced.[18] This causes performance degradation and, in the most severe cases, can lead to a fire/explosion. For safety reasons, and to optimise

battery performance and lifetime, battery packs often contain an electronic control system known as a Battery Management System (BMS). The BMS is capable of measuring the current, voltage, and temperature of the battery, as well as several other important parameters.

Resistance is a material's tendency to resist the flow of charge (current). A material with infinite resistance is referred to as a perfect insulator, and a material with zero resistance is referred to as a perfect conductor. In reality, most materials fall somewhere between these two extremes with some amount of energy being lost as heat. Resistance is the opposition to direct current, and impedance, *Z*, is the opposition to alternating current. For more on impedance, see Section 2.13. Voltage *V* (in volts, V), current *I* (in ampere, A) and resistance *R* (in ohms, Ω) are all related to one another via Ohm's Law (Eq. 1.3). This states that the current between two points is directly proportional to the voltage across the points, with the resistance acting as a constant of proportionality.

(Ohm's Law) $$V = IR \tag{1.3}$$

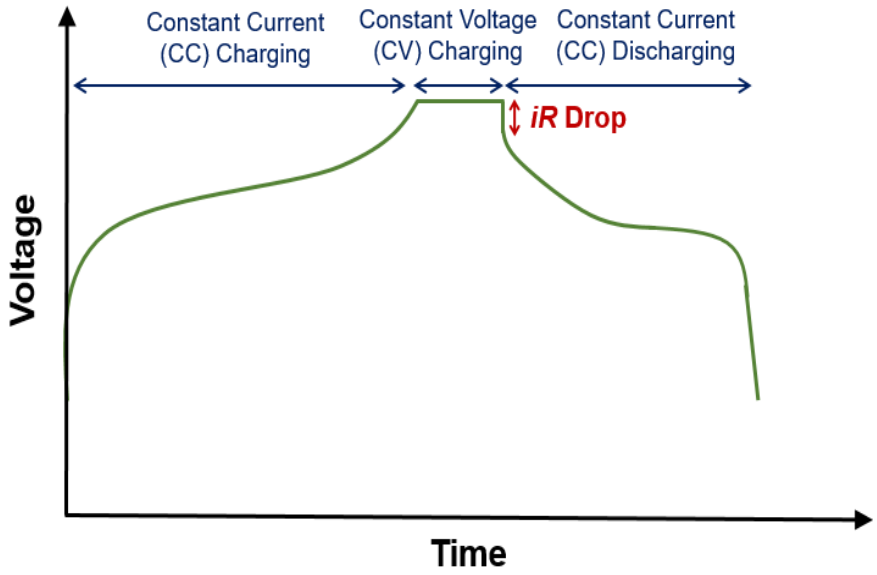

Figure 1.5 Charge and discharge curve of a battery with the *iR* drop indicated.

Each battery in a circuit has an internal resistance associated with it, which is made up of ohmic and non-ohmic (polarisation) contributions.[19] The ohmic resistance exists because the components (electrodes, electrolyte) of a cell are not perfect conductors. It consists of an electronic component (from the resistivity of materials,

e.g. wires and current collectors) and an ionic component due to electrochemical factors, e.g. ion mobility in the electrolyte.[20] The ohmic resistance manifests itself in the cycling profile of a battery as an ohmic (*iR*) drop at the beginning of the cell discharge (Fig. 1.5).[21] Polarisation resistances arise from electrochemical reactions and diffusion processes inside the cell; they increase with battery lifetime. Resistive losses in a battery cause the operating voltage to be lower than what it should be theoretically. This is referred to as an overpotential.[22] Consequently, the cell requires more energy than thermodynamically predicted to drive an electrochemical reaction, with the missing energy lost as heat. The overall internal resistance of a battery varies with chemistry, age, temperature, and discharge current. A larger internal resistance leads to a greater energy consumption, which reduces the efficiency of the battery, and can cause safety issues due to increased heat.

1.1.3 (b) Charge and Coulomb's Law

All charged particles at rest will experience an electrostatic force between one another. The force is attractive if the particles are oppositely charged, and repellent if they are like charges. For two charges, the force acting between them is quantified according to Coulomb's Law (Eq. 1.4).[23] This states that the force F (in newtons, N) acting between two stationary charged species is the product of the magnitude of the charge on object one Q_1 and the magnitude of the charge on object two Q_2 (in coulombs, C), divided by the square of the distance between them r (in metres, m). The term k_e is a proportionality factor and is known as Coulomb's constant or the electrostatic constant. The value of the constant depends on the medium the charges are in (k_e = 8.99 x 10^9 N.m^2.C^{-2} in air).

(Coulomb's Law) $$F = k_e \frac{Q_1 Q_2}{r^2} \quad (1.4)$$

The force is attractive (has a negative sign) if the particles are oppositely charged, and is repulsive (positive) if they have the same signs. The coulomb is the SI unit of electric charge and is equal to the amount of charge transported by a current of one ampere in one second (1 C = 1 A x 1 s). Therefore, 'coulomb counting' becomes a useful way of estimating the state of charge of a battery by measuring the in- and out-flowing current (see Section 1.1.4 (b)).

1.1.3 (c) The Nernst Equation

The Gibbs free energy is the amount of work that can be done by a chemical system (reaction) on its surroundings. Voltage or potential difference can be thought of as the work required to move an electron from one point to another. Therefore, for an electrochemical (redox) reaction, it is possible to relate the Gibbs free energy to the voltage. At an electrode-electrolyte interface, a potential difference develops between the two components. The voltage of an electrode (and that of a battery) is not constant, but changes during (dis)charging, as the concentrations of components in the electrode and electrolyte alter. When the concentration of species across the electrode and electrolyte are at equilibrium, the voltage is referred to as the standard electrode potential.[24] Hence, each half-reaction in an electrochemical cell has a standard electrode potential associated with it. This relation between Gibbs free energy and standard electrode potential (voltage) leads to one of the most important equations in the field of electrochemistry: the Nernst equation (Eq. 1.5).

(Nernst Equation) $$\boldsymbol{\Delta G = -nFE} \quad (1.5)$$

This states that the change in Gibbs free energy ΔG (in kJ mol^{-1}) is equal to the product of the number of electrons transferred n, Faraday's constant F (in C mol^{-1}) and the standard electrode potential E (in volts). A joule is defined as the energy required to move a charge of one coulomb through a potential difference of one volt (1 J = 1 C.V). Faraday's constant is the magnitude of electric charge per mole of electrons and is equal to 96,485 C mol^{-1} (the elementary positive charge of an electron, 1.60×10^{-19} C, multiplied by the Avogadro constant, 6.02×10^{23} mol^{-1}).[25] If ΔG has a negative sign, the electrochemical reaction occurs spontaneously, and if it is positive, it does not. For a battery, the change in Gibbs free energy denotes the change in internal energy during the ion and electron insertion/extraction. This is dependent upon the interaction of atoms/electrons in the electrode, and, therefore, the chemistry of the transition metal(s), as well as the structure of the electrode.[12] These factors ultimately determine the electrochemical potential of the electrode.

The Gibbs free energy of an electrode is mainly dependent upon site energy.[13] Different positions within the crystal structure possess different site energies and, hence, produce different potentials when ions are inserted into/extracted from them.

The lower the site energy of a lithium/sodium in the electrode structure, the greater its stability. This means more energy is consumed to transfer it from the occupied site to a free state, and the higher the electrochemical potential. The insertion/extraction of alkali metal ions to/from either octahedral, tetrahedral or prismatic sites result in different ΔG.[26] The main classes of crystal structures for Li-ion insertion cathodes are layered, spinel and olivine (Fig. 1.6).[27]

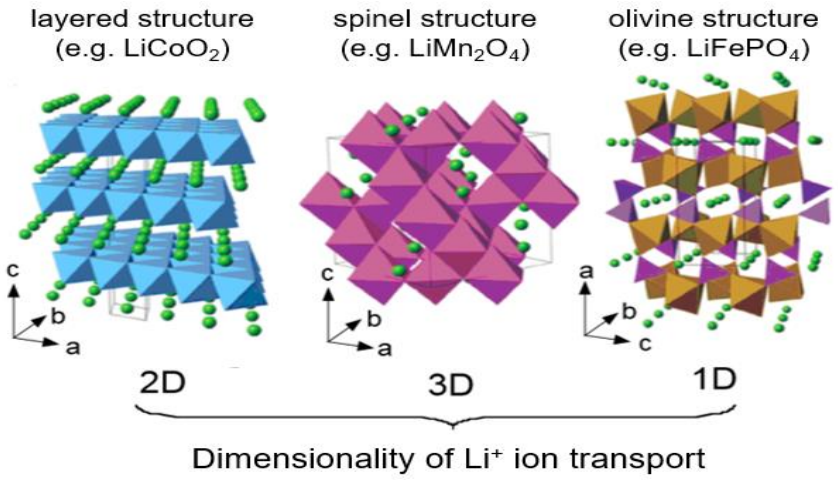

Figure 1.6 Crystal structures of the three main classes of insertion cathodes for Li-ion batteries. Adapted from reference 27.

Spinel and olivine crystal structures exhibit flat potential plateaux in their charge-discharge profiles,[28,29] whereas layered electrodes display sloping profiles.[30] A sloping region in the voltage plot indicates that a change in free energy results in a voltage change, in accordance with the Nernst equation. A flat section corresponds to a region where the removal/insertion of Li^+ does not lead to a significant alteration in electrochemical potential. When subjected to the insertion/extraction of Li^+ ions, the robust 3D frameworks of spinel/olivine crystal electrodes exhibit negligible change to their structures, retaining the same site energy and displaying an almost constant electrochemical potential.[13] However, the layered structures are distorted to a larger extent leading to a slight alteration in site energy and a sloping potential profile. As well as the three ordered crystalline structures, there are also disordered rock salts, which have received a lot of interest in recent years as promising cathodes.[31] Rather than containing separate, distinct layers of Li^+ ions and transition metal elements, these possess randomly assigned cations. Disordered rock salts also exhibit a sloping charge-discharge voltage profile.

1.1.3 (d) Theoretical Capacity/Faraday's Laws

Perhaps the most important characteristic of a battery is its capacity. This is the discharge current the electrochemical device is capable of delivering over time and has units of ampere hour (Ah). It is a measurement of the charge stored by a battery (1 Ah = 3,600 C), and is determined by the mass of active material. As batteries are often used for mobile devices, where weight is an important factor, it is often more useful to think in terms of specific capacity, which has units of Ah kg^{-1} (or mAh g^{-1}).

Faraday's laws of electrolysis relate the theoretical capacity of an electrode to the amount of active material it contains.[32] They can be summarised mathematically by Equation 1.6:

$$\textbf{(Faraday's Laws)} \qquad \boldsymbol{Q = \frac{nF}{M}} \qquad (1.6)$$

where Q is capacity (in C), n is the number of electrons transferred (unitless), F is Faraday's Constant (96,485 C mol^{-1}), and M is the molar mass of the electrode after discharge (g mol^{-1}). The use of Faraday's Laws to calculate the theoretical capacity of a lithium cobalt oxide cathode is given below.

Discharge: $CoO_2 + Li^+ + e^- \rightarrow LiCoO_2$

The molar mass of LCO is 97.87 g mol^{-1}, therefore, using Equation 1.6:

$$Q = \frac{1 \times 96{,}485\ C\ mol^{-1}}{97.87\ g\ mol^{-1}} = 985.8\ C\ g^{-1}$$

$$\div 3{,}600$$

$$Q = 0.2738\ Ah\ g^{-1}$$

$$\times 1{,}000$$

$$\boldsymbol{Q = 274\ mAh\ g^{-1}}$$

In reality, the capacity exhibited by an electrode is likely to be lower than its theoretical one for a variety of different reasons. In the case of lithium cobalt oxide, it is only practically possible to extract ~ 50% of the lithium from the material, before the electrode begins undergoing irreversible, detrimental structural changes.[33]

1.1.3 (e) Capacitance

Capacitance *C* (in Farads, F) is the ability of a body to store electrical charge. It is measured as the ratio of electric charge of a system to its corresponding electric potential (Eq. 1.7).[34]

$$C = \frac{Q}{V} \qquad (1.7)$$

The most commonly encountered example of capacitance is in capacitors. A capacitor is a device that stores electrical energy in an electric field. Energy is stored purely through the physical separation of electrostatic charges, and there is no chemical or phase changes during charge/discharge (such as in a battery). The most basic capacitor design is a parallel plate one, which consists of two conductive (usually metallic) plates separated by an insulating region (Fig. 1.7). The insulator may be a vacuum or some form of dielectric, e.g. air. The non-conductive region prevents DC current passing through the capacitor. When a capacitor is connected to a DC power supply it is charged: a potential difference is applied across the two parallel plates causing electrons to build up on one plate and the other to become electron-deficient. Hence, an electric field is created, the strength of which decreases with increasing separation distance. When the potential is removed, the plates remain charged and the stored energy can be discharged through an external load.

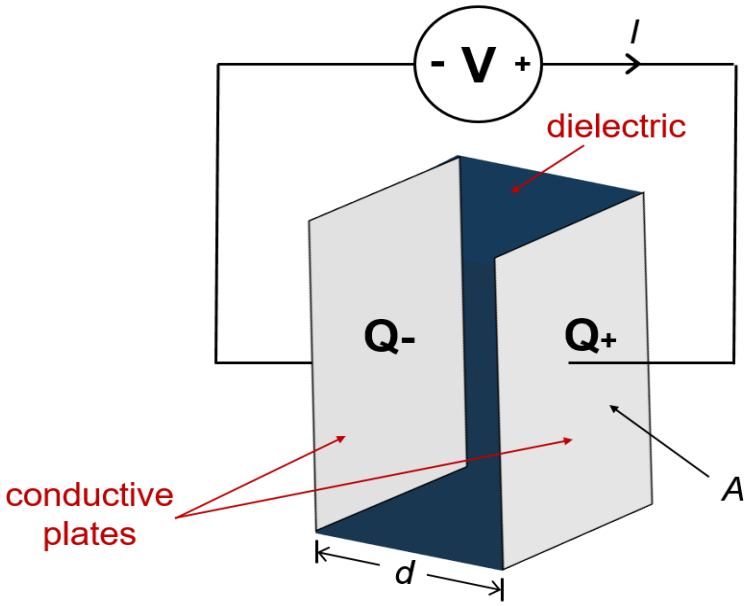

Figure 1.7 A schematic of a parallel plate capacitor.

A dielectric is a type of insulator that can be polarised by an applied electric field (dipoles can align), but does not allow charge to actually flow through it.[35] Permittivity is a measure of polarisability of a dielectric (how easily it forms instantaneous dipoles). A material with high permittivity polarises more in response to an applied electric field than a material with a low permittivity, and is therefore capable of storing more energy. The dielectric constant ε' (also known as the relative permittivity, ε_r) is the absolute permittivity of a material ε relative to that of a vacuum of free space e_0 , and is given by Equation 1.8. The dielectric constant is unitless, and both ε and e_0 are in F cm^{-1}. The vacuum of free space is the absolute permittivity of a vacuum and has a value of 8.854 x 10^{-14} F cm^{-1}. Dielectric constant values range from 1 for a vacuum (by definition) to about 2 x 10^{14} for materials that possess high polarisability.

$$\varepsilon' = \frac{\varepsilon}{e_0} \tag{1.8}$$

The permittivity of the dielectric in a capacitor is important for determining the overall capacitance of the device. The higher the permittivity of the medium used, the greater the capacitance will be. In a parallel plate capacitor, the capacitance is also proportional to the surface area of the conducting plates A (in cm^2) and inversely proportional to the separation distance d between them (in cm); this leads to Equation 1.9.

(Capacitance) $$\boldsymbol{C = \frac{e_0 \varepsilon' A}{d}} \tag{1.9}$$

There are several strategies which have been looked at to increase the capacitance of modern-day devices. One method is to 'interleave' additional plates within the capacitor body, which increases the overall surface area of each parallel plate; such a construction is employed in the widely-used multilayer ceramic capacitors (MLCCs).[36] Another is to coat the metallic plates with a porous electrode material, e.g. activated carbon, and use a liquid electrolyte as the dielectric. This setup leads to the formation of electrical double layers at the electrode-electrolyte interface, which have very high surface areas, and low separation distances of a single layer of solvent molecules. Such devices are referred to as supercapacitors.[37]

Resistance (in Ω) and capacitance (F) are geometry-dependent terms, and so it is often more useful to think in terms of resistivity ρ (Ω.cm) and permittivity ε (F cm^{-1}).

$$\rho = R\frac{A}{d} \tag{1.10}$$

$$\varepsilon = C\frac{d}{A} \tag{1.11}$$

An electrical circuit, which contains resistors and capacitors, may be characterised by its *RC* time constant (Eq. 1.12). This is represented by the symbol τ and has the units of seconds (1 Ω = 1 s F^{-1}).

(Time Constant) $$\boldsymbol{\tau = RC = \rho\varepsilon} \tag{1.12}$$

Capacitance and *RC* time constants are important when it comes to discussing impedance spectroscopy later on in this work (see Section 2.13).

1.1.4 Definitions

1.1.4 (a) C-Rate

Table 1.1 C-rate and charging/discharging time.

C-rate	(Dis)charge Time
5C	12 minutes
2C	30 minutes
1C	1 hour
C/2 (0.5C)	2 hours
C/5 (0.2C)	5 hours
C/10 (0.1C)	10 hours
C/20 (0.05C)	20 hours

The term C-rate is used to specify the speed at which a battery is charged or discharged relative to its capacity. A 1C rating means that the cell is discharged in

one hour. Therefore, for a 100 Ah battery, a current of 100 A is drawn for one hour. A 2C rating means that the cell is (dis)charged twice in one hour, so for a 100 Ah cell, a current of 200 A is provided. A C/2 (0.5C) rate confers that the cell takes 2 hours to dis(charge) so a current of 50 A is used. Table 1.1 shows some examples of the charge/discharge times at various C-rates. While, in theory, a 2C rate should deliver the same amount of capacity in 30 minutes as a 1C rate does in an hour, in reality, a higher current often results in a greater amount of internal resistive losses, thus lowering the actual achievable capacity.

1.1.4 (b) State of Charge and Depth of Discharge

The state of charge (SoC) of a battery is how much energy it presently holds compared to the maximum it may possess. It is an important parameter as it indicates how much longer the battery will last for before it needs to be recharged. It is the available capacity expressed as a percentage of the cell's current maximum capacity (Eq. 1.13), e.g. the capacity at its last full charge, rather than the rated capacity of the cell when it was manufactured. This is an important distinction because the capacity of a battery decreases over time (this is known as capacity fading), hence, the state of charge is a measure of the short-term capability of a battery. A complementary way of presenting a battery's SoC is to refer to its depth of discharge (DoD). The depth of discharge is the percentage of the capacity which has been removed from a fully charged cell (Eq. 1.14). Hence, as the depth of discharge increases, the state of charge decreases. A battery that has been fully discharged has 100% DoD and 0% SoC, whereas a battery which is fully charged has 0% DoD and 100% SoC. In this work, the term state of charge is used when referring to a battery undergoing charging, and the depth of discharge when referring to one undergoing discharging.

$$\boldsymbol{SoC} = \frac{\boldsymbol{Current\ Cap.}}{\boldsymbol{Current\ Max.Cap.}} \times \mathbf{100}\% \qquad (1.13)$$

$$\boldsymbol{DoD} = \frac{\boldsymbol{Current\ Max.Cap.} - \boldsymbol{Current\ Cap.}}{\boldsymbol{Current\ Max.Cap.}} \times \mathbf{100}\% \qquad (1.14)$$

There are several different methods available for estimating the state of charge. The most widespread technique for determining the SoC of lithium-ion batteries, and the

one that will be used in this study, is the coulomb counting method.[38] This is based on the principle that charge is the integral of current with respect to time (Eq. 1.2). Therefore, the capacity of a cell can be calculated by measuring the current entering (charging) or leaving (discharging) a cell and integrating (accumulating) this over time.

1.1.4 (c) State of Health and Cycle Life

The state of health (SoH) of a battery gives a measurement of its general condition, and its ability to deliver its specified performance, compared with when it was first manufactured. It is a crude indicator of battery lifetime and gives an idea as to how much longer the battery will last for before it needs replacing. It is calculated as a percentage of the current total capacity of the cell compared with the capacity when it was new, which is also referred to as the nominal capacity (Eq. 1.15). Hence, a battery has a 100% SoH after being manufactured, which then decreases over time.

$$\boldsymbol{SoH} = \frac{\boldsymbol{Current\ Discharge\ Cap.}}{\boldsymbol{Nominal\ Discharge\ Cap.}} \times \mathbf{100}\% \qquad (1.15)$$

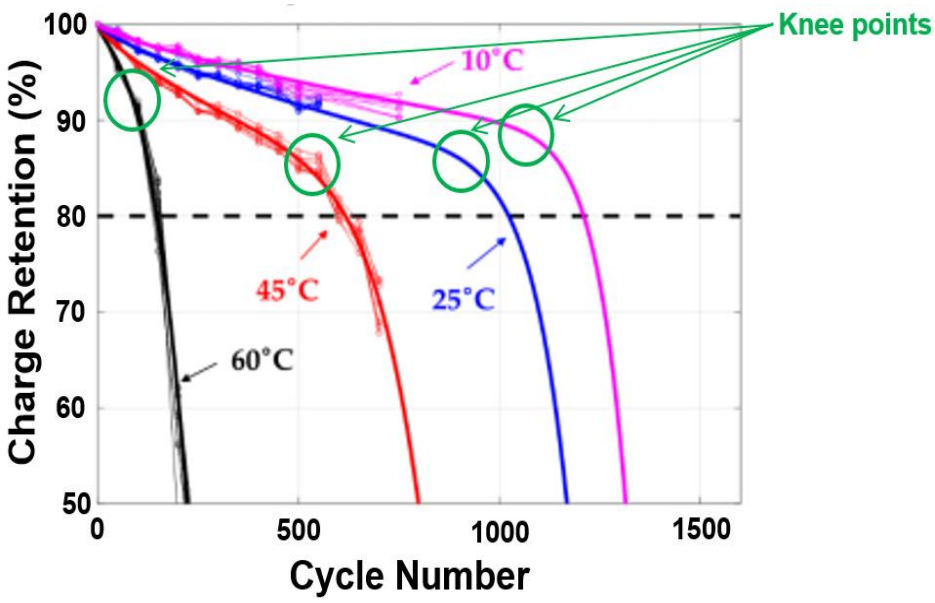

Figure 1.8 Lithium-ion batteries cycled at different temperatures with their knee points indicated. Adapted from reference 39.

The cycle life of a battery is how many cycles it is capable of during its lifetime, or more precisely, how many cycles a battery is capable of before it fails to meet

specific performance criteria. For many battery applications, particularly mobile ones, the end of practical operation for a cell is often deemed as when its state of health drops below 80%. The capacity decay of lithium-ion batteries is characterised by a gradual linear decline in capacity up to a certain point, before transitioning to a more dramatic reduction. This change in gradient of the capacity plot is often referred to as the 'knee point' (Fig. 1.8).[39] The 'knee point' signals the beginning of the end of operational life of the battery, as its capacity rapidly fades after this. As there is no widely accepted standard approach or algorithm for identification of the 'knee point', its location is subjective to the visual inspector, and, therefore, is considered more of a region than occurring at one particular charge/discharge cycle.

1.1.4 (d) Specific Energy and Specific Power

Table 1.2 Comparison of approximate energy densities for three Li-ion battery chemistries, from active material to battery pack level.[40–42]

Chemistry	Specific Capacity	Nominal Voltage	Energy Density (Material Level)	Energy Density (Cell Level)	Energy Density (Pack Level)
$LiCoO_2$	165 mAh g^{-1}	3.6 V	600 Wh kg^{-1}	175 Wh kg^{-1}	140 Wh kg^{-1}
$LiFePO_4$	140 mAh g^{-1}	3.2 V	450 Wh kg^{-1}	130 Wh kg^{-1}	105 Wh kg^{-1}
$LiMn_2O_4$	120 mAh g^{-1}	3.7 V	450 Wh kg^{-1}	130 Wh kg^{-1}	105 Wh kg^{-1}

Batteries have a nominal (average) voltage. This is the battery's voltage at 50% depth of discharge. The specific energy (Wh kg^{-1}), or gravimetric energy density, is calculated by multiplying the specific capacity by nominal voltage (Eq. 1.16).

$$\boldsymbol{Specific\ Energy = Specific\ Cap. x\ Nominal\ Voltage} \quad (1.16)$$

Watt-hour is the unit of energy for electrochemical devices (1 J = 1 W.s). Care should be taken when mentioning the energy density of a battery as this can refer to either the active material or the composite electrode, or alternatively, the device at the cell or pack level.[‡] A range of different Li -ion battery chemistries and their

[‡] In this thesis, the term 'energy density' refers to the active material, unless stated otherwise.

corresponding energy densities are given in Table 1.2. There is a decrease in energy density at each higher level of the battery assembly process, due to the presence of a greater amount of inactive components (Fig. 1.9).[43] The energy density decreases by approximately 15% on going from the active material to electrode level, due to the current collector, binder and conductive additive. There is then a further 65% reduction from the electrode to the cell level because of the weight of the anode, separator, electrolyte, cell case etc., and finally a 20% decrease on going from the cell to battery pack level, due to components such as packaging and connecting wires. Consequently, for Li-ion cathode materials, there is approximately a four-fold decrease in energy density between the active material and end battery pack level.

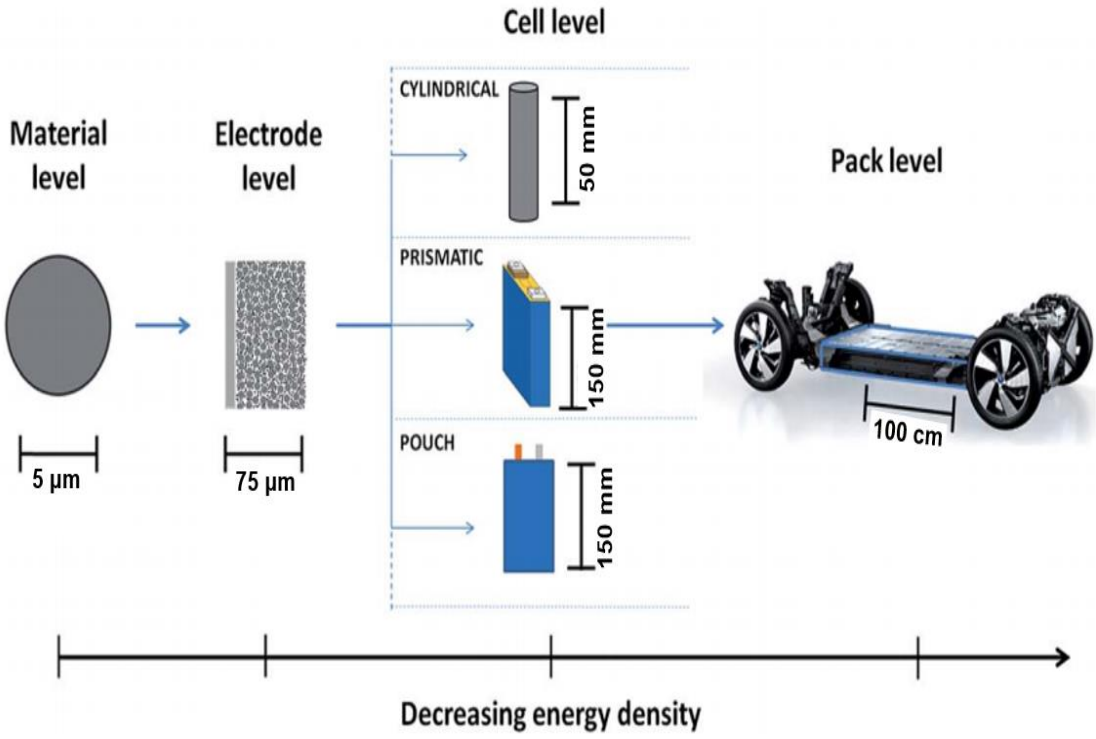

Figure 1.9 The energy density of the battery decreases from the active material to electrode, cell, and pack level. Adapted from reference 43.

There are three main cell formats used in commercial electric vehicles: cylindrical, prismatic and pouch cells (button or coin cell formats are used for other applications). Each of these designs has its own advantages and drawbacks. It is also possible to express the energy density of a battery in the form of volumetric energy density (Wh l^{-1}). This is a measure of how much energy a battery contains in comparison to its volume. Once again, this decreases moving up through the

assembly chain, but not in proportion to gravimetric energy density. For example, while there is a 20% decrease in going from cell to the pack level in terms of specific energy, the volumetric energy density decreases by over 50% due to the amount of space taken up by the packaging, wiring and cooling system.

Power *P* is the rate at which energy is transferred, and is measured in watts. A watt is the work done when a current of 1 A flows across a potential difference of 1 V (Eq. 1.17), hence, 1 W = 1 V.A. Specific power (W kg^{-1}), is the maximum available power per unit mass. It is also possible to think about power in terms of power density (W l^{-1}). Batteries for specific applications such as power tools are geared towards possessing a high specific power, rather than a large specific energy.

(Power) $$\boldsymbol{P = VI} \tag{1.17}$$

1.1.4 (e) Faradaic/Coulombic Efficiency

The faradaic or coulombic efficiency of a battery describes how efficiently charge is transferred around the electrochemical system. For a cathode, it is the ratio of discharge capacity to charge capacity (for the same cycle), and is given by Equation 1.18. A higher coulombic efficiency equates to a longer battery cycle life and is therefore desirable. Lithium-ion batteries have one of the best coulombic efficiencies, which is usually over 99%. After charging a battery it is not possible to re-insert all of the lithium back into the cathode. This can be due to a variety of reasons, e.g. parasitic side reactions between the electrolyte and anode which consume lithium. In theory, a cell which has zero internal resistance and is free of all side reactions will have a coulombic efficiency of 100%.

$$\boldsymbol{Coulombic\ Eff.} = \frac{\boldsymbol{Discharge\ Cap.}}{\boldsymbol{Charge\ Cap.}} \times \mathbf{100}\% \tag{1.18}$$

1.1.4 (f) Round Trip (Energy) Efficiency

While the faradaic/coulombic efficiency of a battery describes how efficiently charge is transferred around the electrochemical system, it can often be more useful to think in terms of energy efficiency (Eq. 1.19). This takes into account also the voltage at which a battery is charged/discharged and, hence, the total amount of energy

retrieved. Often a battery is discharged at a lower voltage than it is charged at, leading to a lower specific discharge energy. This difference in voltage is referred to as potential hysteresis.[13] This occurs partly due to an internal cell resistance, which is most pronounced as the *iR* drop between the end of charge and the start of discharge. Furthermore, more energy is required to remove Li^+/Na^+ ions from the host lattice and electrons from the transition metals on charging (and promote them from the ground state) than is accompanied with the opposite processes on discharge. The combined result of these effects is that the energy spent during charge is higher than that delivered during discharge, resulting in an energy efficiency less than 100%.

$$\boldsymbol{Energy\ Eff.} = \frac{\boldsymbol{Specific\ Charge\ Energy}}{\boldsymbol{Specific\ Discharge\ Energy}} \times \mathbf{100}\% \quad (1.19)$$

Energy efficiency is also sometimes referred to as round trip efficiency because it is the energy retrieved in a round trip around the storage system. It is a critical factor in assessing the usefulness of a storage technology. The higher the round trip efficiency, the less energy lost during storage, and the more efficient the system is as a whole. Batteries tend to have a round trip efficiency around 85-95% (depending on the chemistry), which is higher than most other storage technologies, e.g. hydroelectricity (70-85%), compressed air (40-70%).[44]

1.2 Sodium-Ion Batteries

1.2.1 Overview

The significant growth in interest in sodium-ion batteries over the past decade has been demonstrated by a dramatic rise in the number of patents and publications. There has been approximately 80 times the number of peer-reviewed papers published on Na-ion technology in the last 10 years (2010-2020) than existed in total prior to this date.[§]

Interest in sodium-ion batteries stems from concerns surrounding current lithium-ion technology. Lithium metal can only be found in certain regions globally, with

[§] Based on article search in the database of Web of Science (September 2020).

relatively few known deposits in Europe.[45] Current resources are being depleted at a steadily increasing rate, and the cost of lithium metal is increasing.[46] In contrast, sodium is the fourth most abundant metal in the Earth's crust, and Na metal is only a fraction of the cost of lithium[47] (Table 1). Furthermore, a major component of most lithium-ion cells is cobalt, which is toxic, relatively expensive, and there are also human rights concerns surrounding its supply chain.[48] Lithium and sodium have relatively similar chemistries, meaning that current manufacturing for LIBs can be easily transferred to Na-ion. Due to these different factors, is predicted that when fully-commercialised, sodium-ion technology will be 30% cheaper to manufacture than Li-ion.[49] Furthermore, lithium-ion batteries are susceptible to overcharging, which can lead to thermal runaway, whereas sodium-ion cells have improved thermal stability and can be stored at 0 V, which means that they can be transported more safely.[50] However, there are a number of challenges associated with sodium-ion batteries stemming from the larger size and lower reduction potential of Na. This means it is difficult to achieve cell voltages as high as seen with LIBs, and the theoretical capacity of the metal is much lower.[51]

Table 1.3 Lithium versus sodium characteristics.[45,51]

Category	Lithium	Sodium
Abundancy	20 ppm	23,000 ppm
Cost	$1500/ton	$150/ton
Ionic Radius	76 ppm	106 ppm
Atomic Weight	6.9 g mol^{-1}	23 g mol^{-1}
Voltage vs. SHE	-3.04 V	-2.70 V
Theoretical Capacity of metal	3,829 mAh g^{-1}	1,165 mAh g^{-1}

Sodium and lithium-ion batteries both operate on the same basic principles. During charging, Li^+/Na^+ metal ions move out of the cathode, travel through the electrolyte, before inserting into the anode. At the same time, electrons travel through an external circuit. During discharging, the reverse process occurs and the electrons do

work. Crucial to this is the presence of a partially permeable separator, which allows ions to pass through, but is an electronic insulator and so prevents a short circuit between the two electrodes. The structure of an Na-ion cell is shown in Figure 1.10. Unlike with lithium, sodium metal does not react with aluminium at low voltages to form an alloy at the anode, so this can be used instead of a more expensive copper or nickel current collector.[52]

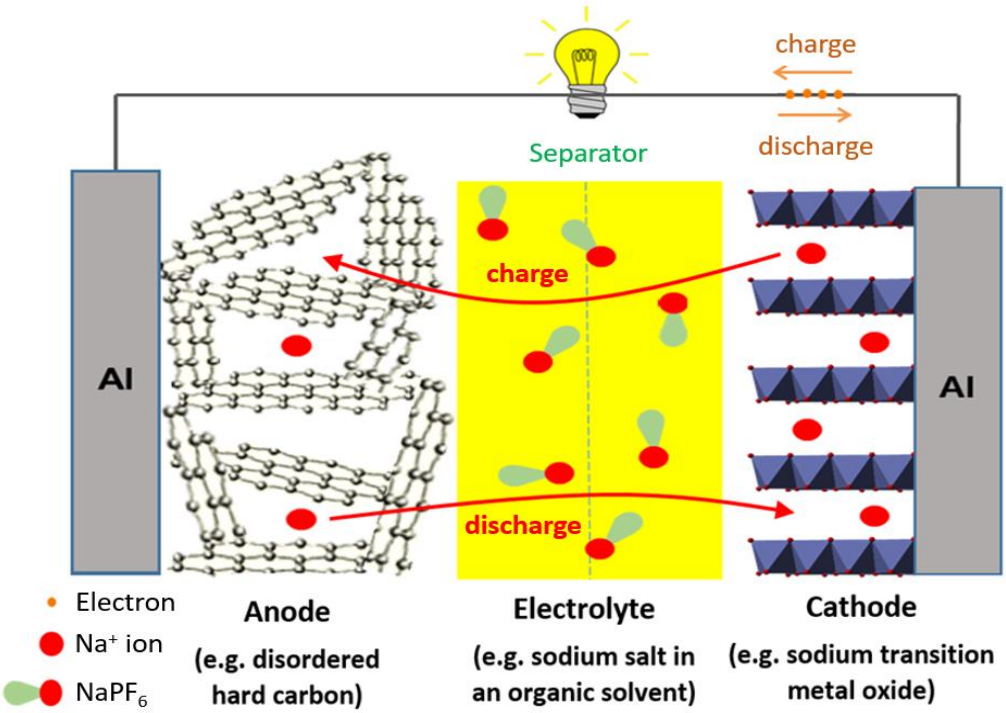

Figure 1.10 Schematic of a sodium-ion battery.

1.2.2 Anodes

Another important difference between lithium and sodium-ion batteries is the type of anode material used. Whereas LIBs use sheets of graphite for intercalating Li^+ ions at the anode, sodium ions are too large to fit between these so, instead, some alternative material must be used. A wide range of these have been examined, primarily carbon and alloy-based structures. Crucial to this selection is consideration of the solid electrolyte interphase (SEI).[53] This forms by reaction between the electrolyte and anode during the first charge when the salts and solvent in the electrolyte are reduced by raising the voltage.[54] Similarly with lithium-ion cells, SEI formation leads to capacity fading.[55] While a stable SEI layer is necessary, as it

limits further electrolyte-electrode reaction,[56] its thickness must be controlled, as over time an increase can lead to performance degradation and limit cycle life.[57]

The SEI layer that forms on carbon-based materials is usually the most stable,[58] and thus this is one of the reasons these materials have received the most development to date as Na-ion anodes. Hard carbons were amongst the first materials looked at for SIBs.[59,60] These showed modest capacity (200 mAh g^{-1}) but inferior cycling stability and coulombic efficiency. Work done by Jeff Dahn's group around the year 2000[61] was able to raise this to 300 mAh g^{-1}, which was more in line with LIBs. Carbonaceous materials have the advantage that the electrochemical potential of C is close to Na metal.[62] However, this also means that a high current density/depth of discharge represents a safety hazard as sodium plating can occur, which leads to dendrite formation, and eventually a short circuit.[62] This problem can be circumvented through use of expanded graphite (Fig. 1.11), which is prepared by the oxidation and partial reduction of graphite.[63,64] This has a higher voltage and shows improved safety, although a slight reduction in energy density (284 mAh g^{-1}). [63]

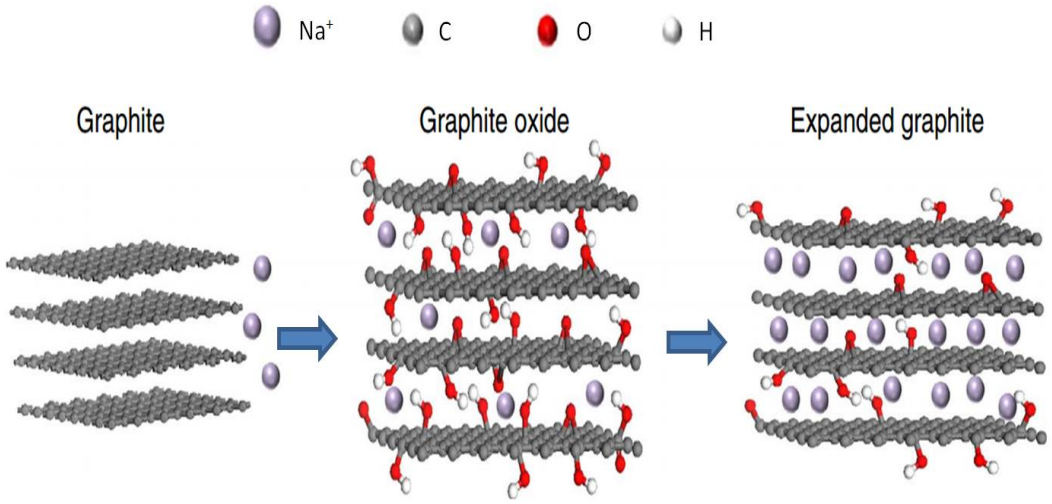

Figure 1.11 Sodium storage in expanded graphite. Adapted from reference 63.

Significant work has also taken place on sodium alloy materials. Research performed in Asia demonstrated a tin sulfide anode capable of achieving 400 mAh g^{-1}.[65] Phosphorous-based structures have also been studied, and are capable of achieving a theoretical capacity much higher than metallic sodium.[66] More recently, major advances have come about by an abandonment of conventional materials in favour of

alternative designs. Antimony nanoparticles anchored on interconnected carbon nanofibres have been shown to give a high performance anode,[67] as do MoS_2 nanoflowers (400 mAh g^{-1}).[68] Low potential titanium oxides have also been extensively studied. The well-known spinel $Li_4Ti_5O_{12}$ anode for LIBs is able to also accommodate Na^+ ions, and possesses one of the best cyclabilities to date among these oxide anode materials.[69]

1.2.3 Electrolytes

The electrolyte in SIBs must be able to efficiently shuttle Na^+ ions between electrodes over time, while retaining good stability. The ionic conductivity is dependent upon the concentration of charge carriers, as well as the viscosity and permittivity of the electrolyte medium, whereas crucial to the chemical stability is the ability to form an effective SEI layer. Electrochemical stability is also important, and the electrolyte must be able to operate across a wide voltage window. As with their LIB counterparts, the ionic conductivity of Na-ion solid electrolytes trails substantially behind those of liquid ones. Thus, the major electrolytes currently looked at for SIBs are based on solutions of salts in mixtures of either organic solvents or ionic liquids (ILs).

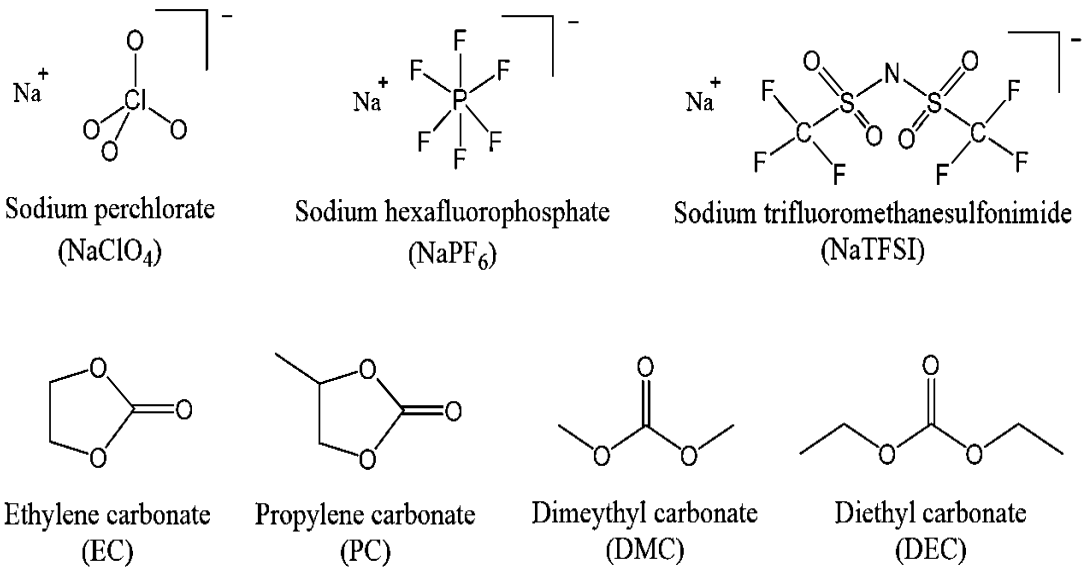

Figure 1.12 Most commonly used salts and solvents in Na-ion battery electrolytes.

Non-aqueous electrolytes consist of a sodium salt dissolved in some organic solvent. Most salts researched to date use the same weakly coordinating anions as in lithium-ion batteries (Fig. 1.12), e.g. chlorate (ClO_4^-) and hexafluorophosphate (PF_6^-).[70] One advantage of chlorate over PF_6^-, is that the latter can react to give toxic hydrogen fluoride gas.[71] The trifluoromethanesulfonimide ($TFSI^-$) anion is also problematic in that it corrodes aluminium.[72] Most solvents looked at so far have been carbonates, such as propylene carbonate (PC), as these have a high dielectric constant, large electrochemical window, and low volatility. Each of these has its own advantages and disadvantages, which has led to mixtures being looked at. A comprehensive study by Bhide *et al.*[73] found that $NaPF_6$ has the highest conductivity amongst Na-ion salts: 12 mS cm^{-1} in an ethylene carbonate (EC) : dimethyl carbonate (DMC) solvent system.[74] Subsequent work by Rosa Palacín suggested that an EC:PC:DMC mixture is the optimum solvent for SIBs.[75]

While non-aqueous liquids are the most promising sodium-ion battery electrolytes to date, the flammability of the organic electrolytes poses potential safety problems. Therefore, ionic liquids - an ionic salt doped with some sodium salt equivalent – are being developed as an alternative. So far, the fluorosulfonimide ions (FSI^- and $TFSI^-$) have proved the most promising for use with these. NaTFSI with imidazolium-TFSI ILs show an ionic conductivity as high as 5.5 mS cm^{-1}.[76] Chang and co-workers even claim that for certain electrodes, FSI-based ILs are capable of outperforming organic electrolytes.[77] However, ionic liquids are plagued with a number of drawbacks: they are more viscous than their organic-based counterparts, so require a higher operating temperature (generally at least > 50 ºC), and purity and dryness are often an issue.[70] To date, ILs have shown great potential, but still are yet to surpass non-aqueous electrolytes for sodium-ion battery use.

1.2.4 Cathodes

By far the most research which has taken place into sodium-ion batteries has been on their cathode materials. Similar to lithium-ion technology, the capacity of the cathode component of the cell trails behind that of the anode. Hence, improving the working voltage and specific capacity of cathode materials is key to enhancing Na-ion battery energy density, and enabling them to compete alongside Li-ion

technology. The biggest challenge to their design is limiting the volume change that occurs due to larger sodium ion (de-)insertion. Furthermore, sodium ions prefer octahedral or prismatic coordination, whereas lithium ions tend to adopt either octahedral or tetrahedral.[45] This means that sodium and lithium compounds are not necessarily isostructural, leading to different electrochemical properties. This can be either advantageous or detrimental, and a number of promising materials now exist with energy densities exceeding those of graphite/$LiMn_2O_4$, as shown in Figure 1.13.[78] (Note that for this figure, the energy content at the active material level of a graphite/$LiMn_2O_4$ and graphite/$LiCoO_2$ cell is taken as 300 and 380 Wh kg^{-1} respectively; ~ 65% the energy density of just the active cathode material).

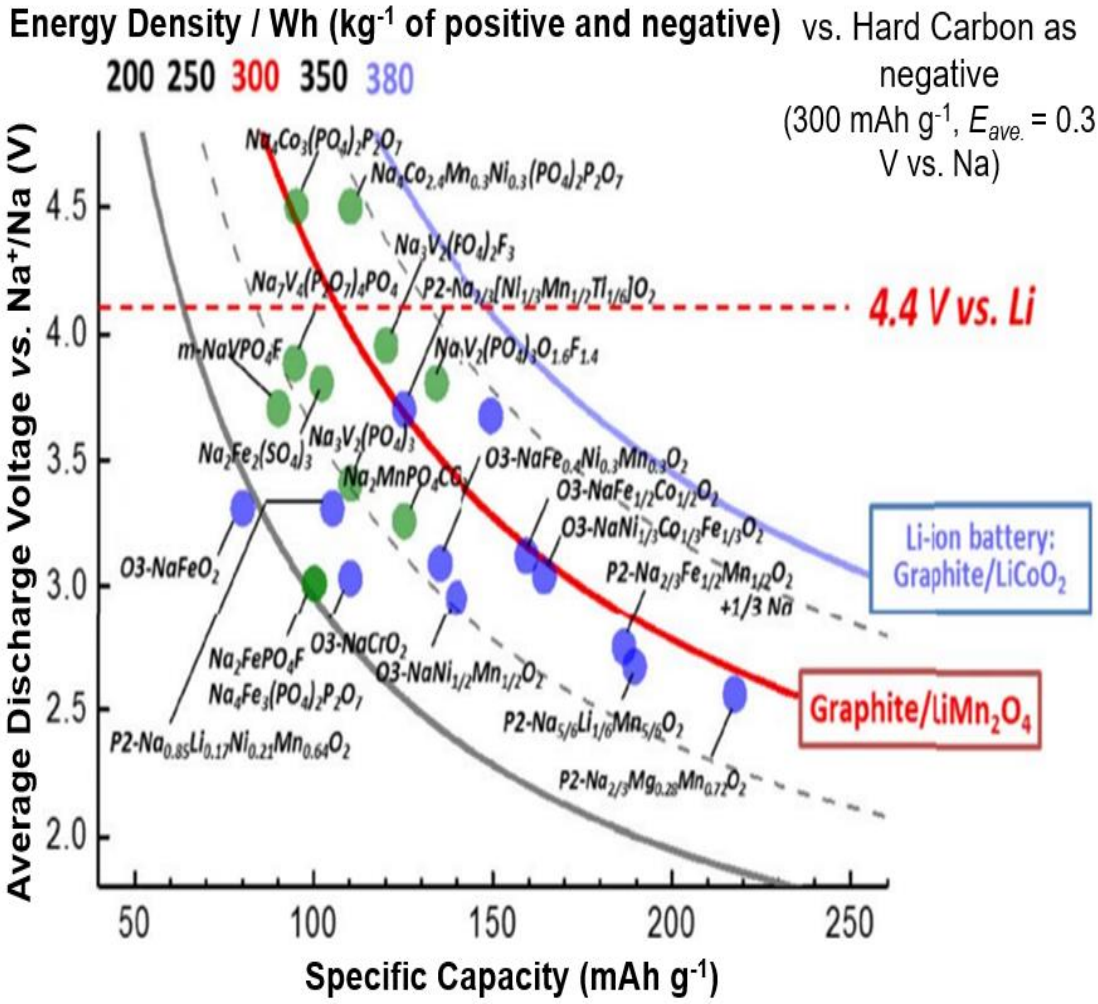

Figure 1.13 Average voltage against specific capacity for Na-ion cathodes. Energy density is given based on weight of active materials only (using hard carbon with a reversible capacity of 300 mAh g^{-1} and $V_{ave.}$ = 0.3 V). Adapted from reference 78.

The two main classes of Na-ion cathode materials can be broken down into polyanionic compounds and transition metal oxides. Polyanionic materials are promising cathode candidates due to their robust covalent framework, which confers suitable conductivity channels for Na^+ ions, and ensures good stability.[62] The most common LIB polyanionic cathode is LiT_MPO_4 (T_M = Mn, Fe, Co, Ni), with lithium iron phosphate being used for applications worldwide.[79] However, sodium analogues have proven disappointing due to the lack of obvious channels for diffusion.[80] More recent work has focused on pyrophosphates, $Na_2T_MP_2O_7$, as well as sulfates/fluorosulfates. Of these, $NaFeSO_4F$ was surprisingly found to have a higher ionic mobility than $LiFeSo_4F$, from pellet impedance measurements.[81] Possibly the most well-known polyanionic compound, however, is the type of material referred to as an Na Super Ionic Conductor (or NASICON).[82] This has an open 3D framework built-up of corner-sharing T_MO_6 and XO_4 polyhedra: $A_nT_MT_M'(XO_4)_3$, which form large tunnels, and have an ionic conductivity above 10^{-3} S cm^{-1}.[83] The vanadium-based NASICON phosphate $Na_3V_2(PO_4)_3$, has yielded some of the most interest so far amongst polyanionic compounds, due to its high energy density (~ 400 Wh kg^{-1}),[84] however, it is limited in its commercial potential due to the toxicity and cost of vanadium.

Sodium transition metal oxides were historically the first compounds considered as cathode materials for Na-ion batteries.[85–87] The chemistry of these is complicated as many different phases and polymorphs exist as the Na to transition metal ratio changes. The reduction of β-$NaMnO_2$ produces $Na_{0.44}MnO_2$.[47] This material has S-shaped tunnels, and was first looked at in sodium-metal polymer cells by Doeff *et al.* during the 1990s.[88] Vanadium-based oxides, $Na_xV_2O_5$, are also well reported in the literature for Na-ion cathode materials,[89,90]which may possess channel structures. A more recent paper on $Na_{1.25}V_3O_8$ nanowire looks particularly encouraging, with a capacity of ~ 100 mAh g^{-1} up to 1000 cycles.[91] However, it has been research done on layered oxides which has shown the most potential for Na-ion cathode materials to date; these have been studied extensively over the past few years.

1.3 Layered Sodium Oxides and Na-Ion Cathode Materials

1.3.1 Classification and Structure

Layered sodium transition metal oxides are a popular choice of cathode material for Na-ion batteries because they have easy-to-synthesize, simple structures, which are capable of high redox potentials and specific capacities. Importantly, they do not show any decrease in ionic conductivity compared to LIB materials.[92] Furthermore, the larger sodium cation means that unfavourable alkali ion/transition metal mixing is not expected to occur, as is seen with Li-ion.[45] Since 2010, the substitution of elements into these oxide layers has been a key focus of Na-ion cathode development. Electrochemically active elements can be used to raise the operating voltage of the battery, as well as bring about a smoother charge-discharge profile, while incorporating a small amount of electrochemically inactive elements can enhance stability and result in a better cycle life.[93]

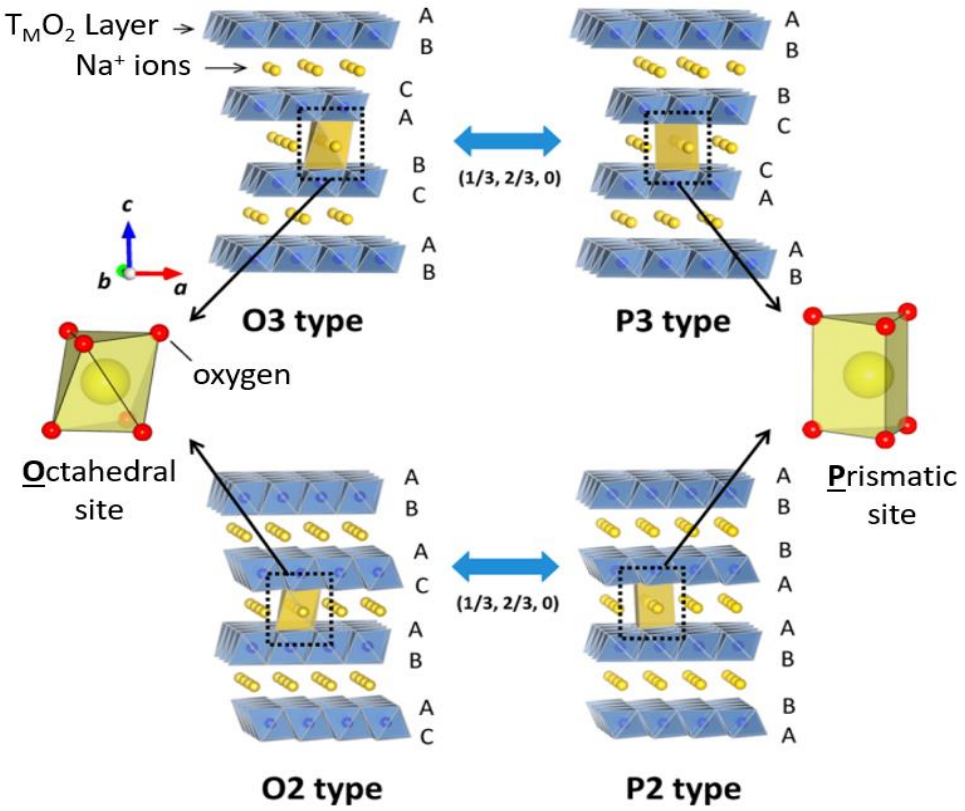

Figure 1.14 Classification of layered sodium transition metal oxide polymorphs. Adapted from reference 47.

The structure and classification of layered oxides were first laid out in a seminal paper by Claude Delmas in 1980.[94] The layered structure is built of sheets of edge-sharing T_MO_6 octahedra, with alkali ions inserted between these metal oxide slabs. The stacking of these sheets with different orientations gives rise to polymorphism. Sodium-based materials, $Na_xT_MO_2$ form cation-ordered rock salt superstructures, which can be classified into four major groups: O3, P2, O2, and P3 (Fig. 1.14). The letters indicate the environment in which the Na^+ ion is located: either octahedral (O) or prismatic (P), and the number is how many oxide sheets form the repeat unit in the c-direction. The O3- and P2-type phases are the most common. The O3 phase ($0.7 \leq x \leq 1$) consists of close packed ABCABC oxide layer stacking, and the P2-type phase ($0.6 \leq x \leq 0.7$) a close packed ABBA array. Note that it is only the TMO_6 layer that is rock salt-like in these compunds, and the rock salt ordering is lost in the third dimension. Hence, the term 'layered rock salt type structure' is more accurate when referring to these materials.

The intercalaction electrochemistry of these layered oxides is heavily dependent upon the structure of the phase, including the amount of sodium and the stability of the structures to Na (de-)insertion. A general characteristic of these polymorphs is that the O3 phase has a higher sodium content than its P2 counterpart, and so the latter consequently has much more vacancies in its structure. Hence, the O3 polymorph has a greater initical charge capacity due to a larger sodium reservoir, whereas the P2 phase is thought to generally afford better electrochemistry due to its higher ionic conductvity. This comes about because Na^+ ion hopping in O-layered structures must take place through unfavourable interstitial tetrahedral sites. In the P-phases, in contrast, there is an on open path for diffusion through adjacent prismatic sites.[95,96]

Sodium extraction during cycling generally induces phase transitions.[47] During this process, the T_MO_2 planes undergo gliding, and move from octahedral accommodation of the sodium ions to prismatic and vice versa. For example, the extraction of Na^+ ions from O3 creates vacancies and allows sodium at prismatic sites to be energetically stabilised, thus forming the P3 polymorph ($x \approx 0.5$) with ABBCCA stacking.[97] The extraction of sodium ions from between the T_MO_6 slabs leads to greater repulsion between oxygen layers, which in turn results in an

expansion of the T_MO_6 interlayer distance.[98] This leads to Na^+ ions occupying prismatic sites due to the large Na ionic size. Sodium ions occupy two different types of trigonal prismatic sites: Na1 contacts the two T_MO_6 octahedra of the adjacent slabs along its face, whereas Na2 contacts the six surrounding T_MO_6 octahedra along its edges (Fig. 1.15). Adjacent Na1 and Na2 sites are too close together (considering the Na^+ ionic radius) to be occupied simultaneously.[7]

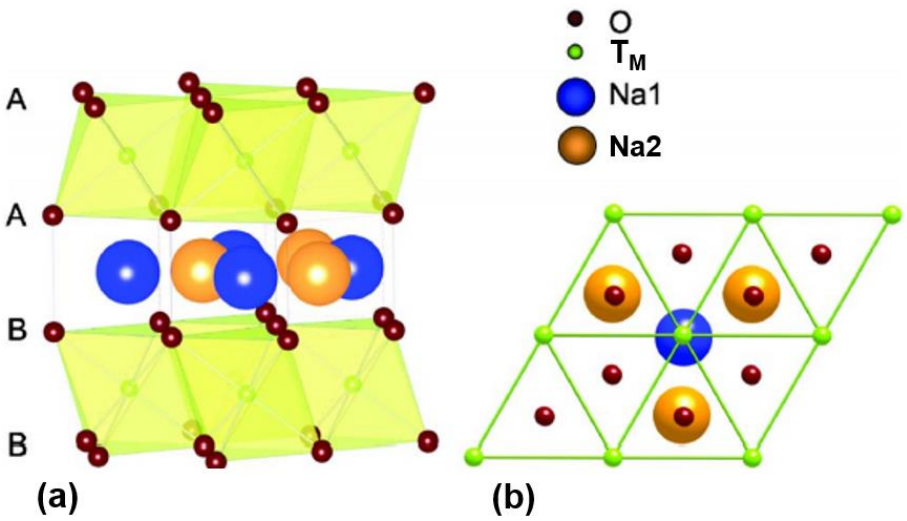

Figure 1.15 Crystal structure of P2-NaT_MO_2. (a) View perpendicular to the *c*-axis to show the AABB oxygen stacking. (b) View parallel to the *c*-axis to show relative positions of Na1 and Na2. Adapted from reference 98.

The P2 phase is generally more stable structurally as it does not undergo slab gliding to O2 (ABACAB) unless a lot of Na is removed (~ 70%).[92] Desodiation shifts the phase toward O2 due to gliding ($\pi/3$ rotation) of the TMO_6 octahedra and contraction of the crystal structure, reducing the interlayer distance.[7] An O3/P3 transtion to O2/P2 is not possible without high temperature, as it requires the breaking/reforming of T_M-O bonds. Addressing these phase transitions is a major challenge to enhancing electrochemical reversibility and cyclability in these layered oxide materials.

1.3.2 Single Transition Metal Oxides

A range of layered single transition metal oxides, NaT_MO_2 (T_M = Ti, V, Cr, Mn, Fe, Co, Ni), were investigated for their electrochemical properties as far back as the 1980s.[87,99,100] Sodium cobalt oxide was the first layered oxide to be studied for Na

insertion.[85] The trigonal O3 phase is able to de-intercalate around 0.5 Na while undergoing a phase transition to monoclinic P3.[99] However, as one of the driving forces behind Na-ion battery research is the use of cheaper, more sustainable elements compared with Li-ion, research into Na-ion cathodes has primarily focused on using more environmentally friendly elements than cobalt.

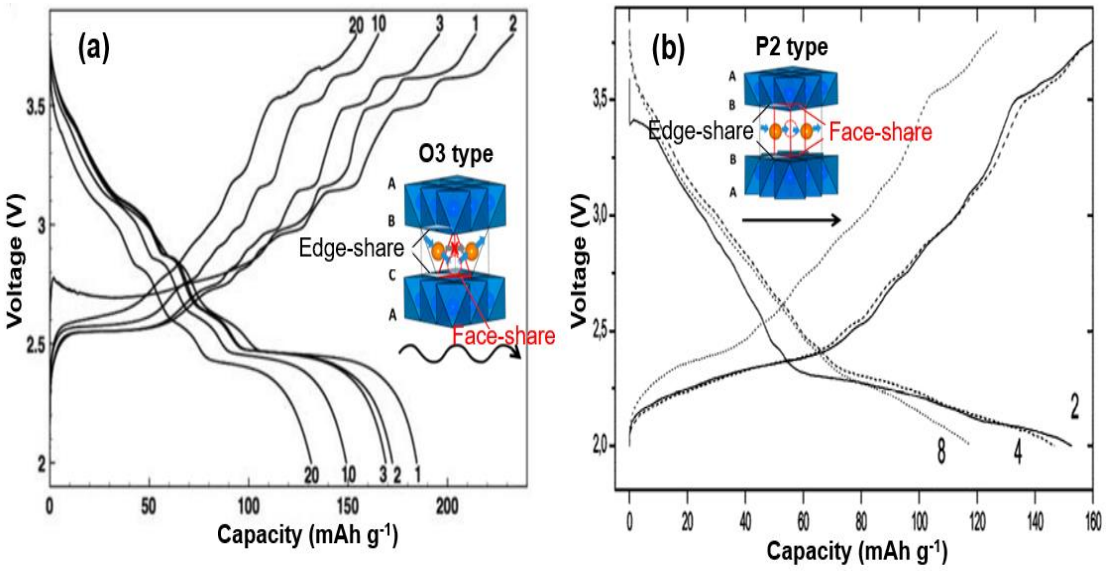

Figure 1.16 The charge-discharge profiles of (a) O3 α-$NaMnO_2$, and (b) P2-$Na_{0.6}MnO_2$, cycled over the voltage range 2.0 – 3.8 V. The different Na migration paths are shown as insets. Adapted from references 47, 106 and 107.

One of the most early studied and well characterised single transition metal oxides was sodium manganese oxide, Na_xMnO_2. This compound can form either a 3D structure with tunnels (x = 0.4 and 0.44), or a 2D layered structure (x = 1.0 and 0.7). The 2D phases can be either O3 low temperature monoclinic α-NaMnO2, O3 high-temperature orthorhombic β-NaMnO2, or a range of sodium-deficient P2-type phases.[101] These materials have been extensively studied by Grey and co-workers,[102–104] and the conduction in all of them is found to be limited by the Jahn-Teller effect of high-spin Mn^{3+}, which encourages electronic localisation and unfavourable Na^+/electron binding, lowering the diffusion rate.[86,105] The α-$NaMnO_2$ polymorph is the most stable; 0.8 Na can be reversibly de-intercalated, giving an initial capacity > 180 mAh g^{-1}.[106] The P2-$Na_{0.6}MnO_2$ cathode by comparison shows a discharge capacity of just *ca.* 140 mAh g^{-1} (2–3.8 V) (Fig. 1.16).[107] It is suspected

that moisture uptake may play a role in destabilising the structure of this P2-type layered oxide.[108]

Similar to the sodium manganese oxides, the Jahn-Teller effect is also of importance in the structure and properties of $NaNiO_2$. This material can be synthesized stoichiometrically due to the presence of low-spin Ni^{3+}, which induces really strong Jahn-Teller distortion.[97] This alters the lattice parameters, forming an O3 hexagonal unit cell above 220 ºC, and a distorted monoclinic one below.[99] When this material was initially studied *ca.* 30 years ago, it was thought to only (de-)intercalate ~ 0.2 Na,[109] but more recently, a capacity of 123 mAh g^{-1}, and coulombic efficiency > 99%, has been demonstrated between 1.25-3.75 V by Ceder *et al*.[110]

Layered sodium iron oxide also exists as two polymorphs, α-$NaFeO_2$ and β-$NaFeO_2$,[111] although only the low temperature ordered honeycomb structure, α-$NaFeO_2$, is known to be electrochemically active (80 -100 mAh g^{-1}).[112] The structure of this O3 phase is stable up to ~ 0.1 Na removal, with Mossbauer spectroscopy indicating Fe^{4+} formation.[99] Both O3-$NaVO_2$ (120 mAh g^{-1}) and P2-$Na_{0.7}VO_2$ (100 mAh g^{-1}) have also been reported in the literature.[113] In contrast, there are relatively few Ti^{3+} systems, as these are highly reducing. While some of these single T_M systems display good reversible capacity over a suitably wide voltage range, their electrochemistry has more importantly been used as the basis for other more complex systems.

1.3.3 Multiple Metal Oxides

Some of the best capacities so far have been achieved with layered oxides containing multiple metal elements in addition to sodium. A cooperative effect between different transition elements, Mn, Fe, Ni, Co etc., can help to activate the redox reaction at a target voltage, thus enabling a smoother charge-discharge profile. Furthermore, inactive spectator elements, such as Mg and Ti, are considered as a way of enhancing capacity retention and improving structural stability.[97]

Of the binary O3 polymorphs, $Na[Fe_xMn_{1-x}]O_2$ ($0.5 \leq x \leq 1$) has been well studied, and found to have a discharge capacity as high as 105 mAh g^{-1} (at $x = 0.5$).[52] Increasing the manganese concentration in this system improves performance by

reducing the reliance on the $Fe^{3+/4+}$ redox reaction and the Jahn-Teller distortion caused by high-spin Fe^{4+}. Nickel works in a similar way in O3-$Na[Fe_{1-x}Ni_x]O_2$ ($0.5 \leq x \leq 0.7$) by suppressing polarisation during cycling through limiting Fe^{4+} formation. This material has a capacity of 112 mAh g^{-1} and a coulombic efficiency of ~ 90% (x = 0.5).[114] However, of all the O3 phases studied, the $Na[Ni_{1/2}Mn_{1/2}]O_2$ cathode developed by Komaba and co-workers is one of the most promising to date, and has received much attention from other research groups around the world.[115,116] This material is capable of achieving around 125 mAh g^{-1} (2.2-3.8 V), with 75% capacity retention after 50 cycles.[117] X-ray absorption spectroscopy shows via a combination of X-ray absorption near edge structure (XANES) and extended X-ray absorption fine structure (EXAFS) that nickel is the only redox active element in this structure – manganese remains as Mn^{4+}, while Ni^{2+} goes to Ni^{4+}, via Ni^{3+} (Fig. 1.17).

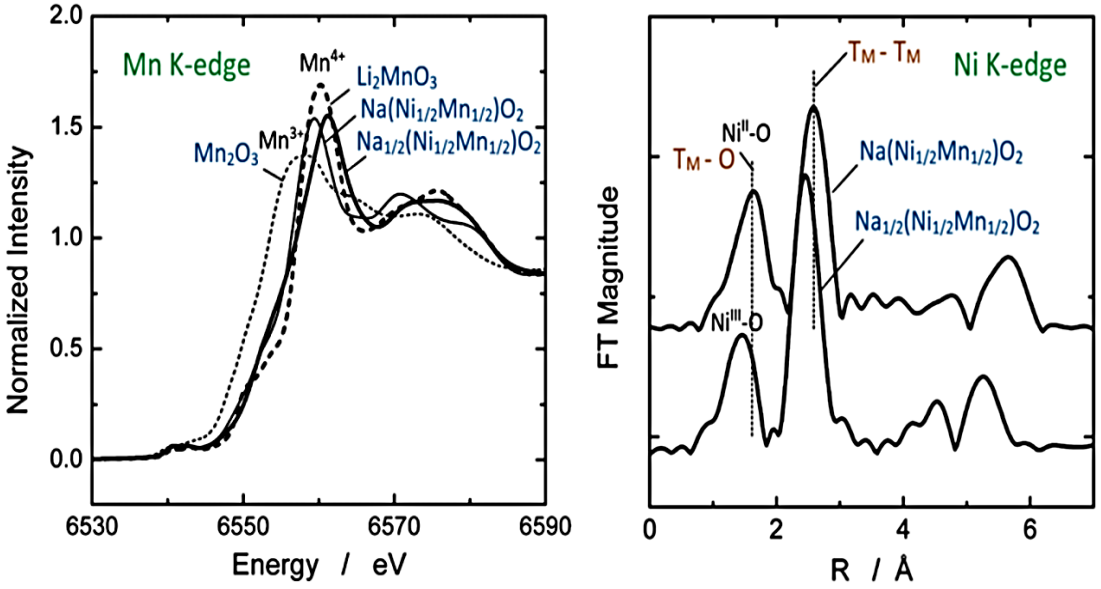

Figure 1.17 XANES spectrum at the Mn K-edge (6539 eV), and EXAFS spectrum at the Ni K-edge. Adapted from reference 117.

Similar to O3, there has been much development of binary P2-type polymorphs. The compound P2-$Na_x[Ni_{1/3}Mn_{2/3}]O_2$ shows a lower initial capacity than O3-$Na[Ni_{1/2}Mn_{1/2}]O_2$,[118] but exhibits superior structural stability and capacity retention due to the P2-O2 transition occurring at a higher voltage.[119] The P2-type polymorph $Na_{2/3}[Fe_{1/2}Mn_{1/2}]O_2$ has a capacity of 190 mAh g^{-1} (1.5-4.2 V)[52] and an energy density of 520 Wh kg^{-1}, which is greater than that of some well-established Li-ion cathodes ($LiMn_2O_4$ and $LiFePO_4$). However, the material undergoes an irreversible

phase change above 3.4 V,[120] and Na-Fe-Mn systems are known to be quite hygroscopic.[121] Various research groups have investigated the effect of doping layered sodium oxide P2 materials with electrochemically inactive magnesium[122] and titanium.[123] The Bruce Group, in Oxford, found that a small amount of magnesium, such as in P2-$Na_{2/3}[Mn_{1-x}Mg_x]O_2$ ($0 \leq x \leq 0.2$), improves the overall performance without compromising the capacity much (150 mAh g^{-1} for $x = 0.2$).[124] Furthermore, these materials are found to possess smoother charge-discharge profiles (less phase transitions) as Mg^{2+} decreases polarisation by suppressing the Jahn-Teller distortion of Mn^{3+}.[125] Work performed in Japan found that $Na_{0.67}[Mg_{0.28}Mn_{0.72}]O_2$ is capable of an anomalous capacity beyond 200 mAh g^{-1}, which is thought to be due to an oxide ion contribution induced by the magnesium.[126] A small amount of titanium is also thought to enhance long-term cycling performance.[127] For example, Ti^{4+} improves stability and cyclability in P2-$Na_{2/3}[Ni_{1/3}Mn_{2/3-x}Ti_x]O_2$ by suppressing Na^+/vacancy ordering and restricting the P2-O2 phase transition.[128]

Layered oxides containing more than two metals in addition to sodium have proven to be useful in boosting electrochemical performance. A sodium analogue of the well-known Lithium Nickel Manganese Cobalt Oxide (NMC) cathode, O3-$Na[Ni_{1/3}Mn_{1/3}Co_{1/3}]O_2$, developed by Tarascon and colleagues, is capable of 0.5 Na (de-)intercalation and a capacity of 120 mAh g^{-1}.[129] The ternary P2-$Na_{0.67}[Mn_{0.65}Fe_{0.2}Ni_{0.15}]O_2$, is one of the most promising, with a discharge capacity greater than 200 mAh g^{-1}, and 70% capacity retention after 50 cycles.[130] These layered ternary[131], and even quarternary[132] metal oxides, have gained increasing attention in recent years, as researchers try and find ways of increasing the energy density of sodium-ion cathode materials, whilst achieving good structural and electrochemical stability.[133]

1.3.4 Mixed Phase Systems

The structure of the layered sodium oxide cathode hugely affects its electrochemical properties. The well-known O3 and P2 polymorphs each possess their own intrinsic strengths and weaknesses. The O3 phase has a higher sodium reservoir, and shows much more reversible capacity. However, structural degradation occurs above 4 V,[117] and the material is prone to complex phase transitions. The P2 polymorphs, in

contrast, possess greater rate capability, and are generally more stable. However, they are prone to over-extraction of sodium at high voltages, and their specific capacity is limited by the large number of unoccupied Na^+ ion sites.[134] Recently, research groups have looked into cathodes made up of a mixture of these two layered phases in order to overcome their individual limitations, and combine the high energy of the O3 with the high power of the P2. This is sometimes referred to as utilising a 'synergetic' effect.

Despite the fact that earlier studies on lithium-ion batteries reported the co-existence of P- and O-phase intergrowth,[135] which was later confirmed in sodium-ion batteries by phase diagram work,[136] until very recently, Na-ion cathode research has almost exclusively been restricted to phase pure materials. The first mixed phase material reported was in 2014 by Johnson and co-workers, when the partial substitution of Na for lithium formed $Na_{0.7}[Li_{0.3}Ni_{0.5}Mn_{0.5}]O_{2+\delta}$ with mixed phase intergrowth.[137] This has a discharge capacity of 130 mAh g^{-1} and high rate performance. A year later, scientists started with P2 as the major phase and introduced some O3 to form $Na_{0.66}[Li_{0.18}Mn_{0.71}Ni_{0.21}Co_{0.08}]O_{2+\delta}$, which has one of the highest energy densities of all reported SIB materials so far – 640 Wh kg^{-1},[138] however, this material is limited in its charge retention.

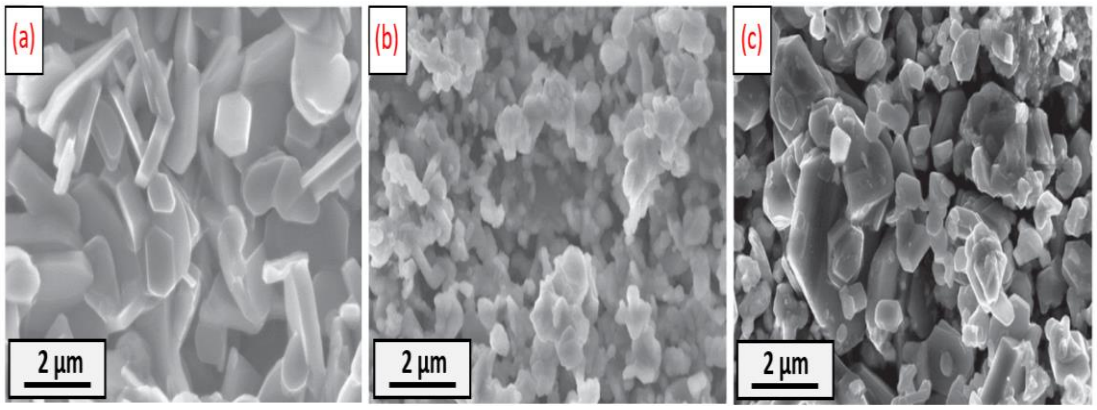

Figure 1.18 SEM images of (a) P2-, (b) O3-, and (c) mixed P-/O-$Na_x[Mn_yNi_zFe_{0.1}Mg_{0.1}]O_2$. Adapted from reference 139.

One of the most comprehensive works done to date on mixed phase layered sodium oxides was performed by Passerini and co-workers at the Helmholtz Institute in 2015.[139] This compared the performance of O3, P2 and mixed phase quaternary

$Na_x[Mn_yNi_zFe_{0.1}Mg_{0.1}]O_2$ ($0.67 \leq x \leq 1$; $0.5 \leq y \leq 0.7$; $0.1 \leq z \leq 0.3$). It was found that the type of material produced could be fine-tuned to either the O3, P2 or mixed phase material by modifying the synthesis conditions. A larger quantity of transition metals in higher oxidation states, such as Mn^{4+}, favours P2, whereas low charge Ni^{2+}, along with more sodium, favours the O3. Quenching also increases the likelihood of forming O3, whereas slow cool leads to P2. Hence, utilising intermediate conditions such as 0.76 equivalent Na^+, with slow cooling, leads to a mixture of O- and P-phases. These results are confirmed by SEM images (Fig. 1.18). Appropriate reaction conditions[108] are required in order to get the beneficial effects arising from intimate mixing of the polymorphs, and blending P2 and O3 phases together post-synthesis does not suffice. The best electrochemical performance is obtained for the mixed phase material, e.g. ~ 125 mAh g^{-1} after 50 cycles, compared to just 90 and 110 mAh g^{-1} for the O3 and P2 polymorphs respectively, with superior charge retention also present in the mixed phase cathode. It is thought that this reduced capacity fading arises from the volume changes associated with the phase transitions in the O3 and P2 structures cancelling each another out in the mixed phase material. This lowers the overall volume change for the electrode and reduces strain, leading to a high energy density of 490 Wh kg^{-1}.

Other O3/P2 biphasic compounds have since been investigated. A range of sodium-deficient layered oxides $Na_x[Ni_{0.2}Fe_{x-0.4}Mn_{1.2-x}]O_2$ were synthesized via conventional solid state reaction.[140] Tuning the sodium content was found to lead to a different O3 : P2 ratio with x = 0.78 found to be the optimal cathode design - 86 mAh g^{-1} with 90% charge retention after 1,500 cycles. The introduction of lithium into $Na_{0.67}[Mn_{0.55}Ni_{0.25}Ti_{0.2-x}Li_x]O_2$ leads to a hybrid O3/P2 structure, with improved performance.[141] Li was found to mainly reside on the T_M site so that the P2 phase dominates, with some Li on Na sites to generate an O3 minority component. Another Li-substituted mixed phase material, $Na_{0.67}[Li_{0.18}Mn_{0.8}Fe_{0.2}]O_2$, was capable of 125 mAh g^{-1} and a high coulombic efficiency.[142] Despite the great promise these mixed phase cathodes display, there has been little work performed in this area relative to the large field of sodium-ion battery research. In particular, understanding the structures and electrical properties of these mixed phase layered O3/P2 materials, and how they differ to their single-phase components is lacking.

1.4 Performance Limiting Factors in Batteries

A key criterion with respect to rechargeable batteries is cycle life, i.e. how many cycles a battery can undergo before significant loss of performance. All batteries experience reduction in performance during storage, as well as cycling.[143] This can be due to a variety of degradation (ageing) mechanisms, which can be associated with one or more of the components/interfaces of a cell. Degradation leads to decrease in (energy) capacity and/or power.[144] Identifying performance limiting factors in batteries, and ways in which these can be overcome, are large areas of interest within the battery research community.

For lithium-ion cells, degradation pathways can be divided into three possible primary processes:[145]

- Loss of the lithium metal
- Loss of the active cathode/anode material
- Deterioration of ionic transport through components and across interfaces

The first two of these affect the thermodynamic behaviour of the cell, whereas the last impacts the cell kinetically. Loss of the Li metal component or of the active cathode/anode material results in an irreversible drop in capacity. A deterioration of ionic transport leads to a rise in internal cell resistance, which is monitored by measuring the impedance. This increase in resistance means that the cell's power capability drops. Certain ageing routes cause both a fall in capacity and power. An impedance increase, and the associated fall in capacity, can often be reversed by changing the operating conditions of the battery e.g. cycling at a lower C-rate.

Table 1.4 Summary of the major known degradation mechanisms in Li-ion cells.[146]

Cause	Effect	Result
Electrolyte decomposition	Loss of lithium metal, deterioration of ionic transport	Capacity fade, impedance rise
Solid electrolyte interphase (SEI)	Loss of lithium metal, deterioration of ionic transport	Capacity fade, impedance rise
Binder decay	Loss of lithium metal, loss of active electrode material, deterioration of ionic transport	Capacity fade, impedance rise
Particle contact loss	Loss of active electrode material, deterioration of ionic transport	Capacity fade, impedance rise
Particle cracking (solvent co-intercalation)	Loss of active electrode material, deterioration of ionic transport	Capacity fade, impedance rise
Metal plating	Loss of lithium metal	Capacity fade
Transition metal dissolution	Loss of active electrode material	Capacity fade
Structural disordering/unfavourable phase transitions	Loss of active electrode material	Capacity fade
Changes in porosity	Deterioration of ionic transport	Impedance rise
Decrease in electrode surface area	Deterioration of ionic transport	Impedance rise
Oxidation of conductive additive	Deterioration of ionic transport	Impedance rise
Current collector corrosion	Deterioration of ionic transport	Impedance rise
Separator pore blocking	Deterioration of ionic transport	Impedance rise

A summary of the major degradation mechanisms in lithium-ion batteries is given in Table 1.4. These mechanisms can be related to either the individual active cell components: electrolyte, positive or negative electrode, as well as a deterioration in inactive materials: binder, separator, current collector etc. Many of the degradation mechanisms are linked to one another. For instance, electrolyte decomposition, changes in electrode porosity and decrease in surface area may all be connected to

the formation of the solid electrolyte interphase. SEI formation, growth and decay is one of the most well established and problematic ageing mechanisms in LIBs.[147] An ionically-conducting, electronically-insulating, and mechanically robust SEI is essential for a long Li-ion battery life. However, the SEI consumes lithium (causing a fall in capacity), and also limits the power due to a decrease in porosity and usable surface area of the electrode, thus restricting the transfer of Li^+ ions across the electrode-electrolyte interface. An analogous surface film has also been reported to form at the cathode,[148] sometimes referred to as a solid permeable interphase (SPI) or cathode electrolyte interphase (CEI),[149] but this has been less extensively studied, and its impact on cell ageing is, therefore, not so well understood.

Lithium plating, where Li^+ ions are reduced to Li metal, is also another major cause of capacity loss,[150] as it depletes the inventory of usable lithium. Furthermore, Li metal reacts with the electrolyte to exacerbate its decomposition, thus lowering its conductivity, while also contributing to the SEI. Lithium plating also causes dendrites to form, which increases the probability of a short circuit. Inhomogeneity, poor mass balance, and geometric misalignment of the electrodes, all increase the risk of metal plating.[151]

Volume changes in the electrodes during repetitive Li^+ insertion/removal can cause mechanical disintegration,[57] which leads to particle contact loss that hinders the electronic pathway. In most severe cases, particle cracking occurs; this can be brought about by solvent molecules intercalating between graphite sheets, and can lead to active particle isolation.[152] Structural changes in the electrode bulk during cycling are particularly problematic for the cathode. For materials such as layered oxides, phase changes occur, which are accompanied by volume changes that distort the crystal lattice and cause mechanical stress over time.[153] Jahn-Teller distortion of certain transition metal elements, and cation exchange between Li and T_M, also have an effect.[154] This can lead to structural disordering, which can restrict the pathways for Li^+ ion diffusion. Transition metal dissolution from the cathode not only hinders the redox activity of this electrode, but T_M can also deposit on the surface of both the cathode and anode, increasing their impedances.[155] This is most prominent for manganese-containing materials, e.g. $LiMn_2O_4$.[156] Figure 1.19 illustrates some of the most commonly reported degradation mechanisms in Li-ion cells.

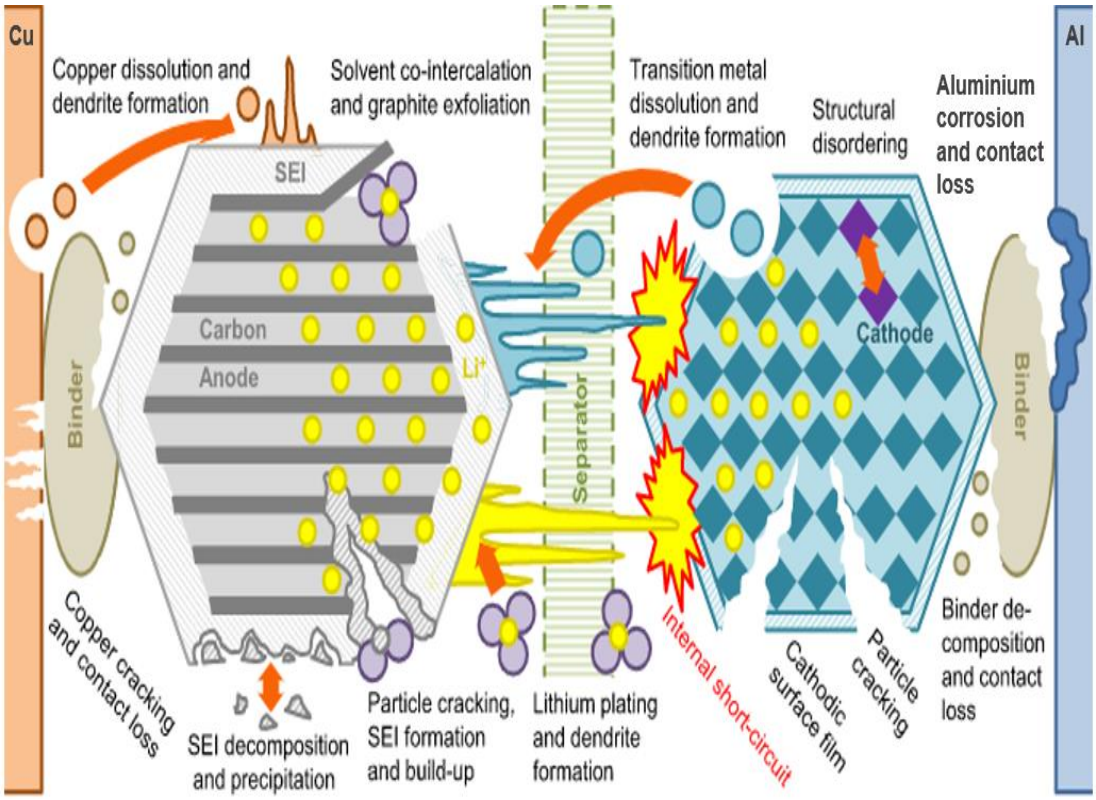

Figure 1.19 Schematic showing some of the known degradation mechanisms in a lithium-ion cell. Adapted from reference 152.

The inactive components of a battery also contribute to cell ageing. The binder can react with lithium in the anode to give LiF, which causes the binder to decay.[157] This in turn leads to degradation of the mechanical properties of the electrode, which causes a rise in cell impedance due to disruption of the electronic conduction network. Furthermore, lithium/active material particle isolation can occur due to binder breakdown, which leads to a drop in capacity.[158] At high voltages, oxidation of conductive carbon additives takes place, which also decreases the electronic conductivity of the electrode.[159] In addition to this, the current collector can corrode if it reacts with the electrolyte. This is particularly problematic for the copper current collector at the anode, which at a low enough cell voltage can be oxidised to Cu^{2+} ions. These ions then dissolve in the electrolyte and, when the voltage is raised again, plate onto the anode surface.[160] Furthermore, stress induced during cycling changes the structure of pores in the separator and leads to lower Li^+ ion mobility. This is caused primarily by dendrite growth, however, high temperatures can also

cause the softening of separators and the closing of their pores.[151] Electrolyte decomposition products may also deposit in them and hinder Li^+ ion diffusion.[161]

Many of the aforementioned ageing routes can be mitigated by careful selection of the materials, e.g. correct binder, active material, and operating the battery in optimal conditions, e.g. temperature, C-rate, and voltage window. High temperatures exacerbate electrolyte decomposition and cause the SEI to break down, as well as enhancing transition metal dissolution.[147] Low temperatures restrict Li^+ ion diffusion in the anode, which intensifies Li metal plating.[162] High C-rates increase the cell temperature and also cause lithium deposits because the transport rate of Li^+ ions from the electrolyte exceeds the insertion rate, resulting in lithium accumulating at the anode surface.[163] Good mass balance and geometric alignment of the electrodes is important to avoid the plating mechanism.[151] Avoiding fully charging and discharging cells has also proven optimal for prolonging the cycle life for Li-ion technology.[164] Too high a voltage can cause electrolyte decomposition and film formation on cathode particles,[165] as well as lithium plating,[166] while too deep a discharge can result in current collector corrosion.[160] It is also possible to pre-treat the electrodes and current collectors, as well as using electrolyte additives, to aid with SEI formation.[57] Doping of the cathode structures can help to mitigate phase changes, as well as tuning the voltage range they operate at.[153] Contaminants, in particular water, contributes to cell degradation. It reacts with the electrolyte salt $LiPF_6$ to form HF, which is very reactive, and can attack various active and passive components of the cell.[167] Therefore, preventing moisture uptake during cell assembly and cycling is hugely important.

While extensive research has taken place over the past few decades into the causes and effects of lithium-ion battery ageing, much is still unknown about the precise pathways that occur. The exact mechanisms of capacity/power fading, and their prevention are of great interest to the battery research community. While determining the causes of performance loss and cycle life limitation in sodium-ion batteries is also of the utmost importance with regards to realising their commercial potential, similar studies into studying the degradation (ageing) mechanisms of sodium-ion technology have yet to materialise to any great extent.

1.5 Impedance Spectroscopy of Batteries

1.5.1 Studying Performance Limiting Factors in Batteries

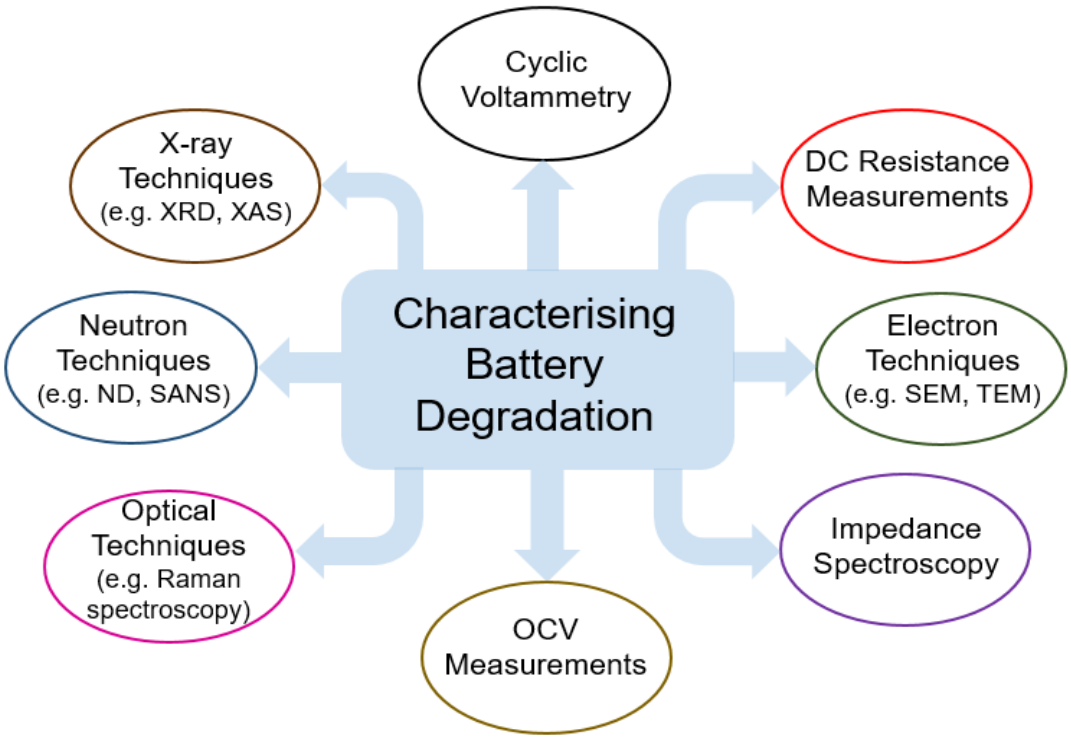

Figure 1.20 Some of the main characterisation techniques used to study battery ageing.

Evaluating ageing mechanisms in batteries is a difficult topic. Several attempts have been made, which vary in complexity and accuracy for separating effects. A summary of the main techniques used to characterise battery degradation is provided in Figure 1.20. These different strategies can be divided into those that take place either *ex situ* (outside the battery) or *in situ* (inside the battery). *Ex situ* techniques are also referred to as post-mortem analysis, as they are performed after the cell has been cycled and disassembled. The battery is deconstructed into its various parts and analysis (Raman spectroscopy, X-ray techniques, etc.) performed on the separate components.[168] It can be difficult to preserve the various parts of the cell 'intact', without contamination of the materials to be studied, and sample preparation prior to performing certain measurements such as SEM/TEM, may introduce artefacts into the results. Furthermore, destructive testing eradicates the ability to gather

information on dynamic processes that occur during battery operation, therefore curtailing its usefulness.

In situ techniques can be further divided into those that take place *ex operando* (outside the cell functioning) and *in operando* (taken during the cell functioning). Custom built *in situ* cells, needed for atomic force microscopy (AFM), neutron studies etc., normally require a specialist design, which diverges from a conventional coin, pouch cell setup, i.e. larger electrode geometry, a vacuum etc.[151] The compatibility between electrochemical cell designs and experimental setup may introduce features which affect the electrochemical performance, and, hence, impact degradation processes.

Cyclic voltammetry provides information about electrode polarisation curves that are of interest for characterising ageing effects.[169] However, the response is a composite of all electrochemical processes, and data analysis using this technique is, therefore, quite complex. Open circuit voltage measurements take place *ex operando*, as the cell must be paused from charging/discharging. OCV measurements are dependent upon the different degradation modes occurring inside the battery, and by developing a suitable model and diagnostic algorithm, may be used to extract important cell parameters, such as state of health.[152] However, OCV readings only give information on degradation of the thermodynamic behaviour of a cell and not the kinetic one. DC resistance measurements are able to provide information on a cell's kinetics by measuring the voltage drop in response to a load.[170] While this provides information on the total resistance inside the battery, it does not allow for a separation of the different individual resistive components, and, hence, allow the user to identify the problem interfaces and rate-limiting steps inside the cell.

Electrochemical impedance spectroscopy (EIS) is a non-destructive technique which provides a considerable amount of information in a relatively short space of time, while preserving integrity of the battery.[169] It allows *in operando* dynamic measurements during battery cycling as well as *ex operando* measurements at various states of charge and discharge. In EIS, a small AC signal is applied over a wide frequency range and the response measured (a more detailed explanation of the theory of impedance spectroscopy is given in Chapter II). As the measurement occurs across a wide frequency range, it enables the separation of different

components and processes within the cell, which operate on different timescales (Fig. 1.21). Furthermore, EIS is particularly sensitive to systems that contain several impedance elements, including bulk components and interfaces, which makes it well-suited to study a multi-component device such as a battery.[146]

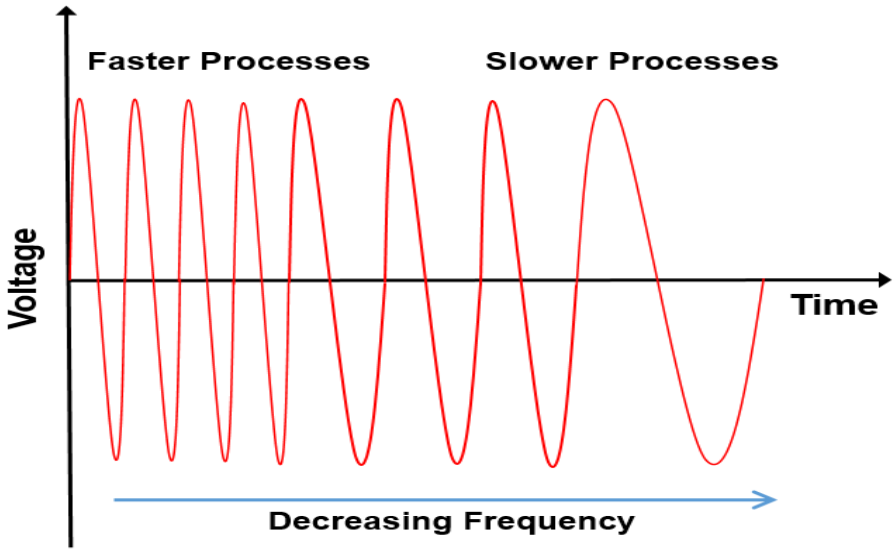

Figure 1.21 Impedance scan showing the separation of processes operating on different timescales.

Although the interpretation of collected EIS results is not always straightforward, the analysis of generated data may be aided through the use of models in the form of equivalent electrical circuits.[171] These help to assign different parts of the obtained impedance spectrum to different components and processes inside the electrochemical cell. As well as being used to analyse battery kinetics, electrochemical impedance spectroscopy can also extract important behavioural parameters.[171] An impedance measurement can be conducted at any point during a battery's lifetime and at any point during its (dis)charging cycle. The generated spectrum is dependent upon the state of health of the battery and its state of charge. Therefore, by performing EIS measurements for a battery at various predefined SoC and SoH values, it may be possible to deduce relationships between certain EIS parameters from equivalent circuits and the state of the cell. Thus, it may then be possible in future to estimate the SoC and SoH value of a battery from impedance spectroscopy measurements. All of the above makes EIS one of the most powerful techniques for studying performance limiting factors in batteries. As a result of this,

there have been several research studies conducted in this field, looking at different systems and setups for performing impedance measurements, as well as various analysis strategies examined for interpreting the results obtained.

1.5.2 Two-Electrode Impedance Studies

One of the earliest comprehensive reviews into impedance spectroscopy of batteries was by Huet in 1998.[172] This article investigated the relationship between the various impedance parameters encountered in the EIS spectra of lead-acid and nickel-cadmium batteries. While it was found that impedance testing was an effective method for detecting potentially problematic cells, the author concluded that further work was needed to accurately extract SoC and SoH values from measurements. One of the earliest works into impedance spectroscopy on high power lithium-ion batteries was performed by *Zhang et al.* in the year 2000.[173] This studied the capacity fade of Sony LCO/graphite cells, and noted the increase in the interfacial resistance at these electrodes during cycling. This work was the first full-cell study,[**] and followed on from previous papers which looked at $LiCoO_2$ and graphite electrodes separately (*vs.* a Li metal counter electrode).

More recently, in 2011, two highly cited papers have been published by the Sauer Group in Germany. In the first of these, tests were carried out on a commercial cylindrical 6.5 Ah high power Li-ion cell.[174] The cathode consisted of nickel-cobalt-aluminium and the anode, graphite. The influence of temperature (-30 – 50 °C) and SoC on the impedance response was investigated. The impedance spectra were found to consist of two major components (arcs), which increased in size at lower temperature. Furthermore, the low-frequency arc increased below 30% SoC, which the authors attribute to a combination of a rise in charge-transfer and diffusion resistance. The second publication follows on from the first and focuses on using these data for the modelling of impedance spectroscopy for high power LIBs.[175] Equivalent circuit models were developed and the estimated parameters from these used to predict the voltage from current, temperature and SoC. It is hypothesised that it is possible to use these battery models to predict vehicle range, battery lifetime etc.

[**] In this work, the term 'half-cell' refers to active material *vs.* either sodium or lithium metal, and 'full-cell' to *vs.* a non-metallic counter electrode.

One limitation to analysing two-terminal EIS data is that it can often be difficult to deconvolute impedance components that have similar time constants (*RC* products), and separate out the resistive contributions at each electrode.[176] Half-cell measurements can be used to study separately the impedances associated with the two electrodes but may not accurately reflect the processes occurring in a full-cell battery at different states of charge and discharge. An alternative strategy is the use of symmetric cells in which two cells are disassembled and the cathode of one is replaced with the anode of the other, and vice versa.[177,178]

Khalil Amine and co-workers at Argonne National Laboratory were some of the first researchers to look at these symmetric cell setups. In 2001, they took some 18650 (cylindrical) cells with a $LiNi_{0.8}Co_{0.2}O_2$/graphite chemistry, as well as some in-house built coin cells, and deconstructed and reassembled them to form symmetric cells.[177] These were in the fully charged state and their impedances were measured over time. The resistance at each electrode was found to increase with storage time, but to stabilise after around three weeks. The impedance at the cathode was found to be significantly greater than at the anode, which the authors attributed to an increase in the charge-transfer resistance. They also produced another paper using the same sort of experimental setup.[179] They reported in this that power fading for these stored symmetric cells was accelerated at greater SoC, and with a higher temperature.

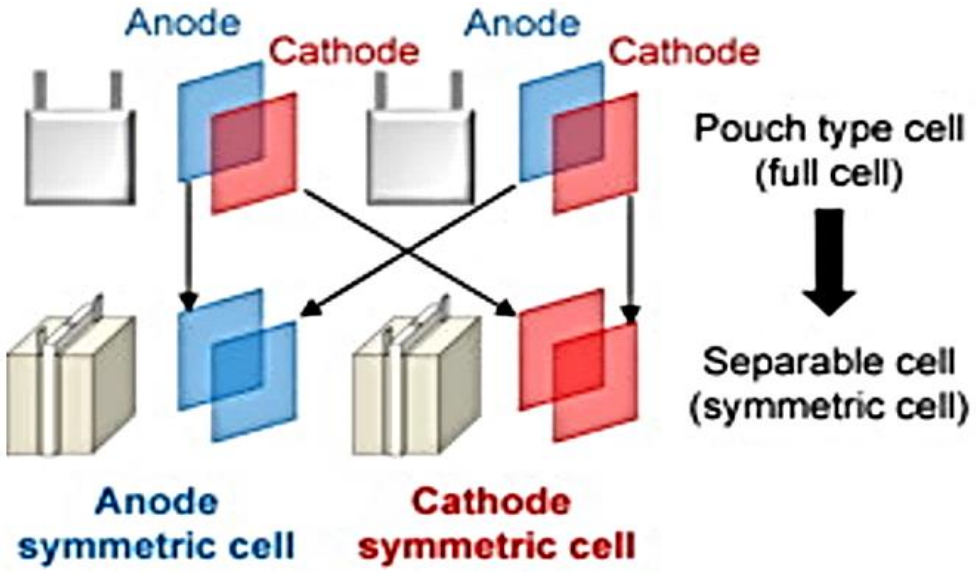

Figure 1.22 Schematic showing the preparation of symmetric pouch cells. Adapted from reference 178.

Later, researchers in Japan studied symmetric pouch cells.[178] These were developed from 5 Ah Li-ion (LCO/carbon) batteries consisting of 7 x 7 cm electrode sheets. The standard full-cells were first charged and discharged over two cycles, before being disassembled and symmetric cells constructed using a newly designed separable cell module (Fig. 1.22). These cells were also found to possess a larger cathode resistance compared with the anode. However, it was discovered that the process of fabricating the symmetric cells resulted in an artificial growth in certain impedances such as the charge-transfer resistance at the cathode. Gordon *et al.*, a few years later, studied modifications induced by the sample preparation protocol in symmetric cell work.[180] They found that impedance measurements are highly sensitive to the deconstruction and reassembly of the cells. They claim it is better to avoid washing/drying electrodes to preserve their interfaces and state of lithiation intact. Otherwise, a rinsing of the electrodes in dimethyl carbonate and a gentle drying is optimal.

Such approaches using symmetric cells are limited because they are unable to be charged and discharged in the same way as a fully functioning conventional battery. This means that the arduous process of disassembling and reassembling cells must therefore be carried out repeatedly, in order to gather information at different states of charge and states of health. Furthermore, as has been mentioned, the process of disassembling and reassembling cells is thought to possibly introduce additional artefacts/impedances, which may affect the validity of collected results.

1.5.3 Three-Electrode Impedance Studies

One way in which researchers have tried to circumvent the previous limitations of conventional two-electrode and symmetric cell EIS studies, is via a three-electrode setup. A three-electrode cell design incorporates a spectator reference electrode, which does not interfere with the cycling of the battery.[181] An example of one of the earlier setups is given in Figure 1.23. The battery is charged/discharged as usual, but as well as recording the impedance across the entire cell, the impedances of the cathode and anode can be individually measured separately against the reference. It is therefore possible to monitor how each electrode contributes to the overall impedance of the battery.

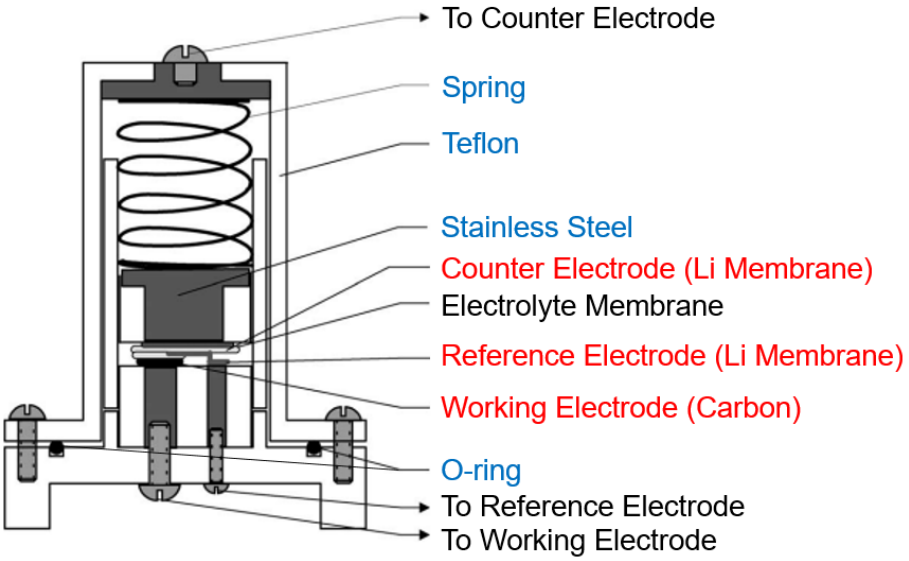

Figure 1.23 An example of a three-electrode test cell. Adapted from reference 181.

One of the earliest studies into this type of three-electrode setup was work performed by Nagasubramanian in the year 2000 on 18650 (cylindrical) cells.[182] This communication paper presents two- and three-electrode EIS results for commercial Sony cells at different temperatures between -40 and 35 °C. A Li reference electrode was inserted in the mandrel hole that runs along the length of the cell at the centre. This and a follow-up paper[183] were able to separate out the impedances of the two electrodes and determined the cathode resistance to dominate over the anode for these LIBs. Another highly cited study was performed in the year 2000 by Song *et al* on $LiCoO_2$/graphite batteries.[181] Three-electrode measurements were performed on purpose-built test cells (Fig. 1.23), as well as retrofitted commercial prismatic cells. This paper highlighted the advantage of using a three-electrode cell over half-cell (two-electrode) configurations, by showing a direct comparison. However, one limitation with the study was that a ground impedance correction had to be performed in order to get good agreement between the full-cell measurement and anode + cathode spectra.

Since these early studies, a number of different three-electrode configurations for lithium-ion batteries have been reported using a variety of cell types and reference electrodes.[184] Tarascon and co-workers tested various shapes, positions and types of reference electrodes to determine the most reliable and accurate configuration.[185] These results are displayed in the current *vs.* working potential plots in Figure 1.24.

The reference electrode needs to maintain a stable potential under prolonged and extensive testing and not interfere with the normal cell operation. Furthermore, the reference electrode should be non-polarisable and have a low internal resistance. Hence, in the graph below, a suitable reference electrode candidate should possess a vertical line. Therefore, lithium metal and lithium titanate (LTO, $Li_4Ti_5O_{12}$) meet this criteria, whereas silver has its voltage affected by current flow, and is therefore discounted. Other studies have favoured LTO over Li metal at high current densities,[186] as the latter is known to react with the electrolyte.[187]

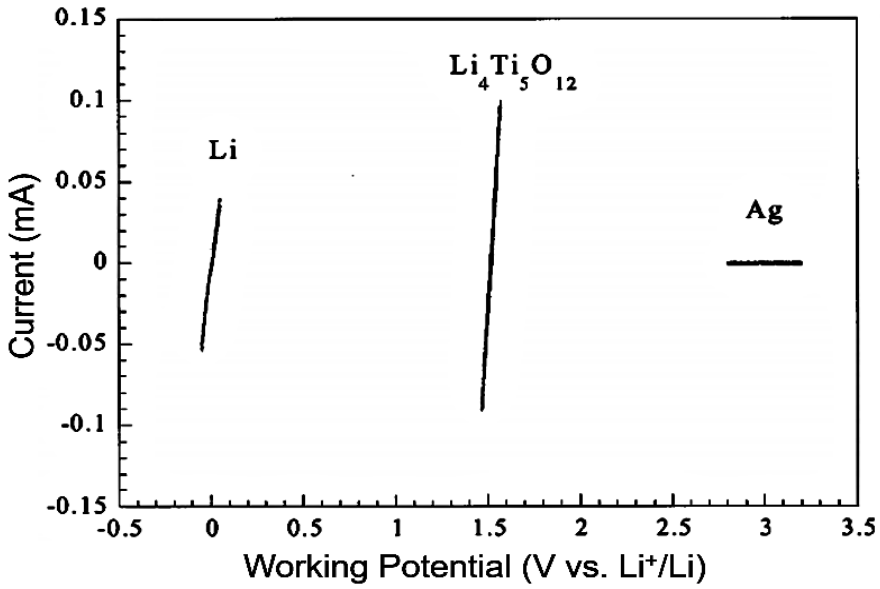

Figure 1.24 Polarisation curves at 0.2 mV s^{-1} for three different reference electrodes. Adapted from reference 185.

The study by Tarascon uses a plastic Li-ion battery with the LTO reference electrode sitting in the centre, directly between the two active electrodes. Impedance was followed as function of cycle number and storage time. When the validity of the measurement was checked, less than 5% difference was found between the sum of the half-cell impedance results and the two-electrode measurement in the real part (Z_{real}) of the spectrum and less than 10% difference in the imaginary region (Z_{imag}). Impedance is performed as a function of the electrode potential during the first (formation) cycle as well as a function of the number of charge-discharge cycles. The resistances and capacitances are quantified using equivalent circuits. The rate performance of the cell is said to be limited by the charge-transfer resistance at the cathode, whereas capacity loss during storage is mostly attributed to the negative

electrode and, more precisely, to the instability of its passivating layer. Another study by researchers in Taiwan a couple of years later used a similar three-electrode plastic cell configuration on 750 mAh LCO/mesocarbon microbead (MCMB) batteries.[188] The authors claim that in a fully charged battery the main contribution to the resistance comes from the SEI of the anode; whereas, in a fully discharged state, the contribution comes from the charge-transfer resistance at the cathode. SEM and energy dispersive X-ray spectroscopy (EDX) were also performed to complement the impedance results.

One of the main issues with early three-electrode EIS studies is that few checked the validity of the experimental setup, through summing the individual impedances of the cathode and anode, and comparing the combined spectra with the impedance of the full-cell.[189] This is a significant omission as three-electrode impedance measurements may suffer from measurement artefacts associated with distortions caused by electrical/electrochemical and geometrical asymmetry in the experimental setup. These effects have been detected and reported by several authors in the field over the years.[190,191]

Much research into the origin of these impedance artefacts, and strategies for overcoming them, has been performed at the Karlsruhe Institute of Technology (KIT), in Germany, over the past decade. In a paper dating back to 2012,[192] researchers there claimed that geometrical asymmetry in three-electrode impedance measurements is created by misalignment of the cathode and anode, which affects the reference electrode potential. They assert this results in quantitative scaling factors (shifting) of the impedance response for the two electrodes. Electrochemical asymmetry is due to different kinetics at each electrode, and can lead to inductive artefacts. Both geometrical and electrochemical asymmetries result in an inhomogeneous electrolyte current density at the reference electrode, which may be responsible for distortions in the measured impedance spectra, e.g. cross contamination of the electrode responses.[193] These may show up as additional artificial components in the impedance spectrum. An example of geometrical and electrochemical asymmetry in a three-electrode cell with identical (symmetric) electrodes is displayed in Figure 1.25. The impedance response of each electrode is

shifted relative to each other, and there is evidence of an inductive loop at high frequency for electrode 2, and a second artificial semi-circle for electrode 1

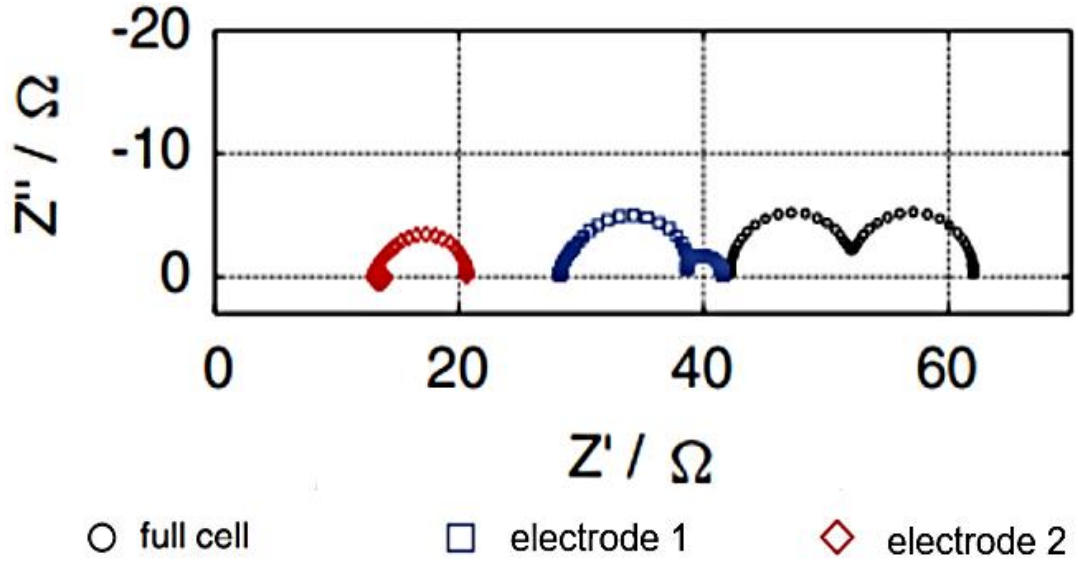

Figure 1.25 Simulated impedance spectra for a three-electrode cell possessing both geometrical and electrochemical asymmetry. Both the cathode and anode are identical (the cell is symmetric). Adapted from reference 192.

Care must be taken, therefore, to ensure that the design of the battery does not affect the cell performance and electrode impedances.[194] It is important to have good geometrical alignment of the two electrodes, with the reference equidistant between the two. Keeping the electrolyte and separator resistances low is also thought to help. The researchers at KIT used finite element modelling extensively to evaluate the reliability of different three-electrode setups.[193,195] They have investigated how the shape and position of the reference electrode may affect the impedance results, as well as the geometry of the cell setup and location of the reference.

The most popular three-electrode cell geometries are point-,[196] wire-[197] or ring-type.[198] A point-type reference electrode is a small piece of, say, Li metal for Li-ion batteries, which is placed away from the centre of the cell. A wire-type reference is similar to the point-type but extends within the electrolyte into the centre of the cell. A ring-type, often utilised in coin cells, surrounds the centre of the battery. Some examples of the different types of three-electrode cell setups used are displayed in Figure 1.26.[193,194,199]

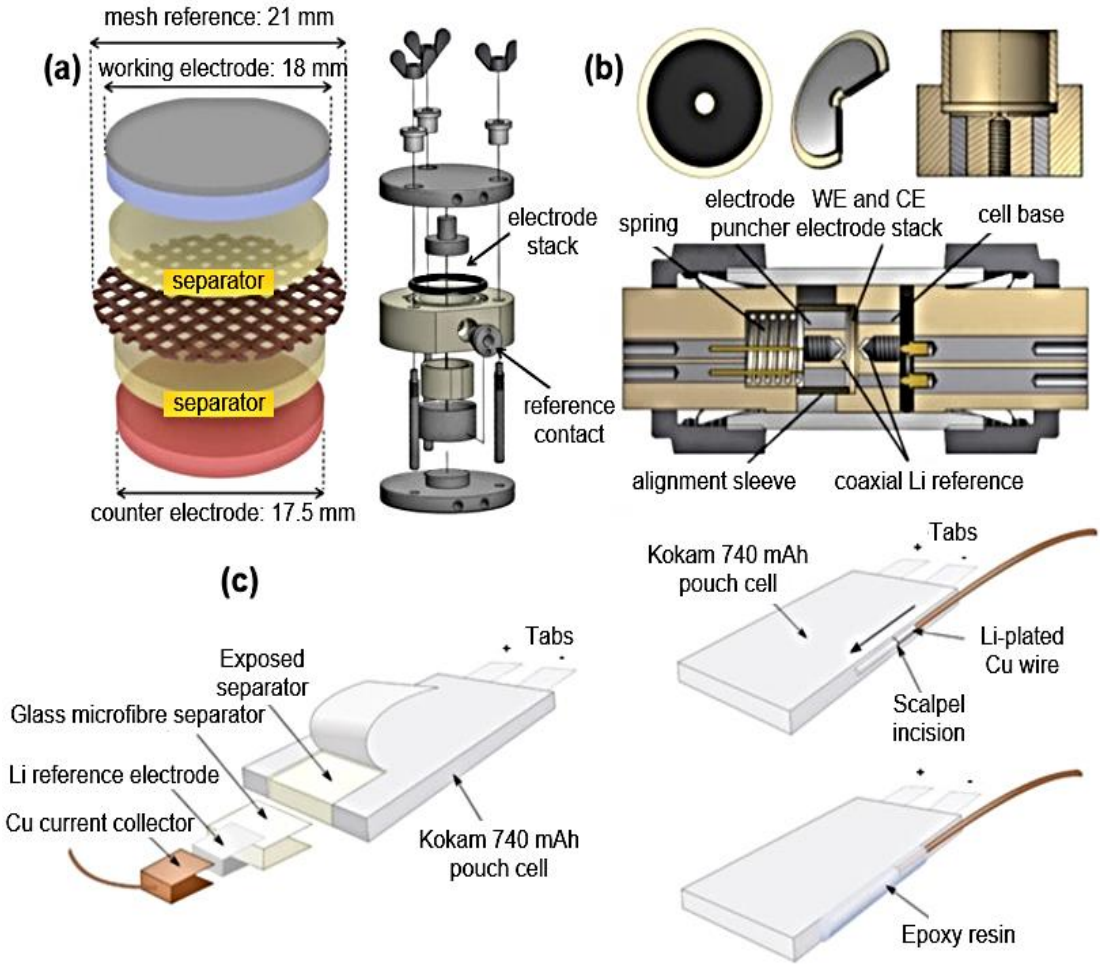

Figure 1.26 Some of the different three-electrode cell designs: (a) coin cell, where a mesh reference electrode is placed between two separators;[193] (b) coaxial cell developed from a modified Swagelok;[194] (c) commercial pouch cells retrofitted with a third reference electrode.[199] Adapted from references 193, 194 and 199.

The coin cell in (a) used a bespoke mesh reference electrode, in place of a more conventional type.[193] Researchers at KIT compared a range of reference electrode geometries and found that this design gave the largest potential for error-free EIS measurements. The cathode is NMC, lithium metal as the anode, and LTO as the reference. The electrochemical and geometrical asymmetries are negligible because the mesh is efficient at measuring the potential between the electrodes, where the current distribution is homogeneous. However, the greater surface area of the mesh creates multiple transport paths which leads to an additional polarisation process within the cell and can cause distortions at certain frequencies.

The design in (b) was developed to overcome limitations with the imprecise electrode alignment and an asymmetric reference electrode geometry of Swagelok

cells.[194] The cell used lithium iron phosphate and lithium metal. Typically, in a three-electrode Swagelok cell (also known as a T-cell), the reference electrode contacts the electrolyte/separator at its outer rim. The reference voltage is susceptible to fluctuation under changing current, such as during impedance measurements, and can lead to a distortion of data: artificial loops are often seen in the impedance response. In the design used by these authors, the reference electrode is moved to a coaxial position in combination with precise alignment of the electrode stack. This led to improved performance, but the measurements were still limited, particularly in the high frequency region.

In design (c), a commercial pouch cell was retrofitted with a reference electrode, in order to monitor the behaviour of the individual positive and negative electrodes, using two different methods: "patch" and "wire".[199] The "patch" method, where a U-shaped piece of Li metal encases the electrode stack, lead to significant disruption in the battery structure and to deterioration in cell performance. However, the "wire" method, where a Li-plated Cu wire was inserted down one side of the pouch, gave a performance close to that of a conventional two-electrode cell in terms of capacity and voltage. However, this design was not tested for EIS measurements.

Recently, a paper by Petr Novak's group attempted to address the issues with accurate and reliable three-electrode measurements: cell geometry, electrode arrangement, and having one electrode with a much higher impedance than the other.[200] The authors came up with an in-house cell design (Fig. 1.27) to circumvent this, which uses ring electrodes arranged concentrically around a reference electrode. The reliability of the impedance spectra was confirmed by using symmetric electrodes, which gave reproducible and overlapping responses. However, the long-term cycling stability is hindered by the O-rings used, which are thought to swell with the electrolyte.

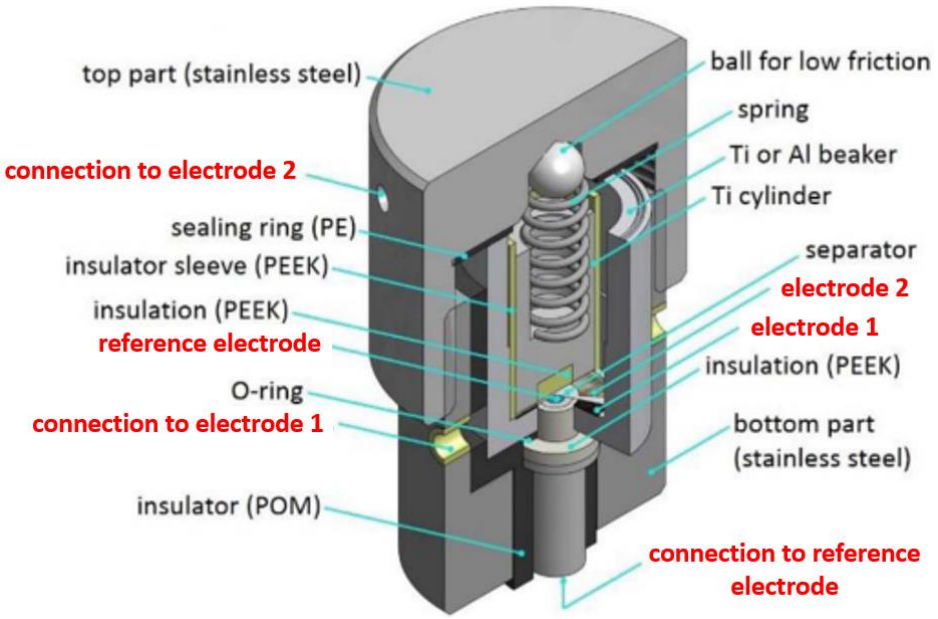

Figure 1.27 Drawing of a three-electrode EIS cell built for ring electrodes aligned concentrically, with a reference electrode in the centre. Adapted from reference 200.

Many other papers over the years have dealt with trying to assign the different components in the impedance response to various processes inside the battery, with varying successes.[201–203] A study by Michel Armand and co-workers used commercial 5.7 Ah LMO/graphite pouch cells taken from an electric vehicle.[204] A three-electrode configuration is fabricated by retrofitting an LTO reference electrode into the cell. EIS measurements are performed at different SoC and SoH. The authors claim that the high-frequency response in the impedance spectrum reflects porosity effects and the graphite particles–composite matrix electric transfer. The SEI layer and charge-transfer phenomena are thought to be in the medium and medium to low frequency domains respectively, and their impedance contributions depend on the Li content of the graphite particles.

The most recent progress in this field has been made by Hubert Gasteiger's group since 2017. They developed a general transmission line equivalent circuit model to analyse the impedance of a high-voltage $LiNi_{0.5}Mn_{1.5}O_4$ (LNMO) cathode.[205] A full-cell Swagelok setup (*vs.* graphite) is used with a gold wire micro-reference for three-electrode impedance measurements in both, non-blocking conditions (where charge-transfer reactions are able to occur occur) at a potential of 4.4 V, and in a blocking configuration achieved at 4.9 V. This is performed over 85 cycles at 40 °C. The

authors claim a superior equivalent circuit to conventional approaches and an impedance analysis strategy which enables *in situ* quantification of the cycle dependent charge-transfer, contact, and pore resistances, over the course of extended charge/discharge cycling. From follow-up studies,[206] they assert that the origin of the dominating high-frequency semi-circle is not related to the charge-transfer or surface film resistance, but to the contact resistance between the cathode and the current collector.

In a separate paper by the same group, the authors use their three-electrode Swagelok cell setup to measure the anode impedance at non-blocking conditions (10% SOC) and blocking conditions (0% SOC) in a graphite/LNMO full-cell.[207] By simultaneously fitting EIS spectra in blocking and non-blocking conditions using a general transmission line model, the anode impedance is able to be deconvoluted into contributions of a) the separator resistance, b) the charge-transfer resistance, and c) the ionic contact resistance evolving at the separator/anode electrode interface. They propose that the main contributor to a rising anode impedance is the ionic contact resistance. It is claimed that this is most likely caused by manganese dissolution from the high-voltage cathode (LNMO), as the same phenomenon is not detected for an LFP cathode.

1.5.4 Beyond Lithium-Ion Impedance Studies

While numerous studies have taken place into using impedance spectroscopy to probe the performance limiting factors in lithium-ion batteries, there has been very little research performed to date on 'beyond lithium' technology. A paper published in 2010 looked at how the EIS spectra changed for Li-air batteries with cycling, and how this was linked to capacity fade.[208] It was found that a build-up of discharge products decreases the porosity of the cathode, which in turn increases the cell resistance.

Other papers have looked at impedance growth in lithium-sulfur (Li-S) batteries. Figure 1.28 shows the schematic for sulfur particles in the cathode prior to (a), and after (b), being reduced.[209] By analysing the changes in impedance spectra as a function of temperature and DoD, an equivalent circuit model was proposed (c). The

resistance R_{el} is the electrolyte, R_{bulk} is the contact resistance in the bulk of the electrode, and R_{ct} represents the charge-transfer resistance. The terms CPE_{dl} and CPE_{diff} refer to the constant phase elements of the electrode double layer and Li^+ ion diffusion respectively. The authors suggest that the middle-frequency impedance component, which is attributed to the charge-transfer resistance, is the most significant factor in the capacity fade of these Li-S batteries, a claim which has since been supported by other papers.[210]

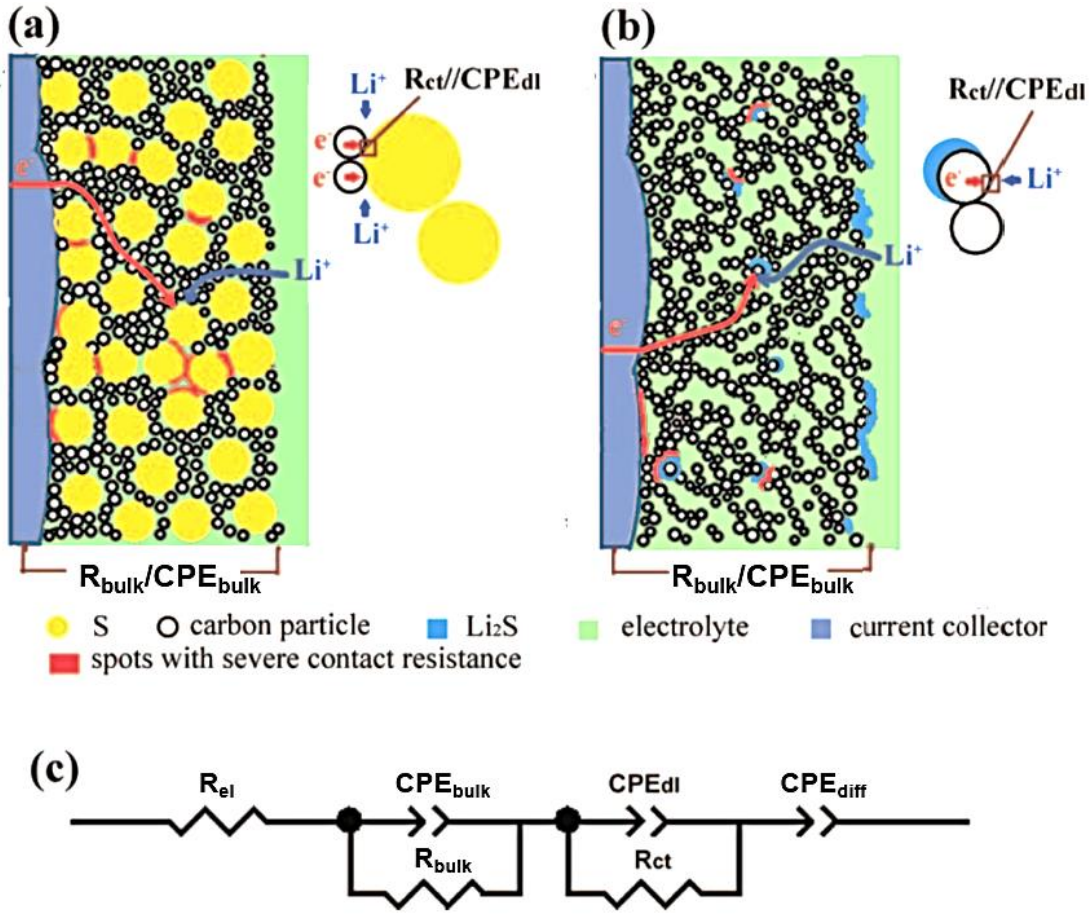

Figure 1.28 Schematic of physical/chemical processes involved in the cathode of a lithium-sulfur battery: (a) sulfur particles prior to being reduced; (b) sulfur particles after being reduced; (c) the proposed equivalent circuit for the lithium-sulfur cell. Adapted from reference 209.

Reports of impedance measurements performed on sodium-ion batteries in the literature are relatively scarce. The vast majority of these have been half-cell measurements to study the kinetics of individual cathode/anode materials, rather than trying to identify ageing mechanisms in full-cell Na-ion batteries. A paper by Park *et*

al. in 2013[211] outlined a new sodium-ion cathode material, $Na_{1.5}VPO_{4.8}F_{0.7}$, with an energy density of ~ 600 Wh kg^{-1}, and ~ 84% capacity retention after 500 cycles. Impedance spectroscopy showed that the charge-transfer resistance in the electrochemical half-cell decreased with decreasing Na content (Fig. 1.29), which the authors claimed suggested that the reaction kinetics was rapidly improved as more Na vacancies were generated in the structure. Researchers in the US have also investigated the transport properties and interfacial kinetics of P2- type layered oxide materials $Na_{2/3}[Ni_{1/3}Ti_{2/3}]O_2$ and $Na_{2/3}[Ni_{1/3}Mn_{1/3}Ti_{1/3}]O_2$ using: DC conductivity, potentiostatic intermittent titration technique (PITT), and impedance spectroscopy.[212] Due to its faster ionic/electronic transport in the pristine/intercalated states, and faster interfacial kinetics, the manganese-doped material was found to exhibit an improved rate performance.

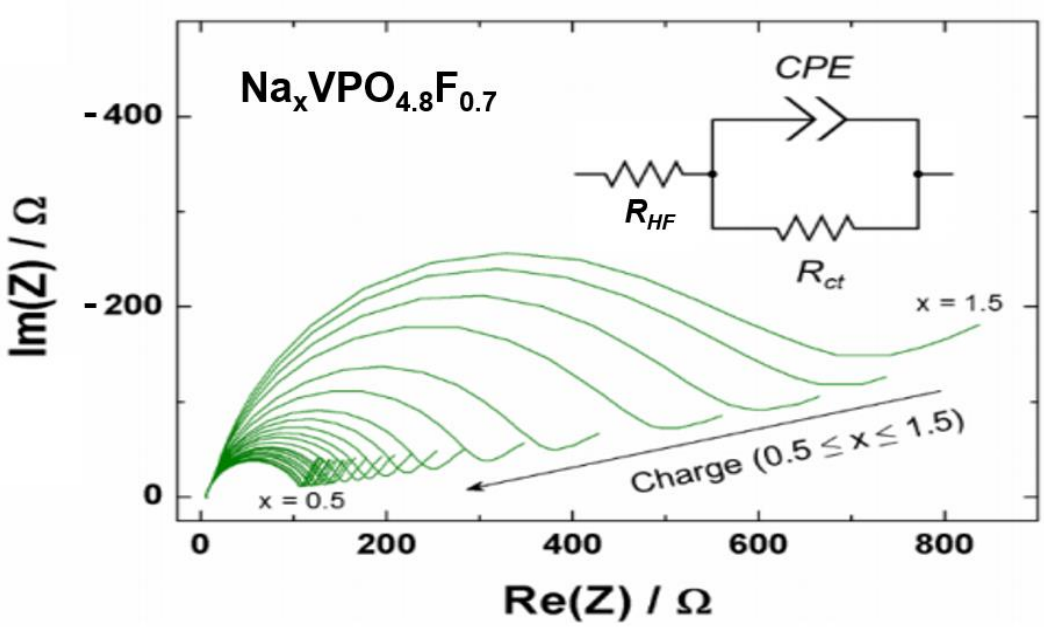

Figure 1.29 The evolution of EIS spectra as the $Na_xVPO_{4.8}F_{0.7}$ *vs.* sodium metal half-cell is charged. The size of the arc reduces with decreasing Na content. The inset shows the equivalent circuit for the fitting of the EIS spectra. R_{HF}, R_{ct} and *CPE* represent the high frequency resistance, charge-transfer resistance, and constant phase element, respectievly. Adapted from reference 211.

More recently, in 2017, a paper by the Goodenough Group aimed to address the large interfacial resistance that occurs in all solid-state Na-ion batteries between the cathode and the electrolyte by replacing a NASICON material ($Na_3Zr_2(Si_2PO_{12})$) with a plastic-crystal (Fig. 1.30).[213] $Na_3V_2(PO_4)_3$ was used as the cathode and

sodium metal as the anode. Resistances were evaluated by EIS, and equivalent electrical circuits used to divide the total cell resistance into contributions from the electrolyte, cathode, and anode. It was found from impedance measurements that addition of the plastic-crystal electrolyte into the cathode significantly reduces interfacial resistances on the cathode side, hence, suggesting an improved performance.

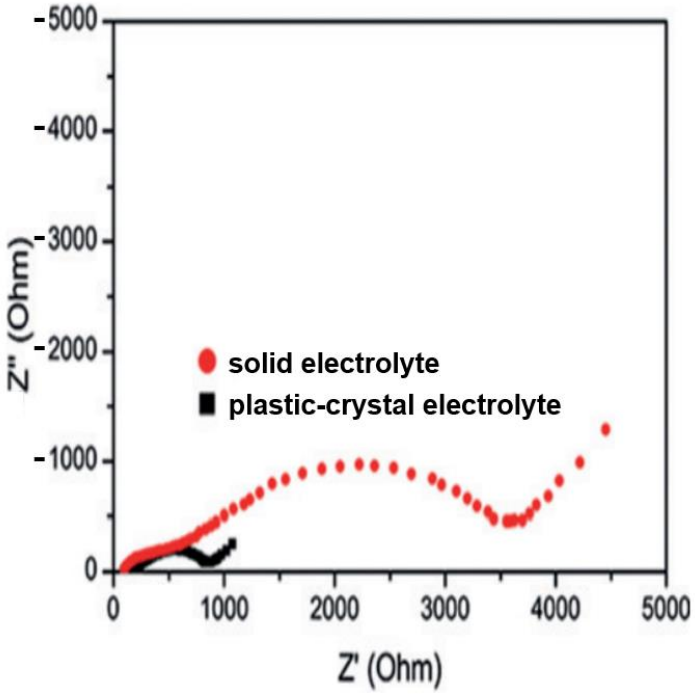

Figure 1.30 The initial EIS profiles of solid-state cells with the $Na_3Zr_2(Si_2PO_{12})$ solid electrolyte particles or the plastic-crystal electrolyte in the cathode. Data shows a reduced resistance for when a plastic-crystal electrolyte is used. Adapted from reference 213.

In 2018, researchers in Japan utilised a symmetric cell approach to study the $Na_2FeP_2O_7$ cathode in temperatures ranging from 25 to 90 °C using an ionic liquid electrolyte.[214] They used equivalent circuits to divide up the different resistive components inside the cell, and claimed that improvements in rate capability at increased temperature originated from a decrease in the charge-transfer resistance. However, importantly, these studies did not employ a three-electrode cell design, which would have allowed for a more accurate assignment of the separate parts of the impedance spectrum to different components and processes inside the cell.

1.6 Aims

To date, layered oxides have demonstrated the greatest potential, and received the most attention, as cathodes for sodium-ion batteries. Of these, the mixed phase class of materials have shown particular promise, but are relatively unexplored. In particular, it is not well understood how the structure and properties of these lead to an enhanced electrochemical performance over conventional single phase materials.

Electrochemical impedance spectroscopy is a grossly undervalued technique for the characterisation of Na-ion batteries. The electrical properties of the active cathode materials have not been extensively studied, even though they are likely to play an important role in the overall cell performance. This has been particularly overlooked for the promising mixed phase systems, despite these materials possessing a unique complex structure which requires unravelling. Full-cell impedance measurements also offer a useful tool for identifying electrochemical processes inside batteries and understanding the sources of capacity fading and cell degradation. Crucially, three-electrode measurements afford a separation of the different components at each electrode, which allows for greater analysis and, hence, a better understanding. Previous EIS studies for lithium-ion batteries fail to check the validity of the experimental setup, and also do not plot data using a wide range of different formalisms, thus limiting their interpretation and usefulness.

Using impedance spectroscopy, with in-depth analysis, to investigate the electrical properties of mixed phase layered sodium-ion cathodes, from raw active material to their performance in a full battery, is a previously unexplored area, which will be addressed in this work. The aim of this thesis is to identify and overcome degradation mechanisms in layered oxide sodium-ion cells. This includes two major objectives:

(i) To better understand the structure-composition-properties-performance relationship in layered oxide sodium-ion cathodes (chapters III-IV).

(ii) To use three-electrode impedance spectroscopy to determine the performance limiting factors in prototype commercial Na-ion batteries (Chapters V-VII).

1.7 References

1 International Renewable Energy Angency, *Electricty Storage and Renewables: Costs and Markest to 2030*, IRENA, Abu Dhabi, 2017.

2 Avicenne Energy, Worldwide Rechargeable Battery Market 2019-2030, Avicenne, Paris, 2019.

3 K. Mizushima, P. C. Jones, P. J. Wiseman and J. B. Goodenough, *Mater. Res. Bull.*, 1980, **15**, 783–789.

4 Y. Meesala, A. Jena, H. Chang and R. S. Liu, *ACS Energy Lett.*, 2017, **2**, 2734–2751.

5 G. Zubi, R. Dufo-López, M. Carvalho and G. Pasaoglu, *Renew. Sustain. Energy Rev.*, 2018, **89**, 292–308.

6 D. Deng, *Energy Sci. Eng.*, 2015, **3**, 385–418.

7 J.-Y. Hwang, S.-T. Myung and Y.-K. Sun, *Chem. Soc. Rev.*, 2017, **46**, 3529-3614.

8 J. B. Robinson, D. P. Finegan, T. M. M. Heenan, K. Smith, E. Kendrick, D. J. L. Brett and P. R. Shearing, *J. Electrochem. En. Conv. Stor.*, 2018, **15**, 011010(1)-011010(9).

9 P.K. Nayak, L. Yang, W. Brehm and P. Adelhelm, *Angew. Chem. Int. Ed.*, 2018, **57**, 102-120.

10 Green Car Congress, *Faradion demonstrates proof-of-concept sodium-ion electric bike*, https://www.greencarcongress.com/2015/05/20150515-faradion.html, (accessed August 2020).

11 J. Newman and K. E. Thomas-Alyea, *Electrochemical Systems*, John Wiley & Sons, Hoboken, 2004.

12 J. Gao, S.-Q. Shi and H. Li, *Chin. Phys. B.*, 2016, **25**, 018210(1)-018210(24).

13 C. Liu, Z. G. Neale and G. Cao, *Materials Today*, 2016, **19**, 109-123.

14 W. R. Browne, *Electrochemistry*, Oxfrod University Press, Glasgow, 2018.

15 J. B. Goodenough and K. S. Park, *J. Am. Chem. Soc.*, 2013, **135**, 1167–1176.

16 J. B. Goodenough and Y. Kim, *Chem. Mater.*, 2010, **22**, 587–603.

17 A. Manthiram, in *Lithium Batteries: Science and Technology*, ed. G.-A. Nazri and G. Pistoia, Springer, 2003, ch. 1, pp. 3-41.

18 Q. F. Yuan, F. Zhao, W. Wang, Y. Zhao, Z. Liang and D. Yan, *Electrochim. Acta*, 2015, **178**, 682–688.

19 V. Pušara, A. Mulaosmanović and A. Fazlić, *Battery Internal Resistance Measurement - AC Method Phase Calculation Algorithm*, http://www.amforum.org/site/journal/2017/resAC.pdf, (accessed September 2020).

20 Energizer, *Energizer Technical Bulletin: Battery Internal Resistance*, https://data.energizer.com/PDFs/BatteryIR.pdf, (accessed July 2020).

21 B. Saha and K. Goebel, presented in part at the Annual Conference of the Prognostics and Health Management Society, 2009, San Diego, October, 2009.

22 J. Kasnatscheew, U. Rodehorst, B. Streipert, S. Wiemers-Meyer, R. Jakelski, I. C. Laskovic and M. Winter, *J. Electrochem. Soc.*, 2016, **163**, A2943-A2950.

23 M. A. Salam, *Electromagnetic Field Theories for Engineering*, Springer, Singapore, 2014.

24 R. G. Compton and G. H. Sanders, *Electrode Potentials*, Oxford University Press, New York, 1996.

25 A. C. Fisher, *Electrode Dynamics*, Oxford University Press, New York, 1996.

26 J. B. Goodenough, *Acc. Chem. Res.*, 2013, **46**, 1053–1061.

27 C. Julien, A. Mauger, K. Zaghib and H. Groult, *Inorganics*, 2014, **2**, 132–154.

28 L.-X. Yuan, Z.-H. Wang, W.-X. Zhang, X.-L. Hu, J.-T. Chen, Y.-H. Huang and J. B. Goodenough, *Energy Environ. Sci.*, 2011, **4**, 269-284.

29 J.-K. Park, *Principles and Applications of Lithium Secondary Batteries*, John Wiley & Sons, Weinheim, 2012.

30 E. Antolini, *Solid State Ionics*, 2004, **170**, 159–171.

31 R. J. Clément, Z. Lun and G. Ceder, *Energy Environ. Sci.*, 2020, **13**, 345–373.

32 J. Zhang, L. Zhang, H. Liu, A. Sun and R.-S. Liu, *Electrochemical Technologies for Energy Storage and Conversion*, John Wiley & Sons, Singapore, 2011.

33 H.-L. Guo, H.-F. Lin, Y.-C. Yang, C.-H. Cheng, Y.-R. Tsai and F.-M. Wang, *J. Solid State Electrochem.*, 2020, **160**, 1-11.

34 V. K. Mehta and R. Mehta, *Principle of Electrical Engineering and Electronics*, 2006, S. Chand & Company Pvt. Ltd., New Delhi, 1996.

35 A. J. Moulson and J. M. Herbert, *Electroceramics : materials, properties, applications*, John Wiley & Sons Chichester, 2003.

36 R. P. Deshpande, *Capacitors: Technology and Trends*, Tata McGraw Hill, New Delhi, 2012.

37 P. Simon, T. Brousse and F. Favier, *Supercapacitors Based on Carbon or Pseudocapacitive Materials*, John Wiley & Sons, London, 2017.

38 Woodbank Communications Ltd., *Electropaedia: Battery State of Charge Determination*, https://www.mpoweruk.com/soc.htm, (accessed September 2020).

39 W. Diao, S. Saxena, B. Han and M. Pecht, *Energies*, 2019, **12**, 2910(1)-2910(9).

40 Q. Liu, X. Su, D. Lei, Y. Qin, J. Wen, F. Guo, Y. A. Wu, Y. Rong, R. Kou, X. Xiao, F. Aguesse, J. Bareño, Y. Ren, W. Lu and Y. Li, *Nat. Energy*, 2018, **3**, 936–943.

41 C. Nan, J. Lu, C. Chen, Q. Peng and Y. Li, *J. Mater. Chem.*, 2011, **21**, 9994-9996.

42 A. Swiderska-Mocek, *J. Solid State Electrochem.*, 2014, **18**, 1077–1085.

43 D. Andre, S.-J. Kim, P. Lamp, S. F. Lux, F. Maglia, O. Paschos and B. Stiaszny, *J. Mater. Chem. A*, 2015, **3**, 6709-6732.

44 A. Zablocki, *Fact Sheet: Energy Storage*, Environmental and Energy Study Institute, Washington DC, 2019.

45 M. D. Slater, D. Kim, E. Lee and C. S. Johnson, *Adv. Funct. Mater.*, 2013, **23**, 947–958.

46 The Economist, *Clean energy: An increasingly precious metal* | The Economist, https://www.economist.com/business/2016/01/14/an-increasingly-precious-metal, (accessed June 2020).

47 N. Yabuuchi, K. Kubota, M. Dahbi and S. Komaba, *Chem. Rev.*, 2014, **114**, 11636–11682.

48 Chemistry World, *A battery technology worth its salt*, https://www.chemistryworld.com/features/a-battery-technology-worth-its-salt/3010966.article#/, (accessed September 2020).

49 Faradion Ltd., *Technology Benefits: Cost Savings*, https://www.faradion.co.uk/technology-benefits/cost-savings/, (accessed September 2020).

50 X. Xia and J. R. Dahn, *Electrochem. Solid-State Lett.*, 2012, **15**, A1-A4.

51 H. Pan, Y.-S. Hu and L. Chen, *Energy Environ. Sci.*, 2013, **6**, 2338-2360.

52 N. Yabuuchi, M. Kajiyama, J. Iwatate, H. Nishikawa, S. Hitomi, R. Okuyama, R. Usui, Y. Yamada and S. Komaba, *Nat. Mater.*, 2012, **11**, 512-517.

53 E. Peled, *J. Electrochem. Soc.*, 1979, **126**, 2047-2051.

54 D. Guyomard and J. Tarascon, *Adv. Mater.*, 1993, **38**, 1221-1231.

55 M. Pinson and M. Bazant, *J. Electrochem. Soc.*, 2013, **160**, A243-A250.

56 H. J. Ploehn, P. Ramadass and R. E. White, *J. Electrochem. Soc.*, 2004, **151**, A456-A462.

57 J Vetter, P. Novák, M. R. Wagner, C. Veit, K.-C. Möller, J. O. Besenhard, M. Winter, M. Wohlfahrt-Mehrens, C. Vogler and A. Hammouche, *J. Power Sources*, 2005, **147**, 269–281.

58 V. A. Agubra and J. W. Fergus, *J. Power Sources*, 2014, **268**, 153–162.

59 S. Komaba, W. Murata, T. Ishikawa, N. Yabuuchi, T. Ozeki, T. Nakayama, A. Ogata, K. Gotoh and K. Fujiwara, *Adv. Funct. Mater.*, 2011, **21**, 3859–3867.

60 K. Tang, L. Fu, R. J. White, L. Yu, M.-M. Titirici, M. Antonietti and J. Maier, *Adv. Energy Mater.*, 2012, **2**, 873–877.

61 D. A. Stevens and J. R. Dahn, *J. Electrochem. Soc.*, 2000, **147**, 1271-1273.

62 D. Kundu, E. Talaie, V. Duffort and L. F. Nazar, *Angew. Chemie Int. Ed.*, 2015, **54**, 3431–3448.

63 Y. Wen, K. He, Y. Zhu, F. Han, Y. Xu, I. Matsuda, Y. Ishii, J. Cumings and C. Wang, *Nat. Commun.*, 2014, **5**, 4033(1)-4033(10).

64 Y.-X. Wang, S.-L. Chou, H.-K. Liu and S.-X. Dou, *Carbon*, 2013, **57**, 202–208.

65 D. Chao, P. Liang, Z. Chen, L. Bai, H. Shen, X. Liu, X. Xia, Y. Zhao, S. V. Savilov, J. Lin and Z. X. Shen, *ACS Nano*, 2016, **10**, 10211–10219.

66 M. Dahbi, M. Fukunishi, T. Horiba, N. Yabuuchi, S. Yasuno and S. Komaba, *J. Power Sources*, 2017, **363**, 404–412.

67 H. Hou, M. Jing, Y. Yang, Y. Zhang, W. Song, X. Yang, J. Chen, Q. Chen and X. Ji, *J. Power Sources*, 2015, **284**, 227–235.

68 P. Zhang, F. Qin, L. Zou, M. Wang, K. Zhang, Y. Lai and J. Li, *Nanoscale*, 2017, **9**, 12189–12195.

69 Y. Liu, J. Liu, M. Hou, L. Fan, Y. Wang and Y. Xia, *J. Mater. Chem. A*, 2017, **5**, 10902–10908.

70 A. Ponrouch, D. Monti, A. Boschin, B. Steen, P. Johansson and M. R. Palacín, *J. Mater. Chem. A*, 2015, **3**, 22–42.

71 J. Chen, Z. Huang, C. Wang, S. Porter, B. Wang, W. Lie and H. K. Liu, *Chem. Commun. Chem. Commun*, 2015, **51**, 9809–9812.

72 T. D. Hatchard and M. N. Obrovac, *J. Electrochem. Soc.*, 2014, **161**, 1748–1752.

73 A. Bhide, J. Hofmann, A. Katharina Dürr, J. Janek and P. Adelhelm, *Phys. Chem. Chem. Phys.*, 2014, **16**, 1987–1998.

74 A. Ponrouch, E. Marchante, M. Courty, J.-M. Tarascon and M. R. Palacín, *Energy Environ. Sci.*, 2012, **5**, 8572-8583.

75 A. Ponrouch, A. Rémidedry, D. Monti, A. E. Demet, J. M. Ateba Mba, L. Croguennec, C. Masquelier, P. Johansson and M. R. Palacín, *Energy Environ. Sci.*, 2013, **6**, 2361-2369.

76 D. Monti, E. Jónsson, M. R. Palacín and P. Johansson, *J. Power* Souces, 2014, **245**, 630-636.

77 H. C. Chen, J. Patra, S. W. Lee, C. J. Tseng, T. Y. Wu, M. H. Lin and J. K. Chang, *J. Mater. Chem. A*, 2017, **5**, 13776–13784.

78 K. Kubota and S. Komaba, *J. Electrochem. Soc.*, 2015, **162**, A2538–A2550.

79 G. X. Wang, S. L. Bewlay, K. Konstantinov, H. K. Liu, S. X. Dou and J.-H. Ahn, *Electrochim. Acta*, 2004, **50**, 443–447.

80 S. Ong, V. Chevrier, G. Hautier and A. Jain, *Energy & Environ. Sci.*, 2011, **4**, 3680-3688.

81 P. Barpanda, J.-N. Chotard, N. Recham, C. Delacourt, M. Ati, L. Dupont, M. Armand and J.-M. Tarascon, *Inorg. Chem.*, 2010, **49**, 7401–7413.

82 N. Anantharamulu, K. Koteswara Rao, G. Rambabu, B. Vijaya Kumar, V. Radha and M. Vithal, *J. Mater. Sci.*, 2011, **46**, 2821–2837.

83 R. Fuentes, *Solid State Ionics*, 2001, **140**, 173–179.

84 K. Chayambuka, G. Mulder, D. L. Danilov and P. H. L. Notten, *Adv. Energy Mater.*, 2018, **8**, 1800079(1)-1800079(49).

85 C. Delmas, J. Braconnier, C. Fouassier and P. Hagenuller, *Solid State Ionics*, 1981, **3**–**4**, 165–169.

86 A. Mendiboure, C. Delmas and P. Hagenmuller, *J. Solid State Chem.*, 1985, **57**, 323–331.

87 J. Tarascon and G.W. Hull, *Solid State Ionics*, 1986, **22**, 85–96.

88 M. M. Doeff, M. Y. Peng, Y. Ma and L. C. De Jonghe, *J. Electrochem. Soc.*, 1994, **141**, L145-L147.

89 K. West, B. Zachau-Christiansen, T. Jacobsen and S. Skaarup, *Solid State Ionics*, 1988, **28**–**30**, 1128–1131.

90 S. Tepavcevic, H. Xiong, V. Stamenkovic, X. Zuo, M. Balasubramanian, V. B. Prakapenka, C. S. Johnson and T. Rajh, *ACS Nano*, 2012, **6**, 530-538.

91 Y. Dong, S. Li, K. Zhao, C. Han, W. Chen, B. Wang, L. Wang, B. Xu, Q. Wei, L. Zhang, X. Xu and L. Mai, *Energy Environ. Sci.*, 2015, **8**, 1267–1275.

92 S.-W. Kim, D.-H. Seo, X. Ma, G. Ceder and K. Kang, *Adv. Energy Mater.*, 2012, **2**, 710–721.

93 Y. Fang, L. Xiao, Z. Chen, X. Ai, Y. Cao and H. Yang, *Electrochem. Energy Rev.*, 2018, **1**, 294–323.

94 C. Delmas, C. Fouassier and P. Hagenmuller, *Phys. B+C*, 1980, **99**, 81–85.

95 A. Van der Ven, G. Ceder, M. Asta and P. D. Tepesch, *Phys. Rev. B*, 2001, **64**, 184307(1)-184307(17).

96 C. Delmas, A. Maazaz, C. Fouassier, J.-M. R?au and P. Hagenmuller, *Mater. Res. Bull.*, 1979, **14**, 329–335.

97 M. H. Han, E. Gonzalo, G. Singh and T. Rojo, *Energy Environ. Sci.*, 2015, **8**, 81–102.

98 Y. S. Meng, Y. Hinuma and G. Ceder, *J. Chem. Phys.*, 2008, **128**, 104708(1)-104708(8).

99 S. Miyazaki, S. Kikkawa and M. Koizumi, *Synth. Met.*, 1983, **6**, 211–217.

100 C. Delmas, *Mater. Sci. Eng. B*, 1989, **3**, 97–101.

101 J.-P. Parant, R. Olazcuaga, M. Devalette, C. Fouassier and P. Hagenmuller, *J. Solid State Chem.*, 1971, **3**, 1–11.

102 J. Billaud, R. J. Clément, A. R. Armstrong, J. Canales-Vázquez, P. Rozier, C. P. Grey and P. G. Bruce, *J. Am. Chem. Soc.*, 2014, **136**, 17243–17248.

103 J. Bréger, K. Kang, J. Cabana, G. Ceder and C. P. Grey, *J. Mater. Chem.*, 2007, **17**, 3167-3174.

104 R. J. Clément, P. G. Bruce and C. P. Grey, *J. Electrochem. Soc.*, 2015, **162**, A2589–A2604.

105 X. Li, X. Ma, D. Su, L. Liu, R. Chisnell, S. Ong, H. Chen, A. Toumar, J.-C. Idrobo, Y. Lei, J. Bai, F. Wang, J. W. Lynn, Y. S. Lee and G. Ceder, *Nat. Mater.*, 2014, **13**, 586-592.

106 X. Ma, H. Chen and G. Ceder, *J. Electrochem. Soc.*, 2011, **158**, A1307-A1312.

107 A. Caballero, L. Hernán, J. Morales, L. Sánchez, J. Santos Peña and M. A. G. Aranda, *J. Mater. Chem.*, 2002, **12**, 1142–1147.

108 J. M. Paulsen and J. R. Dahn, *Solid State Ionics*, 1999, **126**, 3–24.

109 J. J. Braconnier, C. Delmas and P. Hagenmuller, *Mater. Res. Bull.*, 1982, **17**, 993–1000.

110 P. Vassilaras, X. Ma, X. Li and G. Ceder, *J. Electrochem. Soc.*, 2012, **160**, A207–A211.

111 Y. Takeda, J. Akagi, A. Edagawa, M. Inagaki and S. Naka, *Mater. Res. Bull.*, 1980, **15**, 1167–1172.

112 J. Zhao, L. Zhao, N. Dimov, S. Okada and T. Nishida, *J. Electrochem. Soc.*, 2013, **160**, A3077–A3081.

113 D. Hamani, M. Ati, J.-M. Tarascon and P. Rozier, *Electrochem. commun.*, 2011, **13**, 938–941.

114 X. Wang, G. Liu, T. Iwao, M. Okubo and A. Yamada, *J. Phys. Chem. C*, 2014, **118**, 2970-2976.

115 P.-F. Wang, Y. You, Y.-X. Yin and Y.-G. Guo, *J. Mater. Chem. A*, 2016, **4**, 17660–17664.

116 T. Yu, H. Ryu, G. Han and Y. Sun, *Adv. Energy Mater.*, 2020, **10**, 2001609(1)-2001609(8).

117 S. Komaba, N. Yabuuchi, T. Nakayama, A. Ogata, T. Ishikawa and I. Nakai, *Inorg. Chem.*, 2012, **51**, 6211–6220.

118 H. Wang, B. Yang, X.-Z. Liao, J. Xu, D. Yang, Y.-S. He and Z.-F. Ma, *Electrochim. Acta*, 2013, **113**, 200–204.

119 Q. Liu, Z. Hu, M. Chen, C. Zou, H. Jin, S. Wang, S. Chou and S. Dou, *Small*, 2019, **15**, 1805381(1)-1805381(24).

120 S. Kalluri, K. Hau Seng, W. Kong Pang, Z. Guo, Z. Chen, H.-K. Liu and S. X. Dou, *ACS Appl. Mater. Interfaces*, 2014, **6**, 8953–8958.

121 N. Yabuuchi and S. Komaba, *Sci. Technol. Adv.* 2014, **15**, 043501(1)-042501(29).

122 G. Singh, N. Tapia-Ruiz, J. M. Lopez Del Amo, U. Maitra, J. W. Somerville, A. R. Armstrong, J. Martinez De Ilarduya, T. Rojo and P. G. Bruce, *Chem. Mater.*, 2016, **28**, 5087–5094.

123 Y. J. Park, J. U. Choi, J. H. Jo, C. Jo, J. Kim and S. Myung, *Adv. Funct. Mater.*, 2019, **29**, 1901912(1)-1901912(10).

124 J. Billaud, G. Singh, A. R. Armstrong, E. Gonzalo, V. Roddatis, M. Armand, T. Rojo and P. G. Bruce, *Energy Environ. Sci.*, 2014, **7**, 1387-1391.

125 R. J. Clément, J. Billaud, A. Robert Armstrong, G. Singh, T. Rojo, P. G. Bruce and C. P. Grey, *Energy Environ. Sci.*, 2016, **9**, 3240–3251.

126 N. Yabuuchi, R. Hara, K. Kubota, J. Paulsen, S. Kumakura and S. Komaba, *J. Mater. Chem. A*, 2014, **2**, 16851–16855.

127 S. Guo, J. Yi, Y. Sun and H. Zhou, *Energy Environ. Sci.*, 2016, **9**, 2978–3006.

128 H. Yoshida, N. Yabuuchi, K. Kubota, I. Ikeuchi, A. Garsuch, M. Schulz-Dobrick and S. Komaba, *Chem. Commun.*, 2014, **50**, 3677-3680.

129 M. Sathiya, K. Hemalatha, K. Ramesha, J.-M. Tarascon and A. S. Prakash, *Chem. Mater.*, 2012, **24**, 1846–1853.

130 D. Yuan, X. Hu, J. Qian, F. Pei, F. Wu, R. Mao, X. Ai, H. Yang and Y. Cao, *Electrochim. Acta*, 2014, **116**, 300–305.

131 J. H. Stansby, W. M. Dose, N. Sharma, J. A. Kimpton, J. M. López del Amo, E. Gonzalo and T. Rojo, *Electrochim. Acta*, 2020, **341**, 135978(1)-135978(9).

132 J. Y. Hwang, S. T. Myung and Y. K. Sun, *J. Phys. Chem. C*, 2018, **122**, 13500–13507.

133 Y. Lyu, Y. Liu, Z. E. Yu, N. Su, Y. Liu, W. Li, Q. Li, B. Guo and B. Liu, *Sustain. Mater. Technol.*, 2019, **21**, e00098(1)-e00098(21).

134 K. Kubota, N. Yabuuchi, H. Yoshida, M. Dahbi, S. Komaba, *MRS Bulletin*, 2014, **39**, 416-422..

135 J. M. Paulsen and J. R. Dahn, *J. Electrochem. Soc.*, 2000, **147**, 2478-2485.

136 Y. Lei, X. Li, L. Liu and G. Ceder, *Chem. Mater.*, 2014, **26**, 5288-5296.

137 E. Lee, J. Lu, Y. Ren, X. Luo, X. Zhang, J. Wen, D. Miller, A. DeWahl, S. Hackney, B. Key, D. Kim, M. D. Slater and C. S. Johnson, *Adv. Energy Mater.*, 2014, **4**, 1400458(1)-1400458(8).

138 S. Guo, P. Liu, H. Yu, Y. Zhu and M. Chen, *Angewandte Chemie*, 2015, **54**, 5894-5899.

139 M. Keller, D. Buchholz and S. Passerini, *Adv. energy Mater.*, 2016, **6**, 1501555(1)-1501555(11).

140 X. Qi, L. Liu, N. Song, F. Gao, K. Yang, Y. Lu, H. Yang, Y.-S. Hu, Z.-H. Cheng and L. Chen, 2017, **9**, 40215-40223.

141 Z. Y. Li, J. Zhang, R. Gao, H. Zhang, L. Zheng, Z. Hu and X. Liu, *J. Phys. Chem. C*, 2016, **120**, 9007–9016.

142 M. Bianchini, E. Gonzalo, N. E. Drewett, N. Ortiz-Vitoriano, J. M. López Del Amo, F. J. Bonilla, B. Acebedo and T. Rojo, *J. Mater. Chem. A*, 2018, **6**, 3552–3559.

143 M. Broussely, P. Biensan, F. Bonhomme, P. Blanchard, S. Herreyre, K. Nechev and R. J. Staniewicz, in *J. Power Sources*, Elsevier, 2005, **146**, 90–96.

144 R. B. Wright, J. P. Christophersen, C. G. Motloch, J. R. Belt, C. D. Ho, V. S. Battaglia, J. A. Barnes, T. Q. Duong and R. A. Sutula, *J. Power Sources*, 2003, **119**–**121**, 865–869.

145 F. M. Kindermann, J. Keil, A. Frank and A. Jossen, *J. Electrochem. Soc.*, 2017, **164**, E287–E294.

146 M. R. Palacín, *Chem. Soc. Rev.*, 2018, **47**, 4924–4933.

147 J. Cabana, B. J. Kwon and L. Hu, *Acc. Chem. Res.*, 2018, **51**, 299–308.

148 K. Edström, T. Gustafsson and J. Thomas, in *Lithium-Ion Batteries*, ed. P. B. Balbuena and Y. Wang, Imperial College Press, London, 2004, ch. 8 pp. 337–364.

149 M. R. Palacín and A. de Guibert, *Science*, 2016, **351**, 1253292(1)-1253292(7).

150 M. M. Kabir and D. E. Demirocak, *Int. J. Energy Res.*, 2017, **41**, 1963–1986.

151 L. A. Middlemiss, A. J. R. Rennie, R. Sayers and A. R. West, *Energy Reports*, 2020, **6**, 232–241.

152 C. R. Birkl, M. R. Roberts, E. McTurk, P. G. Bruce and D. A. Howey, *J. Power Sources*, 2017, **341**, 373–386.

153 R. Hausbrand, G. Cherkashinin, H. Ehrenberg, M. Gröting, K. Albe, C. Hess and W. Jaegermann, *Mater. Sci. Eng. B Solid-State Mater. Adv. Technol.*, 2015, **192**, 3–25.

154 J. H. Lee, J. K. Hong, D. H. Jang, Y. K. Sun and S. M. Oh, *J. Power Sources*, 2000, **89**, 7–14.

155 C. Zhan, T. Wu, J. Lu, K. Amine, *Energy Environ. Sci.*, 2018, **11**, 243-257.

156 A. Du Pasquier, A. Blyr, A. Cressent, C. Lenain, G. Amatucci and J. M. Tarascon, *J. Power Sources*, 1999, **81**–**82**, 54–59.

157 R. Spotnitz and J. Franklin, *J. Power Sources*, 2003, **113**, 81–100.

158 D. Y. W. Yu, M. Zhao and H. E. Hoster, *ChemElectroChem*, 2015, **2**, 1090–1095.

159 S. Ko, Y. Yamada, L. Lander and A. Yamada, *Carbon*, 2020, **158**, 766–771.

160 S. T. Myung, Y. Hitoshi and Y. K. Sun, *J. Mater. Chem.*, 2011, **21**, 9891–9911.

161 R. Kostecki, L. Norin, X. Song and F. McLarnon, *J. Electrochem. Soc.*, 2004, **151**, A522-A526.

162 M. Petzl, M. Kasper and M. A. Danzer, *J. Power Sources*, 2015, **275**, 799–807.

163 J. C. Burns, D. A. Stevens and J. R. Dahn, *J. Electrochem. Soc.*, 2015, **162**, A959–A964.

164 Power Electronics, *Proper Care Extends Li-Ion Battery Life*, https://www.powerelectronics.com/markets/mobile/article/21859861/proper-care-extends-liion-battery-life, (accessed Sep 2020).

165 P. Dong, D. Wang, Y. Yao, X. Li, Y. Zhang, J. Ru and T. Ren, *J. Power Sources*, 2017, **344**, 111–118.

166 Q. Liu, C. Du, B. Shen, P. Zuo, X. Cheng, Y. Ma, G. Yin and Y. Gao, *RSC Adv.*, 2016, **6**, 88683–88700.

167 S. F. Lux, I. T. Lucas, E. Pollak, S. Passerini, M. Winter and R. Kostecki, *Electrochem. commun.*, 2012, **14**, 47-50.

168 T. Waldmann, A. Iturrondobeitia, M. Kasper, N. Ghanbari, F. Aguesse, E. Bekaert, L. Daniel, S. Genies, I. J. Gordon, M. W. Löble, E. De Vito and M. Wohlfahrt-Mehrens, *J. Electrochem. Soc.*, 2016, **163**, 2149–2164.

169 U. Tröltzsch, O. Kanoun and H.-R. Tränkler, *Electrochim. Acta*, 2006, **51**, 1664–1672.

170 I. Buchmann, *Batteries in a portable world : a handbook on rechargeable batteries for non-engineers*, Cadex Electronics, Richmond, 4th edn, 2016.

171 T. Osaka, T. Momma, D. Mukoyama and H. Nara, *J. Power Sources*, 2012, **205**, 483–486.

172 F. Huet, *J. Power Sources*, 1998, **70**, 59–69.

173 D. Zhang, B. S. Haran, A. Durairajan, R. E. White, Y. Podrazhansky and B. N. Popov, *J. Power Sources*, 2000, **91**, 122–129.

174 D. Andre, M. Meiler, K. Steiner, C. Wimmer, T. Soczka-Guth and D. U. Sauer, *J. Power Sources*, 2011, **196**, 5334–5341.

175 D. Andre, M. Meiler, K. Steiner, H. Walz, T. Soczka-Guth and D. U. Sauer, *J. Power Sources*, 2011, **196**, 5349–5356.

176 J. Li, E. Murphy, J. Winnick and P. A. Kohl, *J. Power Sources*, 2001, **102**, 294–301.

177 C. H. Chen, J. Liu and K. Amine, *J. Power Sources*, 2001, **96**, 321–328.

178 T. Momma, T. Yokoshima, H. Nara, Y. Gima and T. Osaka, *Electrochim. Acta*, 2014, **131**, 195–201.

179 K. Amine, C. H. Chen, J. Liu, M. Hammond, A. Jansen, D. Dees, I. Bloom, D. Vissers and G. Henriksen, *J. Power Sources*, 2001, **97**–**98**, 684–687.

180 I. J. Gordon, S. Genies, G. Si Larbi, A. Boulineau, L. Daniel and M. Alias, *J. Power Sources*, 2016, **307**, 788–795.

181 J. Y. Song, H. H. Lee, Y. Y. Wang and C. C. Wan, *J. Power Sources*, 2002, **111**, 255–267.

182 G. Nagasubramanian, *J. Power Sources*, 2000, **87**, 226-229.

183 G. Nagasubramanian, *J. Appl. Electrochem.*, 2001, **31**, 99–104.

184 R. Raccichini, M. Amores and G. Hinds, *Batteries*, 2019, **5**, 12(1)-12(24).

185 M. L. Dollé, F. Orsini, A. S. Gozdz and J.-M. Tarascon, *J. Electrochem. Soc.*, **148**, A851-A857.

186 F. La Mantia, C. D. Wessells, H. D. Deshazer and Y. Cui, *Electrochem. commun.*, 2013, **31**, 141–144.

187 D. Rahner, *J. Power Sources*, 1999, **81-82**, 358-361.

188 M.-S. Wu, P.-C. J. Chiang and J.-C. Lin, *J. Electrochem. Soc.*, 2004, **152**, A47-A52.

189 G. Hsieh, S. J. Ford, T. O. Masona and L. R. Pederson, *Solid State Ionics*, 1996, **91**, 192-201.

190 S. Fletcher, *Electrochem. commun.*, 2001, **3**, 692-696.

191 S. Klink, D. Höche, F. La Mantia and W. Schuhmann, *J. Power Sources*, 2013, **240**, 273–280.

192 M. Ender, A. Weber and E. Ivers-Tiffée, *J. Electrochem. Soc.*, 2011, **159**, A128-A136.

193 J. Costard, M. Ender, M. Weiss and E. Ivers-Tiffée, *J. Electrochem. Soc.*, 2017, **164**, A80–A87.

194 S. Klink, E. Madej, E. Ventosa, A. Lindner, W. Schuhmann and F. La Mantia, *Electrochem. Commun.*, 2012, **22**, 120–123.

195 M. Ender, J. Illig and E. Ivers-Tiffée, *J. Electrochem. Soc.*, 2017, **164**, A71–A79.

196 Y. Hoshi, Y. Narita, K. Honda, T. Ohtaki, I. Shitanda and M. Itagaki, *J. Power Sources*, 2015, **288**, 168–175.

197 J. Landesfeind, D. Pritzl and H. A. Gasteiger, *J. Electrochem. Soc.*, 2017, **164**, A1773–A1783.

198 M. Itagaki, K. Honda, Y. Hoshi and I. Shitanda, *J. Electroanal. Chem.*, 2015, **737**, 78–84.

199 E. McTurk, C. R. Birkl, M. R. Roberts, D. A. Howey and P. G. Bruce, *ECS Electrochem. Lett.*, 2015, **4**, A145–A147.

200 C. Bünzli, H. Kaiser and P. Novák, *J. Electrochem. Soc.*, 2015, **162**, A218–A222.

201 T. R. Jow, M. B. Marx and J. L. Allen, *J. Electrochem. Soc.*, 2012, **159**, A604–A612.

202 L. Wang, J. Zhao, X. He, J. Gao, J. Li, C. Wan and C. Jiang, *Int. J. Electrochem. Sci*, 2012, **7**, 345–353.

203 J. Illig, M. Ender, T. Chrobak, J. P. Schmidt, D. Klotz and E. Ivers-Tiffée, *J. Electrochem. Soc.*, 2012, **159**, A952–A960.

204 I. A. J. Gordon, S. Grugeon, H. Takenouti, B. Tribollet, M. Armand, C. Davoisne, A. Débart and S. Laruelle, *Electrochim. Acta*, 2017, **223**, 63–73.

205 J. Landesfeind, D. Pritzl and H. A. Gasteiger, *J. Electrochem. Soc.*, 2017, **164**, A1773–A1783.

206 D. Pritzl, A. E. Bumberger, M. Wetjen, J. Landesfeind, S. Solchenbach and H. A. Gasteiger, *J. Electrochem. Soc.*, 2019, **166**, A582–A590.

207 D. Pritzl, J. Landesfeind, S. Solchenbach and H. A. Gasteiger, *J. Electrochem. Soc.*, 2018, **165**, A2145–A2153.

208 M. Mirzaeian and P. J. Hall, *J. Power Sources*, 2010, **195**, 6817–6824.

209 Z. Deng, Z. Zhang, Y. Lai, J. Liu, J. Li and Y. Liu, *J. Electrochem. Soc.*, 2013, **160**, 553–558.

210 N. A. Cañas, K. Hirose, B. Pascucci, N. Wagner, K. A. Friedrich and R. Hiesgen, *Electrochim. Acta*, 2013, **97**, 42–51.

211 Y.-U. Park, D.-H. Seo, H.-S. Kwon, B. Kim, J. Kim, H. Kim, I. Kim, H.-I. Yoo and K. Kang, *J. Am. Chem. Soc.*, 2013, **135**, 13870-13878.

212 R. Shanmugam and W. Lai, *J. Electrochem. Soc.*, 2015, **162**, 8–14.

213 H. Gao, L. Xue, S. Xin, K. Park and J. B. Goodenough, *Angew. Chemie*, 2017, **129**, 5633–5637.

214 J. Hwang, K. Matsumoto and R. Hagiwara, *J. Phys. Chem. C*, 2018, **122**, 26857–26864.

Chapter II

Experimental

2.1 Solid State Synthesis

All samples reported in this thesis were synthesized by conventional solid state reaction (shake 'n' bake). Starting reagents were dried according to the conditions set out in Table 2.1. Sodium peroxide (Na_2O_2) was placed directly into a glove box upon being received from the supplier. Amounts of reagents were weighed using a balance, mixed and ground with acetone (*Fisher Scientific*) using an agate pestle and mortar, before being placed into a gold crucible and heated in a furnace.

Table 2.1 Purity, supplier and drying temperature of starting reagents.

Reagent	Purity	Supplier	Drying Temperature
Na_2CO_3	≥ 99%	Sigma Aldrich	180 °C
Na_2O_2	≥ 99%	Alfa Aesar	Undried
Mn_2O_3	≥ 99%	Sigma Aldrich	625 °C
MnO_2	≥ 99%	Sigma Aldrich	180 °C
NiO	≥ 99%	Sigma Aldrich	800 °C
MgO	≥ 99%	Sigma Aldrich	1000 °C

Samples were mixed for 30 minutes initially, before being pre-reacted at a lower temperature of ~ 700 °C. Subsequent grindings of the partially reacted mixtures took place for 20 minutes, with compounds synthesized between 700 and 1000 °C. For certain materials, powders were pressed into 'green' pellets prior to the firing. A muffle furnace was used for materials synthesized and cooled in air. Synthesis in other atmospheres (O_2/N_2) took place in a tube furnace.

2.2 X-Ray Diffraction

Powder X-ray diffraction (PXRD) is the main technique used for identifying non-molecular, crystalline, inorganic solids. Each crystalline material has its own characteristic XRD pattern (a 'fingerprint'). The diffraction pattern of most inorganic solids can be found in the Powder Diffraction File (PDF) database.[1] The matching of an experimental diffractogram collected for an unknown sample to a known pattern in the database is known as phase analysis/identification. Crystal structure determination is another important use of X-ray diffraction. After an internal standard has been employed for peak position calibration, pattern indexing (assigning Miller indices) and lattice parameter determination can be performed, as well as calculation of the unit cell volume. Full crystal structure determination, including finding the fractional coordinates of the atoms present in the cell, e.g. by Rietveld refinement, can also be performed (see Section 2.3).

When X-rays interact with matter, they can either be scattered or absorbed. If there is no loss of energy on scattering, the scattered X-rays are coherent with the incident beam; these are the type used in X-ray diffraction (XRD) experiments. Crystals, which have regular repeating structures, are able to diffract radiation that has a wavelength similar to interatomic separations. The most universal approach to treating diffraction by crystals is via Bragg's Law.[2] The Bragg approach to the X-ray diffraction is to treat the crystal as a simplified series of layers/planes. For some simple crystal structures, the planes may also correspond to layers of atoms, but this is not usually the case. The derivation of Bragg's Law is shown in Figure 2.1.[3]

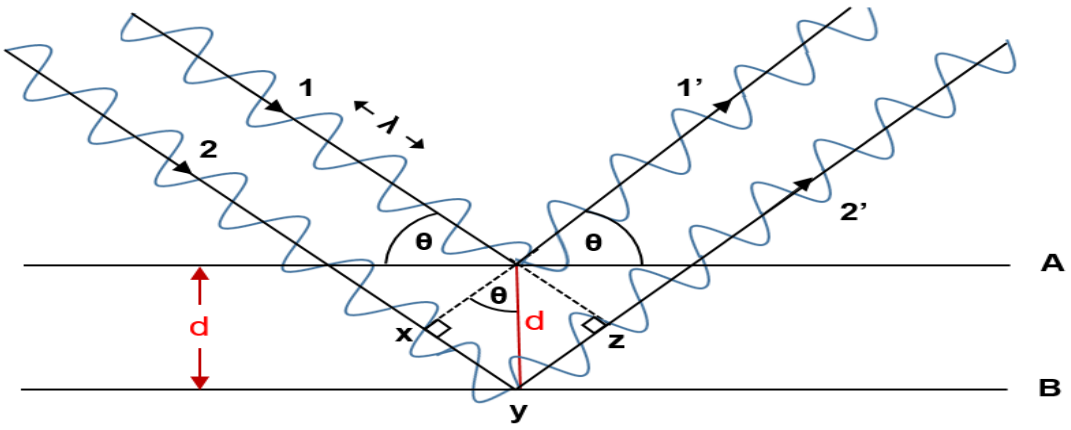

Figure 2.1 Derivation of Bragg's Law.[3]

In the X-ray diffraction of crystals, some X-rays are reflected off a plane with the same angle of reflection as the angle of incidence, and others are reflected by succeeding planes. In Figure 2.1, X-ray beams 1 and 2 are reflected by adjacent planes within the crystal, A and B. The angle of incidence for each X-ray beam is also known as the Bragg angle, θ, and the distance between pairs of planes is referred to as the d-spacing, d. In the Bragg approach, the only X-ray beams of interest are those which undergo constructive interference because destructive interference causes a cancellation of the diffracted X-rays, and, therefore, no resultant peak in the diffraction pattern. Constructive interference occurs when the phase difference between waves/beams is an even multiple of π (180°), and the waves are referred to as being in-phase. Destructive interference occurs when the difference is an odd multiple of π, and the waves are said to be out of phase. For XRD, we are only interested in what conditions reflected beams 1' and 2' are in-phase. Beam 22' has to travel an extra distance, *xyz*, compared with beam 11'. Therefore, for 1' and 2' to be in-phase, *xyz* must equal a whole number of wavelengths:

$$n\lambda = xyz \tag{2.1}$$

where λ is the wavelength of the incident beam and n is an integer (referred to as the order of reflection). Basic trigonometry also tells us that the following is true for Figure 2.1.

$$xy = yz = dsin\theta \tag{2.2}$$

$$\text{and} \quad xyz = xy + yz \tag{2.3}$$

$$\therefore \quad xyz = 2dsin\theta$$

$$\textbf{(Bragg's Law)} \quad \boldsymbol{n\lambda = 2\,dsin\theta} \tag{2.4}$$

For a given set of planes, several solutions of Bragg's Law (Eq. 2.4) are usually possible, for n = 1, 2, 3, etc. It is customary, however, to set n = 1.[3] In crystals with thousands of planes, Bragg's Law imposes a stringent condition on the angles at which reflection may occur. If the incident angle is incorrect by more than a few tenths of a degree, cancellation of the reflected beams is usually complete.

The diffractometer used for phase identification and structure determination on powder samples in this work was a linear position sensitive detector (PSD), Mo $K\alpha_1$ ($\lambda = 0.70926$ Å). Patterns were collected in the range from 5 to 40 ° with a scan rate of 0.1 °. An internal silicon standard of SRM 640e from the National Institute of Standard and Technology (NIST) was added for 2θ peak position calibration, prior to pattern indexing and lattice parameter determination. The WinXPOW software (version 3.05 of STOE & Cie GmbH, Germany) was used for the analysis of collected XRD data.

2.3 Rietveld Refinement

The X-ray diffraction of powder samples results in a pattern characterised by reflections (peaks in intensity) at certain 2θ positions, for which the d-spacings may be calculated. The height, width and position of these peaks can be used to determine many aspects of the material's structure. One approach to this, and the most popular in use today, is the Rietveld refinement method, first reported in 1969,[4] which has become extremely valuable as a method to confirm structural details of powdered samples. The Rietveld method uses a non-linear least squares approach to refine a theoretical line profile until it matches/fits the measured profile. Each iteration of the refinement is dependent on the results generated by the last, and multiple refinement iterations eventually converge to a possible solution. The Rietveld method is a whole pattern refinement in which the experimental powder XRD profile is compared with a calculated profile (including all structural and instrumental parameters) whose parameters are adjusted by refinement.

A starting model of a crystal structure which is close to the final structure is required to commence the refinement and generate the calculated patterns. For a known structure type, this means that reasonable initial estimates for the values of some refinable (free) parameters are required, including peak shape, unit cell dimensions, and coordinates of the atoms in the crystal structure. The outcome of the refinement is dependent on the quality of the collected data, the quality of the model (including initial approximations), and the experience of the user. A good high resolution XRD (or neutron diffraction) data set is often required for the refinement. This is to try and

ensure that all the intensities of each individual peak can be determined, since there is a tendency for peaks to overlap - especially at lower 2θ angle. Due to this, a longer data acquisition time (especially using Mo radiation) is desirable, and since the Rietveld method is a whole pattern refinement, which includes the background scatter, a good signal to noise ratio is important to avoid any unaccounted peak intensities. Nowadays, there are numerous widely available software packages for performing Rietveld refinements. The GSAS (General Structure Analysis System) with graphical user interface EXPGUI was used for the refinements presented in this work.[5,6]

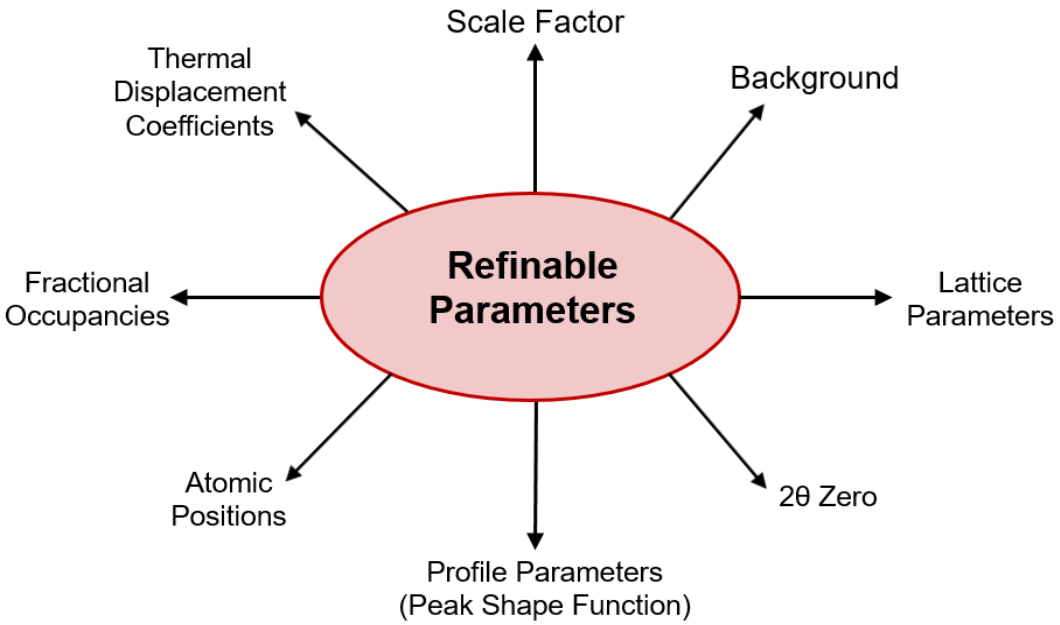

Figure 2.2 Parameters refined using the Rietveld method.

Several parameters are refined during the Rietveld process, summarised in Figure 2.2.[7] For a full explanation on each of these see Appendix A. Each refinement is unique and there is no definitive list of parameters to include and the order in which to refine them; it is left up to the user to determine the best sequence. If too many variables are refined at once, the least squares fitting will be destabilised, or a false minimum may be produced wherein some of the structural parameters are incorrect. The strategy, therefore, should be to proceed with caution: refine each variable one-by-one and then either fix them at their refined values or allow the number of refined parameters to increase gradually. A damping factor can be used during the early

steps of refinement to avoid the refined model drifting away from the initial value. Several residual/reliability factors (R-factors) can be used to assess the quality of a single crystal structure refinement (Eqs. 2.5-2.7).[8] From these, a goodness of fit (Eq. 2.8) can be calculated, which can be used as a numerical figure of merit for quantifying the quality of the refinement.

Profile R-factor:
$$R_p = \frac{\sum_i |y_i(obs) - y_i(calc)|}{\sum_i |y_i(obs)|} \quad (2.5)$$

Weighted Profile R-factor:
$$R_{wp} = \left\{ \frac{\sum w_i [y_i(obs) - y_i(calc)]^2}{\sum w_i [y_i(obs)]^2} \right\}^{\frac{1}{2}} \quad (2.6)$$

Expected Profile R-factor:
$$R_{exp} = \left\{ \frac{N - P}{\sum w_i [y_i(obs)]^2} \right\}^{\frac{1}{2}} \quad (2.7)$$

Goodness of fit:
$$\chi^2 = \left(\frac{R_{wp}}{R_{exp}}\right)^2 \quad (2.8)$$

where $y_i(obs)$ = intensities of observed data at step i
$y_i(calc)$ = intensities of calculated data at step i
w_i = weighting factor at step i
N = number of data points
P = number of parameters

The profile R-factor (R_p) is an equation used to determine the difference between calculated and observed data. However, the weighted profile R-factor (R_{wp}) is more useful as it also considers the standard deviation of the background and peak intensities. The expected profile R-factor (R_{exp}) is used to assess the quality of data being used. Ideally, the refined R_{wp} values should approach the statistical R_{exp}, and the goodness of fit (χ^2) should be as close to 1 as possible. When assessing the quality of a refinement, R_{wp} and χ^2 are often quoted in the results. However, it is usual practice to also present graphically the experimental and calculated profiles together with a difference profile and markers showing the positions of the expected Bragg peaks. All this information considered together is used to assess the quality of the refinement.

2.4 Scanning Electron Microscopy

Scanning electron microscopy (SEM) passes a focused electron beam across the surface of a sample in order to generate an image. The electrons in the beam interact non-destructively with the sample, and the signals (electrons and X-rays) produced make it possible to obtain information about surface topography, particle morphology, and chemical composition of the material studied. Objects can be magnified up to 300,000 times using this technique, and it is possible with high-performance machines to obtain resolution below 1 nm.[9] For conventional scanning electron microscopes, a magnification up to 30,000 is achievable, equating to a spatial resolution 50 – 100 nm, meaning that areas 1 – 5 μm in width can be imaged.

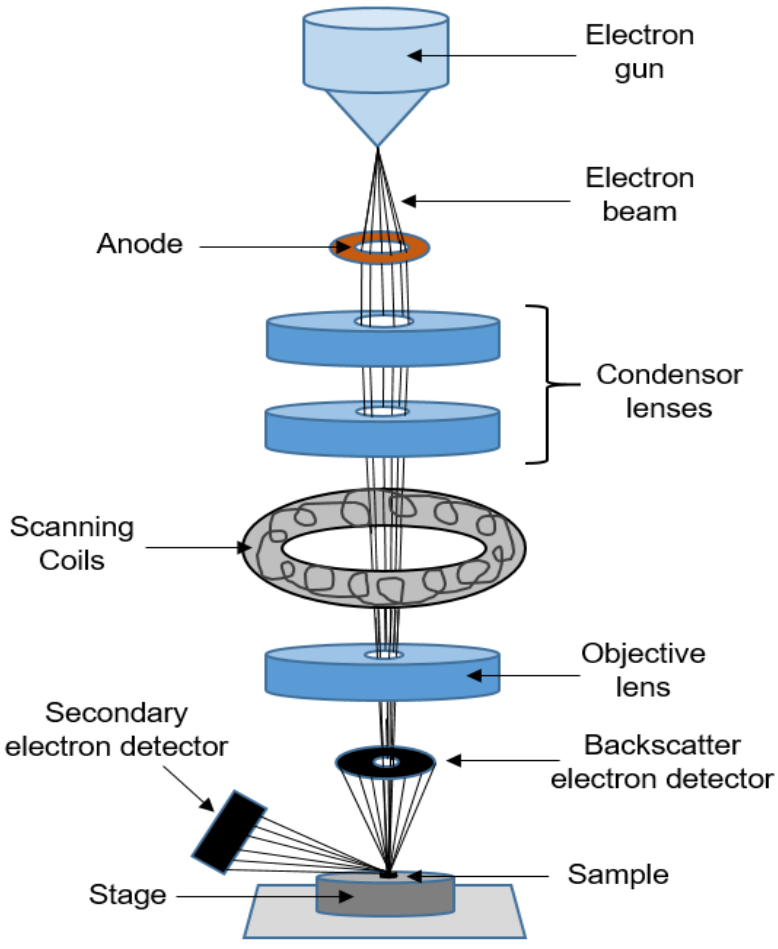

Figure 2.3 Scanning electron microsocpe.[10]

A schematic of a scanning electron microscope is shown in Figure 2.3.[10] The entire machine is operating under vacuum in order to prevent electrons interacting with air

particles. Electrons are generated by a suitable source, e.g. tungsten filament or a field emission gun. The electron beam is accelerated through a high voltage by an anode and passes through a system of apertures and electromagnetic lenses to produce a thin, focused beam. The position of the beam is controlled by the scanning coils, which are used to raster the beam across the surface of the specimen. As the beam scans the surface of the sample and interacts with atoms, electrons are produced which are collected by detectors. The most common mode of SEM operation is using a secondary electron (SE) detector, which registers electrons emitted from the outer surface of the sample (inelastic interactions). Backscattered electrons (BSEs) are electrons from the primary beam, which are reflected back after elastic interactions between the beam and the sample. BSEs originate from deeper regions of the sample than SEs, which means that they contain different information about the sample. Secondary electrons can be used to construct a physical image of the surface, whereas BSEs, which are more sensitive to atomic number, can be used to obtain chemical composition information.

In the work in this thesis, samples prepared for SEM were placed on carbon coated stubs to mitigate any charging effects during imaging. Determination of microstructure information was performed with an Inspect F50 scanning electron microscope (SEM) (FEI, Oregon, USA) using an accelerating voltage of 20 kV and a probe diameter of 6 – 10 mm. Data were recorded and analysed using LINK ISIS software.

2.5 Thermogravimetric Analysis

Thermogravimetric analysis (TGA) measures the mass change of a sample as a function of temperature. It is a widely used technique in materials science to characterise and verify solid substances. It can provide information about physical phenomena, such as phase transitions, the uptake and loss of atmospheric species; as well as chemical phenomena, such as thermal decomposition and solid-gas reactions (oxidation/reduction).[11] The specimen under investigation is subjected to a controlled temperature programme, which may consist of heating/cooling steps as well as regions of constant temperature (isotherms). A TGA instrument (Fig. 2.4) consists of

a sample pan, which resides inside a furnace, connected to a high precision micro balance.[12] A thermocouple near the pan monitors the sample temperature and is linked up to a temperature programmer and controller. A TGA run often takes place in the presence of flowing gas, which may be inert or reactive. An oxidising atmosphere, e.g. air, oxygen, combusts organic materials and oxidises metals. The TGA curves (thermograms) produced by the instrument may help to assess thermal and oxidative stability of the sample, product lifetime, decomposition temperatures, as well the moisture and volatile content of the material.

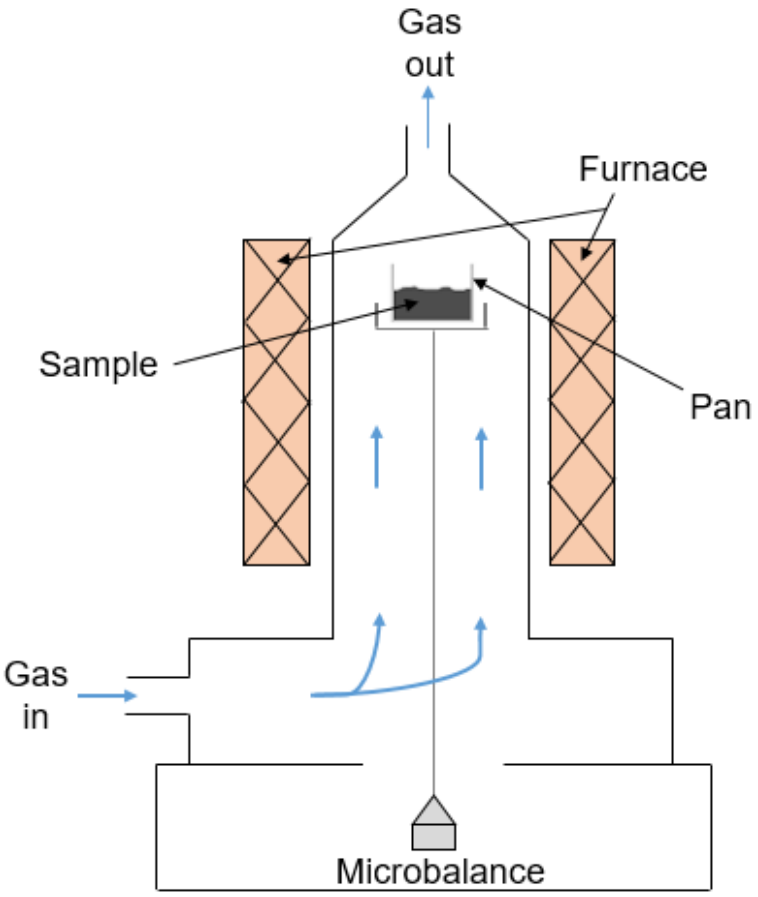

Figure 2.4 A simplified schematic of a TGA instrument.[12]

In this work, measurements were performed in either flowing air, nitrogen, or oxygen, using a PerkinElmer Pyris 1 or a PerkeElmer TGA 4000 (PerkinElmer, Massachusetts, USA). Pyris Manager software was used for data analysis. For each measurement, 10-20 mg of powder sample was placed in an alumina crucible. The heating/cooling rate was fixed at 5 °C/min, and the measured temperature ranges varied according to each sample.

2.6 Differential Scanning Calorimetry

Differential scanning calorimetry (DSC) is a thermoanalytical technique used to study how physical properties of a material are affected by change in temperature. The technique works by determining the amount of heat needed to maintain the same temperature between a sample and an inert reference (Fig. 2.5).[13] A sample of known mass is heated/cooled and changes in heat flow are measured simultaneously for both the sample and reference. The difference in input energy required to match the temperature of the sample to that of the reference corresponds to an alteration in the heat capacity of the material. Results from the experiment are output as DSC curves of heat flux *vs.* temperature or time, with peaks indicating heat absorptions (endotherms) and releases (exotherms). These heat changes may be caused by a thermal event, such as melting, decomposition, loss of solvents, or a polymorphic transition. TGA and DSC are often used together because the two techniques provide complementary information. DSC expands the capability of TGA as it makes it possible to observe reactive changes which occur without the loss/gain of mass.

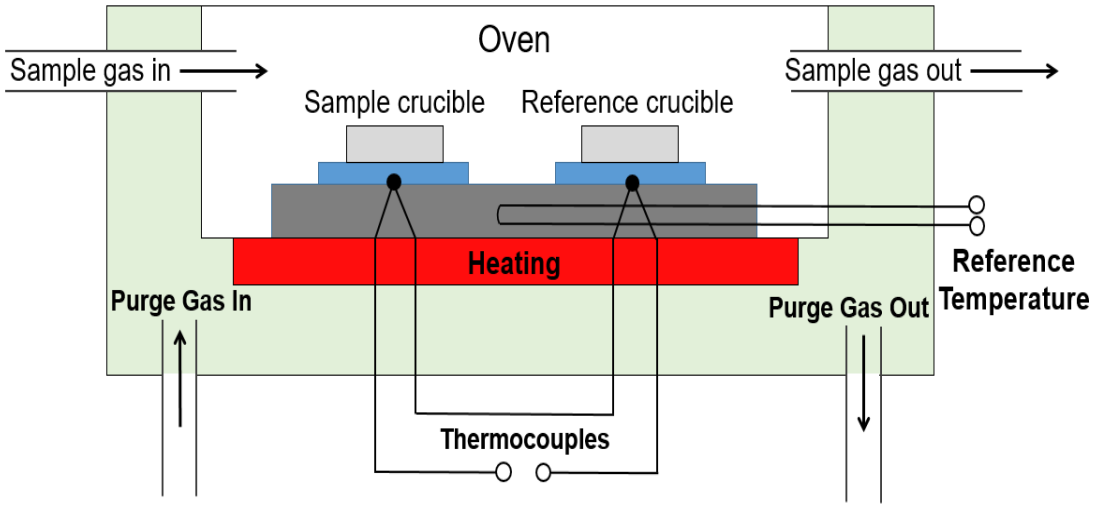

Figure 2.5 A schematic of a DSC instrument.[13]

For each measurement in this study, 20-30 mg of powder sample was placed in an alumina crucible, and heated at 5 °C/min heating/cooling rate, in an air/argon (80/20) atmosphere. The sample temperature was compared with that of an inert reference material (an empty alumina crucible). The measured temperature ranges were

dependent on the sample. The data were collected using a NETZSCH 404 C thermal analyser (Netzsch, Selb, Germany) and analysed using Proteus Analysis software.

2.7 Battery Assembly

Positive electrode (cathodes) were prepared by mixing dried active material, carbon black conductive additive and polyvinylidene fluoride (PVDF) binder with N-methyl-2-pyrrolidone (NMP) in a THINKY ARE-250 non-contact planetary mixer to form a uniform slurry. This was then cast onto carbon-coated aluminium foil. For graphite anodes, the procedure was slightly different, and a mixture of styrene-butadiene (SBR) and carboxymethyl cellulose (CMC) was used as the binder, in a water solvent, which was cast onto a carbon-coated copper foil current collector. The separators used in cells to isolate the two electrodes from one another were cut from glass microfibre filter paper (GF/A, Whatman), which were soaked in liquid electrolyte prior to cell assembly. Lithium-ion electrolyte used was 1 M $LiPF_6$ in 1:1 EC : DMC, supplied by Sigma-Aldrich. Sodium-ion electrolytes were prepared in a glove box with the solvent mixture dried over molecular sieves prior to dissolution of the dried salt.

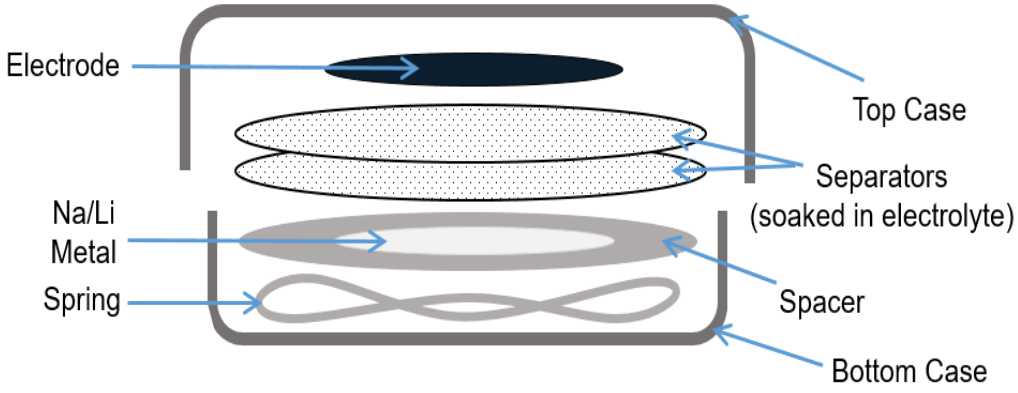

Figure 2.6 A schematic of a 2032 coin cell.

All cells were assembled in an argon-filled glove box. Half-cell in this work refers to active material *vs.* either sodium or lithium metal and full-cell to *vs.* a non-metallic counter electrode. Electrochemical half-cell testing was performed using CR2032 coin cells (Fig. 2.6) with a metal-disk, 11 mm in diameter, as the negative electrode. Steel coin cells were used for Li-ion battery research, and aluminium-clad ones for

Na-ion work. The latter were used to try and avoid passivation of the steel by the Na-ion electrolyte at higher voltages. Circular positive electrodes, 12 mm in diameter, were punched from cathode coatings. Cell casings, spacers, springs, separators and electrodes were all dried in an 80 °C vacuum oven for 16 h prior to being taken into the glove box for battery assembly.

Full-cell testing took place using a pouch cell configuration. Square positive electrodes (20 x 20 mm) were cycled against negative electrodes (22 x 22 mm). The anode was slightly larger than the cathode to try and prevent alkali metal plating. Electrodes were punched using cutting dies along with a hydraulic swing arm clicker press. Laminate-type prismatic pouch cells (7 x 5 cm) containing aluminium current collector tabs to connect the electrodes to the battery tester were dried at 70 °C overnight before being taken into the glove box for battery assembly.

2.8 Four-Point Probe Conductivity Measurements

In conventional two-terminal resistivity measurements, there is an impedance associated with the leads connected to the sample. For semiconducting materials, it is necessary to eliminate this contact/lead resistance in order to obtain a more accurate resistivity measurement. In a four-point probe conductivity setup (Fig. 2.7), the points of the instrument are usually in a line, with a current passed between the two outside points and the voltage measured between the two inner ones.[14] For a semiconducting thin film, such as an electrode sheet, the value measured by the instrument is given in terms of a sheet resistance R_s (Eq. 2.9).

$$R_s = \frac{\boldsymbol{\pi}}{ln2}\left(\frac{V}{I}\right) \tag{2.9}$$

This is reported in Ω/□, which is dimensionally equal to Ω, but is exclusively used for sheet resistance. The resistivity ρ of the electrode coating (in Ω cm) can then be calculated by multiplying the sheet resistance by the thickness t (in cm) of the coating (Eq. 2.7).

$$\rho = R_s \times t \tag{2.10}$$

Therefore, from a four-point probe conductivity measurement, it is possible to calculate the resistivity of the sample, providing that the thickness of the coating is known.

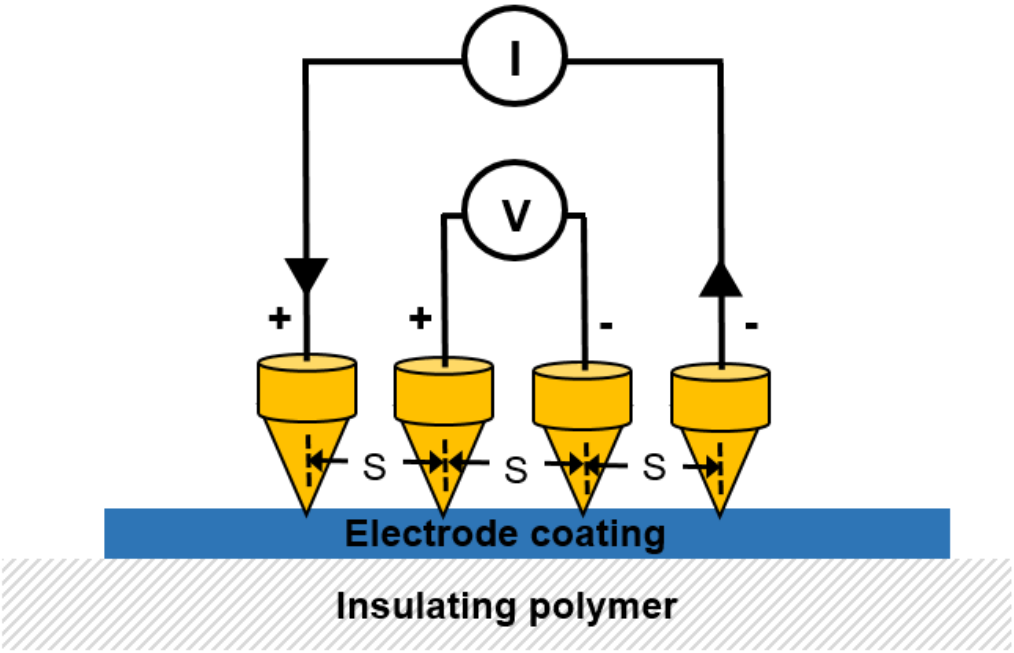

Figure 2.7 Four-point probe conductivity measurement of an electrode coating.

A Jandel cylindrical four-point probe was used for the measurements conducted in this work. The probe consists of four equally spaced tungsten metal tips, each with a radius of 500 μm and a 1 mm spacing (*S*) between them. For an accurate four-point probe measurement, the thickness of the film must be less than 40% of the probe spacing, and the edges of the sheet from the probe must be at least four times *S*.[15] Therefore, this setup is capable of measuring samples < 400 μm thick which have an area > 0.64 cm^2. The electrode coatings were deposited on a layer of 75 μm thick insulating polyester (PET) film, so that there was not a short circuit during the measurement via the Al current collector. The coating was then cut into smaller sheets which were dried in a 60 °C vacuum oven. Some of the coatings were calendered at 80 °C using an electric hot rolling press machine (MSK-HRP-01, MTI, Richmond, CA, USA). The electrode sheets were pressed to various densities by varying the gap size between the rolls. After calendering, the coatings were again dried in a vacuum oven at 60 °C for 16 h, before the four-point probe conductivity measurements were performed.

2.9 Constant Current/Constant Voltage Cell Testing

One of the primary ways to characterise a potential new battery technology is cell cycling, where a battery is charged and discharged over several cycles and its performance monitored and analysed. Manufacturers and scientists will normally use advanced battery cyclers, which possess multiple channels and are capable of high precision currents, in order to test cells under different conditions. The voltage of a battery is a measurement of the difference in electric potential (charge) between the two electrode terminals. Prior to cycling a cell, it may have an open circuit voltage (OCV) close to zero, or slightly negative if there is a modest excess of electrons at the positive terminal (cathode). During charging of a battery, electric current is forced through it. This is done by the charger generating a voltage higher than the voltage of the cell. An external variable power supply makes it possible to build up a positive (positive polarisation) or negative potential difference at the working (positive) electrode in order to charge/discharge the battery. Once the cell begins to charge, electrons are forced from the positive to the negative terminal, meaning there are more electrons now at the negative (anode) terminal, and, as a result of this, the overall voltage of the cell is positive. During discharge, a voltage is generated by the battery cycler which is lower than the terminal voltage of the cell, meaning that electrons flow in the opposite direction, thus lowering the cell voltage.

Cell cycling can take place using either the constant current (CC) method, constant voltage (CV), or a combination of both (CC/CV). An example of a CC/CV charging profile for a battery is given in Figure 2.8. Under constant current conditions, the battery cycler limits the amount of current to a pre-determined level until a set voltage is reached. The amount of current used is often based on the capacity rating of the cell and set as a function of C-rate (see Section 1.1). The switch from CC to CV at the top of charge occurs seamlessly and the current then tapers off to a minimum value as the battery saturates. Charging ends when the current decreases below a set percentage of the capacity rating of the cell, e.g. when the current drops to below 0.02C. The bulk of the charge comes from the constant current step, and a constant voltage at the end is implemented in order to try and maximise the capacity utilised.

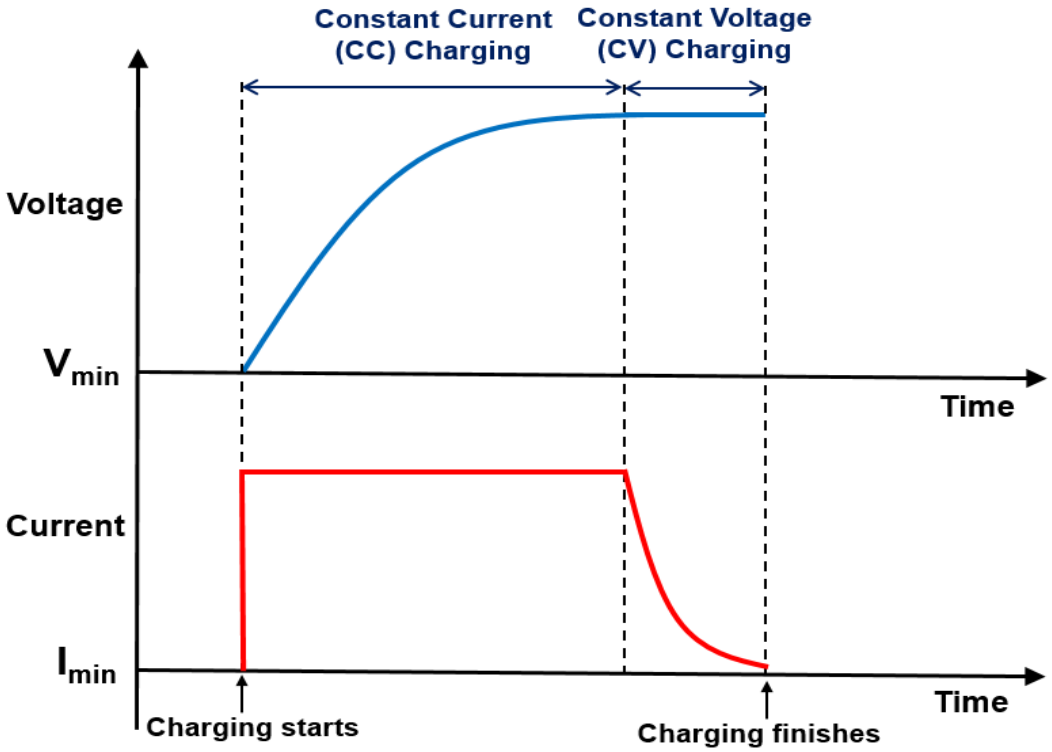

Figure 2.8 Constant current/constant voltage (CC/CV) charging profile.

Constant current/constant voltage is the preferred method for cycling a lithium-ion battery because it is safe and efficient.[16] If a constant voltage step was applied to an empty cell, the charging current would likely be so high that it would damage the battery. Similarly, the constant voltage step allows the battery to continue drawing current until it is fully charged, without increasing the voltage beyond the limit of the cell. During discharge, a constant current is used, with a lower voltage limit set to prevent the battery from over-discharging. Similar to the four-point probe setup, battery testers usually have separate pairs of wires for current and voltage in order to increase the accuracy of the measurements. Just a few microamps of current flowing in the voltage leads will create some error when measuring the potential difference. The current and voltage leads should be kept as far away from each other as is physically achievable, in order to minimise electromagnetic coupling, and then come together as close to the battery as possible.

Constant current mode is sometimes referred to as galvanostatic testing and constant voltage as potentiostatic. Both cycling conditions operate by injecting different amounts of current through the cell; however, in galvanostatic testing, the cell current signal is measured and determines how much current is injected, whereas in

potentiostatic testing, it is the voltage which is measured and controlled. Battery cyclers provide multi-purpose test functions for research laboratories. They are able to simulate battery loading and can be automated with a custom program written by the user. In this study, electrochemical CC/CV testing on half-cells and two-electrode full-cells was performed using a Maccor Series 4000 Automated Test System. Three-electrode cells were cycled using a Solartron Potentiostat 1470E. All cells were held in temperature-controlled environmental chambers. The *Maccor Information Management System (MIMS) Client* and *Scribner MultiStat* softwares were used for data analysis.

2.10 Cyclic Voltammetry

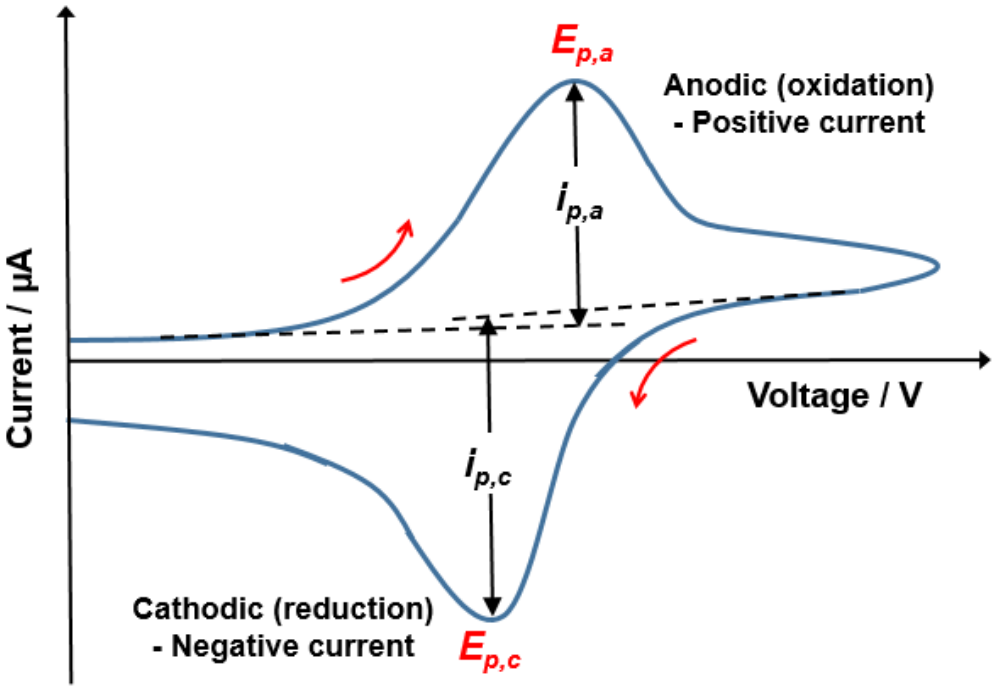

Figure 2.9 A typical cyclic voltammogram (CV) profile showing the characteristic peak anodic ($i_{p,a}$) and cathodic ($i_{p,c}$) currents, as well as the potentials ($E_{p,a}$ and $E_{p,c}$) at which these are reached.

Cyclic voltammetry (CV) is a potentiodynamic technique which is able to yield important thermodynamic and kinetic information on the electrochemical behaviour of battery materials.[17] The technique works by applying a potential scan across a cell, whilst measuring the current response. The voltage is increased linearly (at a

constant scan rate) up to a pre-set limit, at which point the scan is reversed, and continues down to a lower voltage cut-off. This process can occur once or several times. The measured current is plotted against the applied voltage in order to give a cyclic voltammogram trace (Fig. 2.9). During the forward (anodic) 'sweep', the current will increase sharply when there is an oxidation reaction (loss of electrons from the material). Similarly, in the reverse (cathodic) sweep, the current will fall sharply when there is a reduction reaction (gain of electrons). Hence, the voltammogram contains peaks which correspond to redox reactions occurring in the materials inside the battery. The position and magnitude of the peaks yield important information about these redox reactions, including their reversibility. In addition to identifying the various redox processes that occur, CV can also be used to obtain information on the reaction kinetics of electrochemical reactions, including ion diffusion.[18]

In this work, cyclic voltammetry was used in order to try and identify and study the different redox reactions occurring in sodium-ion cathode materials. Two-electrode half-cells were built using a coin cell design, with the active cathode material being tested *vs.* sodium metal. Hence, the Na metal disk served as both the reference and counter electrode for the testing procedure. Multiple scans were performed for each cell that was tested, between upper and lower voltage limits. The experiment was performed using a multichannel potentiostat (1470E) supplied from Solartron Analytical. While the CV technique is fairly straightforward to perform, the analysis of voltammograms, and the assignment of peaks to specific redox processes within electrode materials, is much more difficult. The shapes of voltammograms are dependent upon such parameters as particle size, electrolyte concentration and electrode thickness, as well as a range of experimental conditions, e.g. temperature and scan rate.[19]

2.11 Galvanostatic Intermittent Titration Technique

Rechargeable batteries function by transferring ions between the two electrodes. During cycling, Li^+/Na^+ ions must be able to diffuse through the bulk of the electrode to the surface, in order to reach the electrode/electrolyte interface, and

similarly the reverse process needs to occur at the opposite electrode. The ease at which Li^+/Na^+ ions move through the electrode is measured by the chemical diffusion coefficient, $D_{Li}{}^+/D_{Na}{}^+$. As the rate of mass transport through the electrode (solid state diffusion) is often the rate-limiting step in the charge/discharge of a cell, *D* is an important parameter which is inherently linked to the rate capability and power output of a battery. Galvanostatic intermittent titration technique (GITT) is a useful electrochemical method which can be employed to obtain the diffusion coefficients of electrodes in batteries.[20]

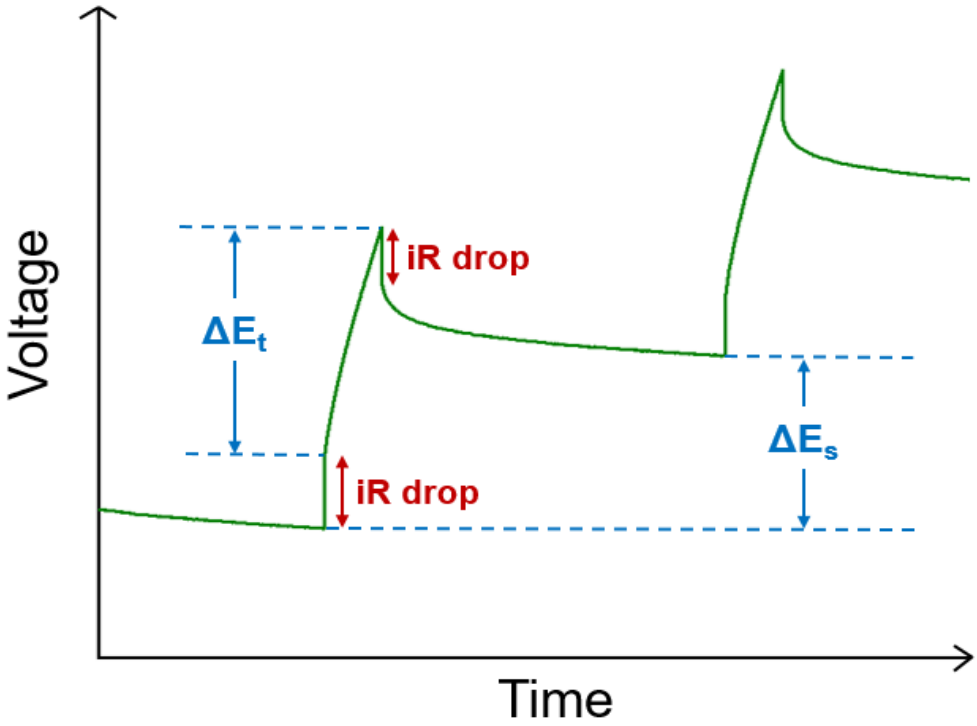

Figure 2.10 A section of a galvanostatic intermittent titration curve vs. time. The *iR* drops are labelled together with ΔE_t and ΔE_s for one charge step.

During the GITT procedure, the battery undergoes a current pulse followed by a period of relaxation. The pulse creates a Li^+/Na^+ concentration gradient in the electrode, and, during the subsequent relaxation period, this disappears and the distribution of alkali ions returns to equilibrium. This sequence of pulses and relaxations is repeated until the cell is fully charged. The battery is then discharged in a similar manner, but this time using a negative current. An example of what the voltage-time profile looks like for the GITT procedure is shown in Figure 2.10. During the current pulse, the voltage quickly increases to a value proportional to the

iR drop, before gradually increasing for the remainder of the pulse (ΔE_t).[21] This voltage increase is proportional to the concentration gradient induced in the electrode by the pulse. During the relaxation stage, the potential decreases sharply to begin with, once again due to the *iR* drop, before slowly decaying to a voltage where the electrode is in equilibrium (the cell has reached its open circuit voltage). The difference between the OCV after the relaxation period and at the start of the current pulse is referred to as the steady-state potential difference (ΔE_s). Hence, the greater the value of ΔE_s, the quicker the Li^+/Na^+ concentration gradient in the electrode disappears. During the discharge part of a GITT procedure, the same processes happen in reverse, the voltage drops during the negative current pulse and then increases again during the relaxation period.

After performing a GITT protocol, providing that small currents are used for short durations, Equation 2.11, which is based on Fick's Law,[22] can be used to calculate the chemical diffusion coefficient (*D*), where τ (s) is the duration of the current pulse; n_m (mol) is the number of moles; *Vm* ($cm^3\ mol^{-1}$) is the molar volume of the electrode; *S* (cm^2) is the electrode area; ΔE_s (V) is the steady-state voltage change, and ΔE_t (V) is the voltage change during the current pulse. A number of assumptions are made in calculating *D* using this equation, including that current distribution through the electrode is uniform, diffusion is one-dimensional, and that volume/structural changes in active materials are negligible.[23]

$$\textbf{(Diffusion Coefficient)} \quad \boldsymbol{D = \frac{4}{\pi\tau}\left(\frac{n_m V_m}{S}\right)^2\left(\frac{\Delta E_s}{\Delta E_t}\right)^2} \qquad (2.11)$$

The value given for the diffusion coefficient is most likely estimated to an order of magnitude, since the value is dependent upon a square of a combination of experimental values, and, therefore, uncertainties in experimental data are amplified. Galvanostatic intermittent titration technique can be performed using a standard laboratory battery cycler. In this study, the GITT protocol was performed using a Maccor Series 4000 Automated Test System, with the cells held in temperature-controlled environmental chambers. The *Maccor Information Management System (MIMS) Client*, along with *ViewData*, were used for data analysis.

2.12 *In Operando* X-Ray Diffraction

The electrochemical performance of batteries is inherently linked to the structures of the solid state materials they possess and the changes these undergo during cycling. A major cause of known cell degradation is unfavourable structural changes, e.g. phase transitions, in the electrode materials during charge/discharge.[24] Therefore, to be able to optimise existing materials and develop novel high-performing electrodes, a thorough understanding of the structural properties and stability of these during battery operation is required. *In operando* X-ray diffraction offers a non-destructive and real-time way to observe structural processes occurring at the electrodes during battery operation.[25] The technique has the advantage over *ex situ* measurements in that it measures the dynamic real-time response during cycling, which is necessary to detect the formation of intermediate, metastable (non-equilibrium) phases; this provides a greater depth of understanding into how batteries function and degrade. Furthermore, with XRD measurements performed *ex situ*, it is not always possible to know the exact voltage data is being recorded at as, after removing the battery from the cycler, the cell will resort to its OCV. Performing XRD scans, while electrochemically testing the cell simultaneously, enables the user to correlate both electronic and structural changes accurately, which provides a greater insight into the complex reaction mechanisms occurring inside the battery.

A photograph of the *in operando* XRD setup used in this work is shown in Figure 2.11. A pouch cell design was used to conduct the measurements with the X-ray diffractometer operating in transmission mode (the X-ray beam passing through the battery). The cell consists of an aluminium pouch containing electrodes deposited on carbon-coated Al current collectors and two glass fibre separators soaked in electrolyte solution. The advantage of using this cell design is that it is commonly used in laboratories as a prototype for scaled-up, mass produced pouch batteries and, therefore, is not too far removed from what is used commercially. The pouch was mounted on a stage which has a mechanism to apply pressure to the cell for proper operation. The current collector tabs of the cell had crocodile clips placed on them, which were in turn connected to wires that ran through the back of the XRD machine to a battery cycler positioned outside the diffractometer.

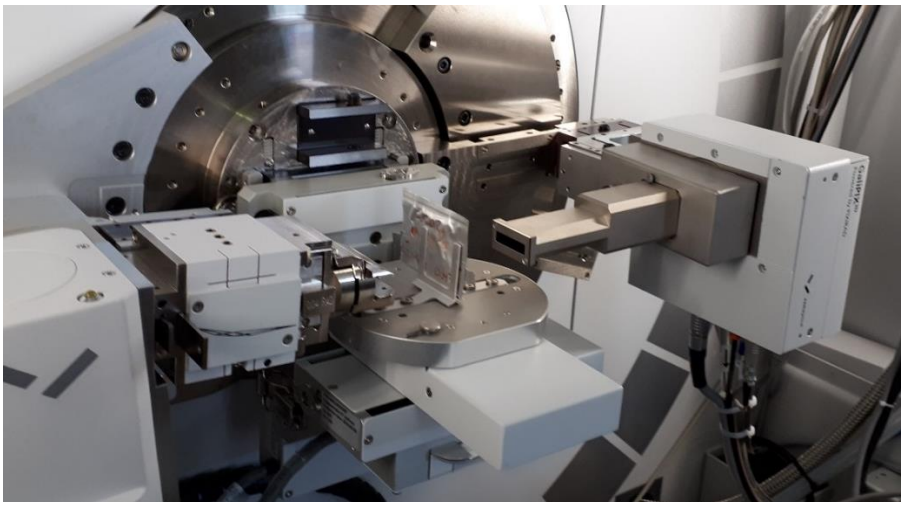

Figure 2.11 *In operando* XRD experimental setup.

Scans were performed using a Malvern Panalytical Empyrean X-ray diffractometer, with a high-performance hybrid pixel GaliPIX^{3D} Detector with CdTe sensor. The Empyrean supports an accelerating voltage of 60 kV and a tube current of 36 mA, which enables high-intensity 22.16 keV Ag radiation for pouch cell research. Data were recorded over the 2θ scan range 5 - 25 ° with a stepsize of 0.1 °. Each XRD pattern took ~ 16 min to record. The pouch cell underwent CC/CV cycling using a Maccor Series 4300 Automated Test System. The *Maccor Information Management System (MIMS) Client* software was used for data analysis. The *Data Collector* software, along with HighScore (versions 5.5 and 4.9 of Malvern Panalytical, respectively) were used for processing collected XRD data.

2.13 Electrochemical Impedance Spectroscopy

2.13.1 Theory

Electrochemical impedance spectroscopy (EIS) is a technique used to gain information about the electrical properties of materials and their interfaces. A material can be either insulating (a dielectric) or exhibit some level of conductivity. The conduction can be either ionic or electronic, and may be either short-range (AC) or long-range (DC).[26] Long-range conduction is diffusive and is due to the random motion of charge carriers over extended distances, whereas short-range conduction is sub-diffusive (dispersive), due to the correlated motion of charge carriers over short

distances.[27] Broadly speaking, impedance can be thought of as the AC analogue to DC resistance, and includes a frequency-dependent reactance component, made up of a combination of capacitive and inductive contributions. The electrical properties of a material comprise transport, polarisation and magnetic processes, which can be considered as resistive, capacitive and inductive effects, respectively.

In impedance spectroscopy, an AC signal is applied over a wide frequency range and the characteristic response measured. The technique may be used to investigate the dynamics of bound or mobile charges in the bulk or interfacial regions of any kind of solid or liquid. In doing so, it may be possible to distinguish between, and measure, different electrical property types. Impedance spectroscopy has the advantages that it is *in situ*, non-destructive, and can be used on a variety of materials and devices. However, while the technique is relatively straightforward to use, analysis and interpretation of collected data is often less so.

For an introduction to the concepts of resistance and capacitance see Section 1.1. In impedance spectroscopy, an electric stimulus (a known voltage or current) is applied to a system and the response (resulting current or voltage) measured.[28] The voltage V delivered by mains AC electricity varies sinusoidally with time t and can be represented by Equation 2.12:

$$V = V_0 sin\omega t \tag{2.12}$$

where V_0 is the amplitude signal and ω is the radial frequency (radians/second), which is calculated from frequency f (Hz) using Equation 2.13.

$$\omega = 2\pi f \tag{2.13}$$

For a pure resistor, there is no phase difference between the voltage and current signals. In an impure resistive linear (or a pseudo-linear) system, the current response (I) is a sinusoid at the same frequency but shifted in phase (ϕ), and has a different amplitude (I_0):

$$I = I_0(sin\omega t - \phi) \tag{2.14}$$

This is illustrated in Figure 2.12. An expression analogous to Ohm's Law (Eq. 1.2) allows us to calculate the overall impedance Z of the system:

$$\boldsymbol{V = IR} \qquad \textbf{(Ohm's Law)}$$

$$Z = \frac{V}{I} = \frac{V_0 \sin(\omega t)}{I_0 \sin(\omega t - \phi)} = Z_0 \frac{\sin(\omega t)}{\sin(\omega t - \phi)} \qquad (2.15)$$

The impedance is therefore expressed in terms of a magnitude and a phase shift and is a vector quantity. In order to ease the handling of circuits with multiple components, the impedance can be expressed in terms of complex exponential functions through the use of Euler's relationship (Eq. 2.16).

$$\textbf{(Euler's Formula)} \quad \boldsymbol{e^{j\omega t} = cos\omega t + jsin\omega t} \quad (\text{where } j = \sqrt{-1}\,) \qquad (2.16)$$

Equation 2.15 then becomes the following where *Im* is used to designate the imaginary component of the complex number:

$$Z = Z_0 \frac{Im\left(e^{j\omega t}\right)}{Im\left(e^{j(\omega t - \phi)}\right)} \qquad (2.17)$$

which can be rewritten as

$$Z = Z_0 \frac{e^{j\omega t}}{e^{j\omega t}.e^{-j\phi}}$$

Therefore, the impedance is a frequency-dependent complex number characterised by the ratio of voltage to current and the phase angle shift between them, Φ:

$$\boldsymbol{Z^* = \frac{V}{I} = Z_0 e^{j\phi} = Z_0(cos\phi + jsin\phi) = Z' + jZ''} \qquad (2.18)$$

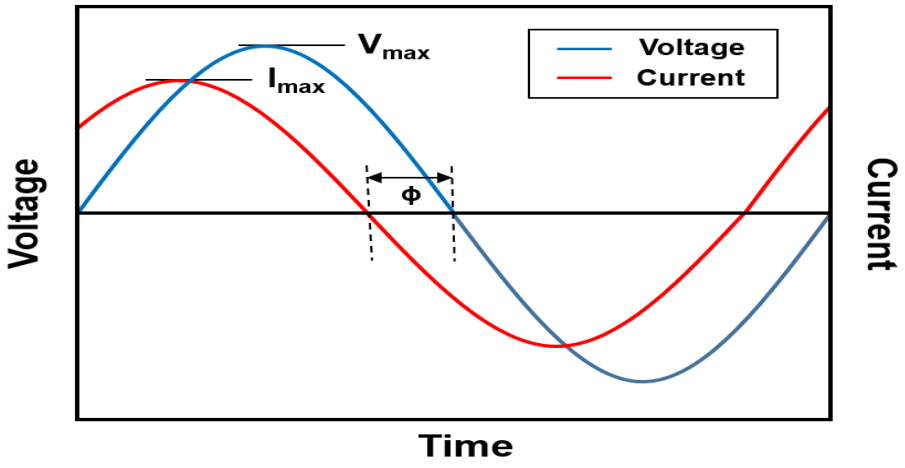

Figure 2.12 Relationship between the sinusoidal AC voltage signal and current response.

As mentioned previously, for a perfect resistor there is no phase difference between the voltage and current signals and so, at all frequencies, the impedance of a resistor is given by Equation 2.19. Hence, the impedance of a resistor is real and takes the value of the resistor's resistance at all frequencies. The impedance of a pure capacitor, on the other hand, has only an imaginary component, and is inversely proportional to the product of ω and capacitance C (Eq. 2.20).[29] The impedance of an inductor also only possesses an imaginary component and is proportional to the product of ω and inductance L, (Equation 2.21). The derivations for the impedances of a capacitor and inductor are given in Appendix B.

Resistor: $$Z^* = R \tag{2.19}$$

Capacitor: $$Z^* = \frac{1}{j\omega C} \tag{2.20}$$

Inductor: $$Z^* = j\omega L \tag{2.21}$$

The j term can be removed from the denominator of Equation 2.20 through the following:

$$Z^* = \frac{1}{j\omega C} \times \frac{j}{j}$$

$$= \frac{j}{j^2 \omega C}$$

As

$$j^2 = -1$$

hence

$$Z^* = -\frac{j}{\omega C}$$

While resistance is always positive, reactance can be positive or negative. Therefore, in accordance with the above equations, a capacitive reactance translates into a negative imaginary impedance and an inductive reactance translates into a positive imaginary impedance.

While impedance spectroscopy is a relatively easy technique to use, the difficulty usually lies in performing a meaningful interpretation of the results obtained. It is often beneficial to plot gathered data using different complex formalisms to highlight separate features of it. There are four commonly-used formalisms to represent collected data: impedance, Z^*; admittance, Y^*; permittivity, ε^*, and electrical modulus, M^*.[30] These formalisms are inter-related by Equations 2.22-2.25.

$$\text{Impedance:} \quad Z^* = (Y^*)^{-1} \tag{2.22}$$

$$\text{Admittance:} \quad Y^* = j\omega C_0 \varepsilon^* \tag{2.23}$$

$$\text{Permittivity:} \quad \varepsilon^* = (M^*)^{-1} \tag{2.24}$$

$$\text{Electrical modulus:} \quad M^* = j\omega C_0 Z^* \tag{2.25}$$

The blank capacitance C_0 is the capacitance for the same volume of free space as that of the sample being measured and is given by Equation 2.26, where e_o is the vacuum of free space (8.854×10^{-14} F cm^{-1}), d is the thickness of the region under consideration (cm) and A the surface area (cm^2).

$$C_0 = e_o \frac{A}{d} \tag{2.26}$$

Impedance spectroscopy data may also be presented in different graphical ways to highlight separate features of the results. The use of complex plane plots, also known as Nyquist plots, is one of the most common graphical presentations, in which the imaginary (reactive) component Z'' is plotted against the real (resistive) component Z' using the same linear scales. Spectroscopic plots may also be used, in which either the real or imaginary component, on a linear scale, is plotted against frequency on a logarithmic scale. These various ways of data presentation give different weightings to a data set and can aid greatly in subsequent analysis and interpretation.

Real world materials and devices are a combination of resistive, capacitive and inductive processes. Hence, the electrical properties of these can be represented by networks of R, C and L components. When performing analysis of impedance results, models are used in the form of equivalent electrical circuits, comprised to a first approximation of resistance and capacitance elements (inductance can often be

neglected), with the objective of assigning these to different physical processes and components within the material/device. Each electrically distinct region of a sample can be represented by its own parallel *RC* element. The origin of this may be understood by considering an ideal insulator (dielectric). In an equivalent electrical circuit, this would be best represented by a capacitor, which would capture all the charge and prevent it from passing through the material. However, in reality, ideal insulators do not exist and DC current is able to 'leak' through. Therefore, a more accurate description of such a component is a 'leaky capacitor'.[31] This can be represented electrically by placing a resistor in parallel with a capacitor. The capacitor describes the insulating dielectric properties of the material, but the resistor describes the leakage behaviour, as DC current is able to pass through the resistor and bypass the capacitor, thus evading the charge storage device. At low frequency, the impedance of the capacitor is high (Eqn. 2.20), so current mainly flows through the resistor, and as the frequency increases, more current flows through the capacitor. The magnitude of *R* controls the degree to which the capacitor leaks and the magnitude of *C* controls the permittivity of the medium which makes up the resistor. Hence, to a first approximation, each electrically distinct component of a sample may be represented by a parallel *RC* element, which is characterised by a unique time constant, τ (in seconds), given by the magnitude of the *RC* product (Eq. 1.12). In impedance spectroscopy, electrical components and parallel *RC* elements are separated on a frequency scale according to their time constants. This allows the electrical make-up of a material to be evaluated.

$$\boldsymbol{\tau = RC} \qquad \textbf{(Time Constant)}$$

Conduction can be thought of as the movement (hopping) of charge carriers (ions/electrons). There is often a significant and variable time delay between successive charge carrier 'hops'. The overall conductivity of the system is determined not by the time taken for an individual hop, but by the residence or waiting times between sequential hops. The residence time determines the *R* value of the time constant, and because it is an average value, broad relaxation processes are detected by impedance spectroscopy, rather than sharp resonances (as seen with other spectroscopic techniques e.g. NMR, IR). Broad relaxations are detected at different frequencies with a relaxation maxima given by Equation 2.27. The term

ω_{max} represents an angular frequency where the real and imaginary components of impedance have the same value. Hence, at this frequency, equal amounts of current are flowing through the resistor and capacitor. This relationship is of fundamental importance for understanding impedance spectroscopy.

$$\omega_{max} RC = 1 \qquad (2.27)$$

There is an activation barrier associated with a charge carrier hop. If the average residence time depends only on the activation barrier, independent of other processes in the structure, this overall conduction is given by an ideal parallel *RC* element. Increasing the temperature of the sample increases the vibrational energy of ions/electrons and increases the success rate for a hop. This in turn causes the average site residence to decrease and, hence, *R* is reduced. Very resistive processes may occur at such a low frequency that measuring them by impedance spectroscopy at room temperature would take an unfeasibly long time. By increasing the temperature, these phenomena can be brought into the 'frequency window' of the measurement. Similarly, extremely conductive processes that occur at very high frequencies may be observed by cooling the sample down.

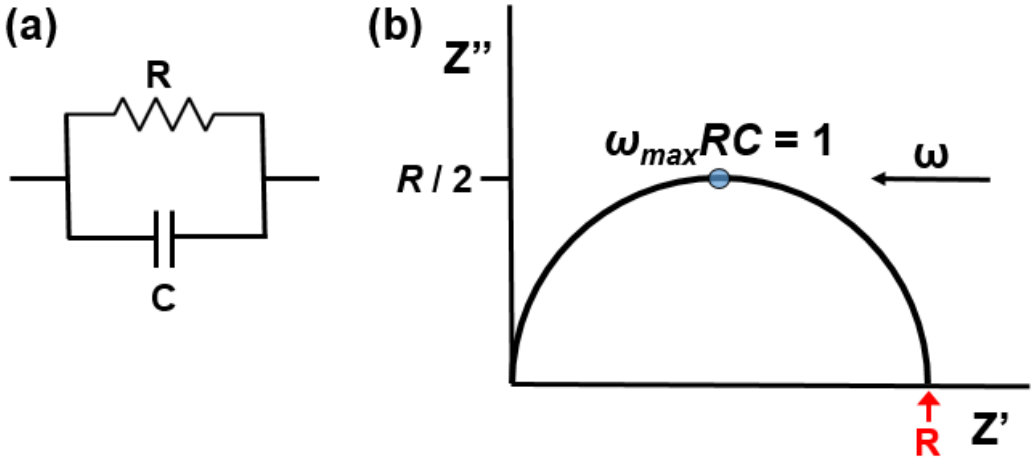

Figure 2.13 A parallel RC element (a) and its impedance complex plane plot (b).

A parallel *RC* element along with its impedance complex plane plot are shown in Figure 2.13. In order to understand the origin of this graphical presentation and the derivation of the *Z** equation, it is important to first be aware of the principle that impedances add in series and admittances add in parallel. The admittance is also the

reciprocal of impedance (Eqn. 2.22). Therefore, the summation of the reciprocals of equations 2.19 and 2.20, gives the admittance for a parallel *RC* element:

$$Y^* = \frac{1}{R} + j\omega C \tag{2.28}$$

The impedance can then be derived as follows:

$$Z^* = (Y^*)^{-1} = \frac{1}{\frac{1}{R} + j\omega C}$$

$$= \frac{1}{\frac{1}{R}(1 + j\omega RC)}$$

$$= \frac{R}{1 + j\omega RC} \tag{2.29}$$

In order to separate real, *Z'* and imaginary, *Z''* components, the numerator and denominator are both multiplied by the complex conjugate of the denominator (1 - *jωRC*):

$$Z^* = \frac{R(1 - j\omega RC)}{(1 + j\omega RC)(1 - j\omega RC)}$$

$$= \frac{R - j\omega R^2 C}{1 - j^2\omega^2 R^2 C^2} \tag{2.30}$$

As

$$j^2 = -1$$

hence

$$Z^* = \frac{R - j\omega R^2 C}{1 + (\omega RC)^2}$$

$$Z^* = \frac{R}{1 + (\omega RC)^2} - j\frac{\omega R^2 C}{1 + (\omega RC)^2} \tag{2.31}$$

As the imaginary component is purely capacitive, it is written with a negative *j*, and the notation for the complex impedance in this instance is:

$$Z^* = Z' - jZ''$$

Therefore, by combining the preceding derivation with Equation 1.12, we get:

$$Z' = \frac{R}{1 + (\omega\tau)^2} \qquad (2.32)$$

$$Z'' = \frac{R\omega\tau}{1 + (\omega\tau)^2} \qquad (2.33)$$

Hence, the *Z** complex plane plot (Fig. 2.13) takes the form of a semicircle with a maximum frequency that occurs according to Equation 2.27, with height *R*/2. Impedance data plotted in such a way for an ideal parallel *RC* element is said to exhibit a Debye-like response. The diameter of the semicircle, and low frequency intercept on the Z' axis, is *R* (this is found when ω = 0).

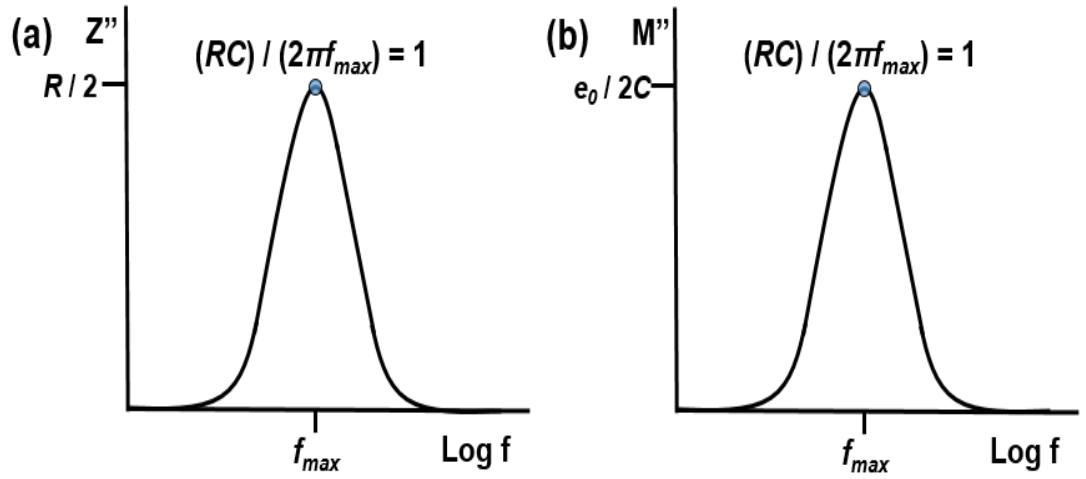

Figure 2.14 Spectroscopic plots for a parallel *RC* element: (a) *Z''* and (b) *M''*.

Most materials and devices consist of multiple electrically distinct regions. Hence, we can represent this electrically as several parallel *RC* elements connected together in series. As mentioned previously, data from impedance spectroscopy measurements may be presented using different complex formalisms, and in different graphical formats, to highlight separate features of the results. Figure 2.14 presents data as a spectroscopic *Z''* plot in (a) and *M''* plot in (b), which allows separate visualisation of the *Z''*, *M''* components against frequency on a logarithmic scale. A spectroscopic plot of *Z''* against log frequency (a) is scaled according to *R*, meaning that for a series of parallel RC elements, the largest *Z''* peak will

correspond to the most resistive component. For an ideal parallel *RC* element, Z''_{max} = R/2, and for a perfect Debye peak, the full width half maximum (FWHM) will measure 1.14 decades on the log *f* scale.[32] The electrical modulus *M''* spectroscopic plot (b) is scaled according to C_0/C and has a maximum value at $C_0/2C$ (the C_0 terms are changed to e_0 if data has been geometry corrected prior to plotting it). This means that for a series of parallel *RC* elements, the component with the largest *M''* peak possesses the smallest capacitance.

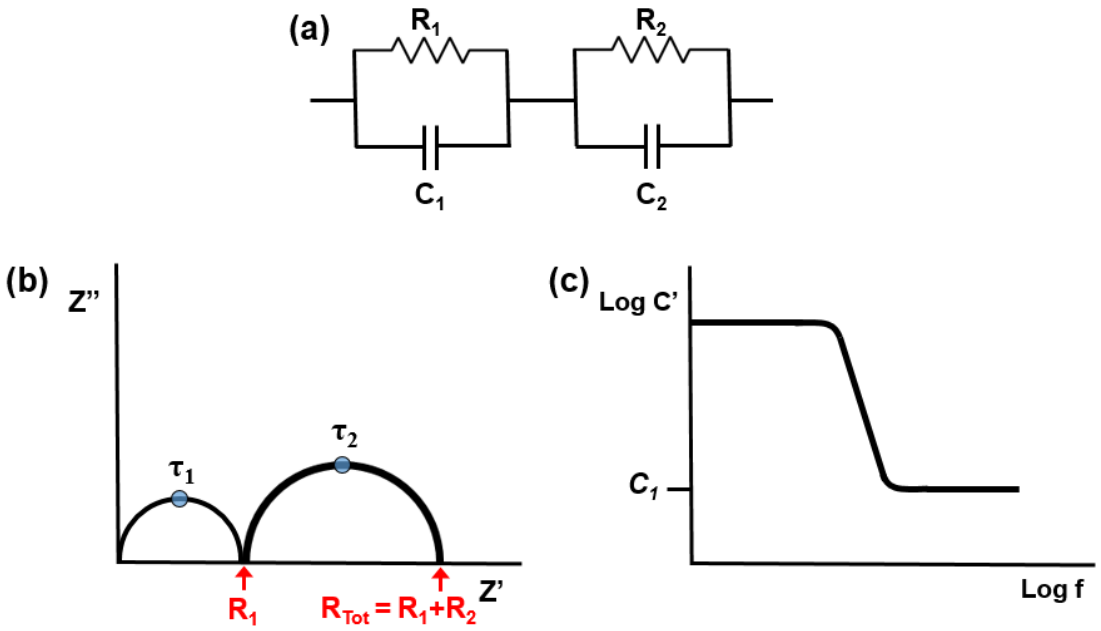

Figure 2.15 (a) A series combination of two parallel *RC* elements, (b) corresponding impedance complex plane plot, (c) corresponding spectroscopic plot of capacitance *C'* on a logarithmic scale.

For the circuit shown in Fig. 2.15 (a) of two parallel *RC* elements connected in series, we can simply add together the impedances of the separate components. The resulting impedance complex plane plot (b) therefore consists of two semicircles of diameters R_1 and R_2. The total DC resistance (R_{Tot}) of the system can be calculated by adding the separate resistive components together:

$$R_{Tot} = R_1 + R_2 + \cdots \qquad (2.34)$$

If the time constants for the *RC* elements are separated by at least two orders of magnitude, then the components are well separated in the impedance response and there are two distinct semicircles,[31] as is shown in Figure 2.15. However, if the time

constants are more similar, then a composite arc is formed in the complex plane plot, and it is less easy to distinguish between the separate components. In such a case, the total resistance is still readily obtained but a data fitting procedure is required to deconvolute the total resistance into its separate components. In such an instance, it can be useful to examine a combined *Z''/M''* spectroscopic plot, as these formalisms give different weightings to data, as was previously discussed.

Another useful data presentation to help in separating different electroactive regions within a sample is a plot of capacitance *C'* against log *f* (c), where *C'* is just the geometry corrected capacitance, given by:

$$C' = C\frac{d}{A} \qquad (2.35)$$

To a first approximation, each plateau (constant capacitance region) in the *C'* plot can be assigned to a separate electroactive region. Hence, the high frequency plateau in (c) is attributed to the limiting high frequency capacitance, C_1. However, the value of each plateau is often just an approximation of the capacitance of the component assigned to it. In reality, each plateau is a composite value, with multiple contributions coming from separate *RC* components.

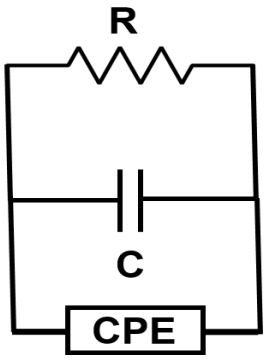

Figure 2.16 A parallel *RC* element with a contant phase element (*CPE*) connected in parallel.

As mentioned previously, the residence time between successive ion/electron hops, determines the *R* value of the time constant. If the average residence time depends only on the activation barrier, independent of other processes in the structure, this overall conduction is given by an ideal parallel *RC* element. In reality, however,

other factors are at play e.g. the availability of vacant sites, interaction between charged species. These constraints to independent conduction steps present themselves in impedance data in the form of distorted/depressed semicircles in the complex plane plot and asymmetric *Z''*, *M''* peaks, whose peak maxima no longer coincide.[33] Therefore, an additional component, a constant phase element (*CPE*), is required to account for the frequency dependency of the response and represent departure from ideality.[34] A constant phase element is a combined variable resistor and variable capacitor, and is often placed in parallel to the *RC* element (Fig. 2.16).[35] The impedance of a constant phase element is defined as:

$$Z^* = \frac{1}{(j\omega)^n Y_0} \qquad (2.36)$$

where Y_0 is a constant and $0 < n < 1$. For a value $n = 1$ the *CPE* reduces to a perfect capacitor, and for $n = 0$ it is a resistor. When the parameter is assigned a value between 0 and 1 it is a non-ideal capacitor with a resistive component. Constant phase elements are successful in providing good fits to data in all formalisms. No other function that has been used previously to model non-ideality has achieved this degree of data analysis and universal applicability.[31]

2.13.2 Impedance Spectroscopy for Electroceramics

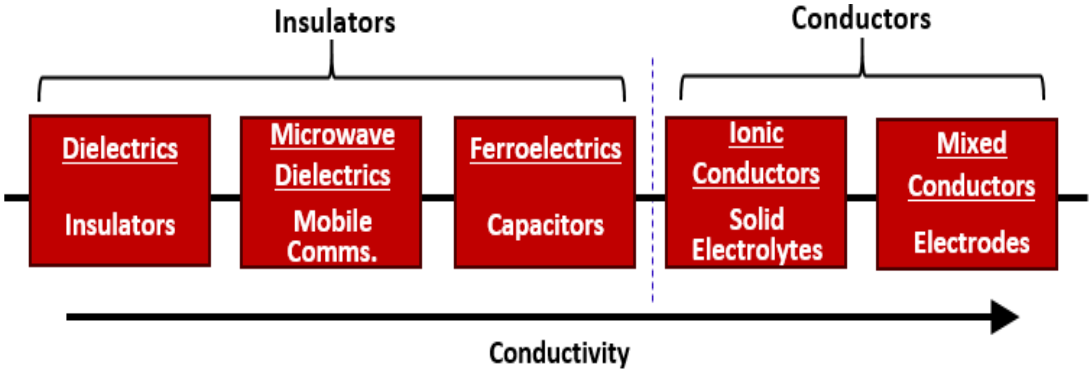

Figure 2.17 Examples of electroceramic materials studied by impedance spectroscopy.

An electroceramic is an inorganic solid, usually a polycrystalline oxide, possessing electrical properties that can be exploited for useful applications.[36] These electrical properties depend on both the overall crystal and defect structure of the solid, as well

as any interfaces present within the material. Properties may range from insulating to a variety of conduction types (Fig. 2.17). Impedance spectroscopy enables the overall electrical properties of the sample to be divided into component parts, which can then be systematically studied or modified. It is the only widely-applicable technique for characterising the electrical microstructure of materials. The total resistance of the solid is measured and, through appropriate data analysis, can be deconvoluted into contributions from different regions within the sample's structure. Furthermore, the technique makes it possible to determine the nature of the conducting species (ions/electrons).

The brickwork layer model (BLM)[37] is a useful approach for analysing impedance spectroscopy of electroceramics (Fig. 2.18). In this, an electrode is applied to either side of an idealised solid, assumed to consist of cubic conductive grains, referred to as the bulk of the material, surrounded by thin high-resistive grain boundaries. Each of these electroactive regions - bulk, grain boundary, sample-electrode interface – has a resistance and capacitance associated with it; and so to a first approximation, an electroceramic may be modelled by several parallel *RC* elements connected in series. Hence, each electrical component of the solid possesses a different time constant and, therefore, they can be separated out according to frequency in the generated impedance spectrum and characterised one by one. The physical origins of these electrical properties can then be determined by varying the temperature, atmosphere etc.

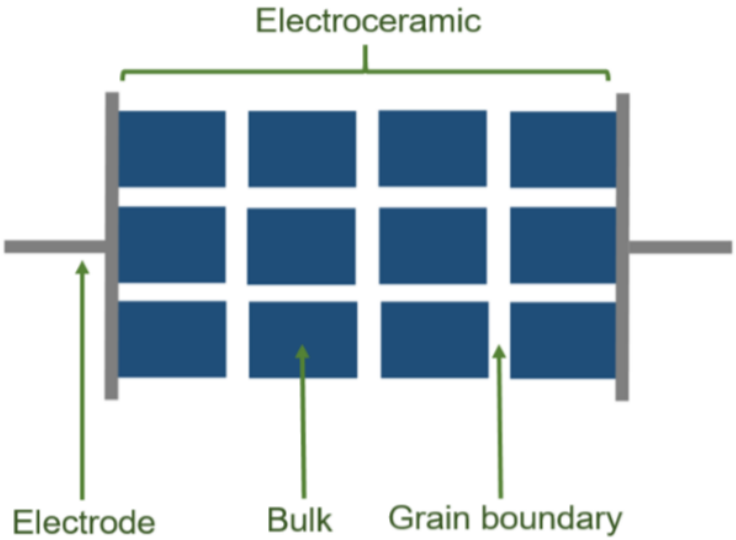

Figure 2.18 Brickwork layer model (BLM) for an electroceramic.

In an electroceramic, the grain boundary resistance is assumed to be greater than the bulk of the sample. The origin of this may be due to resistive impurity phases at the grain boundaries and/or space charge effects.[38–40] Assuming the relative permittivity of the grain boundary and the bulk are the same, then in accordance with Equation 1.9, the grain boundary will have a larger capacitance, as it is thinner. As the bulk has a smaller resistance and capacitance than the grain boundary, it possesses a smaller time constant (Eq. 1.12). The time constant is inversely proportional to frequency (Eq. 2.27), and, therefore, this component of the electroceramic will appear at a higher frequency in the EIS spectrum. Hence, the bulk of an electroceramic is usually the highest frequency component in an impedance complex plane plot. The capacitance values of the different electroactive components in the solid will vary by several orders of magnitude, depending on the geometry of the regions responsible. A capacitance in the picofarad region is typical for a sample bulk (for a material with permittivity ~ 10), with thinner regions of the electroceramic possessing higher capacitances. A summary of typical capacitance values is provided in Table 2.2.[41] Hence, by calculating the capacitance for each arc in an impedance complex plane plot through use of Equation 2.27, it may be possible to determine which region of the sample is being measured at a particular frequency. Plotting data as C' against f on logarithmic scales also allows for a quick separation of the different phenomena, at least in theory, with each showing up as a plateau.

Table 2.2 Capacitance values and their possible interpretations.[41]

Capacitance / F cm^{-1} *	Phenomenon
10^{-12}	Bulk
10^{-11}	Minor, second phase
10^{-11} – 10^{-8}	Grain boundary
10^{-10} – 10^{-9}	Bulk ferroelectric
10^{-9} – 10^{-7}	Surface layer
10^{-7} – 10^{-5}	Sample-electrode interface
10^{-4}	Electrochemical reactions

* Capacitance values are corrected for overall sample geometry of the electroceramic, rather than geometry of region or phenomena.

In a well-sintered dense ceramic, the grain boundary will usually possess a capacitance 2-3 orders of magnitude greater than the capacitance of the bulk.[31] However, in a poorly sintered ceramic, which contains some porosity, the capacitance values may be more similar. This results in less well separated components (arcs) in the impedance complex plane plot and makes it difficult to distinguish between the different regions. Impedance data can therefore be used as an indicator for quality of a ceramic and be used to refine fabrication procedures. A way of gaining greater insight into the origin of the different features in a complex plane plot is by presenting data as combined *Z''*/*M''* spectroscopic plots.[42] The bulk component usually has the smallest capacitance as a consequence of its geometry, so the *M''* spectroscopic plot can be used to identify this component of a data set. The capacitance of the bulk can then be calculated, as the maximum has a value corresponding to $e_0/2C$, which in turn can be used to estimate the resistance of the bulk from Equation 2.27. Furthermore, the largest *Z''* peak in the data set indicates the most resistive component, which is often the grain boundary.

If the dominant *Z''* and *M''* peaks in combined *Z''*/*M''* spectroscopic plots occur at separate frequencies, then the impedance response has both a bulk and grain boundary contribution, and the electroceramic is electrically heterogeneous. If the combined *Z''*/*M''* spectroscopic plots show only single overlapping peaks at the same frequency, then the material can be described as electrically homogeneous with the response dominated by the bulk; there is no significant grain boundary impedance. However, if the peaks have broadened significantly and are slightly offset, this indicates that here is some degree of electrical bulk inhomogeneity in the sample. The origin of this heterogeneity might be the existence of regions with small deviations in dopant level compared to one another, or possibly core-shell microstructures, where there is a compositional gradient from the surface of grains to their interior.[43] Impedance data for a sample possessing core-shell microstructures may even possess two bulk-related *M''* peaks if the time constants of the core and shell are different enough.[44] The formation of core-shells is dependent upon ceramic processing conditions, and, hence, it is important to remember that impedance data is controlled by the fabrication procedure used, as well as the material present.

From impedance data and appropriate equivalent circuit analysis, values for the resistances and capacitances of the different electroactive regions may be determined. Furthermore, from similar impedance measurements over a range of temperatures, activation energies E_a (eV) may be calculated for the different regions of the electeroceramic via the Arrhenius equation:

(Arrhenius Equation) $$\sigma = Ae^{\frac{-E_a}{kT}} \quad (2.37)$$

where σ is conductivity in siemens (S), A is a pre-exponential factor/constant (S), k is the Boltzmann constant (8.6173 x 10^{-5} eV K^{-1}), and T the absolute temperature (K). By obtaining the resistance at different temperatures from impedance data, Arrhenius plots may be constructed of the logarithm of conductivity σ against reciprocal temperature $1/T$.[45] For a single rate-limited thermally activated process, an Arrhenius plot gives a straight line, from which the activation energy can be determined via the gradient. If a similar E_a is obtained for the bulk and grain boundary components, this often indicates a poorly sintered (porous) ceramic.[31] The values of the activation energies can be used to help identify the type of conduction in the electoceramic, i.e. whether it is ionic of electronic.

The nature of the mobile charge species can also be inferred from examining low frequency impedance data. For electronically-conducting electroceramics, electrons are able to cross freely between the sample and electrode, so there is no resistive barrier associated with this and thus no response in the impedance spectrum. For ionic conductors, on the other hand, ions are not usually able to move between the sample and electrode, and, therefore, there is a build-up of ions at the sample-electrode interface. In such an instance, this contact is referred to as a blocking/double layer capacitor (C_{dl}). The sample-electrode interface is a very thin region of the electroceramic, and, therefore, this phenomenon shows up at low frequency, as a spike, in the EIS spectrum.[46] Such a spike is indicative of ionic conduction in the sample, and its imaginary impedance is given by Equation 2.38.

$$Z'' = -\frac{1}{\omega C} \quad (2.38)$$

Ideally, the spike should be vertical and, therefore, represented in an equivalent circuit by a capacitor connected in series to the rest of the impedance components.

However, a high surface roughness usually results in an inclined spike, and a constant phase element is, therefore, often more suitable to model the response.[47,48]

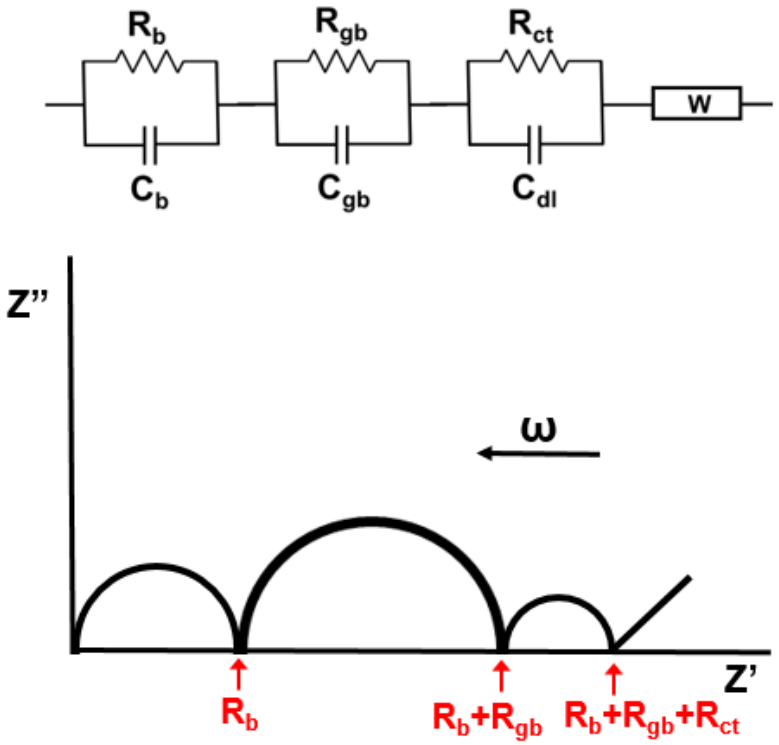

Figure 2.19 Schematic, idealised impedance spectrum of an ion conducting electroceramic showing bulk (b), grain boundary (gb), charge-transfer (ct) and Warburg (W) components.

Depending on the nature of the ionically-conducting system, electrode reactions may also occur. This is where there is electron exchange with ions at the two electrodes. There will be a resistance associated with this, referred to as a charge-transfer resistance (R_{ct}), which is placed in parallel to the double layer capacitor in the equivalent circuit.[49] Hence, for such systems, the low-frequency spike collapses to an additional arc,[50] which will have a capacitance in the microfarad region, consistent with Table 2.2. When this occurs, there will also be an additional component at low frequency, an inclined spike which represents the impedance associated with the solid state diffusion of ions to/from the electrodes.[51] The electrode is said to be partially blocking, and such a scenario is also indicative of ionic conduction in the material. When the spike is at an angle of 45° to the *Z'* (real) axis, this indicates infinite diffusion, and is referred to as a Warburg impedance *W*,[52] which takes the form of a constant phase element where n = 0.5. Figure 2.19 shows an idealised

impedance complex plane plot, along with the appropriate equivalent circuit, for a material exhibiting ionic conduction. At very high temperatures or very low frequencies, the Warburg element will also eventually collapse to an arc, as ions are able to diffuse through the entire thickness of the electrode.

Often, the charge-transfer and diffusion controlled regions at low frequency in the impedance spectrum are not well defined. The observed electrode response depends on the relative magnitudes of *Rct* and *W*.[52] If the electrode reactions proceed quickly, such as at high temperatures, the charge-transfer component may be small and difficult to observe in the impedance spectrum. Hence, the Warburg element dominates the response at low frequency in such an instance, and the circuit in Figure 2.19 can be approximated without the charge-transfer resistance and double layer capacitance. A low-frequency spike indicates that a significant amount of ionic conduction is present in the sample, but there may also be a degree of electronic conductivity also. For mixed conductors with a larger amount of electronic conduction there is no spike, but another arc at low frequency due to a parallel electronic pathway.[53] The circuit for an ionic conductor is then modified by placing an additional resistor in parallel with the sample (R_e), and a second in parallel with the Warburg element ($R_{w,e}$); as shown in Figure 2.20.[54]

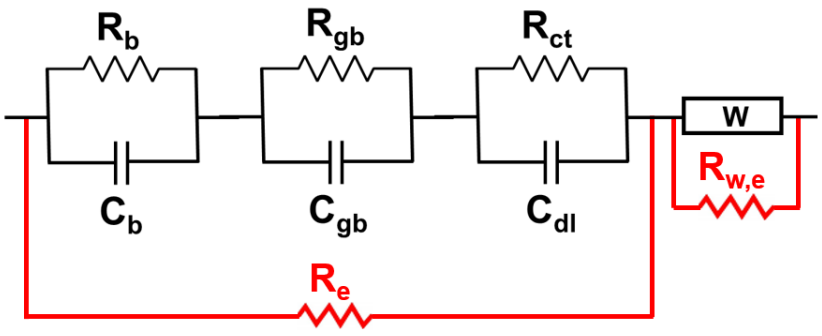

Figure 2.20 Equivalent electrical circuit for a mixed conductor.

In this work, pellets were pressed with 0.4 tons pressure and heated at the desired sintering temperature for 1 h. Platinum or gold electrode paste was painted on both sides of the pellet and dried by heating in a furnace. Impedance measurements performed in air, at room temperature and above, were collected with an Agilent E4908A analyser at 100 mV AC with a sweep frequency from 10 Hz to 1 MHz in

air. Low temperature impedance measurements were carried out using an Oxford Instrument cryocooler and an Agilent E4980A Precision LCR meter over the frequency range from 20 Hz to 1 MHz with 100 mV alternating voltage. Data collected in N_2/O2, at room temperature and above, used a Solartron 1260 analyser at 100 mV AC over the frequency range 10^{-1} to 10^6 Hz. Impedance data were corrected for overall pellet geometry and for blank capacitance of the conductivity jig. Analysis was performed using *ZView* software.

2.13.3 Characterisation of Batteries by Electrochemical Impedance Spectroscopy

All batteries possess an internal resistance, which is defined as an opposition to current flow. This is made up of a contribution of electronic and ionic resistances. Electronic resistance originates from the resistivity of the component materials of a battery and their interfaces. Ionic resistance is controlled by electrochemical factors, e.g. conductivity of the electrolyte, ion transfer across the electrode-electrolyte interface, diffusion through the electrode.[55] An increase in the internal resistance of a battery over time can indicate declining battery capacity or degradation,[56] hence, it is an important parameter for analysing cell performance. The internal resistance of a battery can be measured and monitored via a number of different methods.

The DC internal resistance (DCIR) measurement works by applying a brief step (dis)charge current (pulse) and measuring the voltage drop.[57] Only the DC resistance is obtained, with no information on the reactance of the system, meaning it is not possible to separate out different resistive contributions within the cell. In essence, the battery is treated as one large resistor using this technique. Furthermore, the measured value is dependent upon voltage amplitude and duration, and time taken to record data.[58] The instantaneous voltage drop after the current pulse is due to ohmic resistance (current collectors, electrolyte), however, a further drop will occur due to electrochemical processes (charge-transfer, diffusion). Hence, a different time taken to record the measurement will give a different value. The 1,000 Hz AC internal resistance (ACIR) test is another method. A 1 kHZ signal excites the battery and Ohm's Law used to calculate the resistance. However, similar to DCIR, this method

only gives information at a single point in time, which is dependent on the feature in the impedance spectrum at this frequency. The advantages of electrochemical impedance spectroscopy are that it is a non-destructive technique and provides a considerable amount of information across a wide frequency range in a relatively short space of time, while preserving the integrity of the battery. Furthermore, as the technique is particularly sensitive to systems that contain several impedance elements, including bulk components and interfaces, this makes it particularly well-suited for studying a battery, which is a multi-component device.

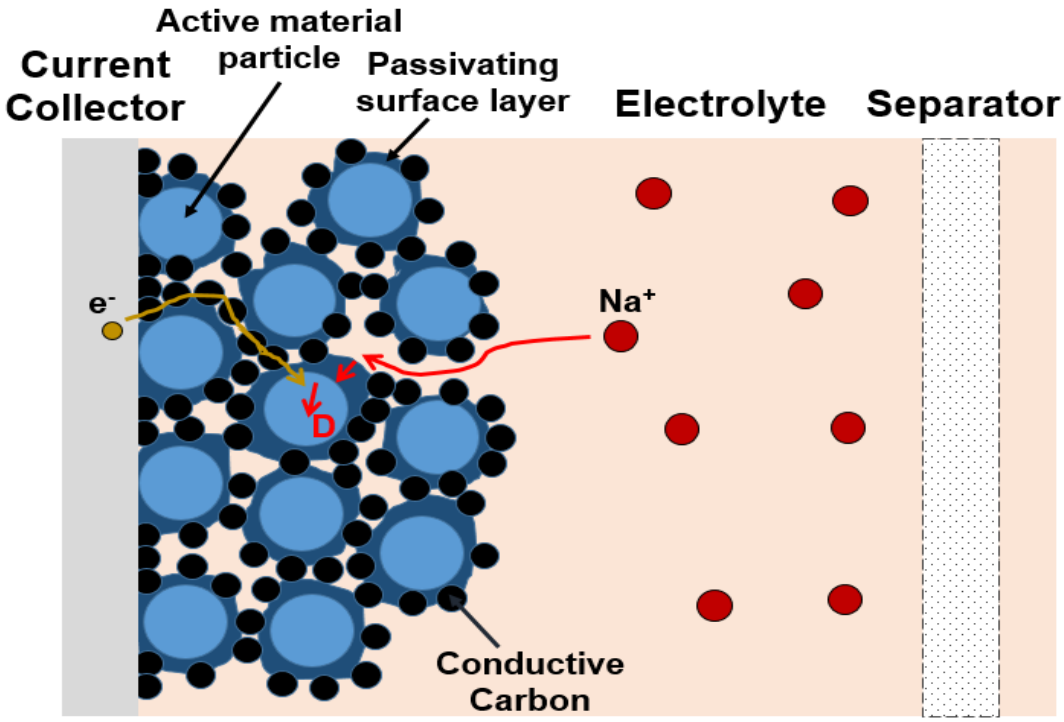

Figure 2.21 Kinetic steps in a sodium-ion battery.

A standard battery consists of two electrodes, an electrolyte, separator and current collectors. The different kinetic processes that occur inside a sodium-ion battery are illustrated in Figure 2.21.[59] The electrode is a porous structure, consisting of active material and conductive carbon additive particles, held together by a binder. The electrolyte conducts sodium ions, which are able to pass through the permeable separator. At the electrode, the Na^+ ions move into the electrolyte-filled cavities. There is an ionically-conducting passivating layer at the surface of the active material particles, formed by decomposition reactions. Electrons travel from the

current collector to the active material via hopping between particles. This leads to the formation of a double layer at the electrode-electrolyte interface where there are electrons at the surface of electrode particles and a layer of ions in the electrolyte surrounding them. At the active material surface, a charge-transfer reaction occurs where a positively charged ion and electron pair up to maintain local electroneutrality. The ion then diffuses (*D*) into the bulk of the electrode. Each of these kinetic steps inside a battery operates on a unique time scale (and thus possesses its own individual time constant). Therefore, conducting the EIS measurement across a wide frequency range allows for the dynamics of each elemental step to be analysed separately and, hence, each component of the cell to be characterised one by one. In this way, it may be possible to differentiate between individual resistive contributions inside the battery and, therefore, in doing so, determine what the major performance limiting factor is, i.e. identify the rate-limiting step. This can then be potentially overcome (its resistance reduced) to enhance the operation of the battery.

As with electroceramics, the analysis of impedance spectra for batteries may be aided through the use of models in the form of equivalent electrical circuits. These help to assign different parts of the obtained impedance spectrum to different components and processes inside the electrochemical cell. The Randles equivalent electrical circuit (Fig. 2.22), first proposed in 1947,[60] is one of the simplest models for describing processes at an electrochemical interface. It consists of an electrolyte solution resistance (R_s) in series with a double layer capacitance (C_{dl}), which is in parallel with a charge-transfer resistance (R_{ct}). The capacitor is often replaced with a constant phase element (*CPE*) because the characteristics of the double layer are non-ideal e.g. due to surface roughness. The rate of the charge-transfer reaction is controlled by the diffusion of reactants from the electrode surface, and so a Warburg element (*W*) is placed in series with R_{ct}. In real electrochemical systems, such as a battery, impedance spectra are often very complicated and the Randles circuit may not be appropriate. However, it is often a useful starting point for the development of other more complex models.

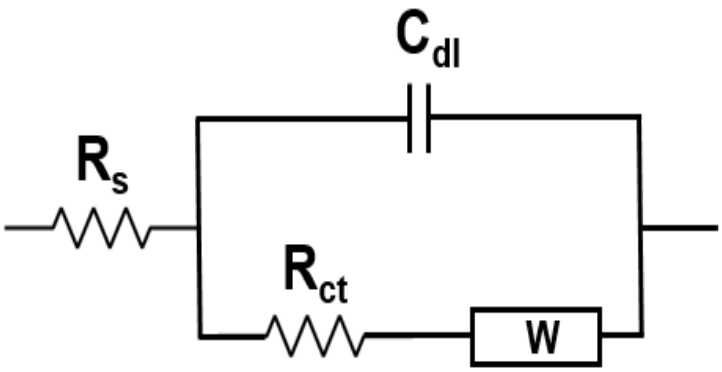

Figure 2.22 The Randles equivalent circuit.[60]

As well as being used to analyse specific kinetic properties of battery materials, electrochemical impedance spectroscopy can also be used to obtain important behavioural parameters. An impedance measurement can be conducted at any point during a battery's lifetime and at any point during its (dis)charging cycle. The generated spectrum is dependent upon the state of health of the battery and its state of charge. Therefore, by performing EIS measurements for a battery at various predefined SoC and SoH values, it may be possible to deduce relationships between certain EIS parameters from equivalent circuits and the state of the cell. Thus, it may then be possible in future to estimate the SoC and SoH value of a battery from impedance spectroscopy measurements.[61] This is not always straightforward, as battery impedance may increase and decrease during the course of a battery's lifetime. Therefore, often multiple model parameters are required for confident estimation.

To perform EIS on batteries, a frequency response analyser (FRA) is typically used in combination with an electrochemical interface. The electrochemical interface applies a constant voltage (CV) or constant current (CC) and the FRA superimposes a small AC signal, usually in the range mHz–MHz, and measures the response.[62] A multiplexer connects the FRA to the battery test system. A typical setup is shown in Fig. 2.23. The battery is connected using four wires — two for current flow and two for cell potential. This is in order to improve the accuracy of the EIS measurement as just a few microamps of current flowing in the voltage leads will result in an impedance error in both the real and imaginary components. The FRA outputs a signal to the cell via the counter electrode (I-) and the signal is returned through the

working electrode (I+). It also connects to a pair of reference electrode points (V+ and V-) to measure the voltage across the cell.

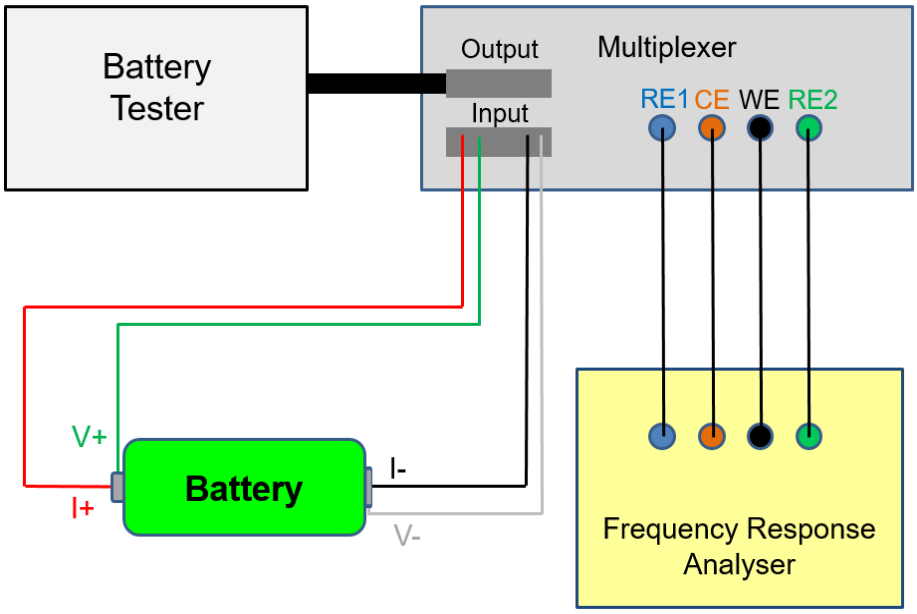

Figure 2.23 Experimental setup for impedance measurement of a battery.

EIS may be used to characterise either the static or dynamic impedance of a battery.[63] Dynamic measurements are conducted on the battery during charge/discharge by performing an EIS scan while simultaneously applying a DC bias across the cell. This allows for information to be obtained during operation of the battery, and is useful for determining the minimum (de)-insertion voltage for electrodes, as well as enabling any intermediary reactions/species to be detected and monitored. Static EIS, in contrast, is performed when the battery is at rest. For such a measurement, a reproducible steady state is required to ensure validity.[64] Therefore, an open circuit voltage is applied before conducting the measurement to ensure that the voltage does not vary significantly during the EIS measurement. Similarly, an additional rest period or open circuit may be implemented following the impedance scan to allow the cell to 'recover' from any changes that occur during the EIS run, prior to continuing with the cell cycling.

Impedance spectroscopy can also be used in either potentiostatic (constant voltage) or galvanostatic (constant current) mode.[61] Potentiostatic mode, where a voltage is applied at each frequency and the resultant current measured, is most common. The

current responds at the same frequency as the applied voltage but may be shifted in phase. In order to ensure a steady state, EIS usually is carried out with a small potentiostatic signal amplitude of 10 mV so that the cell response is pseudo-linear (in phase). If the system is non-linear, the response contains harmonics of the input signal frequency.[65] However, for larger batteries, which possess smaller impedances, even a signal this small can produce enough current that changes the state of the device. Therefore, for such a system, galvanostatic EIS may be favoured, as a relatively small change in voltage may result in a large DC current, whereas large changes in current usually result in only small changes in voltage.[66] There can also be a problem of OCV drift when performing potentiostatic measurements, which is not an issue for galvanostatic EIS. Care must be taken, however, to ensure that correct current amplitude is chosen when performing a glavnostatic measurement; for batteries, an amplitude of $\leq 5\%$ of the (dis)charge current is recommended.[67]

An idealised spectrum for a metal-ion battery is shown in Fig 2.24 together with its equivalent circuit. There is also often a tail below the real Z' axis at higher frequencies, not shown, which is due to inductive effects associated with the battery and/or the experimental setup. With decreasing frequency, the first feature is a non-zero ohmic resistance where the spectrum intersects the real Z' axis at high frequency; it is represented in the equivalent circuit by a resistor (R_{HF}). The two semi-circles, usually of different size, are each represented by a parallel *RC* element. To account for, and model, a non-ideal or distorted semi-circle, a constant phase element (*CPE*), is added in parallel with the parallel *RC* element. The fourth feature, at low frequency, is frequently an inclined spike, which can be a non-ideal capacitor represented by a *CPE* or a Warburg element (where $n = 0.5$) if the spike is at 45° to the Z' axis.

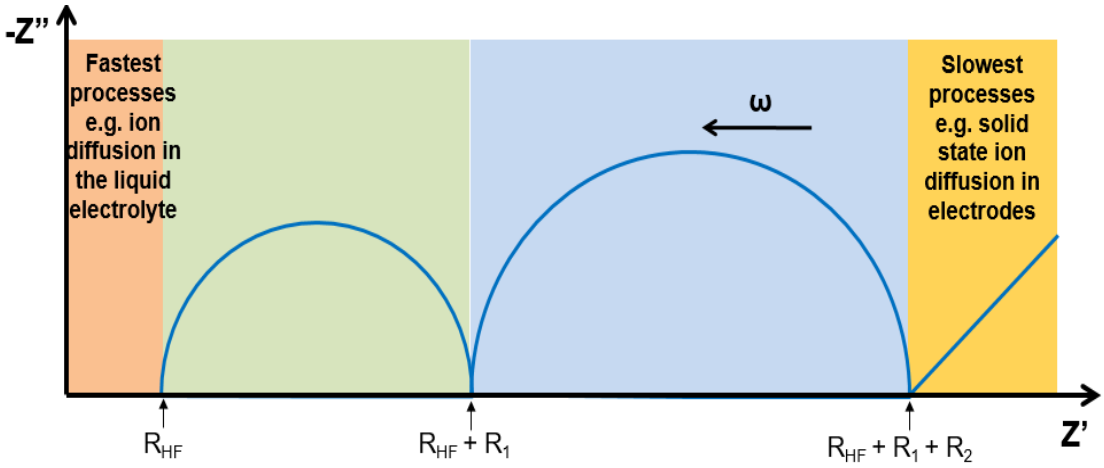

Figure 2.24 Schematic idealised complex plane plot for a battery together with its ideal equivalent electrical circuit.

The impedance spectrum shows a separation of processes in the battery, dependent upon time-scale. The high-frequency section consists of the fastest processes, which make up the ohmic resistance: ionic conductivity of the electrolyte, separator and the electron conductivity in the current collector and wires. The electrolyte resistance dominates this response as the diffusion of solvated ions is the slowest process of them. There is no polarisation (capacitance) associated with these processes (at least for a highly concentrated salt electrolyte),[59] and, therefore, they are represented by only a resistor placed in series to the impedance of the rest of the cell. The slowest process in a battery will be solid state diffusion of Li^+/Na^+ ions in the bulk of the electrode, and, hence, this is seen at low frequency as a spike. The remainder of the components in the mid-frequency range will account for the rest of the cell: charge-transfer, the passivating surface layer etc.

Figure 2.24 shows an idealised impedance spectrum, but in reality, data obtained is much more complex. Hence, when carrying out impedance measurements, it can be difficult to interpret the generated spectrum due to the overlapping of processes with similar time constants. It may be possible to an extent to afford better separation of the components through cooling down the system, which causes resistances and subsequently, the difference between time constants to increase. Half-cell measurements can also be used to study the cathode and anode separately, however, the impedances associated with the electrodes in this setup may not reflect the processes occurring in a full-cell battery at different states of charge and discharge.

Measurements may also be made on symmetric cells in which the two cells are disassembled and the cathode of one is replaced with the anode of the other, and vice versa.[68] However, such approaches are limited as symmetric cells cannot be charged and discharged in the same way as a fully functioning battery. The arduous process of disassembling and reassembling cells must therefore be carried out repeatedly, in order to gather information at different states of charge and states of health. For these reasons, a three-electrode cell setup is often preferred. A three-electrode cell design incorporates a spectator reference electrode, which (at least in theory) does not interfere with the cycling of the battery. The battery is then charged/discharged as usual, but as well as recording the impedance across the entire cell, the impedances of the cathode and anode can be measured separately against the reference. It is therefore possible to monitor how each electrode contributes to the overall impedance of the battery.[62]

In this work, two-electrode cells were tested using a Maccor Series 4000 Automated Test System. The layered oxide cathode was connected to the positive terminal and the carbon anode to the negative terminal using banana clips. AC impedance measurements were performed using a frequency response analyser (Solartron Modulab). All cells were held at a constant temperature of 30 ± 0.5 °C using a Maccor Temperature Chamber. Three-electrode cell measurements were performed using a potentiostat with a parallel frequency response analyser (Solartron Pstat 1470E/FRA 1455A). Three intrinsic EIS scans were made using different methods for connecting the Solartron equipment to the electrodes. In the first, the impedance of the cell was measured without using the reference electrode. In the second, the impedance of the working electrode (layered oxide) was measured against the reference (Li/Na metal) electrode, and, in the third, the counter electrode (carbon) was measured versus the reference electrode. All cells were held at a constant temperature of 30 ± 0.5 °C using a MMM FRIOCELL Incubator.

Each battery was left for 32 h at 30 °C prior to cycling to allow time to equilibrate. An impedance measurement was then performed before beginning to cycle the cell. The cells were cycled under constant current/constant voltage (CC/CV) conditions, with four hours for equilibration after each charging/discharging step, prior to performing an impedance scan. AC impedance measurements were performed in

static potentiostatic mode by varying the frequency with a perturbation signal amplitude of 10 mV (peak to peak) from 10 mHz to 100 kHz for two-electrode cells and 10 or 50 mHz to 1 MHz for three-electrode measurements. An additional one-hour open circuit voltage (OCV) hold after running EIS allowed the cell to return to a steady state. Data acquisition was performed using *MIMS* and *Multistat* software for two- and three-electrode cells respectively. *ZView* software was used for impedance data analysis.

2.14 References

1 International Centre for Diffraction Data, PDF-4+ XRD Database 2020, ICDD, Newton Sqaure, 2020.

2 W. H. Bragg and W. H. Bragg, *Proc. R. Soc. London. Ser. A, Contain. Pap. a Math. Phys. Character*, 1913, **88**, 428–438.

3 A.R. West, S*olid State Chemistry and its Application*s *Student Edition*, John Wiley & Sons, Chichester, 2nd edn, 2014.

4 H. M. Rietveld, *J. Appl. Crystallogr.*, 1969, **2**, 65–71.

5 A. C. Larson and R. B. Von Dreele, *General Structure Analysis System (GSAS) Report LAUR 86-748*, Los Alamos National University, Los Alamos, 2004.

6 B. H. Toby, *J. Appl. Crystallogr.*, 2001, **34**, 210–213.

7 R. A. Young, *Rietveld Method.pdf*, Oxford University Press Inc., New York, 1993.

8 V. K. Pecharsky and P. Y. Zavalij, *Fundamentals of powder diffraction and structural characterization of materials*, Springer US, New York, 2005.

9 S. K. Sharma, D. S. Verma, L. U. Khan, S. Kumar and S. B. Khan, *Handbook of Materials Characterization*, Springer International Publishing, Cham, 2018.

10 B. J. Inkson, in *Materials Characterization Using Nondestructive Evaluation (NDE) Methods*, ed. G. Hübschen, I. Altpeter, R. Tschuncky and H.-G. Herrmann, Elsevier Inc., 2016, ch. 2, pp. 17–43.

11 R. Bottom, in *Principles and Applications of Thermal Analysis*, ed. P. Gabbott, Blackwell Publishing Ltd, Oxford, 2008, ch. 3, pp. 87–118.

12 S. Ogata, S. Homma, A. Sasahira, F. Kawamura, J. Koga and S. Matsumoto, *J. Nucl. Sci. Technol.*, 2004, **41**, 135–141.

13 W. Steinmann, S. Walter, M. Beckers, G. Seide and T. Gries, *Thermal Analysis of Phase Transitions and Crystallization in Polymeric Fibres, Applications of Calorimetry in a Wide Context - Differential Scanning Calorimetry, Isothermal Titration Calorimetry and Microcalorimetry*, https://www.intechopen.com/books/applications-of-calorimetry-in-a-wide-context-differential-scanning-calorimetry-isothermal-titration-calorimetry-and-microcalorimetry/thermal-analysis-of-phase-transitions-and-crystallization-in-polymeric-fibers, (accessed May 2020).

14 Bridge Technology, *Four-Point Probe Manual*, http://four-point-probes.com/four-point-probe-manual/, (accessed May 2020).

15 T. G. Santos, *Characterization of FSP by electrical conductivity*, https://www.sciencedirect.com/science/article/pii/B9780857094681500050, (accessed May 2020).

16 The Battery University, *Charging Lithium-Ion Batteries – Battery University*, https://batteryuniversity.com/learn/article/charging_lithium_ion_batteries, (accessed May 2020).

17 N. Elgrishi, K. J. Rountree, B. D. McCarthy, E. S. Rountree, T. T. Eisenhart and J. L. Dempsey, *J. Chem. Educ.*, 2018, **95**, 197–206.

18 X. Huang, Z. Wang, R. Knibbe, B. Luo, S. A. Ahad, D. Sun and L. Wang, *Energy Technol.*, 2019, **7**, 201801001(1)-201801001(13).

19 T. Kim, W. Choi, H.-C. Shin, J.-Y. Choi, J. Man Kim, M.-S. Park and W.-S. Yoon, *J. Electrochem. Sci. Technol*, 2020, **11**, 14-25.

20 M. D. Levi and D. Aurbach, *Potentiostatic and Galvanostatic Intermittient Titration Techniques*, https://onlinelibrary.wiley.com/doi/full/10.1002/0471266965.com125, (accessed May 2020).

21 Metrohm, *Galvanostatic Intermittent Titration Technique*, https://www.ecochemie.nl/download/Applicationnotes/Autolab_Application_Note_BAT03.pdf, (accessed May 2020).

22 A. Fick, *Ann. der Phys. und Chemie*, 1855, **170**, 59–86.

23 D. W. Dees, S. Kawauchi, D. P. Abraham and J. Prakash, *J. Power Sources*, 2009, **189**, 263–268.

24 J. P. Pender, G. Jha, D. H. Youn, J. M. Ziegler, I. Andoni, E. J. Choi, A. Heller, B. S. Dunn, P. S. Weiss, R. M. Penner and C. B. Mullins, *ACS Nano*, 2020, **14**, 1243–1295.

25 Y. Shen, E. E. Pedersen, M. Christensen and B. B. Iversen, *Rev. Sci. Instrum.*, 2014, **85**, 104103.

26 X. Vendrell and A. R. West, *J. Electrochem. Soc.*, 2018, **165**, F966–F975.

27 U. Ahmadu, in *Advanced Sensor and Detection Materials*, ed. A. Tiwar and M. M. Demir, John Wiley & Sons, Hoboken, 2014, ch. 9, 265-308.

28 E. Barsoukov and J. R. Macdonald, *Impedance spectroscopy : theory, experiment, and applications*, John Wiley & Sons, Hoboken, 2nd edn, 2005.

29 A. Lasia, *Electrochemical impedance spectroscopy and its applications*, Springer, New York, 2014.

30 I. M. Hodge, M. D. Ingram and A. R. West, *J. Electroanal. Chem. Interfacial Electrochem.*, 1976, **74**, 125–143.

31 A. R. West, Solid State Chemistry and its Applications, John Wiley & Sons., Chichester, 2nd edn, in press.

32 P. G. Bruce and A. R. West, *J. Electrochem. Soc.*, 1983, **130**, 662-669.

33 K. Srinivas, P. Sarah and S. V Suryanarayana, *Bull. Mater. Sci.*, 2003, **26**, 247-253.

34 A. R. West, D. C. Sinclair and N. Hirose, *Journal of Electroceramics*, 1997, **1**, 65-71.

35 M. A. Hernández, N. Masó and A. R. West, *Appl. Phys. Lett.*, 2016, **108**, 152901(1)-252901(4).

36 A. J. Moulson and J. M. Herbert, *Electroceramics : materials, properties, applications*, John Wiley Sons, Chichester, 2nd edn, 2003.

37 N. M. Beekmans and L. Heyne, *Electrochim. Acta*, 1976, **21**, 303–310.

38 J. E. Bauerle, *J. Phys. Chem. Solids*, 1969, **30**, 2657–2670.

39 T. van Dijk and A. J. Burggraaf, *Phys. Status Solidi*, 1981, **63**, 229–240.

40 C. Kjølseth, H. Fjeld, Ø. Prytz, P. Inge Dahl, C. Estournès, R. Haugsrud and T. Norby, *Solid State Ionics*, 2010, **181**, 268–275.

41 J. T. S. Irvine, D. C. Sinclair and A. R. West, *Adv. Mater.*, 1990, **2**, 132–138.

42 D. C. Sinclair, *Bol. Soc. Esp. Cerám Vidrio*, 1995, **34**, 55-65.

43 P. Y. Foeller, PhD thesis, The University of Sheffield, 2017.

44 G. Wang, J. Li, X. Zhang, Z. Fan, F. Yang, A. Feteira, D. Zhou, D. C. Sinclair, T. Ma, X. Tan, D. Wang and I. M. Reaney, *Energy Environ. Sci.*, 2019, **12**, 582–588.

45 E. J. Abram, D. C. Sinclair and A. R. West, *Journal of Electroceramics*, 2003, **10**, 165-177.

46 D. C. Sinclair and A. R. West, *Phys. Rev. B*, 1989, **39**, 13486–13492.

47 R. D. Armstrong, T. Dickinson and P. M. Willis, *J. Electroanal. Chem.*, 1974, **53**, 389–405.

48 E. Butchereit, M. Schreiber and J. Schoonman, *Solid State Ionics*, 1994, **69**, 1–12.

49 C. K. Lee, D. C. Sinclair and A. R. West, *Solid State Ionics*, 1993, **62**, 193–198.

50 P. Quintana and A. R. West, *Solid State Ionics*, 1987, **23**, 179–182.

49 J. T. S. Irvine, M. Lacerda and A. R. West, *Mater. Res. Bull.*, 1988, **23**, 1033–1038.

50 K. Jackowska and A. R. West, *Journal of Applied Electrochemistry*, 1985, **15**, 459-468.

51 J. T. S. Irvine, M. Lacerda and A. R. West, *Mater. Res. Bull.*, 1988, **23**, 1033–1038.

52 K. Jackowska and A. R. West, *Journal of Applied Electrochemistry*, 1985, **15**, 459-468.

53 N. Masó and A. R. West, *Chem. Mater.*, 2015, **27**, 1552–1558.

54 X. Vendrell and A. R. West, *J. Am. Ceram. Soc.*, 2019, **102**, 6100-6106.

55 Energizer, *Energizer Technical Bulletin*, https://data.energizer.com/PDFs/BatteryIR.pdf, (accessed: May 2020).

56 Y. Bao, W. Dong and D. Wang, *Energies*, 2018, **11**, 1073(1)-1073(11).

57 Neware Technology Limited, *DCIR - Direct Current Internal Resistance*, https://www.neware-usa.com/products/applications/dcir, (accessed: September 2020).

58 A. Barai, K. Uddin, W. Widanage, A. McDordon and P. Jennings, *Sci. Rep.*, 2018, **8**, 1-13.

59 M. E. Orazem and B. Tribollet, *Electrochemical impedance spectroscopy*, John Wiley & Sons, Hoboken, 2008.

60 J. Randles, *Disc. Faraday Soc.*, 1947, **1**, 11-19.

61 F. Huet, *J. Power Sources*, 1998, **70**, 59–69.

62 L. A. Middlemiss, A. J. R. Rennie, R. Sayers and A. R. West, *Energy Reports*, 2020, **6**, 232–241.

63 J. Huang, H. Ge, Z. Li and J. Zhang, *Electrochim. Acta*, 2015, **176**, 311–320.

64 U. Tröltzsch, O. Kanoun and H.-R. Tränkler, *Electrochim. Acta*, 2006, **51**, 1664–1672.

65 Gamry, *Basics of Electrochemical Impedance Spctroscopy*, http://www.gamry.com/application-notes/EIS/basics-of-electrochemical-impedance-spectroscopy/, (accessed May 2020).

66 J. Harper, *Non-linear system analysis: The application of Electrochemical Impedance Spectroscopy to the study of fuel cells and batteries operated under load*, https://www.ameteksi.com/-/media/ameteksi/download_links/documentations/library/solartonanalytical/modulab%20ecs/anml02%20non%20linear%20systems%20analysis%20a4.pdf?la=en, (accessed May 2020).

67 Gamry, *EIS: Potentiostatic or Galvanostatic Mode?*, https://www.gamry.com/application-notes/EIS/eis-potentiostatic-galvanostatic-mode/, (accessed May 2020).

68 C. H. Chen, J. Liu and K. Amine, *J. Power Sources*, 2001, **96**, 321–328.

Chapter III

Structural Characterisation and Electrical Properties of Mixed Phase Na[Ni,Mg,Mn,Ti]O_2

3.1 Introduction

As mentioned in Chapter I, layered oxides have, to date, been one of the most researched sodium-ion cathode material systems.[1] These possess a rock salt type structure (Fig. 3.1.) consisting of a O-Na-O-T_M-O stacking sequence. The structure is built of sheets of edge-sharing T_MO_6 octahedra, with Na^+ ions inserted between the metal oxide slabs. The covalently bonded T_MO_2 layers allow for the reversible extraction/insertion of sodium ions from the interlayer Na planes. The packed sodium sheets confer a high theoretical specific capacity, and, depending on the transition metals used, the cathode can be tailored to operate at high redox potentials. A combination of these properties means that large energy densities, rivalling those of certain Li-ion materials, are possible when used in sodium-ion batteries.

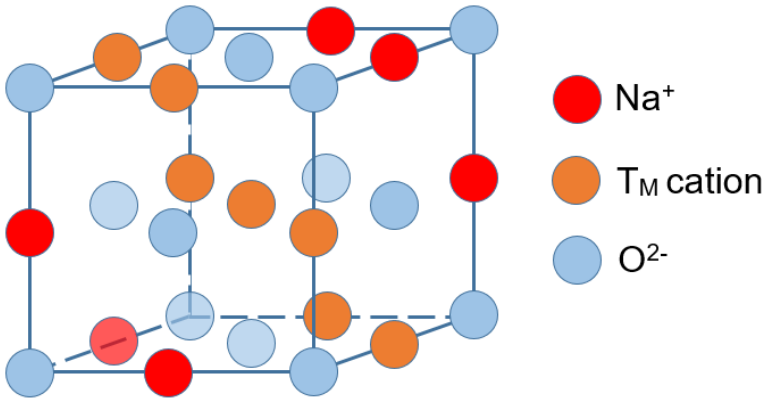

Figure 3.1 Unit cell of a layered rock salt.

Some of the best layered oxide cathodes made so far contain a combination of several transition metals in the oxide sheets: $T_MT_M'T_M''…O_2$.[2] As well as electrochemically active elements, such as Ni and Mn,[3] inactive spectator elements, e.g. Mg and Ti, are utilised to enhance capacity retention and lead to a smoother

voltage profile.[4] Hence, in theory at least, a cooperative effect between these different transition metals can allow for an ideal battery system to be designed. The structure of the layered sodium oxide cathode and the amount of Na contained in it also hugely affect the electrochemical properties of the battery. In sodium-based materials, the stacking of the T_MO_2 sheets with different orientations gives rise to polymorphism.[5] The cation-ordered rock salt superstructures that form can be divided into O (octahedral) and P (prismatic) phases depending on the environment in which the Na^+ ion is located. Of these, the O3- and P2-type polymorphs are the most common to date,[6] where the number denotes how many oxide sheets are contained in a single cell unit. These O3 and P2 phases each possess their own intrinsic strengths and weaknesses. The O3 polymorph has a higher sodium reservoir, however, the material is prone to unfavourable complex phase transitions during cycling. The P2 phases, in contrast, tend to possess greater stability; however, cell performance is limited by the large number of unoccupied Na^+ ion sites they possess[7,8] Recently, research has taken place into cathodes made up of a mixture of these two layered phases in order to overcome their individual limitations and combine the high energy of the O3 with the high power of the P2.[9,10] However, much is still unknown about the structures and electrical properties of these unique complex multiphase systems and how these give rise to a favourable electrochemical performance.

In this chapter, a promising novel mixed phase layered sodium quaternary transition metal oxide, $Na[Ni,Mg,Mn,Ti]O_2$, is studied as a potential Na-ion cathode candidate. The structure and thermal stability of the material is examined using a variety of different characterisation techniques. The electrical properties of the material are also investigated using impedance spectroscopy. Electrochemical testing is performed employing both half- and full-cell battery setups.* Finally, *in operando* XRD is carried out in order to try and gain a better understanding of how the unconventional structure of the multiphase layered oxide relates to its electrochemical performance.

* In this chapter, half-cell refers to when the anode is sodium metal, and full-cell when it is carbon.

3.2 Experimental

3.2.1 Materials

The Na[Ni,Mg,Mn,Ti]O_2 layered rock salt type structure used in this work was a commercial product obtained from Faradion, and was used as-received. The layered compound had been prepared by solid state synthesis. Acetone, isopropanol and N-Methyl-2-pyrrolidone (NMP) solvents were obtained from Sigma-Aldrich UK Ltd.

3.2.2 X-Ray Diffraction

Phase analysis used a STOE Stadi P X-ray diffractometer, Mo $K\alpha_1$ (λ = 0.70926 Å) with a linear position sensitive detector (PSD) at an accelerating voltage of 40 kV and a tube current of 45 mA. Data were recorded over the 2θ scan range 5 - 40 ° with a step size of 0.1 °. A Ge monochromator was used to remove $K\alpha_2$ and K_β, in order to leave $K\alpha_1$ monochromatic radiation. Qualitative phase analysis was performed using the PDF-4+ software, and patterns compared with PDF cards from the International Centre for Diffraction Data (ICDD).[11]

In operando XRD was performed using a Malvern Panalytical Empyrean X-ray diffractometer, Ag $K\alpha$ (= 0.5608 Å) with a hybrid pixel detector, at an accelerating voltage of 60 kV and a tube current of 36 mA. Data were recorded over the 2θ scan range 12 - 15 ° with a stepsize of 0.1 °. Each XRD pattern took ~16 min to record.

3.2.3 Materials Characterisation

Scanning Electron Microscopy (SEM). Prior to analysis, samples were deposited on carbon-coated tape and mounted on aluminium stubs. Determination of microstructure information was carried out using an Inspect F50 microscope with a field emission gun (FEG) operating at 20 kV.

Thermogravimetic Analysis (TGA). For each measurement, 10-20 mg of powder sample was placed in an alumina crucible. The heating/cooling rate was fixed at 5 °C/min, but the measured temperature ranges varied according to each sample. The

measurements performed in flowing air and nitrogen used a PerkinElmer Pyris 1 (PerkinElmer, Massachusetts, USA). The measurements performed in oxygen were taken using a PerkinElmer TGA 4000. Pyris Manager software was used for data analysis.

Differential Scanning Calorimetry (DSC). For each measurement, 20-30 mg of powder sample was placed in an alumina crucible and heated/cooled between 25 and 1000 °C at 5 °C/min heating/cooling rate, in an air/argon (80/20) atmosphere. The temperature of the sample was compared with that of an inert reference material (in this case an empty alumina crucible). The data were collected using a NETZSCH 404 C thermal analyser (Netzsch, Selb, Germany) and analysed using Proteus Analysis software.

Impedance Spectroscopy. Pellets were pressed with 0.4 tons pressure and heated at the desired temperature for 1 h. Platinum paste was painted on both sides of the pellet and dried by heating in a furnace. Impedance data were collected with an Agilent E4908A analyser at 100 mV AC with a sweep frequency from 10 Hz to 1 MHz in air. Impedance data were corrected for overall pellet geometry and for blank capacitance of the conductivity jig. Analysis was performed using ZView software.

3.2.4 Electrochemical Testing

Electrode sheets were supplied by the Warwick Manufacturing Group (WMG). The composite cathode they supplied consisted of the active material component $Na[Ni,Mg,Mn,Ti]O_2$, which had been mixed with polyvinylidene fluoride (PVDF) binder and C65 carbon black conductive additive in a 89 : 6 : 5 weight ratio. For the anode, a non-graphitizable commercially-available carbon had been mixed with PVDF and C45 carbon black in a 88.1 : 9 : 2.9 weight ratio. WMG formed slurries of both of these with NMP before these mixtures were drawn down onto carbon-coated aluminium foil. These were then dried and stored at 60 °C in a vacuum oven before battery assembly took place in our lab. The average mass loading for the positive electrode sheet was 15-17 mg/cm^2 and 8.5-9.0 mg/cm^2 for the anode. The separators used in the Na-ion cells to isolate the two electrodes from one another were cut from GF/A glass microfiber filter paper (Whatman). The electrolyte used was a solution of

0.5 M sodium hexafluorophosphate in an ethylene carbonate : diethyl carbonate : propylene carbonate (1:2:1) mixture. This was prepared in the glove box, with the solvent mixture dried over molecular sieves for 16 h prior to dissolution of the salt. Electrochemical testing was performed using a Maccor Series 4000 Automated Test System. All cells were held in temperature-controlled environmental chambers.

An argon-filled (H_2O, O_2 < 0.1 ppm) glove box was used for battery assembly (MBraun, Germany). Electrochemical half-cell testing was performed using aluminium CR2032 coin cells with a Na metal-disk, 11 mm in diameter, as the counter electrode. Circular positive electrodes, 12 mm in diameter, were punched from the Na[Ni,Mg,Mn,Ti]O_2 cathode coating. Cell casings, spacers, springs and separators were all dried in an 80 °C vacuum oven for 16 h prior to being taken into the glove box for battery assembly.

Full-cell testing took place using Na[Ni,Mg,Mn,Ti]O_2 positive electrodes with a discharge capacity per unit area of 2.5 mAh/cm^2 (20 x 20 mm, thickness: 0.155 mm) cycled against negative hard carbon electrodes (22 x 22 mm, thickness: 0.135 mm). Laminate-type prismatic pouch cells (7 x 5 cm) containing aluminium current collector tabs (MTI) to connect the electrodes to the battery tester were dried at 70 °C overnight before being taken into the glove box. For galvanostatic intermittent titration technique (GITT) measurements to determine the diffusion coefficient (D_{Na^+}), a current pulse of 0.1C was applied during charge and 0.2C during discharge, for 10 min, followed by a relaxation time of 1 h.

3.3 Results and Discussion

3.3.1 Structural Characterisation and Thermal Stability

Phase analysis of the as-received Na[Ni,Mg,Mn,Ti]O_2 powder from Faradion was performed using powder X-ray diffraction (PXRD). The diffractogram (Fig. 3.2) suggests that this is a mixed phase layered rock salt type structure, consisting of one O3 and one P2 polymorph. The two nominal phases that make up the material are the layered sodium oxides O3-Na-[$Ni_{0.5}Mn_{0.5}$]O_2 (PDF: 01-082-9602)[12] and P2-$Na_{0.64}$[$Mn_{0.8}Mg_{0.2}$]O_2 (PDF: 04-022-8282).[13] A small amount of the starting material, NiO, appears to be present as an impurity. The strongest peak from the cubic NiO pattern, (200), can be indexed as a shoulder on the P2 (103) peak; all the remaining NiO peaks overlap with the O3 phase. As the P2 polymorph is sodium deficient, this means that a more accurate formula for this mixed phase layered oxide is $Na_x[Ni_{1-a-b-c}Mg_aMn_bTi_c]O_2$.

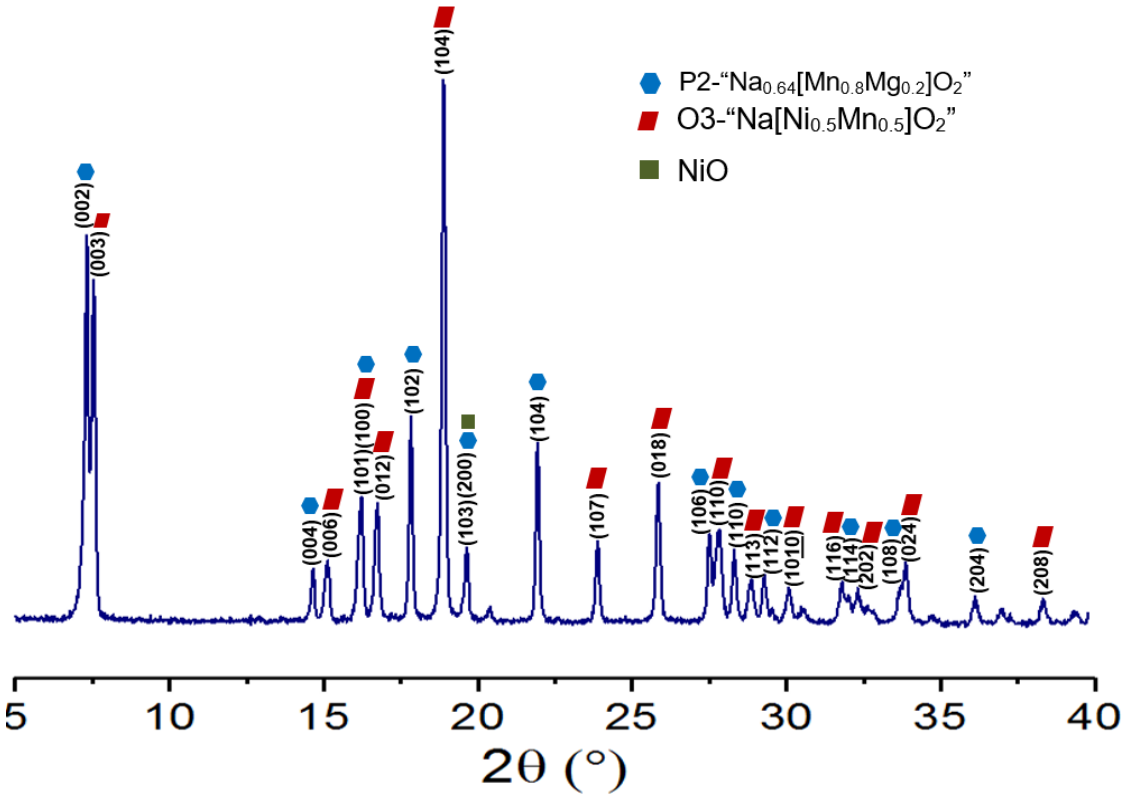

Figure 3.2 The PXRD pattern of mixed phase Na[Ni,Mg,Mn,Ti]O_2 collected by MoPSD with λ = 0.7093 Å. The two polymorphs are indicated as hexagonal P2 phase ⬣, and trigonal O3 phase ▰. A minor impurity of cubic NiO is marked with ■.

The crystal structures of each individual polymorph are displayed in Figure 3.3. The O3 phase (a) consists of close packed ABCABC oxide layer stacking with the sodium ions occupying the octahedral sites between the layers. The P2-type phase (b) has a close packed ABBA array with sodium intercalated into trigonal prisms. The O3 polymorph has a rhombohedral lattice with space group $R\bar{3}m$, and is isostructural with α-NaFeO2. The P2 material possesses $P6_3/mmc$ symmetry in a hexagonal lattice. Both of the nominal formulae: O3-"Na-[$Ni_{0.5}Mn0_{.5}$]O_2"[14] and P2-"$Na_{0.64}[Mn_{0.8}Mg_{0.2}]O_2$"[15] are regarded in the literature as individual sodium-ion battery cathodes. The $Na[Ni_{0.5}Mn_{0.5}]O_2$ is one of the most popular O3 phases and was the first system to operate at a higher voltage (4.5 V).[12] Studies performed elsewhere on magnesium doping in the earth-abundant P2-$Na_{2/3}[Mn_{1-x}Mg_x]O_2$ polymorph were found to reduce the amount of Jahn-Teller active Mn^{3+}, leading to better capacity retention, smaller cell polarisation, and a smoother voltage profile.[16]

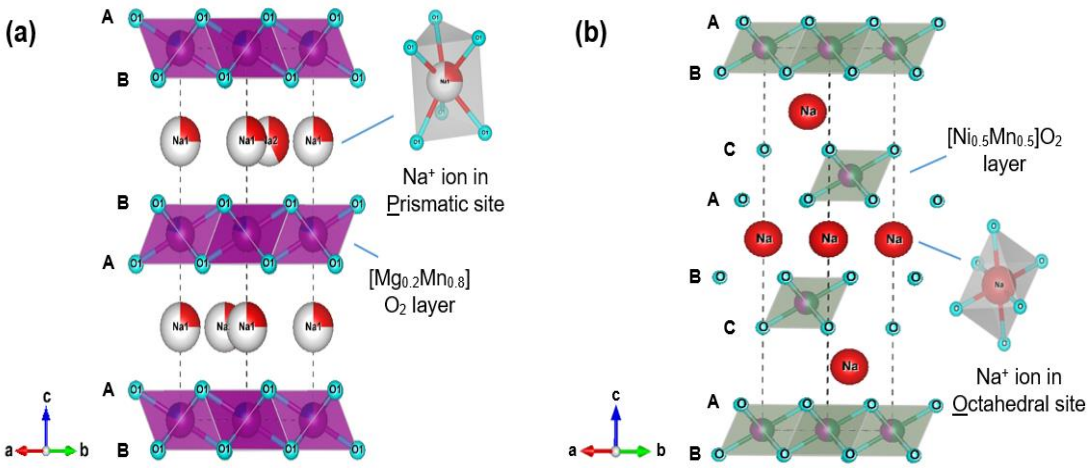

Figure 3.3 Schematic illustrations of the crystal structures of (a) P2-$Na_{0.64}[Mn_{0.8}Mg_{0.2}]O_2$[13] and (b) O3-$Na[Ni_{0.5}Mn_{0.5}]O_2$[12] drawn using the computer program VESTA.[17]

It is important to point out that as $Na[Ni,Mg,Mn,Ti]O_2$ is a commercial cathode supplied by Faradion, while the nominal phases it contains are known, their exact compositions are not. All of the elements in this layered oxide are highly abundant and relatively low cost. Nickel and manganese are the major non-sodium metals in the material, with magnesium present to a lesser extent, and titanium the minority element (< 20%). As the layered oxide is a mixture of P2 and O3-type phases, the

sodium stoichiometry is in the region $0.7 < x < 1$. Approximately one third of the non-sodium metals are nickel ions, and the two-electron redox process $Ni^{2+} \rightleftharpoons Ni^{4+}$ allows for two moles of Na^+ to be transferred per mole of nickel ions. The Mn^{4+} ions may then also be reduced to Mn^{3+} from the first discharge onwards, to provide this battery cathode with an enhanced capacity. Mn^{4+} has a small ionic radius, thus leading to a higher crystallographic density.[18] This increases the mixed phase layered oxide's tap density, and hence the overall energy density of the material. While neither Mg^{2+} nor Ti^{4+} are expected to be redox active, their presence is to improve the cycling stability. The Mg^{2+} ion has a tendency to occupy octahedral sites, and therefore, reduces the Jahn-Teller distortion caused by Mn^{3+}, which puts strain on the solid oxide framework.[16] The Ti^{4+} ion is reported to suppress Na^+/vacancy ordering, which leads to structural instability during cycling, as well as preventing unfavourable phase transitions.[19]

To gain a better understanding of the mixed phase $Na[Ni,Mg,Mn,Ti]O_2$ layered oxide, it is important to perform a full structural characterisation of the material, including investigating any changes that occur at different temperatures. The thermal stability of solid state materials is important as this may have serious implications for their processing and applications. The temperature sensitivity of mixed phase sodium-ion cathodes has been previously reported, as fine-tuning the temperature appears to be key in modifying phase formation during synthesis.[20] As layered sodium oxides are prone to a number of complex phase transitions (Section 1.3),[6] it is possible that these may occur when the material is exposed to different heating regimes. The thermal stability of the $Na[Ni,Mg,Mn,Ti]O_2$ powder was investigated by performing *ex situ* XRD after heating the material to either 800, 900 or 1000 °C, and then removing the sample from the furnace at high temperature and leaving it to cool in air (Fig. 3.4).

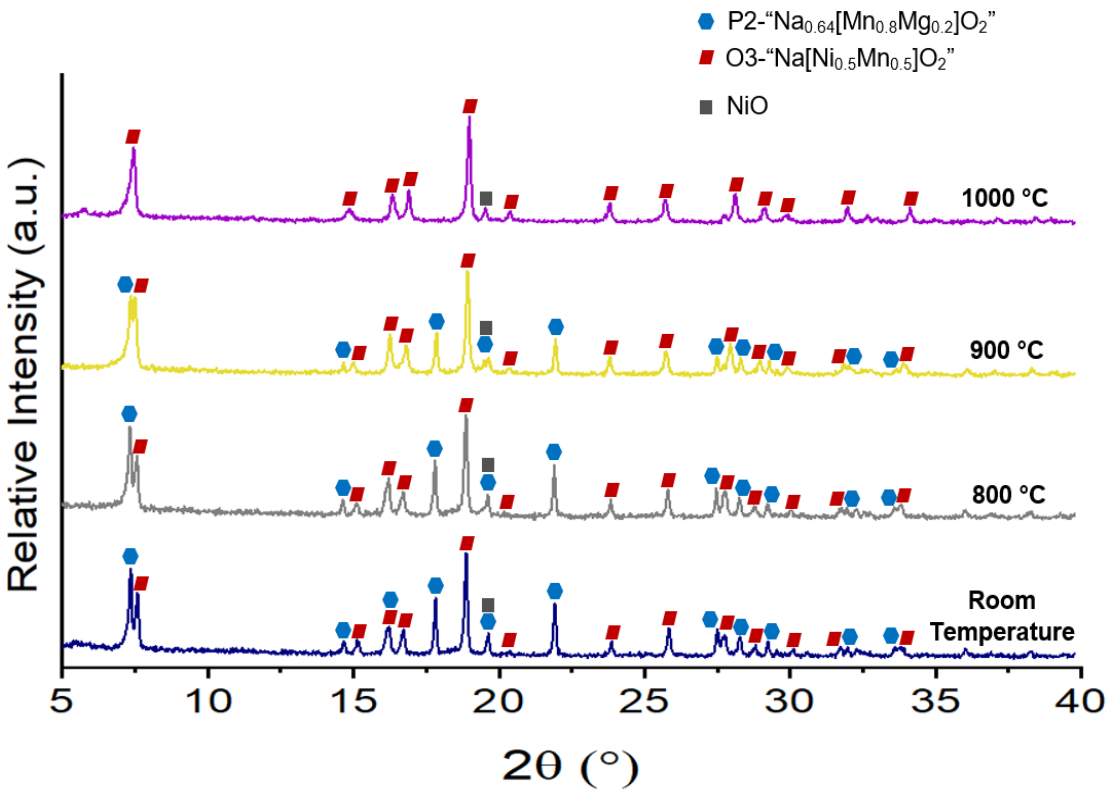

Figure 3.4 XRD patterns of Na[Ni,Mg,Mn,Ti]O_2 fast cooled in air from 800 - 1000 °C to room temperature. The two polymorphs are indicated as hexagonal P2 phase ⬣, and trigonal O3 phase ▰. A minor impurity of cubic NiO is marked with ■. Patterns were collected by MoPSD with λ = 0.7093 Å.

The results indicate that cooling from 800 °C produces a similar XRD to the one performed on the as-received Faradion material, and both phases are clearly present. On heating to 900 °C there appears to be a reduction in the concentration of the P2-type polymorph; on further heating to 1000 °C, P2-"$Na_{0.64}[Mn_{0.8}Mg_{0.2}]O_2$" completely disappears from the XRD pattern, leaving just the O3 phase. Furthermore, the P2 structure does not return on re-heating the 1000 °C-treated material to a lower temperature, such as 800 °C.

Scanning electron microscopy images for the Na[Ni,Mg,Mn,Ti]O_2 material at room temperature (a) and after heating to 1000 °C (b) are depicted in Figure 3.5. Both images contain flake-like primary particles of around 1 – 2 μm in diameter and < 500 nm in length. The sharp edges of the particles in (a) appear to have dulled in (b), indicating perhaps the process of partial melting. The room temperature image on the left also contains smaller particles (< 1 μm), most prominent on the top right, and left hand side of the micrograph, which appear more spherical and agglomerated.

These agglomerates are not present in the micrograph taken in (b) after the sample has been heated to 1000 °C. Hence, these SEM pictures seem to confirm the mixture of O3- and P2-type phases prior to heat treating the sample, whereas just the O3 polymorph is present after heating to 1000 °C.

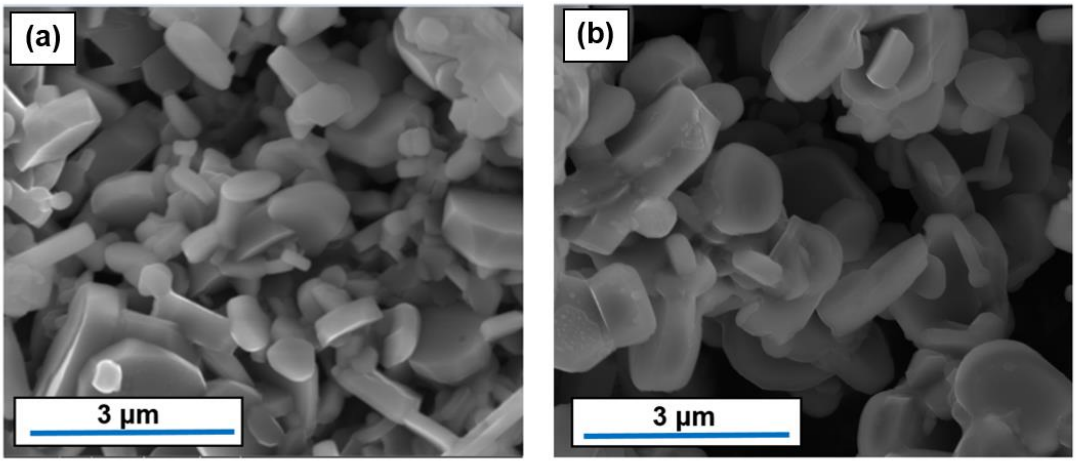

Figure 3.5 SEM images of Na[Ni,Mg,Mn,Ti]O_2 at (a) room temperature, and (b) after heating to 1000 °C.

Stability in air is very important. Many battery cathodes are known to degrade once exposed to the atmosphere,[21] and protection from ambient conditions is often essential for good cell performance.[22] The thermal stability of the Na[Ni,Mg,Mn,Ti]O_2 material, as well as its moisture and oxygen sensitivity, were studied by thermogravimetric analysis (TGA). A TGA run in air, nitrogen and oxygen was made between 25 and 1000 °C with programmed heating/cooling of 5 °C/min (Fig. 3.6). The TGA experiments in (a) were performed on a Na[Ni,Mg,Mn,Ti]O_2 sample which had been stored in a glove box following synthesis. The samples were briefly exposed to the atmosphere (for the maximum of a couple of hours) during removal from the glove box and transfer to the TGA instrument. The measurements in (b) were performed on Na[Ni,Mg,Mn,Ti]O_2 left exposed to the atmosphere for several days. The samples were held at 1000 °C for two hours after each run and prior to cooling.

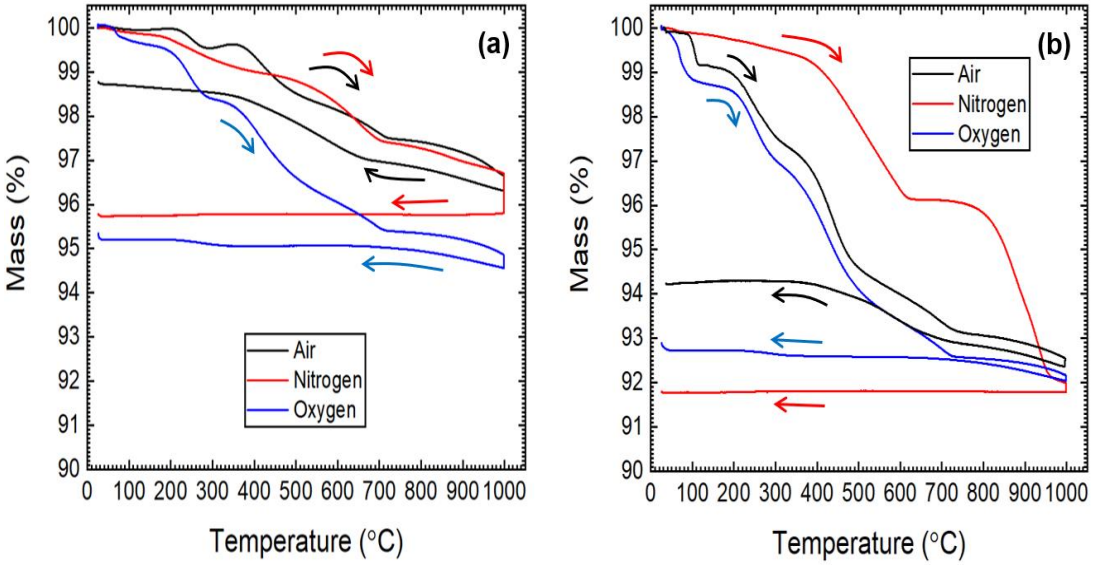

Figure 3.6 TGA of Na[Ni,Mg,Mn,Ti]O_2 stored in a glove box (a), and after exposure to the atmosphere for several days (b), under different gases.

Each TGA plot consists of different regions of continuous mass loss, interrupted by approximately flat plateaux. In each gas, the samples exposed to atmospheric conditions for longer experienced more significant mass loss. For the powder stored in the glove box (a), samples run in air and nitrogen both lost about 3-4% of their initial mass during heating to 1000 °C, whereas in oxygen the sample lost ~ 5%. The Na[Ni,Mg,Mn,Ti]O_2 exposed to air regained the majority of its mass on cooling, the sample in oxygen regained a relatively small amount, and the sample under nitrogen none. For the samples exposed to the atmosphere for longer (b), in all three gases the samples lost around 7-8% of their total mass, with the Na[Ni,Mg,Mn,Ti]O_2 exposed to air regaining ~ 1.5% of its total mass on cooling, the sample in oxygen a relatively small amount, and the sample under nitrogen, once again, none. These results demonstrate that storage conditions for this layered rock salt type structure are of the utmost importance, and that the material is prone to the uptake of atmospheric species.

For every TGA run, each individual plot can be split into approximately four different regions, as outlined in Figure 3.7 for Na[Ni,Mg,Mn,Ti]O_2 stored in a glove box. Stage 1 shows a small decrease in mass up to 125 °C; region 2, between 125 and 300 °C, a more significant loss; stage 3 (300 - 720 °C) indicates the greatest loss in mass; and finally a further, more moderate decrease is seen above 700 °C at stage

4. Stage 4 appears to be reversible on cooling in both air and oxygen atmospheres, whereas stage 3 is reversible only in air.

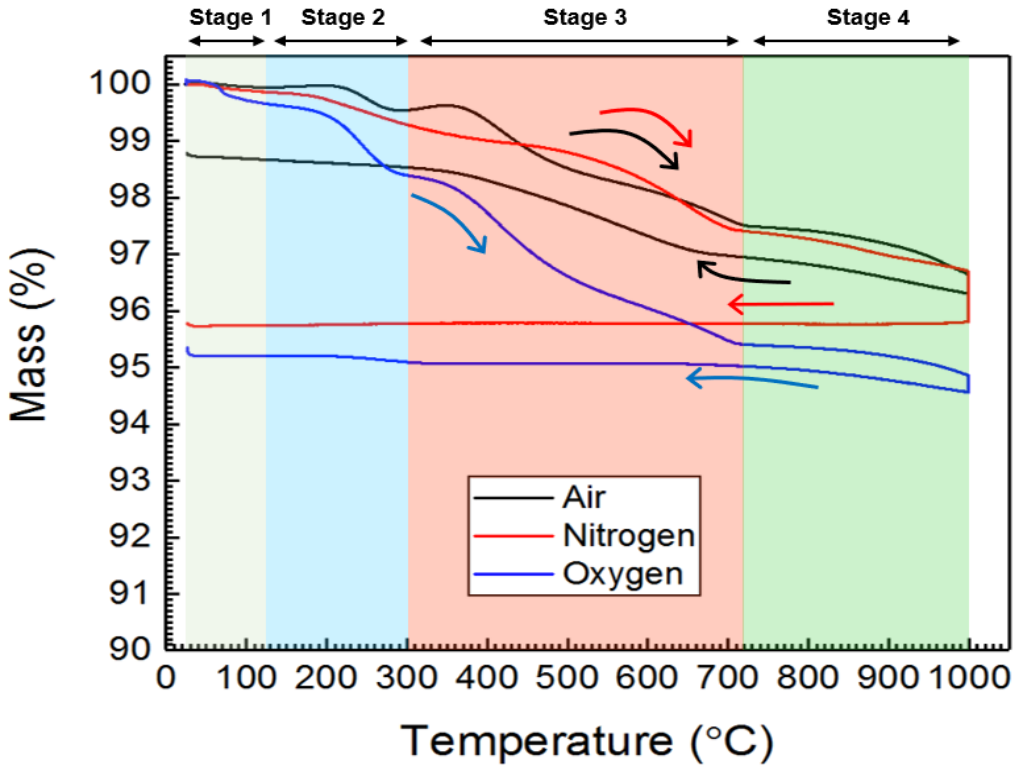

Figure 3.7 The Na[Ni,Mg,Mn,Ti]O_2 TGA profile for a sample stored in the glove box, with the different mass loss regions indicated.

These results can be interpreted as follows. The plots in air and oxygen follow similar profiles during heating, but there is a greater loss of mass on heating in O_2. This is an unusual occurrence and suggests that volatile compounds are more easily formed in a higher partial pressure of oxygen. Stage 4 is reversible in both oxygen and air atmospheres, whereas stage 3 is only reversible in air. This suggests that stage 4 is associated with oxygen loss and stage 3 with CO_2 and H_2O. It is possible that this layered sodium oxide undergoes Na^+/H^+ ion exchange when exposed to water to form NaOH/T_MOOH, and that Na_2CO_3 or $NaHCO_3$ may be synthesized on exposure to CO_2. Importantly, the formation of these insulating species on the surface of Na[Ni,Mg,Mn,Ti]O_2 particles is likely to have a detrimental impact on the performance of the material when tested electrochemically. Furthermore, Na^+/H^+ exchange will result in a loss of sodium, and therefore, a drop in battery capacity.

The sharp drop at the end of stage 4 may be associated with sodium evaporation as this is not reversible.

In summary, at low temperatures, below 125 °C (stage 1), the decrease in mass is likely to be due to the loss of weakly bound physisorbed species from the air, such as water. Then, at temperatures above this, there is possibly the loss of more strongly structurally bound H_2O, as well as the decomposition of carbonate ions (as seen in the literature).[23,24] Finally, at high temperatures, for region 4, the mass loss is attributed to the reversible release of oxygen in equilibrium with the gas flow (Eq. 3.1). More work is needed to precisely identify the compounds being lost during each temperature stage in the different gases. Future work could be to perform additional TGA measurements after an initial run in nitrogen to first dry the sample, and using mass spectrometry in combination with TGA (TGA-MS).

$$Na_xT_MO_2 \quad \rightleftharpoons \quad Na_xT_MO_{2-\delta} + \frac{\delta}{2}O_2 \qquad (3.1)$$

In order to try and elucidate the different processes occurring during these TGA experiments, *ex situ* X-ray diffraction data were collected on the studied samples following the runs (Fig. 3.8). The Na[Ni,Mg,Mn,Ti]O_2 sample treated in air was seen to undergo the same P2-O3 phase transition as seen when the sample was rapidly cooled (Fig. 3.4). The powder heated in oxygen also underwent the same phase transition. For the material treated in nitrogen, as well as the P2 polymorph disappearing, there was also the appearance of additional peaks at *ca* 17.1°, 19.2°, 25.6°, and 26.2°. These are indexed as sodium manganese oxide $NaMnO_2$ (PDF: 00-025-0845).[25] There is also a more prominent nickel oxide peak at 19.5°, as well as the emergence of a second NiO peak at 16.9°.

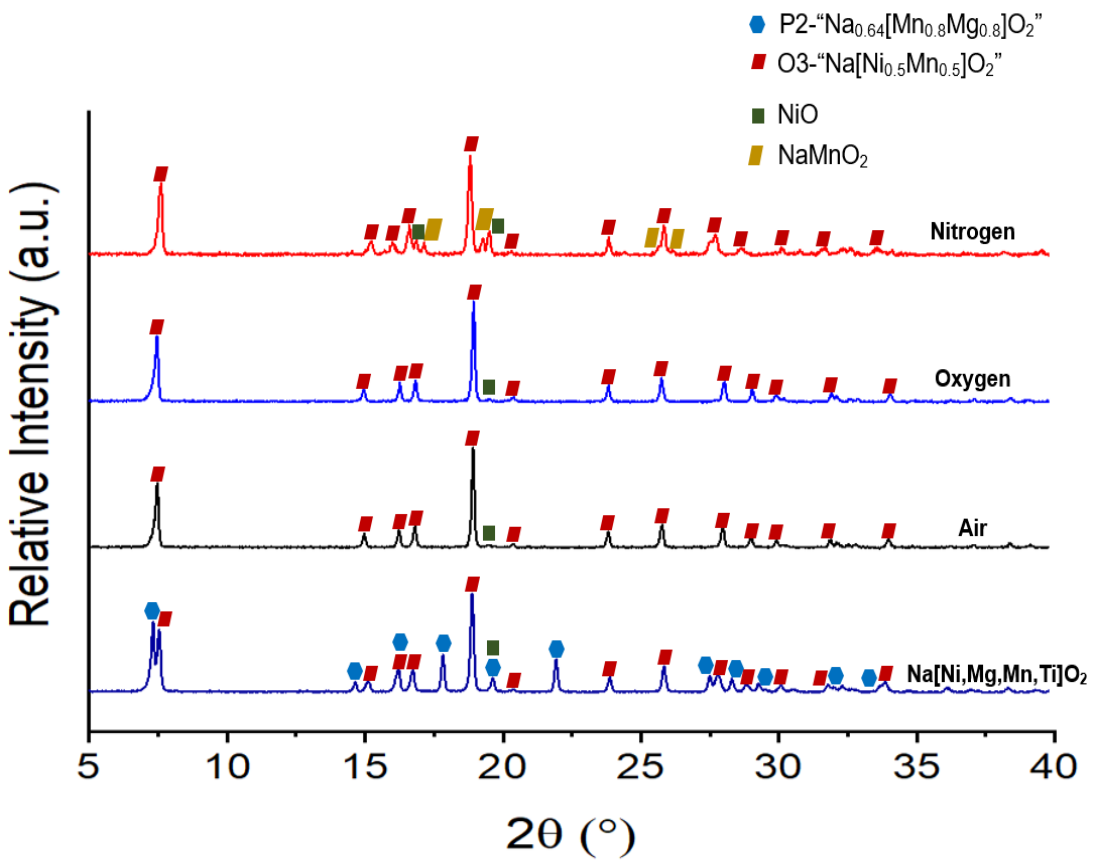

Figure 3.8 XRD patterns of Na[Ni,Mg,Mn,Ti]O_2 after performing TGA under different atmospheres. The two polymorphs are indicated as hexagonal P2 phase ⬢, and trigonal O3 phase ▮. A minor impurity of cubic NiO is marked with ■. A monoclinic $NaMnO_2$ phase ▮ was detected after treatment with nitrogen. Patterns were collected by MoPSD with λ = 0.7093 Å.

These XRD results indicate that high temperature induces the P2-O3 transition, regardless of the atmosphere. The reducing conditions of the low oxygen partial pressure in nitrogen possibly also result in a change of oxidation state of the manganese ion from Mn^{4+} in Na[Ni,Mg,Mn,Ti]O_2 to Mn^{3+} in $NaMnO_2$. In all atmospheres, a temperature-induced major structural reordering of the layered oxide occurs to give a purely O3 polymorph. In nitrogen, a further thermal decomposition reaction takes place to yield several transition metal oxide species. A possible reaction equation for this process is given below (Eq. 3.2).

$$3Na\frac{2}{3}T_MO_2(P2) \rightleftharpoons 2NaT_MO_2(O3) + T_MO + \frac{1}{2}O_2 \qquad (3.2)$$

Another important difference between Na[Ni,Mg,Mn,Ti]O_2 samples heat treated in different atmospheres is that the diffractogram for the material exposed to nitrogen shows that the peaks for the O3 phase have shifted position. This indicates a change in lattice spacing. In a layered oxide structure, the (00*l*) diffraction peaks give information about the interlayer distance of the transition metal sheets and make it possible to investigate any structural changes in the *c*-direction. As Figure 3.9 shows, at low 2θ angle there is a shift of some of the (00*l*) peaks towards higher angle.

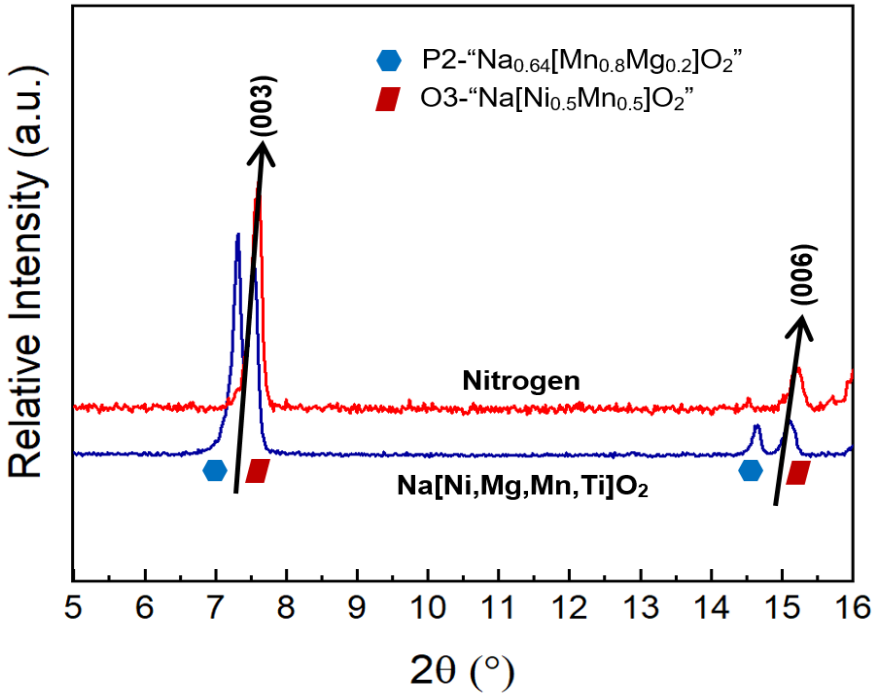

Figure 3.9 *Ex situ* XRD patterns ($5 \leq 2\theta \leq 16$) of Na[Ni,Mg,Mn,Ti]O_2 before and after performing TGA in nitrogen. The two polymorphs are indicated as P2 phase ⬣, and trigonal O3 phase ▰. Diffractograms show the shifting of the (00*l*) peaks for the O3 phase to higher 2θ angle. Patterns were collected by MoPSD with $\lambda = 0.7093$ Å.

A shift in the (00*l*) peak positions to higher diffraction angles indicates a narrowing of the distance between adjacent TMO_2 slabs in the layered rock salt type structure. The above results indicate that this occurs only in a nitrogen atmosphere and not when the sample is heated in air or oxygen. A refinement to find the lattice parameters confirms this: the unit cell parameters for the original mixed phase Na[Ni,Mg,Mn,Ti]O_2 material are calculated as $a = 2.9519(9)$ Å and $c = 16.180(6)$ Å, with a cell volume of $V = 122.10(5)$ Å^3 in a hexagonal setting. After heat treating in a nitrogen atmosphere, the new refined cell parameters are $a_{hex} = 2.9783(15)$ Å,

c_{hex} = 16.098(8) Å, and V_{hex} = 123.67(8) Å^3. Hence, the sample fired in nitrogen experiences a contraction of its unit cell in the *c*-direction, but an expansion in *a* and *b* leads to an overall increase in cell volume. Therefore, the thermal decomposition that occurs on heating in nitrogen, and leads to a breakdown of the layered oxide into transition metal oxides, results in a squashing of the sheets but an overall chemical expansion of the layered rock salt.

An enlargement of the unit cell volume is caused by an increase in average T_M-O bond length within the crystal structure. This corresponds to a weakening of the T_M-O bond strength and, hence, a reduction in the average oxidation state of T_M. As was shown in the XRD results in Figure 3.8, heating Na[Ni,Mg,Mn,Ti]O_2 in N_2 leads to formation of $NaMnO_2$. Mn^{3+} ($t_{2g}^3e_g^1$) is Jahn-Teller distorted, and so the possible formation of more of these ions in the layered rock salt type structure may explain why there is a contraction along the *c*-axis but an elongation along the other axes.

The effects seen here have also been reported previously for similar lithium O3 polymorphs, when treated under comparable conditions. The layered oxides $Li_{2/3}[Mn_{2/3}Ni_{1/3}]O_2$[26] and $Li[Ni_{0.8}Mn_{0.1}Co_{0.1}]O_2$[27] were both found to lose oxygen when fired under nitrogen. The oxygen loss corresponded with interlayer mixing of the cations. This is where cation exchange occurs between Li and Ni due to the similar ionic radii of Li^+ (r_{Li}^+ = 0.76 Å) and Ni^{2+} (r_{Ni}^{2+} = 0.69 Å).[28] Sodium has a much larger ionic radius than any of the transition metals in Na[Ni,Mg,Mn,Ti]O_2 (r_{Na}^+ = 1.02 Å, r_{Ni}^{2+} = 0.69 Å, r_{Mg}^{2+} = 0.72 Å, r_{Mn}^{4+} = 0.53 Å, r_{Ti}^{4+} = 0.61 Å),[28] so interlayer mixing is unlikely to take place. Importantly, a loss of oxygen from this mixed phase layered sodium rock salt type structure must be balanced by a reduction in oxidation state of one or more the transition metals it possesses, which is likely to affect the electrochemical performance of the material.

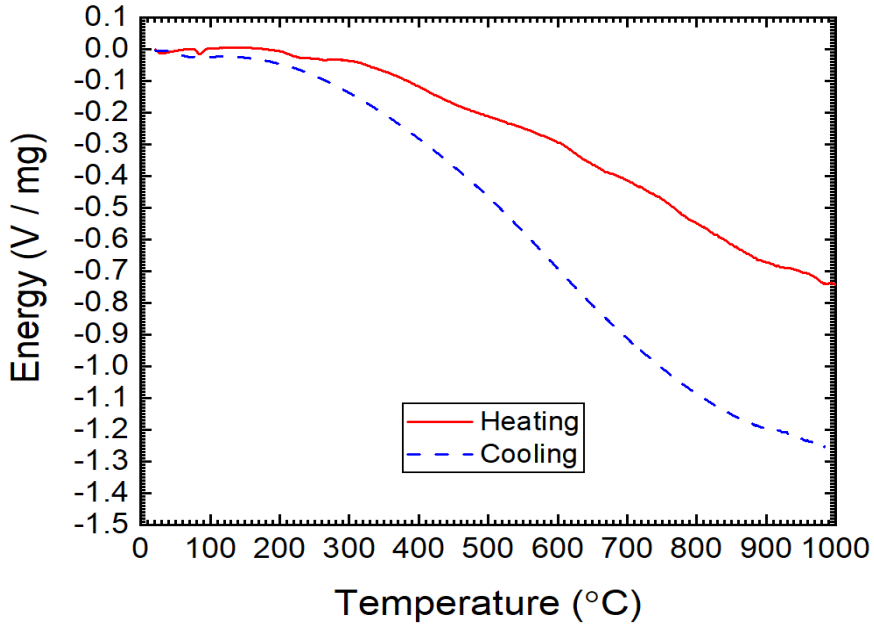

Figure 3.10 DSC curves for Na[Ni,Mg,Mn,Ti]O_2 heated and cooled to 1000 °C in an air/argon (80/20) atmosphere.

In order to obtain further information about the thermal stability of Na[Ni,Mg,Mn,Ti]O_2, DSC was performed. A small endothermic peak is present at around 85 °C on heating, and coincides with the drop in mass seen, during stage 1, in the TGA plots in Figure 3.7. This is attributed to the removal of surface bound water. There are no further endotherms/exotherms present for the rest of the heating/cooling cycle, despite the fact that a structural phase transition is known to occur from *ex situ* XRD data (Fig. 3.8). Hence, these results suggest that the P2-O3 phase transition does not correspond with a significant energy intake/output over a short period of time. Therefore, it is likely that the transformation from P2 to O3 is a slow reordering of the oxygen sub-lattice rather than a sharp bond breaking/forming process.

3.3.2 Electrical Properties

A pellet of the mixed phase Na[Ni,Mg,Mn,Ti]O_2 layered oxide was sintered at 800 °C in air, coated with platinum electrodes, and its electrical properties studied by impedance spectroscopy. A typical impedance dataset is shown in Figure 3.11, with room temperature data presented in four different complementary formats. In (a), the impedance complex plane plot appears to show two separate components – a high-

frequency arc, which passes through the origin, and a larger depressed semi-circle at lower frequency. This is shown more clearly by the inset plot. As the components are not easily separated, and there appears to be significant overlap between them, this suggests that the material is electrically inhomogeneous. This is confirmed by the combined spectroscopic plots in *Z''/M''* in (b). This shows no overlap between the peaks of the separate plots, with the electrical modulus maximum peak not even appearing within the displayed frequency range. Using these same data, plots of log conductance, *Y'*, against log *f*, (c), show what appears to be a plateau at around 100 nS cm^{-1}, and another near 1 µS cm^{-1}, with dispersion to higher conductivity values at higher frequencies. Plots of capacitance, *C'* against frequency, (d), show a plateau with a value 40-100 pF cm^{-1} at mid-frequency, which is typical of a grain boundary capacitance, and the start of a second plateau at higher frequency, ~ 1 pF cm^{-1}, which is typical for the bulk component.

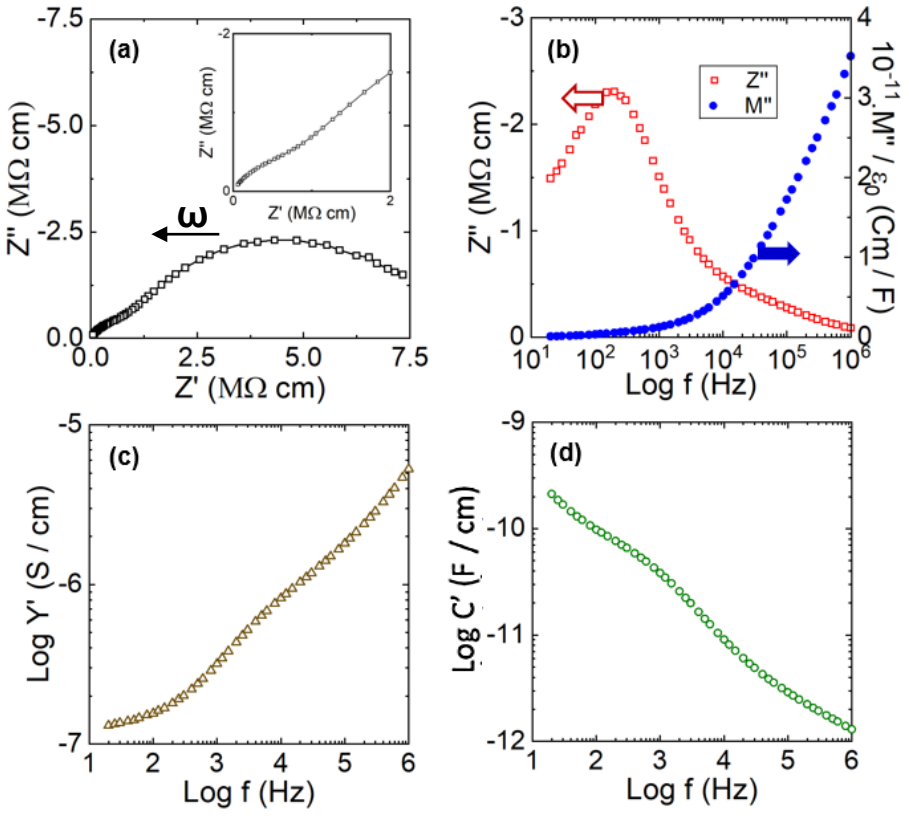

Figure 3.11 Impedance data for Na[Ni,Mg,Mn,Ti]O_2 at room temperature. (a) Impedance complex plane plot. Spectroscopic plots of -*Z''* and *M''* (b), *Y'* (c), *C'* (d). Inset in (a) shows a close up of the impedance complex plane plot at highest frequencies.

The conclusion from these results is that the sample is electrically inhomogeneous with evidence of a grain boundary impedance. The bulk conductivity is given from the poorly-resolved *Y'* plateau, around 1 μS cm^{-1} in (c), which is equivalent to a resistance of ~ 1 MΩ cm. In order to gain further insight into the origin of the different resistances in the sample, impedance measurements were performed over a range of temperatures, with impedance complex plane plots and spectroscopic plots of *C'* and *Z''/M''* displayed in Figure 3.12. The impedance measurements at various temperatures show that the sample contains a number of poorly resolved components. At lower temperatures, -20 and 80 °C, two components are present in the complex plane plot, R_1 and R_2, and at higher temperatures, 120-500 °C, a third component is also detected, R_3. Each of these approximate semi-circles can be modelled by a parallel *RC* element, assumed to be connected in series to one another. These components can be assigned to different features in the electroceramic from the magnitude of the *C'* plateaus.[29] A small plateau in the -20 °C plot, around 3 pF cm^{-1}, indicates that the bulk is the high frequency component. At higher temperatures, the *C'* plots can be used to assign R_2 to the grain boundary, as there is a plateau around 50 pF cm^{-1}. The third component present at higher temperature (R_3) is attributed to surface layer phenomena, as indicated by a small plateau at 10 nF cm^{-1} in the *C'* plot at 500 °C. Complex impedance plots, *Z''*, pick out the most resistive elements in the sample, whereas the electric modulus plots, *M''*, pick out those elements with the smallest capacitance. At all temperatures, the high frequency peak in the *M''* plot, corresponding to the bulk component, is off scale, and measurements at lower temperatures or to higher frequencies are required in order to bring it into the frequency window. The R_2 component, the grain boundary, is present as a peak in the *Z''* plot up to 380 °C. At 500 °C, the R_2 peak is no longer visible, but a second peak representing R_3 and the surface layer phenomena is now present.

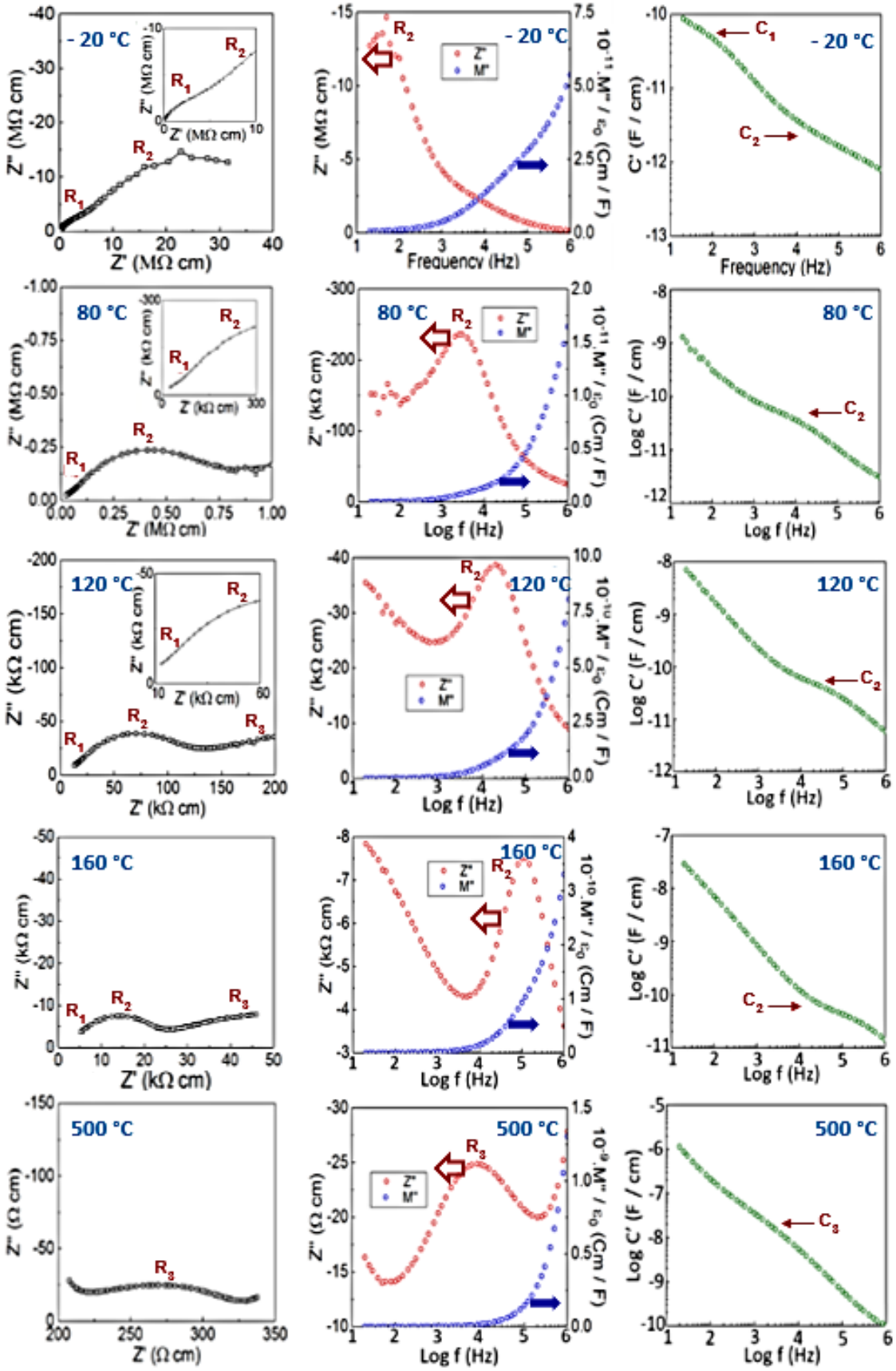

Figure 3.12 Impedance complex plane plots, spectroscopic plots of *Z''/M''* and *C'* for Na[Ni,Mg,Mn,Ti]O_2 at -20, 80, 120, 160 and 500 °C.

The conductivity data at different temperatures were also used to construct Arrhenius plots (Fig. 3.13). These make it possible to compare and quantify conductivity behaviour for different components, as well as to work out the activation energy associated with the conduction. It can be seen from the plots in (a) that the bulk (R_1) has the smallest resistance, with an activation energy of 0.234(4) eV. The grain boundary (R_2) has a higher value of 0.34(1) eV, and the surface layer (R_3) has the greatest resistance, E_a = 0.46(2) eV. The activation energy associated with the total conductivity of the material can also be worked out by adding the individual resistances of the bulk and grain boundary together (b). This shows that the overall conductivity of the material is largely dominated by the grain boundary around room temperature, with a similar activation energy of 0.33(1) eV.

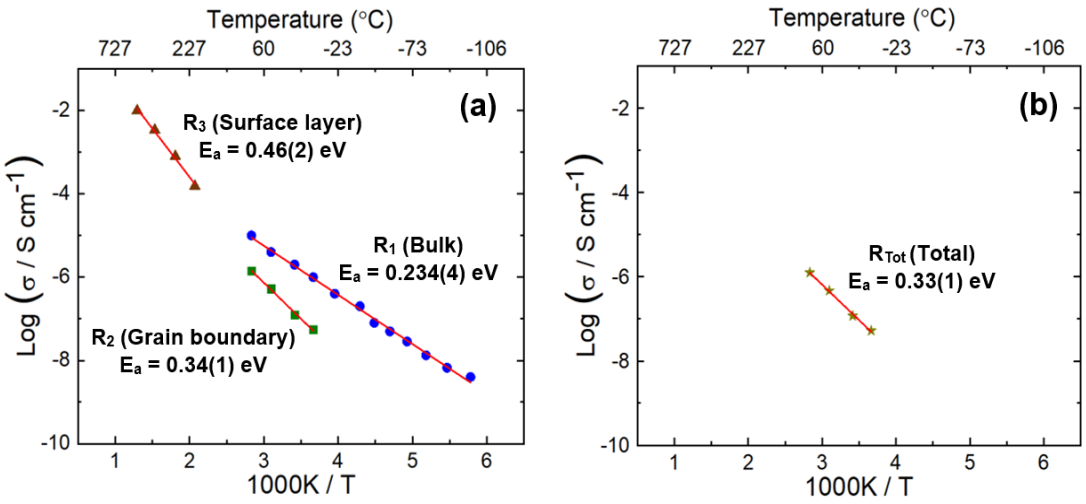

Figure 3.13 Arrhenius plots of Na[Ni,Mg,Mn,Ti]O_2 for its separate individual components (a), as well as its total conductivity (b).

The overall conductivity of the material, as well as that of each individual component, appears to be electronic, as the activation energy for migration of a sodium ion is usually ~ 0.5 eV or greater. There are of course exceptions to this, with very good sodium ion conductors such as NASICON and sodium beta alumina having activation energies of 0.3 ~ eV[30] and ~ 0.2 eV[31] respectively. The absence of an obvious low-frequency spike in the impedance complex plane plot data (Fig. 3.12), which would show the presence of the electrode double layer phenomena, suggests that the material may not be an ionic conductor. However, in the *C'* plot at 500 °C, the values are still increasing beyond 1 μF cm^{-1} at low frequency, which is

likely to be indicative of charge blocking at the sample-electrode interface, and, hence, ionic conduction. Therefore, these measurements suggest that Na[Ni,Mg,Mn,Ti]O_2 is a reasonable mixed conductor, and, hence, support its suitability as a potential sodium-ion cathode material.

3.3.3 Electrochemical Testing

The electrochemical performance of the mixed phase Na[Ni,Mg,Mn,Ti]O_2 material was first evaluated using a half-cell setup *vs.* sodium metal. Charge/discharge curves of the sample in the voltage range 2.5 – 4.3 V, using a specific current of 14 mA g^{-1}, which corresponds to an approximate C-rate of C/10, are shown in Figure 3.14. The voltage-capacity profiles exhibit slopes consisting of a series of poorly-defined small plateaus. An initial charge capacity of ~ 150 mAh g^{-1} was observed, before dropping to around 120 mAh g^{-1} for subsequent cycles. A fairly stable discharge capacity of ~ 120 mAh g^{-1} is seen over the initial 50 cycles.

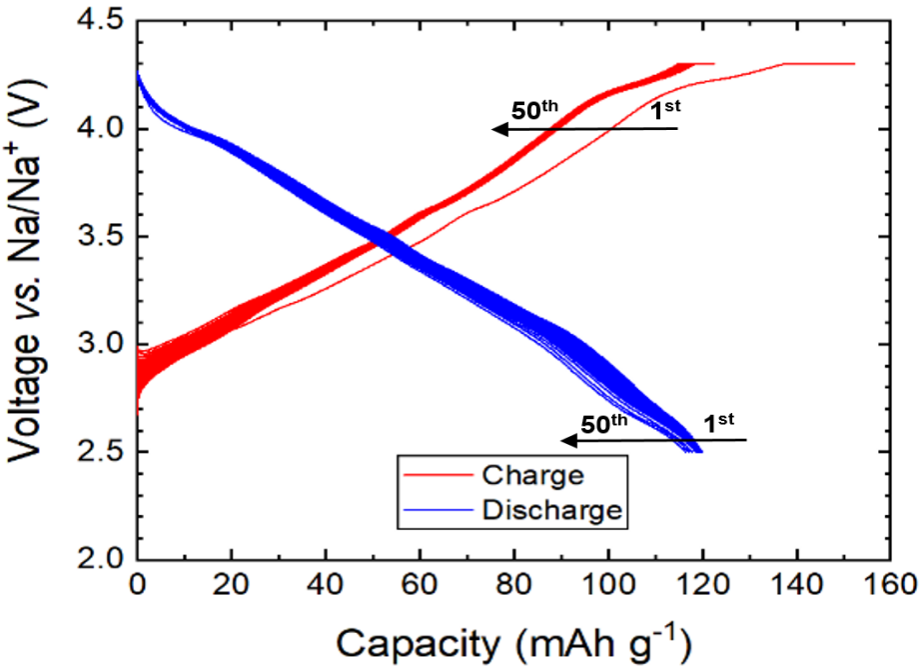

Figure 3.14 Charge/discharge curves in 2.5 - 4.3 V range (*vs.* Na metal) at 14 mA g^{-1} (~ 0.1C), showing 50 cycles for Na[Ni,Mg,Mn,Ti]O_2.

A sloping region of the voltage-capacity profile is indicative of a single phase region where a change in free energy results in a voltage change, in accordance with the

Nernst equation (see Section 1.1). A flat section corresponds to a two-phase region where the removal/insertion of Na^+ does not lead to a significant alteration in electrochemical potential. The sloping voltage-capacity profile seen in Figure 3.14 for Na[Ni,Mg,Mn,Ti]O_2 is typical of a layered electrode structure, e.g. lithium cobalt oxide.[32] The absence of a clearly defined continuously flat section in the voltage-capacity plots means there is no constant two-phase coexistence region, as is seen in many other commercial other Li-ion materials, e.g. lithium iron phosphate ($LiFePO_4$),[33] lithium manganese oxide ($LiMn_2O_4$).[34]

There is a loss of capacity following the first charge of the Na-ion half-cell. There is a voltage plateau during the initial charge around 4.2 V and a shorter one on discharge ~ 4.0 V. Hence, this demonstrates that some of the Na removed from the layered oxide structure at high voltage is not reinserted back into the material on discharge. There are additional plateaus during charge and discharge at 3.6 and 3.5 V respectively. The plateaus occur at a lower voltage on discharge because of an overpotential.[35] This overpotential occurs as more energy is required to remove Na^+ ions from the host lattice and electrons from the transition metals on charging (and promote them from the ground state) than is accompanied with the opposite processes on discharge.[36]

In order to identify the electrochemical reactions involved in the Na[Ni,Mg,Mn,Ti]O_2 cell, cyclic voltammetry was performed at a scan rate of 0.1 mV s^{-1} (Fig. 3.15). A stable trend is obtained through cycling, indicating good structural stability of the electrode. There are a series of current peaks, which can be paired due to a symmetric shape of the cyclic sweep. There are two main pairs of peaks with potential maxima at 4.2 V/4.0 V (anodic/cathodic) and 3.6/3.5 V (matching the plateaus in the voltage-capacity plots in Fig. 3.14). Upon consecutive cycling sweeps, the intensities of these redox peaks slowly decrease and, for the 4.2/4.0 V pair, shift towards a lower voltage value.

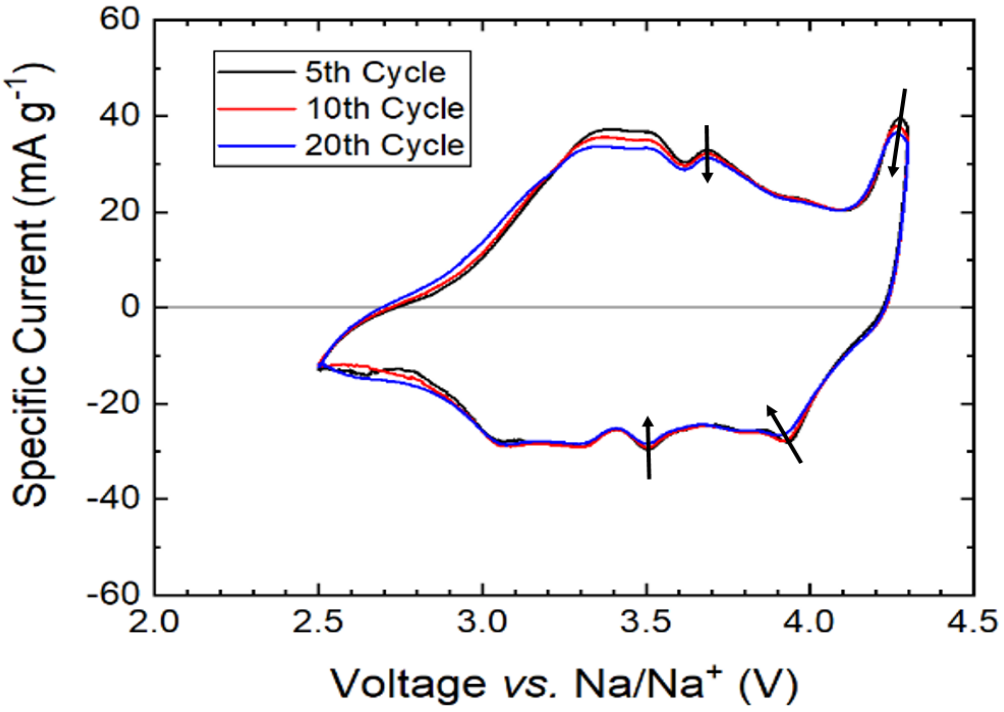

Figure 3.15 Cyclic voltammetry profile of selected sweeps of Na[Ni,Mg,Mn,Ti]O_2 at 0.01 mV s^{-1} between 2.5 and 4.3 V.

The voltage-capacity plots in Figure 3.14 and the cyclic voltammograms in Figure 3.15 illustrate the complex electrochemical behaviour of the mixed phase Na[Ni,Mg,Mn,Ti]O_2 material, indicating that the transition metals are active in wide potential ranges. This is because having a number of different mentals results in a large number of local environments, which leads to (de-)insertion of sodium over a wide range of potentials. This is why multiple broad peaks are seen in the CV profile, as opposed to sharp, well-separated peaks. The most likely redox process to occur in this material during electrochemical testing is a double electron process of the Ni^{2+}/Ni^{4+} redox couple. Based on results seen in the literature for similar systems, manganese ions are likely to be chemically inert under these conditions and only become redox active at lower voltages.[10,37] The anodic peak at 4.2 V exhibits the most significant alteration with cycling, suggesting that changes to the electrode structure at high voltage, upon charging are partially irreversible.

Cycling of the material at different rates of discharge is shown in Figure 3.16. Galvanostatic experiments were performed using coin cells between 2.5 and 4.3 V *vs.* Na^+/Na. Samples were charged at 14 mA g^{-1}, equivalent to a C-rate of ~ 0.1C, and discharged at 14 (low), 28 (moderate), and 140 mA g^{-1} (high) rates,

approximately equivalent to C-rates of C/10, C/5 and 1C respectively. Comparing the rates of discharge, the measured capacity from the highest to lowest follows the sequence 14 mA g^{-1} > 28 mA g^{-1} > 140 mA g^{-1}. The initial discharge capacity after the first cycle was 119, 114 and 94 mAh g^{-1} respectively. After 50 cycles, the capacity, at discharge rates of 14, 28 and 140 mA g^{-1}, was 116, 107 and 82 mAh g^{-1}, equating to respective charge retentions of 98%, 94% and 87%.

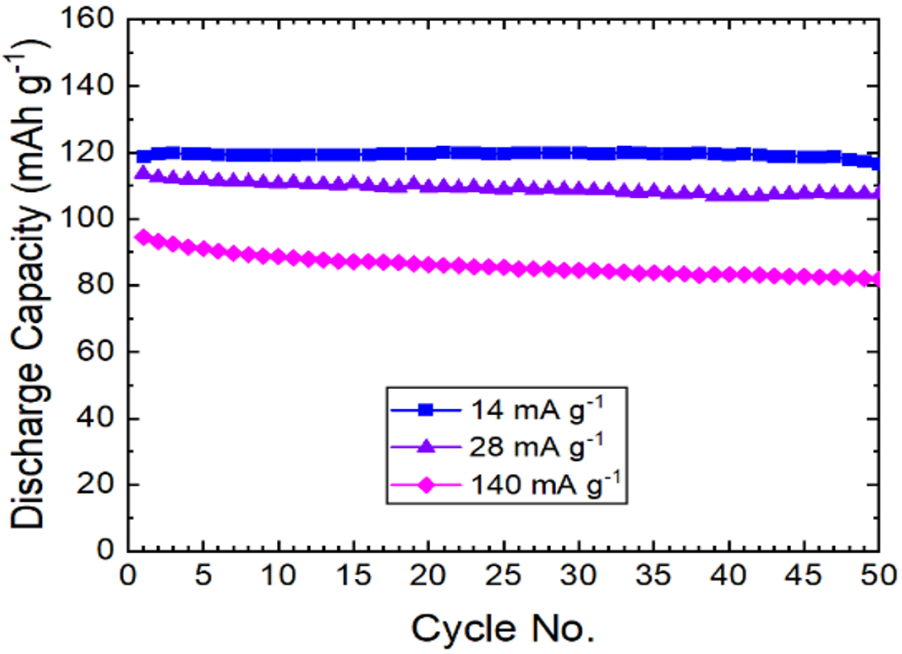

Figure 3.16 Discharge cycling data of Na[Ni,Mg,Mn,Ti]O_2/Na metal half cells over 50 cycles. Samples were charged at 14 mA g^{-1} and discharged at 14, 28 and 140 mA g^{-1} between 2.5 and 4.3 V.

These data presented here are from reproducible cells with very similar electrode loadings: 19 ± 0.5 mg of active material. Results show that a higher C-rate means a lower discharge capacity. This can be explained by a greater discharge current leading to a larger mass transport overpotential.[38] As the Na-ion battery discharges, sodium is pulled from the Na metal anode and forced back into the layered oxide cathode. This creates a concentration gradient where Na^+ ions are high at the surface of the cathode. Gradually, sodium ions diffuse from the surface of the cathode into the bulk to try and rebalance the gradient. However, if the discharge current is too high, Na^+ ions are unable to move into the cathode fast enough to allow further ions to follow suit. This causes a saturation at the surface of the cathode, and, therefore, a

lower amount of Na^+ ions are transferred for the same amount of current, thus resulting in a reduced capacity. Furthermore, cells cycled at a high C-rate exhibit greater capacity fade (lower charge retention). This is because greater mechanical degradation is thought to occur in the cathode particles when cycled with a faster current.[39] Cracks and defects are likely to occur in the cathode structure which trap/isolate Na^+ ions and so prevent them being removed and re-inserted on subsequent cycles.

To further examine the suitability of $Na[Ni,Mg,Mn,Ti]O_2$ for practical application as a sodium-ion battery cathode, a full-cell was assembled where the layered transition metal oxide was cycled against a non-graphitizable hard carbon (the most popular anode material for Na-ion cells). Based on the reversible capacities of the active materials, a typical active mass cell balance (cathode: anode) of around 1.5-1.8 was utilised (mass balance calculations are provided in Appendix C). This represents a cathode-limited cell design, where the capacity is restricted by the amount of Na extracted from the layered oxide during the first charge.

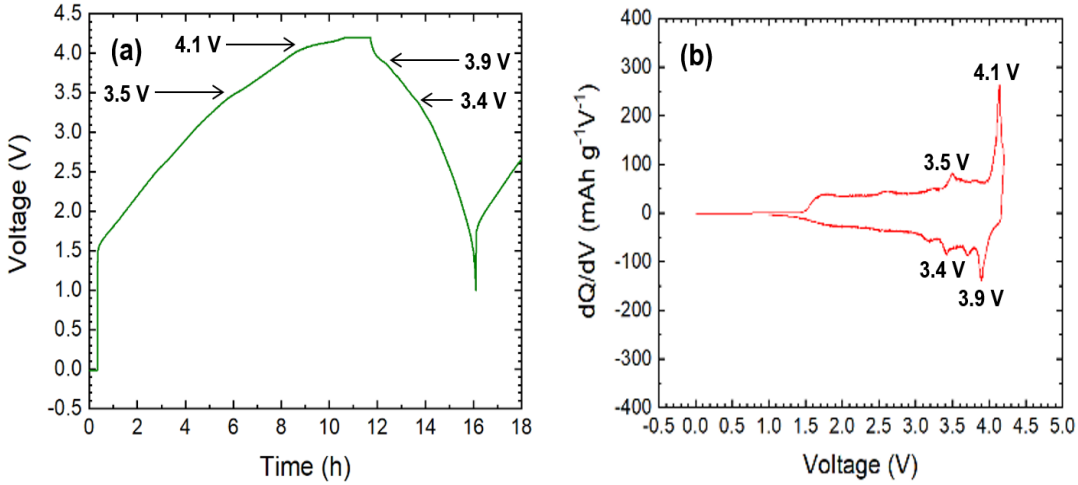

Figure 3.17 (a) Voltage-time profile and (b) differential capacity plot for a $Na[Ni,Mg,Mn,Ti]O_2$/hard carbon cell during the first cycle. The cell was charged at 14 mA g^{-1} up to 4.2 V and discharged at 28 mA g^{-1} down to 1 V. The inflections in the voltage-time profile and corresponding spikes in the differential capacity plot are indicated.

Electrochemical data collected for the cell during the first cycle are displayed in Figure 3.17. The cell was charged using a specific current of 14 mA g^{-1} (~ C/10) and discharged at 28 mA g^{-1} (~ C/5). At 4.2 V; a constant voltage step is used to

complete the charging process. The voltage-time profile in (a) is sloping indicating Na^+ ion (de-)intercalation over a wide potential range. There are two small inflections visible on charging, at voltages of 3.5 and 4.1 V, and two on discharging, at 3.9 and 3.4 V. These are more clearly visible as spikes in the differential capacity plot in (b), and occur at a lower voltage during discharge because of a cell overpotential. The features of the d*Q*/d*V* curves are similar to those observed in the cyclic voltammogram (Fig. 3.15), with sharp well-defined peaks at high voltage and a profile that is diffuse towards lower voltages. Furthermore, as seen with CV data, upon consecutive cycling, the intensities of the peaks in the differential capacity plots slowly decrease and shift towards a slightly lower voltage value for the 4.1/3.9 V pair (see Appendix D).

In Figure 3.18, the discharge rate capability performance within the potential range 1 – 4.2 V is shown. In (a), the cell has been tested for five cycles with discharge currents of 7, 14, 28, 70, 140 and 280 mA g^{-1}, approximately equivalent to discharge rates of C/20, C/10, C/5, C/2, 1C, and 2C, before a final five cycles at 7 mA g^{-1} (C/20). For the cell charging process, (CC/CV), a constant current of 28 mA g^{-1}, equivalent to a ~ C/5 rate has been used for all tests. The cell exhibited a reversible capacity of approximately 131, 130, 128, 122, 116, and 103 mAh g^{-1}, with increasing discharge rate. For the final five cycles at 0.05C, the capacity of the cell returned close to the initial 130 mAh g^{-1}. In Fig 3.18 (b), this cell was tested for ten cycles using equal charge/discharge currents each time of 7 (0.02C), 14 (0.1C), 28 (0.2C), 70 (0.5C), 140 (1C) 280 (2C) and 700 mA g^{-1} (5C). This resulted in reversible capacities of approximately 127, 126, 123, 116, 108, 86 and 30 mAh g^{-1} respectively. The cell was then cycled for a final ten times using a 7 mA g^{-1} (C/20) charge/discharge current, giving a final capacity of around 106 mAh g^{-1}.

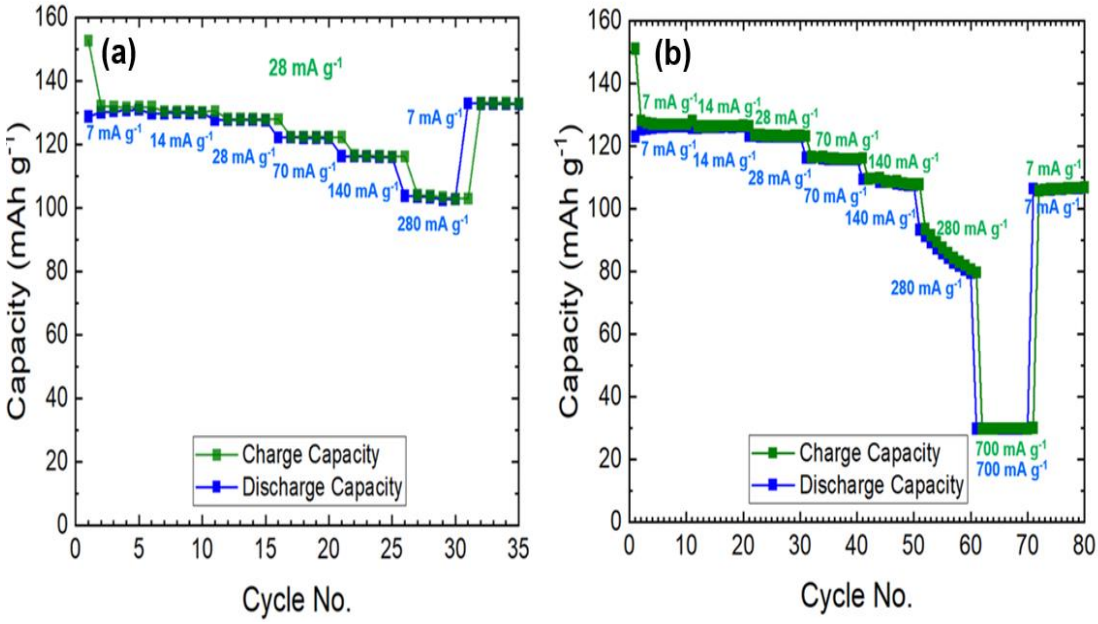

Figure 3.18 Rate capability performance of Na[Ni,Mg,Mn,Ti]O_2/hard carbon full-cell (1-4.2 V) with charge (green) and discharge (blue) capacity curves. A charge rate of 0.2C (28 mA g^{-1}) was used in (a) and variable charge rates, which matched the discharge currents, in (b).

For the rate capability studies in Figure 3.18 (a), Na[Ni,Mg,Mn,Ti]O_2 shows a gradual decline in capacity with increasing discharge current. However, there is a complete recovery when a lower discharge rate of C/20 is used again, even after the high rate cycling at 2C. This suggests that the capacity decrease seen at higher discharge rates is due to an impedance increase, rather than an irreversible loss of sodium.[40] A fast discharge causes an increase in polarisation (resistive) losses due to bottlenecks in the mass/charge transfer of species.[41] The almost complete recovery of capacity when returning to C/20 suggests that the Na[Ni,Mg,Mn,Ti]O_2 electrode possesses good structural stability at higher discharge rates. The capacities for the cell in (b) are similar for the first three charge/discharge currents as observed in (a), within 5 mAh g^{-1} of one another. For the cycles at 70 and 140 mA g^{-1}, the capacity is 6 and 8 mAh g^{-1} lower respectively for the cell charged using a greater current. The real disparity in the performance of the separate cells is noted when the cell in (b) is charged and discharged at a rate of 280 mA g^{-1} (2C). This causes the capacity to gradually decline from 94 to 80 mAh g^{-1} over the ten cycles. The performance in terms of deliverable capacity declines further at the 5C cycling rate. When the cell is cycled once again at a lower rate of 0.05C, there is only an 84% charge retention

from the initial ten cycles. The more significant capacity deterioration and fade in (b) indicates that the battery is less well suited to faster charging compared to discharging.

Many of the capacity fading mechanisms exacerbated by a high cycling rate may be presumed equally likely to occur on charge/discharge, e.g. volume changes and contact loss in the electrode particles.[42] One degradation route, which only occurs significantly on charging, is metal plating on the anode.[43] The insertion potential of carbonaceous materials is close to the potential of Na metal. Over time, the number of vacant sites for Na insertion in the carbon anode decreases, and, with high charge currents, the transport rate of sodium ions from the electrolyte exceeds the insertion rate, resulting in sodium accumulating at the anode surface. This drives the potential of the electrode below 0 V and, as a consequence, sodium plating occurs.[44] The deposited Na metal is then able to react with the electrolyte, thus consuming active sodium and electrolyte, and also causing the loss of electrical contact of some deposited sodium with the anode.[45] This Na can no longer be used in cycling and is known as 'dead sodium'. Furthermore, the reaction between Na metal and electrolyte forms a redundant interfacial film, which increases the anode polarization and, in turn, promotes further anode Na plating.[46] This plating process becomes more prevalent when using high charge currents, and is most likely the explanation for what is observed in Figure 3.18. At the higher charging rates, some of the Na is irreversibly lost, which leads to a drop in capacity which is unrecoverable once the cell is returned to a lower rate. Crucially, the above results point towards an anode issue rather than a cathode one. Hence, importantly, these studies indicate that the mixed phase material, $Na[Ni,Mg,Mn,Ti]O_2$, appears to possess good rate capability when tested as a sodium-ion battery cathode.

Having examined the rate performance of the layered sodium oxide in a Na-ion battery, the cycle life of these cells was also investigated. A $Na[Ni,Mg,Mn,Ti]O_2$/hard carbon cell was charged using voltage limits of 4.2 and 1.0 V, at a specific rate of 14 mA g^{-1} (~ C/10) and discharged at 28 mA g^{-1} (~ C/5). A constant voltage (CV) step was used at 4.2 V to complete the charging process. The resulting cyclability plots (specific capacity and coulombic efficiency *vs.* cycle number) are shown in Figure 3.19. There is an initial delivered discharge capacity of

125 mAh g^{-1} (a), and an average voltage *ca.* 3.2 V vs Na^{+}/Na, equating to an energy density ~ 400 Wh kg^{-1}. To study the long-term cycling performance, the sodium cell is evaluated for 450 cycles (b). High coulombic efficiency is regarded as an important feature for the potential of practical application. For this material, the coulombic efficiencies exceed 99% after the 3rd cycle. There is a charge retention of 79% after 450 cycles of sodium ion extraction and insertion.

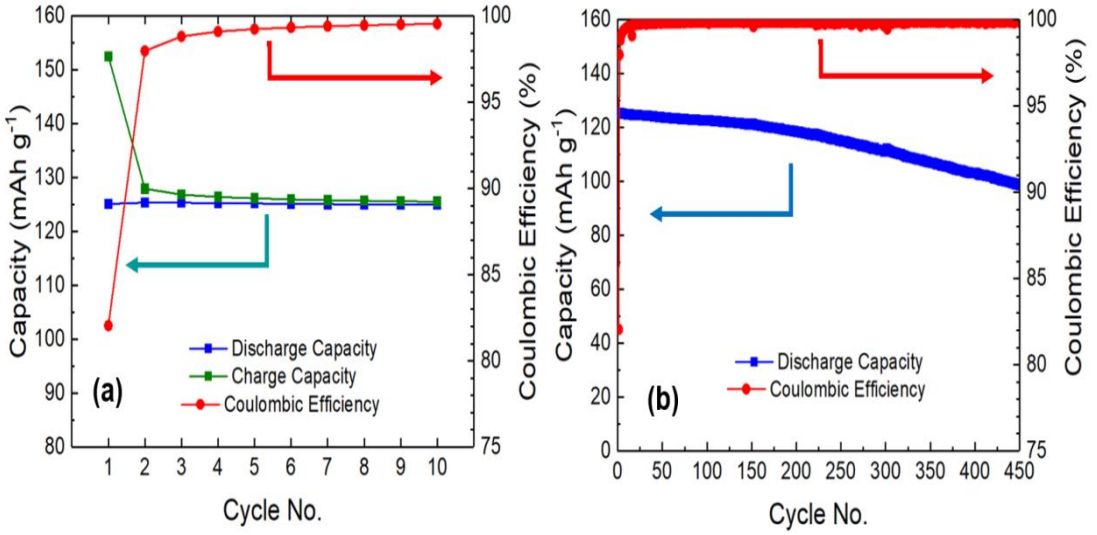

Figure 3.19 Capacity and coulombic efficiency of a Na[Ni,Mg,Mn,Ti]O_2/hard carbon full-cell after (a) 10 and (b) 450 cycles. The cell was charged at 14 mA g^{-1} and discharged at 28 mA g^{-1} between 1-4.2 V.

The discharge capacity and average cell voltage of Na[Ni,Mg,Mn,Ti]O_2 is promising for the use of this material as a sodium-ion battery cathode. Layered sodium transition metal oxides are generally reported to have capacities in the range 100-200 mAh g^{-1},[47] but their cycle life is usually poor, showing significant capacity fading beyond 50-100 cycles.[48] Furthermore, the values obtained for this layered oxide were for a full-cell setup (*vs.* hard carbon anode), whereas most research performed on Na-ion cathodes is only done *vs.* sodium metal (half-cell). Full-cell testing gives a more realistic impression of how the cathode material is likely to perform when employed in a real world battery. The energy density for this layered oxide Na-ion cell of 400 Wh kg^{-1} is comparable with other commercially available lithium-ion cathodes: lithium cobalt oxide (~ 580 Wh kg^{-1}),[49] lithium iron phosphate (~ 450 Wh kg^{-1}).[50] Furthermore, it was found that the specific energy could be improved further by increasing the voltage window (Appendix E). However, despite the relatively

aggressive cycling charge/discharge rates used, ultimately, the cycle life of this sodium-ion battery is lower than most lithium-ion materials. In order to compete commercially with LIBs, sodium-ion cells ideally need to be able to maintain 80% charge retention for > 1,000 cycles, and therefore, further work is required in order to improve the long-term stability of these Na-ion cells.

3.3.4 *In Operando* Studies

In order to elucidate further information on the electrochemical performance of this Na[Ni,Mg,Mn,Ti]O_2 layered cathode, and possibly gain a better understanding of what limits its long-term performance, *in operando* X-ray diffraction was performed. This provides a non-destructive and real-time way to observe structural processes occurring at the electrodes during battery operation. The XRD pattern obtained for a Na[Ni,Mg,Mn,Ti]O_2/hard carbon full-cell prior to cycling (at 0% state of charge) is provided in Figure 3.20. A laminated aluminium pouch cell design was used to conduct the measurements with the diffractometer operated in transmission mode. Precise details on the experimental setup are provided in Chapter II.

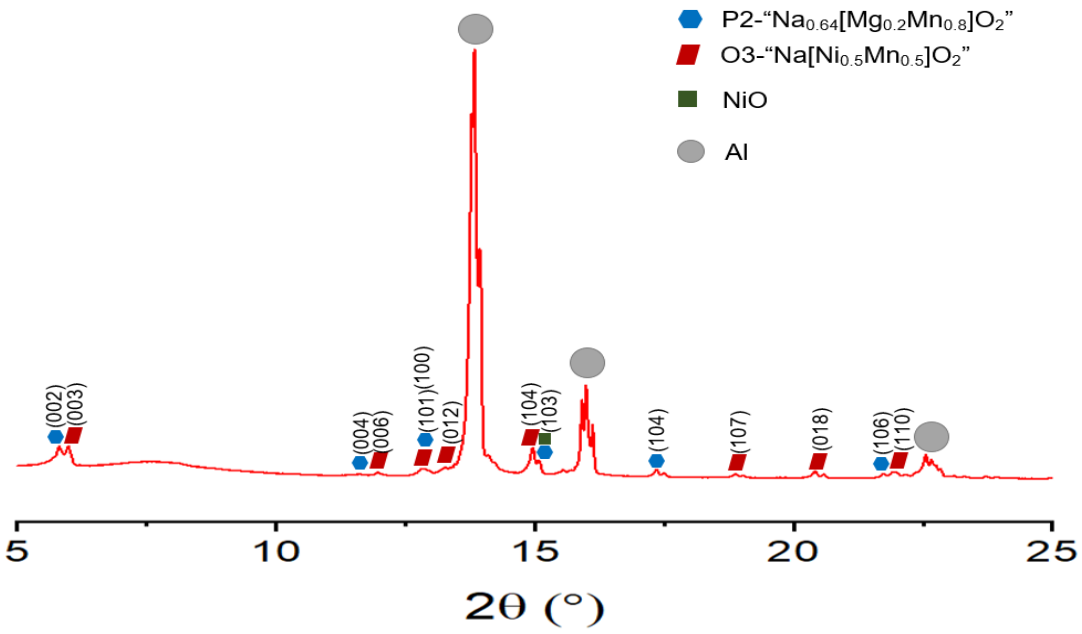

Figure 3.20 The XRD pattern of a Na[Ni,Mg,Mn,Ti]O_2/hard carbon pouch cell at 0% state of charge (prior to cycling), collected by AgPSD with λ = 0.5608 Å. The two polymorphs are indicated as hexagonal P2 phase ⬣, and trigonal O3 phase ▰. A minor impurity of cubic NiO is marked with ■. Reflections from the aluminium of the cell are observed (indicated by ◯).

This X-ray diffraction pattern was obtained using a silver anode as the target metal. The diffractogram is dominated by collections of peaks corresponding to the aluminium within the pouch cell. The pouch itself is laminated Al, and the current collectors are both carbon-coated aluminium. As the hard carbon anode material is amorphous (as well as the glass fibre separators), the remaining peaks must originate from the crystalline Na[Ni,Mg,Mn,Ti]O_2 of the cathode. These peaks can be assigned to the different O3 and P2 polymorphs present within the mixed phase material by converting the 2θ values into d-spacing for both this XRD and the initial diffractogram collected for the raw layered oxide powder using a Mo source (Figure 3.2). Further information on the d-spacing calculations are given in Appendix F.

The *in operando* X-ray diffraction patterns during the first charge and discharge are illustrated in Figure 3.21. The state of charge of the cell is calculated by the coulomb counting method (see Section 1.1). The Na[Ni,Mg,Mn,Ti]O_2/hard carbon cell is charged up to 4.2 V using a specific current of 14 mA g^{-1} (~ C/10), and discharged to 1 V at 28 mA g^{-1} (~ C/5). The collections of peaks from aluminium are indicated by circles and do not shift during cycling. From the changes in XRD reflections, it is clear that there are structural modifications occurring to the electrode during cycling. The most marked alterations in the XRD patterns are indicated by the grey dashed lines; these are most pronounced at the beginning and end of each charge/discharge. The peak intensity ratio of P2 (002) and O3 (003) changes significantly with the variation of sodium content, as is highlighted by the zoomed-in box.

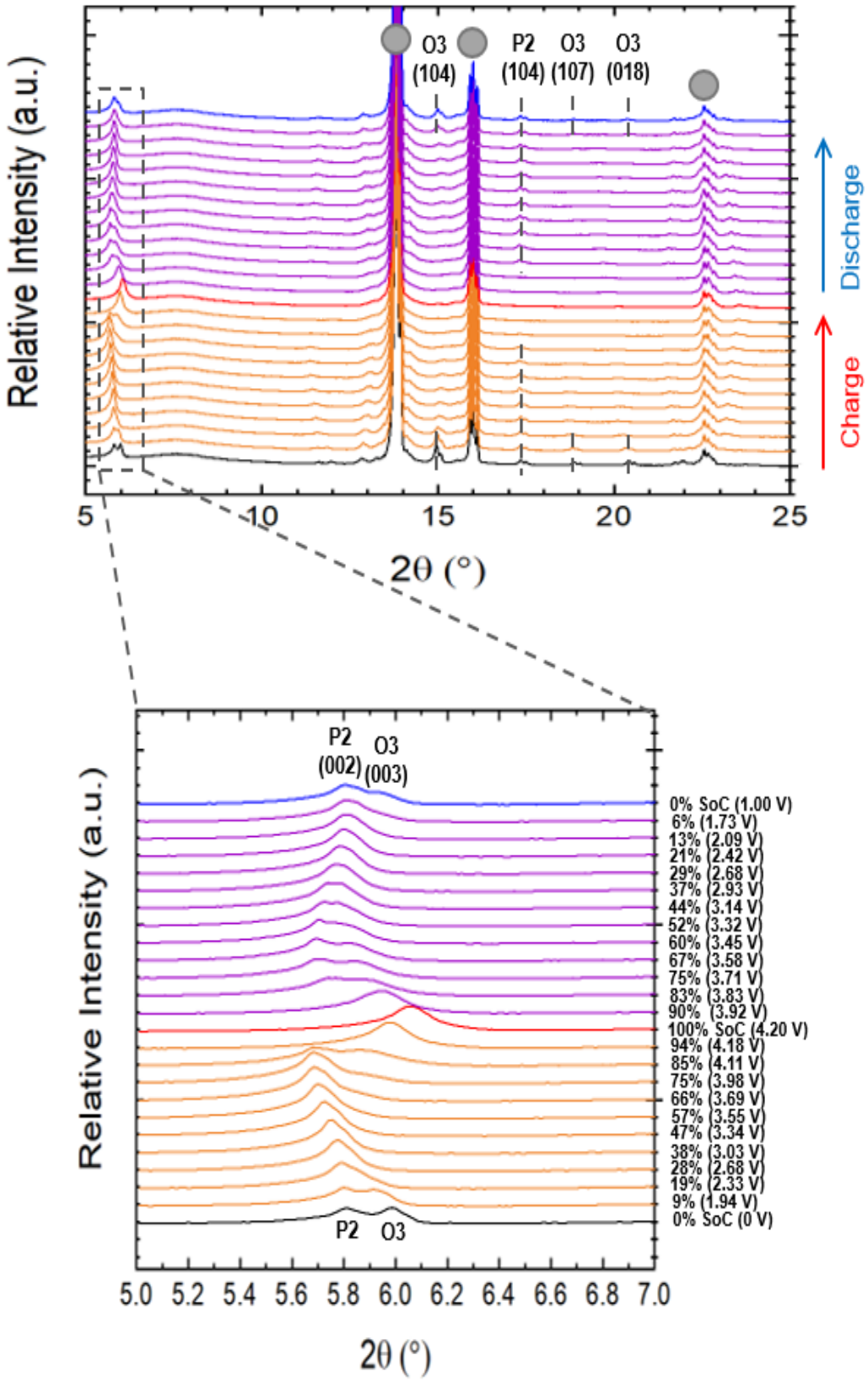

Figure 3.21 *In operando* X-ray diffraction data for a Na[Ni,Mg,Mn,Ti]O_2/hard carbon pouch cell during the first charge and discharge, collected by AgPSD with λ = 0.5608 Å. ○ shows the peaks corresponding to the presence of aluminium. The zoomed-in region shows reflections in the 5-7° range. Each X-ray diffraction pattern was collected for 16 minutes.

Prior to cycling the Na[Ni,Mg,Mn,Ti]O_2 cathode, there is a mixture of the O3 and P2 polymorphs present. During charging, this two phase region lasts up to at least 19% SoC, however, there is a steady decrease in the intensity of the O3 (003) peak. This is also seen in the apparent disappearance of the O3 (104), (107) and (018) reflections. There then appears to be a single phase region from approximately 28 to 66% SoC. The P2 (002) peak shifts towards lower angle until the top of charge; hence indicating that there is likely to be a solid solution formation. The same effect is also observed with the P2 (104) peak. Between 75 and 85% SoC, there is a two phase region again, and above this, possibly a single phase is formed at the top of charge. From 4 – 4.2 V, these P2 peaks disappear and at low angle there is an additional peak present around 5.9° belonging to a separate unidentified phase, which shifts towards higher angle, and broadens, up to 100% SoC. This phase evolution is illustrated in Figure 3.22. The Na[Ni,Mg,Mn,Ti]O_2 electrode structure appears to be reversible as the changes seen during charging of the cell reversed on discharge, and all the peaks in the final discharged pattern returned to the original state (Appendix G). However, it is worth noting that on subsequent cycles, the presence of the O3 phase at low states of charge became less evident, as the peaks belonging to this phase decreased in intensity.

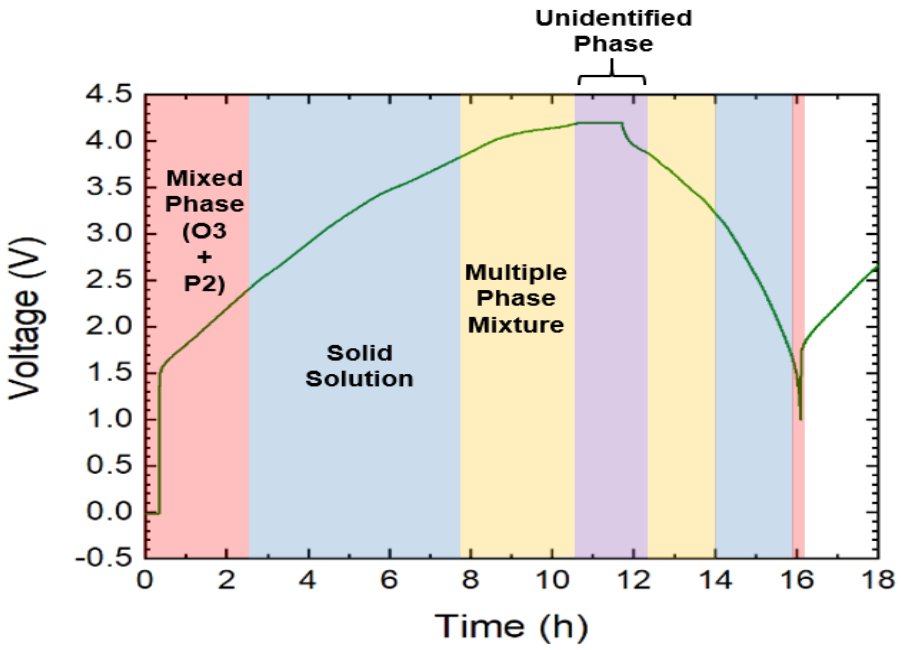

Figure 3.22 Electrochemical charge-discharge profile for the *in operando* XRD Na[Ni,Mg,Mn,Ti]O_2/hard carbon pouch cell, during the first cycle. The different coloured boxes highlight the separate phase regions, indicated by the XRD results.

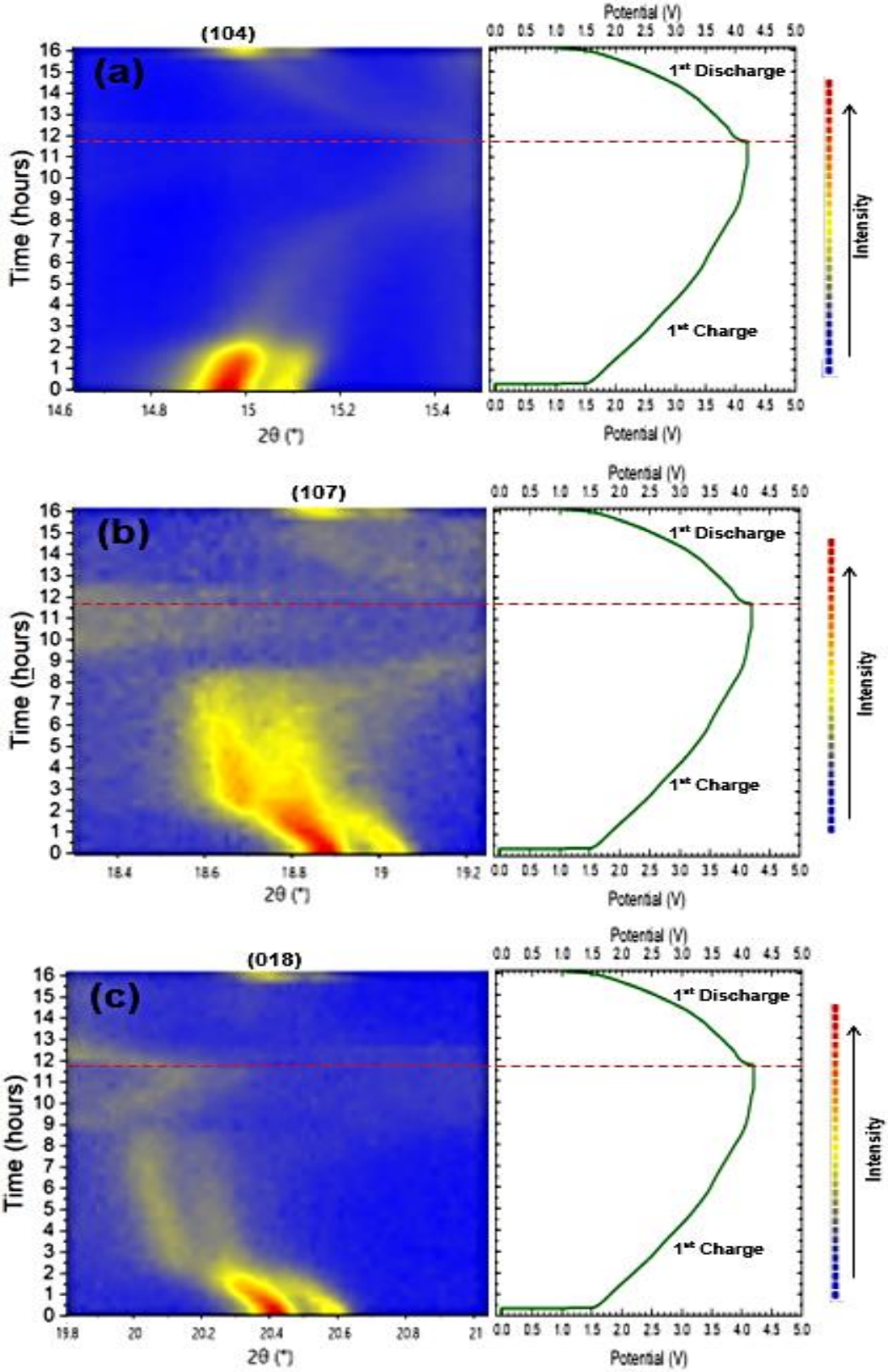

Figure 3.23 Selected 2θ regions of *in operando* XRD data for a Na[Ni,Mg,Mn,Ti]O_2/hard carbon pouch cell during the first charge and discharge, collected by AgPSD with λ = 0.5608 Å. The evolution of the O3 (a) (104), (b) (107), and (c) (018) reflections are highlighted by a colour scale with the potential profile displayed on the right and a red dashed line denoting the top of charge.

In order to aid the analysis of the structural changes during cycling, the evolution for the various reflections can be shown as contour intensity maps. These are presented for the O3 (104), (107) and (018) peaks in Fig. 3.23. While the XRD diffractograms suggest that there is a disappearance of these peaks above ~ 10% SoC, the contour maps show that as well as a significant decrease in intensity there is a movement of the (104) peak (a) to higher angle, and the (107) (b) and (018) (c) peaks to lower 2θ values.

These peak movements are characteristic of T_MO_2 slab gliding and the O3 → P3 transition for layered sodium oxides (Fig. 3.24).[7,51] Sodium ions in the O3-type phase are originally stabilized at edge-shared octahedral sites with ABCABC oxygen packing. The extraction of Na and creation of vacancies allows the T_MO_2 slabs to glide by (1/3, 2/3, 0), and the Na^+ ions become stabilised at prismatic sites with ABBCCA oxygen stacking.[52] The contour intensity maps show that the O3 phase appears at a lower SoC on discharging and the peaks have lower intensity; this suggests that an irreversible change has occurred to the electrode structure during the 1st cycle.

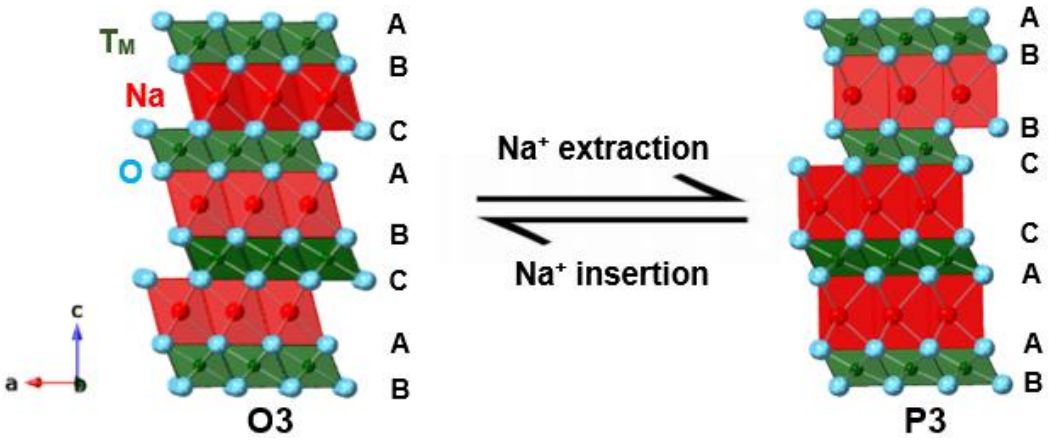

Figure 3.24 Schematic illustration showing the O3-P3 phase evolutions during the Na^+ insertion/extraction process.

Contour maps are also shown for the P2 (104) peak and the low angle region 5.2 – 6.4° of the *in operando* XRD patterns in Figure 3.25. The (104) peak in (a) maintains a steady intensity and shifts very slightly to lower angle on charging up to ~ 4 V. Above this voltage, at the top of charge, the peak disappears and is not seen again until discharging of the Na-ion cell. The low angle 5.2 – 6.4° section in (b) shows the

zoomed-in mixed phase region in Figure 3.22. Above ~ 10% SoC, the O3 polymorph disappears, leaving just the P2 (002) peak in the XRD pattern. Similar to the (104) reflection, there is also a gradual left shift of the P2 (002) peak during charging. At the top of charge, the (002) reflection disappears. However, there is the emergence of a separate peak around 5.9°, which increases in intensity and shifts to higher 2θ angle throughout the remainder of charge. At the top of charge, the angle of the new reflection reaches 2θ = 6.1°. These processes occur in reverse during discharge.

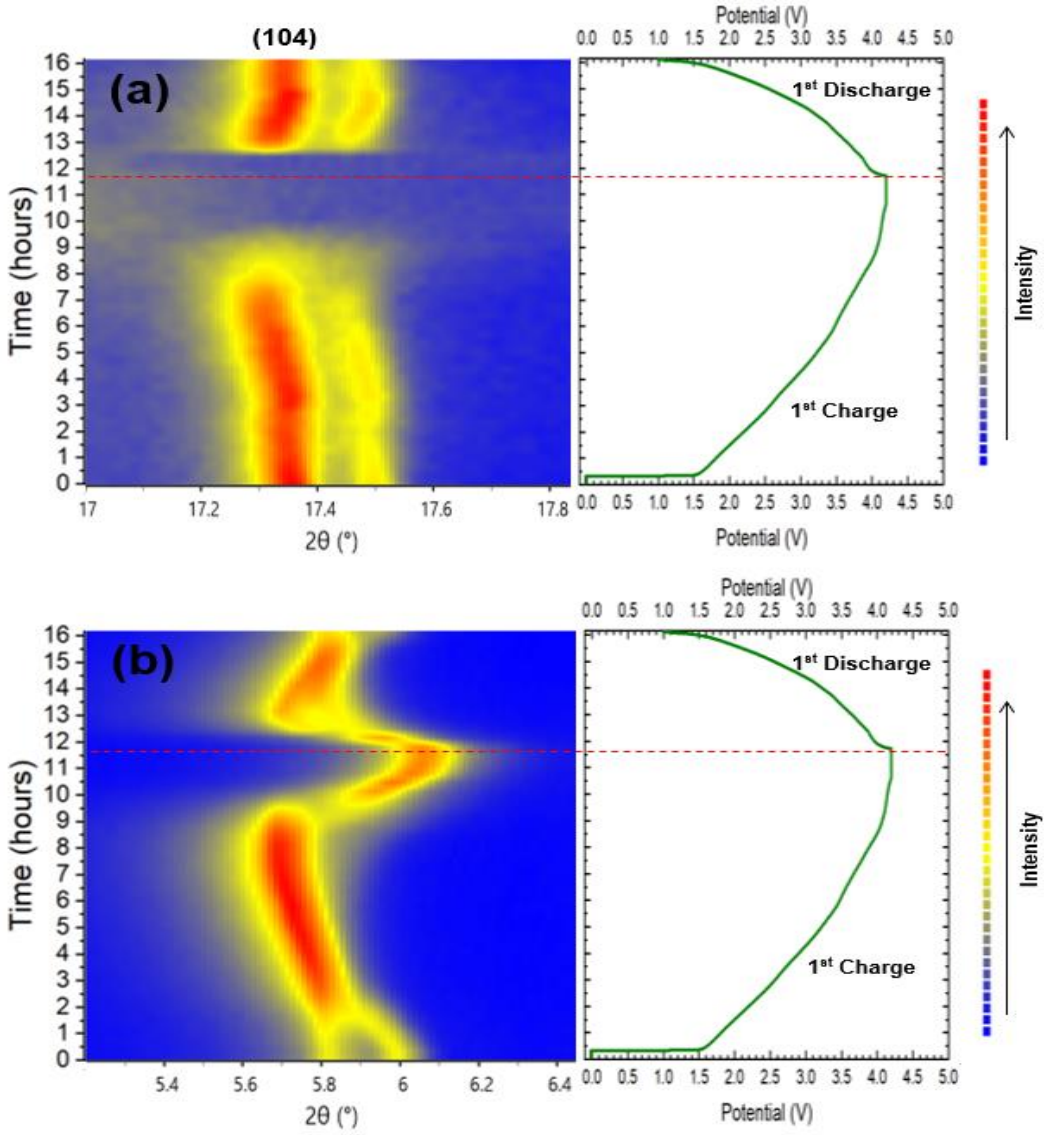

Figure 3.25 Selected 2θ regions of *in operando* XRD data for a Na[Ni,Mg,Mn,Ti]O_2/hard carbon pouch cell during the first charge and discharge, collected by AgPSD with λ = 0.5608 Å. The evolution of the (a) P2 (104), and (b) low angle 5.2-6.4° region are highlighted by a colour scale, with the potential profile displayed on the right and a red dashed line denoting the top of charge.

In a layered rock salt type structure, such as Na[Ni,Mg,Mn,Ti]O_2, the (00*l*) diffraction peaks give important information about the interlayer distance of the transition metal sheets and make it possible to investigate any structural changes in the *c*-direction. The shifting of the P2 (002) peak to lower angle up to 75% SoC (~ 4 V) indicates an increase in interlayer distance and a widening of the distance between adjacent T_MO_2 sheets. This increase is most likely due to reduced screening between adjacent negatively charged oxygen layers when Na^+ ions are removed during desodiation.

Certain P2-type layered sodium oxide compounds have been reported to undergo a phase transition at high voltage to the O2 polymorph by gliding of the transition metal oxide (T_MO_2) slabs, which results in a reordering of the Na sites from trigonal prisms to octahedra.[53] This phase transition is characterised by a sharp disappearance of the original (002) Bragg peak and a new (002') peak suddenly appearing at higher 2θ angle.[54] This is not observed for the *in operando* measurements for the Na[Ni,Mg,Mn,Ti]O_2 material. There is the evolution of a peak, which starts off as a shoulder on the P2 (002) peak, broadening and continually moving towards higher angle. Hence, there is the disappearance of the P2 (002) reflection during charge, and a new reflection appearing at only slightly higher 2θ. This alteration in XRD patterns at high voltage is characteristic of what is termed the "Z" phase, first reported by Delmas *et al.*,[55] and is so called because the precise packing type is unknown. Instead, it can be considered an intergrowth structure between trigonal and octahedral stacking. The appearance of this "Z" type phase coincides with a faint splitting of the P2 (104) reflection to both higher and lower angles of 2θ (Fig. 3.25 a). This splitting is consistent with the "Z" phase not being a solid solution, but rather it can be thought of as a changing structure which evolves between the P2 and O2 phases with an OP4 polymorph, where there is alternating layers of O- and P-type stacking, as an intermediary (Fig. 3.26).[56] The Na^+ ions are located in the P-type layers and the sodium vacancies in the O-type. Upon discharge the "Z" phase transforms back to P2, but the P2 (002) peak now has a weaker intensity (Fig. 3.25 b), thus providing further evidence of an irreversible change, and possibly damage, to the electrode structure.

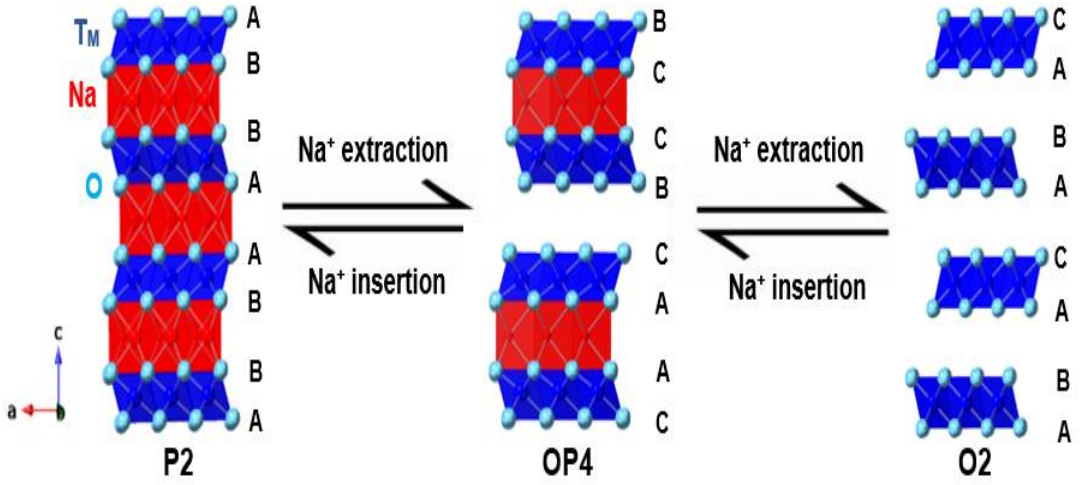

Figure 3.26 Schematic illustration showing the P2-OP4-O2 phase evolutions during the Na^+ insertion/extraction process.

The charging of P2-type layered sodium transition metal oxides occurs by staging.[57] The removal of Na^+ results in stacking faults of highly depleted sodium layers with O-type stacking, randomly distributed within an overall P2 structure. In the absence of Na^+ ions between the oxygen layers to stabilise the trigonal prismatic coordination, and increased repulsion between successive O layers directly facing each other in the P2 arrangement (ABBA), at low sodium content, the T_MO_2 sheets glide in the *a*-*b* plane by (1/3, 2/3, 0) to transform into the O2 structure (ABAC), with the oxygen ions now in octahedral sites.[22] On charging, the ratio of random O-type stacking faults gradually increases. At 50% stacking faults, the ordered OP4 phase (of alternating P- and O-type stacking) forms[56] and, on further charging, a purer O2 polymorph is formed.

The P2 → O2 transition typically results in a severe contraction of the unit cell along the *c*-axis at the top of charge.[58] The P2 → OP4 transition, on the other hand, results in less of a severe volume change, and, therefore, leads to smoother charge/discharge.[59] Hence, the presence of the "Z" phase during cycling of the electrode is advantageous, as the overall volume changes are smaller in magnitude and less abrupt, which should result in a better overall battery cycle life.[60] It is important to bear in mind that the cell used for these measurements has not been optimised for *in operando* measurements. Better XRD data are required to obtain accurate information on bond lengths and lattice parameters from Rietveld

refinements. Furthermore, there may be subtler phase changes and distorted crystal structures present, e.g. O'3, O''3, P'2 polymorphs, during cycling. To determine the exact phase transitions and Na^+/vacancy ordering, an optimum XRD setup is required.

An important consequence of phase transitions during cycling is changes to Na^+ ion mobility in the electrodes. This relates directly to the rate capability and, hence, overall performance of the battery. The conductivity in the $Na[Ni,Mg,Mn,Ti]O_2$ electrode during cycling, and, therefore, the kinetics of Na^+ insertion/extraction, were investigated using galvanostatic intermittent titration technique. A current pulse of 0.952 mA (~ 0.1C) was applied for 10 minutes, followed by a relaxation time of 1 h. The change in voltage during each step was measured and the Na diffusion coefficient (D_{Na^+}) calculated. The detailed GITT equation used is given in Chapter II (Eqn. 2.11). Figure 3.27 shows variation of the Na diffusion coefficient during the first charge of a $Na[Ni,Mg,Mn,Ti]O_2$/hard carbon cell, determined from the GITT profile. Up to 10% SoC, there is a dramatic rise in D_{Na^+} from approximately 1 x 10^{-13} cm^2 s^{-1} to 1 x 10^{-12} cm^2 s^{-1}. The diffusion then stays fairly constant in the electrode until ~ 70% SoC, before a sharp drop off at the top of charge back down to values that fluctuate around 1 x 10^{-13} cm^2 s^{-1}.

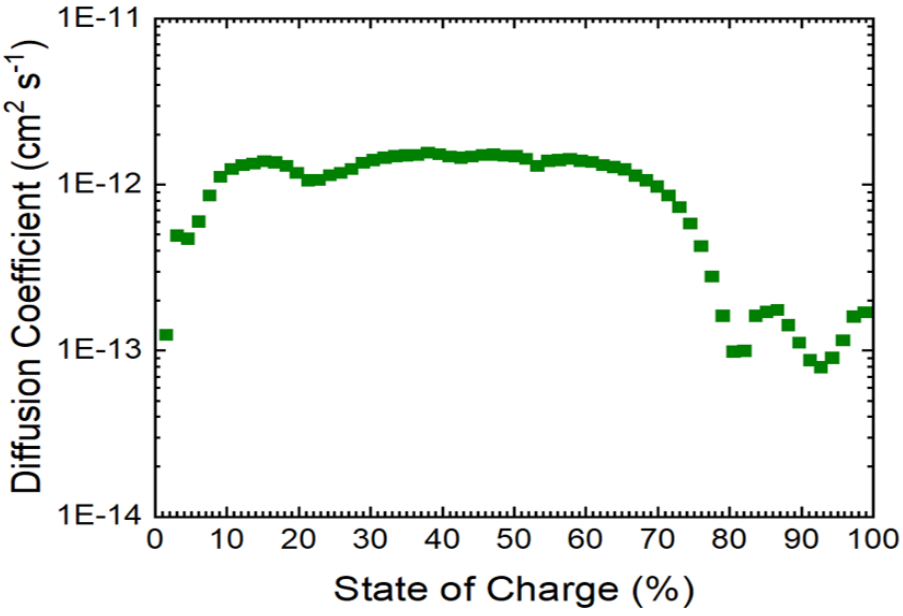

Figure 3.27 Na diffusion coefficients (D_{Na^+}) calculated from GITT measurements in a $Na[Ni,Mg,Mn,Ti]O_2$/hard carbon full-cell as a function of state of charge for the 1st charge.

The change in diffusion coefficient in the Na[Ni,Mg,Mn,Ti]O_2 cathode can be interpreted as follows. At the start of charge, there is a significant increase in Na^+ ion diffusion, which coincides with the disappearance of the O3 phase, as seen by *in operando* XRD measurements. In layered sodium oxides, the P-type structures are thought to generally afford better Na^+ ion diffusion than their O-type counterparts.[61] This is because Na^+ ion hopping in O-layered structures must take place through unfavourable interstitial tetrahedral sites, whereas in the P-phases there is an on open path for diffusion through adjacent prisms. The D_{Na^+} values in the 10 - 70% SoC range of the cell, ~ 1 x 10^{-12} cm^2 s^{-1} are consistent with those previously reported for P2. [62,63] At the top of charge, there is a significant decrease in Na^+ ion mobility. This coincides with the onset of the "Z" phase. Hence, the abrupt decrease in D_{Na^+} at high potentials could be explained by the formation of the OP4 and O2 structures caused by gliding of the T_MO_2 layers, leading to octahedral Na^+ vacancies, which hinders sodium diffusion. Furthermore, these phase changes coincide with a contraction of the *c*-axis, which shrinks the distance between adjacent T_MO_2 slabs and is likely to be of further detriment to Na^+ ion conductivity.[64] Since the GITT measurements were performed using a two-electrode full-cell arrangement, there may be some contribution to the D_{Na^+} values from the conductivity of the hard carbon anode. However, it is suspected that the limiting factor to any Na^+ ion diffusion in the battery will come from the cathode. (This is supported by impedance measurements later on in this thesis - see Chapter V onwards.) In order to rule out completely any contribution from the anode across the charging profile, a three-electrode GITT measurement is required.

3.4 Conclusions

In this chapter, a layered sodium quaternary transition metal oxide, $Na[Ni,Mg,Mn,Ti]O_2$, was studied as a potential sodium-ion battery cathode candidate. The structure and thermal/atmospheric stability of the material was examined using a variety of different characterisation techniques: XRD, SEM, TGA, DSC. Its electrical properties were also investigated using impedance spectroscopy. Electrochemical testing was performed employing both half- and full-cell battery setups. *In operando* XRD was carried out in order to try and gain a better understanding of how the structural changes the layered oxide undergoes during cycling relate to its electrochemical performance.

The $Na[Ni,Mg,Mn,Ti]O_2$ material was found to be a mixed phase layered oxide, consisting of two individual polymorphs, with nominal formulae P2-"$Na_{0.64}[Mn_{0.8}Mg_{0.2}]O_2$" and O3-"$Na[Ni_{0.5}Mn_{0.5}]O_2$". The P2 polymorph was found to disappear on heating above 800 °C, and is not subsequently recovered at lower temperatures. Oxygen loss and transition metal oxidation occurs when the sample is fired at high temperatures in nitrogen, and the layered rock salt type structure was found also to be prone to the uptake of species when exposed to the atmosphere. These are important considerations when considering the preparation, storage and handling of $Na[Ni,Mg,Mn,Ti]O_2$ as a potential Na-ion cathode. From impedance measurements, the activation energy associated with the total conductivity of the material is 0.33(1) eV, and the layered oxide was found to be a mixed conductor, which supports its suitability as a battery electrode. Electrochemical testing revealed the mixed phase material to possess a discharge capacity of 125 mAh g^{-1} (full-cell testing), as well as good rate capability and cycling stability: 95% charge retention after 200 cycles. The material is prone to a number of structural changes during cycling, as indicated by *in operando* XRD results. The O3 polymorph is only present in the bottom ~ 20% state of charge, and at high voltage (> 4 V), there is a significant alteration of the P2 structure, with evidence of the intergrowth "Z" phase.[55] From galvanostatic intermittent titration technique (GITT) measurements, the Na diffusion coefficient (D_{Na^+}) was found to be the highest and, therefore, the electrode the most conductive, when the material possesses predominantly a P2-type structure.

This mixed phase Na[Ni,Mg,Mn,Ti]O_2 layered oxide demonstrates an improved electrochemical performance compared to single phase systems with similar chemistries.[47,48] While this class of O-/P-type mixtures is still relatively unexplored, their superior performance may be explained by a synergistic effect of coupling the O3-type phase, which possesses a larger sodium reservoir, with the P2-type phase, which confers better stability. The presence of different phases within the cathode structure presents increased challenges to understanding the structure and properties of Na[Ni,Mg,Mn,Ti]O_2, and, in particular, its complex electrochemical performance. *In operando* monitoring of the structural evolution of electrode materials is considered crucial for further development of battery technology, and, to our knowledge, this is the first time such XRD data have been reported for a sodium-ion cathode operating in a full-cell. It may be possible to relate the structural changes and diffusion alterations during charge/discharge, observed in this chapter, to modifications in resistances from impedance data, seen later in this thesis. In order to better understand this multiphase system's unique properties, the structures and electrochemical performances of individual O3 and P2 polymorphs will be investigated in the next chapter.

.

3.5 References

1 S. Mariyappan, Q. Wang and J. M. Tarascon, *J. Electrochem. Soc.*, 2018, **165**, A3714–A3722.

2 J. Tang, A. D. Dysart and V. G. Pol, *Curr. Opin. Chem. Eng.*, 2015, **9**, 34–41.

3 P. Manikandan, D. Ramasubramonian and M. M. Shaijumon, *Electrochim. Acta*, 2016, **206**, 199–206.

4 M. H. Han, E. Gonzalo, G. Singh and T. Rojo, *Energy Environ. Sci.*, 2015, **8**, 81–102.

5 C. Delmas, C. Fouassier and P. Hagenmuller, *Phys. B+C*, 1980, **99**, 81–85.

6 N. Yabuuchi, K. Kubota, M. Dahbi and S. Komaba, *Chem. Rev.*, 2014, **114**, 11636–11682.

7 X. Qi, L. Liu, N. Song, F. Gao, K. Yang, Y. Lu, H. Yang, Y.-S. Hu, Z.-H. Cheng and L. Chen, *ACS Appl. Mater. Interfaces*, 2017, **9**, 40215-40223.

8 M. Bianchini, E. Gonzalo, N. E. Drewett, N. Ortiz-Vitoriano, J. M. López Del Amo, F. J. Bonilla, B. Acebedo and T. Rojo, *J. Mater. Chem. A*, 2018, **6**, 3552–3559.

9 E. Lee, J. Lu, Y. Ren, X. Luo, X. Zhang, J. Wen, D. Miller, A. DeWahl, S. Hackney, B. Key, D. Kim, M. D. Slater and C. S. Johnson, *Adv. Energy Mater.*, 2014, **4**, 1400458(1)-1400458(8).

10 S. Guo, P. Liu, H. Yu, Y. Zhu, M. Chen, M. Ishida and H. Zhou, *Angew. Chem. Int. Ed.*, 2015, **54**, 5894-5899.

11 International Centre for Diffreaction Data, PDF-4+, XRD Database 2020, ICDD, Newton Square, 2020.

12 S. Komaba, N. Yabuuchi, T. Nakayama, A. Ogata, T. Ishikawa and I. Nakai, *Inorg. Chem.*, 2012, **51**, 6211–6220.

13 N. Sharma, N. Tapia-Ruiz, G. Singh, A. R. Armstrong, J. C. Pramudita, H. E. A. Brand, J. Billaud, P. G. Bruce and T. Rojo, *Chem. Mater.*, 2015, **27**, 6976–6986.

14 S. Komaba, T. Nakayama, A. Ogata, T. Shimizu, C. Takei, S. Takada, A. Hokura and I. Nakai, in *ECS Transactions*, The Electrochemical Society, 2009, **16**, 43–55.

15 J. Billaud, G. Singh, A. R. Armstrong, E. Gonzalo, V. Roddatis, M. Armand, T. Rojo and P. G. Bruce, *Energy Environ. Sci.*, 2014, **7**, 1387-1391.

16 R. J. Clément, J. Billaud, A. Robert Armstrong, G. Singh, T. Rojo, P. G. Bruce and C. P. Grey, *Energy Environ. Sci.*, 2016, **9**, 3240–3251.

17 K. Momma and F. Izumi, *J. Appl. Crystallogr.*, 2011, **44**, 1272-1276.

18 S. Zheng, K. Zhou, F. Zheng, H. Liu, G. Zhong, W. Zuo, N. Xu, G. Zhao, M. Luo, J. Wu, C. Zhang, Z. Zhang, S. Wu and Y. Yang, *ACS Appl. Mater. Interfaces*, 2020, **12**, 40347–40354.

19 H. Yoshida, N. Yabuuchi, K. Kubota, I. Ikeuchi, A. Garsuch, M. Schulz-Dobrick and S. Komaba, *Chem. Commun.*, 2014, **50**, 3677-3680.

20 M. Keller, D. Buchholz and S. Passerini, *Adv. Energy Mater.*, 2016, **6**, 1501555(1)-1501555(11).

21 Y. You, A. Dolocan, W. Li and A. Manthiram, *Nano Lett.*, 2019, **19**, 182–188.

22 P. Wang, Y. You, Y. Yin and Y. Guo, *Adv. Energy Mater.*, 2018, **8**, 1701912(1)-1701912(23).

23 D. Buchholz, L. G. Chagas, C. Vaalma, L. Wu and S. Passerini, *J. Mater. Chem. A*, 2014, **2**, 13415–13421.

24 J. M. Paulsen and J. R. Dahn, *Solid State Ionics*, 1999, **126**, 3–24.

25 J. P. Parant, R. Olazcuaga, M. Devalette, C. Fouassier and P. Hagenmuller, *J. Solid State Chem.*, 1971, **3**, 1–11.

26 D. Pasero, N. Reeves, L. Gillie, V. Pralong and A. R. West, *J. Electrochem. Soc.*, 2007, **154**, A760-A769.

27 M. S. Idris and A. R. West, *J. Electrochem. Soc.*, 2012, **159**, A396–A401.

28 R. D. Shannon, *Acta Cryst.*, 1976, **32**, 751-767.

29 J. T. S. Irvine, D. C. Sinclair and A. R. West, *Adv. Mater.*, 1990, **2**, 132–138.

30 C. N. R. Rao and J. Gopalakrishnan, *New directions in solid state chemistry*, Cambridge University Press, Cambridge, 1997.

31 S. P. Butee, K. R. Kambale and M. Firodiya, *Processing and Application of Ceramics*, 2016, **10**, 67–72.

32 E. Antolini, *Solid State Ionics*, 2004, **170**, 159-171.

33 L.-X. Yuan, Z.-H. Wang, W.-X. Zhang, X.-L. Hu, J.-T. Chen, Y.-H. Huang and J. B. Goodenough, *Energy Environ. Sci.*, 2011, **4**, 269-284.

34 J.-K. Park, *Principles and Applications of Lithium Secondary Batteries*, John Wiley & Sons, Weinheim, 2012.

35 P. Kumar, P. K. Dwivedi, P. Yadav and M. V. Shelke, in *Emerging Nanostructured Materials for Energy and Environmental Science*, ed. S. Rajendran, M. Naushad, K. Raju and R. Boukherroub, Springer, Cham, 2019, ch. 3, pp. 105-172.

36 C. Liu, Z. G. Neale and G. Cao, *Materials Today*, 2016, **19**, 109-123.

37 Z. Y. Li, J. Zhang, R. Gao, H. Zhang, L. Zheng, Z. Hu and X. Liu, *J. Phys. Chem. C*, 2016, **120**, 9007–9016.

38 PV Education, *Battery voltage and capacity in non-equilibrium*, https://www.pveducation.org/pvcdrom/batteries/battery-voltage-and-capacity-in-non-equilibrium, (accessed April 2020).

39 K. Zhao, M. Pharr, J. J. Vlassak and Z. Suo, *J. Appl. Phys.*, 2010, **108**, 016110(1)-016110(3).

40 M. Coleman, C. K. Lee, C. Zhu, W. G. Hurley, C. K. Lee, C. Zhu and W. G. Hurley, *IEEE Trans. Ind. Electron.*, 2007, **54**, 2550-2557.

41 Y. Liu, Y. Zhu and Y. Cui, *Nat. Energy*, 2019, **4**, 540–550.

42 J. Vetter, P. Novák, M. R. Wagner, C. Veit, K.-C. Möller, J. O. Besenhard, M. Winter, M. Wohlfahrt-Mehrens, C. Vogler and A. Hammouche, *J. Power Sources*, 2005, **147**, 269–281.

43 Z. Li, J. Huang, B. Y. Liaw, V. Metzler and J. Zhang, *J. Power* Sources, 2014, **254**, 168-182.

44 A. P. Cohn, N. Muralidharan, R. Carter, K. Share and C. L. Pint, *Nano Lett.*, 2017, **17**, 1296–1301.

45 J. Christensen and J. Newman, *J. Electrochem. Soc.*, 2005, **152**, A818-A829.

46 Q. Liu, C. Du, B. Shen, P. Zuo, X. Cheng, Y. Ma, G. Yin and Y. Gao, *RSC Adv.*, 2016, **6**, 88683–88700.

47 Q. Liu, Z. Hu, M. Chen, C. Zou, H. Jin, S. Wang, S. Chou and S. Dou, *Small*, 2019, **15**, 1805381(1)-1805381(24).

48 H. Su., S. Jaffer and H. Yu, *Energy Storage Materials*, 2016, **5**, 116-131.

49 L. Zinck, M. Borck, C. Ripp and G. Hambitzer, *Journal of Applied Electrochemistry*, 2006, **36**, 1291-1295.

50 Compute Scotland, *Nextgen Batteries*, https://www.computescotland.com/nextgen-batteries-8472.php, (accessed April 2020).

51 X. Qi, Y. Wang, L. Jiang, L. Mu, C. Zhao, L. Liu, Y. S. Hu, L. Chen and X. Huang, *Part. Part. Syst. Charact.*, 2016, **33**, 538–544.

52 K. Kubota, N. Yabuuchi, H. Yoshida, M. Dahbi and S. Komaba, *MRS Bulletin*, 2014, **39**, 416-422.

53 D. H. Lee, J. Xu and Y. S. Meng, *Phys. Chem. Chem. Phys.*, 2013, **15**, 3304–3312.

54 Z. Lu and J. R. Dahn, *J. Electrochem. Soc.*, 2001, **148**, A1225-A1229.

55 B. Mortemard De Boisse, D. Carlier, M. Guignard, L. Bourgeois and C. Delmas, *Inorg. Chem.*, 2014, **53**, 11197-11205.

56 J. W. Somerville, A. Sobkowiak, N. Tapia-Ruiz, J. Billaud, J. G. Lozano, R. A. House, L. C. Gallington, T. Ericsson, L. Häggström, M. R. Roberts, U. Maitra and P. G. Bruce, *Energy Environ. Sci.*, 2019, **12**, 2223–2232.

57 R. J. Clément, P. G. Bruce and C. P. Grey, *J. Electrochem. Soc.*, 2015, **162**, A2589–A2604.

58 Y. H. Jung, A. S. Christiansen, R. E. Johnsen, P. Norby and D. K. Kim, *Adv. Funct. Mater.*, 2015, **25**, 3227–3237.

59 P.-F. Wang, Y.-B. Niu and Y.-G. Guo, in *Nanostructures and Nanomaterials for Batteries: Principles and Applications*, ed. Y-G. Guo, Springer, Singapore, 2019, ch. 6, 265-312.

60 N. Tapia-Ruiz, W. M. Dose, N. Sharma, H. Chen, J. Heath, J. W. Somerville, U. Maitra, M. S. Islam and P. G. Bruce, *Energy Environ. Sci.*, 2018, **11**, 1470–1479.

61 Y. Sun, S. Guo and H. Zhou, *Energy Environ. Sci*, 2019, **12**, 825-840.

62 G. Singh, N. Tapia-Ruiz, J. M. Lopez Del Amo, U. Maitra, J. W. Somerville, A. R. Armstrong, J. Martinez De Ilarduya, T. Rojo and P. G. Bruce, *Chem. Mater.*, 2016, **28**, 5087–5094.

63 W. L. Pang, X. H. Zhang, J. Z. Guo, J. Y. Li, X. Yan, B. H. Hou, H. Y. Guan and X. L. Wu, *J. Power Sources*, 2017, **356**, 80–88.

64 Z.-Y. Li, R. Gao, J. Zhang, X. Zhang, Z. Hu and X. Liu, *J. Mater. Chem. A*, 2016, **4**, 3453-3461.

Chapter IV

Synthesis and Characterisation of P2-$Na_{0.64}[Mn_{0.8}Mg_{0.2}]O_2$ and O3-$Na[Ni_{0.5}Mn_{0.5}]O_2$

4.1 Introduction

In the previous chapter, it was seen how a mixed phase layered sodium quaternary transition metal oxide, Na[Ni,Mg,Mn,Ti]O_2, possesses good potential as a cathode for Na-ion batteries. This material consists of two individual polymorphs with nominal formulae P2-"$Na_{0.64}[Mn_{0.8}Mg_{0.2}]O_2$" and O3-"Na-$[Ni_{0.5}Mn_{0.5}]O_2$". Each of these separate phases has been reported in the literature[1,2] - both are thought to be capable of high redox potentials *vs.* Na^+/Na and good achievable capacities. However, there are certain limitations to the electrochemical performance of these layered oxides, e.g. poor charge retention. This degradation during cycling is thought to be related in part to the changes their crystal structures undergo on sodium removal/insertion, and is still an ongoing focus of much work.[3] As well as detailed knowledge of the different structural modifications these polymorphs are prone to under various conditions, little is known of the air-stability of these materials, as well as their individual electrical properties, despite these being of the utmost importance to how they behave and perform electrochemically inside a battery.

The crystal structures of each polymorph are displayed in Figure 4.1.[4] The P2 phase (a) consists of close packed ABBA oxygen stacking, including two T_MO_6 octahedra per unit cell. The Na^+ cations are intercalated into trigonal prisms and possess two different sites: either face-sharing with two different TMO_6 octahedra or edge-sharing with six TMO_6 octahedra. The O3-type phase (b) has a close packed ABCABC oxide ion array, with the sodiums occupying the octahedral sites between the layers.[5] There are three TMO_2 sheets per unit cell for this polymorph, with each Na^+ sharing edges with TMO_6 octahedra of the next layer; this results in only one octahedral sodium site. The O3 polymorph has a rhombohedral lattice with space

group $R\bar{3}m$,[6] and is isostructural with α-$NaFeO_2$, whereas the P2 material possesses $P6_3/mmc$ symmetry in a hexagonal lattice.[7]

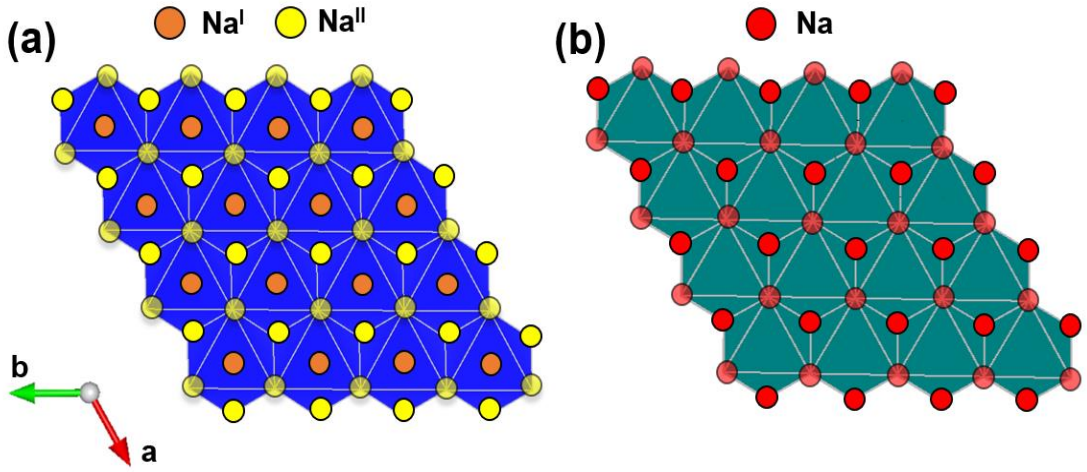

Figure 4.1 Sodium-ion cathode polymorphs. (a) The P2-type crystal structure viewed along the *c*-axis shows that every Na^{I} (face-sharing site) is surrounded by three Na^{II} (edge-sharing) sites, and vice versa. (b) The O3 crystal structure is viewed along the *c*-axis showing that every Na site is edge-sharing.

In this chapter, the synthesis of P2-$Na_{0.64}[Mn_{0.8}Mg_{0.2}]O_2$ and O3-Na-$[Ni_{0.5}Mn_{0.5}]O_2$ will be discussed, including different conditions for trying to achieve phase purity in the latter. The structures of these materials are explored, including the effect of varying the amount of sodium in the P2 layered oxides, and the Ni : Mn ratio in the O3 polymorph. The atmospheric and thermal stability of these compounds will also be investigated. The electrical properties will be characterised via performing impedance spectroscopy on the materials, before testing them electrochemically as cathodes in sodium-ion batteries (*vs.* Na/Na^+). It is hoped that results obtained for these individual polymorphs will help elicit a better understanding of the behaviour and properties of the mixed phase $Na[Ni,Mg,Mn,Ti]O_2$ material.

4.2 Experimental

4.2.1 Synthesis

All samples were synthesized by conventional solid state reaction (shake 'n' bake). The starting reagents used were Na_2CO_3, Mn_2O_3, MnO_2, NiO and MgO. Sodium carbonate and MnO_2 were dried at 180 °C prior to being used. Nickel oxide was dried at 800 °C, magnesium oxide at 1000 °C, and Mn_2O_3 at 625 °C.

Amounts of dried reagents were weighed using a balance, mixed and ground with acetone (*Fisher Scientific*) using an agate pestle and mortar, before being placed into a gold crucible and heated in a furnace. Samples were mixed for 30 minutes initially, before being pre-reacted at a lower temperature of ~ 700 °C. Subsequent grindings of the partially reacted mixtures took place for 20 minutes, with compounds synthesized between 700 and 1000 °C. Intermittent regrinding and phase analysis was carried out after each temperature step. For certain materials, powders were pressed into 'green' pellets prior to the firing. A muffle furnace was used for materials synthesized and cooled in air. Synthesis in other atmospheres (O_2/N_2) took place in a horizontal tube furnace. In this instance, the furnace was purged with the desired gas for 30 minutes at room temperature, prior to executing the heating program. Following synthesis, samples were either stored in an argon-filled glove box or a desiccator.

4.2.2 X-Ray Diffraction

Most samples for X-ray diffraction, were prepared in air. Phase analysis used a STOE Stadi P X-ray diffractometer, Mo $K\alpha_1$ (= 0.70926 Å) with a linear position sensitive detector (PSD) at an accelerating voltage of 40 kV and a tube current of 45 mA. Data were recorded over the 2θ scan range 5 - 40 ° with a step size of 0.1 °. A germanium monochromator was used to remove $K\alpha_2$ and $K\beta$, in order to leave just $K\alpha_1$ monochromatic radiation. An internal silicon standard of SRM 640e from the National Institute of Standard and Technology (NIST) was added for 2θ peak position calibration, prior to pattern indexing and lattice parameter determination. An

air-sensitive sample holder was also employed using a Bruker D2 X-ray diffractometer with Cu *Kα* radiation (λ= 1.5418 Å) used. These samples were prepared in an argon-filled glove box. Patterns were recorded with a scan rate of 0.02° in the 2θ range from 10° to 80°.

The WinXPOW software (version 3.05 of STOE & Cie GmbH, Germany) was used for the analysis of collected XRD data. Qualitative phase analysis used the PDF-4+ software, and compared patterns with PDF cards from the International Centre for Diffraction Data (ICDD).[8] Rietveld refinement was performed using the EXPGUI interface of the GSAS suite of programs.[9,10]

4.2.3 Materials Characterisation

Thermogravimetic Analysis (TGA). For each measurement, 10-20 mg of powder sample was placed in an alumina crucible. The heating/cooling rate was fixed at 5 °C/min, but the measured temperature ranges varied according to each sample. The measurements performed in flowing nitrogen used a PerkinElmer TGA (PerkinElmer, Massachusetts, USA). Pyris Manager software was used for data analysis.

Differential Scanning Calorimetry (DSC). For each measurement, 20-30 mg of powder sample was placed in an alumina crucible and heated in air/argon (80/20) atmosphere from 25 to 1000 °C at 5 °C/min heating/cooling rate, and the sample temperature compared with that of an inert reference material (in this case an empty alumina crucible). The data were collected using a NETZSCH 404 C thermal analyser (Netzsch, Selb, Germany) and analysed using Proteus Analysis software.

Impedance Spectroscopy. Pellets were pressed with 0.4 tons pressure and heated at the desired temperature for 1 h. Platinum or gold paste was painted on both sides of the pellet and dried and hardened by heating in a furnace. Impedance measurements performed in air used an Agilent E4908A analyser at 100 mV AC with a sweep frequency from 10 Hz to 1 MHz. Data collected in O_2 used a Solartron 1260 analyser at 100 mV AC over the frequency range 10^{-1} to 10^{6} Hz. Impedance data were

corrected for overall pellet geometry and for blank capacitance of the conductivity jig. Analysis was performed using ZView software.

4.2.4 Electrochemical Testing

The electrode active materials were mixed with C65 carbon black as the conductive additive and polyvinylidene fluoride (PVDF) as the binder in an 8:1:1 weight ratio. The slurry of the composite was made using N-methyl-2-pyrrolidone (NMP), before these mixtures were drawn down onto carbon-coated aluminium foil. Electrodes were dried at 80 °C for 16 h in a vacuum oven. These were then cut, and pressed between two hot rollers, before being dried and stored at 80 °C in a vacuum oven again, prior to battery assembly. The mass loading for the dried electrode sheets was 2-4 mg/cm^2. The separators used in the Na-ion cells were cut from GF/A glass microfiber filter paper (Whatman). The electrolyte used was a solution of 0.5 M sodium hexafluorophosphate in an ethylene carbonate : diethyl carbonate : propylene carbonate (1:2:1) mixture. This was prepared in the glove box, with the solvent mixture dried over molecular sieves for 16 h, prior to dissolution of the salt.

An argon-filled (H_2O, O_2 < 0.1 ppm) glove box was used for battery assembly (MBraun, Germany). Electrochemical half-cell testing was performed using aluminium CR2032 coin cells with a Na metal-disk, 11 mm in diameter, as the counter electrode. Circular positive electrodes, 12 mm in diameter, were punched from the cathode coatings. Cell casings, spacers, springs, and separators were all dried in an 80 °C vacuum oven for 16 h prior to being taken into the glove box for battery assembly. Electrochemical testing was performed using a Maccor Series 4000 Automated Test System. All cells were held in a temperature-controlled environmental chamber at 25 °C.

4.3 Results and Discussion

4.3.1 Synthesis and Structural Characterisation of P2-$Na_{0.64}[Mn_{0.8}Mg_{0.2}]O_2$

The PXRD patterns of $Na_x[Mn_{0.8}Mg_{0.2}]O_2$ ($0.5 \leq x \leq 1$) are shown in Figure 4.2.The materials were made via a solid state synthesis route by hand grinding the precursors Na_2CO_3, MgO and Mn_2O_3 in stoichiometric amounts. Manganese (III) oxide was used at the starting material as manganese is known to be present in mixed oxidation states (III, IV) when heated in air. For x = 0.64, for example, the Mn has an average oxidation state of +3.7. 'Green' pellets were first fabricated and calcined at 700 °C for 3 hours, before being reground, pressed into pellets again, covered with sacrificial power and reacted at 900 °C for 10 hours. As sodium is volatile and Na loss is known to occur when heated in furnaces at high temperatures, the pellets were covered with excess powder, which acted as a 'buffer'. The final products were removed from the furnace at high temperature, and allowed to cool quickly in air.

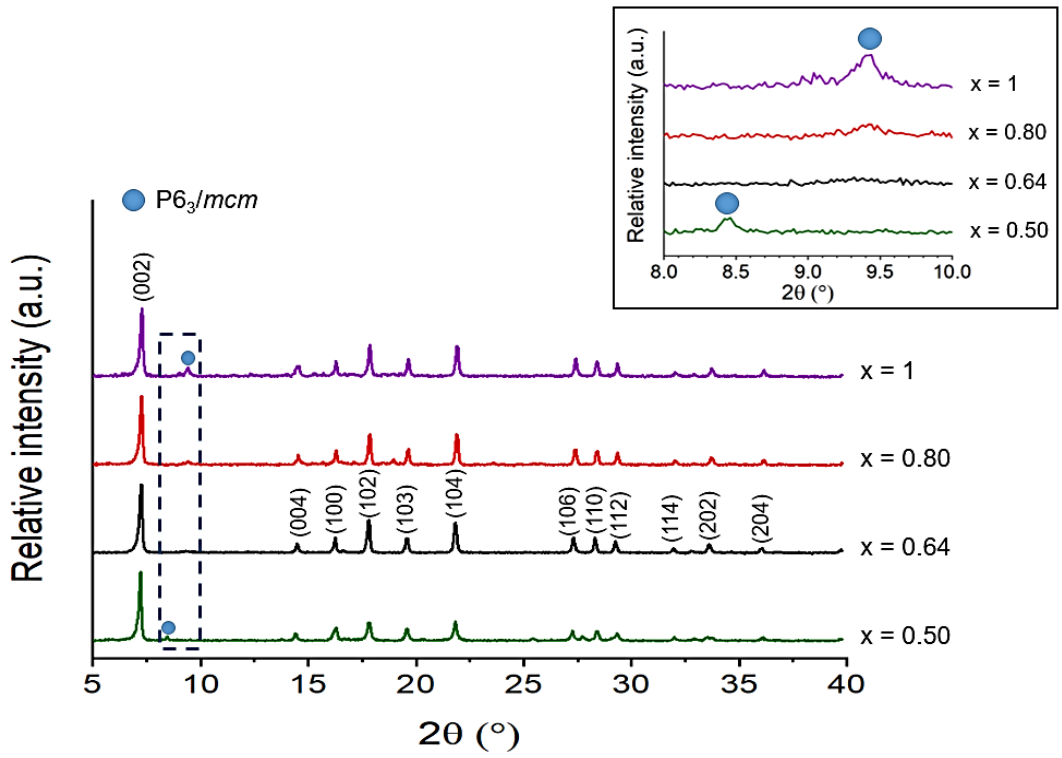

Figure 4.2 The PXRD pattern of P2-$Na_x[Mn_{0.8}Mg_{0.2}]O_2$ for $0.50 \leq x \leq 1$,collected by MoPSD with $\lambda = 0.7093$ Å. Inset shows peak shifting over the range $8° \leq 2\theta \leq 10°$.

The XRD patterns were all indexed using either space group $P6_3/mmc$ or $P6_3/mcm$, which indicates that they form a single phase solid solution. For the x = 0.64 composition, all the peaks are in good accordance with the reported literature of P2-$Na_{0.64}[Mn_{0.8}Mg_{0.2}]O_2$ (PDF 04-022-8282)[11] – a layered rock salt type structure indexed on the hexagonal $P6_3/mmc$ space group. The $P6_3/mcm$ space group possesses different symmetry and reflection conditions from $P6_3/mmc$, which introduces extra small peaks into the XRD pattern,[12] such as the one seen for the x = 0.5, 0.8 and 1 compositions at around 9°. A shift in this peak position to higher 2θ angles was observed for increasing sodium content, as shown by the inset in Figure 4.2.

The structural refinement of P2-$Na_{0.64}[Mn_{0.8}Mg_{0.2}]O_2$ proceeded as described in the methodology section (Chapter II). The starting model and parameters used are given in Appendix H. The thermal parameter or U_{iso} for each atom was set to a default value of 0.025 $Å^2$. The scale factor, background (6 terms of Chebyshev function) and lattice parameters were refined first, and were all allowed to change in the subsequent refinements. The zero-point, followed by the peak profile coefficients, were refined next, which were fixed after convergence. The atomic *z* coordinate of O1 was then refined, before also being fixed. After that, the site occupancies were refined in turn, starting with the occupancies of Mn and Mg, which were refined simultaneously. As these share the same 2a site, the occupancies of these atoms were constrained to add up to 1 (full occupancy at the site). The occupancies of Na1 and Na2 were refined next, simultaneously. The occupancy of the oxygen atom was refined and gave a value close to unity, with no significant improvement to the refinement model. Therefore, it was fixed at 1 for the rest of the refinement. The thermal parameters were not refined at any stage. As a final step, the *z* coordinate of O1, occupancies of Na1, Na2, Mn1 and Mg1, were refined simultaneously, along with the profile terms. This was repeated until no obvious improvements were observed in the χ^2, R_p and R_{wp} values.

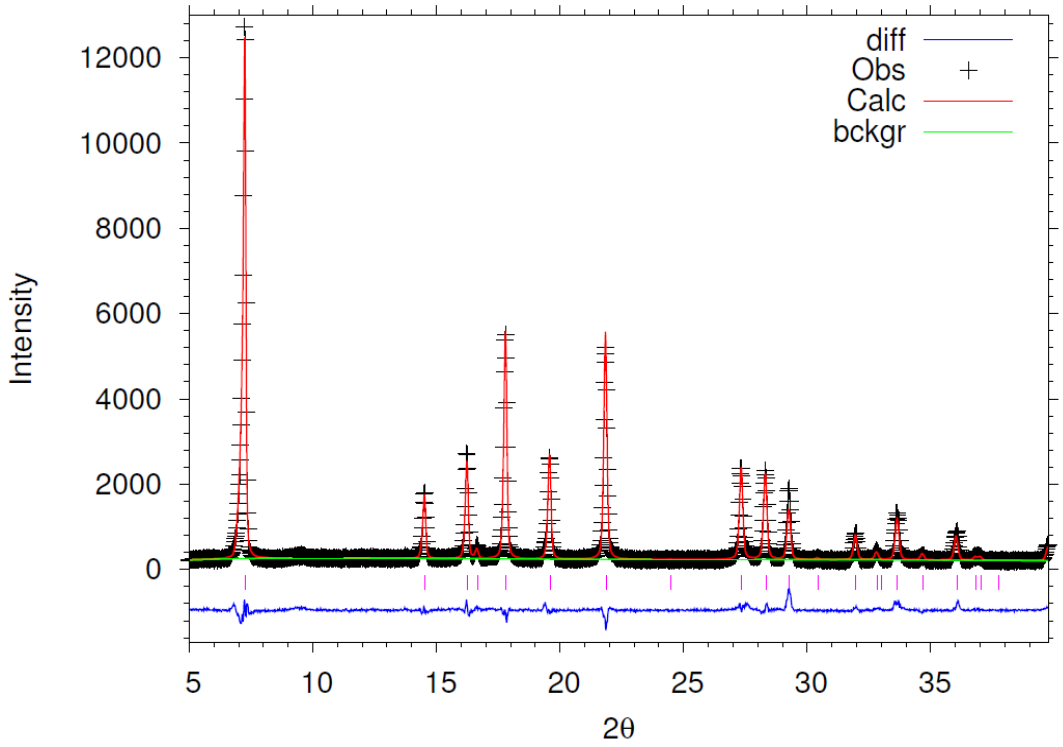

Figure 4.3 Rietveld refinement data for observed (obs), calculated (calc) and difference (diff) profiles of P2-$Na_{0.64}[Mn_{0.8}Mg_{0.2}]O_2$ at room temperature.

Rietveld refinement data (observed, calculated and difference profiles) are presented graphically in Figure 4.3. These data show a good fit between the observed and calculated plots, with only a slight mismatch in intensities for certain peaks. A summary of the final refined parameter results is provided in Table 4.1 Importantly, good statistical parameters were obtained: $\chi 2 = 3.28$, $R_p = 6.27\%$, $R_{wp} = 8.53\%$, along with realistic site occupancies for the different atoms. The occupancy ratio of Mn1 : Mg1 was found to be 0.8 : 0.2. There are two sodium sites for this P2 layered oxide, with the Na1 site being the less occupied of the two. The refined lattice parameters are $a = 2.9017(1)$ Å and $c = 11.235(1)$ Å, which are comparable to those reported in the literature.[11] In order to get more accurate structural data on this material, an X-ray synchrotron or neutron diffraction experiment is required.

Table 4.1 Refined crystallographic parameters for P2-$Na_{0.64}[Mn_{0.8}Mg_{0.2}]O_2$.

Atom	Multiplicity	x	y	z	Occupancy	100 x U_{iso} ($Å^2$)
Na1	2b	0	0	0.25	0.222(4)	2.5
Na2	2d	1/3	2/3	0.75	0.374(5)	2.5
Mn1	2a	0	0	0	0.79(1)	2.5
Mg1	2a	0	0	0	0.20(1)	2.5
O1	4f	1/3	2/3	0.5934(3)	1	2.5

Space group = $P6_3/mmc$, $\chi 2 = 3.28$, $R_p = 6.27\%$, $R_{wp} = 8.53\%$, $a = 2.9017(1)$ Å, $c = 11.235(1)$ Å.

The thermal stability of these layered sodium oxides is important, as it may have serious implications for their processing and applications. Stability in air is also a significant factor when considering the long term storage of these materials, as well as for handling and preparing them as cathodes for Na-ion-ion batteries. The thermal stability of P2-$Na_{0.64}[Mn_{0.8}Mg_{0.2}]O_2$, as well as its moisture and oxygen sensitivity, were studied by TGA and DSC (Fig. 4.4). A TGA run in nitrogen (a) was performed between 25 and 1000 °C with programmed heating/cooling of 5 °C/min. The samples were held at 1000 °C for two hours, prior to the cooling step. The $Na_{0.64}[Mn_{0.8}Mg_{0.2}]O_2$ sample had been stored in a desiccator following synthesis, and then exposed to the atmosphere for several hours, prior to performing the TGA measurement. The TGA profile consists of different regions of continuous mass loss, interrupted by flat plateaus. The sample lost around 3% mass on heating to 700 °C, followed by an additional 3% on heating and holding at 1000 °C. The sample mass remained constant on cooling back to room temperature again.

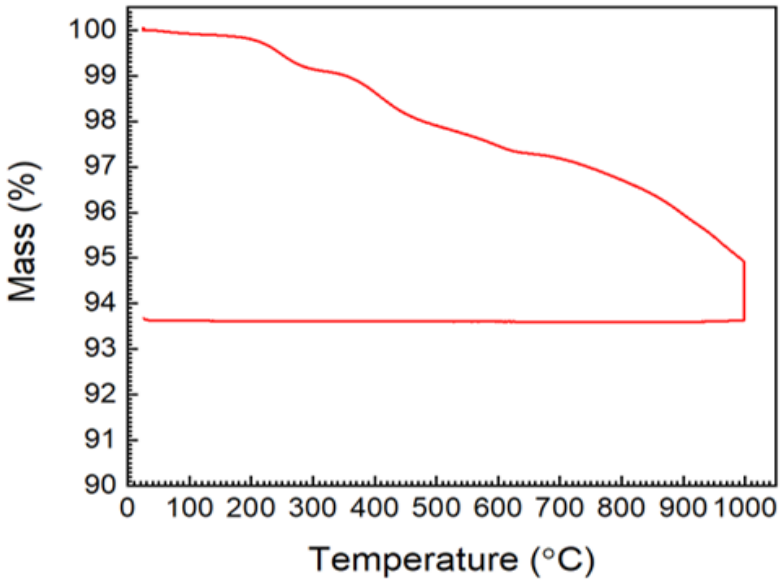

Figure 4.4 TGA profile of P2-$Na_{0.64}[Mn_{0.8}Mg_{0.2}]O_2$ heated and cooled to 1000 °C in nitrogen.

The TGA profile is similar to the one for the $Na[Ni,Mg,Mn,Ti]O_2$ mixed phase material. At lower temperatures, the decrease in mass is likely to be due to the loss of weakly bound physisorbed species from the air, such as water, and possibly the loss of more strongly structurally bound species. It is possible that Na^+/H^+ ion exchange takes place when the sample is exposed to H_2O to form $NaOH/T_MOOH$, and that Na_2CO_3 or $NaHCO_3$ may synthesize on exposure to CO_2. These processes are likely to have a detrimental impact on the electrochemical performance of the material. For certain Na-deficient P2 layered oxides, and under certain conditions, CO_3^{2-} ions and water molecules are reported to insert between the oxide layers at the vacant Na sites (Fig. 4.5), e.g. for $Na_{0.67}[Mn_{0.5}Fe_{0.5}]O_2$[13] and $Na_x[Ni_{0.22}Co_{0.11}Mn_{0.66}]O_2$.[14] These TGA results demonstrate that air-stability for this layered oxide are important, and that the material is prone to the uptake of atmospheric species. The TGA profile for P2-$Na_{0.64}[Mn_{0.8}Mg_{0.2}]O_2$ is a hybrid between the N_2 runs observed for mixed phase $Na[Ni,Mg,Mn,Ti]O_2$ (in Chapter III) for a sample stored in a glove box and one left out in air. Also, the amount of mass lost for this P2 material stored in a desiccator (6%) is intermediate between the amounts lost for these two samples: 4% for the glove box sample and 8% when left out in air. Importantly, storage conditions and air-exposure when handling, investigating, or synthesizing these materials, have been demonstrated as vital considerations for this P2-type layered sodium oxide.

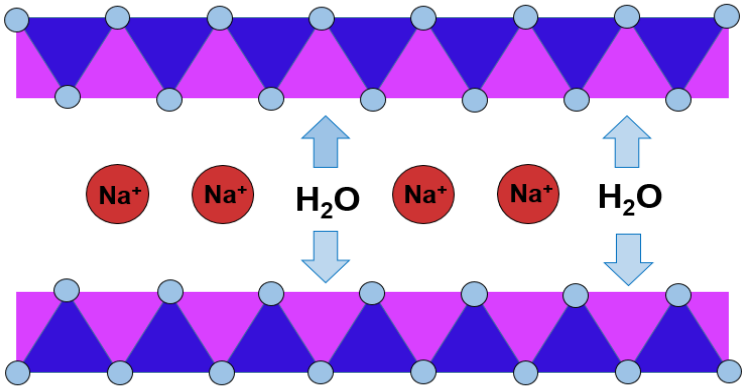

Figure 4.5 Water intercalation between T_MO_6 sheets at sodium deficient sites.

In order to obtain further information about the thermal stability of P2-$Na_{0.64}[Mn_{0.8}Mg_{0.2}]O_2$, DSC was performed (b). These results below show there to be no clear endotherms/exotherms in the plots on heating and cooling, suggesting that the material does not undergo any fast structural phase transitions. While a P2-O3 transition was found to occur in the Na[Ni,Mg,Mn,Ti]O_2 mixed phase material above 800 °C, this does not occur here as the material is synthesized at 900 °C. An XRD was also performed after heating and cooling the material to 1000 °C in the air, and the same XRD pattern was recorded (Appendix I). Hence, interestingly, this suggests that the P2 phase is fairly thermodynamically stable when it is in phase pure form, but possibly only metastable as part of a mixed phase material.

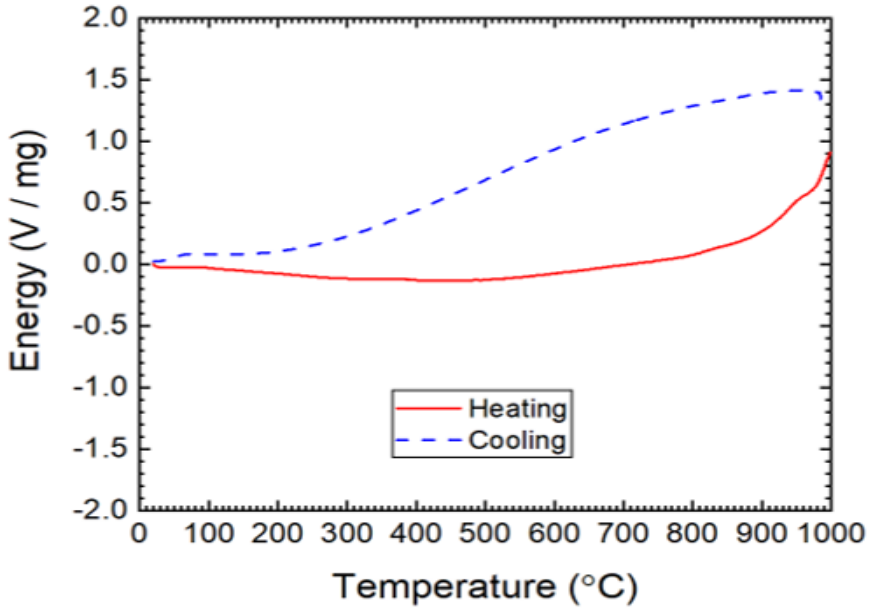

Figure 4.6 DSC curve of P2-$Na_{0.64}[Mn_{0.8}Mg_{0.2}]O_2$ heated and cooled to 1000 °C in an air/argon atmosphere (80/20).

4.3.2 Synthesis and Structural Characterisation of O3-$Na[Ni_{0.5}Mn_{0.5}]O_2$

The precursors Na_2CO_3, NiO and Mn_2O_3 were hand ground in stoichiometric amounts. The mixture was calcined in air at 700 °C for 2 h, before being removed from the furnace at this temperature, reground and heated from 700 to 720 °C. The sample was held at 720 °C for 24 h, removed from the furnace at 720 °C, reground and heated to 740-800 °C. The powder was heated for 24 h at each temperature interval, before a small amount was removed for XRD analysis (Fig. 4.7), the remainder was reground and heated again to the next temperature.

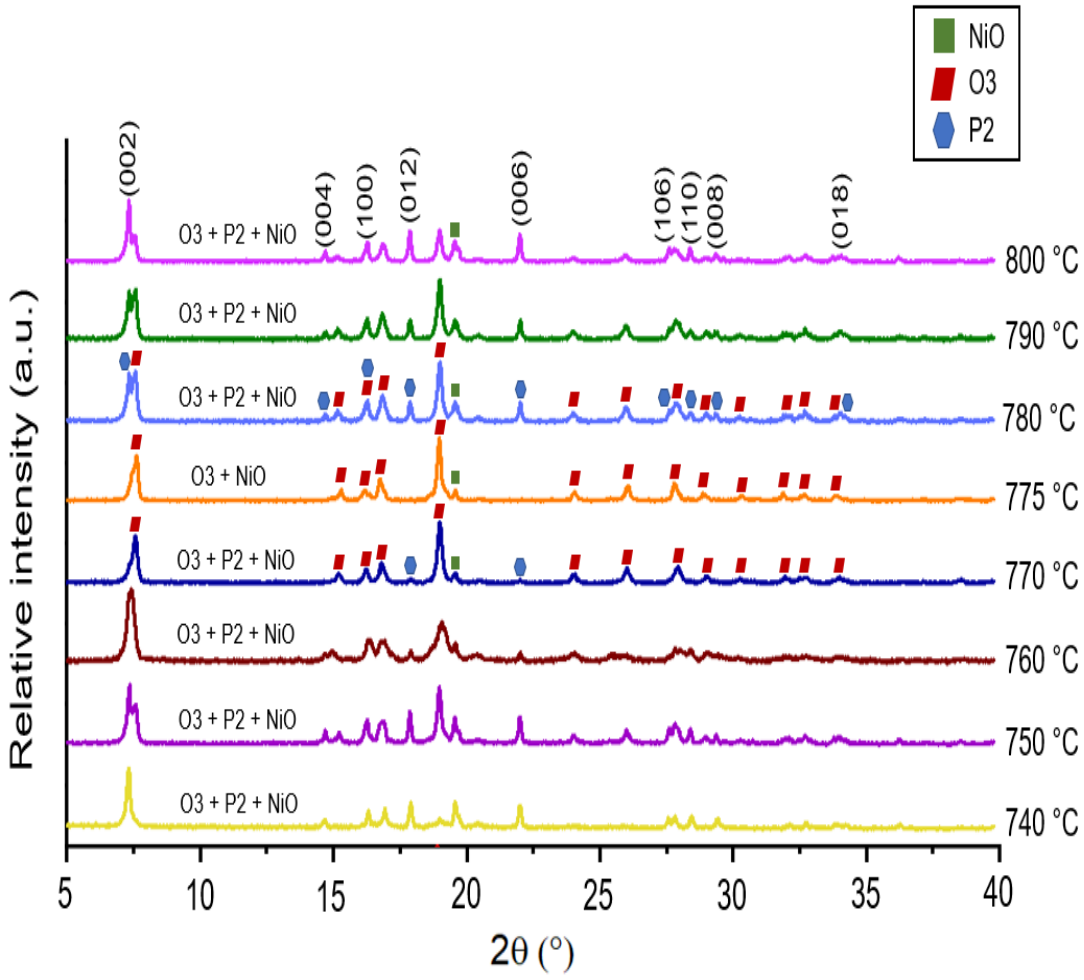

Figure 4.7 XRD patterns for $Na[Ni_{0.5}Mn_{0.5}]O_2$ heated at 740 to 800 °C, collected by MoPSD with λ = 0.7093 Å. Two phases: trigonal O3 (■) and hexagonal P2 (⬢) were observed, as well as starting material cubic NiO (■).

In all of the PXRD patterns in Figure 4.7, there is unreacted nickel (II) oxide present. The XRD pattern of the sample removed from the furnace at 775 °C shows just the targeted O3-$Na[Ni_{0.5}Mn_{0.5}]O_2$ phase, alongside the NiO impurity. For every other temperature, there is evidence of a P2 polymorph. This phase was indexed using the hexagonal $P6_3/mmc$ space group. As a general characteristic of the P2-type layered sodium oxides is Na deficiency, this structure may form due to a loss of sodium on heating in an open air system. A loss of Na in turn means an excess of higher oxidation state manganese is required in the material to balance the charge, hence leading to some unreacted NiO remaining. The synthesis was repeated, targeting temperatures from 770-780 °C, using longer dwell times and more intermittent grinding, but it was not possible to produce phase pure O3-$Na[Ni_{0.5}Mn_{0.5}]O_2$ via this synthesis route.

In order to try and minimise the amount of P2 polymorph present, and obtain phase pure O3-$Na[Ni_{0.5}M_{n0.5}]O_2$, a different synthesis strategy was implemented. Manganese (IV) oxide was used as the starting material as +4 is the oxidation state desired in $Na[Ni_{0.5}Mn_{0.5}]O_2$. The starting materials were ground together in stoichiometric amounts, but with 5 wt.% excess Na_2CO_3 to try and compensate for any sodium lost during the synthesis procedure. The starting materials were ground together and pressed into 'green' pellets. These were then calcined at 700 °C in an oxygen atmosphere for 5 h. The sample was reground, pressed into pellets once more, and heated again in O_2 to 900 °C and reacted at this temperature for 16 h. The synthesis was performed in an oxygen atmosphere to try and maintain the higher +4 oxidation state for the manganese. Although there was not access to the necessary laboratory equipment to perform quenching in O_2, the material was cooled quickly after the reaction had finished (~ 10 °C/min), prior to being removed from the furnace.

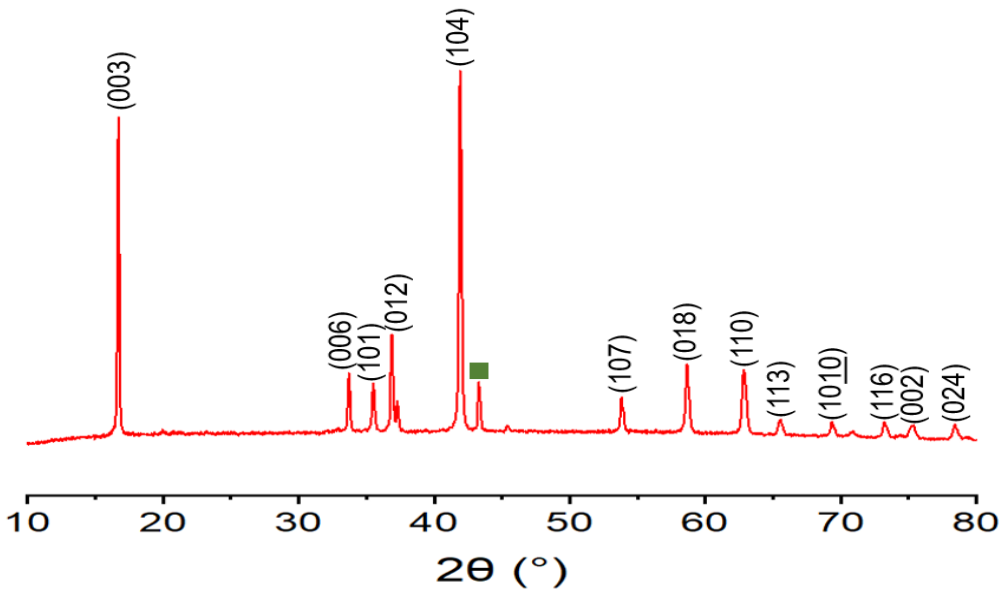

Figure 4.8 The PXRD pattern of O3-$Na[Ni_{0.5}Mn_{0.5}]O_2$ collected by D2 diffractometer with Cu *Kα* radiation (λ = 1.541 Å) using an air-sensitive holder. The starting material cubic NiO is marked with ■.

Following the synthesis procedure, the product was removed from the furnace at 200 °C and immediately transferred to an argon-filled glove box. An XRD was performed with an air-sensitive holder using Cu *Kα* radiation (Fig. 4.8). The O3-$Na[Ni_{0.5}Mn_{0.5}]O_2$ phase was formed, but there is still residual NiO starting material present as a secondary minor phase. The main phase was indexed using the trigonal $R\bar{3}m$ space group. These results suggest that it is not possible to thermodynamically synthesize phase pure O3-$Na[Ni_{0.5}Mn_{0.5}]O_2$ via the shake 'n' bake method, and perhaps alternative synthesis strategies are required, such as ball milling, which uses intensive mixing.

In order to further investigate the structures of these layered sodium nickel, manganese oxides, the ratio of Ni : Mn was altered. A range of $Na[Ni_xMn_{1-x}]O_2$ ($0.33 \leq x \leq 0.5$) materials were prepared via solid state reactions. The samples were synthesized in an oxygen atmosphere, using the same procedure as described previously. As a 5 wt.% excess of Na_2CO_3 was used, the stated Na compositions of the samples are nominal. The PXRD patterns are presented in Figure 4.9. All different compositions showed evidence of the NiO starting material. The x = 0.33 composition has a P2-type structure, compositions in the range $0.4 \leq x \leq 0.45$ have mixtures of O3 and P2-type phases, and x = 0.5, possesses just the O3-type polymorph.

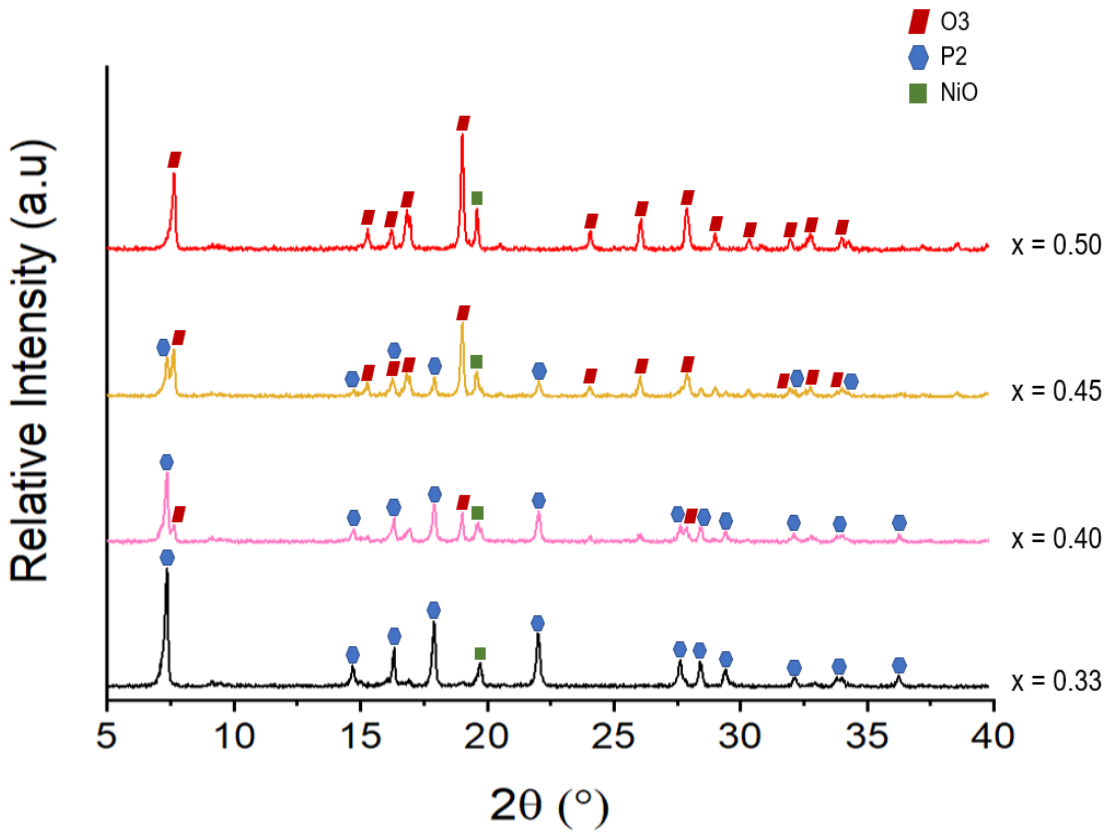

Figure 4.9 XRD patterns for $Na[Ni_xMn_{1-x}]O_2$ for $0.33 \leq x \leq 0.50$, collected by MoPSD with $\lambda = 0.7093$ Å Two phases: trigonal O3 (■) and hexagonal P2 (⬢) were observed, as well as starting material cubic NiO (■).

Nickel oxide is present in all compositions, which is most likely a consequence of sodium evaporation during heating. Less sodium means that a higher ratio of Mn : Ni is required in the layered oxide in order to balance the negative charge on the oxygen, thus resulting in left over NiO. High temperatures and long heating times are required for product formation, but also make Na evaporation more likely, hence why the use of lower temperatures or 'chimie douce' methods e.g. co-precipitation, sol-gel, may be more conducive for synthesizing phase pure O3-$Na[Ni_{0.5}Mn_{0.5}]O_2$. The XRD patterns indicate that reducing the nickel content favours sodium-deficient P2-type formation. This may be because less Ni means there is a greater amount of higher oxidation state Mn in the end compound, and, therefore, less sodium is required to maintain charge neutrality.

The difficulty in synthesizing phase pure $Na[Ni_xMn_{1-x}]O_2$ materials is well documented in the literature.[15] The results reported above share some similarity with those observed by Paulsen and Dahn who found that the P2-$Na_{2/3}[Mn_{1-x}Ni_x]O_2$ class

of layered sodium oxides was only phase pure below x = 1/3.[16] Above this composition, NiO was always present as a secondary phase. The majority of O3-$Na[Ni_{0.5}Mn_{0.5}]O_2$ synthesized in the literature coexists with NiO.[17,18] The only successful synthesis routes are via low temperature methods or, if at high temperature, with prolonged heating and intensive mixing, i.e. ball milling.[15]

For the O3-$Na[Ni_{0.5}Mn_{0.5}]O_2$ powder, the physical changes the material undergoes when exposed to air are clearly visible to the naked eye. Following the synthesis and removal from the furnace, the layered sodium oxide noticeably changes colour and texture over time, becoming darker and stickier. Furthermore, when fabricating pellets of the material in air, these are prone to cracking when left exposed to the atmosphere for prolonged periods of time. The thermal stability of the O3-$Na[Ni_{0.5}Mn_{0.5}]O_2$ sample, as well as its atmospheric sensitivity, were studied by (TGA) and DSC (Fig. 4.10). A TGA run in nitrogen (a) was made between 25 and 950 °C with programmed heating/cooling of 5 °C/min. The samples were held at 950 °C for two hours, prior to cooling. Two samples were run: one which had been stored in the glove box immediately after synthesis until the TGA measurement, and one which had been left out in air for 24 hours prior to the run.

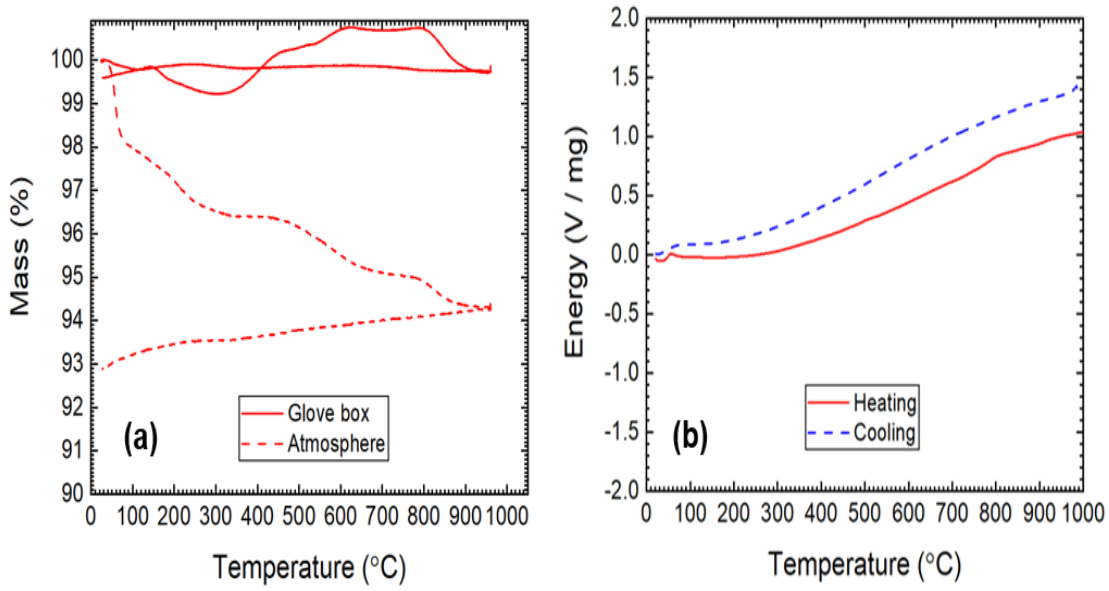

Figure 4.10 Thermal analysis of O3-$Na[Ni,Mn]O_2$: (a) TGA profiles in nitrogen and (b) DSC curve in air/argon (80/20) atmosphere.

The profile for the sample stored in the glove box fluctuated around the 100 wt.% mark, indicating that no significant mass loss/gain occurred. In contrast, the sample left out in air showed a series of regions of continuous mass loss, interrupted by flat plateaus, and a total mass loss of ~ 7 wt.%. These results demonstrate that storage conditions for this O3-$Na[Ni_{0.5}Mn_{0.5}]O_2$ layered oxide are extremely important, and that the material is prone to the uptake of atmospheric species. Both Na_xMnO_2 and Na_xNiO_2 are reported in the literature to be unstable in air.[19] Furthermore, similar O3 layered oxides, e.g. $Na[N_{i0.7}Mn_{0.15}Cu_{0.15}]O2$, are reported to react with water and CO_2 to form NaOH, Na_2CO_3, $Na_2CO_3.H_2O$ and NiO on the particle surfaces.[18] These species are insulating and so are likely to lead to a reduced electrochemical performance in O3-$Na[Ni_{0.5}Mn_{0.5}]O_2$ if they form here. Furthermore, any sodium ions lost either by chemical reaction or Na^{+}/H^{+} exchange will result in a reduced capacity. In order to obtain further information about the thermal stability of the oxide, differential scanning calorimetry was performed (b). The DSC curve possesses no clear, significant endotherms/exotherms on heating and cooling, suggesting that the material does not undergo any fast structural phase transitions; similar to the results observed for phase pure P2-$Na_{0.64}[Mn_{0.8}Mg_{0.2}]O_2$.

4.3.3 Electrical Properties of P2-$Na_{0.64}[Mn_{0.8}Mg_{0.2}]O_2$ and O3-$Na[Ni_{0.5}Mn_{0.5}]O_2$

A pellet of the single phase P2-$Na[Mn_{0.8}Mg_{0.2}]O_2$ layered oxide was sintered at 1000 °C in air, coated with platinum electrodes, and its electrical properties studied using impedance spectroscopy. A typical impedance dataset is shown in Figure 4.11, with data presented in four different complementary formats. In (a), the room temperature impedance complex plane plot appears to show part of an arc, which appears to meet the real (resistive) axis at 10 kΩ cm, and an additional smaller component towards lower frequency. Data is also shown for a measurement taken at 50 °C, which is visible more clearly in the zoomed-in inset. This 50 °C measurement possesses a smaller resistance (~ 1.25 kΩ cm) compared with the room temperature one. The combined spectroscopic plots for *Z''/M''* (at room temperature) in (b) are off-scale, meaning it is not possible to determine the electrical homogeneity of the sample.

Measurements at lower temperature (below room temperature) are required to detect this and shift the measured window to higher frequencies.

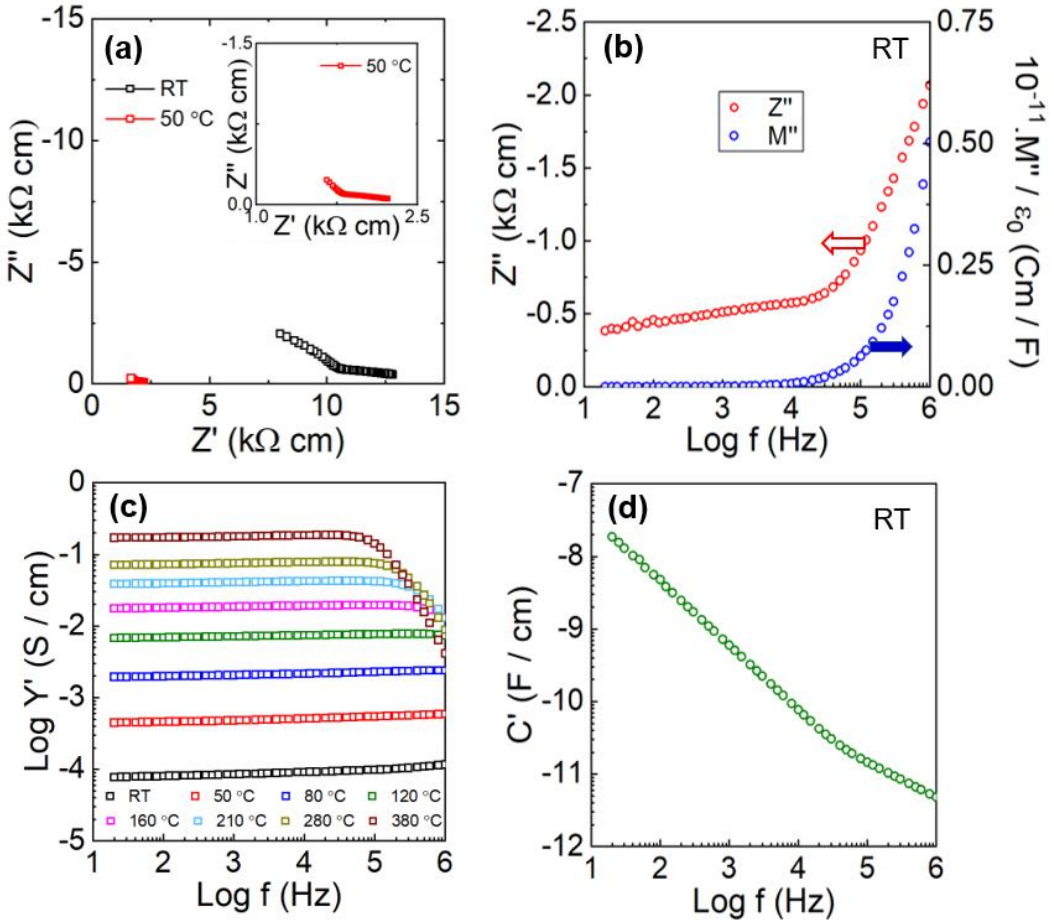

Figure 4.11 Impedance data for P2-$Na_{0.64}[Mn_{0.8}Mg_{0.2}]O_2$. (a) Impedance complex plane plots at room temperature (RT) and 50 °C. Spectroscopic plots of $-Z''$ and M'' (b), Y' (c), and C' (d).

Plots of log conductance, Y', against log f, are presented in (c) for a range of temperatures. These show a frequency-independent plateau with a value ~ 100 μS cm^{-1} at room temperature, and a gradual increase in conductivity as the temperature increases. Capacitance, C' against frequency, (d), show the start of a plateau at higher frequency with a value of ~ 10 pF cm^{-1}. At lower frequencies, C' data increases to high values and at higher temperatures was found to enter the microfarad range. Such a high capacitance is indicative of electrode double layer phenomena, such as would be associated with ionic conduction of, in this case, Na^+ ions.

In order to gain further insight into electrical properties of the P2-$Na_{0.64}[Mn_{0.8}Mg_{0.2}]O_2$ sample, impedance measurements at different temperatures were used to construct an Arrhenius plot (Fig. 4.12). Arrhenius plots make it possible to work out the activation energy associated with the conduction in the material. As it was not possible to measure the bulk of the material without going to below room temperature, an Arrhenius plot was constructed using the total resistance of the bulk added to the grain boundary.

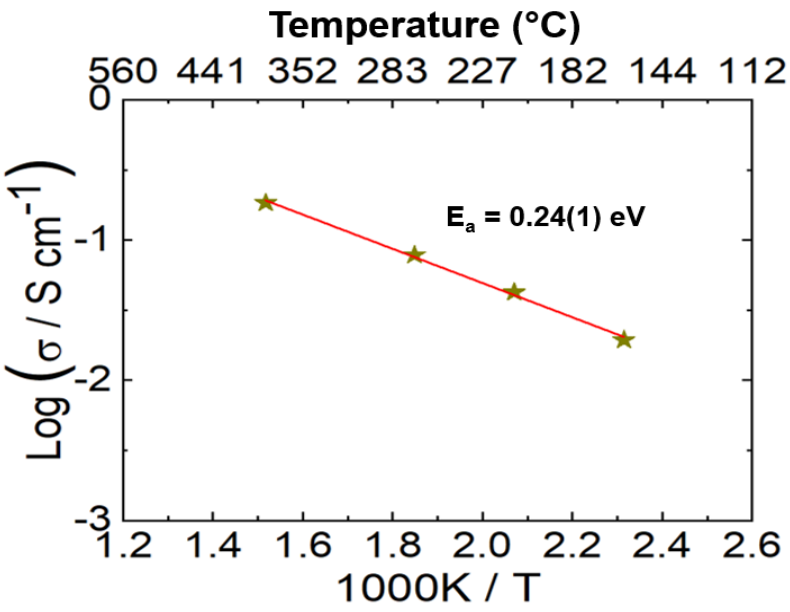

Figure 4.12 Arrhenius plot of P2-$Na_{0.64}[Mn_{0.8}Mg_{0.2}]O_2$.

These results above show that the conductivity of single phase P2-$Na_{0.64}[Mn_{0.8}Mg_{0.2}]O_2$ is much more conductive than the mixed phase $Na[Ni,Mg,Mn,Ti]O_2$ layered rock salt type structure studied in Chapter III. The activation energy associated with the total conductivity of P2-$Na_{0.64}[Mn_{0.8}Mg_{0.2}]O_2$ is 0.24(1) eV, which is lower than that for the mixed phase material, 0.33(1) eV. Hence, this indicates a lower activation energy for Na^+ ion conduction in the phase pure P2 sample. This can be explained by the structure of the P-type polymorph, which due to its sodium deficiency possesses an open wide path for diffusion through adjacent prismatic sites.[20] This confers a low activation energy barrier for Na^+ ion hopping.

Impedance measurements were also performed on the O3-$Na[Ni_{0.5}Mn_{0.5}]O_2$ material. As this layered oxide was found to possess high atmospheric sensitivity,

measurements were performed in dry O_2 in order to replicate the conditions in which the material was synthesized. A pellet of O3-Na[$Ni_{0.5}Mn_{0.5}$]O_2 was sintered at 900 °C in oxygen, coated with gold electrodes, and its electrical properties studied by impedance spectroscopy. Complex plane *Z** plots of O3-Na[$Ni_{0.5}Mn_{0.5}$]O_2 are shown in Figure 4.13. These all possess a large depressed non-ideal semi-circle. With increasing temperature, the arc decreases in size, indicating a reduced resistance. The arc crosses the real (resistive) axis at ~ 7.5 MΩ cm at 280 °C and around 0.375 MΩ cm at 500 °C. At lower temperatures, data becomes noisier, especially towards low frequency. This indicates that the impedance instrument is at the limit of what it is able to measure, and the sample is too resistive to extract usable data. At room temperature, it was not possible to extract resistances from data due to how resistive the material was and, subsequently, how noisy the measured impedance response was.

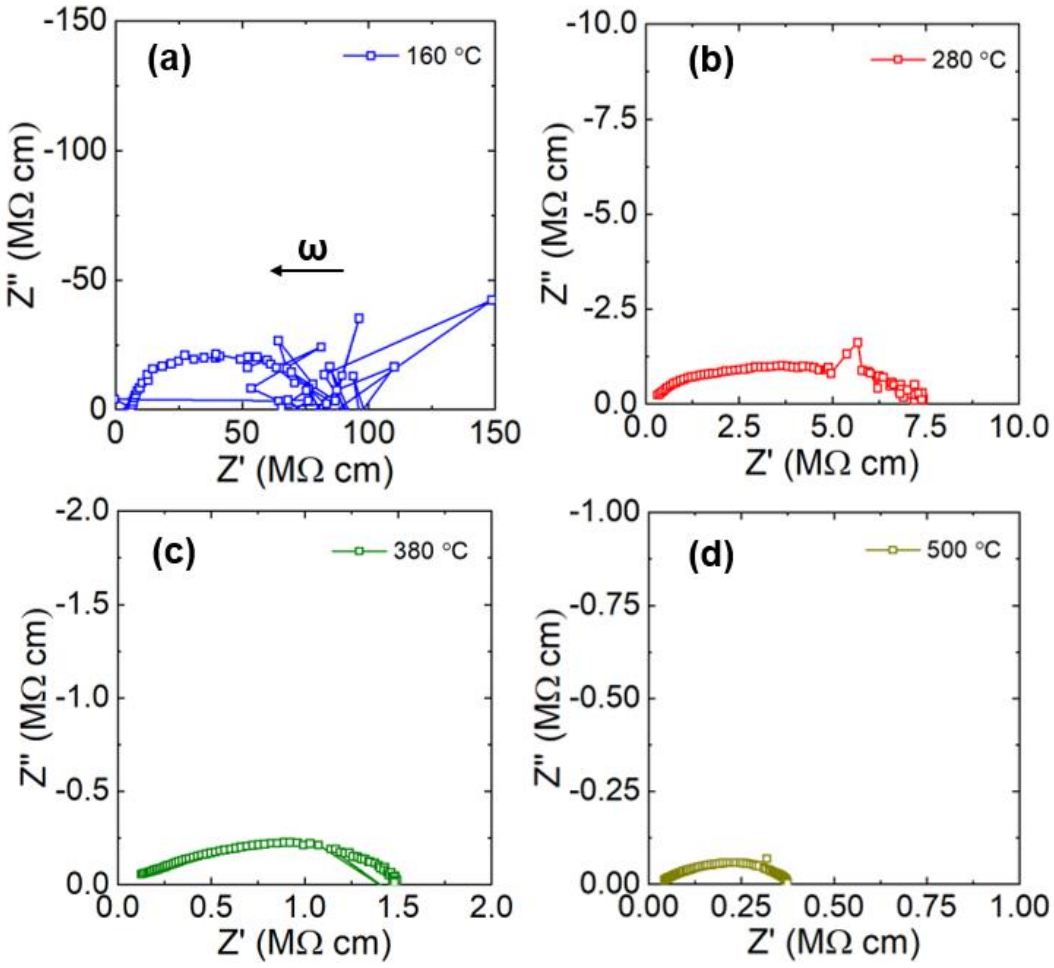

Figure 4.13 O3-Na[$Ni_{0.5}Mn_{0.5}$]O_2: Impedance complex plane plots *Z** at 160 °C to 500 °C in O_2.

Figure 4.14 shows impedance spectra for O3-Na[$Ni_{0.5}Mn_{0.5}$]O_2 using a range of different complex formalisms and graphical presentations. The capacitance as a function of frequency is displayed in Figure 4.14 (a). There are no clear visible plateaus in the plot, however, the capacitance is still increasing beyond 1 x 10^8 F cm^{-1} at low frequency, indicating the possibility of a sample-electrode interface response and a double layer phenomena. The corresponding capacitance of the Nyquist arc at 500 °C in Fig. 4.13 (d) is 1.2 x 10^{-9} F cm^{-1}, which is calculated from ωRC = 1. This is consistent with a grain boundary contribution to the impedance. Combined *Z''*/*M''* spectroscopic plots in (b) show an offset between the peak maxima of *M''* and *Z''*, which implies the electrical heterogeneity of the sample. The conductivity (*Y'*) versus frequency at different temperatures is shown in (c). The *Y'* plot shows a dispersion at higher frequencies, which could be associated with Jonscher power law behaviour,[21] and a nearly frequency independent plateau towards lower frequencies. Data is increasingly noisy at lower temperatures.

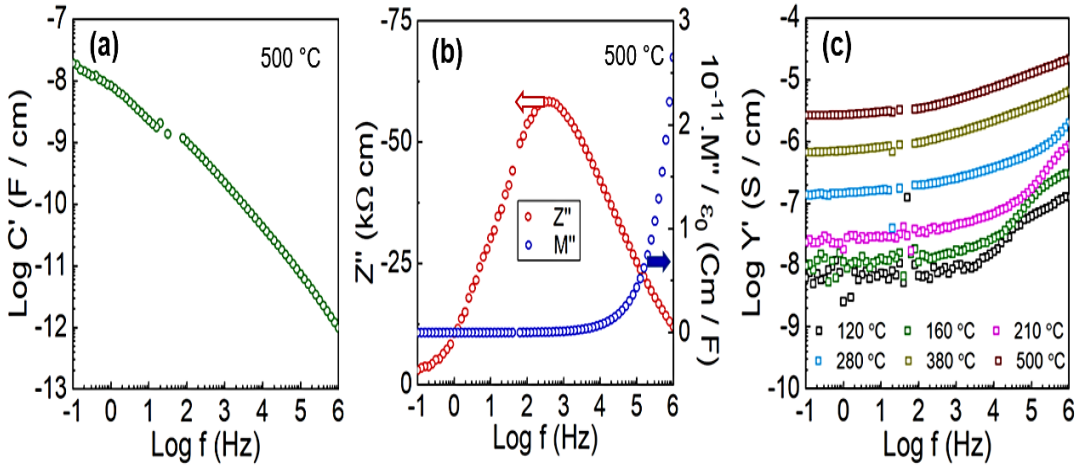

Figure 4.14 O3-Na[$Ni_{0.5}Mn_{0.5}$]O_2: spectroscopic plots of *C'* (a), -*Z''* and *M''* (b), *Y'* (c), in O_2.

In order to gain further insight into electrical properties of the O3-Na[$Ni_{0.5}Mn_{0.5}$]O_2 sample, impedance measurements at different temperatures were used to construct Arrhenius plots (Fig. 4.15). The separate bulk and grain boundary conductivities are given in (a). The bulk is found to be more conductive than the grain boundary at the temperatures measured, and has a lower activation energy of 0.43(2) eV compared with 0.511(1) eV for the grain boundary. The activation energy associated with the total conductivity of the material (bulk + grain boundary) is given in (b). This shows

that the overall conductivity of the material is largely dominated by the grain boundary at these temperatures, with a similar activation energy of 0.503(1) eV.

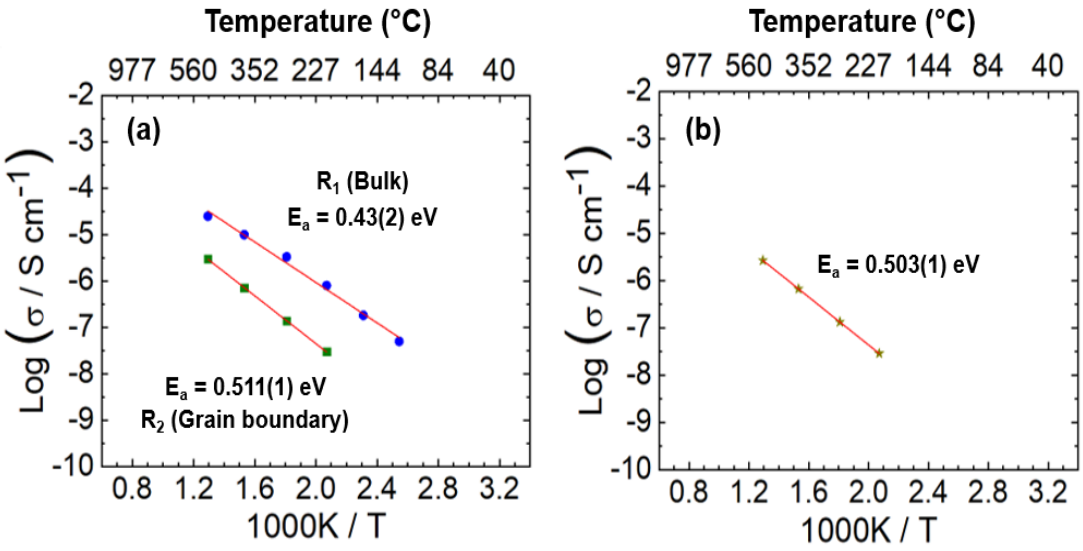

Figure 4.15 Arrhenius plots of O3-Na[$Ni_{0.5}Mn_{0.5}$]O_2 for its separate bulk and grain boundary components (a), as well as its effective total (bulk + grain boundary) conductivity (b).

Extrapolating the Arrhenius plots for O3-Na[$Ni_{0.5}Mn_{0.5}$]O_2 to room temperature would give extremely high resistances - of the order of gigaohms. So it is possible to say with some confidence that this O3 polymorph is much less conductive than the P2 phase, as well as less conductive than the Na[Ni,Mg,Mn,Ti]O_2 mixed phase material studied in Chapter III. Furthermore, the activation energy associated with the effective total conductivity of O3-Na[$Ni_{0.5}Mn_{0.5}$]O_2 (0.503(1) eV) is much higher than for the P2 material (0.24(1) eV), and all E_a values are higher than those of the corresponding mixed phase Na[Ni,Mg,Mn,Ti]O_2 components. Hence, this indicates a higher activation energy for Na^+ ion conduction in this O3 sample. This can be explained by considering the material's solid state structure. In O-phases, sodium ions occupy octahedral sites. In order to jump from one to the next, the Na^+ ion must go via a tetrahedral site, where there is size discrepancy and the ion experiences strong repulsion from cations in the T_MO_2 sheets.[22] Hence, crossing through an octahedral-tetrahedral face, gives rise to a high activation barrier for Na^+ ion migration in these layered oxides.

4.3.4 Electrochemical Testing of P2-$Na_{0.64}[Mn_{0.8}Mg_{0.2}]O_2$ and O3-$Na[Ni_{0.5}Mn_{0.5}]O_2$

Electrochemical testing of P2-$Na_{0.64}[Mn_{0.8}Mg_{0.2}]O_2$ and O3-$Na[Ni_{0.5}Mn_{0.5}]O_2$ was performed using coin cells between 2.5 and 4.3 V *vs.* Na^+/Na. A voltage window and charge/discharge currents were selected, which are directly comparable with those used to test the mixed phase $Na[Ni,Mg,Mn,Ti]O_2$ material in Chapter III. Cycling of the phase pure P2-$Na_{0.64}[Mn_{0.8}Mg_{0.2}]O_2$ layered oxide at different rates of discharge is shown in Figure 4.16. Samples were charged at 14 mA g^{-1}, and discharged at 14, 28, and 140 mA g^{-1} rates. The P2 cells discharged at 14 and 28 mA g^{-1} have similar capacities of around 45 mAh g^{-1}. The cell discharged at 140 mA g^{-1} possesses a significantly lower initial capacity, but it steadily rises across the first 25 cycles, finishing at around 18 mAh g^{-1}.

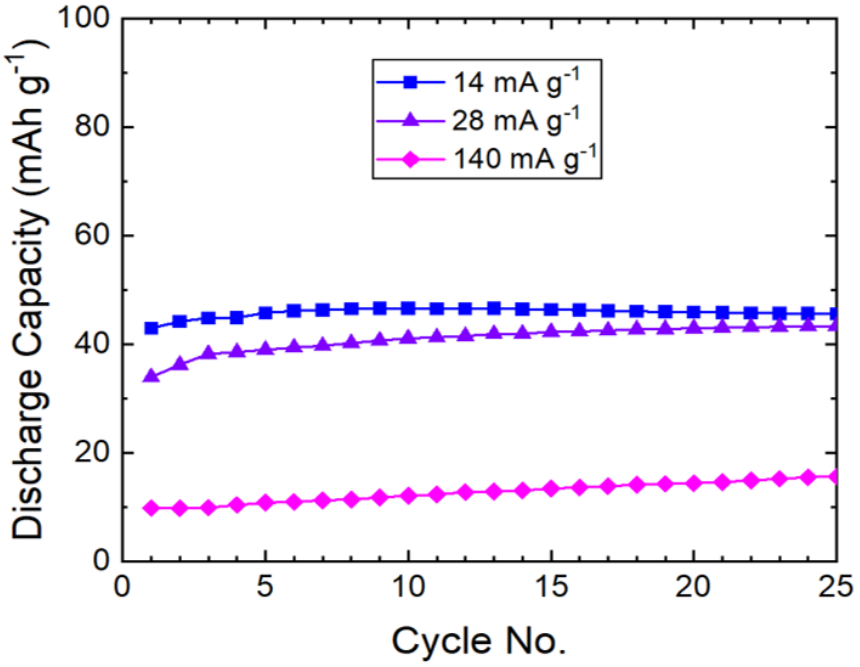

Figure 4.16 Discharge cycling data of P2-$Na_{0.64}[Mn_{0.8}Mg_{0.2}]O_2$/Na metal half cells over 25 cycles. Samples were charged at 14 mA g^{-1} and discharged at 14, 28 and 140 mA g^{-1} between 2.5 and 4.3 V.

The capacities obtained for P2-$Na_{0.64}[Mn_{0.8}Mg_{0.2}]O_2$ as a cathode material correspond to the Mn^{3+}/Mn^{4+} redox reaction. These discharge capacities are quite low compared to other similar P2 materials in the literature,[23,24] which is most likely due to the narrower voltage window these cells are being operated at. The Na-ion

battery is not discharged below its OCV of 2.5 V. Hence, the limited sodium extracted during the first charge is all that is reinserted back into the layered cathode structure. Discharging to a lower capacity would insert Na into the sodium deficient sites from the sodium metal counter electrode. Furthermore, going to higher voltages would also increase the capacity by utilising more of the initial pre-existing Na reservoir. A capacity of 45 mAh g^{-1} is only equivalent to ~ 0.18 Na. Similar P2 layered oxides, e.g. $Na_{0.67}[Ni_{0.33-x}Mg_xMn_{0.67}]O_2$ materials, are reported to possess a large voltage plateau at 4.2-4.4 V,[25,26] which is unlikely to have been fully exploited here. However, while these capacities seem quite low, importantly, the stability looks promising for this layered oxide. By avoiding a higher voltage, it is possible oxygen layer gliding and P2-O2 phase transitions are avoided, which are structurally damaging and are thought to result in poor charge retention.[27]

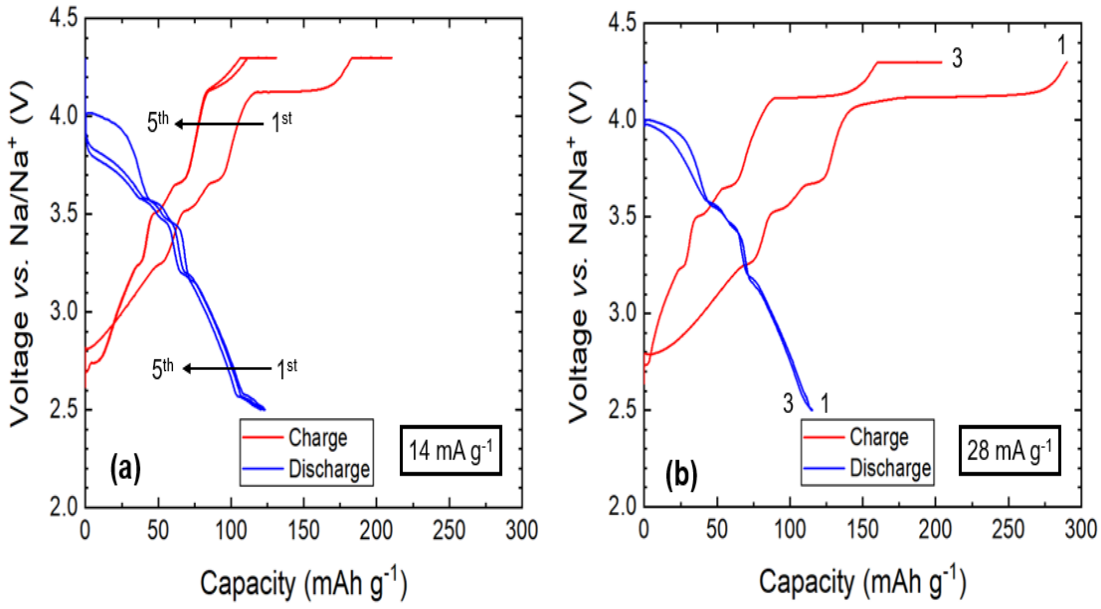

Figure 4.17 Charge/discharge curves in 2.5 - 4.3 V showing the first few cycles for O3-$Na[Ni_{0.5}Mn_{0.5}]O_2$/Na metal half cells. Cells were charged at 14 mA g^{-1} and discharged at (a) 14 and (b) 28 mA g^{-1}.

The electrochemical performance of the O3-$Na[Ni_{0.5}Mn_{0.5}]O_2$ layered oxide was evaluated using a half-cell setup *vs.* sodium metal. Charge/discharge curves of the sample in the voltage range 2.5 – 4.3 V, using a specific charge current of 14 mA g^{-1} and a discharge current of 14 mA g^{-1} (a) and 28 mA g^{-1} (b), are shown in Figure 4.17. The voltage-capacity profiles exhibit slopes consisting of a series of plateaus.

A discharge capacity of around 125 mAh g^{-1} is achieved for both cells across the first couple of cycles, which is fairly high for a sodium-ion cathode, and slightly above that seen for the mixed phase Na[Ni,Mg,Mn,Ti]O_2 material under the same testing conditions. However, after the first couple of cycles, the electrochemical performance was found to rapidly deteriorate and the capacity sharply drop off.

The stepwise voltage plateaux seem to be reasonably reversible. There is an extra capacity during the initial charge, which may be attributed to electrolyte decomposition above 4 V. The series of voltage plateaus is indicative of Na^+/vacancy ordering and structural transitions during cycling. Hence, the trigonal O3 structure is likely to transform into various P3 and O3 phases with different crystal structures as Na is extracted and inserted. These transitions confer poor long-term stability for the O3-Na[$Ni_{0.5}Mn_{0.5}$]O_2 material as a cathode, as these structural changes lead to large volume changes and overpotentials.[28] As with the P2 class of materials, there is likely to be a trade-off between capacity and stability once again when tailoring the voltage range to be utilised for this layered oxide.

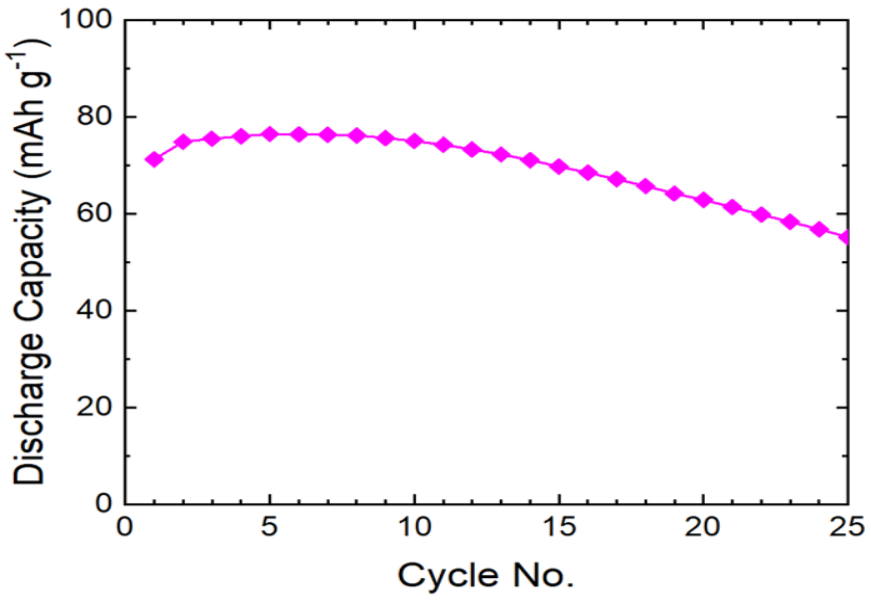

Figure 4.18 Discharge cycling data of O3-Na[$Ni_{0.5}Mn_{0.5}$]O_2/Na metal half-cell over 25 cycles. Samples were charged at 14 mA g^{-1} and discharged at 140 mA g^{-1} between 2.5 and 4.3 V.

The instability of the O3-type material is best demonstrated by the capacity *vs.* cycle number plot shown in Figure 4.18. This Na-ion half-cell was charged at 14 mA g^{-1}

and discharged at 140 mA g^{-1} (approximately 1C). The initial discharge capacity is 80 mAh g^{-1}, which is approximately 33% less than what is achieved at lower discharge rates. Hence, this suggests that rate kinetics are poor for this material, as suggested by impedance results performed on the raw electroceramic. Beyond 10 cycles the capacity rapidly declines, and after 25 cycles it is below 60 mAh g^{-1} (~ 75% charge retention). Hence, while the O3-$Na[Ni_{0.5}Mn_{0.5}]O_2$ material possesses a much higher specific capacity than P2-$Na_{0.64}[Mn_{0.8}Mg_{0.2}]O_2$, the stability and charge retention do not appear to be as good, thus limiting the overall performance of the material, and curtailing its use as an Na-ion cathode.

4.4 Conclusions

In this chapter, the P2-$Na_{0.64}[Mn_{0.8}Mg_{0.2}]O_2$ and O3-Na-$[Ni_{0.5}Mn_{0.5}]O_2$ layered oxides were synthesized and characterised. The structures of these oxide materials were explored, including the effect of varying the amount of sodium in the P2-type material and the Ni : Mn ratio in the O3 polymorph. The structure and thermal/atmospheric stability of these materials were examined using a variety of different characterisation techniques: XRD, TGA, DSC. Their electrical properties were also investigated using impedance spectroscopy. Finally, electrochemical testing was performed by employing half-cell battery setups *vs.* metallic sodium.

A solid solution was found to form for P2-$Na_{0.64}[Mn_{0.8}Mg_{0.2}]O_2$ ($0.5 \leq x \leq 1$). The $x \approx 2/3$ material was indexed using the $P6_3/mmc$ space group, and had its detailed structure resolved by Rietveld refinement. The O3-$Na[Ni_{0.5}Mn_{0.5}]O_2$ polymorph was found to form over a narrow temperature range when synthesized in air. Synthesis in an oxygen atmosphere was also performed - both routes resulted in residual NiO precursor. Hence, this helps account for the NiO impurity present in the mixed phase $Na[Ni,Mg,Mn,Ti]O_2$ in Chapter III. The Ni : Mn ratio in these layered oxide materials was altered by synthesizing $Na[Ni_xMn_{1-x}]O_2$ ($O.33 \leq x \leq 0.5$) materials. A lower nickel content favoured the formation of a sodium-deficient P2 phase over the O3 one. Both P2-$Na_{0.64}[Mn_{0.8}Mg_{0.2}]O_2$ and O3-Na-$[Ni_{0.5}Mn_{0.5}]O_2$ materials are prone to the uptake of atmospheric species when exposed to air, as found by TGA measurements. DSC results showed no indication of fast structural phase transitions occurring in either material on heating.

From impedance measurements, the conductivity of the layered oxides was as follows: P2-$Na_{0.64}[Mn_{0.8}Mg_{0.2}]O_2$ > mixed phase $Na[Ni,Mg,Mn,Ti]O_2$ > O3-Na-$[Ni_{0.5}Mn_{0.5}]O_2$. The activation energies suggest that Na^+ ion hopping occurs most easily in the P2-type material and is significantly hindered in the O3-phase. Electrochemical testing revealed the P2-$Na_{0.64}[Mn_{0.8}Mg_{0.2}]O_2$ material to have a low discharge capacity of only around 45 mAh g^{-1}, but good initial cycling stability. The O3-$Na[Ni_{0.5}Mn_{0.5}]O_2$ layered oxide showed a much higher specific capacity (~ 125 mAh g^{-1}), but possesses poor charge retention.

Results found in this chapter raise important concerns over the preparation, storage and handling of layered oxide materials as potential Na-ion cathodes. Possible future work is to perform XRD measurements after exposing the material to air/moisture, and after TGA/DSC runs. Further Rietveld analysis would also be useful to try and determine the degree of Na/Ni mixing, if any, in the materials synthesized in this chapter, as well as quantitative phase analysis to determine the amount of residual NiO. Inductively coupled plasma mass spectrometry (ICP-MS) may also prove advantageous for accurate elemental analysis. Further synthesis work is required to produce phase pure O3-$Na[Ni_{0.5}Mn_{0.5}]O_2$.

While P2-$Na_{0.64}[Mn_{0.8}Mg_{0.2}]O_2$ and O3-Na-$[Ni_{0.5}Mn_{0.5}]O_2$ have been well studied in the literature, this is the first time their electrical properties have been investigated by impedance spectroscopy. Results obtained help to provide further information on the structure-property-performance relationship in these layered oxide Na-ion cathode materials. In order to obtain greater insight, using a wider temperature range is desirable to allow for better separation and analysis of all the individual components in the impedance response. Due to the phase transitions that are reported to occur in these materials during cycling,[2,11] impedance measurements on the P3 and O2 structures would also provide greater insight into the electrochemical performances.

Cell testing of P2-$Na_{0.64}[Mn_{0.8}Mg_{0.2}]O_2$ and O3-Na-$[Ni_{0.5}Mn_{0.5}]O_2$ can help explain the promising behaviour of the $Na[Ni,Mg,Mn,Ti]O_2$ mixed phase sample as an Na-ion cathode. The O3-$Na[Ni_{0.5}Mn_{0.5}]O_2$ layered oxide has a high specific capacity, and the P2-$Na_{0.64}[Mn_{0.8}Mg_{0.2}]O_2$ material appears to possess good cycling stability. Hence, a combination of these two effects is seen in the mixed phase system. Importantly, it is essential to remember that P2-$Na_{0.64}[Mn_{0.8}Mg_{0.2}]O_2$ and O3-Na-$[Ni_{0.5}Mn_{0.5}]O_2$ are the nominal phases in the $Na[Ni,Mg,Mn,Ti]O_2$ mixed phase material, and not the exact compositions of the polymorphs. For instance, there is also titanium present. Doping O3 materials with Ti^{4+} is reported to suppress the abrupt phase transformation via the gliding of the transition metal layer, and lead to an enhanced electrochemical performance.[29] Future work could be to explore the effect of replacing the Mn^{4+} ions with Ti^{4+} in each of the individual phases that have been studied.

4.5 References

1 J. Billaud, G. Singh, A. R. Armstrong, E. Gonzalo, V. Roddatis, M. Armand, T. Rojo and P. G. Bruce, *Energy Environ. Sci.*, 2014, **7**, 1387-1391.

2 S. Komaba, N. Yabuuchi, T. Nakayama, A. Ogata, T. Ishikawa and I. Nakai, *Inorg. Chem.*, 2012, **51**, 6211–6220.

3 T. Yu, H. Ryu, G. Han and Y. Sun, *Adv. Energy Mater.*, 2020, **12**, 2001609(1)-2001609(8).

4 S. Guo, Y. Sun, J. Yi, K. Zhu, P. Liu, Y. Zhu, G. Z. Zhu, M. Chen, M. Ishida and H. Zhou, *NPG Asia Mater.*, 2016, **8**, e266(1)–e266(9).

5 C. Delmas, C. Fouassier and P. Hagenmuller, *Phys. B+C*, 1980, **99**, 81–85.

6 S. Komaba, T. Nakayama, A. Ogata, T. Shimizu, C. Takei, S. Takada, A. Hokura and I. Nakai, *ECS Transactions*, 2009, **16**, 43–55.

7 U. Maitra, R. A. House, J. W. Somerville, N. Tapia-Ruiz, J. G. Lozano, N. Guerrini, R. Hao, K. Luo, L. Jin, M. A. Pérez-Osorio, F. Massel, D. M. Pickup, S. Ramos, X. Lu, D. E. McNally, A. V Chadwick, F. Giustino, T. Schmitt, L. C. Duda, M. R. Roberts and P. G. Bruce, *Nat. Chem.*, 2018, **10**, 288-295.

8 International Centre for Diffraction Data, PDF-4+, XRD Database 2020, ICDD, Newton Square, 2020.

9 A. C. Larson and R. B. Von Dreele, *General Structure Analysis System (GSAS) Report LAUR 86-748*, Los Alamos National University, Los Alamos, 2004.

10 B. H. Toby, *J. Appl. Crystallogr.*, 2001, **34**, 210–213.

11 N. Sharma, N. Tapia-Ruiz, G. Singh, A. R. Armstrong, J. C. Pramudita, H. E. A. Brand, J. Billaud, P. G. Bruce and T. Rojo, *Chem. Mater.*, 2015, **27**, 6976–6986.

12 T. Lonkai, D. G. Tomuta, U. Amann, J. Ihringer, R. W. A. Hendrikx, D. M. Tobbens and J. A. Mydosh, *Phys. Rev. B*, 2004, **69**, 134108(1)-134108(10).

13 V. Duffort, E. Talaie, R. Black and L. F. Nazar, *Chem. Mater.*, 2015, **27**, 2515–2524.

14 D. Buchholz, L. G. Chagas, C. Vaalma, L. Wu and S. Passerini, *J. Mater. Chem. A*, 2014, **2**, 13415–13421.

15 R. Fielden and M. N. Obrovac, *J. Electrochem. Soc.*, 2015, **162**, A453–A459.

16 J. M. Paulsen and J. R. Dahn, *Solid State Ionics*, 1999, **126**, 3–24.

17 P. F. Wang, Y. You, Y. X. Yin and Y. G. Guo, *J. Mater. Chem. A*, 2016, **4**, 17660–17664.

18 H. R. Yao, P. F. Wang, Y. Gong, J. Zhang, X. Yu, L. Gu, C. Ouyang, Y. X. Yin, E. Hu, X. Q. Yang, E. Stavitski, Y. G. Guo and L. J. Wan, *J. Am. Chem. Soc.*, 2017, **139**, 8440–8443.

19 P. Wang, Y. You, Y. Yin and Y. Guo, *Adv. Energy Mater.*, 2018, **8**, 1701912(1)-1701912(23).

20 C. Delmas, A. Maazaz, C. Fouassier, J.-M. Réau and P. Hagenmuller, *Mater. Res. Bull.*, 1979, **14**, 329–335.

21 D. P. Almond and A. R. West, *J. Electroanal. Chem.*, 1985, **186**, 17–25.

22 K. Kang, Y. S. Meng, J. Bréger, C. P. Grey and G. Ceder, *Science*, 2006, **311**, 977-980.

23 N. Yabuuchi, R. Hara, K. Kubota, J. Paulsen, S. Kumakura and S. Komaba, *J. Mater. Chem. A*, 2014, **2**, 16851–16855.

24 R. J. Clément, P. G. Bruce and C. P. Grey, *J. Electrochem. Soc.*, 2015, **162**, A2589–A2604.

25 G. Singh, N. Tapia-Ruiz, J. M. Lopez Del Amo, U. Maitra, J. W. Somerville, A. R. Armstrong, J. Martinez De Ilarduya, T. Rojo and P. G. Bruce, *Chem. Mater.*, 2016, **28**, 5087–5094.

26 N. Tapia-Ruiz, W. M. Dose, N. Sharma, H. Chen, J. Heath, J. W. Somerville, U. Maitra, M. S. Islam and P. G. Bruce, *Energy Environ. Sci.*, 2018, **11**, 1470–1479.

27 J. W. Somerville, A. Sobkowiak, N. Tapia-Ruiz, J. Billaud, J. G. Lozano, R. A. House, L. C. Gallington, T. Ericsson, L. Häggström, M. R. Roberts, U. Maitra and P. G. Bruce, *Energy Environ. Sci.*, 2019, **12**, 2223–2232.

28 Y. Sun, S. Guo and H. Zhou, *Energy Environ. Sci*, 2019, **12**, 825-840.

29 P.-F. Wang, H.-R. Yao, X.-Y. Liu, J.-N. Zhang, L. Gu, X.-Q. Yu, Y.-X. Yin and Y.-G. Guo, *Adv. Mater.*, 2017, **29**, 1700210(1)-1700210(7).

Chapter V

Two- and Three-Electrode Impedance Spectroscopy of Sodium-Ion Batteries

5.1 Introduction

A crucial measurement used to determine the quality of the cathode material is the discharge capacity. This is for how long a cathode material can deliver a current equal to the discharge rate, at the nominal voltage of the cell, and is therefore intrinsically linked to the energy density of a battery. All batteries will experience, with cycling, some reduction in performance for a variety of reasons. This can take the form of either a fall in capacity or a drop in power. Capacity fading is often expressed in terms of charge retention, and this is an essential value so that the cycle life of a particular battery is known.

A drop in discharge capacity can be due to a variety of degradation (ageing) mechanisms[1] (see Section 1.4 for more on this). Some of these degradation routes are linked to a rise in cell impedance.[2] Therefore, by carrying out a combination of constant-current, constant-voltage (CC/CV) cycling in combination with electrochemical impedance spectroscopy, it should be possible to identify the rate-limiting steps and problem interfaces inside the measured cell. Having knowledge of these may then make it possible to overcome them in order to enhance overall battery performance.

Considerable research has taken place on the application of impedance spectroscopy to lithium-ion batteries for similar purposes,[3] however, such studies have been constrained by their limited analysis. Crucially, so far, no-one in the literature has utilised the full range of different complex formalisms to highlight different aspects of collected data, thus restricting their interpretation of results. Furthermore, when carrying out impedance measurements on full-cells, it can be difficult to interpret data due to the overlapping of processes with similar time constants at both

electrodes. Often, half-cell measurements are required to clarify data and study the two electrodes separately. However, the spectra generated in this way may not exactly reflect the processes occurring at the individual electrodes in a full-cell. A way to circumvent this problem is to use a three-electrode cell design.[4] Thus, in this way, it is possible to monitor how the anode and cathode individually contribute to the overall impedance of the battery, and gain a better insight into fading mechanisms.

In this chapter, electrochemical impedance spectroscopy is applied to full-cell sodium-ion batteries for the first time to try and elucidate their performance limiting factors. This is done using two- and three-electrode designs applied to the commercially-used pouch cell setup. Unlike previous impedance studies on secondary batteries,[5–7] data will be analysed using a range of different complex impedance formalisms in order to allow for a more in-depth analysis.

5.2 Experimental

5.2.1 Cell Components

Sheets of the cathode and anode were supplied by the Warwick Manufacturing Group (WMG). The composite cathode consisted of the active material component, $Na[Ni,Mg,Mn,Ti]O_2$, which had been mixed with polyvinylidene fluoride (PVDF) binder and C65 carbon black conductive additive in a 89 : 6 : 5 ratio. For the anode, a non-graphitizable commercially-available carbon had been mixed with PVDF and C45 carbon black (88.1 : 9 : 2.9). Slurries of both of these were formed with N-methyl-2-pyrrolidone (NMP) before these mixtures were drawn down onto carbon-coated aluminium foil. These were then dried and stored at 60 °C in a vacuum oven before square electrodes were pressed using a die cutting machine. Positive electrodes (cathodes) of 2.5 mAh/cm^2 (20 x 20 mm) were cycled against negative hard carbon electrodes (22 x 22 mm). Prior to cycling, these were all stored in a vacuum oven at 60 °C before being transferred to an argon-filled glove box for cell assembly.

The separators used in the Na-ion cells to isolate the cathode and anode from one another were cut from GF/A glass microfiber filter paper (Whatman). These were dried at 200 °C for 16 h before they were transferred to the glove box. Laminate-type prismatic pouch cells (7 x 5 cm) containing aluminium current collector tabs (MTI) to connect the electrodes to the battery tester were dried at 70 °C overnight before being taken into the glove box. The electrolyte used was a solution of 0.5 M sodium hexafluorophosphate in an ethylene carbonate : diethyl carbonate : propylene carbonate (1:2:1) mixture. This was prepared in the glove box, with the solvent mixture dried over molecular sieves for 16 h, prior to dissolution of the salt.

5.2.2 Cell Designs

Electrochemical measurements were performed using laminate-type prismatic pouch cells assembled in the argon-filled glove box. A pouch cell consists of the cathode stacked on top of the anode, separated by two GF/A separators (Fig. 5.1). These separators were soaked in liquid electrolyte prior to cell assembly. The cells were

then vacuum-sealed with Al current collector tabs sticking out of the pouch for connection to the battery tester.

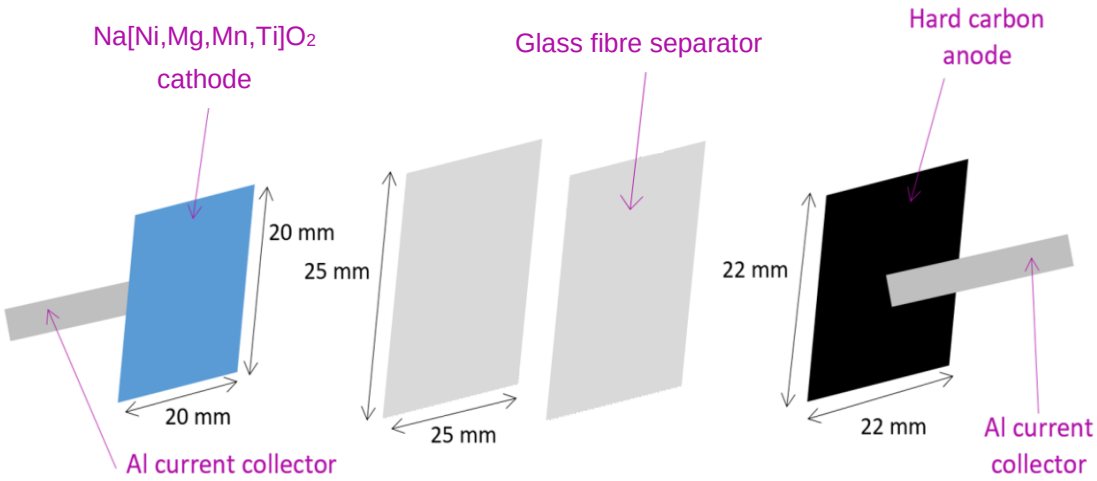

Figure 5.1 Two-electrode pouch cell design.

The three-electrode cell design used in this work is identical to the two-electrode one, except it possesses longer separators (35 x 25 mm). This is to accommodate a third (reference) electrode sandwiched between the two separators, placed above the cathode and anode (Fig. 5.2). This third electrode takes the form of a piece of sodium metal (0.5 x 0.5 cm), which is enclosed inside a folded Al current collector tab.

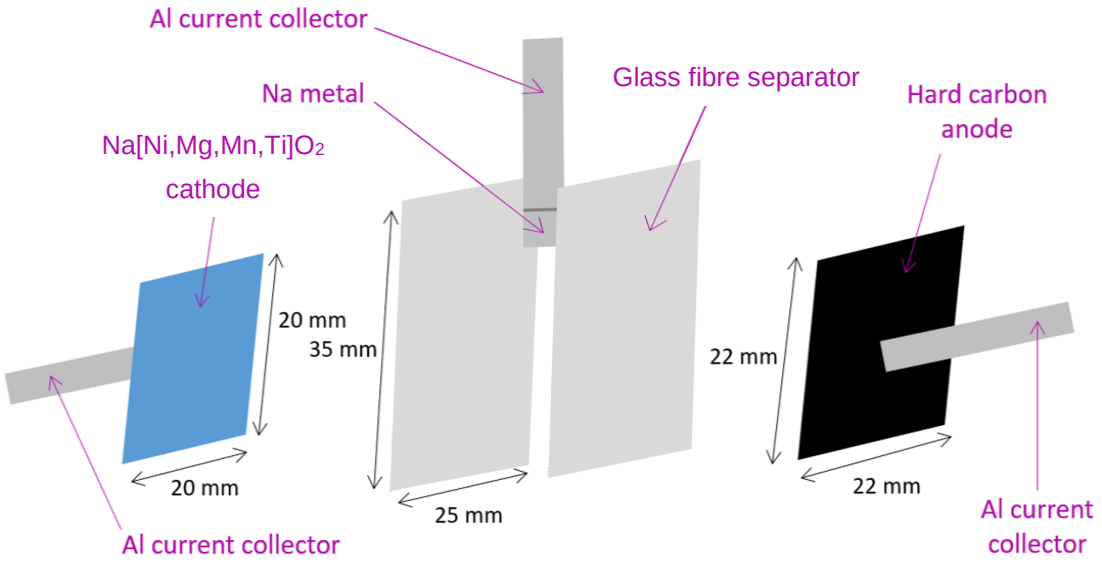

Figure 5.2 Three-electrode pouch cell design.

Four cells were built and tested for each two- and three-electrode design to check the reproducibility of collected results. Analysis of collected data for these showed a close similarity between the cells. This ensures that data presented in this chapter, and conclusions drawn, are representative of a wider population.

5.2.3. Testing Configurations

Two-electrode cells were tested using a Maccor Series 4000 Automated Test System. The Na[Ni,Mg,Mn,Ti]O_2 cathode was connected to the positive terminal and the hard carbon anode to the negative terminal using banana clips (Fig 5.3). AC impedance measurements were performed using a frequency response analyser (Solartron Modulab). All cells were held at a constant temperature of 30 ± 0.5 °C using a Maccor Temperature Chamber.

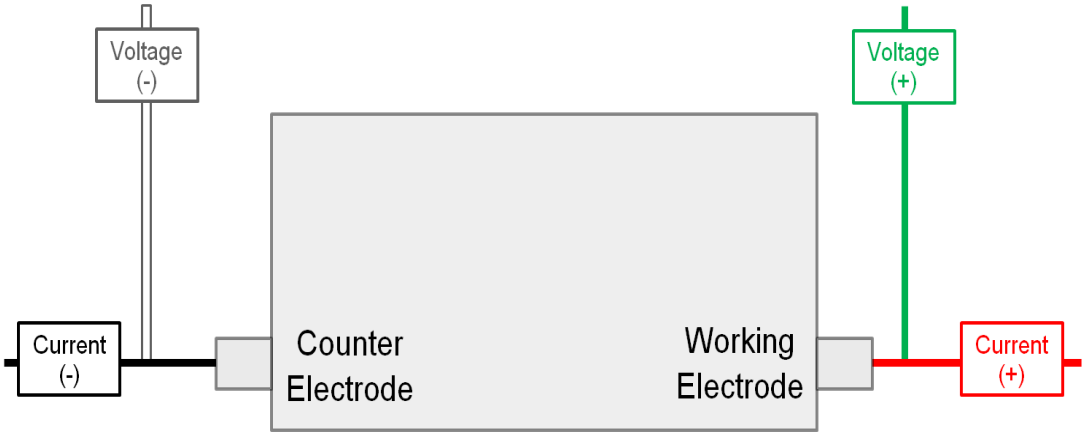

Figure 5.3 Schematic view of the wiring between two-electrode test cells and Maccor Series 4000 Automated Test System.

A schematic diagram of the three-electrode cell and the different interface terminal-to-electrode connections is shown in Fig. 5.4. The Na electrode acts as a voltage reference but experiences no current flow so does not interfere with the cycling of the battery. AC impedance measurements were performed using a potentiostat with a parallel frequency response analyser (Solartron Pstat 1470E/FRA 1455A). This setup is capable of simultaneous high-speed, precision and accurate impedance measurements (the FRA has a measurement accuracy of 0.1%).

All cells were held at a constant temperature of 30 ± 0.5 °C using a MMM FRIOCELL Incubator. Impedance was measured by applying an AC potential between two electrodes and measuring the current between them. Three intrinsic EIS scans were performed simultaneously, using different methods for connecting the Solartron equipment to the electrodes. In the first, the impedance of the cell was measured without using the reference electrode. In the second, the impedance of the working electrode (Na[Ni,Mg,Mn,Ti]O_2) was measured against the reference (Na metal) electrode, and in the third, the counter electrode (hard carbon) was measured versus the reference electrode.

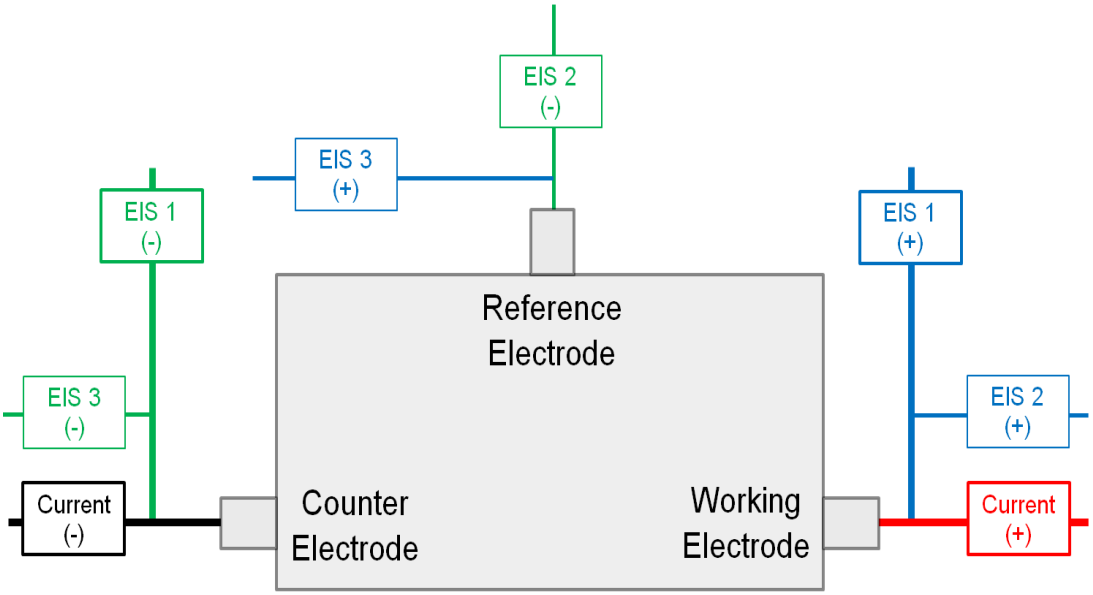

Figure 5.4 Schematic view of the wiring between three-electrode test cells and Solartron 1455A/1470E.

5.2.4 Testing Procedures

Each battery was left for 32 h at 30 °C prior to cycling to allow time to equilibrate. An impedance measurement was then performed before beginning to cycle the cell. The cells were cycled under constant current conditions at a specific current of 14 mA g^{-1} on charging and 28 mA g^{-1} on discharging, between the voltage limits of 4.2 and 1.0 V at 30 °C. On charging, a constant voltage step was applied at 4.2 V until the current dropped below 2.8 mA g^{-1}. The impedance spectra were recorded before every charge and discharge, allowing four additional hours for equilibration after

each charging/discharging step. An additional one-hour open circuit voltage (OCV) hold after running EIS allowed the cell to return to a steady state. AC impedance measurements were performed by varying the frequency with a perturbation potentiostatic signal amplitude of 10 mV (peak to peak) from 10 mHz to 100 kHz for two-electrode cells and 10 mHz to 1 MHz for three-electrode measurements. Data acquisition was performed using *MIMS* and *Multistat* software for two- and three-electrode cells respectively. *ZView* software was used for data analysis.

5.2.5 Geometry Correction

In order to allow a more meaningful interpretation of impedance data collected, a geometry correction was performed (Eq. 5.1). This consisted of dividing the active charge-transfer area, that of the cathode, by the separation between the two electrodes. This was taken as the accumulative thickness of the GF/A separators - each one being 0.26 mm. This allowed data to be plotted in the form of resistivity (Ω cm) and permittivity (F cm^{-1}).

$$Geometry\ correction = \frac{Area\ of\ cathode}{2\ \times Separator\ thickness} \qquad (5.1)$$

$$Geometry\ correction = \frac{2.0\ cm\ \times 2.0\ cm}{2\ \times (2.6\ \times 10^{-2}\ cm)}$$

$$Geometry\ correction = \frac{4.0\ cm^2}{5.2\ \times 10^{-2}\ cm}$$

$$Geometry\ correction = \mathbf{77\ cm}$$

5.3 Results and Discussion

5.3.1 Performance Comparison of Two- and Three-Electrode Cells

The purpose of carrying out three-electrode measurements is to monitor how the anode and cathode individually contribute to the overall impedance of the battery, and subsequently gain a better insight into performance fading mechanisms. However, when using a three-electrode cell setup, it is important that data generated are a meaningful replication of what would be seen for a standard two-electrode battery, so that conclusions drawn from three-electrode measurements can be applied to standard two-electrode batteries. It is therefore necessary to compare the performance of the different cell designs in terms of constant-current, constant-voltage (CC/CV) cycling, before examining the EIS measurements.

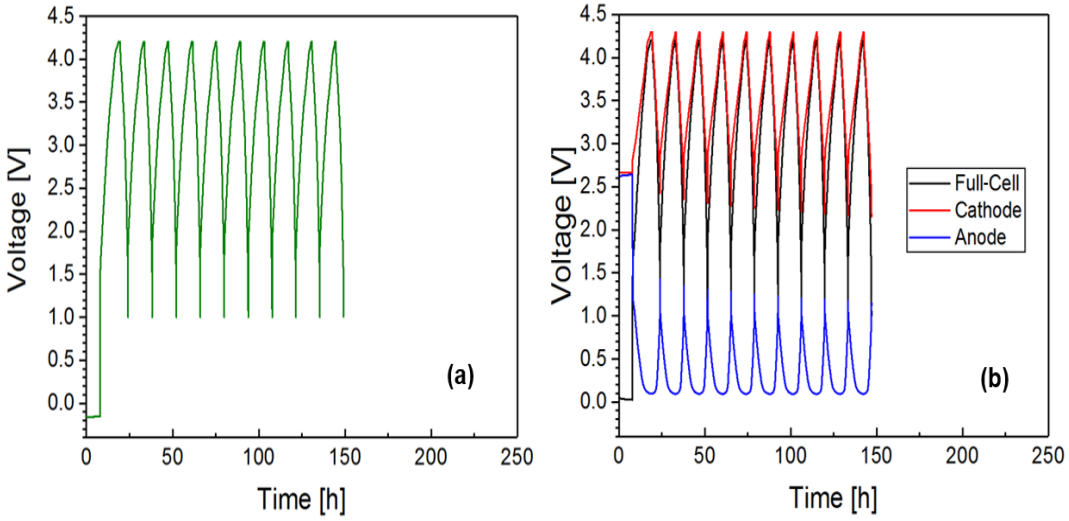

Figure 5.5 Voltage against time during the first ten cycles for a (a) two- and (b) three-electrode cell.

The voltage-time profiles for two- and three-electrode cells are compared in Figure 5.5. Simple charge-discharge measurements were performed on these batteries without EIS. The two-electrode cell (Fig. 5.5 (a)) and the full-cell measurement (Fig. 5.5 (b)) for the three-electrode setup are very similar. The cells were found to have an open circuit voltage close to 0 V in the assembled state. This is measured for 8 h to ensure that it is fairly constant before beginning the cycling. The cells were cycled using a specific current of 14 mA g^{-1} on charging and 28 mA g^{-1} on discharging - this

equates to approximately a 10 h charge and 5 h discharge of the cell. These C-rates were selected so that data could be collected over a reasonable time frame, without using currents which were overly aggressive for the cell.

A faster rate was applied to discharge the battery as less structural strain is thought to be placed on the non-graphitizable carbon anode when removing sodium ions from it. A hard carbon anode is one which lacks long-range crystalline (graphitic) order. Immobilised nanoscale domains exhibit local pseudographitic crystallinity, and at, microsocpic scales, such domains form a structure with closed porosity. Voltage limits between 1.0 and 4.2 V were applied to the cycling procedure, taking into consideration the redox potential of the active electrode materials being used, as well as the stability of these and the electrolyte. A constant voltage step was applied at 4.2 V until the current dropped below 2.8 mA g^{-1} in order to maximise the amount of capacity obtained from the batteries.

For the three-electrode cell, voltage-time profiles for the individual cathode and anode were also plotted in Fig. 5.5 (b). The cathode can be seen to vary between approximately 2.4 and 4.3 V, and the anode between around 1.4 and 0.1 V. The cathode voltage window is consistent with the Na metal reference and the $Ni^{2+/4+}$ redox reaction.[8] The insertion of Na^{+} ions into graphene interlayer spaces is reported to take place > 0.3 V. A lower voltage is thought to move further sodium into micro/nano-pores between 0 - 0.3 V.[9] However, precise sodiation mechnaisms are likely to depend upon the cell components and testing conditions. The full-cell voltage for the three-electrode battery is given by the difference in chemical potential between the cathode and anode (Eq. 5.2).

$$F_{Full-Cell} = V_{Cathode} - V_{Anode} \qquad (5.2)$$

In order to get a clearer picture of how the performances of the cells compare, it is necessary to examine their capacities. The charge, discharge capacity and coulombic efficiency across the first ten cycles, for two- and three-electrode cells, are plotted in Figure 5.6. After the first cycle (from cycle 2 onwards), the $Na[Ni,Mg,Mn,Ti]O_2$ cathode material can be seen to deliver both a charge and discharge capacity of around 125 mAh g^{-1}, and the cell generates an average discharge cell voltage of around 3.2 V, giving a cathode specific energy of 400 Wh kg^{-1}. Both cells possess

high coulombic efficiencies (~ 99%), apart from for cycle 1, thus indicating low polarisation during cycling. The charge capacity for the first cycle of the cell is much higher than subsequent cycles, resulting in a lower coulombic efficiency of approximately 80%.

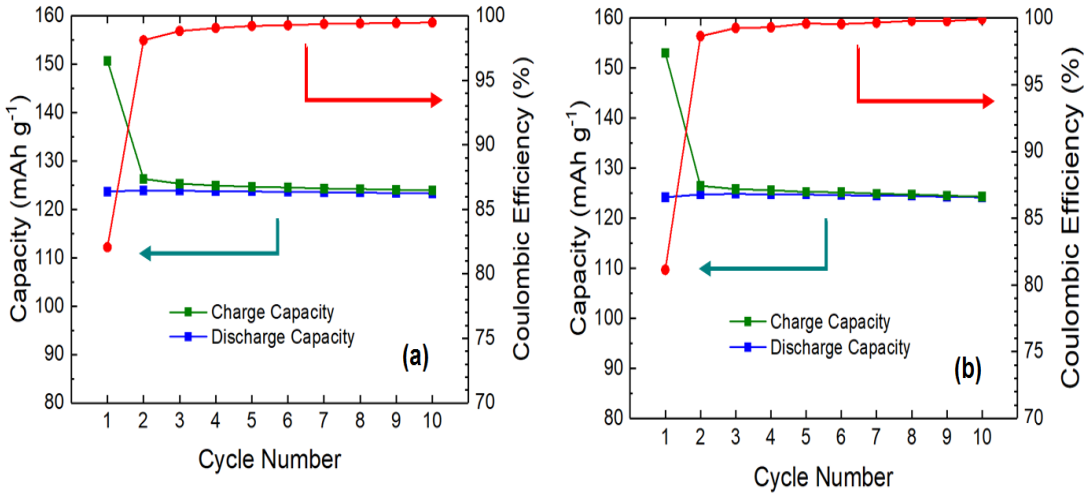

Figure 5.6 Capacity and coulombic efficiency versus cycle number for (a) two- and (b) three-electrode cell.

As the capacities and coulombic efficiencies of the two- and three-electrode cells are virtually indistinguishable, this indicates that the presence of the third reference electrode does not interfere with the performance of the cell. Therefore, this suggests that it should be possible to extract meaningful results from EIS measurements performed on three-electrode cells and apply these to two-electrode batteries.

Standard EIS analysis tools may give wildly inaccurate results on a system that is not at steady state.[10] Hence, a reproducible steady state is a necessary condition for a valid impedance measurement on a battery.[2] In order to ensure this, electrochemical impedance spectroscopy is normally measured using a small excitation signal. This is done so that the cell's response is pseudo-linear. If the system is non-linear, the current response will contain harmonics of the excitation frequency. In order to accurately perform EIS on a cell during cycling, it is necessary to implement a 'rest' period first so that the cell's voltage is not varying significantly.[11] Thus, after every charge and discharge, a 4 h open circuit voltage step was written into the cell testing procedure, prior to performing EIS. An additional 1 h OCV step was implemented following the impedance scan to allow the cell to 'recover' from the EIS run, prior to

continuing with CC/CV cycling. As these rest periods will be significantly present in the battery testing regime when performing EIS, it was first necessary to ensure that the performance of cells under this testing regime does not differentiate significantly from standard cycling of Na-ion batteries, so that the results can be treated as meaningful.

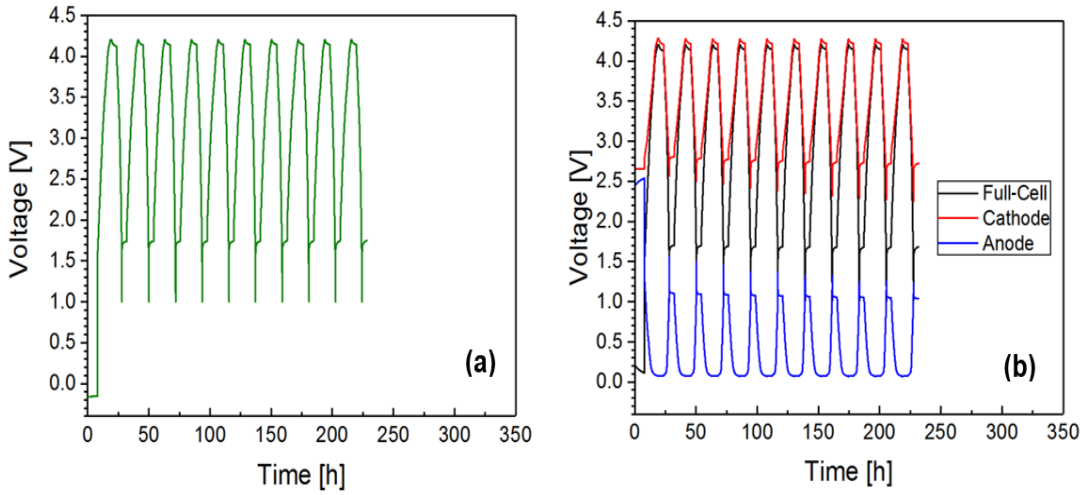

Figure 5.7 Voltage against time during the first ten cycles, including rest steps, for a (a) two- and (b) three-electrode cell.

The voltage-time profiles of two- and three-electrode cells with 4 h rest steps included are shown in Figure 5.7. The OCV step after charging to 4.2 V can be seen as a slight dip at the top of the voltage plateau, with the voltage dropping to close to 4.1 V. After the battery has been discharged to 1 V, an additional 4 h rest period results in the voltage increasing, reaching an OCV close to 1.7 V. Once again, a remarkably similar profile is seen for full-cell data for the three-electrode measurement (Fig. 5.7 (b)). The cathode *vs.* reference electrode measurement has a similar profile to that of the full-cell, but with OCVs after charge and discharge occurring at 4.2 and 2.8 V respectively. Anode data maintains an OCV after charging close to 0.1 V, but after discharging drops from 1.5 to 1.1 V, and then stays constant until the end of the rest period.

The capacities and coulombic efficiencies of the different cell types are compared in Figure 5.8. It can be seen that both of these have charge/discharge capacities (after the 1st cycle) close to 125 mAh g^{-1}, and coulombic efficiencies of around 99%. Importantly, not only is it difficult to distinguish between these two data sets but

they are also almost very similar to the results seen for the standard CC/CV cycling without rests (Fig. 5.6). Hence, these results suggest that the implementation of 'rest' steps does not interfere substantially with the typical performance of these sodium-ion batteries. Therefore, impedance data collected from three-electrode cells should be able to be applied to standard two-electrode Na-ion batteries operating under normal conditions.

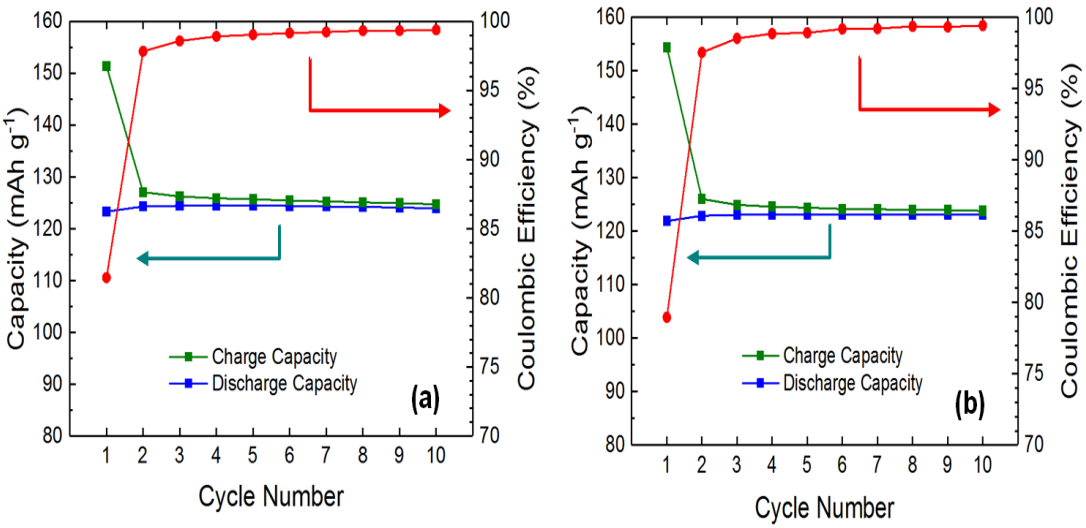

Figure 5.8 Capacity and coulombic efficiency versus cycle number for a (a) two- and (b) three-electrode cell, with rest steps.

Having checked that the cycling of three-electrode cells was comparable with two-electrode batteries, and that implementing 'rest' steps does not interfere with their performances, impedance measurements can be performed. Each AC impedance scan lasts for approximately 40 minutes. As a final check, to ensure that introduction of an EIS step does not dramatically alter the behaviour of the cells, the voltage-time profiles and capacities vs. cycle number were first plotted. The two-electrode voltage-time data (Fig. 5.9 (a)) are closely related to that of cycling with rest periods (Fig. 5.7 (a)). The occasional presence of spikes in the plot corresponds to where EIS has been performed, and is due to a sharp voltage drop sometimes seen when there is a switch from the battery cycler to the frequency response analyser (FRA). The full-cell data for the three-electrode cell (Fig. 5.7 (b)) are once again quite similar to the two-electrode plot. Furthermore, all of the three-electrode spectra – full-cell, cathode and anode - are very similar to what was seen for performing rest steps without introduction of EIS (Fig. 5.7 (b)).

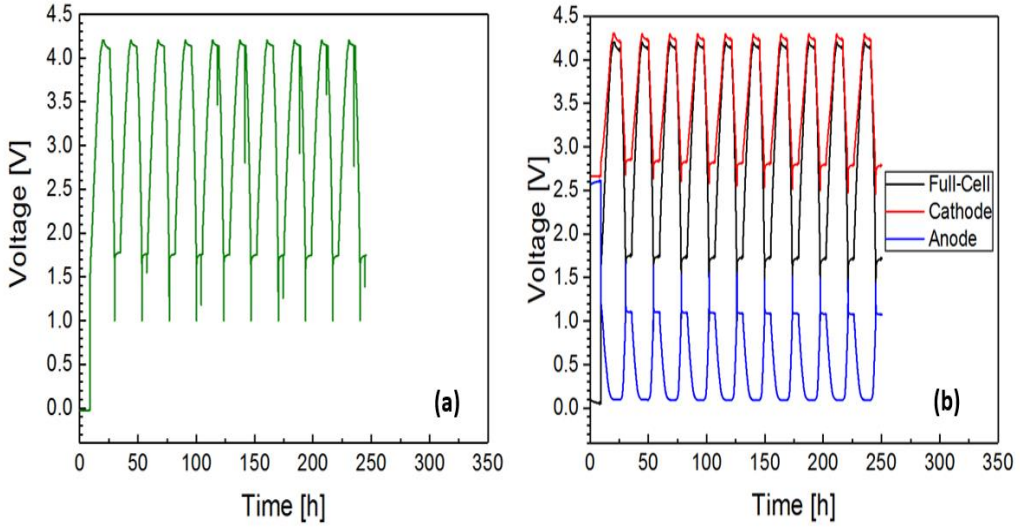

Figure 5.9 Voltage against time during the first ten cycles for a (a) two- and (b) three-electrode cell, with EIS.

The capacity and coulombic efficiency are plotted for the first ten cycles in Fig. 5.10. As seen with previous measurements with and without rest steps, the values are closely related. Both the two- and three-electrode cells possess coulombic efficiencies ~ 99% and a charge/discharge capacity close to 125 mAh g^{-1}. Importantly, this indicates that the introduction of EIS measurements does not significantly alter the cycling behaviour of either the two- or three-electrode cells.

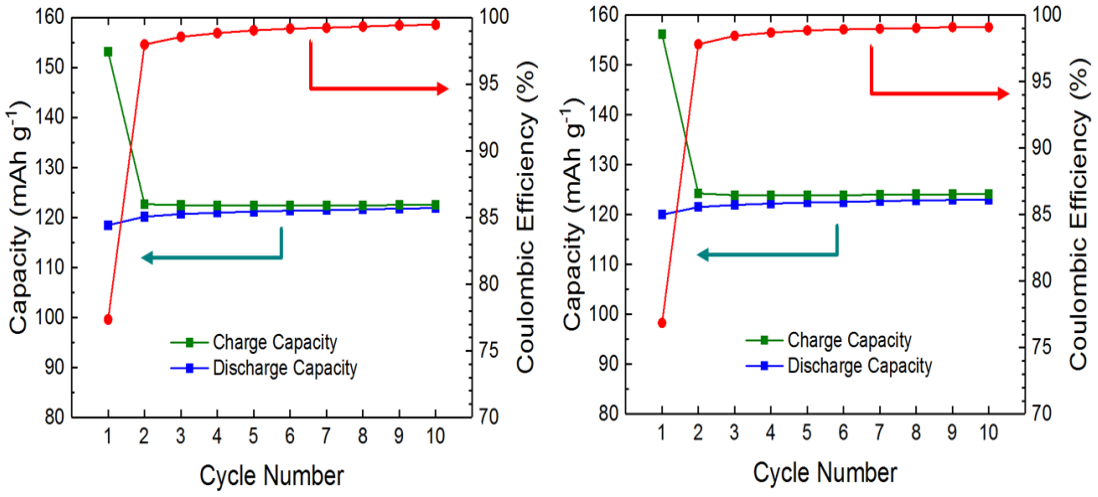

Figure 5.10 Capacity and coulombic efficiency versus cycle number for a (a) two- and (b) three-electrode cell, with EIS.

5.3.2 Two-Electrode Impedance Studies

Upon initial examination, impedance within a battery can be thought to originate from the anode, electrolyte and cathode. Two-electrode EIS measurements on full-cells give an overall picture of the total impedance within the battery; which is made up of contributions from each of these separate components. Simple two-electrode experiments should be useful in theory for determining how the EIS spectrum changes with cycle number, which in turn can be related to the performance degradation of sodium-ion batteries. Furthermore, to elucidate if there is an advantage to performing three-electrode measurements on Na-ion cells, it is necessary to first examine the two-electrode results to see what information can be gathered from these alone. Impedance scans (0.01 - 100,000 Hz) were performed across the first ten cycles for an Na-ion pouch cell with a measurement being carried out after every complete charge/discharge. EIS was also performed prior to cycling the cell in order to gather information about the battery in its assembled state.

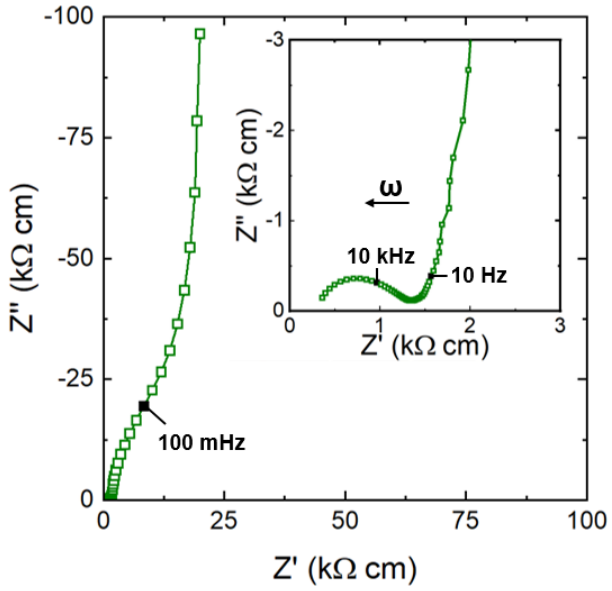

Figure 5.11 Impedance complex plane plot for a two-electrode sodium-ion battery prior to cycling it. Inset shows zoomed-in high-frequency data.

The most common form of plotting impedance data for analysis is in the form of Z'' plotted against Z' on linear scales, also known as a Nyquist plot. Presenting data in this way displays the resistance along the (real) x-axis and reactance (including capacitance) along the (imaginary) y-axis. Such a plot is shown for a sodium-ion

battery, prior to cycling it in Figure 5.11. This data shows what appears to be the start of a semi-circle, which becomes close to a vertical spike at low frequency. This appears as if it would cross the x-axis around 24 kΩ cm. The zoomed-in section reveals another high-frequency arc, crossing the real axis close to 1.5 kΩ cm, with a non-zero intercept at about 250 Ω cm. Hence, these results suggest that prior to cycling the cell, there are three resistances associated with the battery, which from high to low frequency can be labelled as R_{HF}, R_1 and R_2. These have approximate values of 0.25, 1.25 and 22.5 kΩ cm respectively. The low-frequency almost vertical spike also suggests the presence of a component close to a perfect capacitor, C_{LF}. Hence, to a first approximation, the equivalent electrical circuit for this Na-ion battery, prior to cycling it, would consist of two parallel *RC* elements, a resistor, and a capacitor, all connected in series to one another (Fig. 5.12).

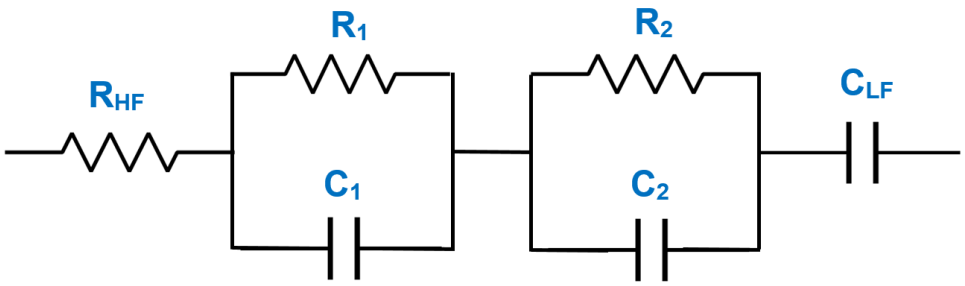

Figure 5.12 The equivalent electrical circuit for a sodium-ion battery prior to cycling it.

It can often be useful to plot data using alternative formalisms to reveal previously unseen features of the data. This is done frequently when analysing impedance results for electroceramics,[12,13] but has not been done before for batteries. One plot which is often very useful is the capacitance plotted against frequency on logarithmic scales. This is displayed in Figure 5.13 for the Na-ion cell prior to cycling it. This data displays two plateaus: one around 50 μF cm^{-1}, increasing to about 120 μF cm^{-1} at the lowest frequencies, and another at about 5 nF cm^{-1} at higher frequency. This low frequency value is in the range, which is indicative of an electrochemical double layer capacitor (~ 1 mF). Therefore, this correlates with the low frequency spike seen in the complex impedance plot (Fig. 5.11).

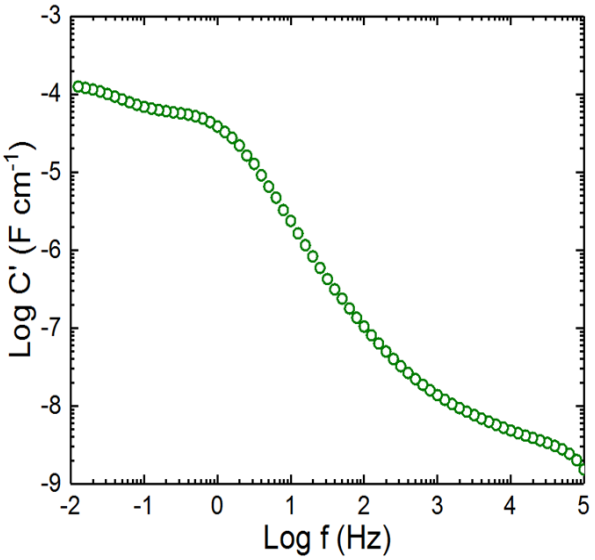

Figure 5.13 Spectroscopic plot of *C'* for a two-electrode sodium-ion battery prior to cycling it.

At the simplest level, the three main possible sources of impedance in a sodium-ion battery are the layered sodium transition metal oxide cathode, the liquid electrolyte, the hard carbon anode, and the interfaces between these different components. As prior to cycling the cell, the carbon anode can be considered a solely electronic conductor (and ionic insulator), and the electrolyte a solely ionic conductor (and electronic insulator), the most likely source of this blocking capacitance is the anode-electrolyte interface (Fig. 5.14). This is due to a build-up of charge on either side of the surface of the anode, which is unable to pass from one side to the other.

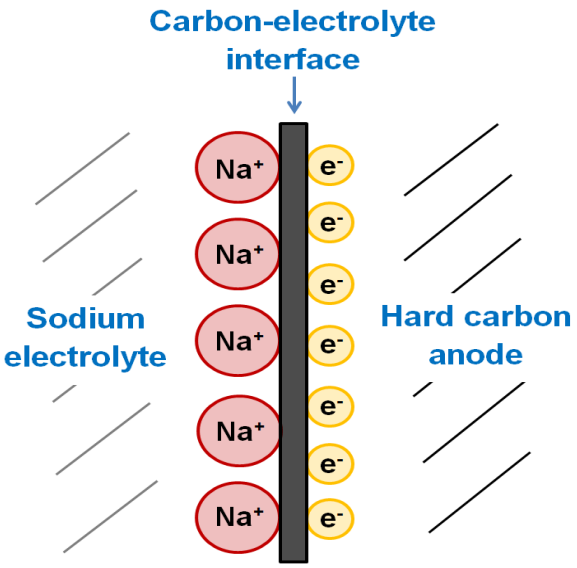

Figure 5.14 Schematic of the carbon-electrolyte interface prior to cycling it.

The impedance within the battery drastically changes after the cell is fully charged for the first time (Fig. 5.15). The Nyquist plot (a) now consists of a semi-circle with a non-zero intercept at about 300 Ω cm, a second arc from approximately 1.25 kΩ cm to 1.6 kΩ cm, and a low-frequency non-vertical spike. This equates to at least three resistive components: 300 Ω cm, 950 Ω cm, and 300 Ω cm. To a first approximation, the equivalent electrical circuit for this Na-ion battery (b) is now two parallel *RC* elements, a resistor, and a Warburg all connected in series to one another. The Warburg impedance element is typically used to reflect diffusion processes, and represents the low-frequency diagonal line in the Nyquist plot. Perhaps the most important thing to note is that the overall resistance within the cell has decreased dramatically from ~ 24 kΩ cm to ~ 1.6 kΩ cm upon the start of cycling.

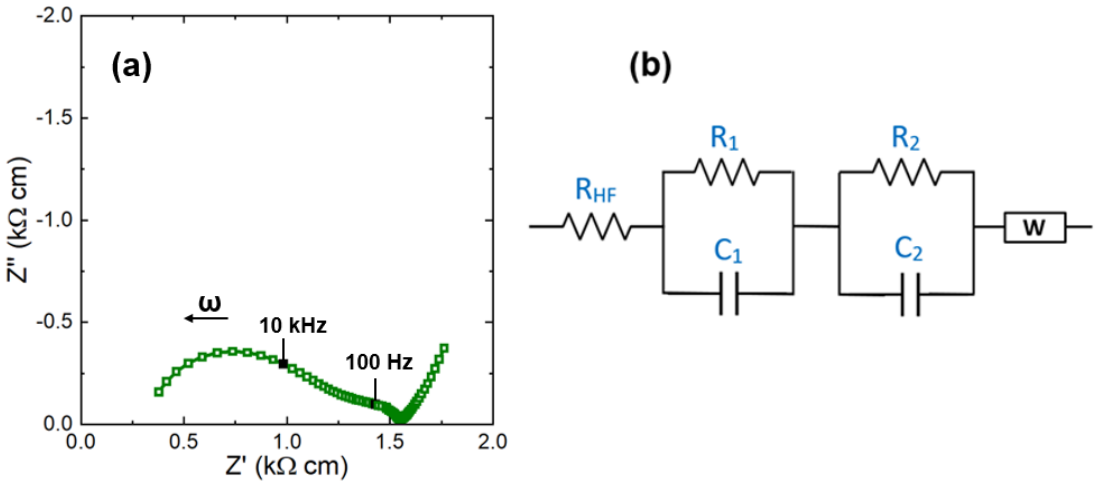

Figure 5.15 Impedance data for a sodium-ion battery after it has first been fully charged. (a) Impedance complex plane plot. (b) Equivalent electrical circuit.

During the first charge of the battery, a current is applied so that sodium ions are removed from the layered transition metal oxide cathode, transported through the liquid electrolyte, and inserted into the hard carbon anode. The battery is then held at constant voltage to ensure that the maximum possible amount of sodium has been deposited into the carbon matrix, and hence, to enhance capacity. The chemical compositions of the cathode and anode change on first charging the battery. The cathodic layered rock salt type structure loses some sodium from its structure, and the anode, which previously possessed none, receives Na. The first charge of

lithium-[14] and sodium-ion[15] batteries is also known to create a solid electrolyte interphase (SEI) on the surface of the anode. This limits further reaction between the anode and alkali metal ions, and is therefore considered essential for efficient operation of a battery. The overall drop in resistance seen when charging up the Na-ion battery could be associated with a reduction in strain from the layered oxide cathode on removal of sodium from its structure, or with the deposition of sodium in the anode and formation of the SEI layer improving the overall conductivity of the battery system. In order to pinpoint what it is that lowers the resistance of the battery upon cycling, a separation of the impedances associated with each electrode would be useful; for instance, by utilising three-electrode measurements.

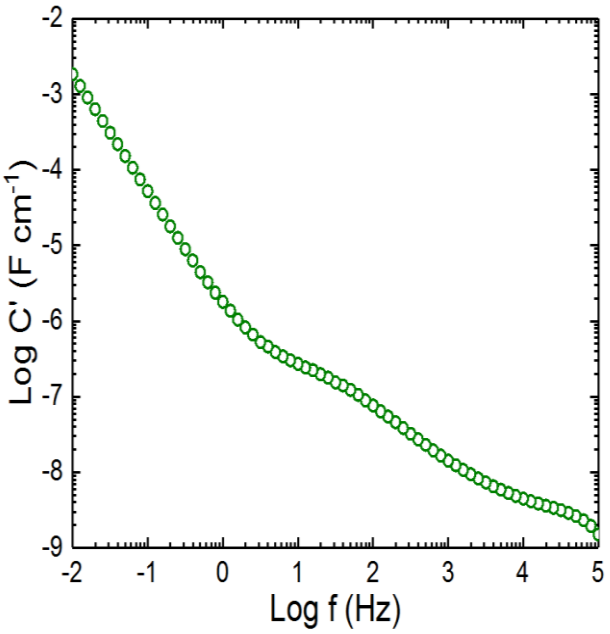

Figure 5.16 Spectroscopic plot of *C'* for a two-electrode sodium-ion battery after it has first been fully charged.

The low-frequency spike in the Nyquist plot (Fig. 5.15) after charging the Na-ion battery indicates the presence of an imperfect blocking capacitor. This is in agreement with what is seen in the capacitance plot (Fig. 5.16) in the charged state. Here, the high-frequency plateau at ~ 5 nF cm^{-1}, which existed prior to cycling the cell, is still present. However, the low-frequency plateau around 10-100 μF cm^{-1} in Figure 5.13 has now been replaced by an increasing capacitance greater than 10^{-3} F cm^{-1} at 0.01 Hz. This indicates that there is now significant charge storage due to an electrochemical process taking place. There is also an additional plateau, which has

appeared around 200 nF cm^{-1}, which could be associated with the creation of the solid electrolyte interphase. Thus, after charging, it appears as if the carbon-electrolyte interface has changed from a perfect capacitor to a leaky capacitor due to Na^+ ions crossing over to the anode side.

Another impedance formalism that can be useful to examine is the electrical modulus, *M''*. Figure 5.17 shows combined spectroscopic plots of *Z''*/*M''* for a sodium-ion battery after it has been fully charged for the first time. There are two peaks present in the *Z''* plot: a large one at high frequency with a value of around 350 Ω cm, corresponding to the semi-circle with the non-zero intercept in the Nyquist plot, and a smaller peak around 100 Hz, with a value of 100 Ω cm, which coincides with the mid-frequency arc in the Nyquist plot. The tail of the *Z''* peak at low frequency is associated with the blocking capacitance from the carbon-electrolyte interface. The rising *M''* at high frequency indicates the possibility of an additional component, however, an EIS scan accessing higher frequencies is required in order to determine this.

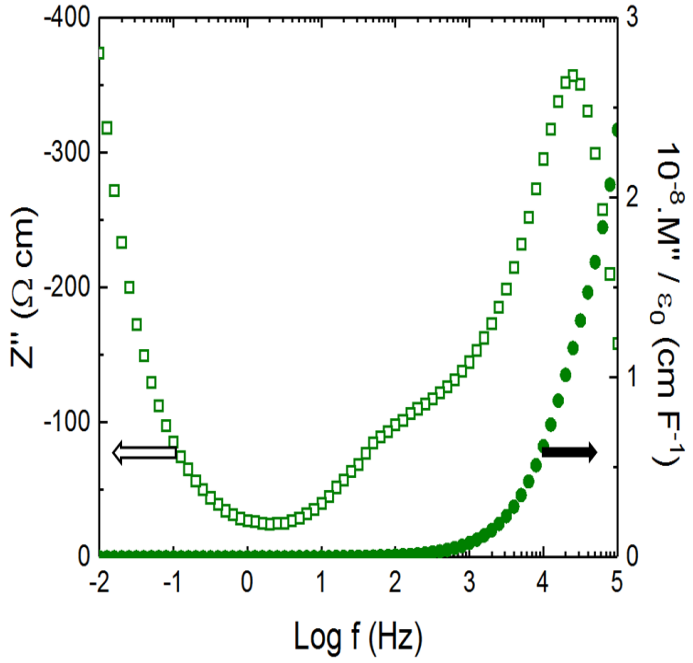

Figure 5.17 Spectroscopic plots of -*Z''* and *M''* for a two-electrode sodium-ion battery after it has first been fully charged.

An impedance measurement was also performed after the battery had first been fully discharged in order to see how the resistances and capacitances inside the cell changed. Figure 5.18 shows impedance spectra using a range of different complex formalisms and graphical presentations, so that all these data can be viewed together simultaneously. The Nyquist plot in (a) shows a high-frequency arc with a non-zero intercept and a larger low-frequency distorted (broadened) semi-circle. There are at least three resistive components with values roughly 0.4, 1.6 and 7 kΩ cm, giving a total cell resistance of ~ 9 kΩ cm. This is much larger than that measured for the battery in the charged state, ~ 1.6 kΩ cm. To a first approximation, the equivalent electrical circuit for this Na-ion battery would now be two parallel *RC* elements and a resistor all connected in series to one another. A significant difference that can be seen on discharging the battery is that there is a change from the high-frequency component dominating the resistance to the low-frequency one. This is seen more clearly in the plot of *Z''/M''*. In the charged state (Fig. 5.17) there is a much larger *Z''* peak for the high-frequency component, and after discharge (Fig. 5.17 (b)), the low-frequency peak is bigger. Using the same discharge data, a plot of capacitance, *C'* against frequency, (c) shows the reappearance of a low-frequency plateau at 50-120 μF cm^{-1}, which resembles what was seen prior to cycling the cell (Fig. 5.13).

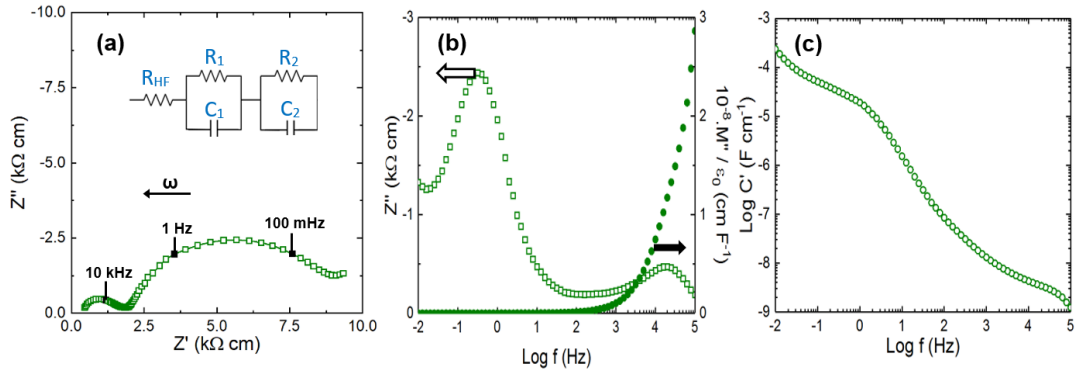

Figure 5.18 Impedance data for a sodium-ion battery after it has first been fully discharged. (a) Impedance complex plane plot with equivalent electrical circuit. Spectroscopic plots of -*Z''* and *M''* (b), *C'* (c).

During discharge of the cell, the direction of current used to charge the battery is reversed. This removes the sodium from the carbon anode, transports it through the electrolyte, and reinserts it back into the layered oxide cathode. The high-frequency arc (a) looks similar to what is seen in the Nyquist plot before the cell is first cycled

(Fig. 5.11), however, the lower frequency component appears to have collapsed into a much smaller arc. This broad response is likely to consist of multiple components - possibly due to contribution from both electrodes - but this is not possible to determine solely from two-electrode measurements. The reappearance of the high capacitance (10-100 μF cm^{-1}) at low frequency (c) is attributed to the removal of all (or close to all) the Na from the carbon anode, thus returning the carbon-electrolyte interface to a close-to perfect double layer capacitor, which existed prior to the start of cycling.

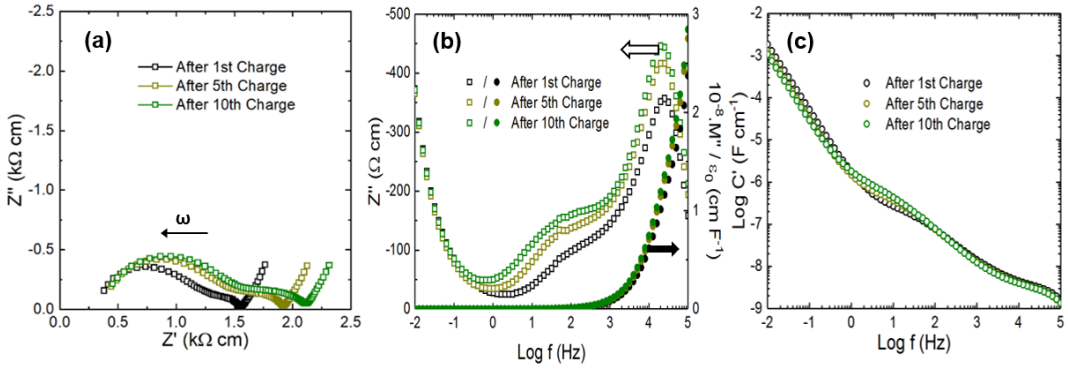

Figure 5.19 Impedance data for a sodium-ion battery after the first, fifth and tenth charge. (a) Impedance complex plane plots. Spectroscopic plots of $-Z''$ and M'' (b), C' (c).

In order to relate a rise in cell impedance to a drop in battery performance with cycle life, it is necessary to apply EIS after successive charges and discharges. This was carried out for the first ten cycles. An impedance dataset in Figure 5.19 presents three different complementary formats for the first, fifth and tenth cycle for a sodium-ion battery in the charged state. In (a), the impedance complex plane plot shows that the resistances of both arcs increase with cycle number. This is seen more clearly for the Z'' values in the combined spectroscopic plots in (b). The high-frequency resistance of the non-zero intercept, however, does not appear to alter significantly with cycling. Plots of capacitance, C' against frequency for the same data, (c), show a slight increase in the capacitance of the mid-frequency plateau on cycling.

The resistances and capacitances for a fully-charged sodium-ion battery across the first ten cycles are shown in Table 5.1. These components correspond with the

equivalent electrical circuit in Fig. 5.15 (b). The total resistance (R_{Tot}) is a sum of the resistances of each individual component (Eq. 2.34). The capacitances of component 1 and 2 were calculated using Eq. 5.3, which is rearranged from Eq. 2.27. The capacitance of the low-frequency spike was calculated using Eq. 5.4, which is a combination of Equations 2.27 and Eq. 2.38.

$$C = \frac{1}{2\pi f_{max} R} \tag{5.3}$$

$$C = -\frac{1}{2\pi f_{max} Z''} \tag{5.4}$$

Table 5.1 Resistances and capacitances for a fully-charged sodium-ion battery across the first ten cycles.

Cycle No.	R_{HF} (Ω cm)	R_1 (Ω cm)	$C_1.10^9$ (F cm^{-1})	R_2 (Ω cm)	$C_2.10^6$ (F cm^{-1})	$W.10^2$ (F cm^{-1})	R_{Tot} (kΩ cm)
1	375	925	6.85	250	6.37	4.26	**1.55**
2	380	995	6.37	325	4.90	4.40	**1.70**
3	390	1000	6.34	370	4.30	4.31	**1.76**
4	400	1000	6.34	450	3.54	4.51	**1.85**
5	400	1050	6.03	470	3.39	4.35	**1.92**
6	400	1100	5.76	460	4.36	4.32	**1.96**
7	400	1100	7.25	490	4.09	4.24	**1.99**
8	400	1100	7.25	515	3.89	4.24	**2.02**
9	440	1110	7.19	525	4.80	4.19	**2.08**
10	450	1140	7.00	530	5.99	4.29	**2.12**

The capacitance values of C_1, C_2 and associated with the low-frequency spike (represented by a Warburg), stay fairly constant with cycling: ~ 7 nF cm^{-1}, ~ 6 μF cm^{-1} and ~ 40 mF cm^{-1} respectively. The high-frequency resistance, R_{HF}, increases only slightly, from 375 to 450 Ω cm, whereas the other two resistances increase more significantly, by about 250 Ω cm each. This results in the overall cell resistance increasing with successive cycles. The total cell resistance (R_{Tot}) is approximately

1.6 kΩ cm for the 1st, 1.9 kΩ cm for the 5th, and 2.1 kΩ cm for the 10th cycle. This is attributed to degradation mechanisms occurring that result in a rise in cell impedance. These could be associated with either the active or inactive components of the battery. For instance, volume changes are known to occur in the active materials with cycling, which result in a change in porosity and subsequently a loss of particle-to-particle contact.[16] Also, a corrosion of the current collectors is known to take place over time.[17] These processes hinder the kinetic transport of charged species and result in a cell impedance rise.

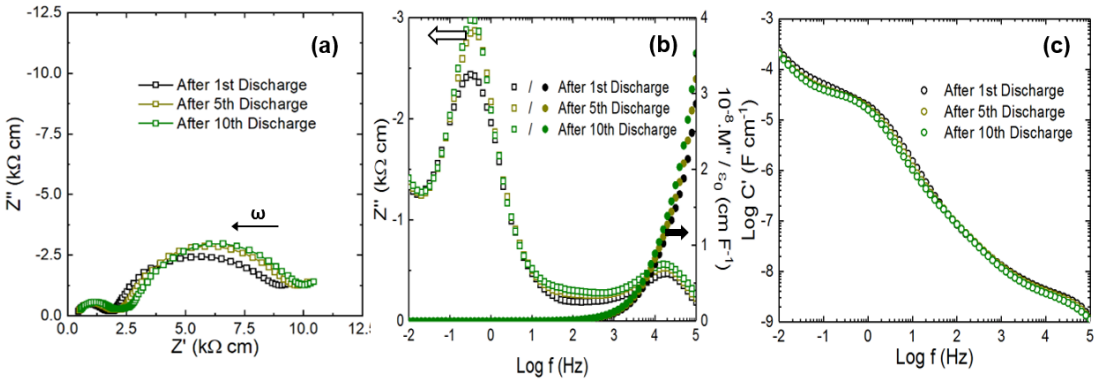

Figure 5.20 Impedance data for a sodium-ion battery after the first, fifth and tenth discharge. (a) Impedance complex plane plots. Spectroscopic plots of -*Z''* and *M''* (b), *C'* (c).

The impedance dataset for a sodium-ion battery in the discharged state is presented in Figure 5.20. Similar to charged data (Fig. 5.19), the high-frequency resistance (non-zero intercept) in (a) does not appear to alter greatly with cycling. The increase in the resistances of the other components is best demonstrated by the combined spectroscopic plots in (b), with the growth in *Z''* peak particularly prevalent for the low-frequency response between the first and fifth discharge. The *C'* plots displayed in (c) do not appear to change much during cycling for the battery in the discharged state.

Table 5.2 displays the resistances and capacitances for the sodium-ion battery in the discharged state, corresponding to the equivalent electrical circuit in Fig. 5.18 (a). The capacitance values of C_1 and C_2 stay fairly constant with cycling: ~ 6 nF cm^{-1} and 60-70 μF cm^{-1} respectively. As the high-frequency resistance does not alter significantly with cycling, by just 100 Ω cm across the first ten cycles, this means it

is probably the resistance associated with the sodium-ion electrolyte, as this is unlikely to change significantly upon charge and discharge for the first few cycles. The value of R_1 increases slightly, by around 280 Ω cm across the first ten cycles, but the most significant resistance rise is for R_2, by almost 1 kΩ cm between cycles 1 and 2. This results in the overall cell resistance increasing from around 9 kΩ cm to 10 kΩ cm between cycles 1 and 2, and again points towards degradation mechanism(s) occurring.

Table 5.2 Resistances and capacitances for a fully-discharged sodium-ion battery across the first ten cycles.

Cycle No.	R_{HF} (Ω cm)	R_1 (kΩ cm)	$C_1.10^9$ (F cm^{-1})	R_2 (kΩ cm)	$C_2.10^5$ (F cm^{-1})	R_{Tot} (kΩ cm)
1	400	1.47	5.41	7.13	7.06	**9.00**
2	440	1.56	6.44	8.00	6.29	**10.0**
3	460	1.54	6.52	8.00	6.29	**10.0**
4	495	1.56	6.46	7.95	6.33	**10.0**
5	500	1.63	6.18	7.88	6.39	**10.0**
6	500	1.63	6.18	7.88	6.39	**10.0**
7	500	1.75	5.74	7.75	6.49	**10.0**
8	500	1.75	5.74	7.75	6.49	**10.0**
9	500	1.75	5.74	7.75	6.49	**10.0**
10	500	1.75	5.74	7.75	6.49	**10.0**

The two-electrode EIS measurements give an insight into how the impedance changes within a sodium-ion battery with cycle number. Prior to cycling the cell, data are best represented to a first approach by two parallel *RC* elements, a resistor and a capacitor all connected in series to one another. The impedance spectrum can be seen to change dramatically upon first charging the cell, with the total cell resistance decreasing significantly also, from about 24 to 1.6 kΩ cm. Charged and discharged data also differ substantially from each other, but to a first approximation both are modelled by a resistor and two parallel *RC* elements. The charged plot also

contains an additional low-frequency non-vertical spike, indicating some blocking capacitance effect, which is attributed to (see later results) the carbon-electrolyte interface. The non-zero high-frequency resistance in the impedance plots is thought to be due to the electrolyte as it does not alter significantly with cycling.

After discharge, the overall cell resistance is far greater, ~ 9 kΩ cm, compared to the battery in the charged state. Successive charges and discharges across ten cycles see the total resistance increasing (around 1.6 to 2.25 kΩ cm and 9 to 10 kΩ cm respectively), indicating that degradation mechanisms are occurring. It appears as if data are easier to analyse by utilising the different complex impedance formalisms, particularly *C'* data, which makes changes upon charge and discharge more visible. While increases in resistances point towards evidence of ageing mechanisms occurring, further work is needed in order to pinpoint what precisely these degradation routes are. Ultimately, in order to analyse where impedances arise from for a multi-component device such as a battery, it is necessary to separate out problem processes/interfaces by use of three-electrode EIS measurements.

5.3.3 Three-Electrode Impedance Studies

Two-electrode measurements are useful for gaining an overview of the rise in cell resistances. However, the technique is constrained when assigning these rises to precise processes and cell components. Three-electrode measurements, where three EIS measurements are performed simultaneously, should make it possible, at least in theory, to distinguish between the impedances of the cathode and anode and measure how resistances associated with each individual electrode change with cycling.

Impedance scans (0.01 – 1,000,000 Hz) were performed across the first ten cycles for an Na-ion three-electrode pouch cell, with a measurement carried out after every complete charge/discharge. EIS was also performed prior to cycling the cell in order to gather information about the battery in its assembled state. It has already been demonstrated that the cycling of two- and three-electrode cells is comparable in terms of capacity and coulombic efficiency (Section 5.3.1). However, in order for meaningful interpretations to be deduced from EIS measurements, it is to be expected that three-electrode full-cell data recorded should resemble closely the

impedance spectra seen for two-electrode batteries. This would mean that the introduction of a reference electrode does not cause the impedance results to differ in any way from what is seen inside a regular two-electrode cell. Figure 5.21 compares two-electrode and three-electrode EIS plots at different states of charge across the first ten cycles. It can be seen in all instances that the impedance complex plane plots look very similar to one another. This indicates that it is possible to extract meaningful results from EIS measurements performed on three-electrode cells and make interpretations that can be applied to commercially-relevant two-electrode batteries.

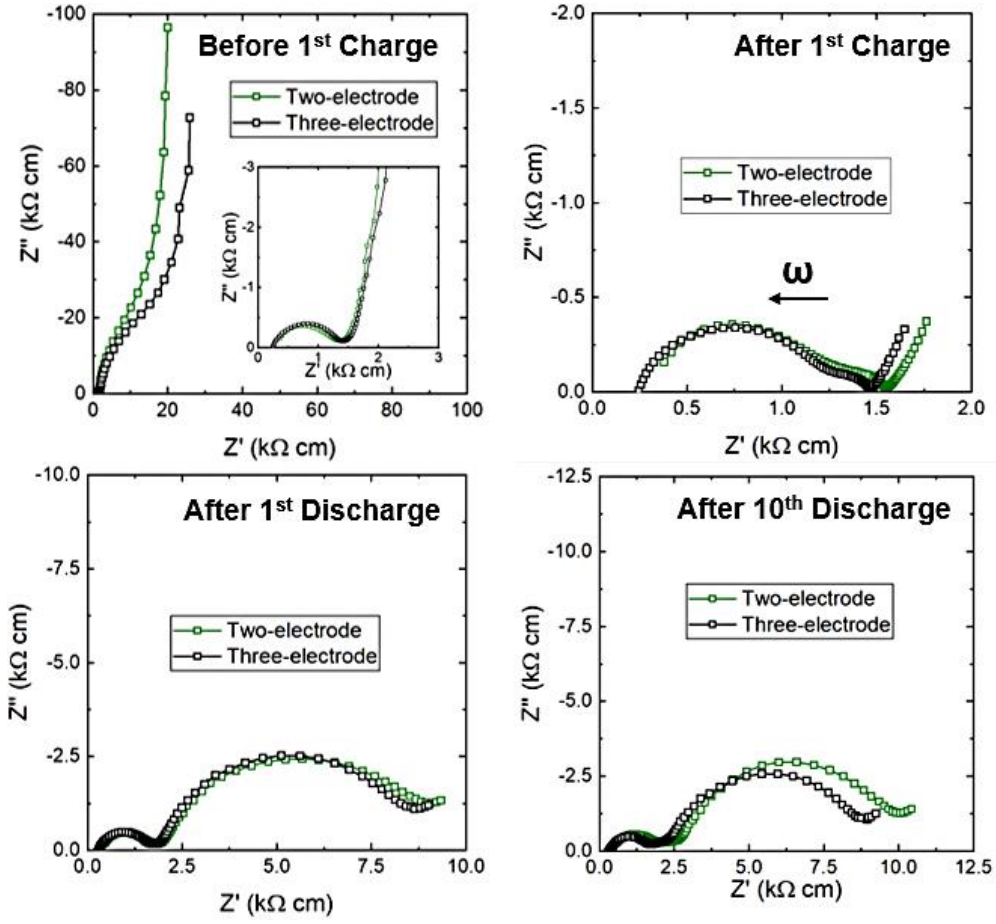

Figure 5.21 Comparison of two- and full-cell three-electrode impedance complex plane plots.

Having proven that three-electrode full-cell impedance measurements are consistent with what are seen for regular two-electrode cell designs, results can be examined and analysed for three-electrode data. Impedance complex plane plots for a three-

electrode sodium-ion battery, prior to cycling, are displayed in Figure 5.22. The full-cell measurement (black) shows what appears to be the start of a semi-circle, which becomes close to a vertical spike at low frequency, and has a total resistance of ~ 24 kΩ cm. The zoomed-in section reveals another high-frequency arc, which crosses the x-axis at around 250 Ω with a resistance of approximately 1.25 kΩ. The cathode data (red) is seen to closely resemble that of the full-cell, especially at high frequency. The only considerable difference is that the cathode data does not contain a low-frequency vertical spike. Hence, this suggests that this feature of the impedance plot must be solely associated with the anode. This is confirmed in data for the anode (blue), which consists of a close-to vertical spike near the origin.

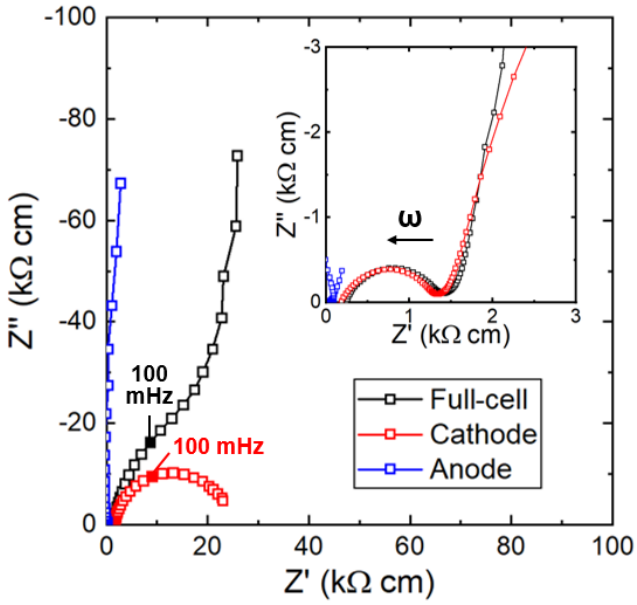

Figure 5.22 Full-cell, cathode and anode impedance complex plane plots for a three-electrode sodium-ion battery prior to cycling. Inset shows zoomed-in high-frequency data.

As with the two-electrode measurements, it can be useful to plot the EIS results using a range of different complex formalisms in order to highlight different aspects of collected data. Figure 5.23 shows the capacitance, *C'*, plotted against the frequency on logarithmic scales for a three-electrode cell prior to cycling it. These spectra agree with the impedance complex plane plots, in that data for the full-cell and cathode measurements closely resemble one another. Both of these possess a low-frequency plateau around 50-120 μF μcm^{-1}, and another at about 5 nF cm^{-1} at

higher frequency. However, the anode capacitance plot is different from these in that while it has two plateaus at the same frequencies, both of these are higher in terms of their capacitance values. There is a more distinct flat plateau at lower frequency with a capacitance of ~ 0.25 mF cm^{-1}, as well as a secondary plateau around 50 nF cm^{-1}. A capacitance in the millifarad range is consistent with an electrochemical double layer effect. Hence, both the impedance complex plane and capacitance plot for anode data from the three-electrode measurement agree with the previous assertion made from the two-electrode results, that the carbon-electrolyte interface is a blocking capacitor prior to performing any cycling. Therefore, from these three-electrode measurements, it is possible to deduce that the anode interface is a blocking capacitance with a very large leakage/charge-transfer resistance, which controls the resistance for a sodium-ion battery in its uncycled assembled state.

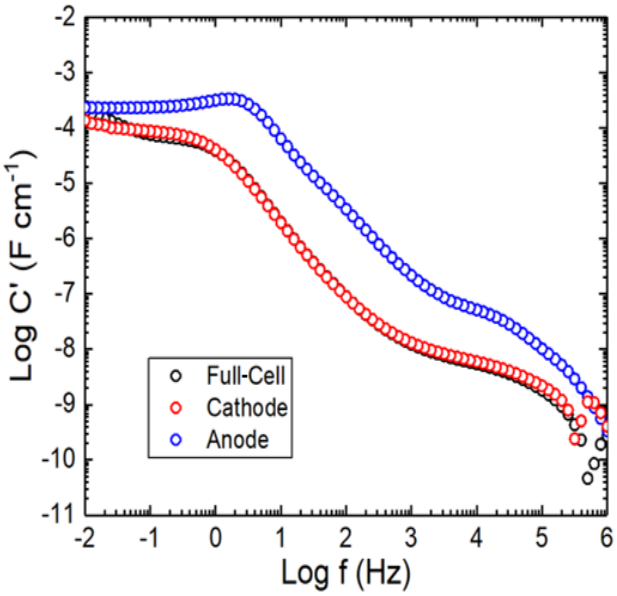

Figure 5.23 Full-cell, cathode and anode spectroscopic plots of *C'* for a three-electrode sodium-ion battery prior to cycling it.

Impedance data for a three-electrode cell after it has first been fully charged are displayed in Figure 5.24. The Nyquist plots (a) for the cathode and full-cell once again closely resemble one another. Both of these are able to be approximately represented by two parallel *RC* elements in series with a resistor representing the non-zero high-frequency intercept, and a Warburg, which represents the diagonal low-frequency spike. The three-resistive components for the cathode, from high to

low frequency, are roughly 190 Ω cm, 950 Ω cm, and 300 Ω cm. The anode measurement has some form of resistive contribution associated with it, as it appears to cross the real axis at low frequency around 100 Ω cm. There is also a long tail at high frequency, with an increasing capacitance. This is most likely to be due to inductive effects from the non-inert component responding to the AC signal. The anodic resistance appears to be responsible for the discrepancy seen between the cathode and full-cell data at low frequency. This is seen more clearly in the *Z''* plot (b), with there being a small hump in the anode spectrum at about 100 Hz. The *C'* plots in (c) are once again similar for the cathode and full-cell data, which both have plateaus with values of 1-10 and ~ 200 nF cm^{-1}. The anode plot has plateaus at the same frequencies, but with higher capacitance values once again: 50-80 nF cm^{-1} and ~ 8 μF cm^{-1} respectively. There is also an increasing capacitance, at low frequency, for both electrodes. This is likely indicating significant charge storage due to electrochemical processes taking place, however, it may also be associated with geometric effects and the measurement of thinner regions at low frequency.

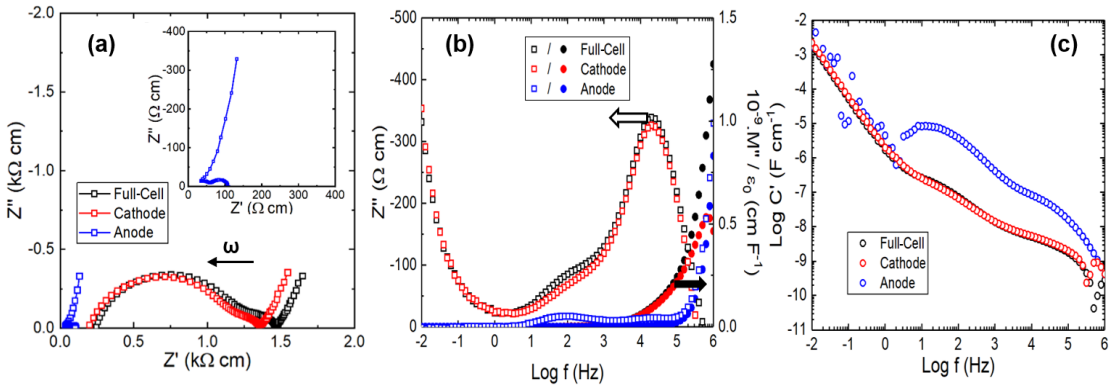

Figure 5.24 Full-cell, cathode and anode impedance data for a three-electrode sodium-ion battery after it has first been fully charged. (a) Impedance complex plane plots with inset showing anode data on an expanded scale. Spectroscopic plots of -*Z''* and *M''* (b), *C'* (c).

These three-electrode impedance measurements make it possible to draw conclusions about sodium-ion batteries that were not possible from two-electrode results alone. There is not much change in the impedance response at high frequency upon beginning to cycle the cell, but there is significant change at low frequency. This is perhaps best illustrated by the capacitance plots. These show a disappearance of the plateaus from 0.01-1 Hz, which have now been replaced by increasing

capacitance values towards low frequency. At the same time, an additional plateau has appeared for each measurement around 10 Hz, which could be associated with changes at the surfaces of the electrodes. It is now clear from the impedance complex plane plots, that the large reduction in resistance upon beginning to cycle the cell is due to the cathode. Hence, removal of Na from the layered oxide cathode results in a dramatic impedance decrease. The low-frequency diagonal spike in the Nyquist plot appears to also be a cathodic effect. Further evidence for this is the absence of a tail in the *Z''* anode plot at low frequency. Hence, this disagrees with our previous assertion from the two-electrode EIS results that the low-frequency spike is due to the diffusion of Na^+ ions into the hard carbon electrode. Instead, from these three-electrode results it is more likely to be due to diffusion processes in the active material of the cathode.

Three-electrode impedance data for a sodium-ion battery after it was fully discharged for the first time are displayed in Figure 5.25. The impedance complex plane plots (a) show that there is a dramatic change in the spectra for each of the measurements compared to charged data. The total resistance for each measurement increases significantly: the full-cell ~ 8.5 kΩ cm, the cathode ~ 6 kΩ cm, and the anode ~ 2.5 kΩ cm. The approximate equivalent circuits for the cathode and full-cell are the same as for the charged state, but it is not clear whether or not a Warburg element is needed to represent a low-frequency spike. This may still be present in the impedance response, but off-scale; EIS scans to lower frequency would be required in order to confirm this. After discharge, while cathode and full-cell data still closely resemble each other at high frequency, there is a much greater disparity at low frequency. This is again demonstrated most clearly by the *Z''* plot in (b). The anode is responsible for making a significant contribution to the full-cell EIS plot at low frequency. Using the same discharge data, plots of capacitance, *C'* against frequency (c), show the reappearance of a low-frequency plateau at ~ 50 μF cm^{-1} for the full-cell and cathode data, and about 0.25 mF cm^{-1} for the anode spectrum. This anodic plot closely resembles what was seen prior to cycling the cell (Fig. 5.13).

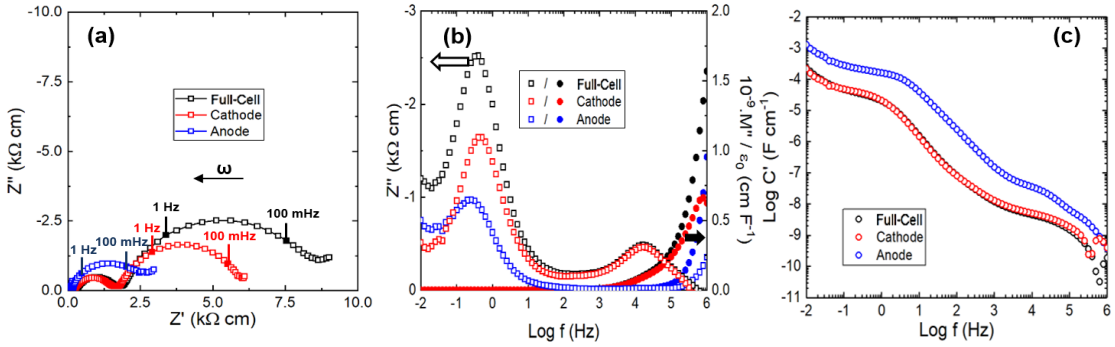

Figure 5.25 Full-cell, cathode and anode impedance data for a three-electrode sodium-ion battery after it has first been fully discharged. (a) Impedance complex plane plots. Spectroscopic plots of $-Z''$ and M'' (b), C' (c).

The total resistance for the cathode appears to have decreased on removing sodium and then re-inserting it into its structure - from around 24 to 6 kΩ cm. However, the total anodic resistance has increased significantly during the same time - from ~ 0.1 to ~ 2.5 kΩ cm. As, after discharge, there is no longer any (significant amount of) sodium in the hard carbon structure, this large anodic resistance may be associated with the solid electrolyte interphase on the surface. From the two-electrode data in Section 5.3.2, it was suggested that the broad resistive arc seen from mid to low frequency (present in the full-cell measurement in Fig. 5.25 (a)) was likely to be due to a contribution from multiple components. It is now confirmed that this response is a combination of the impedances from both the cathode and anode. This is well illustrated in the Z'' plot in (b). From the impedance complex plane plots it appears as if the total resistance for the full-cell measurement (8.5 kΩ cm) is equal to the sum of that for the cathode (6 kΩ cm) and the anode (2.5 kΩ cm). This would suggest that a sum of the cathode and anode impedance spectra give the full-cell EIS spectrum (Eq. 5.5).

$$Z^*_{Full-Cell} = Z^*_{Cathode} + Z^*_{Anode} \quad (5.5)$$

To determine whether Equation 5.5 holds true, the Z' and Z'' values for the anode and cathode at each frequency can be added together and summation EIS plots generated. Figure 5.26 indicates that when the values for the cathode and anode are added together, the combined spectra are remarkably similar to that of the full-cell. This is important in order to check the accuracy of the three-electrode measurements, and is not usually performed in literature. When the validity of the measurement was

checked, less than 6% difference was found between the sum of the anode and cathode impedance results and the full-cell. (The majority of this discrepancy arose from the *Z''* values at high frequency.) Furthermore, unlike with previous experiments, it has been demonstrated that this three-electrode technique works across a range of different complex impedance formalisms.[18] Often when utilising three-electrode measurements, corrections must be applied to the generated impedance spectra.[4,19] The absence of such a requirement here suggests that the novel three-electrode pouch cell configuration used in this work affords a superior measurement than many previous cell designs.

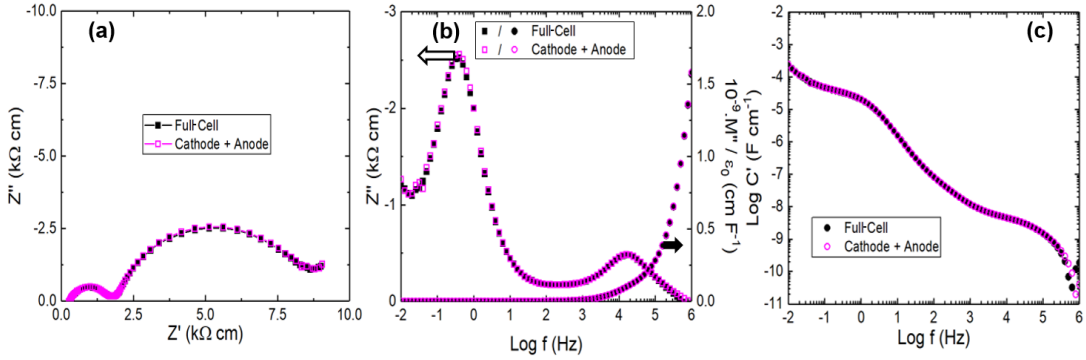

Figure 5.26 Full-cell impedance complex plane plot for a three-electrode sodium-ion battery after it has first been fully discharged and sum of the cathode and anode spectra. (a) Impedance complex plane plots. Spectroscopic plots of -*Z''* and *M''* (b), *C'* (c).

In order to determine how the resistances and capacitances associated with each electrode in a sodium-ion battery change over time, three-electrode EIS measurements were recorded after successive charges and discharges. Figure 5.27 compares impedance spectra for a three-electrode cell after the first and tenth charge. The Nyquist plots in (a) show how the total resistance associated with the full-cell measurement and cathode both increase with cycling: for the full-cell from approximately 1.5 to 1.8 kΩ cm, and cathode from 1.4 to 1.7 kΩ cm. The plot in (b) shows that this increase comes from a combination of both low and high frequency resistive components. The resistance for the anode increases slightly from 100 to 150 Ω cm. In the capacitance plots (c), there appears to be possibly an additional plateau emerging in the anode plot after 10th charge at lower frequency (~ 1 Hz). This has a

capacitance value around 70 μF cm^{-1}. However, it is difficult to say definitively because *C'* anode data is increasingly noisy towards lower frequency.

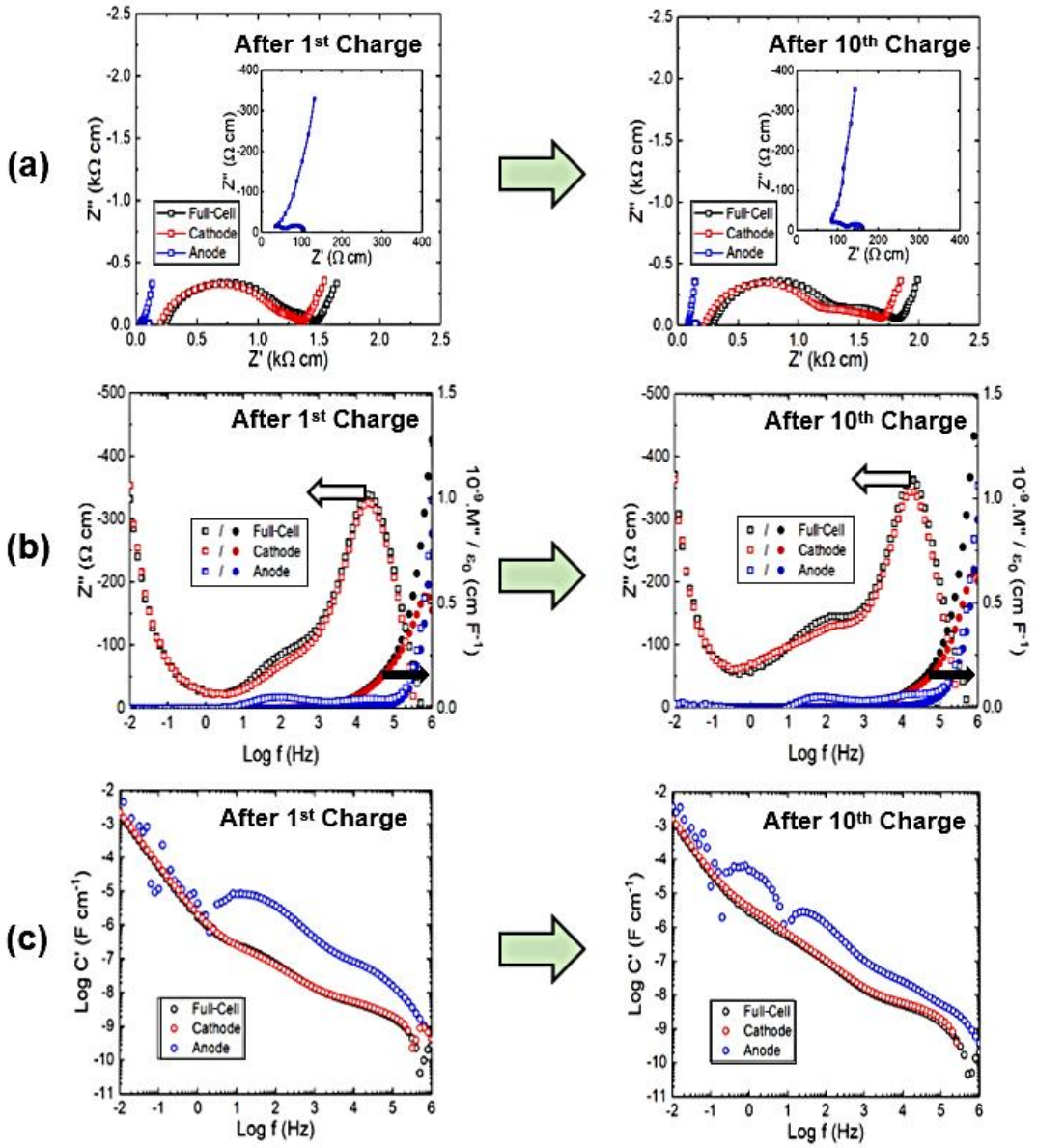

Figure 5.27 Full-cell, cathode and anode impedance data for a three-electrode sodium-ion battery after the first and tenth charge. (a) Impedance complex plane plots with inset showing anode data on an expanded scale. Spectroscopic plots of $-Z''$ and M'' (b), C' (c).

The origin of the increase in overall cell resistance after successive charges is clearly due to a growth in the cathodic contribution to the overall battery impedance. This is primarily as a result of an increase in the resistive contribution from the low-frequency component/arc in the Nyquist plot. This is seen most evidently in the Z''

plot in Fig. 5.27 (b) with the cathode response growing over time. The low-frequency component may be associated with the active oxide material in the cathode, or a charge-transfer process occurring at the surface, but it is not possible to determine this from these measurements alone. The small resistance from the anode does not alter significantly across the ten cycles, indicating that when the battery is charged and the hard carbon anode full of Na, there is a low and constant impedance associated with it.

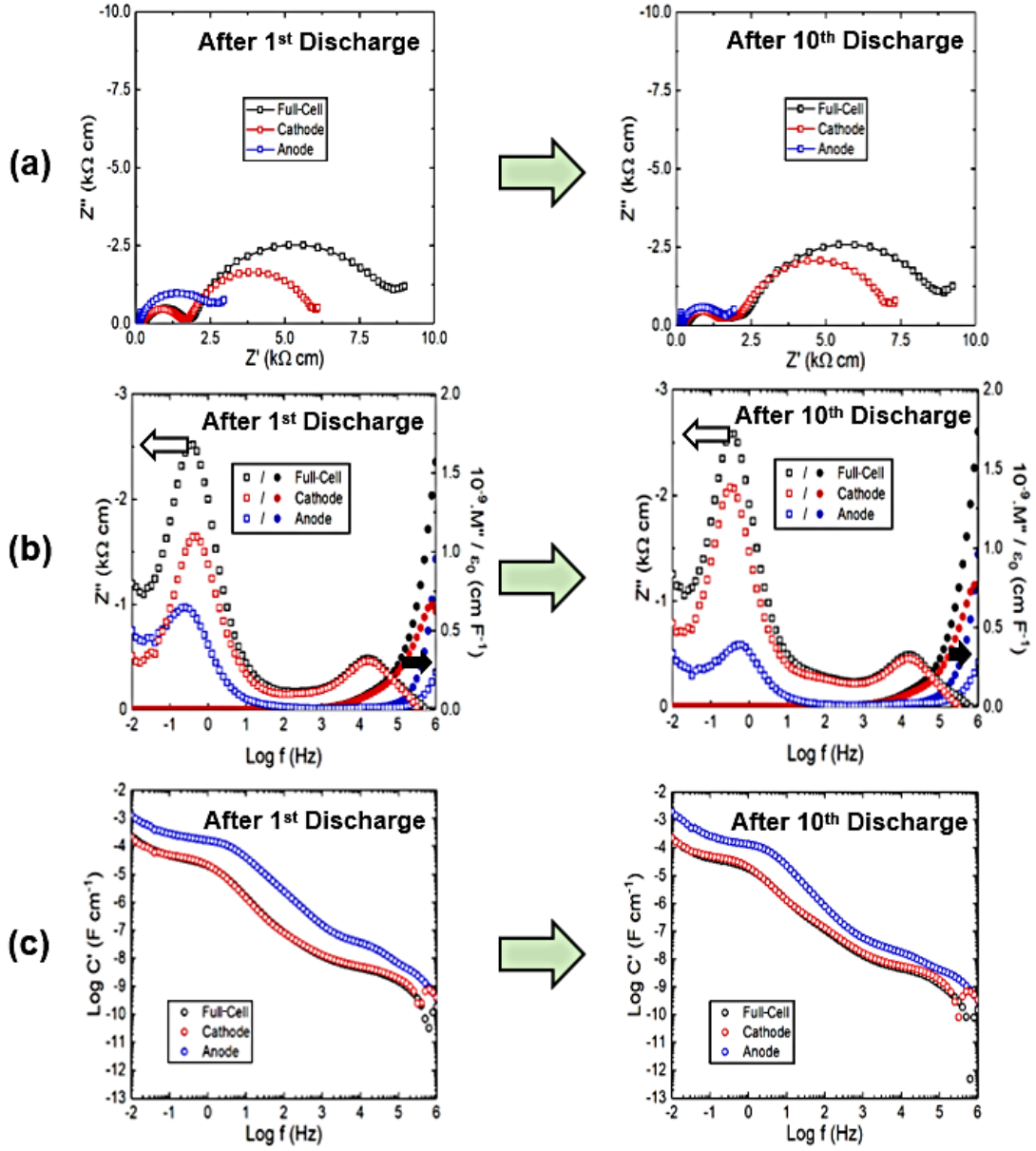

Figure 5.28 Full-cell, cathode and anode impedance data for a three-electrode sodium-ion battery after the first and tenth discharge. (a) Impedance complex plane plots. Spectroscopic plots of $-Z''$ and M'' (b), C' (c).

EIS data were also recorded and plotted using different complex formalisms to compare the impedance spectra after the first and tenth discharge (Fig. 5.28). It can be seen from the Nyquist plots in (a), that unlike with charged data, there is not a significant increase in the resistance of the full-cell, which stays constant at around 8.5 kΩ cm. However, the contributions from each individual electrode can be seen to change. The resistance of the cathode rises from approximately 6 to 7 kΩ cm, and simultaneously the anode decreases from about 2.5 to 1.5 kΩ cm. This change in internal cell resistances over time is again associated with the low-frequency components in the impedance response. This is where the greatest significant change is seen to occur, illustrated most clearly in the *Z''* plots in (b). Here, the peak in the cathode *Z''* plot grows from around 1.6 to 2 kΩ cm, and the anode decreases from ~ 950 to ~ 600 Ω cm. The *C'* plots in (c) show that the capacitance values for each plateau increase very slightly between the first and tenth discharge. The reduction in anodic resistance across the first few cycles may be attributed to a stable solid electrolyte interphase forming over time. The SEI layer is known to form initially during the first cycle, but its chemical composition may continue to alter across the first few successive charges/discharges.[20] Hence, it may be the case that after ten cycles, the initial resistance associated with it has decreased.

5.4 Conclusions

In this chapter, electrochemical impedance spectroscopy was performed on full-cell sodium-ion batteries for the first time. This was done using both two- and three-electrode measurements performed on a commercially-relevant pouch cell type. This novel design was fabricated by inserting a reference electrode between two separators. Measurements were recorded prior to cycling the cell, and after every charge/discharge across the first ten cycles. Results were plotted using different complex formalisms in order to highlight different aspects of collected data, an approach not previously undertaken for analysing impedance measurements for batteries.

Comparison between two- and three-electrode results show that the different cell designs are comparable in terms of voltage-time profiles, capacities, coulombic efficiencies and EIS results. This means that the three-electrode results can be used to make interpretations about commercially relevant two-electrode batteries. Furthermore, it has been demonstrated across a range of formalisms that the sum of the positive and negative electrode impedances is similar to that of the full-cell (within 6% difference). This is better than previously-seen, three-electrode results,[18] and indicates that the novel three-electrode pouch cell configuration used in this works affords a superior measurement to former cell designs. Furthermore, using a range of different complex formalisms to view impedance data was found to afford a more in-depth analysis of the results. Spectroscopic plots of Z'' and C' highlight how components at different frequencies change with cycling and contribute to cell resistances and capacitances.

Two-electrode impedance results show that there is a reduction in overall cell resistance on beginning to cycle sodium-ion batteries. The EIS spectra then differ significantly for whether the cell is in the charged or discharged state, with the total resistance after discharge significantly greater compared to that after charge. There is gradually a growth in total resistance over time in both states, thus indicating the occurrence of degradation (ageing) mechanisms. The three-electrode results indicate that the anode interface is mainly responsible for impedance in sodium-ion batteries prior to cycling. This reduced dramatically on first charging the cell, with the

cathode then dominating the resistance of the battery. This continues to grow after every cycle. The resistance associated with the anode stays fairly small and constant in the charged state (~ 100 Ω cm), whereas it steadily decreases in the discharged, from around 2.5 to 1.5 kΩ cm between cycles 1 and 10.

Overall, results are similar to those seem in lithium-ion batteries in certain ways, such as a dominating cathode impedance during cycling.[21] However, there are noticeable differences, such as a larger decrease in anodic resistance with cycling.[4,18] This discrepancy may be accounted for by a difference in solid electrolyte interphases between lithium- and sodium-ion batteries, which has previously been reported in the literature.[22] The SEI layer in Na-ion batteries is not well understood,[23] and a better comprehension of this may be required to account for the anodic impedances measured in this study. Future work is to try and determine the origin of the large cathodic impedance in sodium-ion cells. This will be looked at in the next chapter.

5.5 References

1 J. Vetter, P. Novák, M. R. Wagner, C. Veit, K.-C. Möller, J. O. Besenhard, M. Winter, M. Wohlfahrt-Mehrens, C. Vogler and A. Hammouche, *J. Power Sources*, 2005, **147**, 269–281.

2 U. Tröltzsch, O. Kanoun and H.-R. Tränkler, *Electrochim. Acta*, 2006, **51**, 1664–1672.

3 D. Andre, M. Meiler, K. Steiner, C. Wimmer, T. Soczka-Guth and D. U. Sauer, *J. Power Sources*, 2011, **196**, 5334–5341.

4 J. Song, H. H. Lee, Y. Y. Wang and C. C. Wan, *J. Power Sources*, 2002, **111**, 255–267.

5 F. Huet, *J. Power Sources*, 1998, **70**, 59–69.

6 G. Nagasubramanian, *J. Power Sources*, 1998, **70**, 59-69.

7 M.-S. Wu, P.-C. J. Chiang and J.-C. Lin, *J.Electrochem. Soc.*, 2005, **152**, A47-A52.

8 Y. S. Meng, PhD Thesis, The Singapore-MIT Alliance, 2005.

9 Y. Wen, K. He, Y. Zhu, F. Han, Y. Xu, I. Matsuda, Y. Ishii, J. Cumings and C. Wang, *Nat. Commun.*, 2014, **128**, 052210(1)-052210(15).

10 Gamry, *Bascis of Electrochemical Impedance Spectroscopy*, https://www.gamry.com/application-notes/EIS/basics-of-electrochemical-impedance-spectroscopy/, (accessed September 2018).

11 K. Bundy, M. Karlsson, G. Lindbergh and A. Lundqvist, *J. Power Sources*, 1998, **72**, 118-125.

12 J. T. S. Irvine, D. C. Sinclair and A. R. West, *Adv. Mater.*, 1990, **2**, 132–138.

13 M. A. Hernández, N. Masó and A. R. West, *Appl. Phys. Lett.*, 2016, **108**, 152901.

14 E. Peled, *J. Electrochem. Soc.*, 1979, **126**, 2047-2051.

15 S. Komaba, W. Murata, T. Ishikawa, N. Yabuuchi, T. Ozeki, T. Nakayama, A. Ogata, K. Gotoh and K. Fujiwara, *Adv. Funct. Mater.*, 2011, **21**, 3859–3867.

16 J. Janek and W. G. Zeier, *Nat. Energy*, 2016, **1**, 1-4.

17 J. W. Braithwaite, A. Gonzales, G. Nagasubramanian, S. J. Lucero, D. E. Peebles, J. A. Ohlhausen and W. R. Cieslak, *J. Electrochem. Soc.*, 1999, **146**, 448-456.

18 M. L. Dollé, F. Orsini, A. S. Gozdz and J.-M. Tarascon, *J. Electrochem. Soc.*, 2001, **148**, A851-A857.

19 G. Hsieh, S. J. Ford, T. O. Masona and L. R. Pedersonb, *Solid State Ionics*, 1996, **91**, 191-201.

20 P. Verma, P. Maire and P. Novák, *Electrochim. Acta*, 2010, **55**, 6332–6341.

21 K. Amine, C. H. Chen, J. Liu, M. Hammond, A. Jansen, D. Dees, I. Bloom, D. Vissers and G. Henriksen, *J. Power Sources*, 2001, **97**–**98**, 684–687.

22 R. Mogensen, D. Brandell and R. Younesi, *ACS Energy Lett.*, 2016, **1**, 1173–1178.

23 Y. Pan, Y. Zhang, B. S. Parimalam, C. C. Nguyen, G. Wang and B. L. Lucht, *J. Electroanal. Chem.*, 2017, **799**, 181–186.

Chapter VI

Investigating the Dominating Cathode Impedance in Layered Oxide Sodium-Ion Batteries

6.1 Introduction

In the previous chapter, it was found that the impedance of the sodium-ion batteries studied was dominated by the cathode component during cycling. There was a large cathodic resistance prior to cycling the cell, which upon first charging, decreased significantly; it then increased again after the cell had been fully discharged. After ten cycles, the cathodic impedance had increased in both the charged and discharged states compared to after the first cycle, indicating the presence of some form of degradation (ageing) mechanisms associated with this electrode.

From a scientific point of view, it is clearly important to have an understanding of what causes this large and changing impedance at the cathode. Furthermore, any new knowledge of this may enable battery researchers and developers to overcome this in their fabrication procedures method in order to enhance the overall cell performance. As well as the state of health of a battery, a crucial parameter with which the impedance is known to vary is the state of charge.[1] Therefore, by performing impedance measurements, and extracting resistances and capacitances at different SoH and SoC, it may be possible to obtain a better understanding of the origin of this large cathodic impedance. As a battery undergoes dramatic changes during the first cycle, having a knowledge of how the impedance varies, in particular during the first charge/discharge, may aid in the analysis.

In this chapter, electrochemical impedance spectroscopy is applied to sodium-ion batteries at varying states of health and states of charge, in order to try and obtain a better understanding of the origin of the dominant cathode impedance. This is

performed using a range of different cell configurations, including three-electrode and symmetric battery designs, applied to the commercially-used pouch cell setup.

6.2 Experimental

6.2.1 Cell Designs

Four batteries were built and tested for each cell design to check the reproducibility of collected results. Analysis of collected data for these showed a close similarity between the cells. This ensures that data presented in this chapter, and conclusions drawn, are representative of a wider population.

6.2.1 (a) Two-electrode cell

Details are outlined in Section 5.2.2

6.2.1 (b) Three-electrode cell

Details are outlined in Section 5.2.2.

6.2.1 (c) Symmetric cathode cell

A symmetric cathode cell used in this work had the same design as a standard two-electrode pouch cell (Fig. 5.1), but the non-graphitizable hard carbon anode component was replaced by an additional Na[Ni,Mg,Mn,Ti]O_2 cathode (Fig. 6.1).

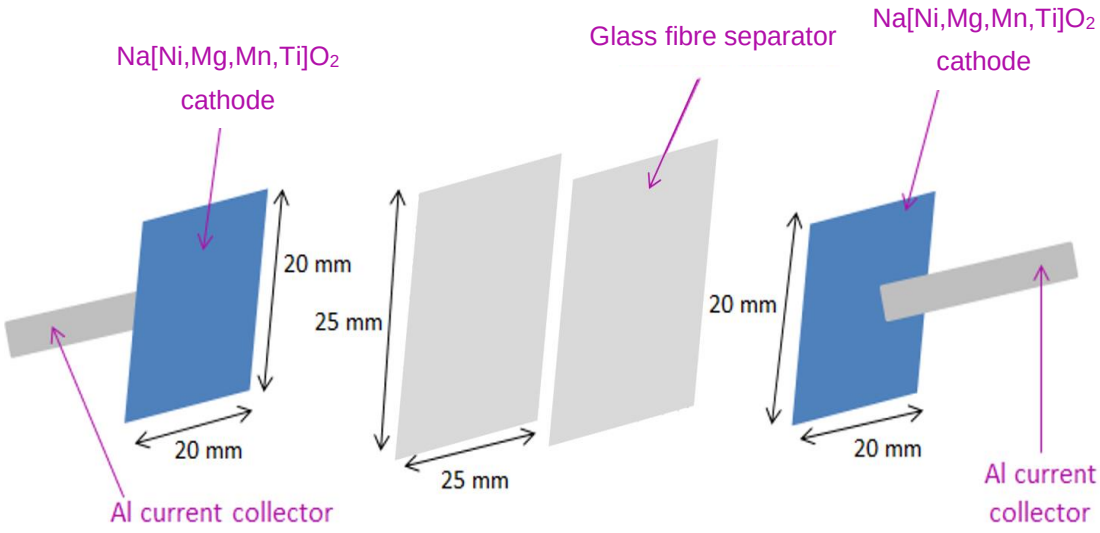

Figure 6.1 Symmetric cathode two-electrode pouch cell design.

6.2.1 (d) Separator cell

In order to measure the resistance of the electrolyte and separators, a 'separator cell' was built and tested. This had the same design as the symmetric cell, but both electrodes were replaced with sheets of aluminium (Fig. 6.2).

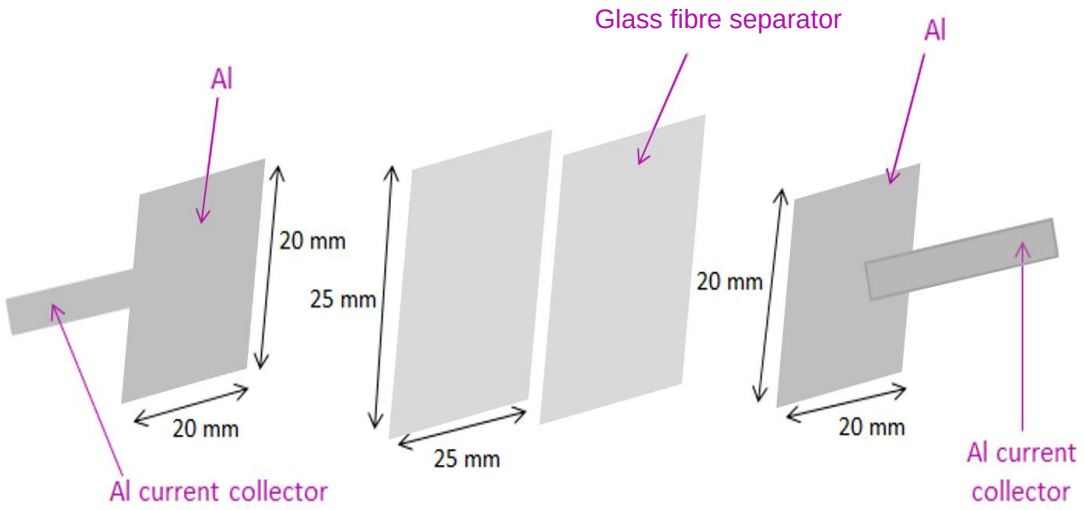

Figure 6.2 Separator cell design.

6.2.1 (e) Conductivity cell

For measuring the resistance of the electrolyte, a BioLogic high temperature conductivity cell (HTCC) was used (Fig. 6.3). The electrolyte was a solution of 0.5 M sodium hexafluorophosphate in an ethylene carbonate : diethyl carbonate : propylene carbonate (1:2:1) mixture. This was prepared in the glove box, with the solvent mixture dried over molecular sieves for 16 h, prior to dissolution of the salt. The conductivity cell was left in the glove box antechamber for 2 h under vacuum, prior to being assembled. A small amount (~ 0.7 ml) of liquid electrolyte was placed in a glass vial inside the glove box. Parallel platinum black electrodes on a glass holder were then lowered into the electrolyte and the lid attached. This formed an air-tight seal so that the electrolyte was not exposed to atmosphere during measurement. The cell had a geometric constant of 1.0 cm^{-1}.

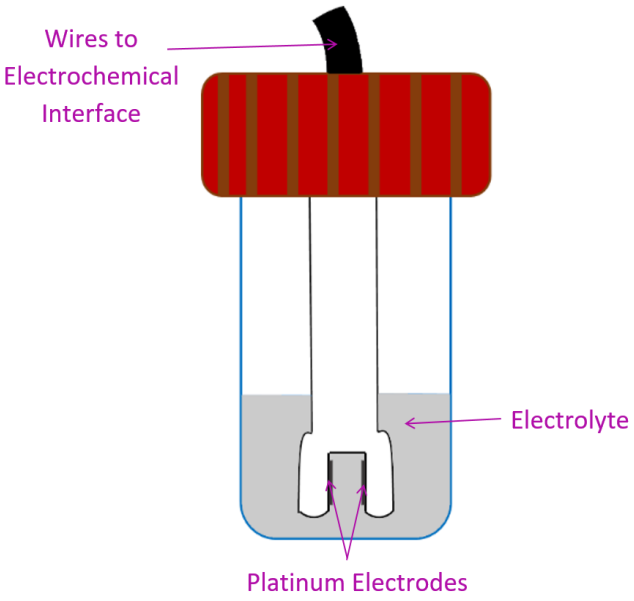

Figure 6.3 Conductivity cell.

6.2.2 Cell Testing Procedures

6.2.2 (a) Two-electrode, symmetric, separator and conductivity cells

The symmetric, separator, and two-electrode cells were tested using a Maccor Series 4000 Automated Test System. The wiring configuration was the same as used for two-electrode cells in Section 5.2.3. AC impedance measurements were performed using a frequency response analyser (Solartron Modulab). Electrolyte conductivity measurements were implemented using the same testing equipment, with the platinum electrodes connected to the electrochemical interface via banana clips. All cells were held at a constant temperature of 30 ± 0.5 °C using a Maccor Temperature Chamber. The cells were left for 32 h at 30 °C prior to performing an EIS scan to allow time to equilibrate. AC impedance measurements were performed by varying the frequency with a perturbation potentiostatic signal amplitude of 10 mV (peak to peak) from 10 mHz to 100 kHz (from 1 Hz for the conductivity cell).

6.2.2 (b) Three-electrode cells

Three-electrode cells were measured using the testing configuration outlined in Section 5.2.3. For cells with EIS performed after every charge/discharge, the testing procedure was also the same as outlined in this section. AC impedance

measurements were performed using a potentiostat with a parallel frequency response analyser (Solartron Pstat 1470E/FRA 1455A). All cells were held at a constant temperature of 30 ± 0.5 °C using a MMM FIOCELL Incubator. For the three-electrode cells with EIS scans performed during charge and discharge, the cells were left at 30 °C for 32 h before impedance measurements were taken. The cells were then cycled under constant current conditions at a specific current of 14 mA g^{-1} on charging and 28 mA g^{-1} on discharging between the voltage limits of 1 and 4.2 V at 30 °C. On charging, the current was applied for 1 h before performing an impedance scan, allowing four additional hours for equilibration before recording the spectra. AC impedance measurements were performed by varying the frequency with a perturbation potentiostatic signal amplitude of 10 mV (peak to peak) from 50 mHz to 1 MHz. An additional one-hour open circuit voltage (OCV) hold after running EIS allowed the cell to return to a steady state. The cell was then charged under a constant current for another hour. This procedure was repeated until a voltage of 4.2 V was reached. A constant voltage step of 4.2 V was then applied until the current dropped below 2.8 mA g^{-1}. Another impedance scan was recorded before the cell was discharged. During discharge, the current was applied for 30 min. before performing an impedance scan, allowing four additional hours for equilibration after each discharging step and a 1 hour OCV hold to allow the cell to return to a steady state afterwards.

6.2.3 Analysis of Cell Data

For the three-electrode cells with EIS performed during charge/discharge, the state of charge was calculated using the traditional coulomb counting method[2] (see Section 1.1). The state of charge (SoC) was estimated from the previous SoC value and the in-and-out flowing current. The capacity is calculated by measuring the current (I) entering (charging) or leaving (discharging) the cell and integrating (accumulating) this with respect to time (t). The charge/discharge capacity of the battery for each cycle is used as a reference. This is calculated by integrating the current between the start and end of fully (dis)charging the cell.

The geometry correction performed on EIS data for the batteries was the same as outlined in Section 5.2.5. As was discussed in Chapter V, it is possible to evaluate

impedance data by fitting equivalent electrical circuits to aid with analysis. In this way, the different responses in a generated EIS spectrum are separated into individual distinct components. When carrying out this method, each semi-circle produced in a complex plane plot is represented by a parallel RC element, and therefore has its own associated resistance and capacitance. An example of how EIS parameters are labelled and extracted from an impedance spectrum in this Chapter is given in Figure 6.4.

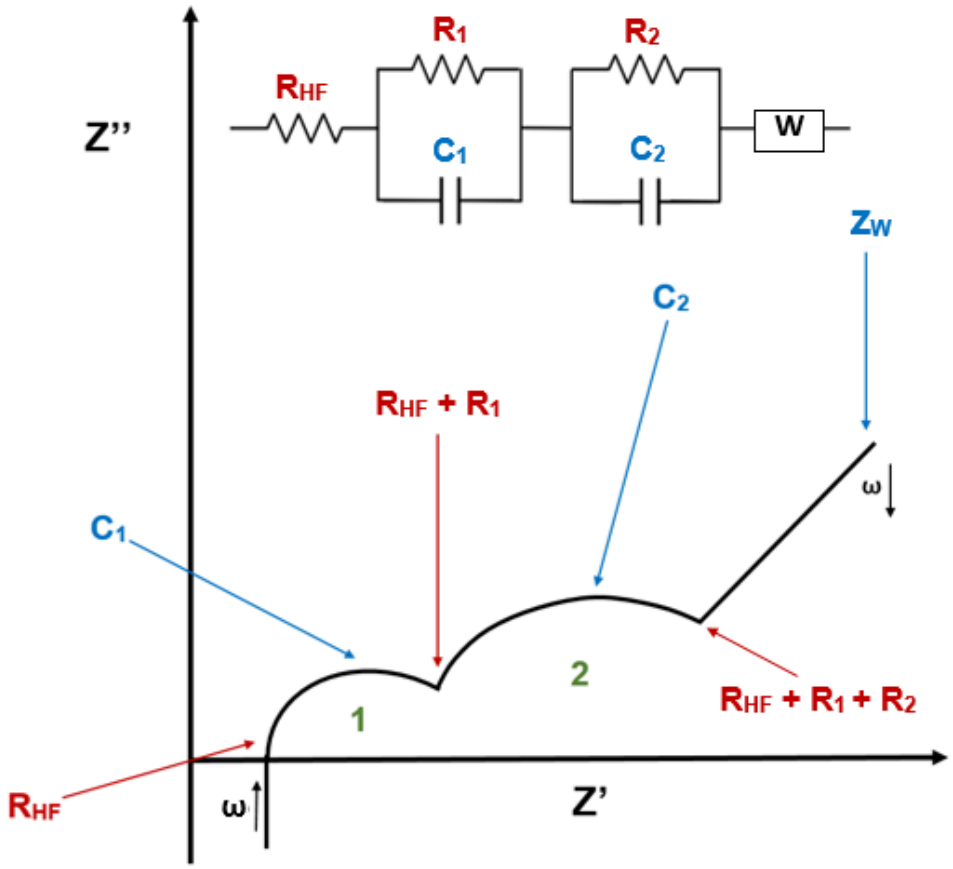

Figure 6.4 Ideal impedance complex plane plot of a sodium-ion battery with labelled parameters and its corresponding equivalent electrical circuit.

The impedance complex plane plot in Figure 6.4 crosses the (real) x-axis at high frequency; this has a resistance associated with it of R_{HF}. The following electrochemical processes can be represented in the simplest way by *RC* elements. The first semi-circle (component 1) then has a resistance R_1 and capacitance C_1 associated with it. A second semi-circle (component 2) towards lower frequency has associated resistance R_2 and capacitance C_2. Resistances are estimated from where

the spectrum meets the (real) x-axis, and capacitances are then calculated using Equation 5.3. When considering the resistances inside a battery, it can often be useful to consider the overall resistance, which is a summation of each individual resistive component in the impedance spectrum (Eq. 2.34). Hence, in this work, when the term 'total resistance (R_{Tot})' is used it refers to the sum of each individual resistance for that particular measurement:

$$R_{Tot} = R_{HF} + R_1 + R_2 + \cdots$$

Finally, a low-frequency spike may be seen, which is represented in the equivalent circuit by a Warburg element or a constant phase element, and has an impedance associated with it, Z_W. The resistance (real part) of the Warburg impedance is calculated from the value of the admittance (Y') at 0.159 Hz using Equation 6.1.

(Warburg Impedance) $$\boldsymbol{Z_W = \frac{1}{Y'}} \qquad (6.1)$$

The origin of this equation is explained in Appendix J. Circuit fitting using a computer software programme was not performed to extract all resistance and capacitance values, but used as a 'sanity check' to ensure values were reasonable. An example of the circuit fitting procedure is provided in Appendix K.

6.3 Results and Discussion

6.3.1 EIS After Charge/Discharge (Three-Electrode Cell)

In the previous chapter, it was seen how the impedances inside a three-electrode cell changed between the first and tenth cycle (Section 5.3.3). Different complex formalisms were used to present EIS data in the charged (Fig. 5.27) and the discharged (Fig 5.28) state. While this gave a general overview, it can also be useful to display graphically how the resistances inside the battery alter across these ten cycles. Figure 6.5 plots the total resistances (Eq. 2.34) for the anode, cathode and full-cell for every cycle, to view more clearly the changes that occur with time.

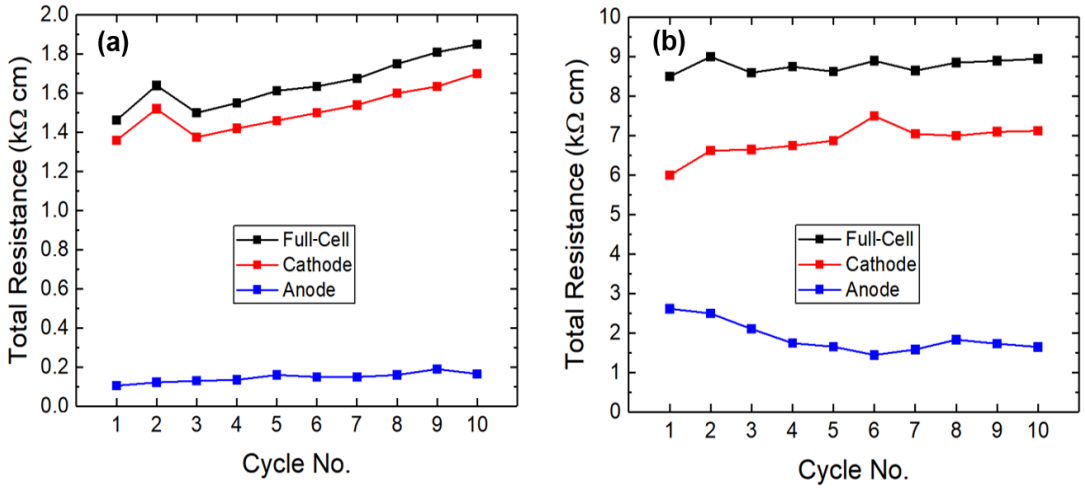

Figure 6.5 The resistances inside a three-electrode cell (a) after charge and (b) after discharge for the first ten cycles.

It can be seen that the resistances for the Na-ion cell in the discharged state are always considerably greater than for when the battery has been fully charged – notice the change in scale of y-axis. For the charged data (a), there is generally a gradual increase in the total full-cell resistance, which goes from around 1.5 to 1.8 kΩ cm across the ten cycles. This consists of a slight increase in the anodic resistance, ~ 100 to ~ 150 Ω cm, as well as a significant rise for the cathode, which increases by approximately 300 Ω cm.

After discharge (b), the full-cell resistance stays more or less constant at around 8.5 kΩ cm. However, there are more significant changes with the resistances associated with each individual electrode. The cathode impedance goes from about 6 to 7 kΩ cm. Meanwhile, the anode shows a significant decline from ~ 2.5 to ~ 1.5 kΩ cm. These two contributions cancel each other out so the change in total full-cell resistance is only small. Crucially, while the anodic resistance stays fairly small and constant after charge and decreases after discharge, in both the charged and discharged states, it is the cathode which clearly dominates the resistance inside the sodium-ion battery. It is therefore intuitive to concentrate on performing a detailed analysis of collected cathode data going forward.

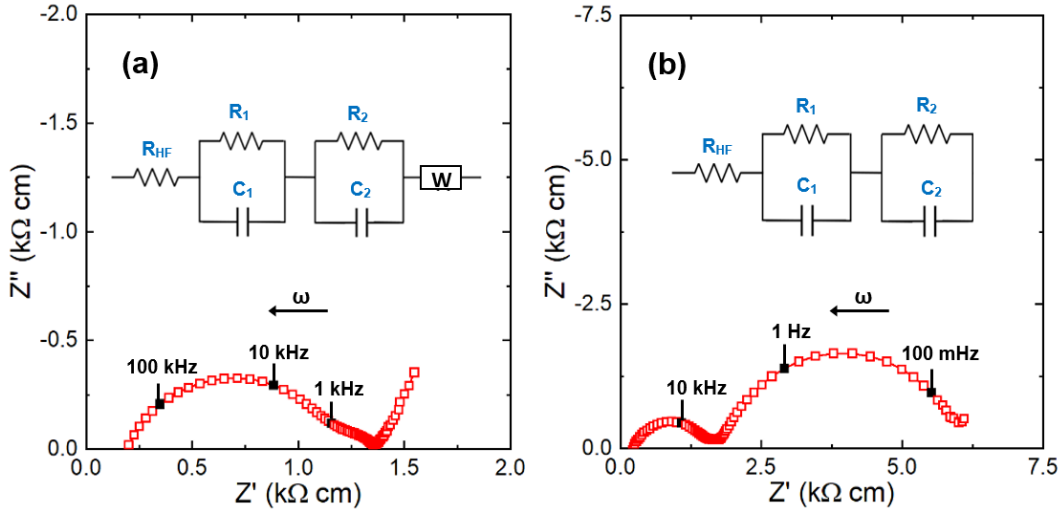

Figure 6.6 Cathode impedance complex plane plot with equivalent electrical circuit for a three-electrode cell (a) after first charge and (b) after first discharge.

In order to gain a better insight into what causes the large cathodic impedance, the impedance complex plane plots for only the cathode measurement for a three-electrode cell are examined. Figure 6.6 displays the cathodic Nyquist plots for a three-electrode cell after it has been first charged and discharged. The impedance complex plane plot (a) for the cathode after the cell has first been charged (sodium removed for the first time) shows three different resistances. The Nyquist plot contains a semi-circle with a high frequency intercept (R_{HF}) around 200 Ω cm. This arc has a resistance associated with it of approximately 1 kΩ cm. There is also a lower frequency small semi-circle with a resistance of ~ 200 Ω cm. Hence, R_{Tot} for this measurement is roughly (0.2 + 1 + 0.2) 1.4 kΩ cm. Finally, at low frequency,

there is a diagonal spike. The equivalent electrical circuit for the cathode after the cell has first been fully charged, to a first approximation, is therefore a resistor, two parallel *RC* elements and a Warburg, *W*, all connected in series to one another, as shown in (a). The Warburg element indicates either diffusion processes taking place during the measurement or a blocking capacitance effect.

After the first discharge (b), the Nyquist plot shows a high-frequency arc with a non-zero intercept and a larger low-frequency semi-circle. There are at least three resistive components with values of around 0.2, 1.5 and 4.3 kΩ cm, giving a total resistance of ~ 6 kΩ cm. To a first approximation, this EIS plot is best represented by a series combination of a resistor and two parallel *RC* elements.

Table 6.1 Cathode resistances and capacitances for a fully-charged sodium-ion battery across the first ten cycles.

Cycle No.	R_{HF} (Ω cm)	R_1 (Ω cm)	$C_1.10^9$ (F cm^{-1})	R_2 (Ω cm)	$C_2.10^6$ (F cm^{-1})	Z_w (kΩ cm)	R_{Tot} (kΩ cm)
1	190	985	8.10	185	6.83	1.40	**1.36**
2	195	1055	7.56	270	4.68	1.55	**1.52**
3	207	843	9.46	325	3.89	1.40	**1.38**
4	208	892	8.94	320	4.97	1.44	**1.42**
5	210	915	8.72	335	5.98	1.48	**1.46**
6	211	939	8.49	350	7.21	1.52	**1.50**
7	214	936	8.52	390	6.47	1.57	**1.54**
8	217	983	8.11	400	7.94	1.63	**1.60**
9	220	980	8.14	435	9.19	1.67	**1.64**
10	220	980	8.14	500	10.1	1.71	**1.70**

Table 6.1 displays how the cathodic resistances and capacitances inside a Na[Ni,Mg,Mn,Ti]O_2/hard carbon sodium-ion battery alter after charge across the first ten cycles. The value of the high frequency resistance (R_{HF}) is very small and increases only slightly across the first ten cycles, from approximately 190 to 220 Ω cm. The value of R_1 is much larger, at around 1 kΩ cm, meaning that it is primarily

responsible for most of the resistance associated with the cathode in the charged state. However, its value stays relatively constant across the ten cycles. The value of the low-frequency resistance, R_2, is reasonably small after the first charge, but increases significantly by about 300 Ω cm, between cycles 1 and 10. Hence, the increase in the total resistance of the cathode (R_{Tot}), from ~ 1.4 to ~ 1.7 kΩ cm, can be accounted for by this increase in the resistance of R_2. The capacitance value of the high-frequency arc, C_1, stays relatively constant across the first ten cycles, around 8-9 nF cm^{-1}, whereas the value of C_2 fluctuates more in the microfarad range. The impedance associated with the low-frequency spike, Z_W, shows a slight general increase from 1.4 to around 1.7 kΩ cm.

Table 6.2 Cathode resistances and capacitances for a fully-discharged sodium-ion battery across the first ten cycles.

Cycle No.	R_{HF} (Ω cm)	R_1 (kΩ cm)	$C_1.10^9$ (F cm^{-1})	R_2 (kΩ cm)	$C_2.10^5$ (F cm^{-1})	R_{Tot} (kΩ cm)
1	220	1.41	7.15	4.38	9.14	**6.00**
2	225	1.43	7.05	4.98	8.04	**6.63**
3	235	1.32	7.64	5.10	7.84	**6.65**
4	235	1.37	7.36	5.15	7.76	**6.75**
5	230	1.40	7.37	5.28	7.58	**6.90**
6	267	1.48	6.77	5.75	6.95	**7.50**
7	250	1.50	6.69	5.25	7.61	**7.00**
8	255	1.50	6.72	5.25	7.61	**7.00**
9	260	1.49	6.74	5.25	9.59	**7.00**
10	255	1.50	6.72	5.25	9.59	**7.00**

Table 6.2 displays the resistances and capacitances of the cathodic components inside a Na[Ni,Mg,Mn,Ti]O_2/hard carbon sodium-ion battery after every discharge across ten cycles. The value of R_{HF} is slightly higher in the discharged state, but increases by roughly the same amount as for charged data, from approximately 220 to 255 Ω cm. The value of the R_1 component is larger than for when the Na-ion

battery is fully charged, ~ 1.5 kΩ cm, however, it stays fairly constant over the first couple of cycles. Unlike in the charged state, where the higher frequency arc dominated the impedance response, the resistance of the cathode after discharge is mainly due to the R_2 component. There is once again an increase in this, and by more than is observed for charged data, as it changes from ~ 4.4 to ~ 5.25 kΩ cm across the first ten cycles. It is, therefore, the low-frequency R_2 component which is once again responsible for the increase in the total cathodic resistance – this time going from about 6 to 7 kΩ cm. The capacitance of C_1 is again steady at around 7 nF cm^{-1}, whereas the capacitance of C_2 fluctuates around 70-100 μF cm^{-1}.

6.3.2 Assigning Cathode Resistive Components

6.3.2 (a) Three-electrode cell data

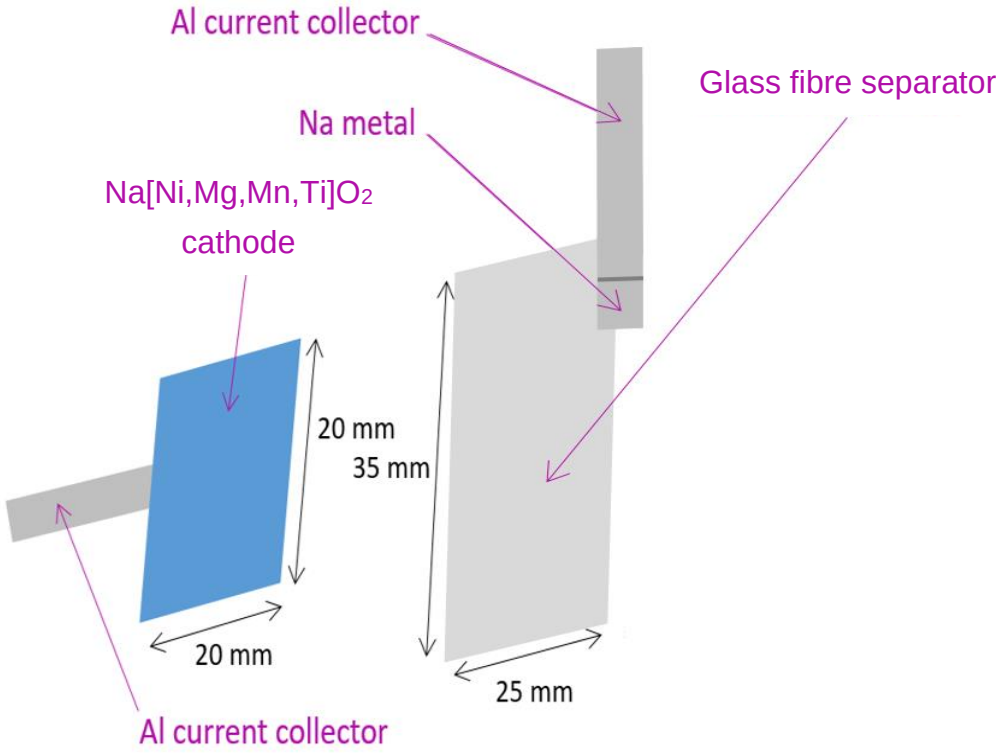

Figure 6.7 The components of a three-electrode cell included in the cathode measurement.

For cathode data obtained from a three-electrode cell, at the simplest level, the different parts of the battery included in the measurement are the cathode, the electrolyte, the separator, the sodium metal, and the aluminium current collectors

(Fig. 6.7). As the resistances associated with metals are so low, it can be assumed that the impedance contribution from the Al current collectors can be ignored. Furthermore, as the reference piece of Na in the three-electrode cells is only small (0.5 x 0.5 cm) and experiences no current flow (and therefore no plating or stripping), it can be assumed that this can also be neglected.

Figure 6.8 shows cathode data ($Na[Ni,Mg,Mn,Ti]O_2$ *vs.* the Na reference electrode) for the EIS scan performed on a three-electrode cell prior to cycling it – this was first presented in Chapter 5. The impedance complex plane plot (a) consists of an arc at high frequency, seen in the inset, which possesses a non-zero intercept with a value of ~ 200 Ω cm. This arc has a resistance of around 1 kΩ cm. There is also a larger distorted semi-circle at lower frequency, with a resistive contribution of approximately 22 kΩ cm, giving a total cathode resistance of ~ 23 kΩ cm. The equivalent electrical circuit for the cathode impedance data (b) can be seen, ideally, to consist of a resistor, representing the non-zero high-frequency intercept, lying in series with two parallel *RC* elements used to represent the two semi-circles.

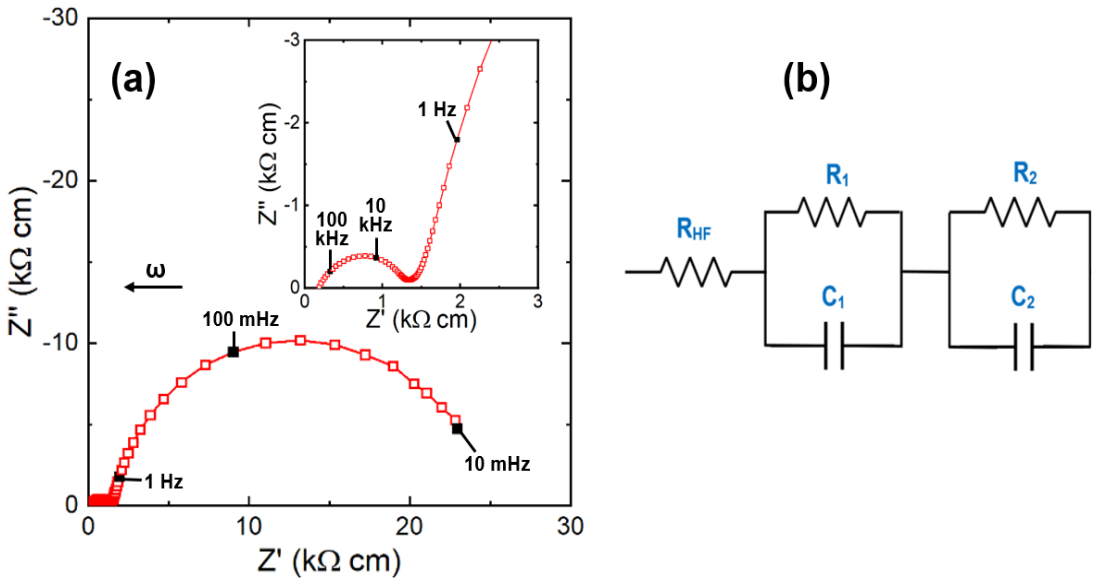

Figure 6.8 Cathode impedance data for a three-electrode cell prior to cycling it. (a) Impedance complex plane plot. (b) Equivalent electrical circuit. Inset in (a) shows zoomed-in high-frequency data.

6.3.2 (b) Symmetric cathode cell data

Figure 6.9 compares an EIS plot for a symmetric cathode cell with cathode data from a three-electrode cell measurement. Note that the frequency response analyser (FRA) used to perform an EIS scan on the symmetric cell is unable to access as high frequencies (100 kHz) compared to the FRA for the three-electrode cell (1 MHz), and, therefore, the symmetric Nyquist plot does not make contact with the real (Z') axis. The symmetric cell is modelled by the same equivalent electrical circuit as used for cathode data. The impedance complex plane plot (a) shows that the resistance for the large semi-circle is about 44 kΩ cm. High-frequency data (b) shows that R_1 for the symmetric cell is roughly 2 kΩ cm. The value of R_{HF} for the symmetric cell appears to be close to the same as that for cathode data, possibly with a slightly lower resistance for the three-electrode measurement.

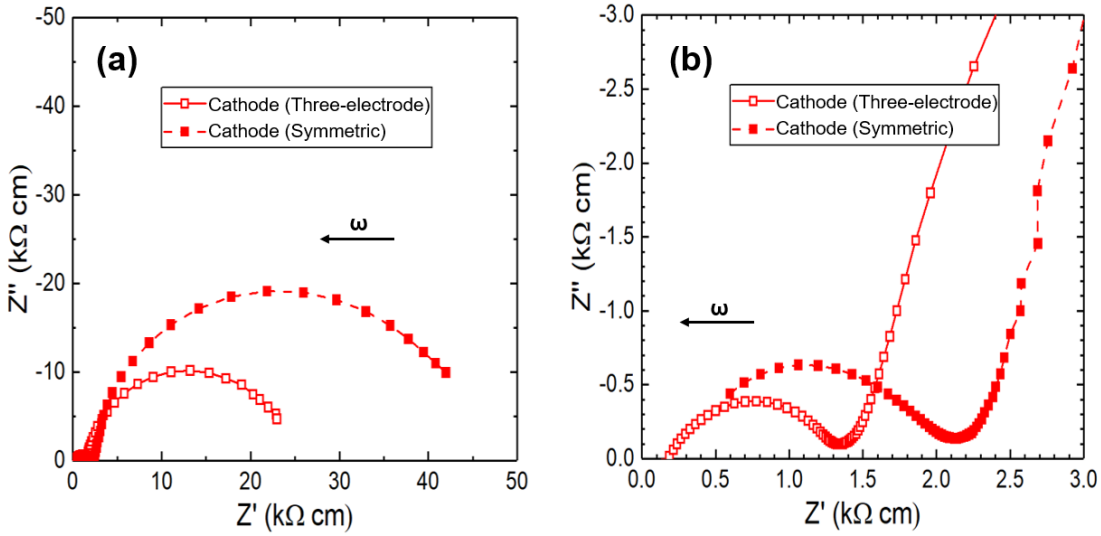

Figure 6.9 Comparison of cathode impedance data for a three-electrode cell and a symmetric cathode cell, prior to cycling. (a) Impedance complex plane plot. (b) Zoomed-in high frequency data.

As the non-zero high-frequency intercept has stayed relatively constant between the two measurements, this indicates that this resistance is associated with something which is more or less the same between the two cells. Therefore, this is likely to be due to the electrolyte. This also agrees with Tables 6.1 and 6.2, which have shown that the value of R_{HF} does not change much with cycling, as would be expected for an impedance from the electrolyte. As the values of R_1 and R_2 approximately double,

this suggests that these resistances are both associated with the cathode as there is just one of these in the three-electrode measurement and two in the symmetric cell. Due to the fact that there is no major reduction in any of the resistances on removal of the piece of sodium metal on going from the three-electrode to symmetric cell, this indicates that the Na metal does not contribute to the impedance of the cell, at least prior to performing any charging/discharging. Further evidence that the sodium reference electrode does not interfere during cycling was seen in Chapter V. The summation spectra for the anode and cathode were very close to the full-cell measurement (Fig. 5.26), which in turn was also very close to data obtained for two-electrode batteries (Fig. 5.21). Hence, this suggests that the Na metal does not cause the impedance spectra to vary considerably on going from a two- to a three-electrode cell, and therefore there is no significant resistance associated with it.

6.3.2 (c) Conductivity and separator cell data

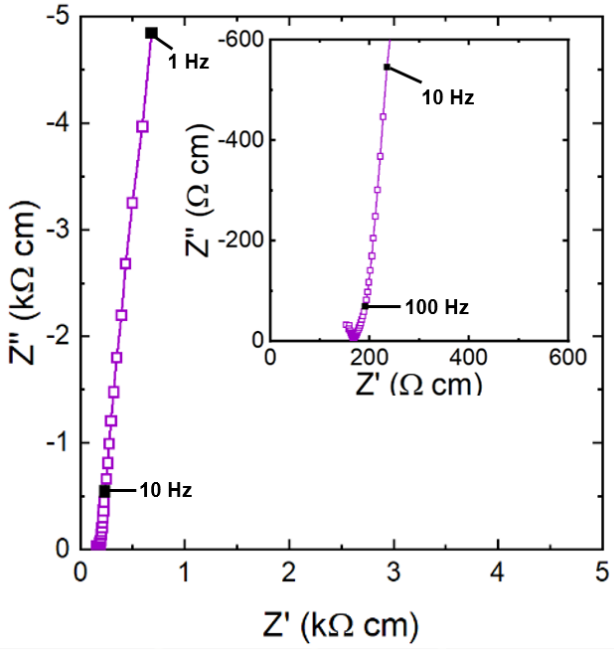

Figure 6.10 Impedance complex plane plot for the sodium electrolyte. Inset shows zoomed-in high-frequency data.

The individual resistance of the electrolyte was measured using a conductivity cell (Fig. 6.3). The impedance complex plane plot (Fig. 6.10) consists of a single resistance at high frequency, with a value of around 150 Ω cm. This appears to be approximately the same, possibly slightly lower, than the high-frequency intercept

for the symmetric and three-electrode cathode data (Fig. 6.9 (b)). Any discrepancy between these intercepts may be accounted for by the fact that when measuring the resistance of the electrolyte using a conductivity cell, there is no separator present. Studies elsewhere have found that separators tend to hinder the conductivity of the liquid electrolyte to a certain extent.[3] In order to determine whether this is the case in this work, a separator cell was constructed and its impedance measured. The separator cell (Fig. 6.2) consisted of two glass fibre separators soaked in the sodium electrolyte. The impedance complex plane plot (Fig 6.11) for the cell possesses a non-zero intercept at high frequency ~ 250 Ω cm. Hence, as this is greater than for the free liquid electrolyte, this suggests that there is an additional resistance associated with the separators used in this work.

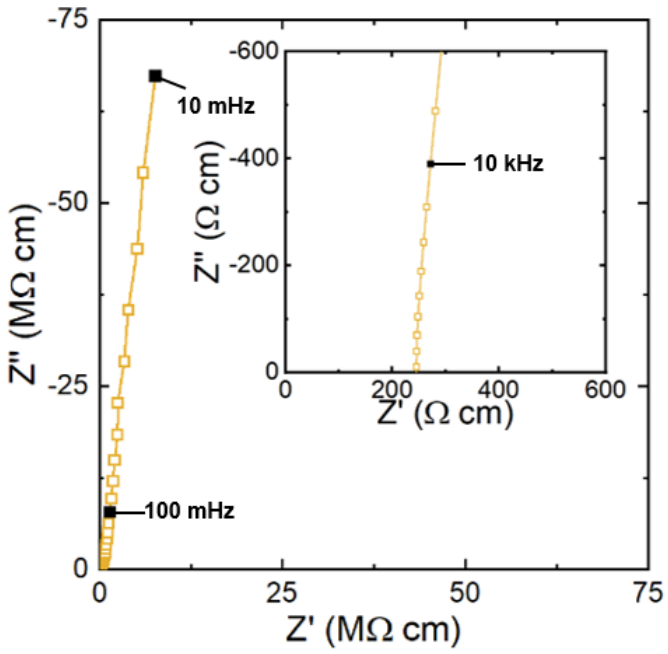

Figure 6.11 Impedance complex plane plot for a separator cell. Inset shows zoomed-in high-frequency data.

Separators have been reported in the literature to hinder the performance of the electrolyte[3]. This is because the resistance of the electrolyte inside the pores of separators is generally greater than the resistance of the free electrolyte. This phenomenon is due to tortuosity.[4] To the simplest approach, tortuosity can be defined as the length of a curved route divided by the most direct, straight pathway

between the two end points. However, at a more involved level, it can be thought of as an effective path length arising from mass transport limitations in porous media.[5]

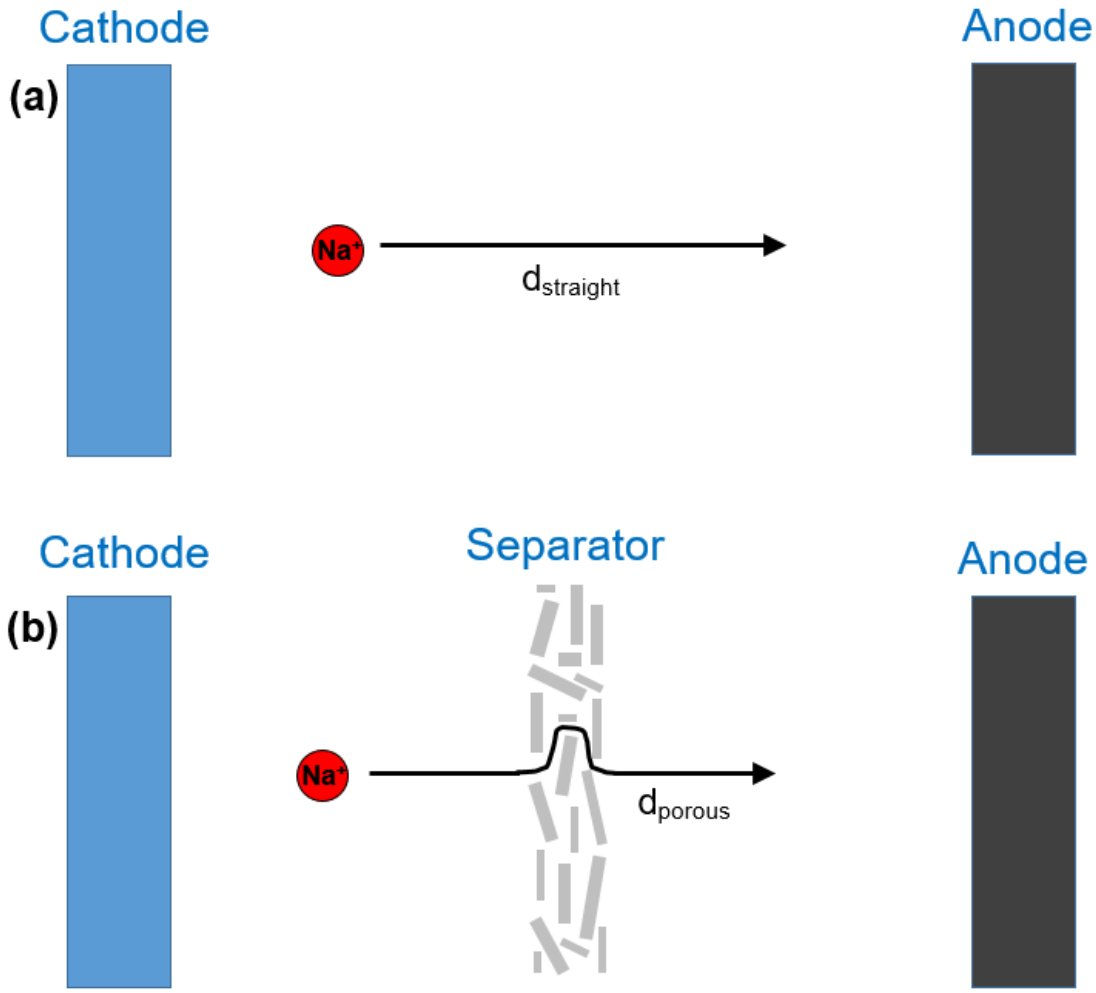

Figure 6.12 Diffusion of a sodium ion through the electrolyte (a) with, and (b) without a separator present.

In previous studies, tortuosity has been used to describe the mass transfer in porous substances, such as the diffusion of Li^+ ions through battery electrodes and separators.[6–8] It can be seen in Figure 6.12 that the path taken for the diffusion of a sodium ion through an electrolyte (a) is longer for when there is a separator present (b). To a first approximation, tortuosity (τ) for such a system is defined by the elongation of the transport path due to the porous structure (d_{porous}) with respect to a straight line ($d_{straight}$), given by Equation 6.2.

$$\tau = \frac{d_{porous}}{d_{straight}} \qquad (6.2)$$

A comparison of Figures 6.10 and 6.11 makes it clear that the value of R_{HF} is greater when there are separators present in the electrolyte, by approximately 100 Ω cm. As has been explained above, this is not because the intrinsic conductivity of the electrolyte has altered but because the path length between the two electrodes has increased. The ratio between the resistivity of the separator soaked in the electrolyte, ρ_{sep}, and the resistivity of the free electrolyte, ρ_{el}, is known as the MacMullin number, N_M,[9] and is a useful way to quantify resistances associated with separators in batteries (Eq. 6.3). As there are two pieces of GF/A in the separator cell used in this work, it is reasonable to assume that one separator would increase the resistance of the electrolyte by half as much, ~ 50 Ω cm. This agrees with R_{HF} for the cathode measurement for a three-electrode cell prior to cycling it being estimated at around 200 Ω cm (Fig. 6.9). Furthermore, it is in keeping with what has been seen in previous studies[10] that have aimed to determine the tortuosity of battery separators. These have found that there is a linear relationship between the measured real resistance and the number of separators.

$$N_M = \frac{\rho_{sep}}{\rho_{el}} \tag{6.3}$$

$$N_M \simeq \frac{200}{150} \simeq \mathbf{1.33}$$

The MacMullin number for the glass fibre separators used in this work is approximately 1.33. Hence, the resistance of the electrolyte coupled with a GF/A separator is 1.33 times higher than the resistance of the free electrolyte. This MacMullin number is much smaller than for other separators seen in the literature (Appendix L).[11] This can be explained by the extremely large pore size that glass fibre separators possess. Commercial separators which possess smaller pores have been reported in the literature to have significantly higher MacMullin numbers; however, these have the advantage of being lighter and thinner than glass fibre, leading to higher volumetric and gravimetric energy densities.

6.3.2 (d) Comparison of different cell data

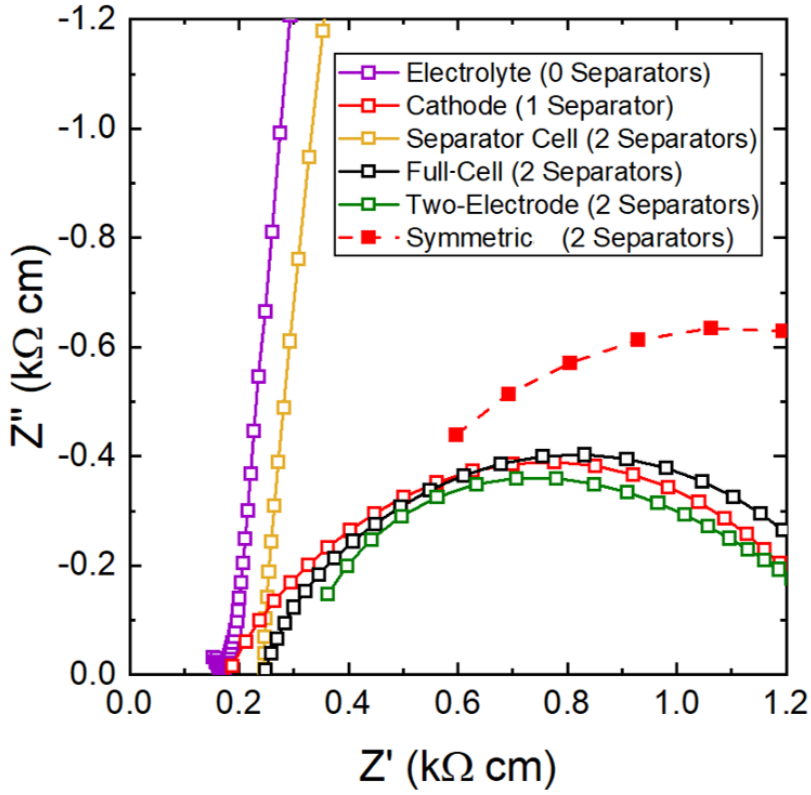

Figure 6.13 Comparison of impedance complex plane plots at high frequency for a range of different cell designs.

Figure 6.13 compares the high-frequency impedance data for a range of different cell designs. The resistance of the free electrolyte measured using the conductivity cell can be seen to possess the lowest value, ~ 150 Ω cm. The impedance plot for the separator cell, which consists of two electrolyte-soaked separators, has a non-zero intercept around 250 Ω cm. The cathode plot for the three-electrode cell crosses the x-axis somewhere between these two values, which is intuitive, considering there is just the one separator in its measurement. Importantly, high-frequency data for the three-electrode full-cell measurement, which consists of two separators, crosses the real axis at the same point as the separator cell. Hence, this indicates that this resistance at high frequency inside sodium-ion batteries is associated with the electrolyte and separators. Furthermore, if the plots for the two-electrode cell and symmetric cathode cells, also both possessing two separators, are extrapolated, they likewise appear to cross the real axis close to the same point, ~ 250 Ω cm. Therefore, it can be concluded with some certainty that the non-zero high-frequency resistance

(R_{HF}) for sodium-ion batteries is due to a combination of the resistance of the electrolyte (R_{el}) and separators (R_{sep}) (Eq. 6.4).

$$R_{HF} = R_{el} + R_{sep} \quad (6.4)$$

The origin of the other two resistive components present in the cathode measurement for the three-electrode cell, R_1 and R_2, still need to be determined. As mentioned previously, a comparison of the impedance complex plane plot for the three-electrode cathode measurement with data for the symmetric cathode cell (Fig. 6.9) appears to show that the values of R_1 and R_2 are approximately double for the symmetric cell. This suggests that these resistances are both associated with the cathode itself, as there is just one of these in the three-electrode measurement and two in the symmetric cell. The capacitance for the first higher frequency semi-circle in Figure 6.8 (component 1) is ~ 10 nF cm^{-1}, and for the lower frequency one (component 2), ~ 0.1 mF cm^{-1}. As capacitance is inversely proportional to the length of the region under consideration, it can be deduced that component 2 is likely to be significantly thinner than component 1 as it has a much larger capacitance.

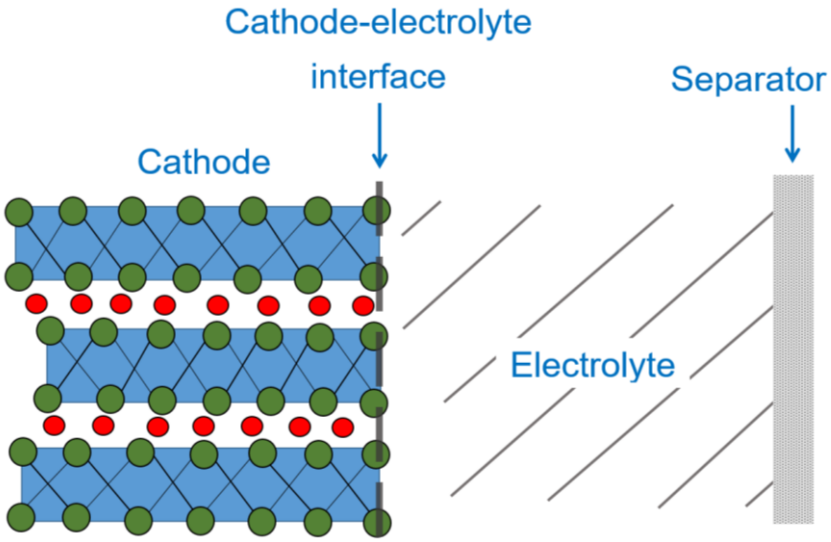

Figure 6.14 Schematic of the different likely components present in the cathodic impedance measurement for a three-electrode cell.

It is reasonable to assume that the resistance of the cathode-electrolyte interface is substantially different from the resistance in the rest of the material.[12] Furthermore, previous work on lithium-ion batteries has noted a significant impedance associated

with Li^+ transport at the interface between the surface of the cathode and the liquid electrolyte.[13] This is referred to as charge-transfer resistance.[14] It is reasonable to assume, therefore, that a similar impedance may be present in sodium-ion cells. Furthermore, as the capacitance of the lower frequency component is a value consistent with an electrochemical double layer, this suggests that R_2 is the resistance associated with the cathode-electrolyte interface. Figure 6.14 displays the likely origins of the different resistances present in impedance data for the cathode measurement of a three-electrode cell. Calendering these layered oxide sodium-ion electrodes appears to be effective in reducing their impedances (Appendix M), and hence, may enhance the performance of these Na-ion batteries. Calendering decreases the porosity of the electrodes, which in turn improves the contact between particles. Thus, this may explain why the cathode bulk resistance decreases with calendering.

6.3.3 EIS During Charge/Discharge (Three-Electrode Cell)

Figure 6.15 displays cathode impedance complex plane plots for a three-electrode cell at various SoC during the first charge of the cell. Prior to cycling, there are two *RC* components (semi-circles present): one at high frequency and a larger arc towards lower frequency. There is also a high-frequency non-zero intercept. It can be seen that after charging the battery slightly, at 8% SoC (~ 1.7 V), there is a drastic change in the impedance complex plane plot. The non-zero intercept and smaller high-frequency semi-circle stay relatively the same size, but the low-frequency semi-circle reduces in size greatly. Charging the cell further to 17% SoC (~ 2.1 V) results in a decrease in resistance of both *RC* components, which is once again particularly noticeable for the lower frequency arc. There is also now a diagonal spike present at low frequency. Once the cell is at 51% SoC, there is a further reduction in both resistances, this time most significant for the higher frequency component. Between half and fully charging the cell there is not much difference in the two impedance spectra. Hence, the most substantial changes appear to occur within the bottom part of the charging profile. Applying a DC bias while performing EIS, indicates that a cell voltage of around 1.4 V is required for the impedance spectra to change

significantly (Appendix N), thus, suggesting that a voltage of this magnitude, or higher, is required to remove Na from the cathode structure.

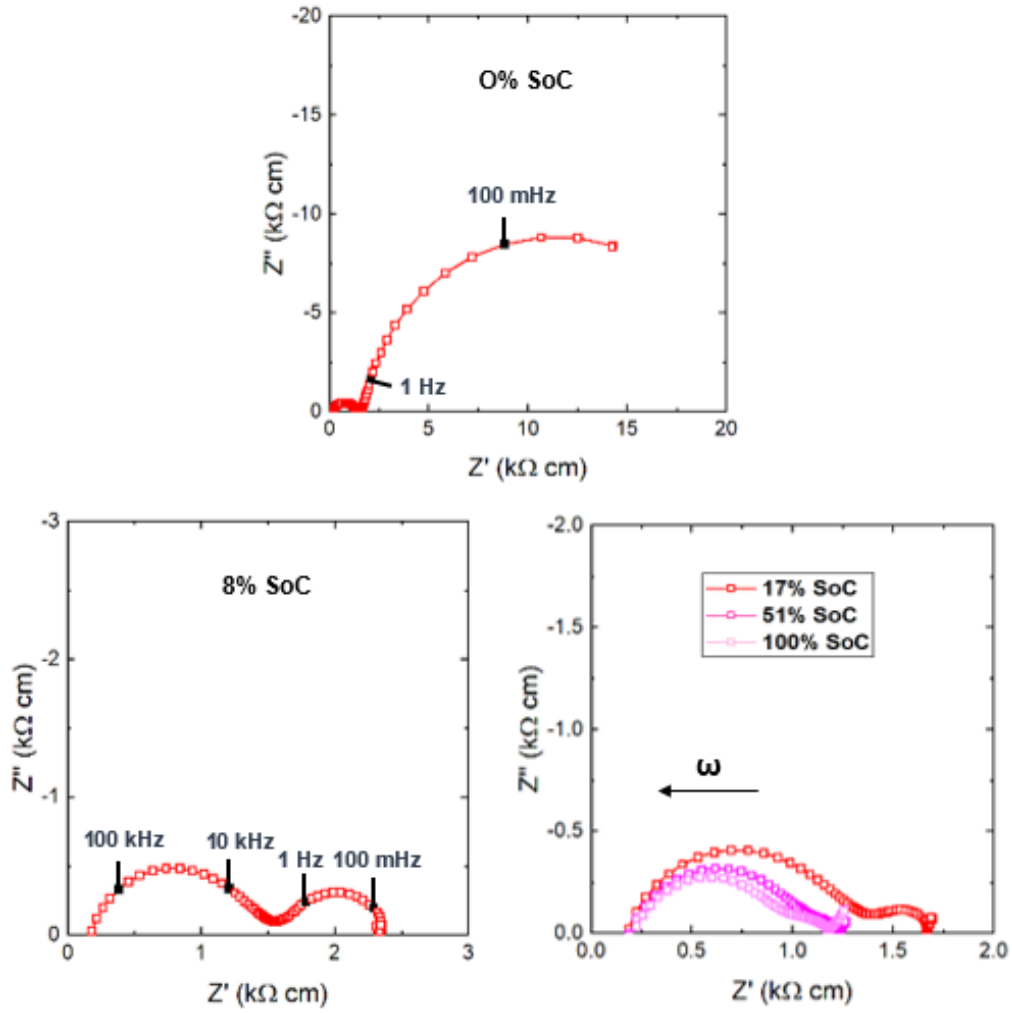

Figure 6.15 Cathode impedance data for a three-electrode cell at different states of charge, during the first charge.

Table 6.3 contains the resistances and capacitances for the different components present in the cathodic impedance complex plane plots at various states of charge. A small gradual increase in R_{HF} occurs with increasing SoC, which rises by a total of about 35 Ω cm during the first charge of the cell. R_1 and R_2 decrease over the same period: R_1 gradually reduces from around 1.3 kΩ cm to about 750 Ω cm. A much more significant decrease in the size of R_2 occurs over the first 8% of charge, from approximately 20 to 1 kΩ cm. There is then a further decrease to ~ 300 Ω cm over the next 9% of charge (up to 17% SoC). The cell then fluctuates around 150-200 Ω cm between 25 and 100% state of charge. A combination of reduction in values of R_1

and R_2 results in an overall decrease in the total cathodic cell resistance. This begins close to 22 kΩ cm at 0% SoC and then shows a gradual general decrease down to ~ 1.1 kΩ cm when the Na-ion battery has been fully charged for the first time. The capacitance associated with the higher frequency *RC* component, C_1, generally increases slightly with SoC, from around 3 to 6.5 nF cm^{-1}. The value of C_2 decreases from ~ 100 to ~ 1.5 μF cm^{-1}. The impedance of the low-frequency diffusion spike, Z_W, decreases from around 1.7 to about 1.2 kΩ cm up to 51% SoC, then stays fairly constant across the top half of the charging regime.

Table 6.3 Cathode resistances and capacitances at different states of charge, during the first charge.

SoC (%)	R_{HF} (Ω cm)	R_1 (Ω cm)	$C_1.10^9$ (F cm^{-1})	R_2 (Ω cm)	$C_2.10^6$ (F cm^{-1})	Z_W (kΩ cm)	R_{Tot} (kΩ cm)
0	175	1275	3.14	20300	98.7	-	**21.8**
8	175	1375	2.91	800	62.9	-	**2.35**
17	178	1213	3.30	274	40.9	1.68	**1.67**
25	182	1093	3.66	155	6.48	1.43	**1.43**
34	180	1045	3.83	160	3.96	1.39	**1.39**
42	190	910	4.39	180	2.80	1.30	**1.28**
51	190	885	4.52	152.5	4.15	1.24	**1.23**
59	188	812	4.92	180	2.77	1.20	**1.18**
68	190	810	4.94	170	5.92	1.20	**1.17**
76	190	835	4.79	210	1.90	1.27	**1.24**
85	200	875	4.57	205	2.77	1.32	**1.28**
100	210	765	6.58	200	1.59	1.22	**1.12**

The small value of R_{HF} is consistent with this being the resistance associated with the electrolyte and separators. The slight increase that occurs during the first charge may be due to the voltage rising outside the stability window of the electrolyte. This may lead to a slight decomposition of the electrolyte, thus raising the resistance. This has

been shown to occur with similar electrolyte systems for Li-ion[15] and Na-ion[16] batteries. As mentioned in the last section, as R_2 is likely, due to its higher capacitance value, to be linked to the cathode-electrolyte interface, this means that the higher frequency *RC* component is most probably related to the bulk of the cathode. In order to balance the overall charge on the cathode, the loss of Na^+ ions from its structure during charging must be accompanied by oxidation of one or more of the transition metals present in the active material. For efficient operation of a battery, there must be a sufficient pathway in the cathode for electrons to hop from Na oxide particles to carbon and then on to the current collector. The mixed valency formed on removing Na^+ ions introduces electron holes, and therefore, increases the p-type conductivity of the system. Furthermore, as more sodium is removed from the cathode during charging, the density of contact between oxide particles and the conductive carbon additive increases.[17] The overall effect of all this is an increase in the conductivity of the electrode system and a decrease in the resistance of R_1.

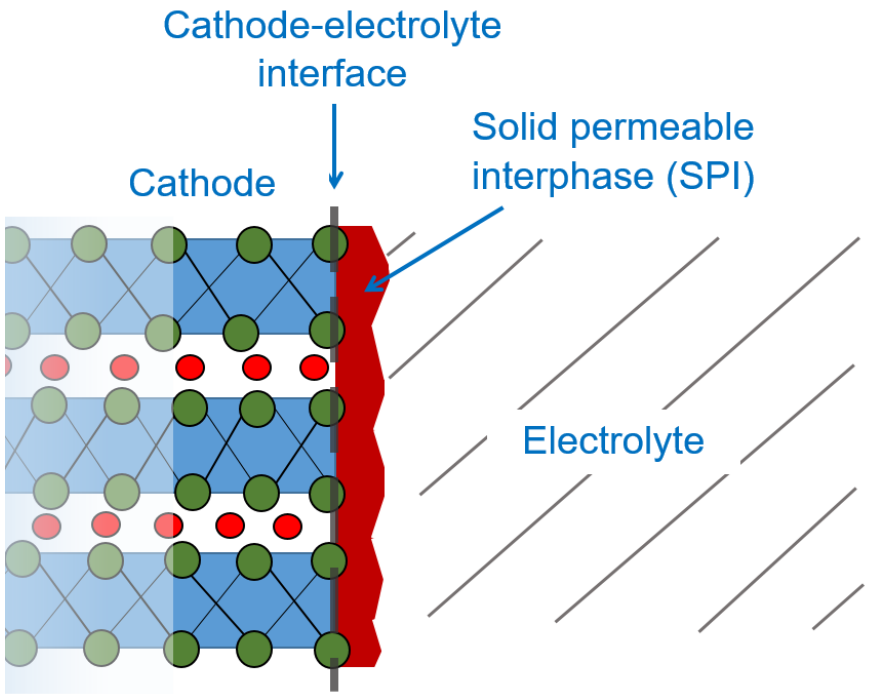

Figure 6.16 Schematic showing a solid permeable interphase (SPI) present on the surface of the cathode.

The lower frequency *RC* component is attributed to the cathode-electrolyte interface. This may consist of a charge-transfer resistance between the solid and liquid,

coupled with a double layer capacitance.[18] The component starts off with a very large resistance, suggesting that there is no sufficient pathway for sodium ions to move between the cathode structure and electrolyte. After 8% charge, this has decreased dramatically as there is an increase in the number of sodium vacancies in the cathode material. The value of C_2 decreases significantly with SoC, thus suggesting that the cathode-electrolyte interface is widening. This may be due to the thickening of a solid layer on the surface of the cathode. As well as a solid electrolyte interphase (SEI) on the surface of the anode, a solid passivation layer has been detected on the cathode in certain lithium-ion systems.[19] To distinguish it from the SEI, this is sometimes referred to as the solid permeable interphase (SPI) (Fig. 6.16).[20] Surface films have been observed on a range of lithium oxide cathode materials, including $LiCoO_2$, $LiNiO_2$ and $Li_2Mn_2O_4$.[21,22] Furthermore, it has been detected for a similar electrolyte system to the one in this work, 1 M $LiPF_6$ in EC:PC (1:1).[23] Much less is known about the SPI layer and its chemical composition,[24] however, it is thought to possibly form from the decomposition of solution components,[25] as well as transition metal dissolution and redeposition from the cathode.[19]

In ionic conduction, solid state diffusion is occurring continuously and spontaneously. A low-frequency spike present in an impedance complex plane plot indicates that diffusion is the rate-limiting step in a sequence of several steps. At low SoC, there is no spike detected. At 17% and above a spike is detected, indicating that diffusion is now the rate-limiting step. Between 17-51% SoC, the resistance of the Warburg impedance, Z_W, decreases. The Warburg impedance is proportional to the Warburg coefficient σ, which is in turn inversely proportional to the diffusion coefficient (Eq. 6.5).[26] In this equation, the molar volume is given by V_M, A is the peak current, F the Faraday constant, E the potential, and x is the mobile Na^+ concentration. Hence, a decrease in the Warburg impedance, indicates an increase in diffusion in the cathode.

$$D = \frac{1}{2}\left[\left(\frac{V_M}{AF\sigma}\right)\frac{\delta E}{\delta x}\right]^2 \qquad (6.5)$$

Similarly, the capacitance of the low-frequency spike can be calculated using Eq. 5.4. A reduction in the capacitance indicates a reduction in charge storage, which in

turn highlights an increase in Na^+ ion diffusion. An increase in diffusion with increasing SoC, may be explained by an increase in the number of vacant Na intercalation sites facilitating greater diffusion in the cathode structure; this has been observed previously for certain lithium-ion systems.[27]

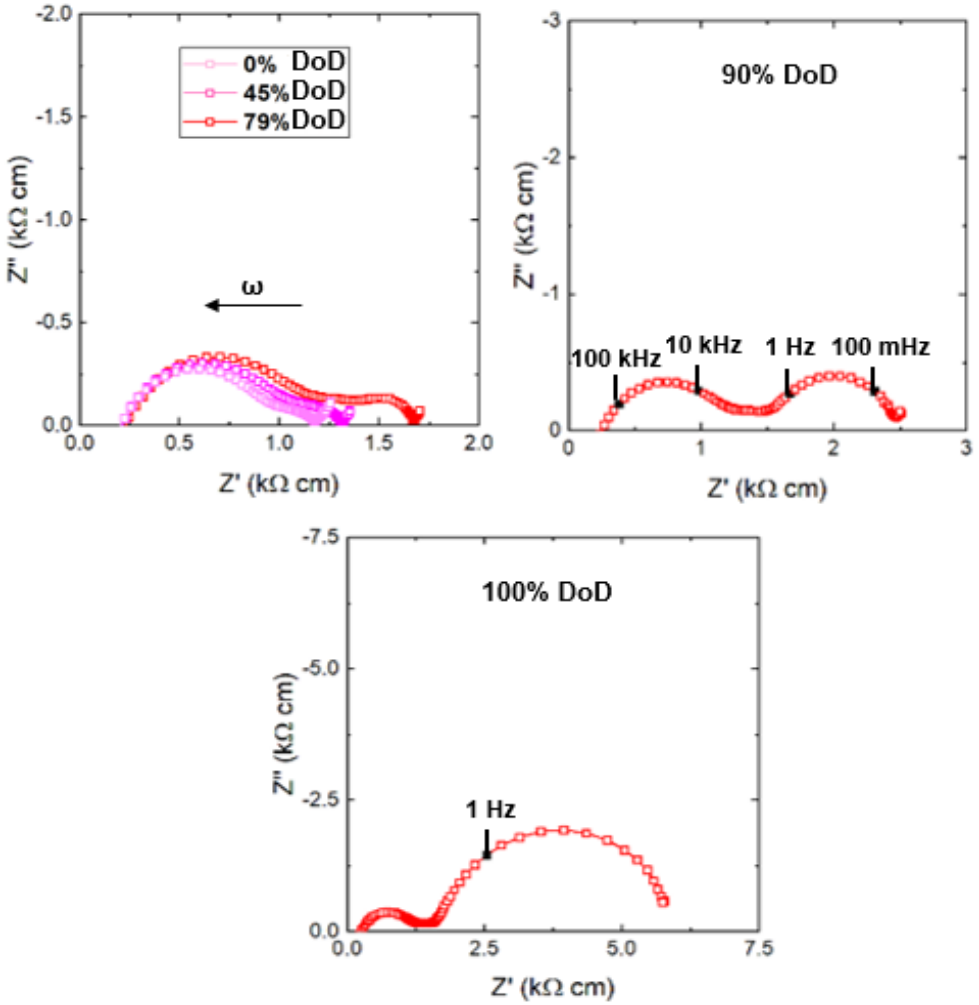

Figure 6.17 Cathode impedance data for a three-electrode cell at different depths of discharge, during the first discharge.

It may also be useful to consider how impedances alter during the first discharge of the cell. Figure 6.17 displays cathode impedance complex plane plots for a three-electrode cell at various depth of discharge (DoD) for cycle 1. From 0 to 45% DoD there is not much change in the shape of the impedance plots, with gradual increases in the resistances of the two arcs, which is most prevalent for the low-frequency component. Then, on increasing to 79% DoD, there is a much more noticeable difference in the plots as R_{Tot} goes from around 1.3 to about 1.7 kΩ cm. Over the last

~ 20% of discharge there is a much more significant change, primarily associated with the lower frequency resistive component, R_2. The value of this increases from around 0.4 to 1.1 kΩ cm between 79 and 90% DoD, before increasing close to 6 kΩ cm once the cell is in the fully discharged state. It can be seen in the plots that an increasing DoD is also accompanied by a reduction in the size of the low-frequency diagonal spike; this is no longer seen at complete discharge. It can be concluded that on discharging the sodium-ion battery, similar to what was observed on charging, the most substantial changes appear to occur when the battery does not have much charge remaining.

To display more clearly the changes that are occurring, the cathode resistances at varying depths of discharge are displayed graphically in Figure 6.18. In (a), the total resistance of the cathode stays fairly constant over the first 80% DoD around 1-1.5 kΩ cm, before increasing up to ~ 2.5 kΩ cm at 90% DoD. It then finally rises near to 6 kΩ cm when the cell is in the fully discharged state. The plot of the high-frequency resistance, R_{HF}, (b), shows a minimal increase from around 220 to 250 Ω cm over the first discharge of the cell. A more substantial difference is noted in the resistance of R_1, in (c), which increases from ~ 800 to ~ 1.2 kΩ cm. This mainly takes place across the last 30% DoD. Finally, the most significant change occurs with the low-frequency R_2 component, (d). This increases slightly from around 200 to 400 Ω cm over the first 80% DoD, before subsequently increasing to approximately 4.25 kΩ cm when the cell has been fully discharged. It is clear from these graphs that R_2 dominates the cathode resistance during the first discharge of a sodium-ion battery; this is most evident in the similarity in the plots of R_{Tot} and R_2.

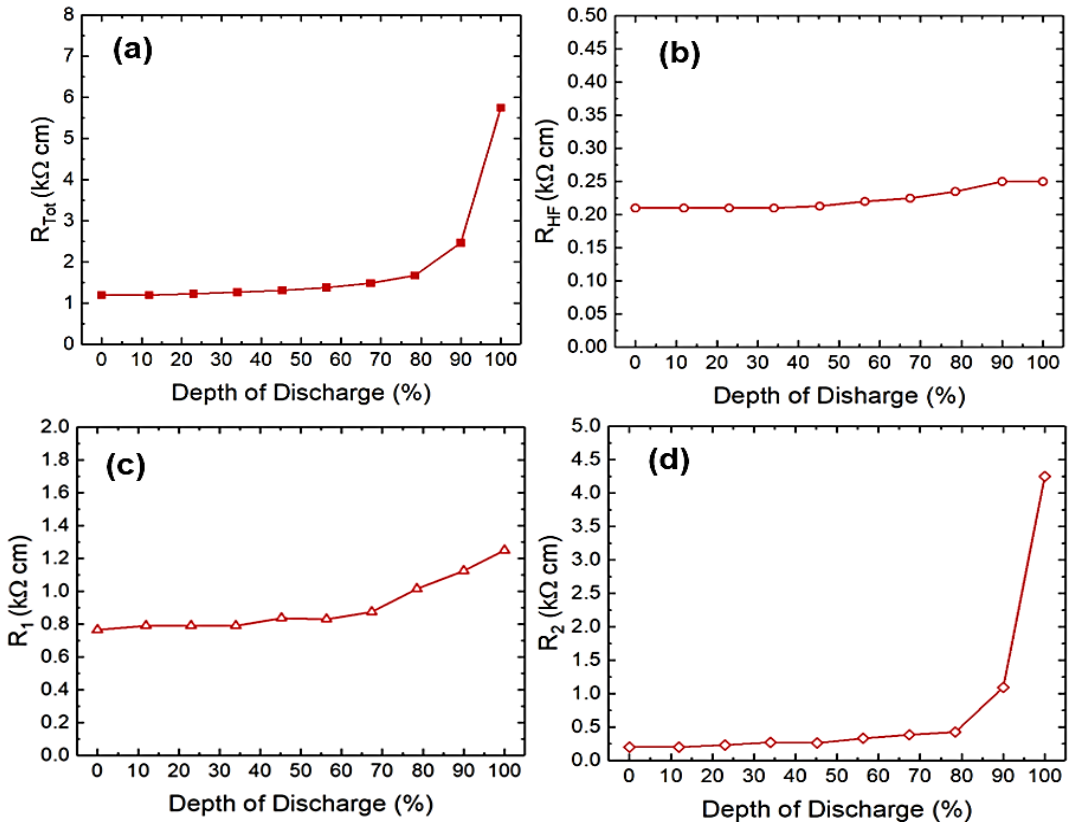

Figure 6.18 Resistances associated with the cathode, for a three-electrode cell at different depths of discharge, during the first discharge: (a) R_{Tot}, (b) R_{HF}, (c) R_1, and (d) R_2.

The changes in cathode resistances that occur during the first discharge can be seen in many ways to have similarities to what happens during the first charge. There is another small gradual increase in the resistance of the electrolyte and separators, R_{HF}. This further suggests that some decomposition of the electrolyte is occurring during the first cycle. With regards to the resistances of the two *RC* components, R_1 and R_2, there is a reversal in trends seen during charge. Instead of a gradual decrease in the resistances there are now progressive increases. The rise in resistance of R_1, which has been previously attributed to the bulk, may be due to a decrease in the p-type conductivity of the cathode, as sodium ions are re-inserted back into the electrode, which is accompanied by a reduction in number of electron holes. The increase in the resistance associated with the cathode-electrolyte interface, R_2, may be explained by the fact that as more Na^+ ions re-enter the cathode structure it becomes increasingly difficult to insert more. Hence, there is a rise in the charge-transfer resistance between the cathode and the electrolyte, which is particularly prevalent above 80% DoD.

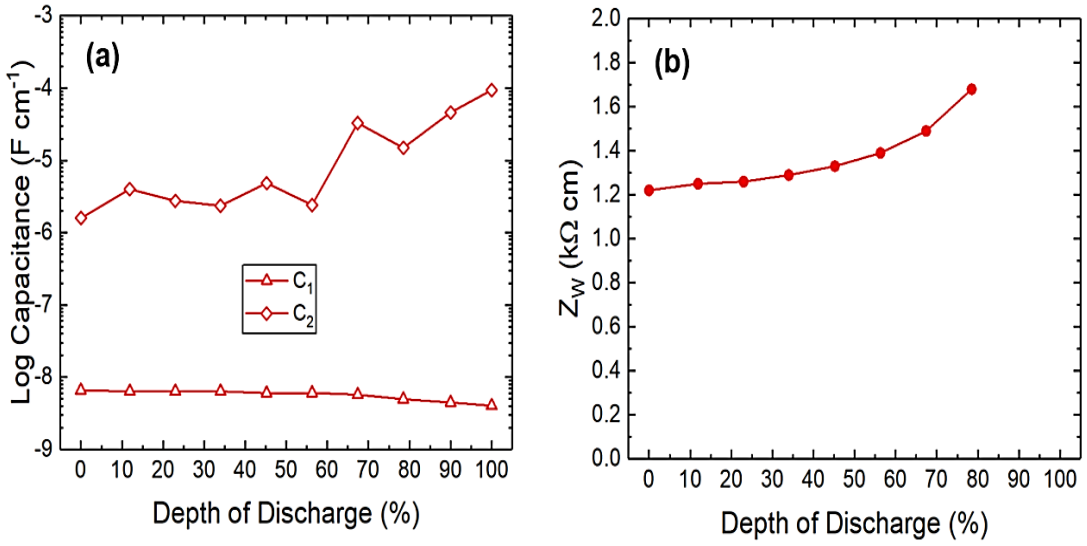

Figure 6.19 Values of EIS parameters associated with the cathode, for a three-electrode cell at different depths of discharge, during the first discharge: (a) capacitances of *RC* elements, (b) impedance of low-frequency spike.

Lastly, the capacitances of the *RC* components and the impedance of the low-frequency spike are plotted (Fig. 6.19). A reversal can be seen to occur with the capacitances compared to what was observed during the first charge (a). The capacitance of C_1, in the nanofarad range, decreases slightly across the first discharge of the cell, but by far the most significant change, once again, is for C_2, which increases from around 1 to 100 μF cm^{-1} between 0 and 100% DoD. The impedance of the low-frequency spike, Z_W, (b) stays more or less constant across the first 50% of discharge, before increasing substantially from ~ 1.3 to ~ 1.7 kΩ cm up to 80% DoD, showing more or less a reversal to what occurred during the first charge of the Na-ion cell.

The increase in the impedance of the low-frequency spike indicates a decrease in diffusion in the cathode structure. This is intuitive with there being an ever increasing amount of sodium present in the electrode with greater DoD, thus reducing the number of vacant Na intercalation sites. The increase in the capacitance of the low-frequency *RC* component, C_2, suggests that the cathode-electrolyte interface is becoming thinner during the first discharge. This may coincide with sodium at the surface of the cathode being forced back into the rock salt type structure during discharge. If indeed a solid permeable interphase (SPI) is forming on the surface of the cathode then it may be dynamic, i.e. its thickness changes with

time.[28] This has been observed for the SEI on the anode in certain lithium-ion battery systems.[29] Furthermore, the SEI in Na-ion systems has been reported to be inferior to its lithium-ion counterpart because it is more soluble, meaning that its thickness is known under certain conditions to decrease over time.[30] Hence, a similar effect may be occurring here with the SPI on the cathode in sodium-ion batteries. This may explain why the capacitance increases at the cathode-electrolyte interface during the first discharge.

6.4 Conclusions

In this chapter, electrochemical impedance spectroscopy has been performed on sodium-ion batteries at varying states of health and states of charge, in order to try and obtain a better understanding of the origin of the large cathode impedance they possess. This was done using a range of different cell configurations, including separator and symmetric battery designs, applied to the commercially-used pouch cell setup. Results were analysed by fitting ideal equivalent electrical circuits to impedance data, and using these to extract resistances and capacitances for the different components present.

Examining EIS data for a three-electrode cell measurement showed that an increasing cathode resistance dominates the impedance inside of sodium-ion batteries across the first ten cycles. Modelling the response using an ideal equivalent circuit found that the cathode impedance spectrum consists of three different resistive components: a small high-frequency non-zero intercept resistance, R_{HF}, and two *RC* elements, with resistances of R_1 and R_2, at medium and low frequencies respectively. Comparison between the impedance results for different cell designs made it possible to assign these separate components to different physical elements of the sodium-ion battery. It was deduced that R_{HF} is due to the resistance of the electrolyte and separators, and that R_1 and R_2 are both associated with the cathode itself. A consideration of the capacitances suggested that R_2, which has a capacitance consistent with an electrochemical double layer (in the microfarad range), is due to the cathode-electrolyte interface. The resistance R_1, which possesses a smaller capacitance, is attributed to the cathode bulk. Across the first ten cycles the cathode-electrolyte interface was found to be primarily responsible for an increase in the total cell resistance.

These findings suggest that the performance limiting factor for these layered oxide sodium-ion batteries is the cathode-electrolyte interface. While much work has been done to date on the interface at the anode in lithium-ion batteries,[31,32] and the existence of the solid electrolyte interphase is well documented,[33,34] much less research has taken place on the interface at the cathode. Hence, in this work, a solid permeable interphase (SPI) on the surface of the cathode may have been detected in

sodium-ion batteries for the first time. From performing impedance measurements during charge/discharge, the resistance of the cathode-electrolyte interface was found to increase dramatically above approximately 80% depth of discharge. These findings have important consequences for sodium-ion battery development, suggesting that to optimise performance and extend battery life, cells should not be discharged below ~ 20% SoC. Furthermore, these results provide an important basis for further work into obtaining accurate and reliable SoC estimates for sodium-ion batteries Future work may include long-term cycling of Na-ion cells to try and estimate state of health (SoH) and battery failure from impedance results. This will be studied in the next chapter.

6.5 References

1 F. Huet, *J. Power Sources*, 1998, **70**, 59-69.

2 Woodbank Communications Ltd., *Electropaedia: Battery State of Charge Determination*, https://www.mpoweruk.com/soc.htm, (accessed September 2020).

3 D. Djian, F. Alloin, S. Martinet, H. Lignier and J. Y. Sanchez, *J. Power Sources*, 2007, **172**, 416–421.

4 I. V. Thorat, D. E. Stephenson, N. A. Zacharias, K. Zaghib, J. N. Harb and D. R. Wheeler, *J. Power Sources*, 2009, **188**, 592–600.

5 D. Kehrwald, P. R. Shearing, N. P. Brandon, P. K. Sinha and S. J. Harris, *J. Electrochem. Soc.*, 2011, **158**, A1393-A1399.

6 N. A. Zacharias, D. R. Nevers, C. Skelton, K. Knackstedt, D. E. Stephenson and D. R. Wheeler, *J. Electrochem. Soc.*, 2013, **160**, A306–A311.

7 J. Cannarella and C. B. Arnold, *J. Power Sources*, 2013, **226**, 149–155.

8 B. Suthar, J. Landesfeind, A. Eldiven and H. A. Gasteiger, *J. Electrochem. Soc.*, 2018, **165**, 2008–2018.

9 K. K. Patel, J. M. Paulsen and J. Desilvestro, *J. Power Sources*, 2003, **122**, 144–152.

10 J. Landesfeind, J. Hattendorff, A. Ehrl, W. A. Wall and H. A. Gasteiger, *J. Electrochem. Soc.*, 2016, **163**, A1373–A1387.

11 M. Kirchhöfer, J. von Zamory, E. Paillard and S. Passerini, *Int. J. Mol. Sci.*, 2014, **15**, 14868–14890.

12 R. Hausbrand, G. Cherkashinin and M. Fingerle, *J. Electron Spectros. Relat. Phenomena*, 2017, **221**, 65–78.

13 J. Illig, M. Ender, T. Chrobak, J. P. Schmidt, D. Klotz and E. Ivers-Tiffée, *J. Electrochem. Soc.*, 2012, **159**, A952–A960.

14 M. Takahashi, S. Tobishima, K. Takei and Y. Sakurai, *Solid State Ionics*, 2002, **148**, 283–289.

15 Y. Qin, H. Lin, Y. Liu and D. Wang, *AIP Conference Proceedings*, 2017, **1890**, 040002(1)-040002(7).

16 H. Zhang, I. Hasa, D. Buchholz, B. Qin, D. Geiger, S. Jeong, U. Kaiser and S. Passerini, *NPG Asia Mater.*, 2017, **9**, e370–e370.

17 Y.-M. Choi and S.-I. Pyun, *Solid State Ionics*, 1997, **99**, 173–183.

18 W. Waag, S. Käbitz and D. U. Sauer, *Appl. Energy*, 2013, **102**, 885–897.

19 J. Cabana, B. J. Kwon and L. Hu, *Acc. Chem. Res.*, 2018, **51**, 299–308.

20 K. Edström, T. Gustafsson and J. Thomas, in *Lithium-Ion Batteries: soli-electrolyte interphase*, ed. P. B. Balbuena and Y. Wang, Imperial College Press, London, 2004, ch. 8, 337–364.

21 D. Aurbach, B. Markovsky, A. Rodkin, E. Levi, Y. . Cohen, H.-J. Kim and M. Schmidt, *Electrochim. Acta*, 2002, **47**, 4291–4306.

22 D. Aurbach, M. D. Levi, E. Levi, H. Teller, B. Markovsky, G. Salitra, U. Heider and L. Heider, *J. Electrochem. Soc.*, 1998, **145**, 3024-3034.

23 A. Würsig, H. Buqa, M. Holzapfel, F. Krumeich and P. Novák, *Electrochem. Solid-State Lett.*, 2005, **8**, A34-A37.

24 M. Gauthier, T. J. Carney, A. Grimaud, L. Giordano, N. Pour, H.-H. Chang, D. P. Fenning, S. F. Lux, O. Paschos, C. Bauer, F. Maglia, S. Lupart, P. Lamp and Y. Shao-Horn, *J. Phys. Chem. Lett.*, 2015, **6**, 4653–4672.

25 H. Duncan, Y. Abu-Lebdeh and I. J. Davidson, *J. Electrochem. Soc.*, 2010, **157**, A528-A535.

26 X. H. Rui, N. Ding, J. Liu, C. Li and C. H. Chen, *Electrochim. Acta*, 2010, **55**, 2384–2390.

27 Y.-M. Choi, S.-I. Pyun, J.-S. Bae and S.-I. Moon, *J. Power Sources*, 1995, **56**, 25–30.

28 E. Peled and S. Menkin, *J. Electrochem. Soc.*, 2017, **164**, A1703–A1719.

29 G. M. Veith, M. Doucet, R. L. Sacci, B. Vacaliuc, J. K. Baldwin and J. F. Browning, *Sci. Rep.*, 2017, **7**, 6326(1)-6326(7).

30 R. Mogensen, D. Brandell and R. Younesi, *ACS Energy Lett.*, 2016, **1**, 1173–1178.

31 M. Winter, W. K. Appel, B. Evers, T. Hodal, K.-C. Möller, I. Schneider, M. Wachtler, M. R. Wagner, G. H. Wrodnigg and J. O. Besenhard, in *Electroactive Materials*, Springer Vienna, Vienna, 2001, pp. 53–66.

32 S. Krueger, R. Kloepsch, J. Li, S. Nowak, S. Passerini and M. Winter, *J. Electrochem. Soc.*, 2013, **160**, A542–A548.

33 P. B. Balbuena and Y. Wang, *Lithium-ion batteries : solid-electrolyte interphase*, Imperial College Press, 2004.

34 P. Verma, P. Maire and P. Novák, *Electrochim. Acta*, 2010, **55**, 6332–6341.

Chapter VII

Long-Term Cycling and Identifying Failure Mechanisms in Layered Oxide Sodium-Ion Batteries

7.1 Introduction

In the previous two chapters, it has been seen that the cathode dominates the resistance inside these layered oxide sodium-ion batteries over the first few (10) cycles. This cathodic impedance continues to grow over time. Analysis of impedance data using a range of different cell configurations, and, by fitting ideal equivalent electrical circuits to collected spectra, indicates that this is most likely due to an increasing resistance at the cathode-electrolyte interface. This is possibly linked to the formation of a solid permeable interphase (SPI) on the surface of the positive electrode.

These first few cycles (especially the first one), are part of the formation procedure that all cells must undergo as part of the manufacturing process, prior to being sold. Hence, it is possible that the beyond these cycles, the results found for impedance measurements may differ significantly. Most rechargeable batteries are required to operate at a high performance for hundreds of cycles, and in the majority of cases, last for a number of years.[1] However, over time, all batteries experience a deterioration in their performance, seen, in part, as a fading in their capacity and power.[2] Therefore, in order to fully evaluate the performance of a cathode material within a commercial context, it is important to examine how it performs across hundreds of cycles – being charged and discharged over thousands of hours. Much of the existing literature of impedance on secondary batteries tends to focus on the first few cycles,[3–5] and is therefore limited in the evaluation of assembled cells and/or their constituent materials for practical commercialisation.

In this chapter, long-term cycling of sodium-ion batteries was performed by charging and discharging ~ 3.2 V Na-ion layered oxide cells for hundreds of cycles. The deterioration in battery performance was monitored by examining the drop-off in discharge capacity and hence the state of health (SoH). Electrochemical impedance spectroscopy is applied at regular intervals to try and correlate a reduction in cell performance with growth in individual resistances, and, therefore, make it possible to identify the failure mechanisms in these sodium-ion batteries.

7.2 Experimental

7.2.1 Cell Designs

Four batteries were built and tested for each cell design to check the reproducibility of collected results. Analysis of collected data for these showed a close similarity between the cells. This ensures that data presented in this chapter, and conclusions drawn, are representative of a wider population.

7.2.1 (a) Two-electrode cell

Details are outlined in Section 5.2.2.

7.2.1 (b) Three-electrode cell

Details are outlined in Section 5.2.2.

7.2.2 Cell Testing Procedures

7.2.2 (a) Two-electrode cells

The two-electrode cells were tested using a Maccor Series 4000 Automated Test System. The wiring configuration was the same as used for two-electrode cells in Section 5.2.3. All cells were held at a constant temperature of 30 ± 0.5 °C using a Maccor Temperature Chamber. Each battery was left for 32 h prior to cycling to allow time to equilibrate. The cells were cycled under constant current conditions at a specific current of 14 mA g^{-1} on charging and 28 mA g^{-1} on discharging, between the voltage limits of 4.2 and 1.0 V. On charging, a constant voltage step was applied at 4.2 V until the current dropped below 2.8 mA g^{-1}. Data acquisition was performed using *MIMS* software.

For cells that underwent EIS measurements, the impedance spectra were recorded prior to cycling, and after every charge and discharge for the first five cycles, allowing four additional hours for equilibration after each charging/discharging step. An additional one-hour open circuit voltage (OCV) hold after running EIS allowed

the cell to return to a steady state. Subsequent impedance scans were performed every five cycles. AC impedance measurements were performed by varying the frequency with a perturbation potentiostatic signal amplitude of 10 mV (peak to peak) from 10 mHz to 100 kHz. *ZView* software was used for impedance data analysis.

7.2.2 (b) Three-electrode cells

Three-electrode cells were measured using the testing configuration outlined in Section 5.2.3. AC impedance measurements were performed using a potentiostat with a parallel frequency response analyser (Solartron Pstat 1470E/FRA 1455A). All cells were held at a constant temperature of 30 ± 0.5 °C using a MMM FIOCELL Incubator. Each battery was left for 32 h at 30 °C prior to cycling to allow time to equilibrate. An impedance measurement was then performed before beginning to cycle the cell. The cells were then cycled under constant current conditions at a specific current of 28 mA g^{-1} on charging and 28 mA g^{-1} on discharging between the voltage limits of 1 and 4.2 V at 30 °C. On charging, a constant voltage step was applied at 4.2 V until the current dropped below 2.8 mA g^{-1}.

The impedance spectra were recorded after every charge and discharge for the first five cycles, allowing four additional hours for equilibration after each charging/discharging step. An additional one-hour open circuit voltage (OCV) hold after running EIS allowed the cell to return to a steady state. Subsequent impedance scans were performed at regular intervals during the course of cycling the cells. AC impedance measurements were performed by varying the frequency with a perturbation potentiostatic signal amplitude of 10 mV (peak to peak) from 10 mHz to 1 MHz. Data acquisition was performed using *Multistat* software. *ZView* software was used for impedance data analysis.

7.3 Results and Discussion

7.3.1 Long-Term Performance of Sodium-Ion Cells

While extensive studies have taken place on the long-term cycling of more technologically mature, commercially-available lithium-ion batteries, the same has not yet been reported for prototype sodium-ion cells. Figure 7.1 shows the charge, discharge capacity and coulombic efficiency over the first 300 cycles for a Na[Ni,Mg,Mn,Ti]O_2/hard carbon sodium-ion battery. These data were collected at charge and discharge rates of ~ C/10 and ~ C/5 respectively, using voltage limits of 4.2 V and 1.0 V. The cell experienced an initial charge capacity of approximately 160 mAh g^{-1} for cycle 1, before the active cathode material cycles reversibly at a specific capacity of 125 mAh g^{-1}. The sodium-ion battery generates an average discharge voltage of around 3.2 V, giving a cathode specific energy of 400 Wh kg^{-1}. The cell possesses a high coulombic efficiency of ~ 99% (apart from for cycle 1), thus indicating low polarisation during cycling. Both the charge and discharge capacities gradually decline over the first ~ 200 cycles, before experiencing an accelerated drop off after this point, which is accompanied by greater fluctuation in the coulombic efficiency.

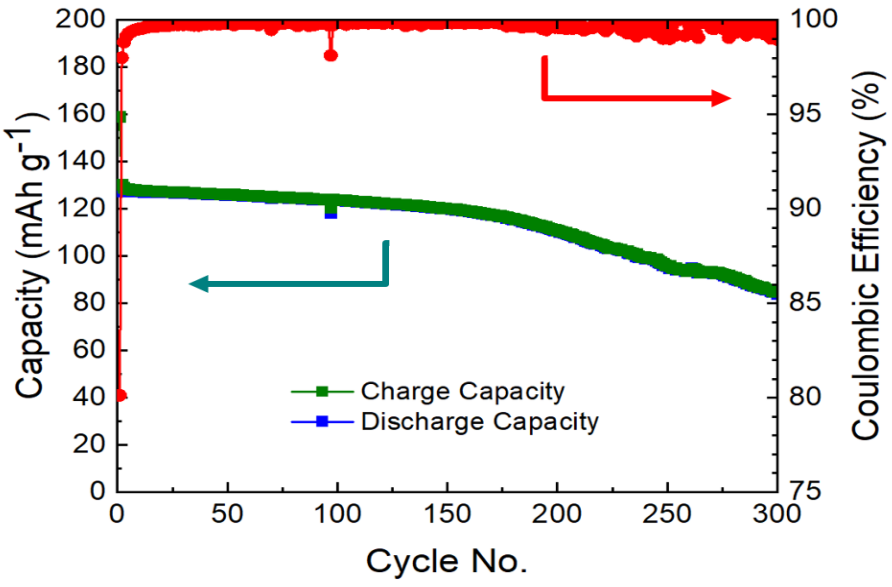

Figure 7.1 Capacity and coulombic efficiency versus cycle number for a layered oxide sodium-ion battery.

The charge capacity for the first cycle of the cell is much higher than subsequent cycles, resulting in a lower coulombic efficiency of approximately 80% for cycle 1. For many secondary battery applications, particularly mobile ones, the end of practical operation of a battery is often deemed as when its state of health drops below 80%.[6,7] For this particular cell, it maintains a charge retention above the 80% threshold for 231 cycles. The performance of the cell can be divided into two sections: a gradual linear decline in capacity up to around cycle 160, and then a more dramatic reduction rate after this point.

Previous studies performed on lithium-ion batteries have referred to this change in gradient of the capacity plot as a 'knee point'.[8,9] The 'knee point' signals the beginning of the end of operational life of the battery, as its capacity rapidly fades after this to the 80% cut-off. As there is no widely accepted standard approach or algorithm for identification of the 'knee point',[10] its location is subjective to the visual inspector, and, therefore, can be considered more of a region than occurring at one particular cycle. Hence, for this particular cell, the 'knee point' can be thought to occur between cycles 150-200. Figure 7.2 shows the approximate 'knee point' for this sodium-ion cell along with linear fits, highlighting the different gradients for the two sections of the plot before and after it.

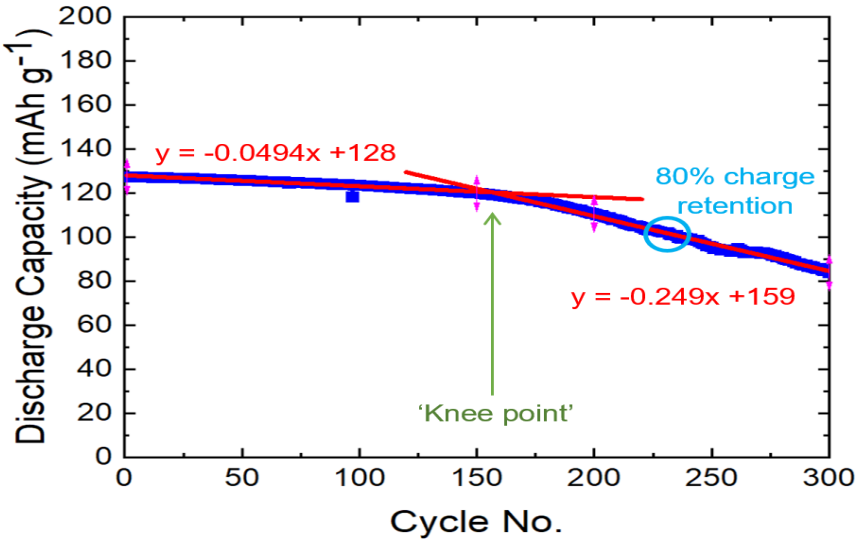

Figure 7.2 Discharge capacity versus cycle number for a layered oxide sodium-ion battery, with the 'knee point' indicated.

In Chapter V, by comparing voltage-time profiles and capacities vs. cycle number for sodium-ion batteries with and without electrochemical impedance spectroscopy in the test procedures, it was seen that the introduction of EIS steps did not dramatically alter the cycling performance of two-electrode cells. This is important as it ensures the EIS results can be used to make interpretations about sodium-ion batteries charged and discharged in a standard way. As this was done only across the first ten cycles, in order to investigate degradation mechanisms which, occur over hundreds of cycles, it is important to first check that EIS does not significantly alter the performance of sodium-ion batteries over longer periods of time.

Figure 7.3 compares the discharge capacity for a two-electrode cell cycled as normal, and one with EIS steps performed after every five cycles. It can be seen from these results that two plots are in close agreement. Importantly, this indicates that the introduction of EIS steps does not appear to significantly affect the cycling performance and degradation rate of these particular sodium-ion cells.

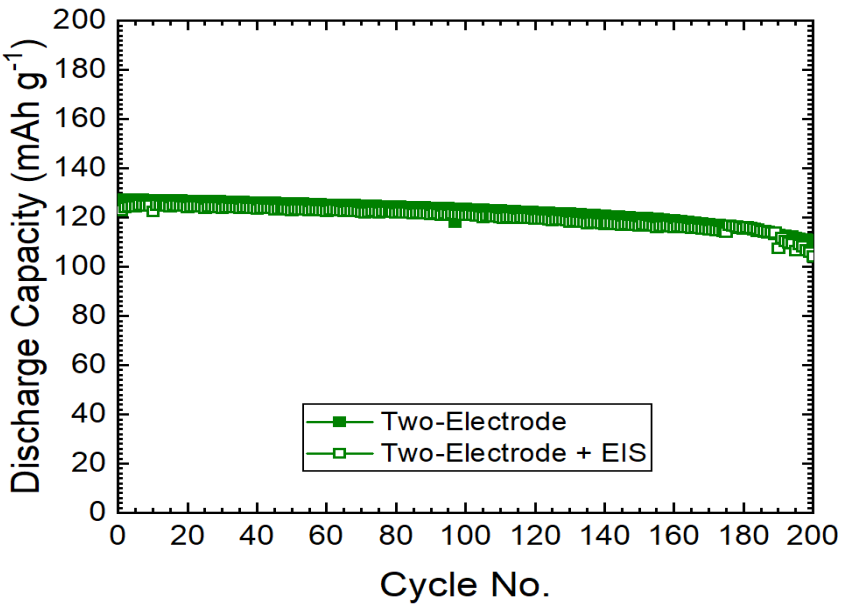

Figure 7.3 A comparison of discharge capacity versus cycle number for a two-electrode sodium-ion cell with and without EIS.

Three-electrode impedance measurements make it possible to distinguish between the impedances of the cathode and anode and monitor how resistances associated with each individual electrode change with cycling. Hence, they give a more

thorough insight into the origin of the different growing resistances within a cycling battery. Therefore, when evaluating the long-term performance of sodium-ion batteries and attempting to determine the main degradation pathways, three-electrode EIS is a particularly important tool.

Figure 7.4 compares the discharge capacities of a standard two-electrode cell undergoing normal charge-discharge cycling and a three-electrode cell subject to EIS runs at regular intervals. Once again, the two plots are very similar to one another, indicating that using the different cell configuration and performing impedance scans does not significantly affect the cycling of the sodium-ion battery. Therefore, this supports that three-electrode EIS results performed over 300 cycles can be used to make interpretations about standard commercially-relevant two-electrode batteries.

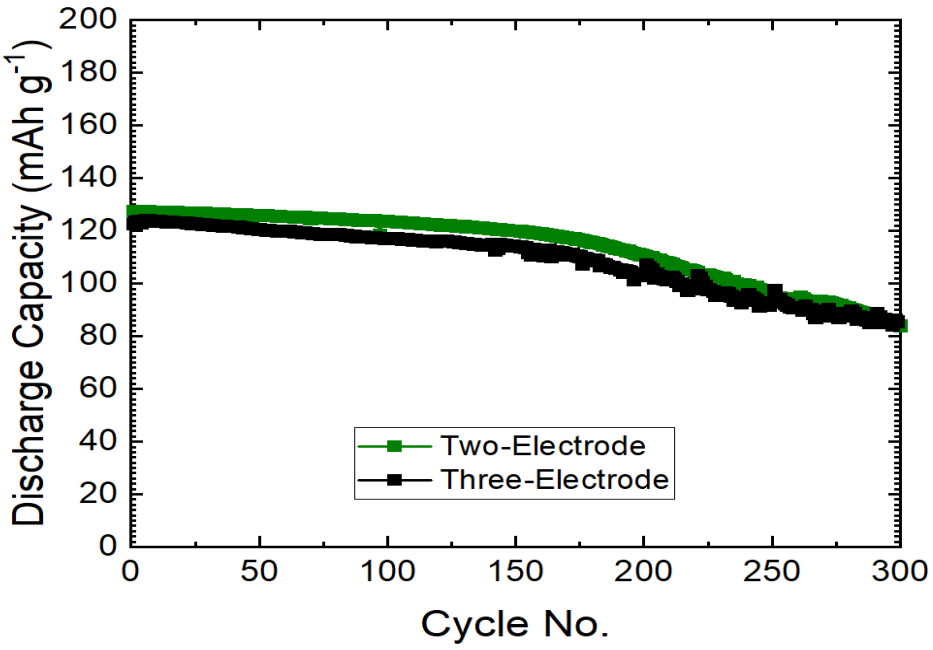

Figure 7.4 A comparison of discharge capacity versus cycle number for a standard two-electrode sodium-ion cell and a three-electrode cell with EIS performed at regular intervals.

7.3.2 Long-Term Impedance Studies of Sodium-Ion Cells

Three-electrode impedance measurements were performed every 20 cycles after charge and discharge up to cycle 120. After this point, in order to study the change in individual resistances at the 'knee point' and the onset of significant capacity fading

mechanisms in greater detail, from cycles 150 to 300 impedance scans were made after every 10th charge and discharge. Figure 7.5 plots the total resistances of the anode, cathode and full-cell in order to monitor the changes that occur with time. As was seen in the previous two chapters, across the first ten cycles the resistances for the Na-ion cell in the discharged state are always considerably greater than for when the battery has been fully charged. This is seen in the change in scale of y-axis for the two graphs in (a) and (b). The maximum resistance seen after charge is ~ 10 kΩ cm, and after discharge it is ~ 26 kΩ cm. Furthermore, as was seen previously for data recorded across the first 10 cycles, the cathode dominates the resistance inside these layered oxide sodium-ion batteries.

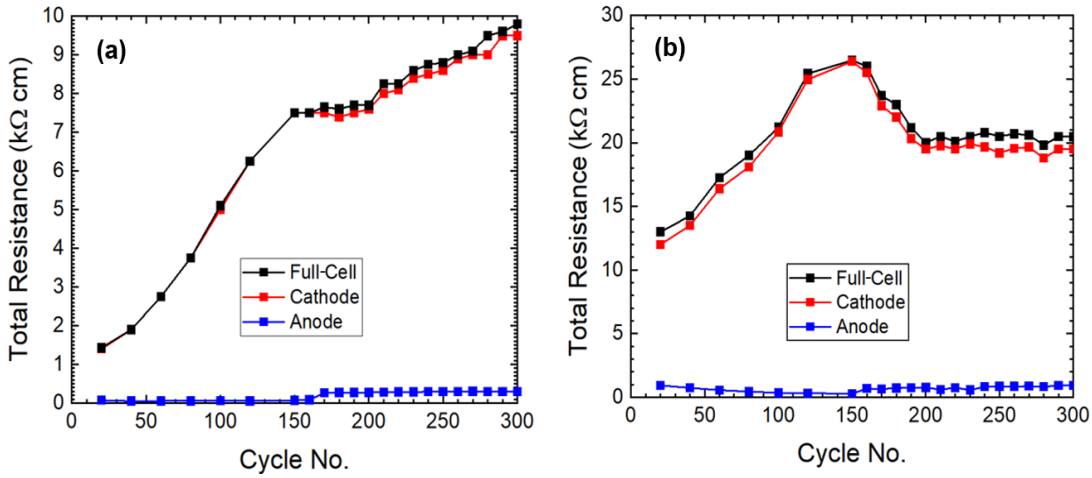

Figure 7.5 The resistances inside a three-electrode layered oxide sodium-ion cell (a) after charge and (b) after discharge for the first 300 cycles.

For the charged data (a), there is a gradual increase in full-cell resistance up to cycle 150, which goes from around 1.5 kΩ cm at cycle 20 to approximately 7.5 kΩ cm. This is solely due to an increase in cathodic resistance, as the resistance of the anode stays fairly small and constant across this period at less than 100 Ω cm. The full-cell and cathode resistances are then fairly constant between cycles 150 and 200, before increasing steadily once again after this point; they are almost both 10 kΩ cm by cycle 300. There is also a change in the anode resistance as it goes from ~ 80 to ~ 250 Ω cm after cycle 160, and then stays fairly constant upon further cycling. This is also seen in there being a greater difference between the cathode and full-cell resistance after this point. After discharge (b), the full-cell resistance approximately doubles between cycle 20 and 150, from around 13 to 26 kΩ cm. During this time,

the cathode follows a similar pattern, while the anode decreases gradually from 1 kΩ cm to ~ 300 Ω cm. From the 160th discharge onwards, the anode resistance steadily increases, reaching almost 1 kΩ cm by the 300th cycle. The dominating cathodic resistance drops near to 20 kΩ cm up to cycle 200, before levelling off after this point.

There is clearly a number of significant changes occurring at both electrodes during the long-term cycling of these layered oxide sodium-ion batteries. An increase is seen in the cathodic resistance up to cycle 150, before it either decreases or remains constant (depending on whether the battery is in the discharged or charged state) after this point. This corresponds with the onset of the 'knee point' where the capacity starts to fall dramatically, see Figure 7.2. There is also a significant increase in the resistance associated with the anode around this same time. Finally, the cathodic resistance experiences another alteration in trend after cycle 200, where it levels off in the discharged state and increases once again for each subsequent cycle after the battery has been charged. This also corresponds with the end of the region where the 'knee point' occurs, after which rapid degradation sets in, leading to the end of operational life of the battery. In order to investigate these changes in more detail, the three-electrode EIS setup will be taken advantage of by studying the behaviour of each electrode, and their resistive components, separately.

7.3.2 (a) Cathode data - Results

Figure 7.6 compares cathode data from three-electrode electrochemical impedance measurements performed after the 20th and 40th charge. In order to permit a more in-depth analysis, data are presented using a range of different complex impedance formalisms. The Nyquist plots in (a) show how the total cathode resistance increases with cycling, from ~ 1.4 to ~ 2 kΩ cm. There is also a significant change in shape of the impedance plots after 20 and 40 cycles. After the 20th charge, the impedance complex plane consists of a semi-circle with a non-zero high-frequency intercept at about 160 Ω cm, a second arc from approximately 800 Ω cm to 1.4 kΩ cm, and a low-frequency non-vertical spike. This is a similar profile to what was seen in the previous two chapters for the first ten cycles and equates to the presence of at least three resistive components.

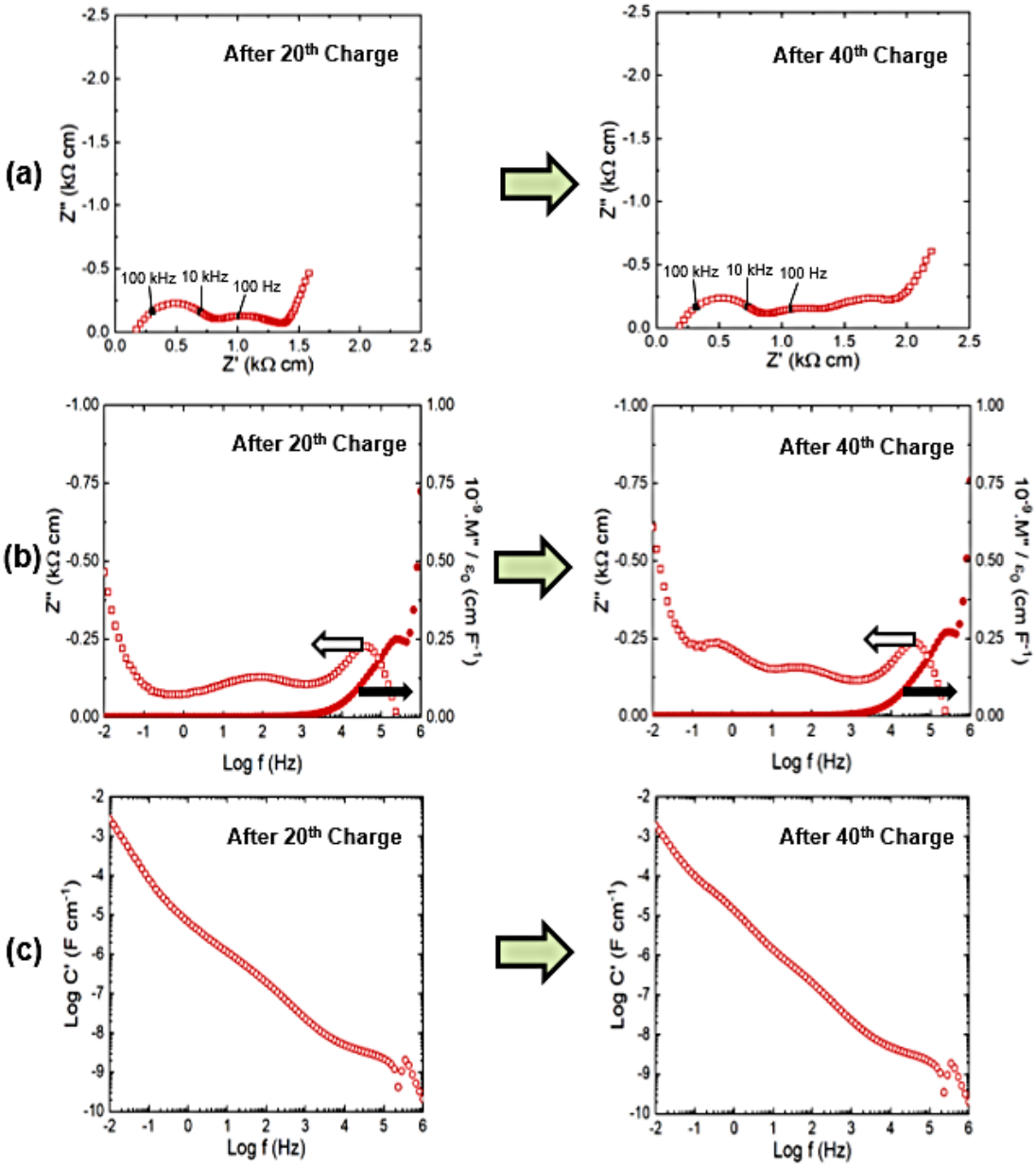

Figure 7.6 Cathode impedance data for a three-electrode layered oxide sodium-ion battery after the 20th and 40th charge. (a) Impedance complex plane plots, spectroscopic plots of $-Z''$ and M'' (b), C' (c).

After 40 cycles, there is an additional arc at lower frequency and, hence, an additional resistive component. It is the emergence of this third arc which is primarily responsible for the growth in overall cathodic resistance across this period. This is seen more clearly in the Z'' plots in (b). Between the two cycles, the peaks at high and medium frequency do not alter much, but there is clearly the appearance of an additional poorly resolved peak around 0.5 Hz. The capacitance plots in (c) also

show an additional poorly-resolved plateau emerging after 40th charge at this same frequency.

The low-frequency spike seen in the Nyquist plots in (a) may be due to diffusion in the solid electrode structure or it could be a capacitive effect. In the previous chapter, the arc at high frequency was attributed to the cathode bulk, and the more capacitive component at lower frequency, as seen after 20th charge in (a), to the cathode-electrolyte interface. At the cathode-electrolyte interface, there are two separate processes occurring: the solvation/desolvation of sodium ions, as well as the possible migration of charged species through any sort of surface layer that has formed. If the time constants of these two processes have similar magnitudes, then they will merge in the EIS spectrum to give one depressed semi-cicle;[11] such is the case after 20th charge. However, after 40 cycles, the time constants are now sufficiently different so that these two processes show up as different components in the impedance response. To a first approximation, the equivalent electrical circuit for this sodium-ion battery after 40th charge is shown in Figure 7.7.

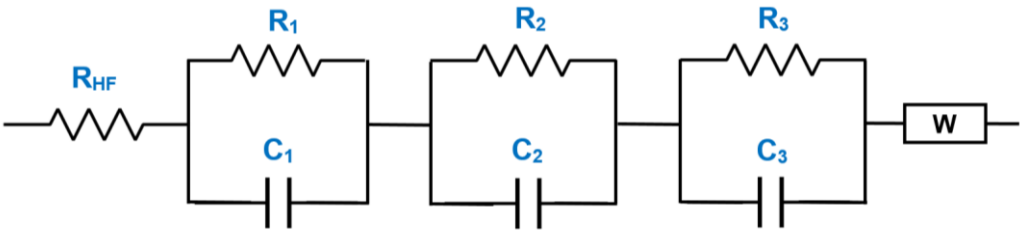

Figure 7.7 An ideal equivalent electrical circuit for this layered oxide sodium-ion battery after the 40th charge.

In order to gain further insight into degradation processes occurring at the cathode during prolonged cycling, it is important to compare and contrast what has been viewed so far in the charged state with discharged data. Figure 7.8 shows cathode impedance spectra for a three-electrode cell after the 20th and 40th discharge. The Nyquist plots in (a) possess a large low-frequency arc and a smaller high-frequency semi-circle, shown in the zoomed-in insets. There is also evidence in these zoomed-in sections of a third component between the two *RC* elements, present from around 1.5 to 2.5 kΩ cm.

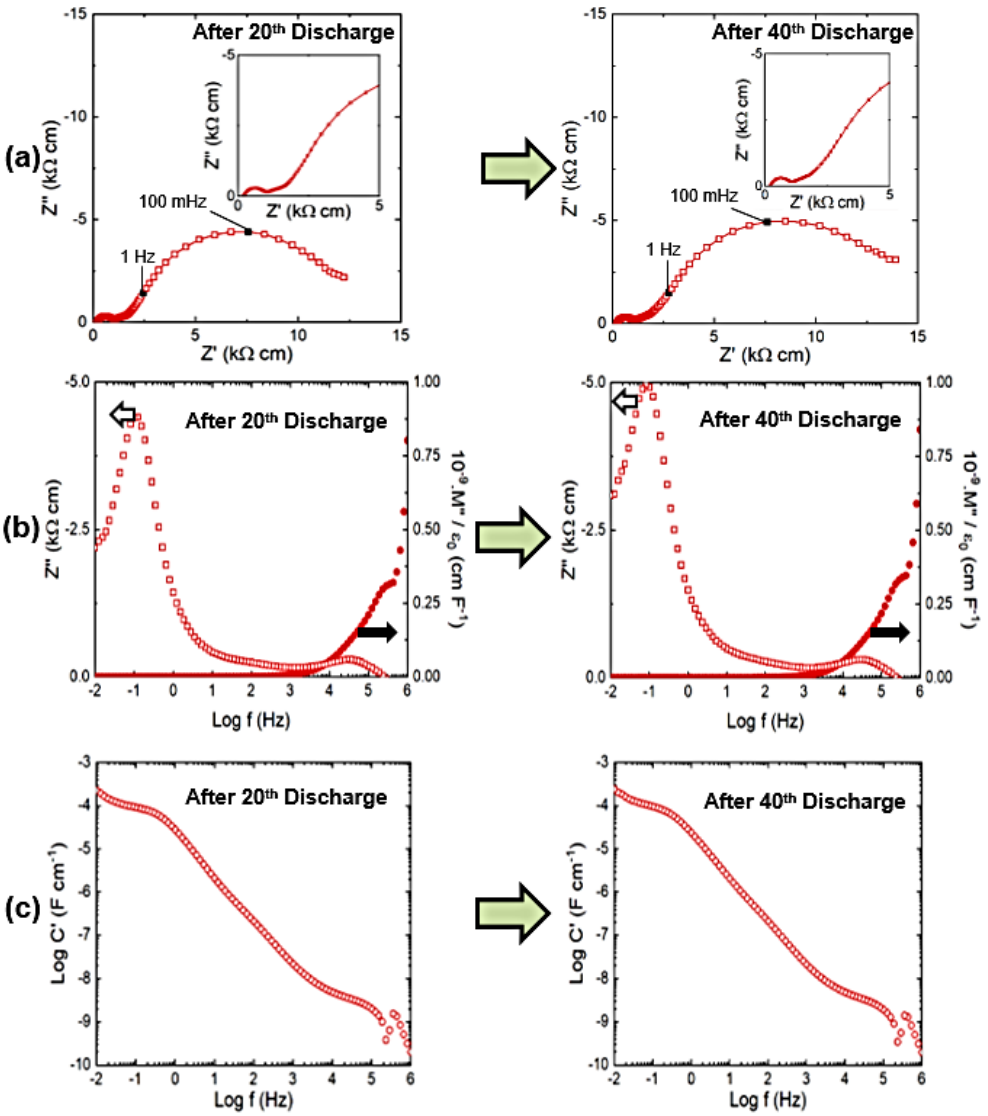

Figure 7.8 Cathode impedance data for a three-electrode layered oxide sodium-ion battery after the 20th and 40th discharge. (a) Impedance complex plane plots with inset showing high-frequency data on an expanded scale. Spectroscopic plots of $-Z''$ and M'' (b), C' (c).

The total cathode resistance increases over these 20 cycles, from approximately 12.5 to 15 kΩ cm, which from the Z'' plots in (b) can be seen to be due primarily to an increase in the low frequency resistive component. In the capacitance plots (c), there is evidence of a plateau at low frequency in the millifarad region, and one at higher frequency of the order of nanofarads. This cathode discharge data in the impedance complex plane plot in Fig. 7.8 (a) can be ideally modelled by the same equivalent electrical circuit as the one given in Fig. 7.7, but it is not clear whether or not a Warburg or additional capacitive element is needed to represent a low-frequency spike. This may still be present in the impedance response, but off-scale.

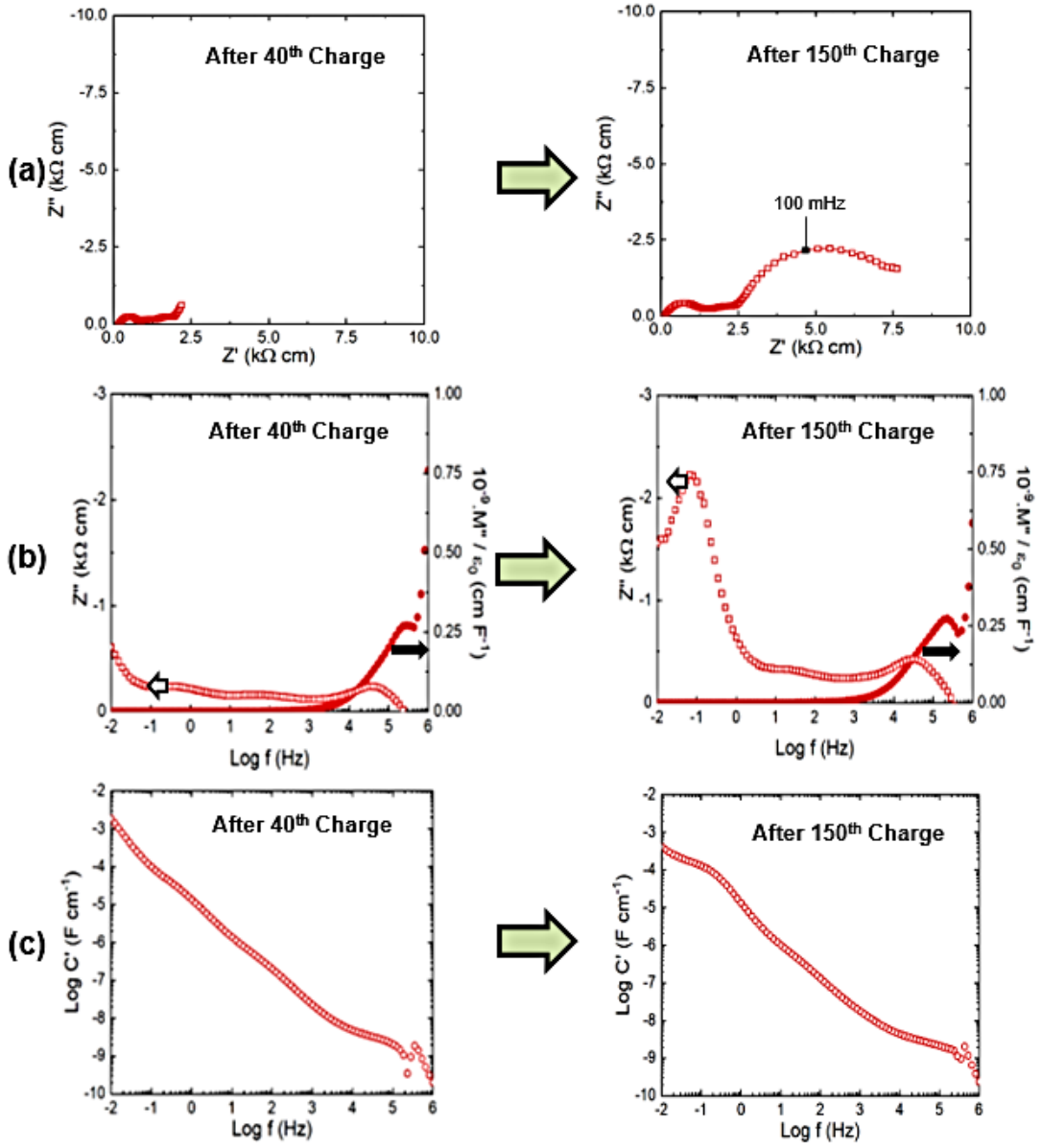

Figure 7.9 Cathode impedance data for a three-electrode layered oxide sodium-ion battery after the 40th and 150th charge. (a) Impedance complex plane plots. Spectroscopic plots of $-Z''$ and M'' (b), C' (c).

Impedance data comparing the 40th and 150th charge are plotted using different complex formalisms in Figure 7.9. It can be seen from the Nyquist plots in (a) that there is a significant increase in the resistance of the cathode: from approximately 2 to around 7.5 kΩ cm. This change in internal electrode resistance over time appears to be associated primarily with a growth in the low-frequency component in the impedance response. This is where the most significant change is seen to occur, and is confirmed in the Z'' plots in (b). There is a small peak present at around 0.1 Hz, which grows dramatically to over 2 kΩ cm by cycle 150. The C' plots in (c) also

indicate the presence of a much more well defined plateau present in this low-frequency region after prolonged cycling.

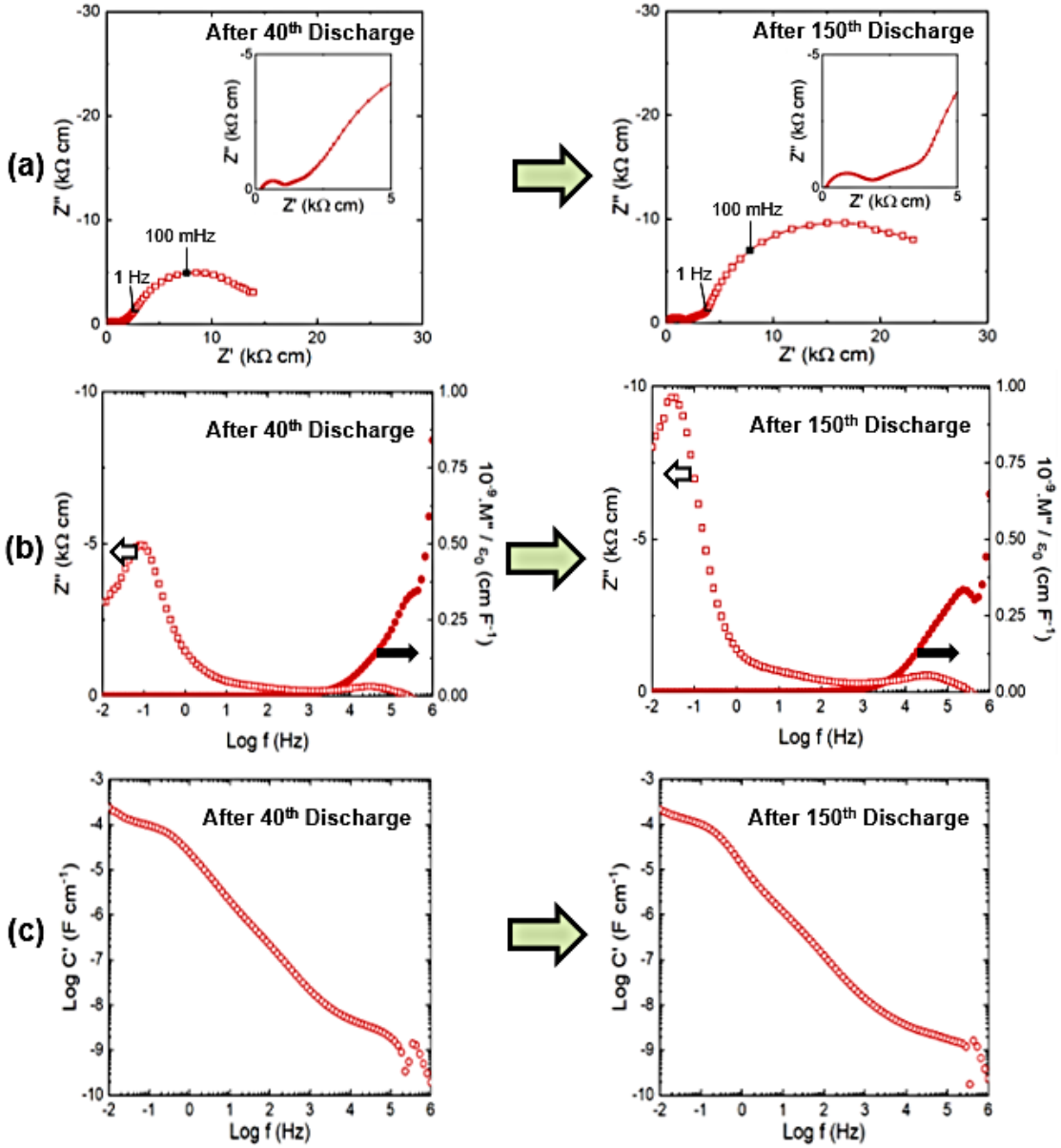

Figure 7.10 Cathode impedance data for a three-electrode layered oxide sodium-ion battery after the 40th and 150th discharge. (a) Impedance complex plane plots with inset showing high-frequency data on an expanded scale. Spectroscopic plots of $-Z''$ and M'' (b), C' (c).

For comparison, cathode impedance data after 40th and 150th discharge are presented in Figure 7.10. The Nyquist plots in (a) show that there is an increase in the total resistance associated with this positive electrode, from approximately 15 to 25 kΩ cm. Similarly, to charged data, it can be seen that this is overwhelmingly due to a

growth in the low-frequency *RC* element. The *Z''* plots in (b) show that over this period, the low-frequency peak at 0.1 Hz roughly doubles from 5 to 10 kΩ cm. The capacitance *C'* data in (c) show two clearly defined plateaus: one in the millifarad and one in the nanaofarard region at low and high frequency respectively. There is also a small poorly-resolved plateau present in the microfarad region between 5-10 Hz, relating to the mid-frequency *RC* component, which is shown in the zoomed-in insets in (a).

In order to see the effects of further cycling on these layered oxide Na-ion batteries, cathode impedance data are displayed in Figure 7.11 for after the 150th, 200th, 230th and 300th charge. The Nyquist plots in (a) show that the total cathodic resistance is fairly constant at around 7.5 kΩ cm between cycles 150-200, before increasing to around 10 kΩ cm up to cycle 300. This is due primarily to an increase in the low-frequency *RC* component. This is shown more clearly in the *Z''* plots in (b), with the peak around 0.1 Hz growing over time. There is also a more modest increase in the R_2 and R_3 resistances as well. The *C'* plots in (c) highlight the three different components present with capacitances of 1.5-4 nF cm^{-1}, 0.35-1.5 μF cm^{-1} and 0.04-0.1 mF cm^{-1} at high, medium, and low frequency respectively.

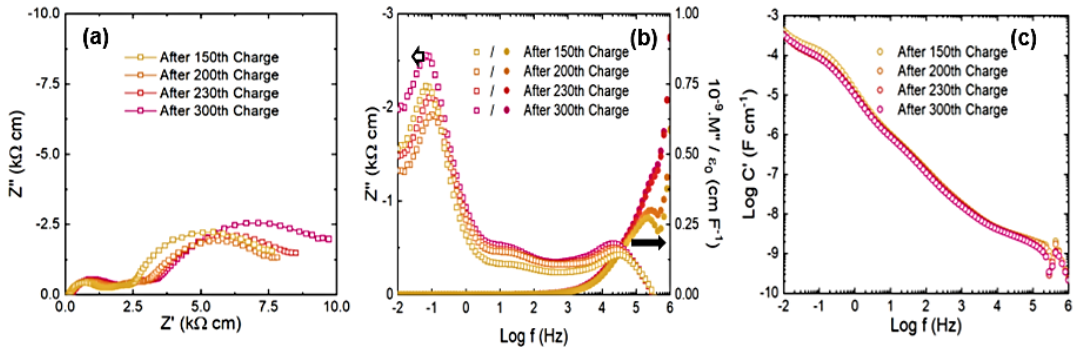

Figure 7.11 Cathode impedance data for a three-electrode layered oxide sodium-ion battery after the 150th, 200th, 230th and 300th charge. (a) Impedance complex plane plots. Spectroscopic plots of -*Z''* and *M''* (b), *C'* (c).

Figure 7.12 displays impedance data after a series of discharges between cycles 150-300. This time, the impedance complex plane plots in (a) indicate a reduction in the total cathodic resistance up to cycle 200, from ~ 27 to ~ 20 kΩ cm, which then appears to stay the same across the last 100 cycles. As shown by the *Z''* spectroscopic plots in (b), this trend is governed by the low-frequency *RC*

component shrinking, which goes from around 22.5 to 15 kΩ cm. The *C'* plots in (c) are similar to those present in Fig. 7.11, indicating that the same three resistive components are present after charge and discharge under prolonged cycling.

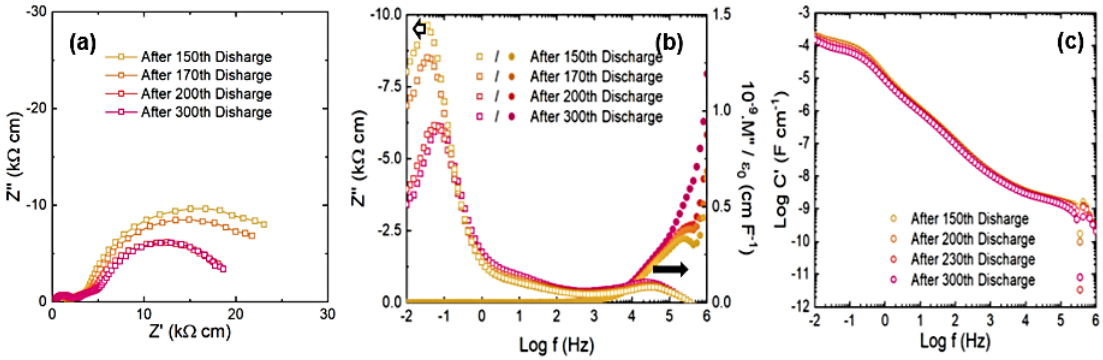

Figure 7.12 Cathode impedance data for a three-electrode layered oxide sodium-ion battery after the 150th, 170th, 200th and 300th discharge. (a) Impedance complex plane plots. Spectroscopic plots of -*Z''* and *M''* (b), *C'* (c).

The cathodic resistances and capacitances seen over the first 300 cycles after charge and discharge are presented in Tables 7.1 and 7.2. The resistances of all three separate RC components - R_1, R_2 and R_3 - are greater when the sodium-ion battery is in the discharged state compared to after it has been charged. All these individual resistances associated with the cathode, as well as the resistance of the non-zero high-frequency intercept, R_{HF}, increase with cycle number. In the charged state, R_{HF} goes from ~ 160 to ~ 220 Ω cm, and after discharge it increases from around 190 Ω cm to 270 Ω cm over the 280 cycles. This increase in resistance likely coincides with a gradual decomposition of the sodium-ion electrolyte with ageing of the battery. The value of the R_1 component goes from ~ 650 Ω cm to almost 2 kΩ cm after charge, and from 810 to > 2.2 kΩ cm in the discharged state of the cell. The mid-frequency resistance, R_2, is close to 600 Ω cm after both the 20th charge and discharge, but increases to 1.15 kΩ cm after 300 charges, and has reached 2.5 kΩ cm by the 300th discharge.

Table 7.1 Cathode resistances and capacitances for a fully-charged layered oxide sodium-ion battery over the first 300 cycles.

Cycle No.	R_{HF} (Ω cm)	R_1 (kΩ cm)	$C_1.10^9$ (F cm^{-1})	R_2 (kΩ cm)	$C_2.10^6$ (F cm^{-1})	R_3 (kΩ cm)	$C_3.10^4$ (F cm^{-1})	R_{Tot} (kΩ cm)
20	162	0.663	5.55	0.575	3.41	-	-	1.40
40	175	0.675	6.72	0.500	3.92	0.550	4.40	1.90
60	170	0.705	6.43	0.525	4.61	1.35	4.14	2.75
80	175	0.725	6.25	0.550	4.40	2.30	5.61	3.75
100	175	0.725	6.25	0.600	4.03	3.50	3.69	5.00
120	175	1.08	4.22	0.650	5.66	4.35	4.51	6.25
150	125	1.38	4.06	1.00	4.53	5.00	4.84	7.50
160	126	1.47	3.79	1.00	4.53	4.90	4.00	7.50
170	141	1.46	3.83	1.05	3.50	4.85	4.05	7.50
180	141	1.56	3.58	1.05	3.50	4.65	3.42	7.40
190	145	1.61	3.48	1.05	3.50	4.70	3.39	7.50
200	145	1.61	4.29	1.25	3.63	4.60	3.46	7.60
210	202	1.55	4.45	1.25	2.94	5.00	3.18	8.00
220	208	1.64	4.2	1.15	3.20	5.10	3.12	8.10
230	213	1.69	4.08	1.10	3.34	5.40	3.63	8.40
240	215	1.79	4.76	1.10	4.12	5.40	2.95	8.50
250	215	1.79	3.86	1.10	4.12	5.50	3.57	8.60
260	215	1.79	3.86	1.15	3.94	5.75	3.41	8.90
270	217	1.78	3.86	1.25	4.47	5.75	4.21	9.00
280	220	1.78	3.87	1.25	3.62	5.75	4.21	9.00
290	215	1.89	4.51	1.15	4.86	6.25	3.87	9.50
300	218	1.88	4.51	1.15	4.86	6.25	3.87	9.50

Table 7.2 Cathode resistances and capacitances for a fully-discharged layered oxide sodium-ion battery over the first 300 cycles.

Cycle No.	R_{HF} (Ω cm)	R_1 (kΩ cm)	$C_1.10^9$ (F cm^{-1})	R_2 (kΩ cm)	$C_2.10^6$ (F cm^{-1})	R_3 (kΩ cm)	$C_3.10^4$ (F cm^{-1})	R_{Tot} (kΩ cm)
20	190	0.810	6.90	0.600	2.15	10.4	1.24	12.0
40	205	0.895	6.24	0.900	4.09	11.5	1.71	13.5
60	198	0.902	6.20	1.15	4.86	14.1	1.71	16.4
80	210	0.940	5.95	1.30	5.30	15.7	1.91	18.1
100	210	0.990	6.96	1.40	6.07	18.2	2.01	20.8
120	205	1.30	4.32	1.60	5.31	21.9	2.07	25.0
150	140	1.76	3.18	1.85	5.66	22.6	2.00	26.4
160	160	1.84	3.04	1.80	5.92	21.7	2.09	25.5
170	175	1.83	3.05	2.00	5.24	18.9	1.95	22.9
180	175	1.93	2.90	2.10	4.99	17.8	2.07	22.0
190	180	1.92	2.91	2.15	4.87	16.1	1.86	20.3
200	180	2.02	2.77	2.30	5.61	15.0	1.99	19.5
210	254	2.00	2.80	2.25	4.65	15.3	1.58	19.8
220	270	2.03	2.75	2.45	5.27	14.8	1.64	19.5
230	263	2.14	2.62	2.60	4.97	14.9	1.62	19.9
240	270	2.13	2.62	2.60	4.97	14.7	1.65	19.7
250	255	2.25	2.49	2.50	5.16	14.2	1.38	19.2
260	254	2.25	3.07	2.50	5.16	14.6	1.35	19.6
270	255	2.25	3.07	2.75	5.79	14.4	1.68	19.7
280	254	2.25	3.07	2.50	5.16	13.8	1.42	18.8
290	254	2.25	3.07	2.50	5.16	14.5	1.67	19.5
300	270	2.23	3.09	2.500	4.19	14.5	1.67	19.5

The resistance of low-frequency component, R_3, changes from approximately 4.4 kΩ cm to 6.25 kΩ cm after charge, and from about 10.4 to ~ 14.5 kΩ cm after discharge. The combined effect of these different increases is to cause the total resistance of the Na-ion battery after charge to increase from around 1.4 to ~ 9.5 kΩ cm. Whereas, after discharge, R_{Tot} goes from approximately 12 to 19.5 kΩ cm. The capacitance value of C_1 generally decreases with electrochemical testing, from around 5.5 to 4.5 nF cm^{-1} and from ~ 7 to ~ 3 nF cm^{-1} after charge and discharge respectively. The mid-frequency component, C_2, fluctuates around 4-5 μF cm^{-1} in both the charged and discharged states, whereas the capacitance of the lower frequency element, C_3, stays fairly constant around 0.4 mF cm^{-1} for after the Na-ion cell has been charged. It has a smaller capacitance, in the 0.1-0.2 mF cm^{-1} range in the discharged state.

7.3.2 (a) Cathode data - Discussion

By examination of their capacitance values, it is possible to try and attribute the different components present in the cathodic impedance response to separate parts of, or processes occurring within, the sodium-ion battery. The high-frequency *RC* element has a capacitance (C_3) in the nanofarad region, the medium-frequency component has a capacitance (C_2) of a couple of microfarads, and the lower frequency arc (C_3) possesses a value of ~ 0.1-1 mF cm^{-1}.

In the previous chapter, the arc at high frequency, with the lowest capacitance and therefore the thickest region, was attributed to the cathode bulk. As was mentioned previously, at the cathode-electrolyte interface there are two separate processes occurring: the solvation/desolvation of sodium ions, as well as the possible migration of charged species through any sort of surface layer that has formed. As a capacitance in the mF region is consistent with that of an electrochemical double layer for a typical energy storage device, it is likely that the lowest frequency component is the charge-transfer resistance coupled with a double later capacitance formed at the cathode-electrolyte interface. Therefore, the second medium frequency component is likely to be the surface layer and diffusion of sodium ions through this region. The different components of the cathode impedance measurement are displayed in Figure 7.13.

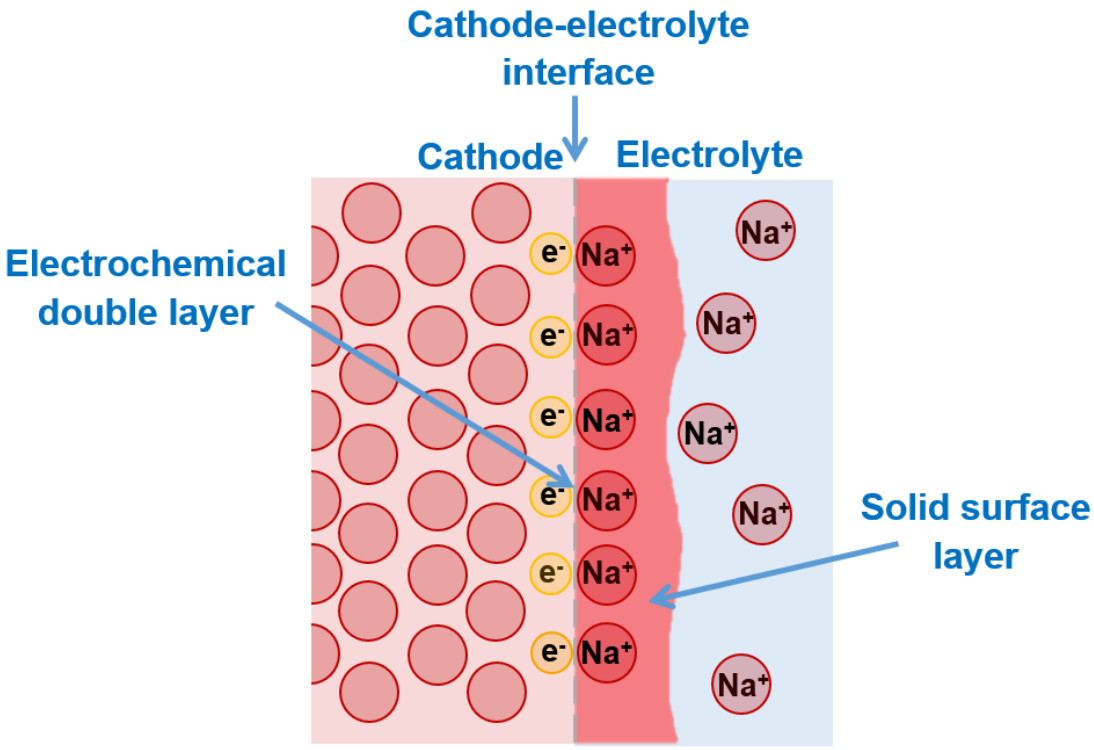

Figure 7.13 A schematic illustrating the components present within the cathode impedance response for a three-electrode measurement of a sodium-ion battery.

From the three-electrode impedance measurements across the first 40 cycles (see Figures 7.6 and 7.8), it appears as if the charge-transfer resistance takes longer to appear in the charged state, and the surface layer resistance longer after discharge. This may be explained by a difference in voltages, which are thought to be important when considering double layer and solid electrolyte/permeable interphase formation.[12] It has been reported for lithium-ion batteries that the SEI is more stable and hence, prevalent at high voltages,[13] which would agree with the effect seen in these Na-ion cells. The resistances of all three separate *RC* components - R_1, R_2 and R_3 - are greater when the sodium-ion battery is in the discharged state compared to after it has been charged. The resistance of R_1, which is attributed to the cathode bulk, could be larger because after discharge there is more sodium in the cathode structure, meaning that there may also be less electron holes, and, therefore, the p-type conductivity of the material decreases. The surface layer resistance, R_2, is also larger after the Na-ion battery has been discharged. This may be related to a smaller concentration gradient of sodium ions inside and outside the cathode, meaning that it takes longer for Na^+ ions to diffuse between the electrode and electrolyte. Finally, the low-frequency resistance, R_3, which is likely to be associated with charge-

transfer at the cathode-electrolyte interface, experiences the most significant increase in the discharged state. This may be because after discharge the cathode structure contains considerably more sodium in it compared with in the charged state. Therefore, it is much more difficult to insert any further sodium into the layered rock salt type structure and, therefore, there is a higher resistance associated with the charge-transfer reaction.

The cathodic resistances and capacitances seen over the first 300 cycles after charge and discharge are also displayed graphically in Figure 7.14. The values of R_1 and R_2 increase steadily in both the charged (a) and discharged (b) states. As the resistance of R_1 is attributed to the cathode bulk, this indicates a reduction in the conductivity of the positive electrode. The capacitance (c) and (d) associated with this *RC* component, C_1, decreases with cycling, thus indicating a thickening of the electrode, and hence a decrease in particle density. This is likely to lead to a decrease in particle-particle contact and, therefore, a larger inter-particle contact resistance. The increase of R_1 occurs most profoundly at cycle 150, at the onset of the 'knee point'.

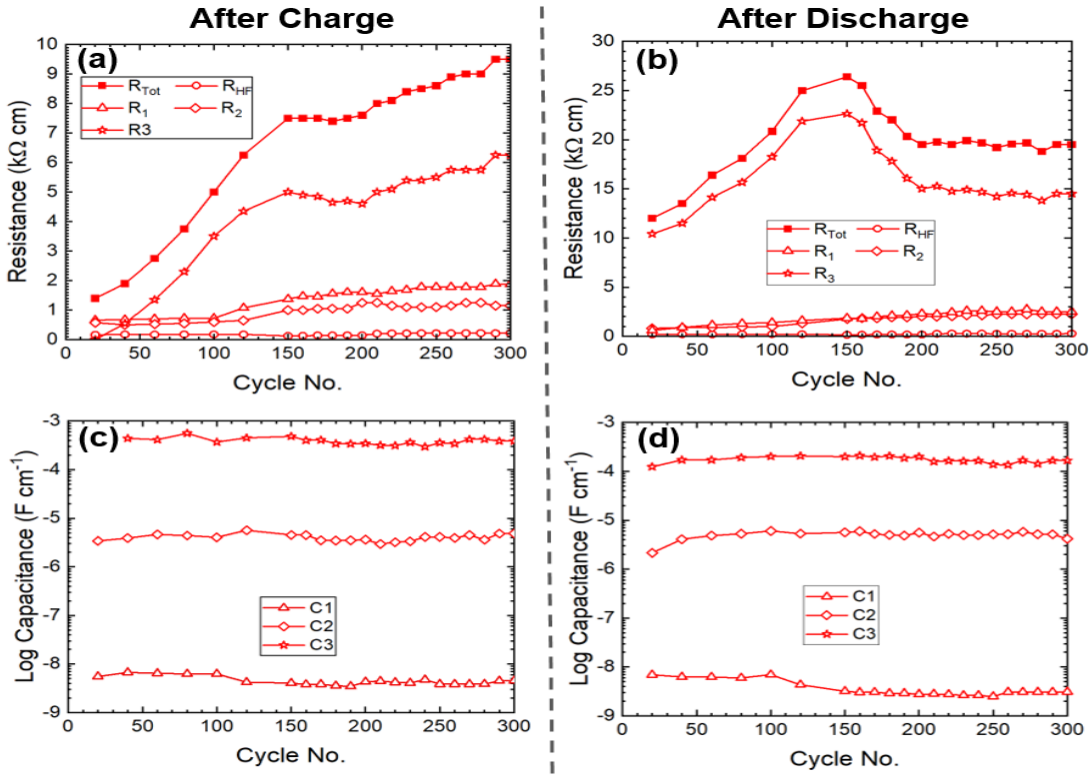

Figure 7.14 A comparison of the cathode resistances and capacitances inside a three-electrode layered oxide sodium-ion battery after charge (a) & (c), and discharge (b) & (d), over 300 cycles.

The value of R_2, attributed to the resistance of the solid layer, which forms on the surface of the cathode, increases with cycling, thus indicating that diffusion through this region is becoming slower, meaning that the surface becomes more insulating under prolonged cycling. An investigation of the capacitance values associated with this component, do not show a significant variation over time, therefore suggesting that there is no significant increase in the thickness of the surface layer with cycling. One possible explanation for the growth in resistance, therefore, is that the composition of the solid permeable interphase may be changing over time as the electrolyte continues to decompose, causing it to become more insulating and resistant to Na^+ ion diffusion.

As can be clearly seen in Figure 7.14, the resistance inside these layered oxide sodium-ion batteries is dominated by the low-frequency component R_3, which is possibly the charge-transfer resistance at the cathode-electrolyte interface. The charge-transfer resistance is related to how easily/quickly sodium ions can de-solvate, i.e. lose their shell of electrolyte solvent molecules, associate with an electron, and become intercalated in the layered oxide rock salt cathode (the process occurs in the opposite direction during charging). The value of R_3 increases up to cycle 150 in both the charged and discharged states of the cell. This may be a combined consequence of both the R_1 and R_2 resistances rising, meaning it takes longer for sodium ions and electrons to reach the cathode-electrolyte interface and for the charge-transfer reaction to occur.

During the cycling of lithium-ion batteries a number of degradation mechanisms associated with the inactive components have been shown to occur: such as binder decay,[14] corrosion of current collector,[15] and the oxidation of conductive carbon additive at high voltage[16]. As these same inactive materials are present in sodium-ion batteries, it is reasonable to presume that similar processes will occur with these also. A combination of these different unfavourable processes will reduce how easily electrons are freed up to associate with intercalating sodium ions from the electrolyte, and hence account for the increase in charge-transfer resistance that is observed.

After cycle 150, and at the ‘knee point’ in the capacity plot, there is a decrease in the value of R_3. This indicates that certain degradation mechanisms are occurring, which

cause a decrease in charge-transfer resistance, but also lead to an acceleration in capacity fading. This decrease in R_3 is not associated with an increase in surface area of the active material particles, as the capacitances of C_2 and C_3 do not show a sustained increase from cycle 150 onwards.

As a cell is a self-contained device with the two electrodes connected by the electrolyte, any processes seen to occur at the cathode may be connected to mechanisms at the anode. Therefore, a consideration of the resistances and capacitances associated with the negative electrode may help to reveal the origin of the major changes seen to occur at the 'knee point' associated with the cathode, and give further insight into the crucial degradation mechanisms, which are eventually responsible for Na-ion cell failure.

7.3.2 (c) Anode data – Results

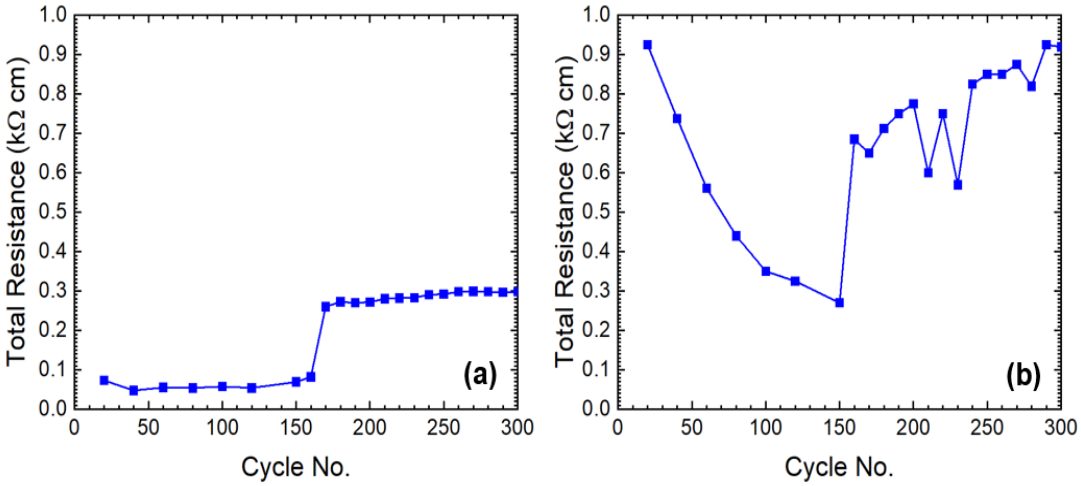

Figure 7.15 The anode resistances inside a three-electrode layered oxide sodium-ion cell (a) after charge and (b) after discharge over the first 300 cycles.

The total resistance of the hard carbon anode inside a full-cell sodium-ion battery over the first 300 cycles is given in Figure 7.15. After charge (a), when the carbon structure is full of Na, the resistance fluctuates between 50-80 Ω cm for the first 160 cycles, before it increases significantly to around 260 Ω cm on the 170th charge. It then grows gradually during the remaining course of cycling up to ~ 300 Ω cm by cycle 300. In the discharged state (b), the total anode resistance after the 1st discharge, once the carbon matrix has been stripped of its sodium content, is > 900 Ω

cm. This then declines to ~ 270 Ω cm by cycle 150, before a sharp increase to around 700 Ω cm on the 160th discharge. The total anodic resistance then shows a general increasing trend, returning to ~ 900 Ω cm again by cycle 300.

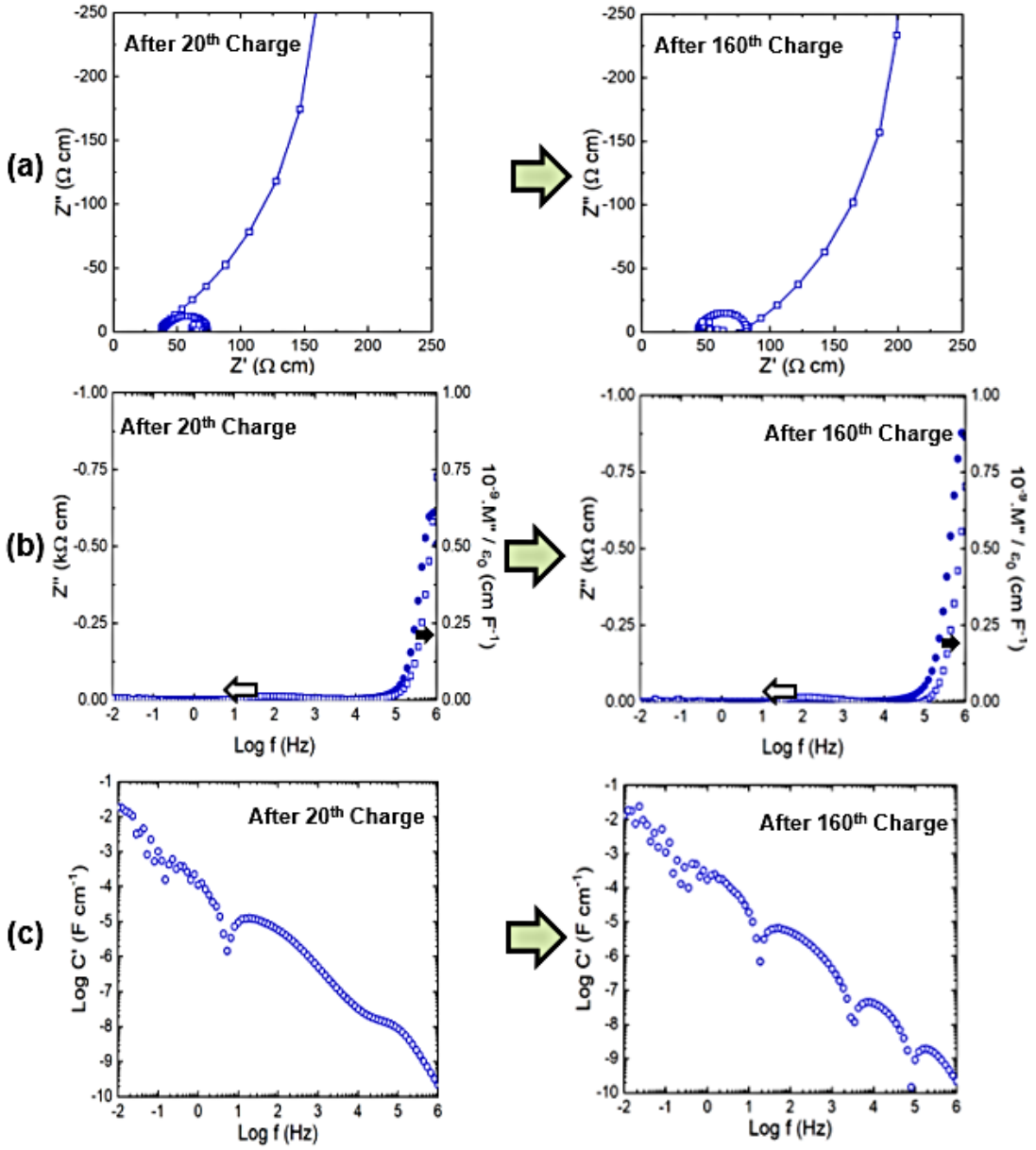

Figure 7.16 Anode impedance data for a three-electrode layered oxide sodium-ion battery after the 20th and 160th charge. (a) Impedance complex plane plots. Spectroscopic plots of -*Z''* and *M''* (b), *C'* (c).

Figure 7.16 compares anode data from three-electrode electrochemical impedance measurements performed after the 20th and 160th charge. The Nyquist plots in (a) show a single arc possessing a constant total resistance of around 750 Ω cm. There is

a long tail at high frequency with an increasing capacitance. This was also seen in earlier anode impedance measurements over the first 10 cycles (see Chapter V), and is most likely due to inductive effects from the non-inert component responding to the AC signal. This is also visible in the *Z''* plots in (b), as well as the single resistance showing up as a small hump around 50-250 Hz. The capacitance plots in (c) appear to show a high-frequency plateau at 10-100 kHz of 10-20 nF cm^{-1}, as well as possibly an additional one in the microfarad region ~ 50 Hz. However, it is difficult to say definitively because *C'* anode data are increasingly noisy towards lower frequency. It is also not possible to pick out any well-defined plateaus in data after 160th charge due to the noisiness of this dataset.

Anode impedance plots for after the 20th and 150th discharge of the Na-ion cell are presented in Figure 7.17. The Nyquist plots in (a) show a large arc, with a smaller component towards medium frequency, visible in the zoomed-in insets. As was seen for charged data, there is also a high-frequency capacitive tail. The total anodic resistance can be seen to decrease from close to 1 k Ω cm to ~ 250 Ω cm, between cycles 20 and 150. This continues the trend, which was seen over the first ten cycles (Chapter V), where the resistance decreased from approximately 2.5 to 1.25 kΩ cm. The *Z''* plots in (b) show that the peak at 0.5 Hz decreases from around 400 to ~ 50 Ω cm during the course of cycling. Plots of capacitance against frequency (c) display that after the 20th discharge there is the same high-frequency plateau in the nanofarad region as was seen after charge, as well as an additional low-frequency plateau at about 0.2 mF cm^{-1}. This is due to the carbon-electrolyte interface which acts as a blocking capacitor once all the sodium has been removed from the negative electrode. There may also be a third component in the microfarad region, present as a small indent in the *C'* plot around 50 Hz. Due to the noisiness of data, once again it is difficult to pick out any well-defined plateaus after 150th discharge.

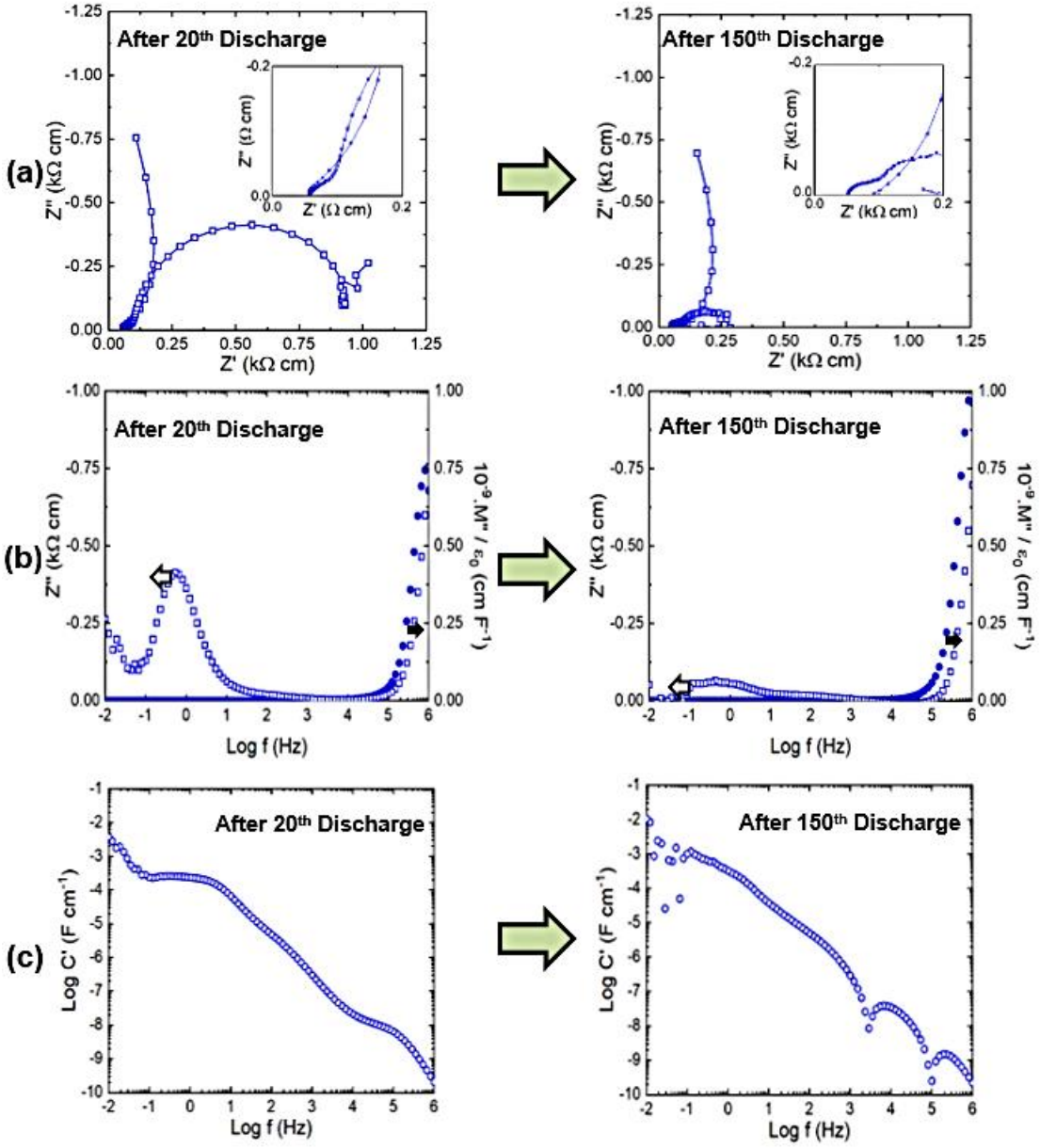

Figure 7.17 Anode impedance data for a three-electrode layered oxide sodium-ion battery after the 20th and 150th discharge. (a) Impedance complex plane plots with inset showing mid-frequency data on an expanded scale. Spectroscopic plots of $-Z''$ and M'' (b), C' (c).

As is shown in Figure 7.15, the major changes in resistance at the anode occur on 170th charge and 160th discharge. Therefore, impedance plots displaying data before and after these changes using a range of different complex formalisms are presented in Figures 7.18 and 7.19. Charged data in Fig. 7.18(a) show that there is a change in the shape of the Nyquist plot between the 160th and 170th charge, with in addition to the same small distorted semi-circle in both, there is the start of an additional arc towards higher frequency in the latter cycle. The total resistance also increases

substantially from around 80 to ~ 250 Ω cm. There is the same small hump present in both *Z''* plots between 50-250 Hz in (b). However, the two spectroscopic plots differ at high frequency, thus indicating there is potentially a poorly resolved additional component present after 170th charge. From the *C'* plots in (c), it is only possible to identify the high-frequency plateau with a capacitance in the nanofarad region after 170th charge.

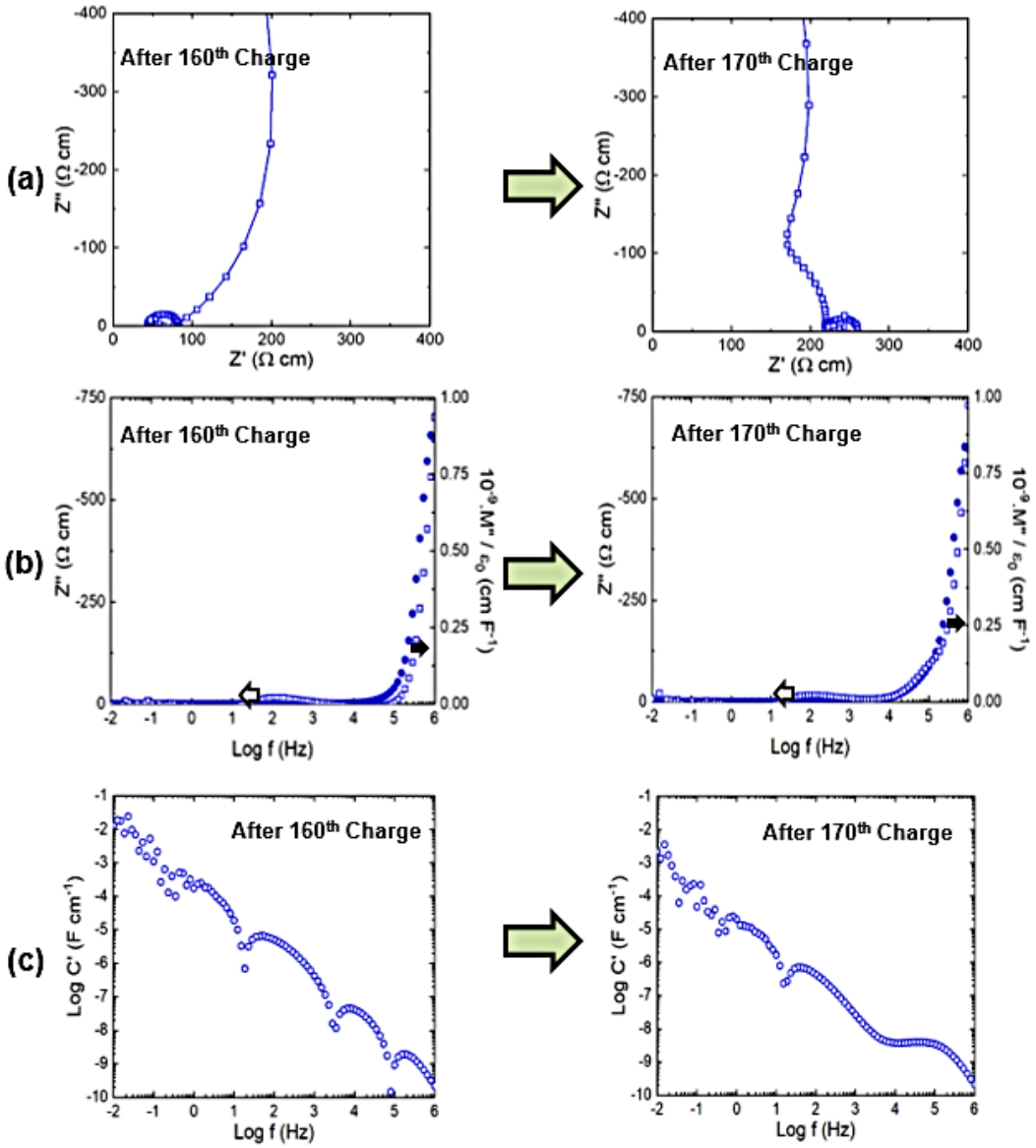

Figure 7.18 Anode impedance data for a three-electrode layered oxide sodium-ion battery after the 160th and 170th charge. (a) Impedance complex plane plots. Spectroscopic plots of -*Z''* and *M''* (b), *C'* (c).

Similarly, there is a change in shape in the Nyquist plots after discharge as shown in Fig 7.19(a). After 160th discharge, there is a larger *RC* component present at higher frequency, which also corresponds with the total anodic resistance increasing from around 250 to ~ 700 Ω cm. This time, in the *Z''* plots in (b), as well as having a peak at 0.5 Hz, there is clearly an additional component present after 160th discharge around 50 kHz. Once again, the *C'* plots in (c) are difficult to analyse due to how noisy they are, but there appears to be an indent in the microfarad region ~ 50 Hz, as well as a flat plateau clearly visible after 160th discharge at high frequency.

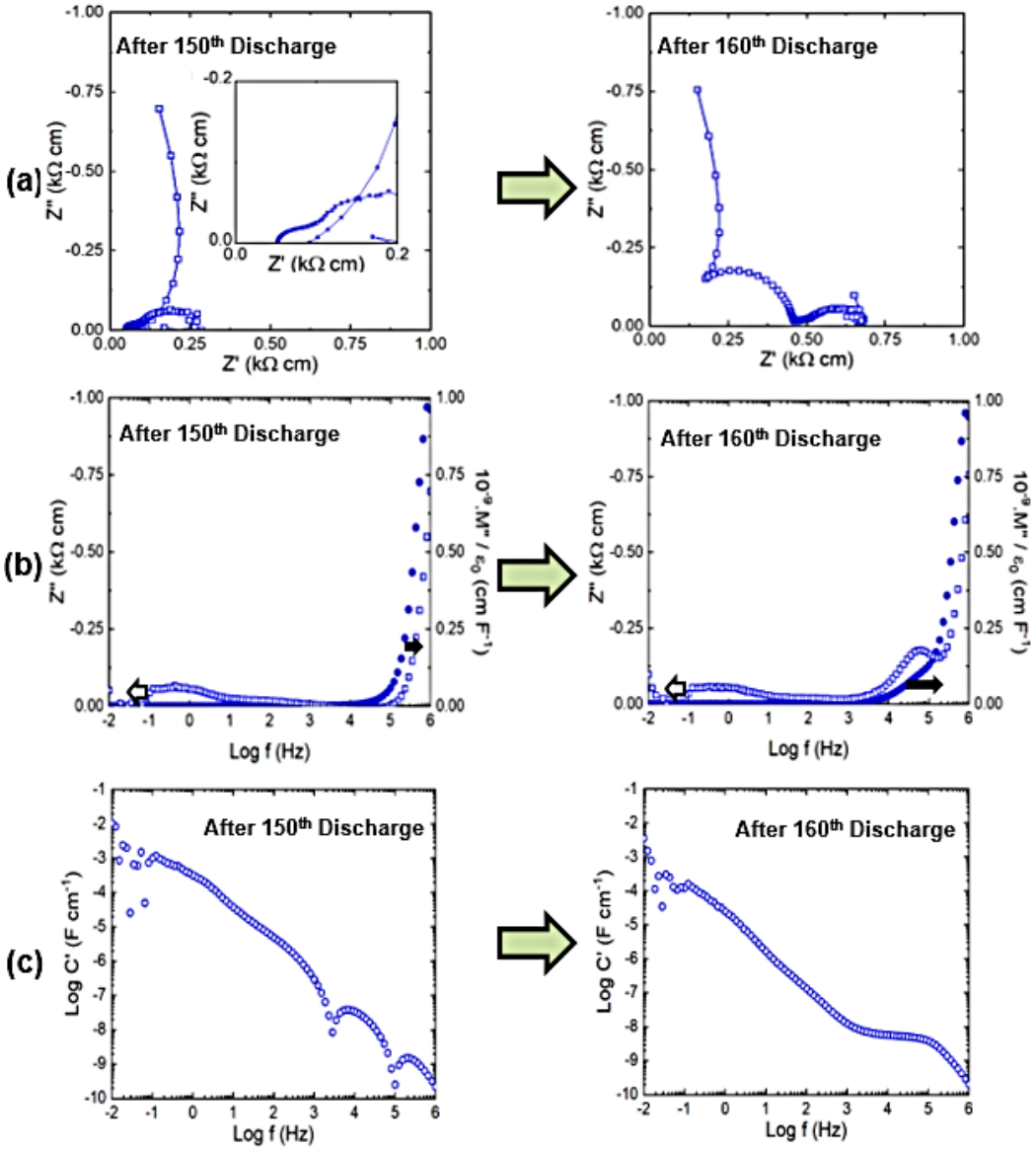

Figure 7.19 Anode impedance data for a three-electrode layered oxide sodium-ion battery after the 150th and 160th discharge. (a) Impedance complex plane plots with inset showing mid-frequency data on an expanded scale. Spectroscopic plots of *-Z''* and *M''* (b), *C'* (c).

In order to see the effects of further cycling on these layered oxide Na-ion batteries, anode impedance data are displayed in Figure 7.20 for after the 170th and 300th charge. The Nyquist plots in (a) possess the same shape, and show that the total anodic resistance increases from around 260 to 300 Ω cm between cycles 170-300. The *Z''* plots in (b) highlight that this is due primarily to an increase in the high-frequency RC component at 50-150 Hz. The *C'* plots in (c) show that successive cycling increases the capacitance of the high-frequency component, thus suggesting the charge storage of the anode increases over time.

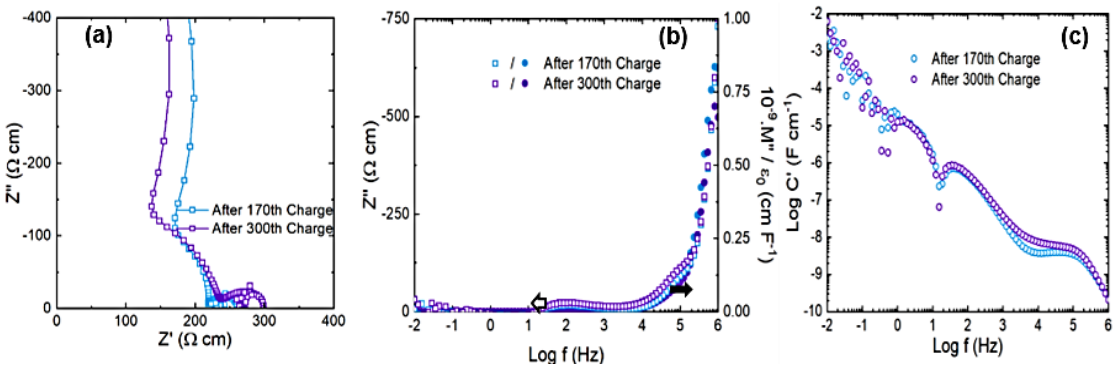

Figure 7.20 Anode impedance data for a three-electrode layered oxide sodium-ion battery after the 170th and 300th charge. (a) Impedance complex plane plots. Spectroscopic plots of -*Z''* and *M''* (b), *C'* (c).

Figure 7.21 displays impedance data after a series of discharges between cycles 160-300. There is a gradual increase in the total resistance, which goes from 700 to 750 to 900 Ω cm on 160th, 200th and 300th discharge. This is again partly due to an increase in the high-frequency *RC* component, but mainly due to an increase in the low-frequency resistance at around 0.5 Hz. There are no significant changes in the capacitance plots in (c), other than possibly a small increase in capacitance with successive cycling.

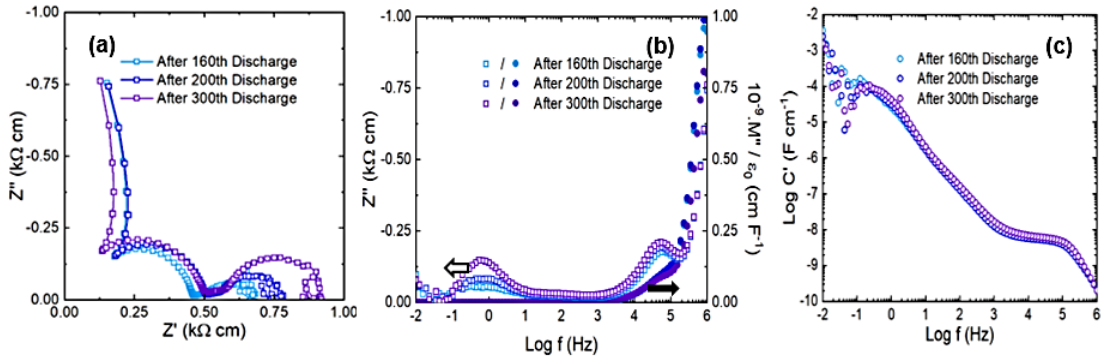

Figure 7.21 Anode impedance data for a three-electrode layered oxide sodium-ion battery after the 160th, 200th and 300th discharge. (a) Impedance complex plane plots. Spectroscopic plots of $-Z''$ and M'' (b), C' (c).

The resistances and capacitances were extracted from the various anode impedance plots reported thus far, and are presented graphically in Figure 7.22. For charged data (a), the summation of R_{HF} and R_1 are plotted from cycle 170 onwards as it is difficult to differentiate between these two components in the impedance complex plane plots. Similar to what was observed for the cathode, the resistances associated with the anode are greatest when the sodium-ion battery is in the discharged state (b): the cathode is saturated with sodium and the anode deficient in it. Also, similar to results seen for the cathode, R_2 makes up a more significant contribution to the total anodic resistance after charge, whereas R_3 is more dominant in the discharged state. In fact, there is no low-frequency RC component visible over 300 cycles in the impedance measurements performed after the Na-ion was fully charged. The medium-frequency resistance, R_2, is approximately 35 Ω cm after both the 20th charge and discharge, and increases to 60 Ω cm by 300th charge, and to 70 Ω cm by the 300th discharge. In the discharged state, R_3 decreases considerably up to cycle 170 from approximately 850 to 150 Ω cm before displaying a reversal in trend and increasing back to ~ 350 Ω cm by cycle 300. The high-frequency R_1 component only becomes visible in the anodic impedance plots from cycle 160 after discharge and cycle 170 after charge. Its resistance fluctuates around 220 Ω cm in the charged state and 380 Ω cm after discharge.

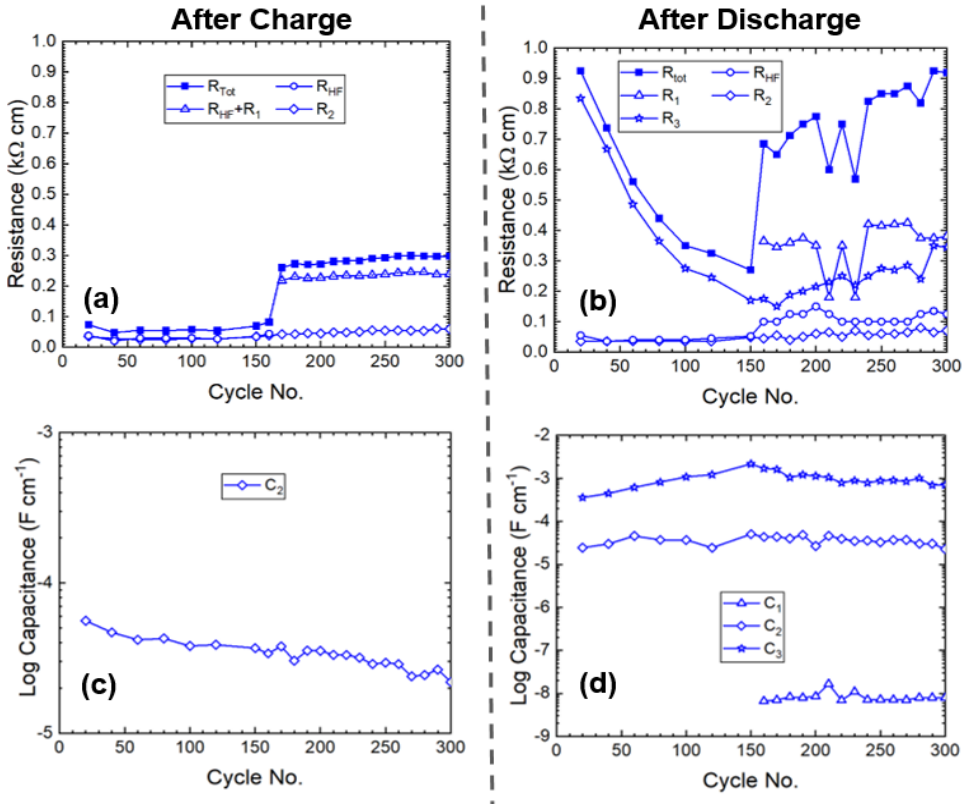

Figure 7.22 A comparison of the anode resistances and capacitances inside a three-electrode layered oxide sodium-ion battery after charge (a) & (c), and discharge (b) & (d), over 300 cycles.

The capacitance value of C_2 (c) generally decreases in the charged state with electrochemical testing, from around 60 to 30 μF cm^{-1}. After discharge (d), it increases from 25 to 50 μF cm^{-1} up to cycle 150, before decreasing back to 25 μF cm^{-1} again by cycle 300. The capacitance C_3 follows a similar trend, going from 0.35 to 3 mF cm^{-1}, before falling back down to around 0.7 mF cm^{-1}. The capacitance of C_1 stays fairly constant around 8 nF cm^{-1} between cycles 170-300 after the sodium-ion battery has been fully discharged.

7.3.2 (c) Anode data – Discussion

The three *RC* components present for impedance measurements of the anode have similar capacitances as the three seen for the cathode: of the order of nanofarads (C_1), microfarads (C_2) and millifarads (C_3) from high to low frequency respectively. Therefore, it can be interpreted that these represent similar processes as were assigned to the positive electrode. The high-frequency component is the resistance associated with the bulk of the electrode (R_1), the second medium frequency

component is attributed to the solid electrolyte interphase (R_2). Finally, as a capacitance in the millifarad region is consistent with that of an electrochemical double layer for a typical energy storage device, it is likely that this low frequency component is the charge-transfer resistance (R_3) coupled with a double layer capacitance formed at the carbon-electrolyte interface.

Data in Figure 7.22 show that the most significant increases in resistance associated with the negative electrode occur after 170th charge (a) and 160th discharge (b). This also corresponds with the 'knee point' and the onset of significant capacity degradation. In the charged state (a), the resistance of the solid electrolyte interphase (R_2) increases gradually with cycling, while the capacitance of the component decreases continuously over time (c). Hence, this indicates a likely thickening of the SEI layer on the anode. A more significant change is that before the 'knee point' there is no considerable resistance associated with the bulk of the electrode, whereas afterwards this resistance dominates in the impedance response, suggesting that the conductivity and possibly the structure of the negative electrode have been altered greatly at this onset of significant capacity degradation. In the discharged state of the cell, the resistance of the SEI also shows a general increase in resistance, doubling from ~ 35 to ~ 70 Ω cm between cycles 20 and 170. Similarly, to what was seen for charged data, at the 'knee point', an additional resistance associated with the bulk of the carbon electrode also becomes apparent, and is the largest resistance over the remaining cycles.

An increase of capacitance C_2 and C_3 after discharge, up to the 'knee point', indicates a likely increase in surface area of the SEI and electrochemical double layer. The continuous insertion and de-insertion of sodium into the carbon electrode results in an expansion and contraction in the inter-graphene layers.[17] Such volume changes in carbon anodes are known to result in cracks and fractures, as are seen with graphite anodes in lithium-ion batteries,[18] and have also been reported to occur with hard carbon.[19] Furthermore, different anode materials have been proven to undergo similar alterations in Na-ion batteries (Fig. 7.23)[20].

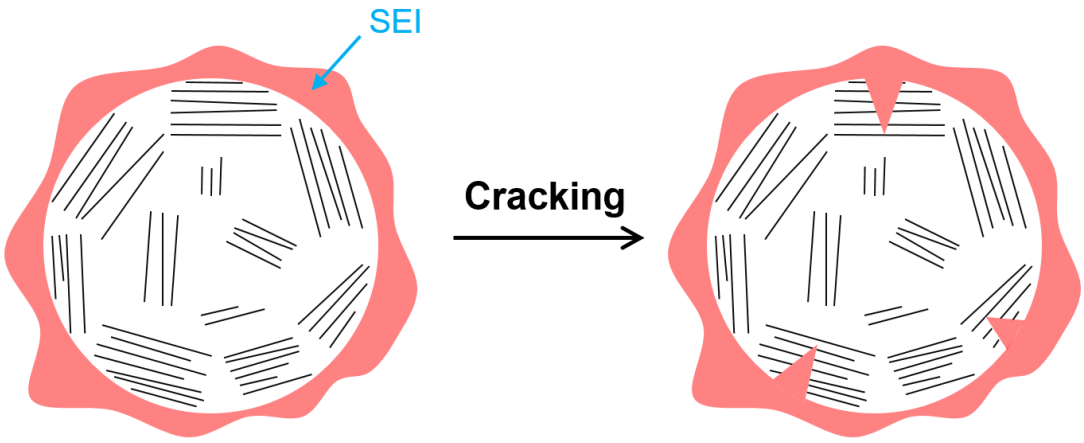

Figure 7.23 Schematic illustration of cracking in sodium-ion battery hard carbon anodes.

The immediate consequence of these structural changes may be to increase the surface area at the particle surface, thus increasing the capacitance of the SEI and reducing the charge-transfer resistance. Hence, a continuous swelling and shrinking of the carbon particles after every Na insertion/removal increases the surface area and means that a transfer of sodium ions and electrons easily takes place. Such a trend may not be seen in the charged state as, once the sodium is back in the structure and the particle expands once more, this may help to reduce the level of deformation present. After cycle 150, the capacitance of C_2 and C_3 now begin to decrease and the charge-transfer resistance also increases. One possible explanation for this is that the thickening of the SEI now outweighs any extra surface area increase due to structural modification

The other most noticeable development visible in these anode data is that at the 'knee point' there is suddenly a considerable resistance associated with the bulk of the electrode, R_1, and hence a decrease in anode conductivity. The resistance of the carbon electrode is negligible to begin with as after discharge, due to its delocalised electrons, it behaves electrically like a metal. After charge, and its insertion of sodium ions, it can be thought of as a mixed conductor, as well as a well-functioning semiconductor.[21] At the 'knee point' there is a sudden decrease in its conductivity, which may be caused by continuous swelling and contracting which has disrupted the electrical conductivity network of the carbon electrode. This may also have a knock-on effect in that it makes the movement of charged species to the surface of

the carbon particles more difficult and, therefore, makes charge-transfer slower, resulting in the increased resistance in the impedance plot at low frequency.

The work done in this chapter has shown that a capacity drop seen at the 'knee point' for these layered oxide sodium-ion batteries is connected with a rise in the cell impedance. An increase in impedance corresponds to a growth in the internal cell resistance and a deterioration in ionic transfer, i.e. how easily ions can move between electrodes during charge and discharge. It was shown in Chapter III that the performance of these layered oxide sodium-ion cells is rate-dependent. A significant amount of capacity loss, including that which occurs at the 'knee point', can be recovered by cycling at a reduced current. A lower cycling rate not only decreases the amount of damage down to electrode particles via cracks, fractures and dislocations,[22] but also allows more time to remove alkali ions trapped in pores within a poorly conducting electrode network; allowing time for them to get to the surface and be extracted. Conversely, a higher C-rate results in electrodes being saturated before all the capacity is able to be utilised. This proves that the fall in capacity in these batteries is not due to an irreversible loss of sodium or of active material, but to a deterioration in ionic transfer within these sodium-ion batteries. The results seen in this section for anode data support this, and suggest that the major ageing mechanisms present within these layered oxide sodium-ion batteries responsible for cell failure are primarily due to mechanical degradation, and not to an irreversible loss of sodium in SEI formation and active material side reactions (chemical degradation).

7.4 Conclusions

In this chapter, the long-term performance of layered oxide sodium-ion batteries was recorded over 300 cycles. Electrochemical impedance spectroscopy was implemented after charge and discharge at regular intervals using a three-electrode setup in order to separate out the responses at the two separate electrodes. This approach was taken in order to try and obtain a better understanding of the origin of the major degradation mechanisms that occur in these cells, which are responsible for eventual battery failure. Results were analysed by fitting ideal equivalent electrical circuits to impedance data, and using these to extract resistances and capacitances for the different components/processes present.

An increasing cathode resistance dominates the impedance inside these layered oxide sodium-ion batteries over 300 cycles. Modelling the response using an ideal equivalent circuit found that the impedance spectrum for this electrode consists of three different *RC* elements, whereas only two are usually observed with Li-ion battery cathodes.[23–26] The low-frequency resistance within the impedance response was found to be the main origin of such a large cathode resistance, which was attributed to the charge-transfer reaction, i.e. the desolvation and insertion of sodium ions.

As with lithium-ion batteries,[8,9] a ‘knee point’ is observed to occur with these layered oxide sodium-ion batteries, after which capacity fading intensifies, eventually resulting in an end to the operational life of the battery. A reduced discharge rate has been proven to recover most of this capacity loss, indicating that the capacity fade is primarily due to a deterioration in ionic transfer rather than an irreversible loss of sodium or of active material. At the ‘knee point’, the resistance associated with the anode significantly increases, which is credited to a decrease in the conductivity of the electrode due to structural degradation caused by successive Na insertion and extraction. On subsequent cycles, it is no longer possible to extract some of the sodium from the anode; this also possibly has a knock-on effect in that the charge-transfer resistance at the cathode now decreases as there is less sodium to insert. In summary, it is hypothesised that while a charge-transfer resistance at the cathode is responsible for a limited capacity over the cycle life of the Na-ion battery,

the major degradation mechanism at fault for eventual end of life is structural degradation of the hard carbon anode.

The long-term cycling of full-cell sodium-ion batteries has not been reported in the literature before. While three-electrode impedance measurements have been performed on lithium-ion batteries, such studies have been curtailed by the limited number of different complex formalisms used in data analysis. In this work, by a more systematic approach, we are able to connect processes occurring at the cathode to those occurring concurrently at the anode, giving greater insight into capacity fading mechanisms. Work is ongoing to try and apply this approach to alternative battery chemistries, and an example of data collected so far for a lithium-ion system is provided in Appendix O.

In the layered sodium-ion batteries, studied in this work, the 'knee point' is attributed primarily to structural degradation of the anode. In order to confirm whether this is the major cause of battery failure, future work could include post-mortem analysis of Na-ion cells, using techniques such as SEM, NMR, XRD etc[27]. Attempts at improving the performance of these Na-ion batteries could be to limit the charge-transfer resistance by altering the particle surface area through increasing electrode porosity, or to limit structural degradation of the carbon anode via nanostructuring techniques.[28] Limited work has taken place in this field for sodium-ion batteries so far.

Furthermore, while the effect of cycling on the degradation of Na-ion batteries has been studied, it would also be useful to examine storage time, as most batteries used in real word situations are subject to a combination of both calendar and cyclic ageing.[29] The cycling conditions used in this work are fairly aggressive compared with what would be expected for practical cell performance in the majority of applications. Nevertheless, the findings made in this chapter, have important consequences for the commercialisation of sodium-ion batteries, suggesting that if their cycle life is to rival that of lithium-ion batteries, the structural stability of the anode needs to be improved.

7.5 References

1 I. Buchmann and Cadex Electronics Inc., *Batteries in a portable world : a* I. Buchmann, *Batteries in a portable world : a handbook on rechargeable batteries for non-engineers*, Cadex Electronics, 4th edn., 2016.

2 R. B. Wright, J. P. Christophersen, C. G. Motloch, J. R. Belt, C. D. Ho, V. S. Battaglia, J. A. Barnes, T. Q. Duong and R. A. Sutula, *J. Power Sources*, 2003, **119**–**121**, 865–869.

3 M. Dollé, F. Orsini, A. S. Gozdz and J.-M. Tarascon, *J. Electrochem. Soc.*, 2001, **148**, A851-A857.

4 C. H. Chen, J. Liu and K. Amine, *J. Power Sources*, 2001, **96**, 321–328.

5 Z. Deng, Z. Zhang, Y. Lai, J. Liu, J. Li and Y. Liu, *J. Electrochem. Soc.*, 2013, **160**, 553–558.

6 O. Erdinc, B. Vural and M. Uzunoglu, *2009 International Conference on Clean Electrical Power*, 2009, 383–386.

7 Apple, *Batteries - Service and Recycling*, https://www.apple.com/batteries/service-and-recycling/, (September 2019).

8 M. Doyle, J. Newman, A.S. Gozdz, C. N. Schmutz and J.-M. Tarascon, *J. Electrochem. Soc.*, 1996, **143**, 1890-1903.

9 J. Neubauer and A. Pesaran, *J. Power Sources*, 2011, **196**, 10351–10358.

10 W. Diao, S. Saxena, B. Han and M. Pecht, *Energies*, 2019, **12**, 2910.

11 P. Kitz, M. Lacey, P. Novák, E. J. Berg. *Anal. Chem.*, 2019, **91**, 2296-2303.

12 A. Würsig, H. Buqa, M. Holzapfel, F. Krumeich and P. Novák, *Electrochem. Solid-State Lett.*, 2005, **8**, A34-A37.

13 C. K. Chan, R. Ruffo, S. S. Hong and Y. Cui, *J. Power Sources*, 2009, **189**, 1132–1140.

14 J. Hassoun, G. Mulas, S. Panero and B. Scrosati, *Electrochem. commun.*, 2007, **9**, 2075–2081.

15 J. W. Braithwaite, A. Gonzales, G. Nagasubramanian, S. J. Lucero, D. E. Peebles, J. A. Ohlhausen and W. R. Cieslak, *J. Electrochem. Soc.*, 1999, **146**, 448-456.

16 F. La Mantia, R. A. Huggins and Y. Cui, *J. Appl. Electrochem.*, 2013, **43**, 1-7.

17 K. Wang, Y. Xu, Y. Li, V. Dravid, J. Wu and Y. Huang, *J. Mater. Chem. A*, 2019, **7**, 3327–3335.

18 V. Agubra and J. Fergus, *Materials*, 2013, **6**, 1310–1325.

19 Z. Lu, Z. Guo, X. Ren and S.-D. Xu, *Int. J. Electrochem. Sci*, 2019, **14**, 3336–3349.

20 J. Wang, C. Eng, Y.-C. Chen-Wiegart and J. Wang, *Nat. Commun.*, 2015, **6**, 7496(1)-7496(9).

21 D. Zhang, B. S. Haran, A. Durairajan, R. E. White, Y. M. Podrazhansky and B. N. Popov, *J. Power Sources*, 2000, **91**, 112-119.

22 A. M. Grillet, T. Humplik, E. K. Stirrup, S. A. Roberts, D.A. Barringer, C. M. Snyder, M. R. Janvrin and C. A Apblett, *J. Electrochem. Soc.*, 2016, **163**, A1859-A1871.

23 M. G. S. R. Thomas, P. G. Bruce and J. B. Goodenough, *J. Electrochem. Soc.*, 1985, **132**, 1521–1528.

24 D. Andre, M. Meiler, K. Steiner, C. Wimmer, T. Soczka-Guth and D. U. Sauer, *J. Power Sources*, 2011, **196**, 5334–5341.

25 L. Wang, J. Zhao, X. He, J. Gao, J. Li, C. Wan and C. Jiang, *Int. J. Electrochem. Sci*, 2012, **7**, 345–353.

26 J. Illig, M. Ender, T. Chrobak, J. P. Schmidt, D. Klotz and E. Ivers-Tiffée, *J. Electrochem. Soc.*, 2012, **159**, A952–A960.

27 T. Waldmann, A. Iturrondobeitia, M. Kasper, N. Ghanbari, F. Aguesse, E. Bekaert, L. Daniel, S. Genies, I. J. Gordon, M. W. Löble, E. De Vito and M. Wohlfahrt-Mehrens, *J. Electrochem. Soc.*, 2016, **163**, 2149–2164.

28 W. Qi, J. G. Shapter, Q. Wu, T. Yin, G. Gao and D. Cui, *J. Mater. Chem. A*, 2017, **5**, 19521-19540.

29 K. L. Gering, S. V. Sazhin, D. K. Jamison, C. J. Michelbacher, B. Y. Liaw, M. Dubarry and M. Cugnet, *J. Power Sources*, 2011, **196**, 3395–3403.

Chapter VIII

Conclusions and Future Work

8.1 Conclusions

Sodium-ion (Na-ion) batteries have received considerable attention in recent years as a cheaper, safer, more sustainable alternative to conventional lithium-ion (Li-ion) technology. Battery cycle life is an important performance criterion with respect to commercialisation of these, as all batteries will experience, with time, some reduction in performance due to a variety of degradation mechanisms. The structure and properties of a novel mixed phase Na[Ni,Mg,Mn,Ti]O_2 layered oxide cathode were investigated in this work via a range of characterisation techniques. By performing a combination of constant-current, constant-voltage (CC/CV) cycling in combination with electrochemical impedance spectroscopy (EIS), it was possible to identify the rate-limiting steps and problem interfaces inside of cells. Identifying such factors allows us to address them and, therefore, enhance overall battery performance.

8.1.1 Structure-Composition-Properties-Performance Relationship in Layered Oxide Sodium-Ion Cathodes

The Na[Ni,Mg,Mn,Ti]O_2 mixed phase layered oxide was found to consist of two individual polymorphs, with nominal formulae P2-"$Na_{0.64}[Mn_{0.8}Mg_{0.2}]O_2$" and O3-"$Na[Ni_{0.5}Mn_{0.5}]O_2$". These polymorphs were also studied separately in the hope this would lead to a better understanding of the multiphase system's properties. A solid solution was found to form for P2-$Na_{0.64}[Mn_{0.8}Mg_{0.2}]O_2$ ($0.5 \leq x \leq 1$), which can be indexed according to the hexagonal space group $P6_3/mmc$. The O3-Na[Ni,Mn]O_2 polymorph was found to form over a narrow temperature range when synthesized in air. Synthesis in an oxygen atmosphere was also performed - both routes resulted in residual NiO precursor, which was also seen in the Na[Ni,Mg,Mn,Ti]O_2 mixed phase

material. The Ni : Mn ratio in these layered oxide materials was altered by synthesizing $Na[Ni_xMn_{1-x}]O_2$ ($0.33 \leq x \leq 0.5$) materials. A lower nickel content favoured the formation of a sodium-deficient P2 phase over the O3 one, and still showed evidence of the NiO starting material.

While phase transitions in these layered oxides have been extensively studied during electrochemical testing, thermally-induced processes are less well known. In the $Na[Ni,Mg,Mn,Ti]O_2$ mixed phase material, the P2 polymorph was found to disappear on heating above 800 °C, and is not subsequently recovered at lower temperatures. Oxygen loss and transition metal oxidation occurs when the sample is fired at high temperatures in nitrogen. DSC measurements indicated that the transformation from P2 to O3 is a slow reordering of the oxygen sub-lattice rather than a sharp bond breaking/forming process. All three layered oxides - $Na[Ni,Mg,Mn,Ti]O_2$, P2-"$Na_{0.64}[Mn_{0.8}Mg_{0.2}]O_2$" and O3-"$Na[Ni_{0.5}Mn_{0.5}]O_2$" - were found prone to the uptake of species when exposed to the atmosphere, as indicated by TGA measurements. These are important considerations when taking into account their preparation, storage, and handling as potential Na-ion cathodes.

The electrical properties of these separate layered oxides were studied by impedance spectroscopy, which has not previously been reported in the literature. The conductivity of these materials was as follows: P2-$Na_{0.64}[Mn_{0.8}Mg_{0.2}]O_2$ > mixed phase $Na[Ni,Mg,Mn,Ti]O_2$ > O3-Na-$[Ni_{0.5}Mn_{0.5}]O_2$. The activation energies suggest that Na^+ ion hopping occurs most easily in the P2-type material and is significantly hindered in the O3-phase. The individual electrical properties of these separate P2 and O3 materials were reflected in the electrochemical measurements performed.

The P2-$Na_{0.64}[Mn_{0.8}Mg_{0.2}]O_2$ layered oxide was found to have a low discharge capacity of only around 45 mAh g^{-1} (*vs.* Na^+/Na), but good initial cycling stability. The O3-$Na[Ni_{0.5}Mn_{0.5}]O_2$ layered oxide showed a much higher specific capacity (~ 125 mAh g^{-1}), but possesses poorer charge retention. Electrochemical testing revealed the mixed phase material to possess a discharge capacity of 125 mAh g^{-1} (full-cell testing at 30 °C), as well as good rate capability and cycling stability: 95% charge retention after 200 cycles. The material is prone to a number of structural changes during cycling, as indicated by *in operando* XRD results. The O3 polymorph is only present in the bottom ~ 20% state of charge, and at high voltage

(> 4 V) there is a significant alteration of the P2 structure, with evidence of the intergrowth "Z" phase. From galvanostatic intermittent titration technique (GITT) measurements, the Na diffusion coefficient (D_{Na^+}) was found to be the highest and, therefore, the electrode the most conductive when the material possesses predominantly a P2-type structure.

8.1.2 Use of Impedance Spectroscopy to Determine Performance Limiting Factors in Prototype Commercial Na-Ion Batteries

Electrochemical impedance spectroscopy was performed on full-cell sodium-ion batteries for the first time. This was done using both two- and three-electrode measurements performed on a commercially-relevant pouch cell type. This novel design was fabricated by inserting a reference electrode between two separators. Measurements were recorded before every charge/discharge across the first ten cycles. Results were plotted using different complex formalisms in order to highlight different aspects of collected data, an approach not previously undertaken for analysing impedance measurements for batteries.

Comparison between two- and three-electrode results shows that the different cell designs are comparable in terms of voltage-time profiles, capacities, coulombic efficiencies and EIS results. This means that the three-electrode results can be used to make interpretations about commercially relevant two-electrode batteries. Furthermore, it was demonstrated across a range of formalisms that the sum of the positive and negative electrode impedances is similar to that of the full-cell (within 6% difference). This is better than previously seen three-electrode results, and indicates that the novel three-electrode pouch cell configuration used in these works affords a superior measurement to former cell designs. Furthermore, using a range of different complex formalisms to view impedance data was found to afford a more in-depth analysis of the results. Spectroscopic plots of Z'' and C' highlight how components at different frequencies change with cycling and contribute to cell resistances and capacitances.

Two-electrode impedance measurements reveal there is a growth in resistance over time, thus indicating the occurrence of degradation (ageing) mechanisms. The three-

electrode results indicate that the cathode is mainly responsible for impedance in sodium-ion batteries across the first ten cycles. This continues to grow after every cycle. The resistance associated with the anode stays fairly small and constant in the charged state (~ 100 Ω cm), whereas it steadily decreases in the discharged, from around 2.5 to 1.5 kΩ cm between cycles 1 and 10. Overall, results are similar to those seem in lithium-ion batteries in certain ways, such as a dominating cathode resistance during cycling. However, there are noticeable differences, such as a larger decrease in anodic resistance over time.

EIS was performed on sodium-ion batteries at varying states of health and states of charge in order to try and obtain a better understanding of the origin of the large cathode impedance they possess. This was done using a range of different cell configurations, including novel separator and symmetric battery designs, applied to the commercially-used pouch cell setup. Results were analysed by fitting ideal equivalent electrical circuits to impedance data, and using these to extract resistances and capacitances for the different components present.

Modelling the EIS data using an ideal equivalent circuit found that the cathode impedance spectrum consists of three different resistive components: a small high-frequency non-zero intercept resistance, R_{HF}, and two *RC* elements, with resistances of R_1 and R_2, at mid and low frequencies respectively. Comparison between the impedance results for different cell designs made it possible to assign these separate components to different physical elements of the sodium-ion battery. It was deduced that R_{HF} is due to the resistance of the electrolyte and separators, and that R_1 and R_2 are both associated with the cathode itself. A consideration of the capacitances suggested that R_2, which has a capacitance consistent with an electrochemical double layer (in the microfarad range), is due to the cathode-electrolyte interface. Across the first ten cycles the cathode-electrolyte interface was found to be primarily responsible for an increase in the total cell resistance.

While much work has been done to date on the interface at the anode in lithium-ion batteries, and the existence of the solid electrolyte interphase is well documented, much less research has taken place on the interface at the cathode. Hence, in this work, a solid permeable interphase (SPI) on the surface of the cathode may have been detected in sodium-ion batteries for the first time. From performing impedance

measurements during charge/discharge, the resistance of the cathode-electrolyte interface was found to increase dramatically above approximately 80% depth of discharge. These findings have important consequences for sodium-ion battery development, suggesting that to optimise performance and extend battery life, cells should not be discharged below ~ 20% SoC. Furthermore, these results provide an important basis for further work into obtaining accurate and reliable SoC estimates for sodium-ion batteries.

The long-term cycling of full-cell sodium-ion batteries has not been widely reported in the literature. While three-electrode impedance measurements have been performed on lithium-ion batteries, such studies have been curtailed by the limited number of different complex formalisms used in data analysis. In this work, by a more systematic approach, we are able to connect processes occurring at the cathode to those occurring concurrently at the anode, giving greater insight into capacity fading mechanisms. The long-term performance of layered oxide sodium-ion batteries was recorded over 300 cycles. Electrochemical impedance spectroscopy was implemented after charge and discharge at regular intervals using a three-electrode setup in order to separate out the responses at the two separate electrodes. This approach was taken in order to try and obtain a better understanding of the origin of the major degradation mechanisms that occur in these cells, which are responsible for eventual battery failure.

An increasing cathode resistance dominates the impedance inside these layered oxide sodium-ion batteries over 300 cycles. Modelling the response using an ideal equivalent circuit found that the impedance spectrum for this electrode consists of three different *RC* elements, whereas only two are usually observed with Li-ion battery cathodes. The low-frequency resistance within the impedance response was found to be the main origin of such a large cathode resistance, which was attributed to the charge-transfer reaction.

As with lithium-ion batteries, a ‘knee point’ is observed to occur with these layered oxide sodium-ion batteries, after which capacity fading intensifies, eventually resulting in an end to the operational life of the battery. A reduced discharge rate has been proven to recover most of this capacity loss, indicating that the capacity fade is primarily due to a deterioration in ionic transfer rather than an irreversible loss of

sodium or of active material. At the ‘knee point’, the resistance associated with the anode significantly increases, which is credited to a decrease in the conductivity of the carbon matrix due to structural degradation caused by successive Na insertion and extraction. On subsequent cycles, it is no longer possible to extract some of the sodium from the anode; this possibly has a knock-on effect in that the charge-transfer resistance at the cathode now decreases as there is less sodium to insert.

In summary, it is hypothesised that while a charge-transfer resistance at the cathode is responsible for a limited capacity over the cycle life of the Na-ion battery, the major degradation mechanism at fault for eventual end of life is structural degradation of the hard carbon anode. These findings have important consequences for the commercialisation of sodium-ion batteries, suggesting that if their cycle life is to rival that of lithium-ion batteries, the structural stability of the anode needs to be improved.

8.2 Future Work

Air-stability of sodium transition metal layered oxides is extremely important for how these materials are prepared, stored, and assembled for electrochemical testing. Degradation in air is likely to lead to an increase in cost and may even jeopardise successful commercialisation of potential Na-ion cathode materials. More detailed work is required, such as thermogravimetric analysis/mass spectrometry, and XRD at the end of TGA runs, to assign precise processes and species to how these layered oxides degrade when exposed to air.

Different synthesis strategies are required to try and produce phase pure O3-$Na[Ni_{0.5}M_{n0.5}]O_2$. Ball milling reactants for long periods of time could help to ensure sufficient mixing of the starting materials. A method that does not rely on high temperatures is desirable to reduce Na loss, e.g. co-precipitation. *In operando* XRD of the P2-$Na_{0.64}[Mn_{0.8}Mg_{0.2}]O_2$ and O3-$Na[Ni_{0.5}Mn_{0.5}]O_2$ individual materials would also be useful to better understand the phase transitions and electrochemical performance of the mixed phase $Na[Ni,Mg,Mn,Ti]O_2$ Na-ion cathode.

The three-electrode impedance results collected in this thesis point towards the electrode-electrolyte interface at both electrodes being critical to degradation mechanisms in sodium-ion batteries. Studying the SEI and SPI via a range of characterisation techniques may help suggest ways to reduce the performance limiting processes that occur and improve cell performance.

In order to confirm the major cause of battery failure, future work could include post-mortem analysis of Na-ion cells, using techniques such as SEM, NMR, XRD etc. Attempts at improving the performance of these Na-ion batteries could involve limiting the charge-transfer resistance by altering the particle surface area through increasing electrode porosity, or to limit structural degradation of the carbon anode via nanostructuring techniques. Limited work for sodium-ion batteries has taken place in this field to date. It is worth mentioning that the cycling conditions used in this study were fairly aggressive and do not represent cell performance in the majority of real-world applications. Furthermore, while the effect of cycling on the degradation of Na-ion batteries has been studied, it would also be useful to examine

storage time, as most batteries used in real world situations are subject to a combination of both calendar and cyclic ageing.

Appendix A – Rietveld Refinement Parameters

Scale Factor

The scale factor adjusts the peak intensities of the calculated profile to be on the same scale as the observed pattern. It is the first parameter to be refined and, usually, it is allowed to refine in every cycle of refinement.

Background

This is used to fit the calculated profile to the background of the observed XRD diffraction pattern. In this work, the Shifted Chebyschev polynomial function with six terms is used to fit the background. This parameter is allowed to refine in every cycle.

Lattice Parameters

These are used to fit the calculated positions of the Bragg peaks to observed data. The lattice parameters are allowed to refine in every cycle.

2θ Zero

The 2θ zero parameter deals with misalignment in the X-ray diffractometer. If an incorrect zero has been set for the machine, then there will be sample displacement, e.g. the height of the powder sample will be wrong. This will then result in a shifting of the peaks for the observed XRD pattern, compared to what is seen in the calculated profile. For a Bragg-Brentano instrument, the sample displacement parameter (*shift*) and the sample transparency correction (*trns*) are refined in order to correct for this.

Profile Parameters (Peak Shape Function)

These are used to get a peak shape in the calculated profile which matches those in the observed XRD pattern. The Pseudo-Voigt function models the effects of instrument design and detector geometry on the width of reflections, as well as any

broadening due to sample effects, e.g. strain and particle size. The Pseudo-Voigt function is a linear combination of Gaussian and Lorentzian functions whose full widths at half maximum (FWHM) are parameterised in GSAS as follows:

Gaussian: $FWHM^2 = U\ tan^2\theta + V\ tan\theta + W$

Lorentzian: $FWHM = X\ tan\theta + Y/cos\theta$

The parameters U, V, W, X, Y are related to stain broadening, crystallite size broadening etc., and together describe the average peak shapes over the whole pattern.

Atomic Positions

The atomic coordinates (*x, y, z*) of each atom in the unit cell can be refined, however, certain atoms may have their positions fixed by the unit cell symmetry. If more than one atom occupies the same site, a constraint can be set up for their atomic positions, fractional occupancies and thermal parameters. Atomic positions should be refined before the fractional occupancies.

Fractional Occupancies

The fractional occupancies of each atom in the unit cell can be refined to check the possibility of partial replacement by other atoms or the presence of site vacancies. Constraints may be applied if one site is shared by more than one atom so that the thermal displacement coefficients and atomic positons are the same for these. An occupancy constraint can be applied if more than one atom occupies the same site, i.e. so that the sum of the individual occupancy should equal 1 (this makes the assumption that the site is fully occupied).

Thermal Displacement Coefficients

The thermal parameter, U_{iso}, is a measure of the magnitude of an atom's vibration/displacement at a particular site. It may not be possible to refine the U_{iso}

values for light elements that do not scatter X-rays well. A high U_{iso} value usually indicates either the presence of some vacancies at that site or that a lighter atom is present. Very small or slightly negative U_{iso} values may mean that additional scattering is needed at that site, i.e. a heavier element or increased occupancy. The U_{iso} values are highly correlated to the fractional occupancies and are usually the last of the parameters to be refined.

Appendix B – Capacitor and Inductor Impedances

Capacitor

An ideal capacitor has a capacitance defined by the ratio of charge Q on each conducting plate to the voltage separating them.

$$C = \frac{Q}{V} \tag{B.1}$$

In practical devices, charge-build up will occur, so the capacitance is more accurately given by the ratio of incremental changes in charge and voltage.

$$C = \frac{dQ}{dV} \tag{B.2}$$

The current of a capacitor is defined as the derivative of charge with respect to time.

$$I = \frac{dQ}{dt} \tag{B.3}$$

Rearranging Equation B.2 and inserting it into Equation B.3 then gives the following:

$$I = C\frac{dV}{dt} \tag{B.4}$$

The voltage delivered by mains AC electricity varies sinusoidally with time t and is given by Equation 2.12. This can be rewritten using Euler's relationship (Eq. 2.16) so that it is expressed in terms of a complex exponential function.

$$V = V_0 Im\left(e^{j\omega t}\right) \tag{B.5}$$

Therefore, Equation B.4 can be rewritten as:

$$I = C\frac{d(V_0 Im\left(e^{j\omega t}\right))}{dt}$$

$$I = CV_0 Im\frac{d\left(e^{j\omega t}\right)}{dt}$$

hence $$I = CV_0 Im(j\omega e^{j\omega t}) \tag{B.6}$$

An expression analogous to Ohm's Law (Eq. 1.3) then allows us to calculate the overall impedance *Z* of the system:

$$\boldsymbol{V = IR} \qquad \textbf{(Ohm's Law)}$$

$$Z = \frac{V}{I} = \frac{V_0 \mathrm{Im}(e^{j\omega t})}{CV_0 \mathrm{Im}(j\omega e^{j\omega t})} \qquad \text{(B.7)}$$

Cancelling like terms leaves us with:

$$\boldsymbol{Z^* = \frac{1}{j\omega C}} \qquad \textbf{(Capacitor)}$$

Inductor

The voltage of an inductor is given by the product of its inductance *L* and rate of change of current passing through it.

$$V = L\frac{dI}{dt} \qquad \text{(B.8)}$$

The current varies sinusoidally with time *t* and is given by Equation 2.14. This can be rewritten using Euler's relationship (Eq. 2.16) so that it is expressed in terms of a complex exponential function.

$$I = I_0 Im\left(e^{j(\omega t - \phi)}\right) \qquad \text{(B.9)}$$

Therefore, Equation B.8 can be rewritten as:

$$V = L\frac{d(I_0 Im\left(e^{j(\omega t - \phi)}\right))}{dt}$$

$$V = LI_0 Im\frac{d\left(e^{j(\omega t - \phi)}\right)}{dt}$$

hence $$V = LI_0 Im(j\omega e^{j(\omega t - \phi)}) \qquad \text{(B.10)}$$

An expression analogous to Ohm's Law (Eqn. 1.3) then allows us to calculate the overall impedance *Z* of the system:

$$\boldsymbol{V = IR} \qquad \textbf{(Ohm's Law)}$$

$$Z = \frac{V}{I} = \frac{LI_0 Im(j\omega e^{j(\omega t-\phi)})}{I_0 Im(e^{j(\omega t-\phi)})} \qquad \text{(B.11)}$$

Cancelling like terms leaves us with:

$$\boldsymbol{Z^* = j\omega L} \qquad \textbf{(Inductor)}$$

Appendix C – Mass Balancing of Sodium-Ion Cells

To a first approximation, in order to maximise battery performance, the capacities of the cathode and anode should equal each other ($Q_{cathode} = Q_{anode}$). The overall capacity (mAh) of each electrode is given by the product of the specific capacity q (mAh g^{-1}) and mass of active material m (g).

$$Q = q \times m \tag{C.1}$$

Due to the differences in specific capacities of the cathode ($q_{cathode}$) and anode (q_{anode}), this requires a careful adjustment of the active mass of each electrode; this is known as "balancing".

If we start off with the assumption that the capacities of the cathode and anode should equal each other then

$$Q = q_{cathode}.m_{cathode} = q_{anode}.m_{anode} \tag{C.2}$$

Equation 2 can be rewritten as

$$\frac{m_{cathode}}{m_{anode}} = \frac{q_{anode}}{q_{cathode}} \tag{C.3}$$

From electrochemical testing results of Na[Ni,Mg,Mn,Ti]O_2 in Chapter III, the specific capacity of this material is approximately 120 mAh g^{-1}. Separate studies performed on the non-graphitizable hard carbon anode material, show it to have a specific capacity of around 225 mAh g^{-1}.

$$\frac{m_{cathode}}{m_{anode}} = \frac{225}{120} = 1.875$$

However, to avoid a risk of metal plating, a slight oversizing of the capacity of negative electrode is often used to achieve better battery safety and cycle life. Therefore, a mass cell balance (cathode: anode) of 1.5-1.8 is utilised.

Appendix D – Differential Capacity Plots

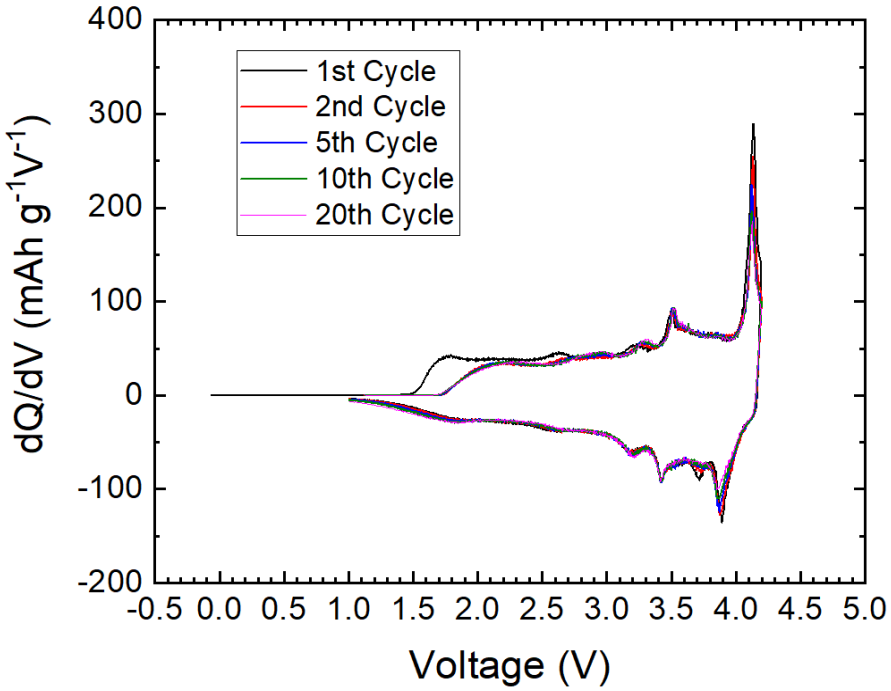

Differential capacity plots for a Na[Ni,Mg,Mn,Ti]O_2/hard carbon full-cell in the voltage range 1-4.2 V at 14mA g^{-1} on charge and 28 mA g^{-1} on discharge, for cycles 1, 2, 5, 10 and 20.

Appendix E – Capacity Plots (1-4.3 V)

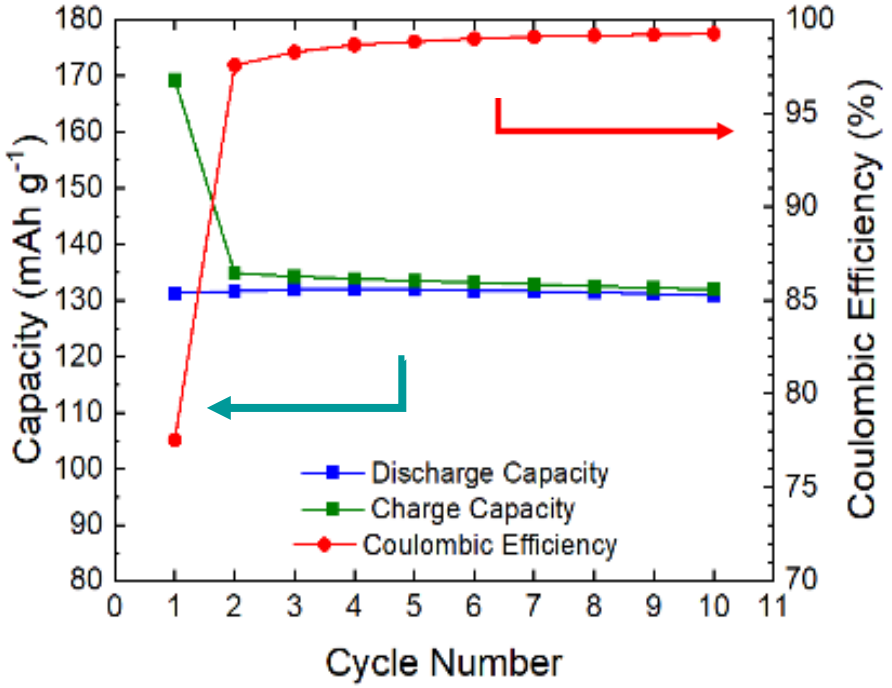

Capacity and coloumbic efficiency of a Na[Ni,Mg,Mn,Ti]O_2/hard carbon full-cell after 10 cycles. The cell was charged at 14 mA g^{-1} and discharged at 28 mA g^{-1} between 1-4.3 V. The capacities achieved are higher than for the 1-4.2 V voltage window.

Appendix F – Bragg's Law Calculations

According to Bragg's Law:

$$\boldsymbol{n\lambda = 2dsin\theta}$$

where: n = diffraction order (usually 1)

λ = X-ray wavelength

d = d-spacing

θ = Bragg angle

Molybdenum X-Ray Source

The X-ray wavelength of molybdenum (Mo $K\alpha_1$) is 0.7093 Å.

$$\boldsymbol{n\lambda = 2dsin\theta}$$

$$0.7093 = 2dsin\theta$$

$$d = \frac{0.7093}{2sin\theta}$$

$$d = \frac{0.35465}{sin\theta}$$

Silver X-Ray Source

The X-ray wavelength of silver (Ag $K\alpha$) is 0.5608 Å.

$$\boldsymbol{n\lambda = 2dsin\theta}$$

$$0.5608 = 2dsin\theta$$

$$d = \frac{0.5608}{2sin\theta}$$

$$d = \frac{0.2804}{sin\theta}$$

Appendix G – *In Operando* XRD Patterns

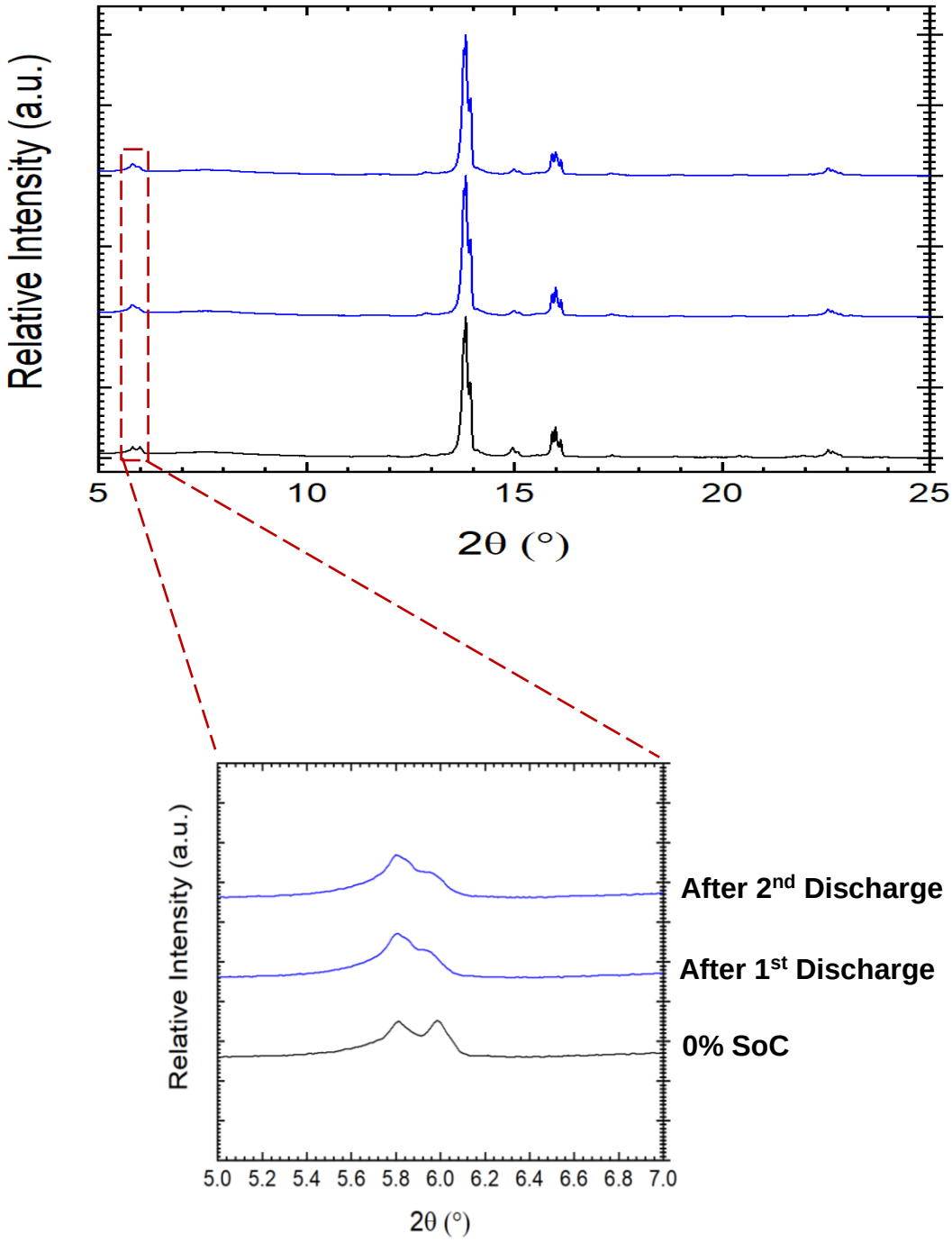

In operando X-ray diffraction data for a Na[Ni,Mg,Mn,Ti]O_2/hard carbon pouch cell before cycling, and after the 1st and 2nd discharge. Collected by AgPSD with λ = 0.5608 Å. The zoomed-in region shows reflections in the 5-7° range. Each X-ray diffraction pattern was collected for 16 minutes.

Appendix H – Starting Rietveld Model of P2-$Na_{0.64}[Mn_{0.8}Mg_{0.2}]O_2$

PDF: 04-022-8282

Atom	Multiplicity	x	y	z	Occupancy	100 x U_{iso} ($Å^2$)
Na1	**2b**	**0**	**0**	**0.25**	**0.218**	**2.5**
Na2	**2d**	**1/3**	**2/3**	**0.75**	**0.421**	**2.5**
Mn1	**2a**	**0**	**0**	**0**	**0.8**	**2.5**
Mg1	**2a**	**0**	**0**	**0**	**0.2**	**2.5**
O1	**4f**	**1/3**	**2/3**	**0.808**	**1**	**2.5**

$a = b = 2.8771$ Å; $c = 11.1672$ Å; Space group = $P6_3/mmc$

Appendix I – XRD Pattern of $Na_{0.64}[Mn_{0.8}Mg_{0.2}]O_2$

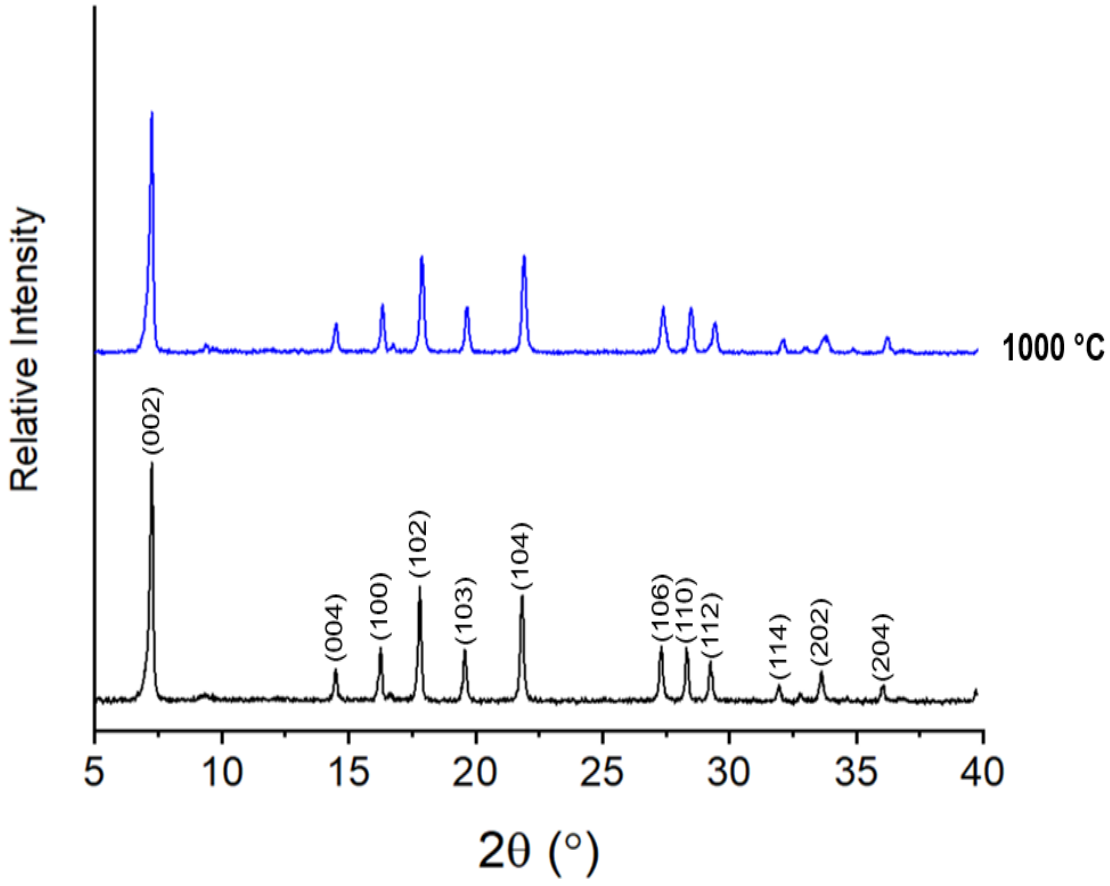

The PXRD patterns of P2-$Na_{0.64}[Mn_{0.8}Mg_{0.2}]O_2$, before, and after heating the sample to 1000 °C, and cooling, in air. Collected by MoPSD with $\lambda = 0.7093$ Å.

Appendix J – Warburg Impedance

The impedance of a constant phase element is defined as:

$$\textbf{(CPE)} \qquad \boldsymbol{Z^* = \frac{1}{(j\omega)^n Y_0}}$$

where Y_0 is a constant and $0 < n < 1$. For a value $n = 1$ the *CPE* reduces to a perfect capacitor, and for $n = 0$ it is a resistor. When the parameter is assigned a value between 0 and 1 it is a non-ideal capacitor with a resistive component.

There is frequently an inclined spike in an impedance spectrum, which can be a non-ideal capacitor represented by a CPE or a Warburg element (where n = 0.5) if the spike is 45° to the Z' axis. The resistance of this spike is the the real value of the impedance, and given by the following equation:

$$Z_W = \frac{1}{\omega^{0.5} Y'} \qquad \text{(I.1)}$$

Hence,

$$\boldsymbol{Z_W = \frac{1}{Y'}} \qquad \textbf{(Warburg Impedance)}$$

when

$$\omega^{0.5} = 1 \qquad \text{(I.2)}$$

Equation I.2 can re-written using Equation 2.13 as:

$$\sqrt{2\pi f_{max}} = 1$$

Squaring both sides gives

$$2\pi f_{max} = 1$$

$$f_{max} = \frac{1}{2\pi}$$

$$f_{max} = 0.159\ Hz$$

Hence, the resistance of the Warburg impedance can be found by reading the real value of the admittance at 0.159 Hz.

Appendix K – Circuit Fitting Example

An example of circuit fitting for cathode data of a three-electrode sodium-ion battery after the cell has been charged for the tenth time, is provided on the next page. Fits to the equivalent circuit are shown for four separate impedance formalsisms. All four formalisms were used while fitting data, in order to give equal weighting to all impedance components over the entire frequency range. Although impedance data covering eight decades of frequency were obtained, data was only fitted between 10^{-2} – 10^{5} Hz. Data were not fitted to higher frequencies due to what are believed to be instrumentation-related inductive effects. Fit quality and accuracy were assessed by visual comparison of fitted and experimental data using data presentation in different impedance formalisms, as well as considering residuals of fits. The goodness of fit was also determined by the sum of squares (chi-squares), which is proportional to the average error between the original data and the calculated values.

To a first approximation, data indicates an equivalent cirucit that contains a resistor, two parallel *RC* elements and a Warburg, *W*, all connected in series to one another. The high frequency components were examined and fitted first. This allows for fewer parameters to be refined. To start with, fitting was attempted using the simplest possibility: a resistor representing the high frequency intercept R_{HF}, connected to a resistor *R* and capacitor *C*, in parallel. Inlcusion of a constant phase element in parallel to these two elements, is then used to account for non-ideality in the equivalent circuit. The requirement of a CPE in parallel was apparent because it represensts the power law dispersion at high frequencies, which is opbserved in both plots of log *Y'* and log *C'* vs log *f* between 10^{4}–10^{6} Hz. A constant phase element can not simiply replace the capacitor as this ignores the frequency-independent premittivity shown in many data sets, paritculary at high frequencies. Therefore, the use of only a resistor and CPE in parallel, does not provide a good fit for all impedance formalisms.

Once a fit of high frequency data was obatined, fitting of the second smaller depressed arc at mid-frequency was attempted. A second element was added in series with the first parallel circuit, in order to represent an additonal series impedance. This section of the impednace spectrum was also fit using a CPE in parallel with an *RC* circuit to

account for the non-idealtiy of the response. Finally, the low-frequency spike was fit by placing an additional CPE in series to model the Warburg impedance.

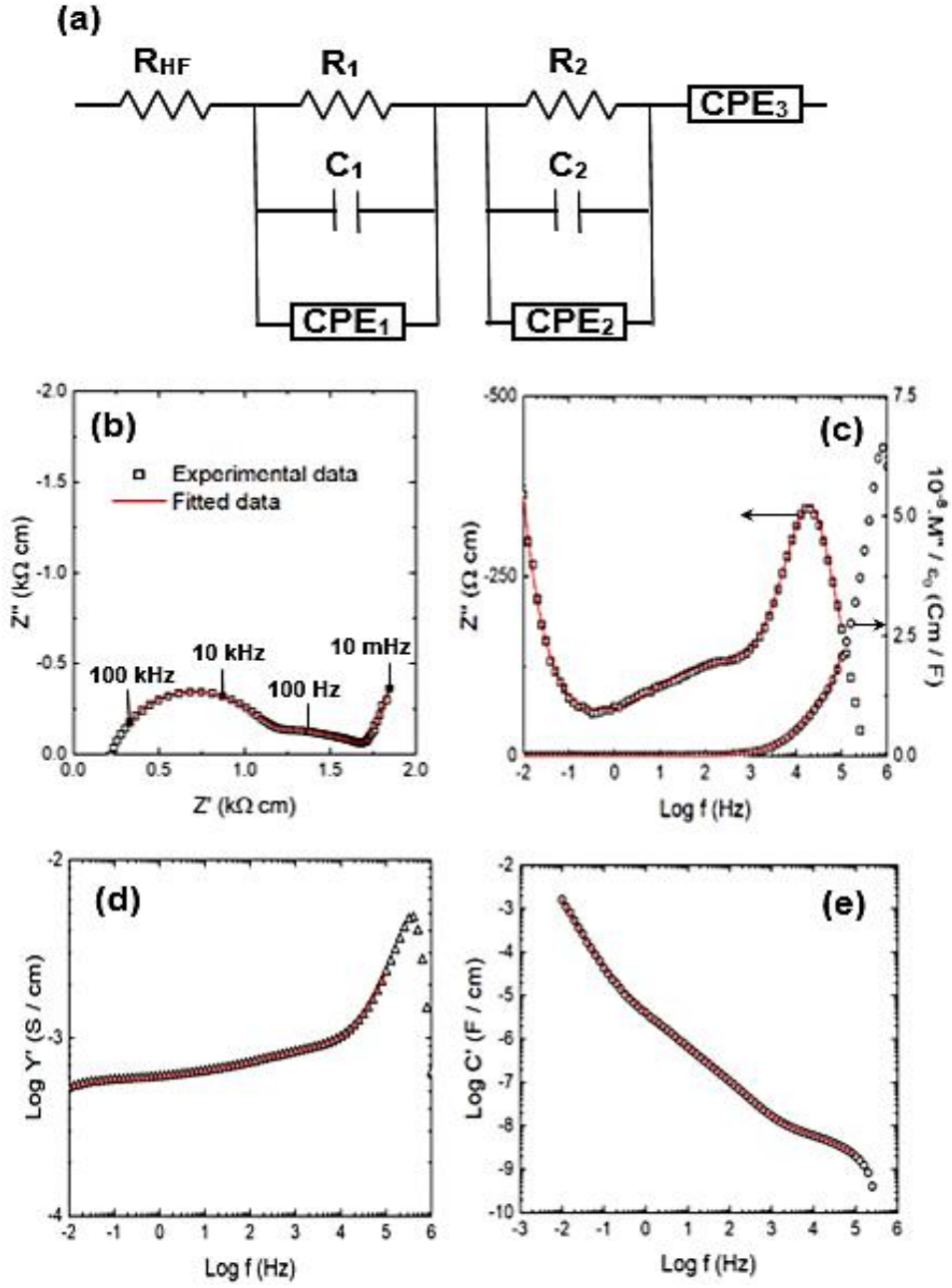

Cathode impedance spectra for a three-electrode sodium-ion cell after the tenth charge. (a) The equivalent electrical circuit used to fit the data. (b) Experimental and fitted data for impedance complex plane plot; the frequencies of some data points are indicated, (c) *Z''/M''* spectroscopic plots, (d) *Y*' spectroscopic plot and (e) *C'* spectroscopic plot.

Appendix L – MacMullin Numbers

Separator	MacMullin Number
Celgard® 2325	11
Celgard® 2500	5
Freudenberg FS2190	3
Polyamide	6
Copa Spacer	3
Separion®	9

MacMullin numbers, reported in the literature, for different types of separator, using a LiTFSI electrolyte.

Appendix M – Calendering Studies

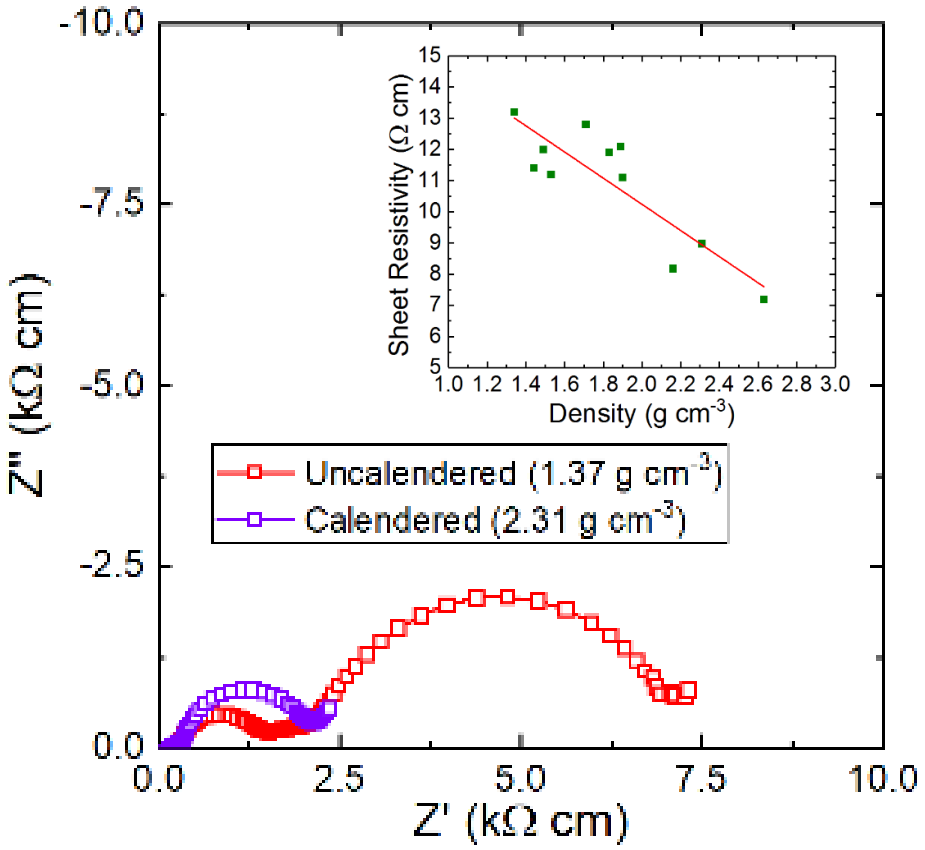

Calendered and uncalendered cathode impedance complex plane plots for a sodium-ion battery after it has been discharged for the tenth time. Four-point probe conductivity measurements, which show how the resistance of the cathode decreases with increasing calendering/electrode density, are provided as an inset.

Appendix N – DC Bias Three-Electrode Measurements

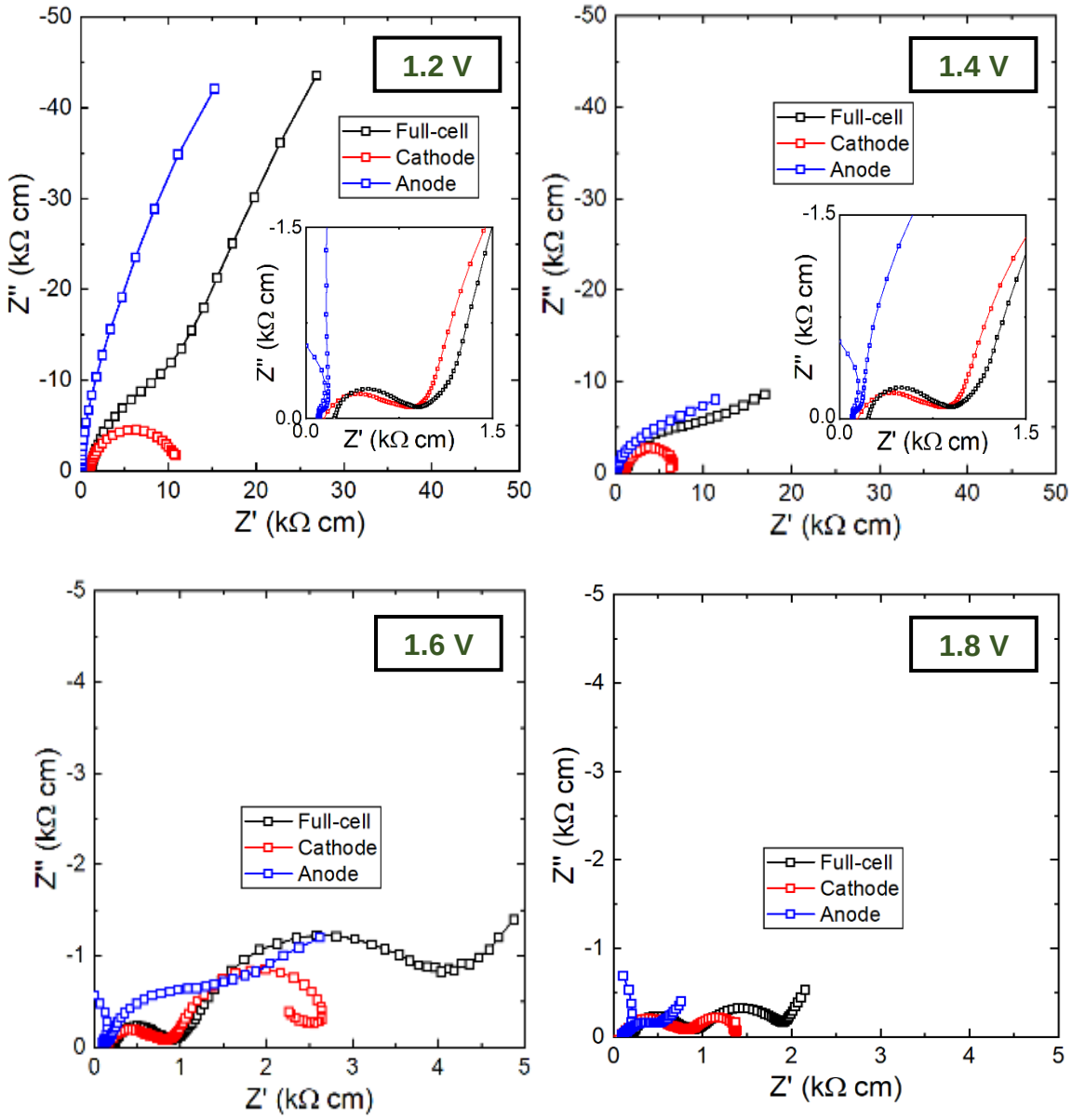

Impedance complex plane plots for a three-electrode cell under the application of different voltages.

Appendix O – Lithium-Ion Impedance Spectra

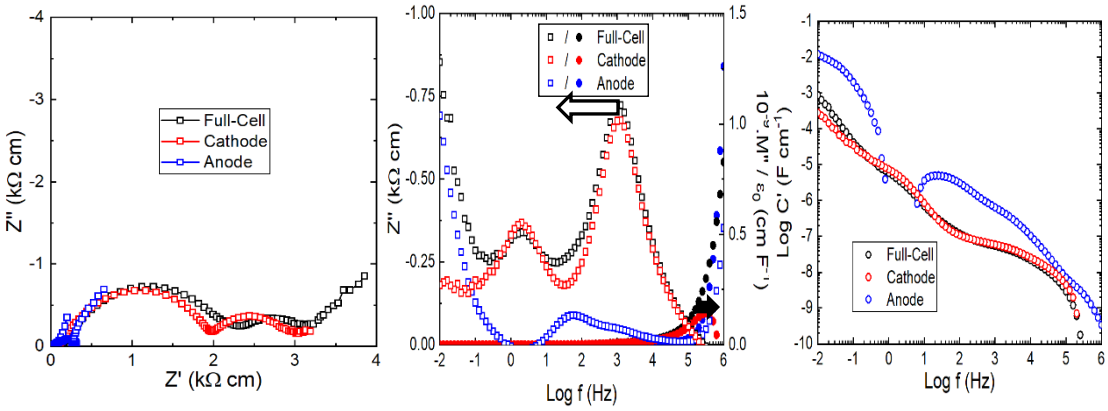

Full-cell, cathode and anode impedance data for a three-electrode lithium-ion battery ($Li[Ni_{0.5}Mn_{0.3}Co_{0.2}]O_2$/graphite) after it has first been fully discharged for the first time.